Long-sought quasiparticle could transform quantum computing p. 1342

Fifty years after the Endangered Species Act, what's next? p. 1348

What Salvadorans feared about bitcoin p. 1375

Science

$15
22 DECEMBER 2023
science.org

AAAS

AI-POWERED FORECASTING

Predicting worldwide weather and cyclone tracks with greater speed and accuracy p. 1416

Are you an early-stage researcher seeking financial support, the freedom to direct your research, and opportunities to advance your professional career? Look to Poland for the FIRST TEAM grant, co-funded by the European Union within the European Funds for Smart Economy Programme.*

First Team

Empowering the New Generation of Researchers

**Eligibility: For PhD holders within 12 years of graduation.*

With up to EUR **0.9 million available**, you can form **an independent research team** to **pioneer innovative studies** in collaboration with leading scientific groups around the world and economic entities in Poland.

Further details on the FIRST TEAM and application process are available at www.fnp.org.pl/en/. Applications must be submitted through a Polish host scientific institution. The announcement of the planned call for proposals is expected in mid-2024.

Connect with a diverse community of 67 researchers from abroad who have already been involved in realization of projects under the FIRST TEAM grant in Poland.

The Foundation for Polish Science holds the distinction of being Poland's foremost non-governmental organisation dedicated to the pursuit of excellence in scientific research across all disciplines. Notably, the Foundation has introduced an array of new funding opportunities designed to foster the development of innovative projects and the commercialisation of their outcomes, funded within the European Funds for Smart Economy 2021-2027 Programme.

European Funds for Smart Economy
Republic of Poland
Co-funded by the European Union
FNP Foundation for Polish Science

CONTENTS

22 DECEMBER 2023 • VOLUME 382 • ISSUE 6677

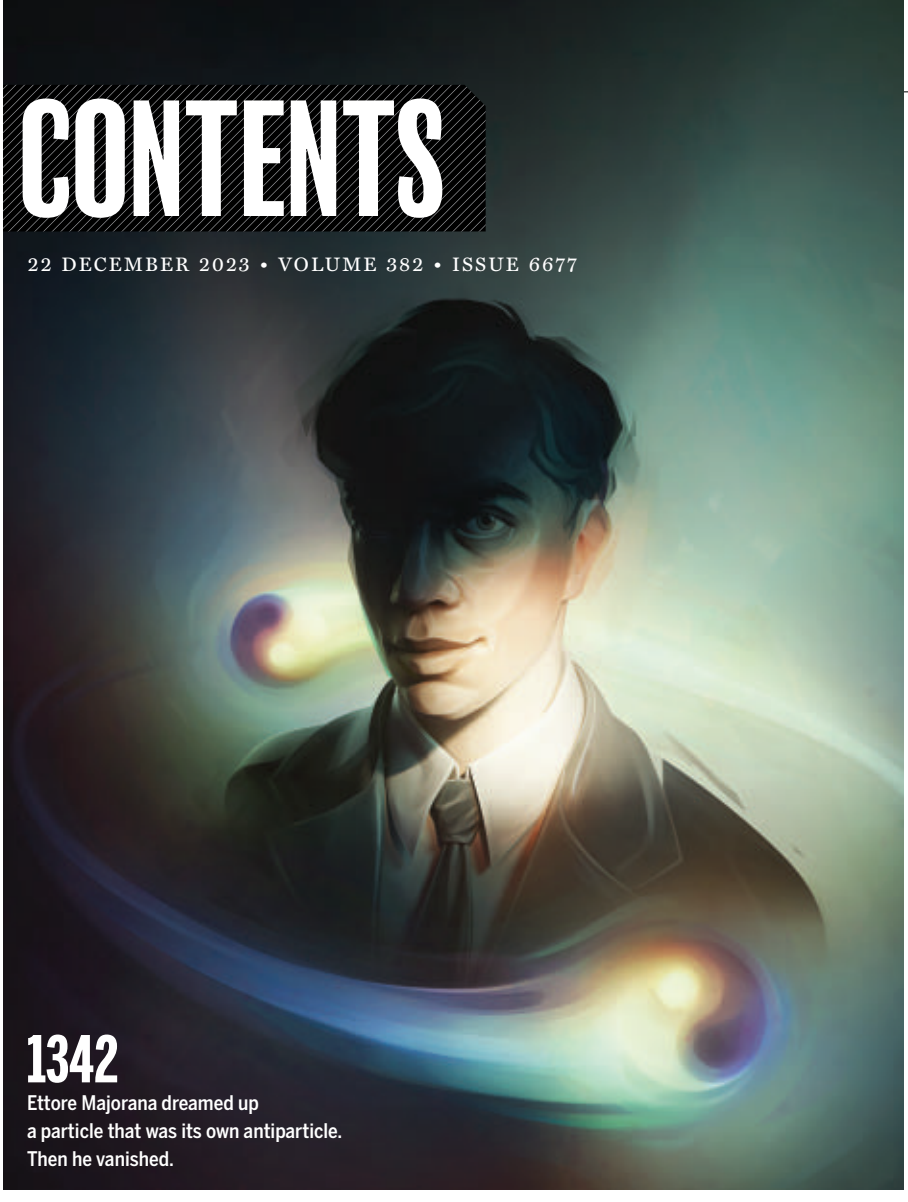

1342
Ettore Majorana dreamed up a particle that was its own antiparticle. Then he vanished.

ILLUSTRATION: OLENA SHMAHALO

NEWS

IN BRIEF

1334 News at a glance

IN DEPTH

1336 NRA donations spike in school shooting counties
Parallel surges for a gun control advocacy group not seen *By M. Wadman*

1337 'Gene drive' may help fight viruses with viruses
CRISPR-engineered herpesviruses can speed spread of genes to viral relatives in mice *By J. Cohen*

1338 NIH advisory group pushes for big pay raise for U.S. postdocs
Though applauded by many, measure would strain lab budgets if adopted *By K. Langin*

1339 San Andreas fault may shake less than once feared
Precariously balanced rocks near Los Angeles hold clues to the hazard of a giant earthquake *By P. Voosen*

1340 Before tunnel collapse, scientists sent warnings
Researchers repeatedly raised concerns about building in Himalayas' unstable geology *By A. Parvaiz*

1341 Chimps remember faces of old friends and family for decades
Recognition ability rivals all other animals, including humans *By A. Gibbons*

FEATURES

1342 The quantum phantom
A ghostly quasiparticle rooted in a century-old Italian mystery could unlock quantum computing's potential—if only it could be pinned down *By Z. Savitsky*
PODCAST

INSIGHTS

POLICY FORUM

1348 A landmark environmental law looks ahead

PERSPECTIVES

1356 Genetic insight on ice sheet history
Octopus DNA reveals timing of the most recent collapse of the West Antarctic Ice Sheet *By A. Dutton and R. M. DeConto*
RESEARCH ARTICLE p. 1384

1357 Deciphering downstream receptor signaling
Advancing drug discovery requires increasingly integrative structural biology approaches *By M. Filizola and J. A. Javitch*
RESEARCH ARTICLE p. 1378

1358 Mimicking polar bear hairs in aerogel fibers
Encapsulated aerogel fibers offer thermal insulation, breathability, and strength *By Z. Sheng and X. Zhang*
RESEARCH ARTICLE p. 1379

1360 Neurosurgery elucidates somatic mutations
Surgical innovation is helping to identify roles for somatic mutations in brain disorders *By E. A. Maury* et al.

1362 Increasing policy support for reducing racial health disparities
Perceiving racial health disparities as unjust could catalyze or halt change *By A. Earl and V. Derricks*
RESEARCH ARTICLE p. 1394

1363 An unexpected role for a glutamate receptor
γ-Aminobutyric acid acts on a glutamate receptor, evoking synaptic plasticity *By I. D. Coombs and M. Farrant*
RESEARCH ARTICLE p. 1389

1365 Endel Tulving (1927–2023)
Explorer, innovator, and theorist of human memory *By R. Cabeza and E. Düzel*

BOOKS *ET AL.*

1366 Data geopolitics
A group of scholars explore the implications of how governments control and restrict digital information *By D. Greenbaum*

1367 Making a digital dupe of Anderson Cooper
Two computer scientists discuss deepfakes and how they made a facsimile of the anchor *By J. Dickman*

Produced by the *Science*/AAAS Custom Publishing Office

New report reveals major change in global enterprise innovation landscape

On October 21, Wuhan University and the Institute of Scientific & Technical Information of China issued a comprehensive report on the current landscape of global enterprise innovation. Titled, "Global Enterprise Innovation Index 2023 (GEII 2023)," the report aims to support enterprises and policymakers across economies in understanding the latest trends of global innovation in science and technology.

Modern societies collectively expect new inventions, new gadgets, new services, new productivity, and new industries—all in the name and notion of innovation. Innovation is a cornerstone of today's economic growth as we know it. For companies around the world, "innovation" has long evolved beyond a buzzword into a deeply rooted philosophy for securing and sustaining business success.

Research on innovation and the impact and prediction thereof is nothing new. However, previous reputable reports on global innovation, such as the *Global Innovation Index* published annually by the World Intellectual Property Organization or the *Technology and Innovation Report* issued by the United Nations Conference on Trade and Development, largely focused on rankings of nations' productivity capacity linked to economic growth. Companies categorized as global enterprises operating businesses in diverse cultures and economies are usually considered a contributing factor to a country or region's innovation status. In a way, these companies could be muffled by their home country's representation through which the enterprises' innovation was primarily described as a part of their home country's R&D investment.

Evaluating and repositioning global enterprises' leadership role in innovation is timely, especially post-pandemic. Science and technology will rely on global enterprises to reach a much broader population than ever. In turn, the global market's demanding emerging industries will drive more fundamental research to advance our understanding of science and realization of new technology.

To provide a comprehensive look at global enterprises' innovation capacity, the Global Enterprise Innovation Index 2023 (GEII 2023) identified three key groups of innovation indicators—knowledge, technology, and collaboration—while subdividing the three groups into nine second-level and 32 third-level indicators. This system broke the existing innovation index format by moving the global enterprises to the center of attention while emphasizing emerging industries, namely new energy, biomedicine, advanced manufacturing, new materials, and next-generation information technology. By shuffling the priorities, the report showed inspiring results while still keeping the world's three major economic regions—Asia, Western Europe, and North America—in context. For example, when looking at combined innovation capacity in all evaluated fields, Japan leads the race with the United States following right after. China has the second largest economy in the world, and has traditionally pivoted around manufacturing, exports, and investment. Now China is showing strong momentum in next-generation information technology. The report also indicated a significant gap Chinese global enterprises need to bridge in innovation capacity to develop at the same level as current enterprise leaders.

"Our newly discovered three-pillar understanding of current world economic development driven by enterprise innovation disclosed a leadership position in global innovation for East Asian enterprises that traditionally was dominated by Western Europe and the United States," writes Ying Huang and Lin Zhang, chief scientists of the report.

Japan has 151 leading innovative global enterprises. The United States secured second place with 147 enterprises, shy of Japan by only four spots. Germany and China took the third and fourth places, with 45 and 41 enterprises, respectively.

This report is just the beginning of a much-needed persistent effort to reflect current economic development. Dean of Wuhan University's Big Data Institute and Director of the GEII 2023 expert committee Feicheng Ma says, "We hope to continue adjusting and optimizing the index system, expanding selection of emerging industries, and systematically peeling back the layers of innovation driven by global enterprises."

Sponsored by

武汉大学（武汉）数据智能研究院
Institute of Data Intelligence, Wuhan University

IMAGE: © JAMESTEOHART/SHUTTERSTOCK.COM

1356 & 1384

Genetic population structure of the circum-Antarctic octopus *Pareledone turqueti* shows that the West Antarctic Ice Sheet collapsed completely during the Last Interglacial.

PHOTO: DAVE BARNES/BAS

LETTERS

1369 Iran's Zayandeh Rud River basin in crisis
By I. Salahshoori and M. N. Jorabchi

1369 Restore the Yangtze River's floodplains *By Z. Mei* et al.

1370 Pakistan's turtle species at risk of extinction
By S. Ahmad and W. Mao

RESEARCH

IN BRIEF

1371 From *Science* and other journals

RESEARCH ARTICLES

1374 Chemistry automation
Autonomous, multiproperty-driven molecular discovery: From predictions to measurements and back *B. A. Koscher* et al.
RESEARCH ARTICLE SUMMARY; FOR FULL TEXT: DOI.ORG/10.1126/SCIENCE.ADI1407

1375 Bitcoin
Are cryptocurrencies currencies? Bitcoin as legal tender in El Salvador *F. Alvarez* et al.
RESEARCH ARTICLE SUMMARY; FOR FULL TEXT: DOI.ORG/10.1126/SCIENCE.ADD2844
PODCAST

1376 Neuroscience
Glia transmit negative valence information during aversive learning in *Drosophila* *T. Miyashita* et al.
RESEARCH ARTICLE SUMMARY; FOR FULL TEXT: DOI.ORG/10.1126/SCIENCE.ADF7429

1377 Transcription
Structural visualization of transcription initiation in action *X. Chen* et al.
RESEARCH ARTICLE SUMMARY; FOR FULL TEXT: DOI.ORG/10.1126/SCIENCE.ADI5120

1378 Signal transduction
Molecular determinants of ligand efficacy and potency in GPCR signaling *F. M. Heydenreich* et al.
RESEARCH ARTICLE SUMMARY; FOR FULL TEXT: DOI.ORG/10.1126/SCIENCE.ADH1859
PERSPECTIVE p. 1357

1379 Textiles
Biomimetic, knittable aerogel fiber for thermal insulation textile *M. Wu* et al.
PERSPECTIVE p. 1358

1384 Ice sheets
Genomic evidence for West Antarctic Ice Sheet collapse during the Last Interglacial *S. C. Y. Lau* et al.
PERSPECTIVE p. 1356

1389 Neuroscience
GluD1 binds GABA and controls inhibitory plasticity *L. Piot* et al.
PERSPECTIVE p. 1363

1394 Social disparities
Highlighting health consequences of racial disparities sparks support for action *R. M. Brown* et al.
PERSPECTIVE p. 1362

1399 Solar cells
Homogenized NiO_x nanoparticles for improved hole transport in inverted perovskite solar cells *S. Yu* et al.

1404 Structural biology
Rab29-dependent asymmetrical activation of leucine-rich repeat kinase 2 *H. Zhu* et al.

1411 Astrochemistry
Polycyclic aromatic hydrocarbons in samples of Ryugu formed in the interstellar medium *S. S. Zeichner* et al.

1416 Weather forecasting
Learning skillful medium-range global weather forecasting *R. Lam* et al.

1422 Superconductivity
Time-reversal symmetry breaking superconductivity between twisted cuprate superconductors *S. Y. F. Zhao* et al.

DEPARTMENTS

1333 Editorial
2024 looms *By H. H. Thorp*

1430 Working Life
Facing fraud in my lab *By R. A. Coleman*

ON THE COVER

Trained on four decades of historical data, GraphCast is an artificial intelligence model that predicts global weather with greater speed and accuracy compared with traditional approaches solving physical equations. It supports severe event predictions, such as cyclone tracking. The photo-illustration depicts Hurricane Nigel viewed from the International Space Station, with a blue mesh representative of the structure that GraphCast uses to process data. See page 1416. *Photo: JSC NASA; Illustration by C. Bickel/*Science*; Adapted from Google DeepMind*

Science Staff 1330
Science Careers 1428

SCIENCE (ISSN 0036-8075) is published weekly on Friday, except last week in December, by the American Association for the Advancement of Science, 1200 New York Avenue, NW, Washington, DC 20005. Periodicals mail postage (publication No. 484460) paid at Washington, DC, and additional mailing offices. Copyright © 2023 by the American Association for the Advancement of Science. The title SCIENCE is a registered trademark of the AAAS. Domestic individual membership, including subscription (12 months): $165 ($74 allocated to subscription). Domestic institutional subscription (51 issues): $2411; Foreign postage extra: Air assist delivery: $107. First class, airmail, student, and emeritus rates on request. Canadian rates with GST available upon request, GST #125488122. Publications Mail Agreement Number 1069624. **Printed in the U.S.A.**
Change of address: Allow 4 weeks, giving old and new addresses and 8-digit account number. **Postmaster:** Send change of address to AAAS, P.O. Box 96178, Washington, DC 20090–6178. **Single-copy sales:** $15 each plus shipping and handling available from backissues.science.org; bulk rate on request. **Authorization to reproduce** material for internal or personal use under circumstances not falling within the fair use provisions of the Copyright Act can be obtained through the Copyright Clearance Center (CCC), www.copyright.com. The identification code for *Science* is 0036-8075. *Science* is indexed in the *Reader's Guide to Periodical Literature* and in several specialized indexes.

Science AAAS

Editor-in-Chief Holden Thorp, hthorp@aaas.org

Executive Editor Valda Vinson

Editor, Research Jake S. Yeston **Editor, Insights** Lisa D. Chong **Managing Editor** Lauren Kmec

DEPUTY EDITORS Gemma Alderton (UK),Stella M. Hurtley (UK), Phillip D. Szuromi, Sacha Vignieri **SR. EDITORS** Caroline Ash (UK), Michael A. Funk, Brent Grocholski, Di Jiang, Priscilla N. Kelly, Marc S. Lavine (Canada), Sarah Lempriere (UK), Mattia Maroso, Yevgeniya Nusinovich, Ian S. Osborne (UK), L. Bryan Ray, H. Jesse Smith, Keith T. Smith (UK), Jelena Stajic, Peter Stern (UK), Valerie B. Thompson, Brad Wible **ASSOCIATE EDITORS** Bianca Lopez, Sarah Ross (UK), Madeleine Seale (UK), Corinne Simonti, Yury V. Suleymanov, Ekeoma Uzogara **SENIOR LETTERS EDITOR** Jennifer Sills **NEWSLETTER EDITOR** Christie Wilcox **RESEARCH & DATA ANALYST** Jessica L. Slater **LEAD CONTENT PRODUCTION EDITORS** Chris Filiatreau, Harry Jach **SR. CONTENT PRODUCTION EDITOR** Amelia Beyna **CONTENT PRODUCTION EDITORS** Anne Abraham, Robert French, Julia Haber-Katris, Nida Masiulis, Abigail Shashikanth, Suzanne M. White **SR. EDITORIAL MANAGERS** Carolyn Kyle, Beverly Shields **SR. PROGRAM ASSOCIATE** Maryrose Madrid **EDITORIAL ASSOCIATES** Aneera Dobbins, Joi S. Granger, Lisa Johnson **SR. EDITORIAL COORDINATORS** Jeffrey Hearn, Alexander Kief, Ronmel Navas, Jerry Richardson, Alice Whaley (UK), Anita Wynn **EDITORIAL COORDINATORS** Maura Byrne, Clair Goodhead (UK), Isabel Schnaidt, Qiyam Stewart, Brian White **ADMINISTRATIVE COORDINATOR** Karalee P. Rogers **ASI DIRECTOR, OPERATIONS** Janet Clements (UK) **ASI OFFICE MANAGER** Victoria Smith **ASI SR. OFFICE ADMINISTRATORS** Dawn Titheridge (UK), Jessica Waldock (UK) **COMMUNICATIONS DIRECTOR** Meagan Phelan **DEPUTY DIRECTOR** Matthew Wright **SENIOR WRITER** Walter Beckwith **WRITERS** Joseph Cariz, Abigail Eisenstadt, Nyla Husain **SENIOR COMMUNICATIONS ASSOCIATE** Zachary Graber **COMMUNICATIONS ASSOCIATES** Kiara Brooks, Haley Riley, Mackenzie Williams, Sarah Woods

News Editor Tim Appenzeller

NEWS MANAGING EDITOR John Travis **INTERNATIONAL EDITOR** David Malakoff **DEPUTY NEWS EDITORS** Rachel Bernstein, Shraddha Chakradhar, Elizabeth Culotta, Martin Enserink, David Grimm, Eric Hand, Kelly Servick, Matt Warren (Europe) **SR. CORRESPONDENTS** Daniel Clery (UK), Jon Cohen, Jeffrey Mervis, Elizabeth Pennisi **ASSOCIATE EDITORS** Jeffrey Brainard, Michael Price **NEWS REPORTERS** Adrian Cho, Jennifer Couzin-Frankel, Phie Jacobs, Jocelyn Kaiser, Rodrigo Pérez Ortega (Mexico City), Robert F. Service, Erik Stokstad, Paul Voosen, Meredith Wadman **CONTRIBUTING CORRESPONDENTS** Warren Cornwall, Andrew Curry (Berlin), Ann Gibbons, Sam Kean, Kai Kupferschmidt (Berlin), Andrew Lawler, Mitch Leslie, Virginia Morell, Dennis Normile (Tokyo), Elisabeth Pain (Careers), Charles Piller, Gabriel Popkin, Joshua Sokol, Richard Stone, Emily Underwood, Gretchen Vogel (Berlin), Lizzie Wade (Mexico City) **CAREERS** Katie Langin (Associate Editor) **COPY EDITORS** Julia Cole (Senior Copy Editor), Hannah Knighton, Cyra Master (Copy Chief) **ADMINISTRATIVE SUPPORT** Meagan Weiland

Creative Director Beth Rakouskas

DESIGN MANAGING EDITOR Chrystal Smith **GRAPHICS MANAGING EDITOR** Chris Bickel **PHOTOGRAPHY MANAGING EDITOR** Emily Petersen **MULTIMEDIA MANAGING PRODUCER** Kevin McLean **WEB CONTENT STRATEGY MANAGER** Kara Estelle-Powers **DESIGN EDITOR** Marcy Atarod **DESIGNER** Noelle Jessup **SENIOR SCIENTIFIC ILLUSTRATOR** Noelle Burgess **SCIENTIFIC ILLUSTRATORS** Austin Fisher, Kellie Holoski, Ashley Mastin **SENIOR GRAPHICS EDITOR** Monica Hersher **GRAPHICS EDITOR** Drew An-Pham **SENIOR GRAPHICS SPECIALISTS** Holly Bishop, Nathalie Cary **SENIOR PHOTO EDITOR** Charles Borst **PHOTO EDITOR** Elizabeth Billman **SENIOR PODCAST PRODUCER** Sarah Crespi **SENIOR VIDEO PRODUCER** Meagan Cantwell **SOCIAL MEDIA STRATEGIST** Jessica Hubbard **SOCIAL MEDIA PRODUCER** Sabrina Jenkins **WEB DESIGNER** Jennie Pajerowski

Chief Executive Officer and Executive Publisher Sudip Parikh

Publisher, Science Family of Journals Bill Moran

DIRECTOR, BUSINESS SYSTEMS AND FINANCIAL ANALYSIS Randy Yi **DIRECTOR, BUSINESS OPERATIONS & ANALYSIS** Eric Knott **MANAGER, BUSINESS OPERATIONS** Jessica Tierney **MANAGER, BUSINESS ANALYSIS** Cory Lipman **MANAGER, WEB ANALYTICS** Samantha Cressman **BUSINESS ANALYSTS** Kurt Ennis, Maggie Clark **FINANCIAL ANALYST** Isacco Fusi **BUSINESS OPERATIONS ADMINISTRATOR** Taylor Fisher **SENIOR PRODUCTION MANAGER** Jason Hillman **SENIOR MANAGER, PUBLISHING AND CONTENT SYSTEMS** Marcus Spiegler **CONTENT OPERATIONS MANAGER** Rebecca Doshi **SENIOR CONTENT & PUBLISHING SYSTEMS SPECIALIST** Jacob Hedrick **SENIOR PRODUCTION SPECIALIST** Kristin Wowk **PRODUCTION SPECIALISTS** Kelsey Cartelli, Audrey Diggs **DIGITAL PRODUCTION MANAGER** Lisa Stanford **SENIOR DIGITAL ADVERTISING SPECIALIST** Kimberley Oster **ADVERTISING PRODUCTION OPERATIONS MANAGER** Deborah Tompkins **DESIGNER, CUSTOM PUBLISHING** Jeremy Huntsinger **SR. TRAFFIC ASSOCIATE** Christine Hall **SPECIAL PROJECTS ASSOCIATE** Shantel Agnew

ASSOCIATE DIRECTOR, BUSINESS DEVELOPMENT Justin Sawyers **GLOBAL MARKETING MANAGER** Allison Pritchard **DIGITAL MARKETING MANAGER** Aimee Aponte **JOURNALS MARKETING MANAGER** Shawana Arnold **MARKETING ASSOCIATES** Ashley Hylton, Mike Romano, Lorena Chirinos Rodriguez, Jenna Voris **SENIOR DESIGNER** Kim Huynh

DIRECTOR AND SENIOR EDITOR, CUSTOM PUBLISHING Erika Gebel Berg **ASSISTANT EDITOR, CUSTOM PUBLISHING** Jackie Oberst **PROJECT MANAGER** Melissa Collins

DIRECTOR, PRODUCT & PUBLISHING DEVELOPMENT Chris Reid **DIRECTOR, BUSINESS STRATEGY AND PORTFOLIO MANAGEMENT** Sarah Whalen **DIRECTOR, PRODUCT MANAGEMENT** Kris Bishop **PRODUCT DEVELOPMENT MANAGER** Scott Chernoff **PUBLISHING PLATFORM MANAGER** Jessica Loayza **SR. PRODUCT ASSOCIATE** Robert Koepke **PRODUCT ASSOCIATES** Caroline Breul, Anne Mason

ASSOCIATE DIRECTOR, INSTITUTIONAL LICENSING MARKETING Kess Knight **BUSINESS DEVELOPMENT MANAGER** Rasmus Andersen **ASSOCIATE DIRECTOR, INSTITUTIONAL LICENSING SALES** Ryan Rexroth **INSTITUTIONAL LICENSING MANAGER** Marco Castellan, Claudia Paulsen-Young **SENIOR MANAGER, INSTITUTIONAL LICENSING OPERATIONS** Judy Lillibridge **SENIOR OPERATIONS ANALYST** Lana Guz **SYSTEMS & OPERATIONS ANALYST** Ben Teincuff **FULFILLMENT ANALYST** Aminta Reyes

ASSOCIATE DIRECTOR, US ADVERTISING Stephanie O'Connor **US MID WEST, MID ATLANTIC AND SOUTH EAST SALES** Chris Hoag **US WEST COAST SALES** Lynne Stickrod **ASSOCIATE DIRECTOR, ROW** Roger Goncalves **SALES REP, ROW** Sarah Lelarge **SALES ADMIN ASSISTANT, ROW** Victoria Glasbey **DIRECTOR OF GLOBAL COLLABORATION AND ACADEMIC PUBLISHING RELATIONS, ASIA** Xiaoying Chu **ASSOCIATE DIRECTOR, INTERNATIONAL COLLABORATION** Grace Yao **SALES MANAGER** Danny Zhao **MARKETING MANAGER** Kilo Lan **ASCA CORPORATION, JAPAN** Rie Rambelli (Tokyo), Miyuki Tani (Osaka)

DIRECTOR, COPYRIGHT, LICENSING AND SPECIAL PROJECTS Emilie David **RIGHTS AND PERMISSIONS ASSOCIATE** Elizabeth Sandler **LICENSING ASSOCIATE** Virginia Warren **RIGHTS AND LICENSING COORDINATOR** Dana James **CONTRACT SUPPORT SPECIALIST** Michael Wheeler

EDITORIAL
science_editors@aaas.org

NEWS
science_news@aaas.org

INFORMATION FOR AUTHORS
science.org/authors/science-information-authors

REPRINTS AND PERMISSIONS
science.org/help/reprints-and-permissions

MULTIMEDIA CONTACTS
SciencePodcast@aaas.org
ScienceVideo@aaas.org

MEDIA CONTACTS
scipak@aaas.org

PRODUCT ADVERTISING & CUSTOM PUBLISHING
advertising.science.org/products-services
science_advertising@aaas.org

CLASSIFIED ADVERTISING
advertising.science.org/science-careers
advertise@sciencecareers.org

JOB POSTING CUSTOMER SERVICE
employers.sciencecareers.org
support@sciencecareers.org

MEMBERSHIP AND INDIVIDUAL SUBSCRIPTIONS
science.org/subscriptions

MEMBER BENEFITS
aaas.org/membership/benefits

INSTITUTIONAL SALES AND SITE LICENSES
science.org/librarian

AAAS BOARD OF DIRECTORS

CHAIR Gilda A. Barabino

PRESIDENT Keith R. Yamamoto

PRESIDENT-ELECT Willie E. May

TREASURER Carolyn N. Ainslie

CHIEF EXECUTIVE OFFICER
Sudip Parikh

BOARD Cynthia M. Beall, Janine Austin Clayton, Kaye Husbands Fealing, Kathleen Hall Jamieson, Jane Maienschein, Robert B. Millard, Babak Parviz, William D. Provine, Juan S. Ramírez Lugo, Susan M. Rosenberg, Vassiliki Betty Smocovitis

Science serves as a forum for discussion of important issues related to the advancement of science by publishing material on which a consensus has been reached as well as including the presentation of minority or conflicting points of view. Accordingly, all articles published in *Science*—including editorials, news and comment, and book reviews—are signed and reflect the individual views of the authors and not official points of view adopted by AAAS or the institutions with which the authors are affiliated.

BOARD OF REVIEWING EDITORS (Statistics board members indicated with **(S)**)

Erin Adams, *U. of Chicago*
Takuzo Aida, *U. of Tokyo*
Leslie Aiello, *Wenner-Gren Fdn.*
Deji Akinwande, *UT Austin*
James Analytis, *UC Berkeley*
Paola Arlotta, *Harvard U.*
Delia Baldassarri, *NYU*
Nenad Ban, *ETH Zürich*
Christopher Barratt, *U. of Dundee*
Franz Bauer, *Pontificia U. Católica de Chile*
Ray H. Baughman, *UT Dallas*
Carlo Beenakker, *Leiden U.*
Yasmine Belkaid, *NIAID, NIH*
Kiros T. Berhane, *Columbia U.*
Joseph J. Berry, *NREL*
Chris Bowler, *École Normale Supérieure*
Ian Boyd, *U. of St. Andrews*
Malcolm Brenner, *Baylor Coll. of Med.*
Emily Brodsky, *UC Santa Cruz*
Ron Brookmeyer, *UCLA* **(S)**
Christian Büchel, *UKE Hamburg*
Johannes Buchner, *TUM*
Dennis Burton, *Scripps Res.*
Carter Tribley Butts, *UC Irvine*
György Buzsáki, *NYU School of Med.*
Mariana Byndloss, *Vanderbilt U. Med. Ctr.*
Annmarie Carlton, *UC Irvine*
Simon Cauchemez, *Inst. Pasteur*
Ling-Ling Chen, *SIBCB, CAS*
Wendy Cho, *UIUC*
Ib Chorkendorff, *Denmark TU*
Chunaram Choudhary, *Københavns U.*
Karlene Cimprich, *Stanford U.*
Laura Colgin, *UT Austin*
James J. Collins, *MIT*
Robert Cook-Deegan, *Arizona State U.*
Virginia Cornish, *Columbia U.*
Carolyn Coyne, *Duke U.*
Roberta Croce, *VU Amsterdam*
Molly Crocket, *Princeton U.*
Christina Curtis, *Stanford U.*
Ismaila Dabo, *Penn State U.*
Jeff L. Dangl, *UNC*
Nicolas Dauphas, *U. of Chicago*
Frans de Waal, *Emory U.*
Claude Desplan, *NYU*
Sandra Díaz, *U. Nacional de Córdoba*
Samuel Díaz-Muñoz, *UC Davis*
Ulrike Diebold, *TU Wien*
Stefanie Dimmeler, *Goethe-U. Frankfurt*
Hong Ding, *Inst. of Physics, CAS*
Dennis Discher, *UPenn*
Jennifer A. Doudna, *UC Berkeley*
Ruth Drdla-Schutting, *Med. U. Vienna*
Raissa M. D'Souza, *UC Davis*
Bruce Dunn, *UCLA*
William Dunphy, *Caltech*
Scott Edwards, *Harvard U.*
Todd A. Ehlers, *U. of Glasgow*
Nader Engheta, *UPenn*
Tobias Erb, *MPS, MPI Terrestrial Microbiology*
Karen Ersche, *U. of Cambridge*
Beate Escher, *UFZ & U. of Tübingen*
Barry Everitt, *U. of Cambridge*
Vanessa Ezenwa, *U. of Georgia*
Toren Finkel, *U. of Pitt. Med. Ctr.*
Natascha Förster Schreiber, *MPI Extraterrestrial Phys.*
Peter Fratzl, *MPI Potsdam*
Elaine Fuchs, *Rockefeller U.*
Caixia Gao, *Inst. of Genetics and Developmental Bio., CAS*
Daniel Geschwind, *UCLA*
Lindsey Gillson, *U. of Cape Town*
Gillian Griffiths, *U. of Cambridge*
Simon Greenhill, *U. of Auckland*
Nicolas Gruber, *ETH Zürich*
Hua Guo, *U. of New Mexico*
Taekjip Ha, *Johns Hopkins U.*
Daniel Haber, *Mass. General Hos.*
Sharon Hammes-Schiffer, *Yale U.*
Wolf-Dietrich Hardt, *ETH Zürich*
Louise Harra, *UCL*
Kelley Harris, *U. of Wash*
Carl-Philipp Heisenberg, *IST Austria*
Christoph Hess, *U. of Basel & U. of Cambridge*
Heather Hickman, *NIAID, NIH*
Hans Hilgenkamp, *U. of Twente*
Janneke Hille Ris Lambers, *ETH Zürich*
Kai-Uwe Hinrichs, *U. of Bremen*
Deirdre Hollingsworth, *U. of Oxford*
Christina Hulbe, *U. of Otago, New Zealand*
Randall Hulet, *Rice U.*
Auke Ijspeert, *EPFL*
Gwyneth Ingram, *ENS Lyon*
Darrell Irvine, *MIT*
Akiko Iwasaki, *Yale U.*
Erich Jarvis, *Rockefeller U.*
Peter Jonas, *IST Austria*
Matt Kaeberlein, *U. of Wash.*
Daniel Kammen, *UC Berkeley*
Kisuk Kang, *Seoul Nat. U.*
V. Narry Kim, *Seoul Nat. U.*
Nancy Knowlton, *Smithsonian*
Etienne Koechlin, *École Normale Supérieure*
Alex L. Kolodkin, *Johns Hopkins U.*
LaShanda Korley, *U. of Delaware*
Paul Kubes, *U. of Calgary*
Chris Kuzawa, *Northwestern U.*
Laura Lackner, *Northwestern U.*
Gabriel Lander, *Scripps Res.* **(S)**
Mitchell A. Lazar, *UPenn*
Hedwig Lee, *Duke U.*
Fei Li, *Xi'an Jiaotong U.*
Ryan Lively, *Georgia Tech*
Luis Liz-Marzán, *CIC biomaGUNE*
Omar Lizardo, *UCLA*
Jonathan Losos, *WUSTL*
Ke Lu, *Inst. of Metal Res., CAS*
Christian Lüscher, *U. of Geneva*
Jean Lynch-Stieglitz, *Georgia Tech*
David Lyons, *U. of Edinburgh*
Fabienne Mackay, *QIMR Berghofer*
Zeynep Madak-Erdogan, *UIUC*
Vidya Madhavan, *UIUC*
Anne Magurran, *U. of St. Andrews*
Ari Pekka Mähönen, *U. of Helsinki*
Asifa Majid, *U. of Oxford*
Oscar Marín, *King's Coll. London*
Charles Marshall, *UC Berkeley*
Christopher Marx, *U. of Idaho*
David Masopust, *U. of Minnesota*
Geraldine Masson, *CNRS*
Jennifer McElwain, *Trinity College Dublin*
Rodrigo Medellín, *U. Nacional Autónoma de México*
Mayank Mehta, *UCLA*
C. Jessica Metcalf, *Princeton U.*
Tom Misteli, *NCI, NIH*
Jeffery Molkentin, *Cincinnati Children's Hospital Medical Center*
Alison Motsinger-Reif, *NIEHS, NIH* **(S)**
Danielle Navarro, *U. of New South Wales*
Daniel Neumark, *UC Berkeley*
Thi Hoang Duong Nguyen, *MRC LMB*
Beatriz Noheda, *U. of Groningen*
Helga Nowotny, *Vienna Sci. & Tech. Fund*
Pilar Ossorio, *U. of Wisconsin*
Andrew Oswald, *U. of Warwick*
Isabella Pagano, *Istituto Nazionale di Astrofisica*
Giovanni Parmigiani, *Dana-Farber* **(S)**
Sergiu Pasca, *Standford U.*
Daniel Pauly, *U. of British Columbia*
Ana Pêgo, *U. do Porto*
Julie Pfeiffer, *UT Southwestern Med. Ctr.*
Philip Phillips, *UIUC*
Matthieu Piel, *Inst. Curie*
Kathrin Plath, *UCLA*
Martin Plenio, *Ulm U.*
Katherine Pollard, *UCSF*
Elvira Poloczanska, *Alfred-Wegener-Inst.*
Julia Pongratz, *Ludwig Maximilians U.*
Philippe Poulin, *CNRS*
Lei Stanley Qi, *Stanford U.*
Simona Radutoiu, *Aarhus U.*
Trevor Robbins, *U. of Cambridge*
Joeri Rogelj, *Imperial Coll. London*
John Rubenstein, *SickKids*
Mike Ryan, *UT Austin*
Miquel Salmeron, *Lawrence Berkeley Nat. Lab*
Nitin Samarth, *Penn State U.*
Erica Ollmann Saphire, *La Jolla Inst.*
Joachim Saur, *U. zu Köln*
Alexander Schier, *Harvard U.*
Wolfram Schlenker, *Columbia U.*
Susannah Scott, *UC Santa Barbara*
Anuj Shah, *U. of Chicago*
Vladimir Shalaev, *Purdue U.*
Jie Shan, *Cornell U.*
Beth Shapiro, *UC Santa Cruz*
Jay Shendure, *U. of Wash.*
Steve Sherwood, *U. of New South Wales*
Brian Shoichet, *UCSF*
Robert Siliciano, *JHU School of Med.*
Lucia Sivilotti, *UCL*
Emma Slack, *ETH Zürich & U. of Oxford*
Richard Smith, *UNC* **(S)**
John Speakman, *U. of Aberdeen*
Allan C. Spradling, *Carnegie Institution for Sci.*
V. S. Subrahmanian, *Northwestern U.*
Sandip Sukhtankar, *U. of Virginia*
Naomi Tague, *UC Santa Barbara*
Eriko Takano, *U. of Manchester*
A. Alec Talin, *Sandia Natl. Labs*
Patrick Tan, *Duke-NUS Med. School*
Sarah Teichmann, *Wellcome Sanger Inst.*
Rocio Titiunik, *Princeton U.*
Shubha Tole, *Tata Inst. of Fundamental Res.*
Maria-Elena Torres Padilla, *Helmholtz Zentrum München*
Kimani Toussaint, *Brown U.*
Barbara Treutlein, *ETH Zürich*
Li-Huei Tsai, *MIT*
Jason Tylianakis, *U. of Canterbury*
Matthew Vander Heiden, *MIT*
Wim van der Putten, *Netherlands Inst. of Ecology*
Ivo Vankelecom, *KU Leuven*
Henrique Veiga-Fernandes, *Champalimaud Fdn.*
Reinhilde Veugelers, *KU Leuven*
Bert Vogelstein, *Johns Hopkins U.*
Julia Von Blume, *Yale School of Med.*
David Wallach, *Weizmann Inst.*
Jane-Ling Wang, *UC Davis* **(S)**
Jessica Ware, *Amer. Mus. of Natural Hist.*
David Waxman, *Fudan U.*
Alex Webb, *U. of Cambridge*
Chris Wikle, *U. of Missouri* **(S)**
Terrie Williams, *UC Santa Cruz*
Ian A. Wilson, *Scripps Res.* **(S)**
Hao Wu, *Harvard U.*
Li Wu, *Tsinghua U.*
Amir Yacoby, *Harvard U.*
Benjamin Youngblood, *St. Jude*
Yu Xie, *Princeton U.*
Jan Zaanen, *Leiden U.*
Kenneth Zaret, *UPenn School of Med.*
Lidong Zhao, *Beihang U.*
Bing Zhu, *Inst. of Biophysics, CAS*
Xiaowei Zhuang, *Harvard U.*
Maria Zuber, *MIT*

CALL FOR PAPERS

SPJ
SCIENCE PARTNER JOURNALS

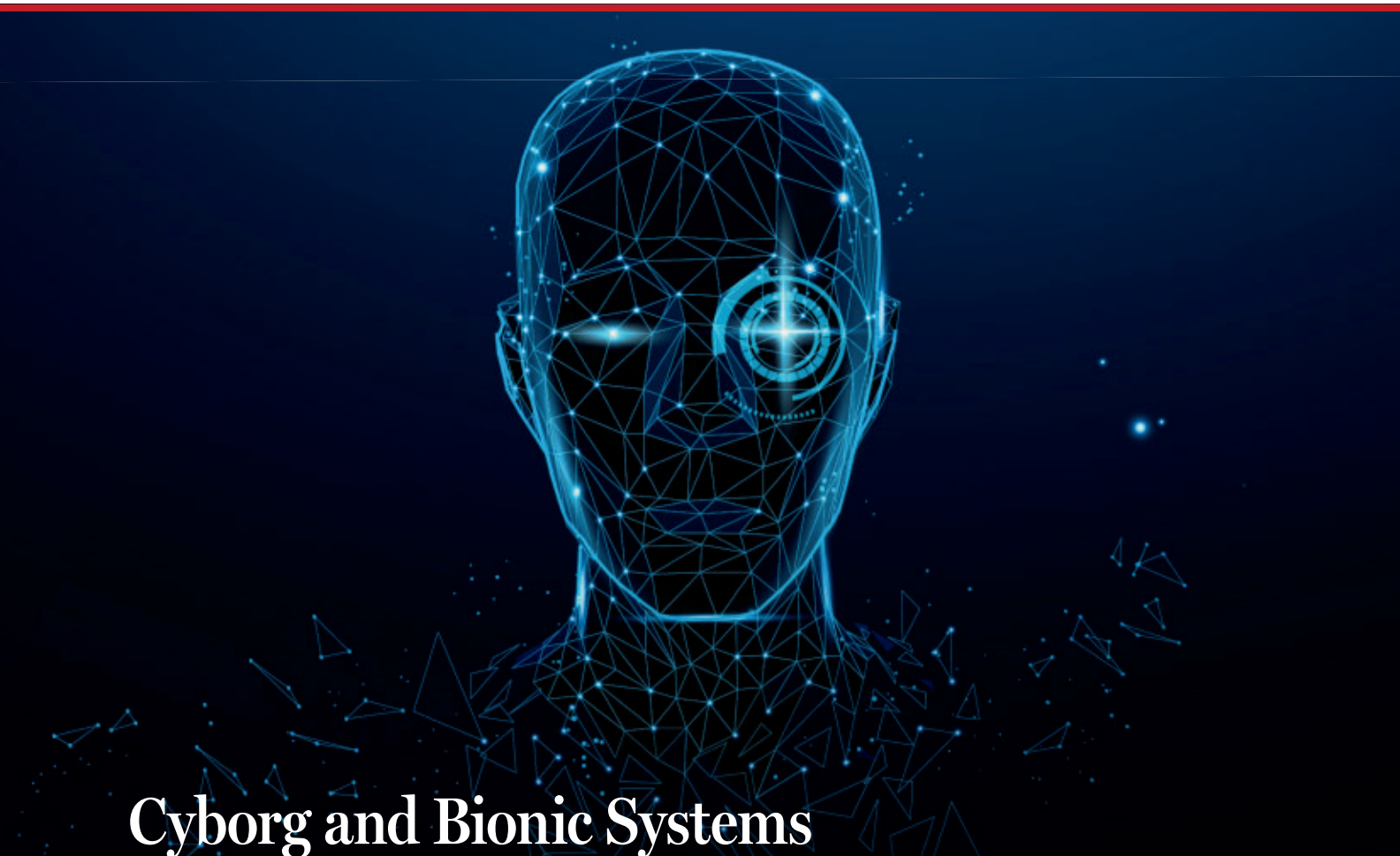

Cyborg and Bionic Systems

Cyborg and Bionic Systems is an online-only, Open Access journal published in affiliation with the **Beijing Institute of Technology (BIT)** and distributed by the **American Association for the Advancement of Science (AAAS).** The journal publishes original, peer-reviewed articles based on fundamental, applied science, or their interaction. *Cyborg and Bionic Systems* promotes the knowledge interchange and hybrid system codesign between living beings and robotic systems. The journal also covers a wide range of fields related to cybernetic organisms (cyborg) and bionic systems (CBS), mainly including robotics, biomedical engineering and neuro-engineering.

Submit your research to *Cyborg and Bionic System* today!

Learn more at **spj.science.org/journal/cbsystems**

The Science Partner Journal (SPJ) program was established by the American Association for the Advancement of Science (AAAS), the nonprofit publisher of the *Science* family of journals. The SPJ program features high-quality, online-only, Open Access publications produced in collaboration with international research institutions, foundations, funders and societies. Through these collaborations, AAAS furthers its mission to communicate science broadly and for the benefit of all people by providing top-tier international research organizations with the technology, visibility, and publishing expertise that AAAS is uniquely positioned to offer as the world's largest general science membership society.

Visit us at **spj.science.org**

@SPJournals **@SPJournals and @CBSystems_**

OPEN ACCESS

ARTICLE PROCESSING CHARGES WAIVED UNTIL JULY 2023

Share **Your Robotics Research** with the **World**.

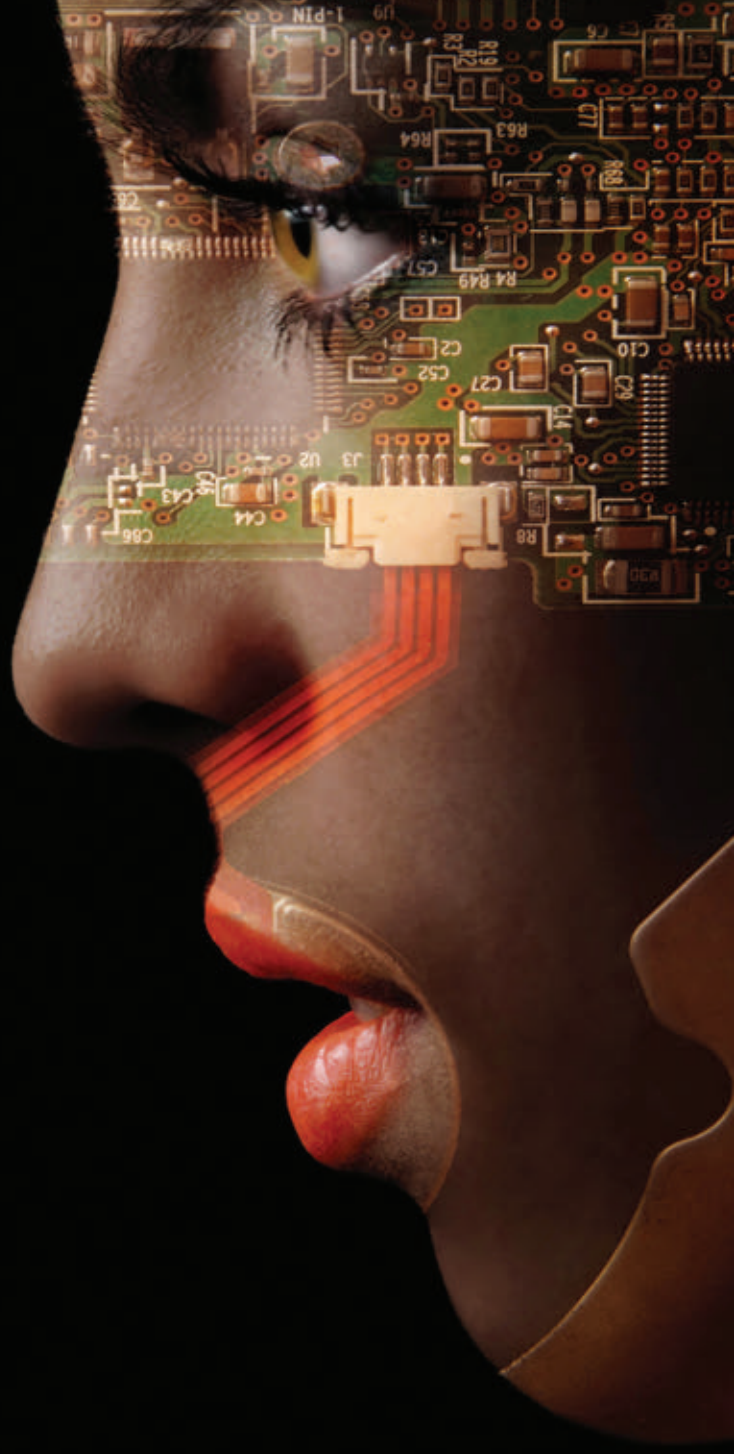

Shaping the future of robotics with high impact research!

As a multidisciplinary online-only journal, *Science Robotics* publishes original, peer-reviewed, research articles that advance the field of robotics. The journal provides a central forum for communication of new ideas, general principles, and original developments in research and applications of robotics for all environments.

Submit your research today. Learn more at: **science.org/journal/scirobotics**

Twitter: @SciRobotics
Facebook: @ScienceRobotics

Science Robotics
AAAS

EDITORIAL

2024 looms

H. Holden Thorp
Editor-in-Chief,
Science journals.
hthorp@aaas.org

Last week, *Science* reflected on major achievements in science in 2023, from weight loss drugs and a malaria vaccine to exascale computing and advances in artificial intelligence. These are all impressive developments and provide yet more testimony to the power of science to continually expand the quality of our lives while deepening our understanding of the world. Even so, it's hard to end the year without some worries about 2024. Wars in Ukraine and Gaza will grind on in the new year, and the United States is headed toward perhaps the most consequential and divisive presidential election in more than 160 years. These events—and similar ones around the world—will challenge the cohesiveness and determination of the scientific community as never before.

The situation in Argentina could be a harbinger of the danger ahead. There, voters elected Javier Milei, "a bombastic, right-wing politician," in the wake of severe economic problems in the country. Milei has vowed to shrink or eliminate the leading science agency in Argentina, which he has said is "unproductive," despite wide international recognition of its importance. Similar cries are likely to emerge in the US election, where an independent-party candidate, Robert F. Kennedy Jr., has already vowed to suspend government-sponsored research on infectious diseases, and Republican primary candidate Vivek Ramaswamy is calling climate change a hoax. Neither has a prayer of winning, but they stand as a warning of how demagogues can mislead voters with their ignorance and exploit a growing sense of suspicion of scientific expertise.

In the US, confidence in science continues to decline and become more polarized. Only 57% of Americans now believe that science has had a positive effect on society, down 16 points since the start of the severe acute respiratory syndrome coronavirus 2 (SARS-CoV-2) outbreak. This division is evident in a recent study showing that although conservatives and liberals have the same tendency to believe conspiracy theories, those beliefs that involve science—such as denials of COVID-19, the efficacy and safety of vaccines, and human-caused climate change—skew far to the right in their level of acceptance. Even unfounded doubts about genetically modified crops, which were once held mostly by those on the left, have moved to the center. With an eroding base of agreement on what counts as well-supported fact, it's now even harder to stand up for science without appearing partisan.

The solution to this is daunting but doable. The scientific community must figure out how to speak out against anti-science attitudes and beliefs without sounding condescending and furthering populist paranoia. It doesn't help that public confidence in US higher education institutions, where most research is conducted, has plummeted to 38%. Last month, US ambassador to Japan Rahm Emanuel was on the mark when he told Sudip Parikh, chief executive officer of the American Association for the Advancement of Science (AAAS, the publisher of *Science*), that scientists need to start speaking with "outside voices." "You can have all your meetings with each other," he said, "share papers, do peer reviews, but still, what you do will be under attack." As these surveys show, this is a problem the scientific community has not cracked. It must look for new ways to reach the public and better support those who are directly engaging with the public and trying to broaden understanding of science as humanity's evolving attempt to discover how the world works and how a deep understanding of nature can be harnessed to benefit everyone, regardless of political persuasion.

> **"We are truly living in two worlds—one of discovery and wonder and one of division."**

Thus, the scientific community must get its own house in better order. It should pay attention to the morale and welfare of trainees and students, call out and address bias and discrimination in its processes, and ensure the production of a reliable scientific record through a correction mechanism that is expedient and transparent. Missteps in these realms make it easier for those who are always looking for the slightest excuse to amplify their attacks on science.

We are truly living in two worlds—one of discovery and wonder and one of division. This means that scientific leadership must be simultaneously bold and pastoral. We all must stand up for science while also caring for the community that produces it. This is no easy task, but it's never been more important.

–H. Holden Thorp

PHOTO: CAMERON DAVIDSON

10.1126/science.adn5404

NEWS

1 in 9

Estimated share of bird species driven extinct by humans, mostly on Pacific islands. The number of extinct species, 1500, is double previous estimates. The new one relies on fossils of species that went extinct before being formally recorded. (*Nature Communications*)

Amateur fossil hunter Steve Etches helped excavate the 2-meter-long fossilized skull of a carnivorous pliosaur.

IN BRIEF

Edited by
Jeffrey Brainard

PALEONTOLOGY

Near-perfect pliosaur skull hints at big bite

A U.K. team that includes amateur fossil hunters is studying the recently discovered skull of a pliosaur, a large, carnivorous marine reptile that dominated ancient oceans about 150 million years ago, news media reported last week. The specimen was found in 2022 embedded in a cliff along Dorset's famed Jurassic Coast, where the pioneering 19th century amateur fossil hunter Mary Anning once discovered skeletons of other marine dinosaurs. Scientists are calling the new skull, about 2 meters long, one of the most complete of its kind. After measuring it, paleontologist Emily Rayfield of the University of Bristol calculated the creature's bite force could have reached 33,000 newtons—about double that of modern-day crocodiles. Other studies have estimated that some pliosaurs' entire bodies measured up to 12 meters long. The fossil has not yet been described in a scholarly article or preprint but is to be featured in a BBC documentary debuting on 1 January 2024.

HHMI wins disability lawsuit

LEGAL AFFAIRS | A Maryland jury last week decided that the Howard Hughes Medical Institute (HHMI) did not discriminate in 2018 when it failed to renew its generous investigator award to Vivian Cheung, an RNA biologist at the University of Michigan who is disabled. In 2014, Cheung learned she has a rare genetic disorder that has impaired her immune system and vision. When she asked the wealthy research philanthropy for employment accommodations, it began to discriminate against her, she alleged in a lawsuit she filed against HHMI in 2020. She said that HHMI threatened to terminate her if she didn't return to her Michigan lab from Maryland, where she had been receiving medical care and doing research. HHMI argued that it didn't renew Cheung's

PHOTO: DAVID STOCK/EYEVINE/REDUX

multimillion-dollar grant because her science wasn't good enough. In 2018, 20 external reviewers gave Cheung 14 C's and six B-minuses. Advocates for disabled scientists had followed the 8-day trial and noted that disability discrimination claims are particularly hard to prove in court.

Scientists help clear mother

FORENSICS | An appeals court in Australia last week officially struck down the convictions of an Australian woman, Kathleen Folbigg, for killing her four young children decades ago. A jury found Folbigg guilty in 2003 for the deaths despite a lack of direct evidence. Since 2019, geneticists and other researchers have gathered and publicized data suggesting her children likely died from undiagnosed medical conditions, which helped Folbigg win a pardon and release from prison earlier this year. On 14 December, she was present in the courtroom as the appeals court called the original evidence used against her at trial "unreliable" and its chief justice spoke of the "substantial and extensive body" of new evidence the scientists had provided. The Australian Academy of Science, which acted as an independent adviser for an official inquiry into the conviction, said Australia should set a standard for the reliability of evidence, as other countries have.

WHO targets disfiguring disease

PUBLIC HEALTH | The World Health Organization (WHO) last week added noma, a disease that disfigures the face and can be fatal if not treated, to its official list of neglected tropical diseases. The designation is intended to attract more research and funding for curbing the disease, also known as cancrum oris and gangrenous stomatitis. More than 30,000 cases are estimated to occur annually, predominantly in malnourished children in remote parts of Africa; specialists suspect more go unreported. WHO says the fatality rate is as high as 90%, although early treatment with antibiotics is effective. Researchers think bacteria and poor oral hygiene help cause the disease, which begins as an inflammation of the gums and evolves into a gangrene that damages the nose, mouth, and eyes. Survivors face stigma, and some need reconstructive surgery. WHO's listing comes after years of advocacy to raise awareness about the disease, including a January request from Nigeria and 32 other countries with significant numbers of noma cases.

PHOTO: CLAIRE JEANTET AND FABRICE CATERINI/INEDIZ/WHO

A 5-year-old girl in Nigeria, her face disfigured by noma, travels with her mother to a hospital for treatment.

Fallen M.D. soon heads to prison

CRIMINAL JUSTICE | Paolo Macchiarini, the former surgeon sentenced to 2.5 years in prison by a Swedish court for aggravated assault against patients he treated, is expected to begin his sentence sometime in coming weeks. As described by a Netflix documentary and the true crime drama *Dr. Death*, three patients died after suffering complications from experimental trachea transplants he performed at the Karolinska Institute; the court ruled that Macchiarini was criminally culpable because he knew the surgeries were unlikely to succeed and disregarded the risks to the patients. On 30 October, Sweden's highest court turned down his appeal, triggering a 90-day deadline for authorities to determine when and where he will report to prison. Sweden does not publicly release such details. Observers say Macchiarini may be imprisoned in Spain, where he lives, because EU rules encourage allowing convicted people to serve their sentence in the country in which they are most likely to be successfully rehabilitated and reintegrated into society.

Compounds nearly diamond-hard

MATERIALS SCIENCE | Researchers reported this month synthesizing carbon nitride materials with a hardness second only to that of diamond, the hardest known mineral. Predicted in the 1980s, such a carbon nitride was first made by a U.S. group in 2016, but the material fell apart if not continually squeezed under intense pressure. Scientists reported on 10 December in *Advanced Materials* that by compressing carbon and nitrogen precursors to pressures similar to those in Earth's mantle, they made three different carbon nitrides, all of which proved to be superhard and stable when the pressure was released. The authors say it's difficult to synthesize more than the tiny amounts they derived, but they speculate these crystals could serve as seeds for growing larger amounts of the material.

CLIMATE POLICY

Fossil fuel pledge panned

Nearly 200 countries agreed last week at the United Nations's 28th Conference of the Parties climate summit to "transition away from" fossil fuels. Some observers called it a political milestone. But many climate scientists described the nonbinding pledge—which asks countries to develop new plans within 2 years to curb greenhouse gas emissions, including methane—as barely a step forward.

> "It's like promising your doctor that you will 'transition away from doughnuts' after being diagnosed with diabetes."
>
> **Michael Mann,** University of Pennsylvania, in *The Guardian*

> "With every empty promise, millions more people will enter the front line of climate change and many will die."
>
> **Friederike Otto,** Imperial College London, in *The Guardian*

NIH not auditing foreign grantees

FUNDING | A federal watchdog office has faulted the U.S. National Institutes of Health (NIH) for failing to collect annual audit reports from foreign grantees. The agency received only 28 of 109 reports required from 55 of its grant recipients that received at least $750,000 in federal funding in fiscal years 2019 and 2020, according to the 14 December report by the Department of Health and Human Services's Office of Inspector General. Most institutions lacking audits were in Europe, Canada, and Africa. NIH responded that it plans to obtain the missing reports by September 2024. In January, the inspector general found that NIH failed to adequately monitor grants to the nonprofit EcoHealth Alliance that included subawards to China's Wuhan Institute of Virology—which some conservatives have accused, without evidence, of sparking the COVID-19 pandemic.

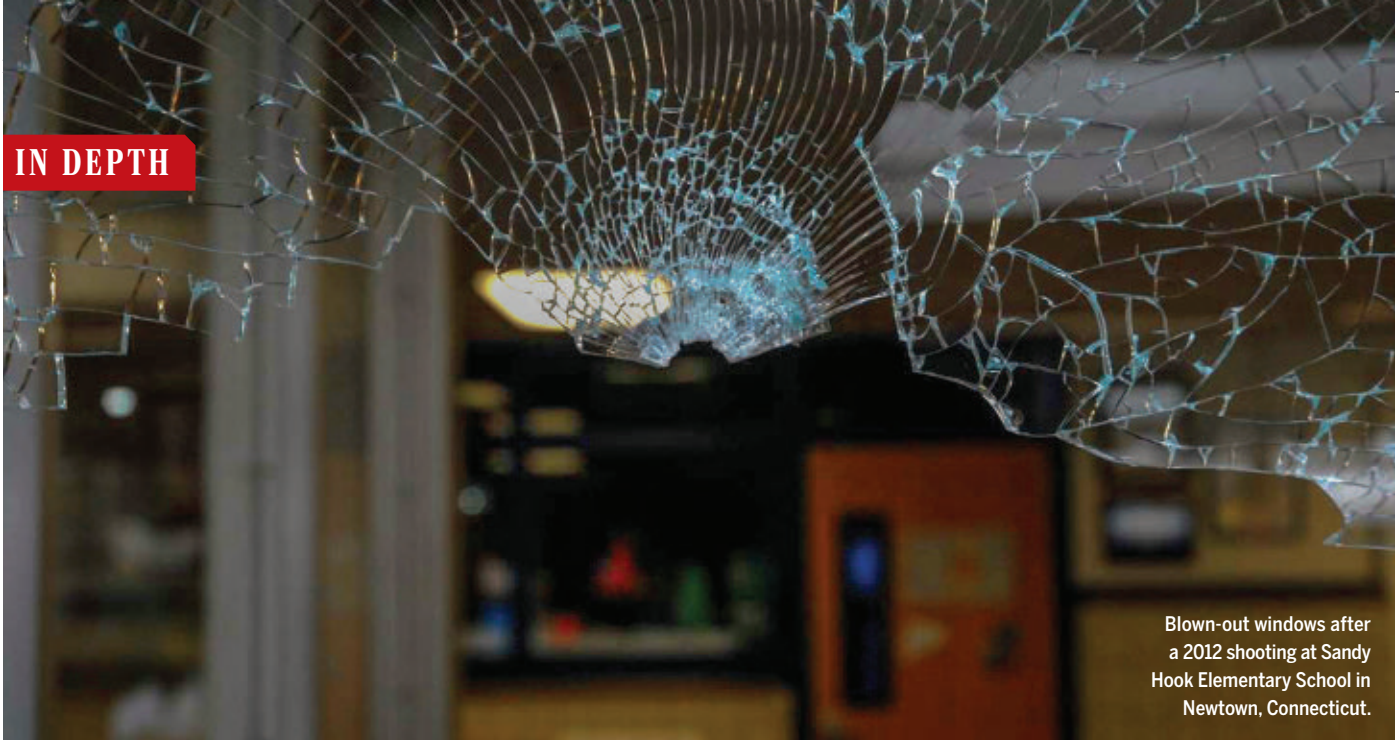

Blown-out windows after a 2012 shooting at Sandy Hook Elementary School in Newtown, Connecticut.

PHOTO: CONNECTICUT STATE POLICE/REUTERS

PUBLIC HEALTH

NRA donations spike in school shooting counties

Parallel surges for a gun control advocacy group not seen

By **Meredith Wadman**

School shootings are tragically familiar in the United States. But a new analysis shows they have a startling consequence. In the very counties where they occur, the National Rifle Association (NRA) sees a surge in donation amounts and in new donors that lasts several years after shootings, according to an analysis of 131 school shootings with at least one fatality between 2000 and 2022.

The finding, published this week in *Science Advances*, echoes well-documented surges in gun purchases and donations to NRA, the leading U.S. gun rights lobbyist, after mass shootings. But the hyperlocal effect is new and revealing, researchers not involved in the study say. "Either there's a fear … that someone is going to take your gun away … and/or a fear that you are somehow less safe and therefore need more guns," says Kerri Raissian, who directs the Center for Advancing Research, Methods, and Scholarship in Gun Injury Prevention at the University of Connecticut. "It says that there is something about this event happening in your county, local to you, that makes this threat more real."

Tobias Roemer, a Ph.D. student in political science at the University of Oxford, which funded the study, used a U.S. Federal Election Commission database to track donations after school shootings in 131 counties as well as in the 2758 counties without such school shootings. He found that donations to NRA's political action committee, the Political Victory Fund, climbed on average $970 per year in the affected counties in the 4 years following a school shooting. The number of individual donors in those counties grew by as much as 40%. He found no parallel surges in NRA donors and donations in unaffected counties. At the same time, donations to the political action committee of Giffords, which lobbies for gun control and research, did not increase in affected counties.

Roemer also found no increase in donations to organizations unconnected to guns, such as antiabortion and abortion rights groups, which ruled out other causes of a more general giving increase, such as a tax benefit deadline. To judge whether donors were responding to active NRA solicitations, he examined the group's advertising buys on Facebook and Instagram and found no increases in the weeks after shootings. Roemer says his paper "focuses on a tangible variable. Money is real. It's not cheap talk."

The results come even as NRA, which did not respond to requests for comment, deals with an ongoing fraud lawsuit from New York state's attorney general.

The study "introduces a novel data set and a very compelling, straightforward … analysis," says Bradley Bartos, a criminologist at the University of Arizona who wrote an accompanying editorial. Laura García-Montoya, a political scientist at the University of Toronto, conducted a similar county-level study published in 2021 that found school shootings with multiple victims drive increases in Democratic electoral support in those counties. The new paper "is showing the other side of the spectrum," she says, adding that the new findings "make a really powerful statement … that … people who support gun rights also feel threatened by school shootings and so they feel the need to help their interest group."

Some academic critics argued the absence of a surge in donations to the Giffords organization does not mean the shootings had no effect on support for gun safety. The group was launched in 2013 and at that time had far lower name recognition than the 150-year-old NRA. And it represents only a slice of the gun control lobby, being one of three leading gun control groups that together outraised NRA by $10 million in the 2021–22 election cycle.

"The paper unfortunately relies on arbitrary slices of data to reach obviously flawed conclusions," says Chris Harris, vice president of communications at Giffords. "Knowledgeable observers on both sides of the gun debate know that the gun safety movement is growing exponentially while the NRA suffers from shrinking membership rolls and shrinking bank accounts." ■

BIOMEDICINE

‘Gene drive’ may help fight viruses with viruses

CRISPR-engineered herpesviruses can speed spread of genes to viral relatives in mice

By **Jon Cohen**

If your immune system or drugs can’t stop a viral infection, why not pit a virus against itself? That’s the provocative idea several labs are pursuing. They are studying whether deliberately introducing engineered viruses into people infected with their natural relatives can “drive” a foreign gene into those viruses that ultimately wipes out an infection.

No lab has knocked down an infection in animals this way yet. But a group has now shown it’s theoretically possible, using a so-called gene drive that harnesses the genome editor CRISPR to perform molecular surgery that spreads a gene among viruses.

So far, efforts to add gene drives to animals such as rodents and mosquitoes to control their numbers have drawn the most attention. In a preprint this month, however, one team reports a similar feat with herpesvirus-1 (HSV-1) in mice. When both engineered and unmodified herpesviruses were inoculated into the rodents, the gene drive converted up to 90% of the viruses—possibly enough to prevent an HSV-1 infection from causing symptoms such as painful cold sores. A second group has succeeded in putting gene drives into HSV-1 that is growing in infected cells in lab dishes.

The viral gene drive work is a long way from curing an infected person. No one knows, for example, what kind of genetic modification the drive should propagate to drive down an infection. But other scientists see its potential. The new studies are “compelling,” says Rebecca Shapiro, a molecular microbiologist at the University of Guelph who has experimented with gene drives in fungi. “This opens up a lot of exciting avenues to use these kinds of gene drive techniques to modify viral populations, and possibly use them as new therapeutics.”

Researchers have developed gene drives mostly in animals that sexually reproduce. They’ve created genetically modified females or males whose odds of spreading a gene to their offspring are significantly higher than 50%—the typical Mendelian chance that a descendant will inherit a particular gene variant. Most experiments aim to spread modifications that kill the offspring or render them sterile, a possible strategy for pest control. This work has only been done in labs so far, however, because of concerns that releasing animals with gene drives could have dire consequences, such as accidentally wiping out an entire species or harming animals that aren’t the target.

Unlike people, viruses don’t have gene-scrambling sex with each other when they replicate. They simply command infected cells to read their genes and produce new viruses. But if multiple virions infect a single cell—as happens with herpesviruses—they often do something akin to sex, randomly swapping genetic sequences inside the nucleus. A gene drive hijacks this natural process, known as recombination, to introduce and spread genetic changes that might ultimately disable a whole population of viruses.

HSV-1, HSV-2, human cytomegalovirus (hCMV), Epstein-Barr virus, and other herpesviruses are particularly attractive candidates for tackling with a gene drive because they can cause lifelong, latent infections that periodically flare and cause symptomatic disease. Some drugs can tamp down viral reactivation, but in people who have compromised immune systems, those drugs often fail and herpesviruses run riot, damaging many parts of the body and even causing death. This is a particular problem with people who have untreated HIV infections or receive organ or bone marrow transplants.

Three years ago, virologists Marius Walter and Eric Verdin at the Buck Institute for Research on Aging demonstrated that a gene drive might be feasible in a herpesvirus. They showed in cell culture experiments that hCMVs endowed with a gene drive built from CRISPR could spread the drive to other hCMVs in infected cells. The gene drive mainly consisted of genetic sequences coding for CRISPR’s two components: a DNA-cutting enzyme known as Cas and a guide RNA that directs the enzyme to a specific place in a viral genome, where it makes a break, enabling a copy of the CRISPR-Cas genetic cassette to insert itself. The researchers attached a gene for a fluorescent marker to the complex so they could track the drive as a chain reaction spread it to yet more herpesviruses.

The study also hinted that a gene drive could reduce, if not eliminate, a viral population. The guide RNA shuttled the drive to park inside a specific viral gene, one encoding a protein that protects the pathogen from immune attack. The insertion disabled the gene, reducing levels of the protective protein and rendering the virus more vulnerable.

The paper, which appeared in *Nature*

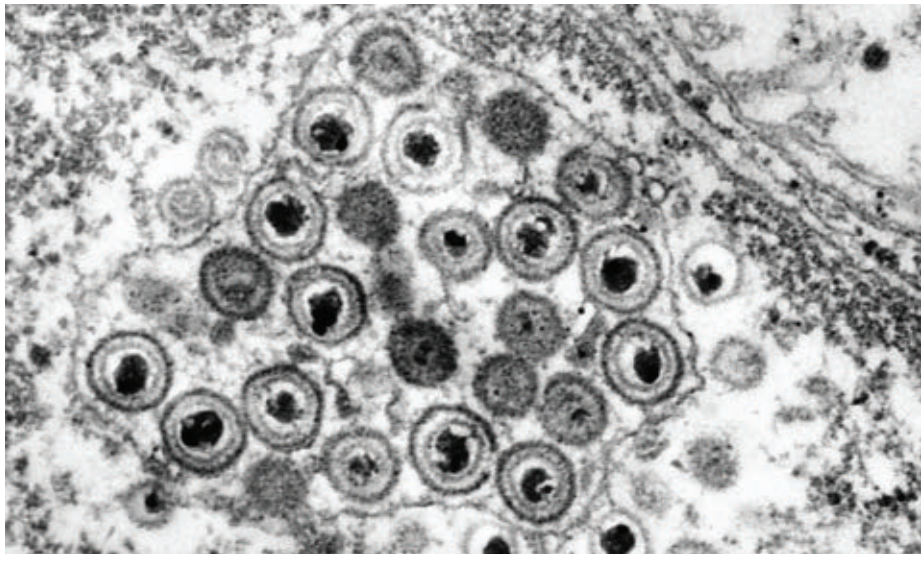

When multiple herpesviruses infect a cell’s nucleus (shown here), they sometimes exchange genes, a behavior a “gene drive” might exploit to wipe them out.

PHOTO: SCIENCE HISTORY IMAGES/ALAMY

Communications in September 2020, received scant attention. "Publishing a paper during a pandemic that's happening with another virus is not a great way of having people notice it," says Walter, who was a postdoctoral researcher in Verdin's lab and has since moved to Keith Jerome's lab at the Fred Hutchinson Cancer Center.

The few researchers who did read it were skeptical, questioning whether a viral gene drive would cripple enough viruses to meaningfully reduce the population, Verdin recalls. "One of the arguments that we heard is, 'Oh, you're never going have enough of the two viruses together in this same cell to actually make it work.'" But the 8 December preprint by Walter, Verdin, Jerome, and colleagues now shows that in at least some infected mouse tissues, a gene drive can spread genes through much of the viral population.

Walter and Verdin view their work as a proof-of-concept experiment, as does a team led by virologist Dai Hongsheng of China's Southern Medical University and his colleagues, which describes its cell culture success with an HSV-1 gene drive in a 4 December preprint on bioRxiv. In tissue cultures, HSV-1 gene drives worked better than the hCMV ones, Dai notes. "The gene drive in HSV-1 spread steadily and at a speed not achievable with hCMV," he says.

But the mouse experiment suggests the HSV-1 gene drive needs to move even faster. As shown by the fluorescent marker gene it carried, the drive spread at different rates across the mice's body regions, with the variation being most pronounced in the brain: In the cortex, the marker propagated to 25% of the viruses, whereas it ended up in as much as 90% of the viruses in the brain stem. Nonetheless, Walter believes the results suggest the technology might one day help people. "You have enough coinfection occurring in vivo for a gene drive to be something that we can potentially use," he says.

All of the involved researchers stress that gene drives for herpesviruses are far from ready for tests in humans. Walter plans future experiments in animal models, hoping to show whether a gene drive can suppress a chronic HSV-1 infection enough to prevent reactivation and disease.

Britt Glaunsinger, a biochemist at the University of California, Berkeley who specializes in studying herpesviruses, sees the promise of the concept, but cautions that the modified viruses could cause disease themselves—especially in immunocompromised people—if the gene drive does not sufficiently weaken the viruses it targets. Still, she wrote in an email, "I look forward to seeing where the field takes this!" ■

WORKFORCE

NIH advisory group pushes for big pay raise for U.S. postdocs

Though applauded by many, measure would strain lab budgets if adopted

By **Katie Langin**

The postdocs who do much of the labor of academic science have long felt overworked and underpaid. If an advisory group to the U.S. National Institutes of Health (NIH) gets its way, conditions for some of these early-career scientists will soon improve. The minimum starting salaries of NIH-supported postdocs should increase to $70,000 in 2024, up from the current minimum of $56,484, the group concluded in a report released last week. "We feel that this is crucial to … protect the U.S. biomedical competitiveness," said co-chair Shelley Berger, an epigeneticist at the University of Pennsylvania, during the presentation unveiling the recommendations.

The group also recommended a 5-year cap on postdoc positions; an expansion of health care, retirement, and child care benefits; increased support for international postdocs; and other measures to improve postdocs' lot. But how lab heads would pay their staff more out of their constrained research grants remains an open question. An NIH spokesperson says the agency's new director, Monica Bertagnolli, will carefully review the report with her leadership team.

Many of the recommendations echo those of a 2012 NIH advisory group. The urgency is greater now, working group members say. "This time will be different because the economy is different," says one, economist Donna Ginther at the University of Kansas. "Potential postdoctoral scholars are skipping the postdoc altogether because they can make more money [elsewhere]."

The proposed salary increase was overdue, some postdocs say. "It has long been clear that systemic change is necessary," says University of California, Santa Cruz postdoc Neal Sweeney, who is president of the union that represents UC postdocs. Postdoc unions at UC and elsewhere have already won raises.

Many PIs see the need for change, but are also left wondering how they would maintain their research programs given the higher postdoc salaries. After the presentation, several attendees worried that junior professors and underresourced institutions such as historically Black colleges and universities might particularly struggle. One attendee also wondered whether the proposed 5-year cap on postdoc positions was feasible given the "practicalities in the real world."

Working group co-chair Tara Schwetz, NIH's deputy director for program coordination, planning, and strategic initiatives, acknowledged the recommendations, if enacted by NIH, "may result in fewer postdocs that are being supported." Given the limits of the budget, "We know that there are priorities and tough decisions that are going to have to be made." Schwetz also emphasized that "it's critical to engage other governmental agencies, organizations, institutions—they're going to be key partners in success."

At the end of the presentation, Bertagnolli emphasized that NIH took seriously its responsibility to "think long and hard" about unanticipated consequences of the proposed recommendations. "This is a big step. I completely agree a critical one. But we just want to do no harm." ■

Salary gap

The minimum salary for starting postdocs funded through the National Institutes of Health (NIH) has consistently been lower than the average starting salaries for U.S. biological and biomedical Ph.D.s in other sectors. A recommended increase would narrow the gap.

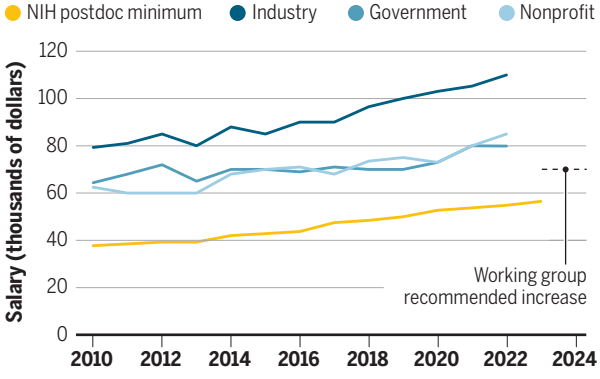

GRAPHIC: C. BICKEL/*SCIENCE*

PHOTO: DYLAN ROOD

Stickers aid the digital re-creation of precarious boulders at Lovejoy Buttes, near Los Angeles.

SEISMOLOGY

San Andreas fault may shake less than once feared

Precariously balanced rocks near Los Angeles hold clues to the hazard of a giant earthquake

By **Paul Voosen**, *in San Francisco*

Someday, a great earthquake will erupt from the San Andreas fault, which cuts through Southern California from Los Angeles to San Francisco. Geologic records make it clear. It has happened, and it will happen again.

But when the Big One does hit, it may be less devastating than once thought, at least near Los Angeles. According to new work presented last week at a meeting of the American Geophysical Union, the ground there will shake up to 65% less violently than official hazard models suggest.

The good news for Angelenos stems from five rocks balanced precariously on top of other rocks in Lovejoy Buttes, a place in northern Los Angeles County that sits just 15 kilometers from the fault. By dating when the rocks first became fragile and analyzing their structures to assess the maximum shaking they could withstand, the researchers could test official predictions against thousands of years of earthquakes. Those predictions have been found wanting, says Anna Rood, a seismic hazard scientist at the Global Earthquake Model Foundation who led the work, which is accepted in *Seismological Research Letters*. "The hazard estimates are totally inconsistent with these precariously balanced rock data."

The new study is a welcome advance for an emerging technique, says Daniel Trugman, a seismologist at the University of Nevada, Reno. "They've applied probably the most rigorous methodology that I've ever seen to try and solve this problem."

"This is good data," adds Mark Petersen, a geophysicist at the U.S. Geological Survey (USGS) who leads development of the U.S. National Seismic Hazard Model. It's too early to incorporate the findings when the hazard maps are updated next month, Petersen says, especially given the maps' conservative nature. But if the findings hold up, Rood says, "There are real implications for the people living in this area." Seismic hazard maps go into building codes, disaster preparation, and land use planning. And if you insure a house in California, she says, "They dictate what your premium will be."

For as long as scientists have sought to calculate seismic hazard, they have struggled to predict the shaking caused by the largest earthquakes, the one-in-10,000-year disasters evident in the geologic record but never experienced in modern times. Paleoseismic techniques offer limited help. Subtle sediment shifts seen in trenches dug across the faults record the ancient quakes but say nothing about the shaking that occurred, which is a complex function of the way a fault ruptures and the local geology. So seismologists construct their shake maps based on extrapolations from historical quakes. "The maps come from the best available science, but there's a lot of uncertainty in them," Trugman says.

The precarious rocks, however, actually witnessed the ancient quakes—and kept standing. Wind and water have eroded these granite rocks, often into hourglass shapes in which boulders perch on top of platforms. During trips in 2021 and 2022, Rood and her co-authors chiseled surfaces up and down the rocks and dated them by measuring levels of beryllium-10, an isotope created when rocks are exposed to the atmosphere and a steady bombardment of cosmic rays. By extracting dates from the narrow neck where the boulders meet their platform, they could determine when the rocks first became precarious. One rock, it turned out, had been teetering in its delicate position for 50,000 years. "That this rock has been recording and surviving these earthquake events for 50,000 years is a crazy amount of data," Rood says.

Like actors in a motion-capture movie, the rocks were also tagged with stickers so their shapes could be digitally re-created. By analyzing the shapes in structural models, the team calculated how much shaking they could take without toppling.

In 2020, Rood had conducted an analysis of precarious rocks along the Hosgri fault near California's Diablo Canyon Power Plant to gauge the earthquake threat to the plant's nuclear reactors. There, too, she found that the hazard was overstated. The large and repeated disagreements with the USGS hazard model suggest researchers may need to "go right back to the basics of earthquake science and check our fundamental understanding," she says.

The use of fragile features to probe past earthquakes is sure to grow. New Zealand has already used similar balanced rocks to lower its estimate of the hazard at Clyde Dam in Otago, the nation's third largest hydroelectric dam. The International Atomic Energy Agency will suggest using fragile features in its new seismic guidelines. And Devin McPhillips, a USGS earthquake geologist, is exploring how sea stacks, ghostly remnants of lost sea cliffs that are prone to collapse, can track the violence of ancient earthquakes along the Cascadia subduction zone in the Pacific Northwest.

Once these analyses mature, they will be able to weed out underperforming ground motion models, McPhillips says. And for now, Californians can enjoy a bit of positivity. "Big earthquakes do happen and will happen again in Southern California. I'm not looking forward to that day," he says. "But maybe I can hold out hope that it won't be quite as damaging." ■

INDIA

Before tunnel collapse, scientists sent warnings

Researchers repeatedly raised concerns about building in Himalayas' unstable geology

By **Athar Parvaiz**

Last month, government officials in India celebrated after rescue teams freed 41 construction workers who had been trapped underground for 17 days when a rock fall sealed a tunnel they were building beneath mountains in northern India. "Everyone involved in this mission has set an amazing example of humanity and teamwork," Indian Prime Minister Narendra Modi said in a statement posted on the social media platform X (formerly Twitter) after the 28 November rescue.

For many Indian researchers, however, the near-disaster was the predictable outcome of officials ignoring repeated warnings from scientists about the dangers of trying to carve what is called the Char Dham National Highway through the unstable geology of the Himalayas. They are hoping the collapse—and problems related to other infrastructure projects—will persuade the government to reconsider building practices, and strengthen a legal challenge to the Char Dham project currently before the nation's Supreme Court. "The repeated disasters … should prompt the government to re-evaluate construction plans and institute preventive measures," says environmental scientist Anjal Prakash of the Bharti Institute of Public Policy at the Indian School of Business.

The Char Dham road has fueled controversy since 2016, when the Modi government made the $1.9 billion effort to upgrade 900 kilometers of roads connecting four popular Hindu pilgrimage sites the centerpiece of a major economic development project. The plan called for widening roads, boring tunnels, and building more than 100 bridges and 3500 culverts in rugged terrain. It required extensive blasting, clearing forests, dumping tons of waste, and slicing massive roadcuts into steep hillsides—all activities that could trigger rockfalls, landslides and floods. But legal analysts say the government sidestepped requirements for a thorough environmental assessment by cutting the project into segments less than 100 kilometers long, below the threshold for review.

In 2019, however, legal challenges from environmental groups prompted the Supreme Court to appoint a 25-member High Powered Committee, led by Ravi Chopra, a prominent environmental scientist, to review the environmental impacts of the project, which was already underway. In a 2020 report, the panel reported that engineers had failed to analyze the geology and hydrology at numerous construction sites, leading to landslides and environmental damage. But the group delivered a split verdict on one contentious issue: the appropriate width of the pavement. A majority supported pavement 10 meters wide, whereas a minority led by Chopra recommended paving be limited to 5.5 meters to reduce safety risks and environmental harm.

After India's military argued it needed the broader roads to defend India's border, the Supreme Court in 2021 backed 10-meter pavement for much of the Char Dham project. In early 2022, Chopra resigned from the panel, writing that the experience had "shattered" his belief that the panel "could protect this fragile ecology," and that he suspected

Pilgrim's path

Much of the Char Dham road project is designed to ease access to Hindu pilgrimage sites in Badrinath, Kedarnath, Gangotri, and Yamunotri.

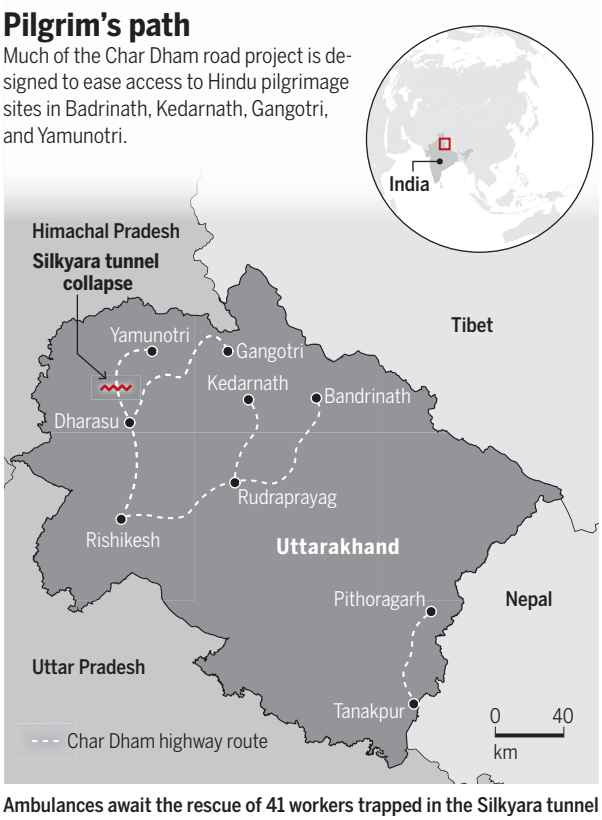

Ambulances await the rescue of 41 workers trapped in the Silkyara tunnel in late November.

CREDITS: (PHOTO) FRANCIS MASCARENHAS/REUTERS; (GRAPHIC) D. AN-PHAM/*SCIENCE*

construction officials would continue to ignore the panel's technical recommendations.

Other infrastructure-related disasters heightened such fears, says Navin Juyal, a former senior geologist at India's Physical Research Laboratory. For example, he says officials have built hydropower dams and other facilities in recently glaciated valleys above 2000 meters, despite warnings from scientists that such areas can be geologically unstable and prone to flooding (a warning echoed by the High Powered Committee). In 2021, a glacial outburst killed more than 140 workers at one such project, the Tapovan Vishnugad Hydropower Plant.

Worries about Char Dam have grown in recent years, especially after rains triggered landslides that caused fatalities. A study of one 250-kilometer-long segment in Uttarakhand found that, after heavy rains in late 2022, widened areas were twice as likely to experience slides than unwidened stretches. That is likely because roadcuts, blasting, and vegetation removal made slopes more likely to fail, the authors wrote in the preprint posted on the EGUsphere server in October.

Given that history, last month's collapse of the 4.5-kilometer-long highway Silkyara tunnel in the state of Uttarakhand came as no surprise to seismologist C. P. Rajendran of the National Institute of Advanced Studies. The tunnel "is itself an example of shoddy construction that ignored the preliminary geological report that warned against the dominating presence of weak unstable rock wedges in the region," he says.

India's Ministry of Road Transport and Highways did not respond to a request for comment. But government officials have told Indian media that engineers were aware the tunnel traversed a "shear zone" of brittle rock. Earlier this month, the ministry appointed a five-member panel to investigate the collapse and report by the end of the month on needed safety measures for the Char Dham project, which is nearly 70% complete.

Rajendran is skeptical that the disaster will catalyze major changes in the government's plans. But the tunnel collapse "has attracted huge public interest," he says. "There is a realization that a disaster-prone road will neither serve any national security purpose nor make the pilgrimage safer." And he hopes the event will persuade the Supreme Court, which is hearing a challenge to the Char Dham project, to impose stiffer construction rules.

Environmental advocate Mallika Bhanot of Ganga Ahvaan, a citizen's group, says the tunnel collapse should teach a broader lesson: India's Himalayan region "can withstand no more unscientific development." ■

Athar Parvaiz is a journalist based in New Delhi and Srinagar.

PHOTO: ANUP SHAH/GETTY IMAGES

ANIMAL BEHAVIOR

Chimps remember faces of old friends and family for decades

Recognition ability rivals all other animals, including humans

By **Ann Gibbons**

Louise hadn't seen her sister or nephew for 26 years. Yet the moment she spotted them on a computer screen, she recognized them, staring hard at their faces. The feat might have been impressive enough for a human, but Louise is a bonobo—one who had spent most of her life at a separate sanctuary from these relatives.

The discovery, published this week in the *Proceedings of the National Academy of Sciences*, reveals that our closest primate cousins can remember the faces of friends and family for years, even decades. The study, experts say, shows that the capability for long-term social memory is not unique to people, as was long believed.

"It's a remarkable finding," says Frans de Waal, a primatologist at Emory University who was not involved with the work. "I'm not even sure we humans remember most individuals we haven't seen for 2 decades." The research, he says, raises the possibility that other animals can also do this, remembering far more than we give them credit for.

Chimpanzee twins Golden and Glitter groom each other in Tanzania.

Trying to figure out whether nonhuman primates remember a face isn't simple. You can't just ask them. So comparative psychologist Christopher Krupenye at Johns Hopkins University and colleagues used eye trackers, infrared cameras that noninvasively map a subject's gaze as they look at images of people or objects.

The scientists worked with 26 chimpanzees and bonobos living in four zoos or sanctuaries in Europe and Japan. The team showed the animals photos of the faces of two apes placed side by side on the screen at the same time for 3 seconds. Some images were of complete strangers; some were of close friends, foes, or family members who had once lived in their same social groups, but whom they hadn't seen in years.

The chimpanzees and bonobos gazed about a quarter-second, or 11% to 14%, longer at the faces of apes they used to know and associated with good times, compared with the faces of strangers. In some cases, the animal hadn't seen the ape depicted on the screen for 5 or 10 years—or, in Louise's case, for more than a quarter-century.

The flicker of recognition was quick but consistent, and matches findings with human infants, who gaze longer at faces of people they know. "It's like when you pass someone on the street you hadn't seen for years and you do a double take," says the study's lead author, Laura Lewis, an evolutionary anthropologist at the University of California, Berkeley. The animals looked longest at the images of apes with whom they had had positive relationships, such as former group mates who had groomed them or played with them. They did not linger as long on former sexual partners, distant acquaintances, or individuals who had hurt or scared them.

Other animals, such as dolphins, elephants, and dogs, use sound or smell to recognize another familiar individual's call or scent. But the ability to use visual cues to remember a friend's face years after parting has long been seen as unique to humans and critical to our ancestors' survival, de Waal says. Humans who recognized a friend or foe could renew alliances and trade food or other goods in hard times, he says. Chimpanzees form large, hierarchical groups, which often break up into smaller groups whose members come and go, sometimes with power struggles. So it makes sense that remembering friends would benefit chimps as well, de Waal says.

Young apes go through intense phases of social learning, similar to human teens, says Rachna Reddy, a biological anthropologist at the University of Utah who was not involved with the work. That may help them make distinctions about whom to trust, she says, particularly for young females in preparation for when they leave their birth group. This study, she says, opens "a window into the incredibly rich interior emotional life of chimpanzees." ■

FEATURES

Ettore Majorana theorized a particle that was its own antiparticle—an idea that could bolster fragile quantum computers.

THE QUANTUM PHANTOM

A ghostly quasiparticle rooted in a century-old Italian mystery could unlock quantum computing's potential—if only it could be pinned down

By **Zack Savitsky**, *in Santa Barbara, California*

Reclusive and disaffected, Ettore Majorana liked to work in the shadows. But after his friend Emilio Segrè dragged him into Enrico Fermi's elite Roman physics club in the late 1920s, Majorana's stature in atomic physics quickly grew. His mostly unpublished premonitions were eerily prescient: Among others, he famously intuited the existence of the neutron from prior experiments. And in 1937, he conjured up a completely new kind of particle. Physicists had learned that every fundamental particle seems to have an antimatter counterpart, an idea Segrè would later earn a Nobel Prize for verifying. Majorana realized the equation that leads to this duality could also describe a single particle with identical matter and antimatter personas, making it prone to annihilate itself.

Months later, the 31-year-old withdrew a large sum from his bank account, took a boat across the Tyrrhenian Sea, and vanished. To this day, nobody's sure what happened to him, and the jury is also still out on whether his proposed particle exists. For example, some physicists still believe the neutrino—a wispy particle that pervades the universe—might be its own antiparticle, which could also help explain why the universe is filled with more matter than antimatter. But tests have so far proved inconclusive.

However, scientists think they are close to approximating a Majorana particle in a much different guise. By confining electrons on flat surfaces, researchers can coax them into peculiar dances that collectively masquerade as a Majorana particle, much as the undulations of a flock of birds might appear like a swimming fish.

If this Majorana quasiparticle could be corralled and controlled, the payoff would be twofold. It's a chance to manifest exotic physics, a thrill on par with smashing out new particles in a collider. More tangibly, the electron dances also promise to fortify quantum computers, transforming the frail devices into practical machines that can realize their promise of vastly speeding up certain computations and simulating the true nature of reality. "It's such a surprising thing that electrons will do this," says Charlie Marcus, a University of Washington physicist and veteran of Majorana research. "And if it turns out that it's really beneficial for quantum computing … that feels like frosting on the cake."

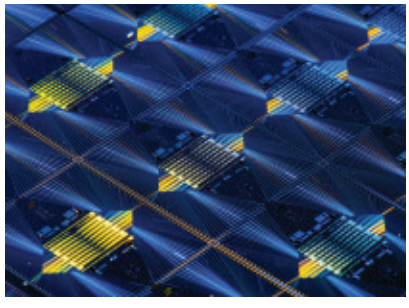

Tiny superconducting loops power Google's Sycamore quantum chips, but they are plagued with errors.

The epicenter for the Majorana hunt is here, in this cushy Southern California beach town that has seen an influx of hundreds of well-paid corporate scientists. Inside a stark black building with tinted windows, Google researchers attempt to engineer the quasiparticle on supercooled chips encased in chilling systems that look like chandeliers. Across the parking lot, Microsoft researchers work to lure it to the ends of a wire 1000 times thinner than a strand of hair. Down the street, scientists at the University of California, Santa Barbara (UCSB) aim to trap it with pencil lead and Scotch tape. They're all pretty sure they've got it—and that they're one step ahead of everybody else.

But like the 85-year hunt for Majorana himself, the field has yet to deliver on tantalizing leads. Contentious false alarms and a muddy mix of corporate and academic interests have left researchers raw and bruised—even as they say they are on the cusp of a breakthrough. "It's a field that has had some hiccups," says Jason Alicea, a theoretical physicist at the California Institute of Technology (Caltech). "But there's a lot of new tendrils that are opening up. There's so much beautiful physics that's waiting to be revealed."

AT AN ATOMIC LEVEL, 2D slices of solid materials can be thought of as giant checkerboards in which the pieces are electrons and the vacant spaces are "holes," which behave like positively charged electrons. Under the right conditions, the motion of electrons and holes can synchronize to behave as a single quasiparticle, in which fragments of the electron appear as if they are physically separated. These quasiparticles are sometimes dubbed "anyons" for their seeming ability to do anything.

A subset of these anyons, for instance, can perform truly unforgettable dances. Split an electron into two virtual pieces and swap their places, and you'll subtly change their identities. When brought back together, the fragments might merge into a single electron—or they might disappear into the vacuum. Shuffling them shifts the probability that they'll converge to make something or nothing, and the outcome depends on all the prior dances they've ever shared with other partners. In this sense, twirling these particles leaves a trail of their past movements, much like braiding hair, in which the order of operations is preserved even if the braid is twisted or tugged. The particles' history is woven into the system's topology, or mathematical shape.

IMAGES: GOOGLE; (OPPOSITE PAGE) OLENA SHMAHALO

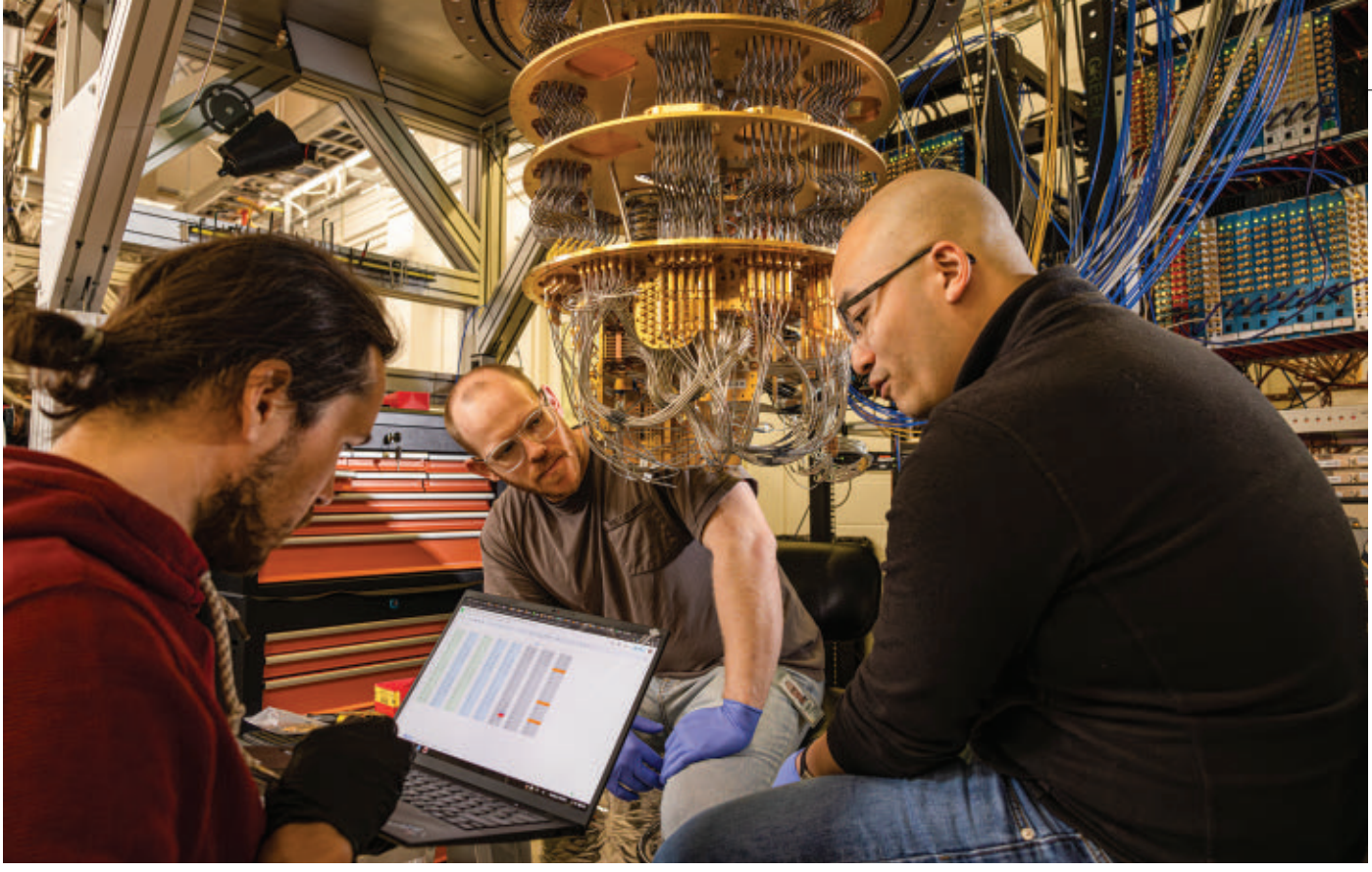

Google engineers huddle under a cooling system designed to chill quantum chips to temperatures colder than the depths of space.

Thanks to a paper in 1997 by the physicist Alexei Kitaev, then at Russia's Landau Institute for Theoretical Physics, this strange electron choreography became the blueprint for a new kind of computer.

Traditional computers rely on transistors, switches that turn electricity off and on, encoding either a 0 or a 1—a "bit" of information. Connect these switches in the right way, and the machine can run any conceivable calculation, although exceptionally complex tasks could take billions of years.

Quantum computers promise to speed up the process by exploiting the strange rules of quantum physics. If your quantum-bit, or "qubit," is made from an object like an atom, it can embody many different superpositions of 0 and 1 states. A relatively small array of qubits, linked through a process called entanglement, can encode a vast number of possible computations. For certain questions, scientists can manipulate those qubits using algorithms that boost the probability of them settling on the correct answer.

In theory, tasks such as simulating chemical interactions and factoring large numbers (the basis for modern cryptography) suddenly become a lot more manageable—making quantum computers both a lucrative gadget and a national security threat.

The catch is that qubits are fragile. Environmental noise can easily disturb them, leading to erroneous changes in their properties or a premature collapse to a definite 0 or 1 state. Because the qubits are entangled, these errors spread like wildfire, and the entire computation goes kaput.

Standard quantum firefighting calls for redundant qubits to correct the errors, but that's proving to be an epic challenge. The heartiest proto–quantum computers today boast hundreds of qubits, far short of the millions or billions they will probably need to operate error-free. "It is turning out to be an engineering nightmare," says Sankar Das Sarma, a theoretical physicist at the University of Maryland.

Kitaev proposed a clever workaround to the problem. In his scheme, the qubits would consist not of atoms, but those special anyon pairs, which can capture quantum information in their dissociated electrons. By entangling multiple anyons and nudging them through the braided series of dances, you can perform calculations that settle on the right answer—which is finally read out by revealing whether the anyons merged into an electron (a 1) or nothing (a 0). Because the electron is effectively split and doesn't exist in any one place, it is impervious to local disturbances.

The challenge then becomes how to get an electron to scatter its tracks so deceivingly. The simplest way is to link an electron and a hole so perfectly that they form two separate entities that are each half-electron and half-hole. These quantum yin-yang particles, both identical and opposite, much like the particles Majorana posited, would have no energy and no charge. With zero energy, the paired quasiparticles would rest securely in a gap between the positive and negative energy levels where electrons and holes can exist, offering extra protection from the noisy world.

Kitaev's idea of harnessing the quasiparticles' built-in error protection is now known as topological quantum computing, and some believe it's the technology's best hope. Without the Majorana at its core, "I personally do not see any hope ever of building a true fault-tolerant quantum computer," Das Sarma says. "Some revolutionary advance is needed."

Around 2004, UCSB mathematician Mike Freedman wrote a letter directly to Microsoft founder Bill Gates promoting the idea of topological quantum computing. A year or so later, the company boldly bought in and established Station Q, initially just a five-person team that met in a seminar room inside the hexagonal oceanfront tower of the prestigious Kavli Institute for Theoretical Physics, which juts out from the UCSB campus like a lighthouse. With a seemingly limitless budget and free range to explore wild ideas, the group was the envy of the fledgling world of topological computing, says Zhenghan Wang, a UCSB mathematician and founding member of Station Q. "It was the perfect place."

BEFORE ETTORE MAJORANA vanished in 1938, he sent a series of cryptic messages to

PHOTO: GOOGLE

his family and colleagues about his impending "sudden disappearance," leading many to suspect he'd taken his own life. But over the following years, purported sightings of Majorana multiplied: as a beggar in Naples, a monk in Calabria, and a vagabond in South America. The search for the ghost of his particle has been similarly confounded by impostors. "There are many, many papers … all of them claim it's Majorana," Das Sarma says. "None of them is Majorana."

Microsoft's opening strategy was to take advantage of the fractional quantum Hall effect, a peculiar behavior of electrons in 2D systems. Under a high magnetic field, electrons in the material take on specific energy levels, and each level can hold a maximum number of electrons. The electrons rearrange themselves to avoid one another, creating a sort of quantum fluid with properties that depend on how large a fraction of a given energy level is filled. If you half-fill the second energy level, for instance, a slight change in the magnetic field should induce ripples in the fluid that seem to be quarter-electron charges, each of which is associated with a Majorana quasiparticle.

Microsoft researchers began to look for these fractional charges in samples of gallium arsenide, a compound often used in solar cells. But after years of trying, scientists couldn't get the material to cooperate: The Majorana's protective energy gap was too small, and applying electrical gates to wrangle the quasiparticles into any useful dance was too challenging.

Just as hope started to wane for the quantum Hall approach, a new proposal emerged: wrapping a superthin nanowire in a fancy superconducting jacket, which allows the electrons inside to link up in a long, single-file chain of pairs. If there's an odd number of electrons in the wire, the unpaired electron should essentially split in half to form two separated Majorana quasiparticles—one at each end of the wire. If you then lay multiple wires across each other in lattice-like frameworks, you can get the Majoranas to dance and braid by having them hop between intersections.

The Microsoft team readily changed horses and began to fund nanowire research. In 2012, one team, led by Leo Kouwenhoven, a physicist at the Delft University of Technology, varied the voltage across the tip of their wire from negative to positive values and reported seeing a small peak in conductance at zero—evidence, they thought, of Majorana pairs residing at zero energy. But theorists soon realized other less interesting electron quasiparticles could also hover around zero energy and mimic that same signature. It was the first of many Majorana mirages.

Some theorists argued that the real Majorana would have a clear signature: a zero-energy conductance peak at a specific value. In 2018, Kouwenhoven's group measured that mark, which at the time was considered a "smoking gun," he says. Microsoft crowned Kouwenhoven the founding director of its new campus in Delft. The company's vice president predicted they'd have a working topological qubit later that year and urged the Department of Energy to invest in the blossoming "quantum economy."

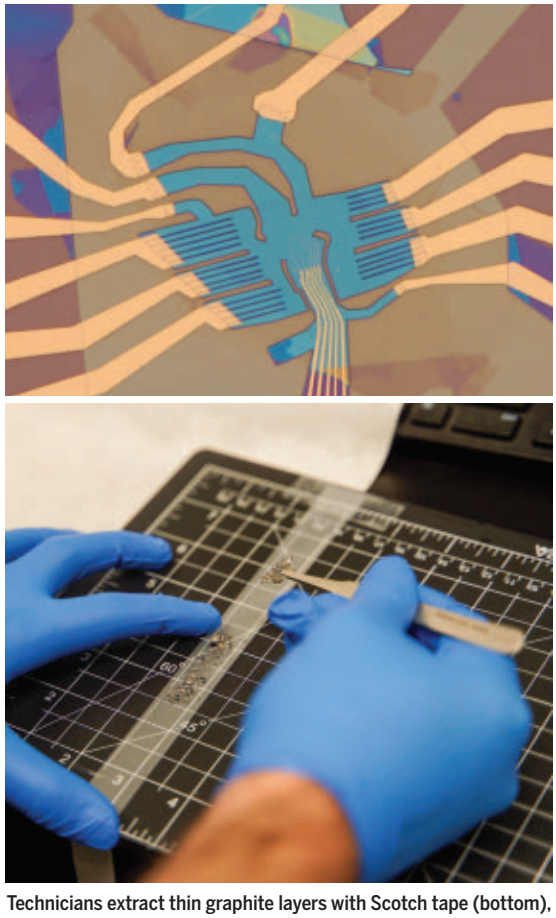

Technicians extract thin graphite layers with Scotch tape (bottom), then carve electrical gates (top) to coax Majoranas into qubits.

PHOTOS: (TOP TO BOTTOM) LIAM COHEN/UCSB; ZACK SAVITSKY

But then the bubble popped. The signal was again shown to be inconclusive. Soon after, Kouwenhoven's paper fell under scrutiny for alleged data manipulation and in 2021 was retracted by *Nature*, which cited a combination of confirmation bias and instrumental miscalibration. In the following years, two similar claims from other groups were retracted by *Nature* and *Science*, and a fourth paper led by Marcus received an editorial expression of concern in *Science*.

The reason researchers kept getting fooled, Kouwenhoven maintains, is that they focused on finding certain signatures without fully understanding the underlying mechanisms. "We jumped over a huge amount of physics," he says. Other scientists suggest the problem runs deeper, pointing to the pressure to deliver results and publish in high-impact journals. Chris Palmstrøm, a UCSB physicist who manufactures nanowires for many experiments, traces it to Microsoft's overzealous push to demonstrate a topological qubit. "They were trying to run before they could crawl," he says. "It was perhaps too early to promise all of this."

Around the time many of these claims fell apart, Microsoft had a culture change. Chetan Nayak, a Microsoft physicist since the dawn of Station Q, took over from Freedman as engineering lead with a business-oriented vision that would focus on commercialization while guarding against intellectual property leaks. "We're not in a mode of exploration," Nayak says. "You need to have everyone focused on this journey, and that's not going to happen with a bunch of academic labs." Microsoft eventually cut most of its funding for its university collaborations and moved the bulk of its quantum computing research in-house.

The shift drove many big names out of the game. "Early in the academic-corporate quantum space … we just had the best of both worlds," laments Marcus, who left Microsoft in 2021. "Then we grew up and the corporate experience changed." Kouwenhoven departed the following year. Earlier this year, Freedman also left Microsoft, and he recently joined the competing Google team across the parking lot.

Fiona Burnell, a theoretical physicist at the University of Minnesota Twin Cities, credits Microsoft's investments with helping lure her into the field, but says the company's secrecy complicates replication efforts. "It's a double-edged sword," she says. Microsoft's latest Majorana publication in June, for example, omits recipes for fabricating nanowires, which the company regards as trade secrets. "Of course, I wish that they would maintain more openness with the academic community," Alicea says. "But maybe it's impossible."

IN 2011, the public prosecutor's office in Rome reopened its investigation into Ettore Majorana's disappearance. Detectives had come across an alleged photograph of

A search for tenacious qubits

Majorana quasiparticles, made from pairs of fractional electrons, could in theory embody the quantum bits (qubits) in an error-free quantum computer. The physical separation of the fractional electrons should protect the quantum information they hold from heat and noise, and computations occur by swapping or braiding their positions. Researchers are hunting for the quasiparticles in three systems.

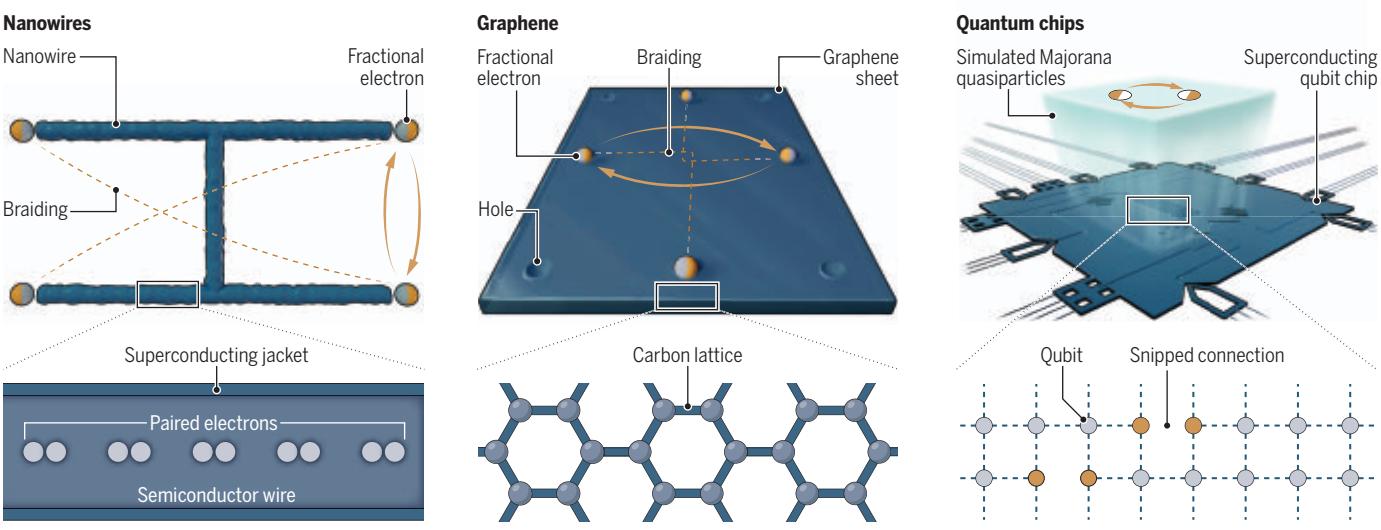

Pairing up electrons within an ultrathin wire can leave an unpaired electron at either end that virtually splits to form Majorana quasiparticles at each end. Shunting them along a nanowire lattice creates braids in the original Majorana pairs.

When magnetic fields are applied to graphene, a single-atom layer of carbon, electrons and positively charged "holes" can virtually split into Majorana pairs. The pairs may be more immune to heat than those in nanowires but harder to control.

Some quantum computing chips consist of error-prone superconducting qubits. Snipping connections between them can simulate the presence of Majorana quasiparticles and distribute information across the qubit array, thereby protecting it.

Majorana from 1955 in Venezuela, where he had supposedly been living under the alias "Mr. Bini." They attempted to match the man's facial structure to an old photo of Majorana and concluded that he had run away to South America, perhaps because he foresaw how his colleagues' work on atomic energy could lead to nuclear weapons. Content with the explanation, the prosecutor's office officially closed the case in 2015. But many were left dissatisfied. Francesco Guerra, a physicist at the Sapienza University of Rome who continues to investigate the case, says the conclusion was "completely ridiculous."

Majorana researchers, similarly vexed by the low standard of evidence, are now pushing to raise the bar. "A photo is not enough," Kouwenhoven says. "We need DNA evidence." The growing agreement is that the only conclusive signature of Majoranas would be to get them to work as qubits. "It's braiding or bust," says Andrea Young, a UCSB physicist.

The present search for Majoranas is proceeding along three primary avenues. The first is the continued effort in nanowires, a torch largely carried by Microsoft. In their June paper, Microsoft researchers reported progress in making their nanowire Majoranas more robust, a feat Nayak likened in a LinkedIn post to "inventing steel."

The Majorana's protection depends on the size of the gap between the quasiparticles' zero-energy state and the electrons' closest available energy level. If the gap is too small, tiny temperature variations will inject energy that can either destroy the Majoranas or create unwanted quasiparticles that might mess with the Majorana signal, particularly if the wire's ends aren't sufficiently separated.

The Microsoft researchers measured the energy gap of their nanowires at 30 microelectronvolts, above the 10 μev needed for them to be confident the signal is real. The next steps are to show that a pair of Majoranas can merge to a 0 or 1 state and to braid two Majorana pairs into a functional qubit. Nayak believes his team can do both. "Internally, we're very convinced," he says. "We're kind of off to the races with this."

The community, however, is largely withholding applause. Some continue to shame Microsoft for safeguarding fabrication methods and parts of its simulations. Others complain the wire is still not clean or long enough to prevent internal disorder in the wire from triggering spurious signals. But even assuming the signal is from Majoranas, the tiny energy gap Microsoft reported would offer limited protection in real world operations, says Mike Zaletel, a theorist at UC Berkeley who previously worked on the nanowires at Station Q. "It's hard to see that they would have a very robust qubit with a gap that small."

At the nearby UCSB, Young is taking a wholly different route to Majorana quasiparticles, one that revives the fractional quantum Hall effect, but in graphene instead of gallium arsenide. Graphene, an atom-thick layer of carbon arranged in a hexagonal array, was first discovered in 2004 when researchers peeled off a layer from graphite using nothing more than Scotch tape. Young and colleagues have since figured out how to stack slivers of graphene and other materials into perfectly clean sandwiches, providing a quantum Hall playground that's thinner than gallium arsenide, where electrons can more easily be coaxed to interact and split into quarter-charges. They also learned how to carve graphite crystals into intricate electrical gates, which they can place on top of their devices to trap and control the quasiparticles.

Recently, Young and colleagues measured the energy gap of the state where Majoranas are expected to form in their graphene, and found it to be about 10 times larger than Microsoft's gap. That should protect a graphene-based qubit at temperatures as high as 5 kelvin—relatively warm for quantum work like this, Young says. "It really finally feels like we have an avenue to attack this legitimately," he says. "I think we will be able to make a qubit without any miracles."

Ali Yazdani, a physicist at Princeton University working on similar graphene sandwiches, uses electron microscopes to create a map of how the energy gap varies across the graphene surface, offering a useful guide for where robust Majoranas might congregate. In a paper now under review, he and his col-

GRAPHIC: A. FISHER/*SCIENCE*

leagues identify multiple spots where the energy gap is "whoppingly huge," he says—even larger than Young's. The two groups have planned experiments to implant the quarter-electron charges and braid their accompanying Majoranas. "It's early days for taking this to the next level, but there is no clear showstopper," Yazdani says.

Already, the graphene efforts have offered "a breath of fresh air" to the community, Alicea says. "It's one of the most promising avenues that I've seen in a while." Since leaving Microsoft, Zaletel has shifted his focus to graphene. "It's clear that this is just where you should do it now," he says.

But not everyone believes they will have enough control over the free-moving quasiparticles in the graphene system to scale up to an array of qubits—or that they can create big enough gaps to keep out intruders. Manipulating the quarter-charge quasiparticles in graphene is much more complicated than moving the Majoranas at the ends of nanowires, Kouwenhoven says. "It's super interesting for physics, but for a quantum computer I don't see it."

Just across the parking lot from Station Q's new office, a third kind of Majorana hunt is underway. In an unassuming black building branded Google AI Quantum, past the company rock-climbing wall and surfboard rack, a dozen or so proto–quantum computers dangle from workstations, hidden inside their chandelier-like cooling systems. Their chips contain arrays of dozens of qubits based on a more conventional technology: tiny loops of superconducting wires through which current oscillates between two electrical states. These qubits, like other standard approaches, are beset with errors, but Google researchers are hoping they can marry the Majorana's innate error protection to their quantum chip.

Error correction on classical computers works by copying one bit's information to additional bits, but that's a challenge in quantum computers, because the laws of quantum mechanics forbid quantum states from being "cloned." Google's workaround (also conceived by Kitaev) is to get the array of qubits to act like a topological material and to store the information nonlocally, smearing it across many qubits so that it's not accessible from any single measurement. Recently, Google engineers brought the Majorana connection a step closer to reality with the help of Cornell University theorist Eun-Ah Kim.

In graduate school, Kim worked on designs for braiding anyons in quantum Hall systems, but she grew frustrated with the endless engineering hurdles. Last year, after Google researchers presented their latest qubit array at Cornell, "I realized that this is the setting where my dream can finally come true," Kim says. She and colleagues learned to group together patches of qubits within Google's array and then remove connections between individual qubits to create imperfections in the grid.

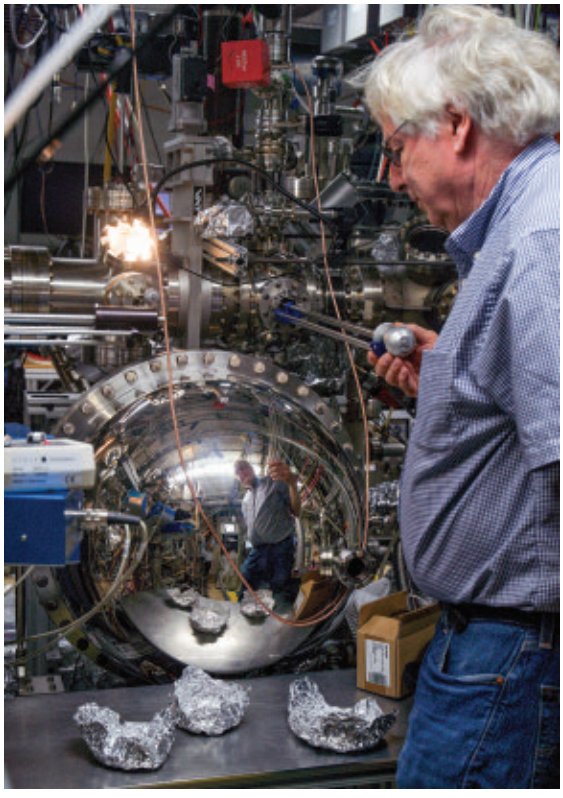

Chris Palmstrøm uses a vacuum-sealed apparatus to construct and clean nanowire devices that may hold Majorana quasiparticles.

In a *Nature* publication in May, the team demonstrated that twirling those imperfections shifts their properties much like braiding Majoranas. The company Quantinuum reported a similar experiment in a preprint around the same time.

Unlike naturally emergent Majoranas, these simulated ones are only stable while errors are manually corrected. But the distinction doesn't matter as long as they help protect the qubits, says Hartmut Neven, founding director of Google Quantum AI. "The question is: What is easier to do?" he asks. "Trying to do it on the low-level hardware is maybe the harder route."

The Google team has yet to use the scheme to actually detect and correct errors. Still, the experiment demonstrates scientists' growing command over quantum systems, Marcus says. "We're beginning to master fire."

OVER THE YEARS, accounts of Ettore Majorana's disappearance have degraded into baseless conspiracies and fictional spin-offs featuring alien abductions and time-travel machines. But Guerra and Nadia Robotti, a historian of physics at the University of Genoa, think the truth is out there. They have uncovered new documents from government, religious, and familial archives that seem to reference Majorana's death about 1 year after his disappearance. For example, one letter written by a Jesuit priest to Majorana's brother in 1939 honors "the mourned Ettore Majorana" and "the beloved extinct."

Guerra and Robotti still do not know where or how he died, but they think his descendants have documents that would shed more light. And 3 years ago, the researchers flew to UC Berkeley to visit the archive of Emilio Segrè, whose friendship with Majorana soured in the years before his disappearance. The researchers came across a folder that, per Segrè's instructions, cannot be opened until the year 2057. Guerra hopes it will contain details that will resolve the case once and for all.

The search for the Majorana quasiparticle is following a similar dynamic. Many researchers are jaded, including Palmstrøm, who says the field's spotty history has eroded his optimism. Even Kitaev, the pioneer, who now works at Caltech and consults for Google, has grown cynical. "Theoretically, it's just beautiful, but in practice it seems that we don't have a suitable technology to make it work well," he says.

And yet, many in the game can't seem to give up the hunt. Palmstrøm continues to meticulously prepare semiconductor nanowires for study, baking them in a foil-wrapped vacuum to expel unwanted gas molecules, scrubbing them with a pressure hose of atomic hydrogen to remove every last contaminating atom, and coating them with a thin superconducting jacket.

Like most Majorana researchers, Palmstrøm does not expect a single triumphant moment of discovery. But he's hooked on the hope that iterations of increasingly precise experiments will gradually bring the long-sought particle into focus.

"We're driven to find the truth," Palmstrøm says. "I think we will." ■

Zack Savitsky is a science journalist in Florida who covers physics and astronomy.

PHOTO: ZACK SAVITSKY

INSIGHTS

POLICY FORUM

Genomics-based detection of inbreeding among southern resident killer whales can help explain the population's lack of recovery.

50 YEARS OF THE ENDANGERED SPECIES ACT

A landmark environmental law looks ahead

In late December 1973, the United States enacted what some would come to call "the pitbull of environmental laws." In the 50 years since, the formidable regulatory teeth of the Endangered Species Act (ESA) have been credited with considerable successes, obliging agencies to draw upon the best available science to protect species and habitats. Yet human pressures continue to push the planet toward extinctions on a massive scale. With that prospect looming, and with scientific understanding ever changing, *Science* invited experts to discuss how the ESA has evolved and what its future might hold. **—Brad Wible**

Drawing from beyond the life sciences

By **Robert L. Fischman**[1] *and* **J. B. Ruhl**[2]

The ESA-implementing agencies, required by the ESA to follow the "best scientific and commercial data," enjoy respect for and build on long traditions of natural science expertise. Less often recognized is that many of the ESA's success stories drew mainly from the social sciences. These offer lessons for how to improve effectiveness of efforts under ESA.

Congress imposed prohibitions in the ESA that can create perverse incentives for landowners who face costs associated with the presence of protected species. For instance, because a certain minimum tree size is required for nesting by endangered red-cockaded woodpeckers, timberland owners were more likely to harvest trees before they reached that size and ESA protections were triggered (*1*). To reduce preemptive habitat suppression, in the 1990s the US Fish and Wildlife Service (USFWS) created a safe harbor program that encourages land managers to voluntarily provide habitat for species—even if temporary (e.g., trees big enough to host owl nests just until they grow to ideal harvest size)—in exchange for immunity from regulatory enforcement. This realigned incentives to generate greater conservation from private property (*2*).

Elinor Ostrom and others have documented the effectiveness of collaborative governance, typified by local, bottom-up, self-enforcing management approaches. The threat of ESA "harm" liability from incidentally injuring a protected animal can prompt large-scale multi-landowner projects that come closer in footprint to the range of a species than could any single property boundary. Rather than navigate ESA compliance property by property, landowners may devise a regional plan that will fulfill the statutory conservation man-

PHOTO: NOAA FISHERIES/VANCOUVER AQUARIUM VIA AP PHOTO

date if they receive immunity for activities consistent with the plan. In this way ESA-implementing agencies created the conditions to spur collaborative conservation efforts pooling economic benefits by leveraging local knowledge, habitat ownership, and less burdensome compliance measures (*3*).

Some ESA agency rules incorporate public-private plans or best-management practices that transform the ESA's harm prohibition—focused on difficult-to-detect consequences such as injury—into programs promoting best practices adapted to particular circumstances in specific places (*4*). For instance, it would be impractical to detect harm from agricultural activities, such as plowing, to California's Mazama pocket gophers nestled in their burrows. But a tailored rule shields from liability any "accepted agricultural or horticultural (farming) practices" if soil disturbance does not penetrate deeper than a foot. That provides a clear standard for both farmers and regulators to track and allows agricultural activities to coexist with species recovery.

Conservation treatments in wildlife management commonly incorporate adaptive management to fine-tune (or abandon) plans to recover or sustain wildlife, iterating to reduce uncertainty through learning by doing (*5*). Yet adaptive management is hardly used to improve the programs and rules themselves that spur and govern adaptive conservation plans. That risks innovation drift if effectiveness is never precisely defined, measured, and used to trigger reevaluation. Agencies have adequately applied science to understand what makes innovations work and to fine-tune agency behaviors. Sometimes conservation science agencies need to turn their observational tools on themselves.

Going forward, an important research priority for the ESA is to understand better how to prompt human behavioral changes. Mere statutory prohibitions are not enough. The agencies should employ lessons from empirically tested models outside of conservation biology, genetics, and other life sciences. Like all environmental law, the ESA is—first and foremost—law governing humans, not the forces of nature.

Updating practices for the genomic era

By **Brenna R. Forester[3], Tanya M. Lama[4], Marty Kardos[5]**

Genetic data have been used for decades in ESA decision-making, most commonly for taxonomy and the delineation of subspecific units. Technological advances have made much larger genomic datasets available for at-risk species, improving the precision and resolution of metrics such as genetic diversity, while bringing previously inaccessible parameters like adaptive differentiation and individual inbreeding within reach. Although inferences from genomics can present challenges to established ESA practices, they also provide opportunities for innovation (*6*).

Genomic data advance ESA implementation in three areas: identification of listable units (i.e., species, subspecies, and distinct population segments), assessments of viability, and development of recovery strategies. Adaptive genomics, which improves our understanding of adaptive differentiation and evolutionary potential, is already being used to inform these three objectives (*7*). For example, these data can help describe "significance" in the designation of distinct population segments, by characterizing a species' adaptive diversity and evolutionary legacy. In a recent case, a small genomic region was found to be associated with the seasonal timing of spawning migration runs, an important life-history trait in Pacific salmon. This discovery challenged established approaches for defining significance in salmonid conservation units, suggesting the need for finer-scale delineations to conserve fish with the early-run life history. However, lack of reproductive isolation and genome-wide similarity among fish with different phenotypes resulted in a recommendation to retain existing larger-scale units. Additional research identifying the dominance patterns and evolutionary history of this genomic region underscored the importance of established guidelines to conserve phenotypic diversity within units, ensuring that recovery actions prioritize retention of early-run alleles to prevent irreversible loss of the phenotype (*8*).

Viability assessments and recovery efforts are also being improved by advances in the detection of inbreeding (mating between close relatives). Small, reproductively isolated populations are particularly susceptible to reduced fitness due to inbreeding (i.e., inbreeding depression). Runs of homozygosity (ROH), large continuously homozygous regions in the genomes of inbred individuals, can now be identified through genomic analysis, and provide greater power to detect inbreeding depression than traditional, pregenomic approaches. For example, endangered southern resident killer whales having more ROH were found to have reduced survival, with population models suggesting that this inbreeding depression has limited population growth. These findings help explain the population's lack of recovery despite efforts to reduce extrinsic environmental threats (*9*). Genomic analysis of inbreeding can also be useful in cases where detailed demographic data are unavailable, for example, to identify declining populations with particularly high inbreeding that might benefit from recovery actions such as genetic rescue.

Genome-scale data will continue to be scarce for at-risk species given the magnitude of the biodiversity crisis. It is therefore critical that genomic inferences are evaluated in the context of population genetic theory, to allow more confident extrapolation to cases where data are lacking (*10*). For example, studies that link genomic variation to fitness can inform the development and validation of more widely and rapidly applicable proxies of genetic health and viability in at-risk species (*11*). Finally, we caution against reliance on advanced interventions such as cloning and gene editing, which are unlikely to be broadly applied to listed species. Across the data-availability spectrum, ensuring the viability of species before they become critically imperiled is best supported by time-tested conservation biology principles: maintaining intact habitats sufficient for large, connected populations across species' ranges to ensure the integrity of ecological and evolutionary processes.

Fostering international conservation

By **Grethel Aguilar Rojas[6]** *and* **Nicholas A. Robinson[7]**

The ESA nationally, and the Convention on International Trade in Endangered Species (CITES) worldwide, protect species at risk of extinction. Created together, these laws are entwined and symbiotic. Sixty years ago, Congress sought to update the Lacey Act of 1900, which criminalizes trade in wildlife taken in violation of state or foreign laws. Meanwhile the International Union for Conservation of Nature (IUCN) was proposing a treaty to curb trade of species listed on IUCN's Red List of Threatened Species. In 1972, IUCN's experts testified in Congress to support enactment of an Endangered Species Act. The US Department of Interior supported IUCN's proposals for a new treaty. The US Department of State led negotiations of the "Washington Convention on International Trade in Endangered Species of Wild Fauna and Flora," which nations signed on 3 March 1973.

On 19 December 1973, the US House of Representatives and Senate both approved the ESA (*12*).

Under the ESA, the USFWS lists species as endangered or threatened regardless of the country in which the species lives. ESA fosters scientific collaboration worldwide to gather data for both ESA's listings and listings under CITES. ESA thus fosters international conservation of habitats and species. Governments know more is needed. When the United Nations Decade on Ecosystem Restoration sunsets in 2030, governments aim to have protected 30% of Earth's ecosystems. In September 2023, 83 nations signed a treaty to conserve marine biodiversity on the high seas. The 2022 Kunming-Montreal Framework of the Convention on Biological Diversity (CBD) sets targets for national action through 2030. In 2015, the US joined 193 nations at the UN endorsing Sustainable Development Goal 15 to halt biodiversity loss by 2030.

This path toward 2030 began in 1973. The ESA established the federal Management and Scientific Authorities that implement CITES. When all 184 nations in CITES confer annually, they expose anew the sixth mass extinction of species. Acknowledging that more than the ESA-CITES approach is needed, IUCN stimulated the negotiation of further treaties, such as the 1979 Convention on Migratory Species (*12*). Expanding on the ESA's ethical premises, IUCN proposed a normative basis for further action, which the UN General Assembly adopted as the 1982 "World Charter for Nature" (*12*). This Charter prescribes principles for protecting genetic viability, ecosystems, and population levels sufficient for survival of species. On the basis of these principles, in 1990 IUCN again proposed a new treaty, which the UN launched as the CBD at the 1992 "Earth Summit" in Rio de Janeiro (*12*). Ironically, controversies about the spotted owl, listed as threatened under the ESA, blocked US plans to sign the CBD in Rio. In 1993, the US did sign the CBD, but Congress has yet to ratify it.

The plight of biodiversity is grave. Success in 2030 and beyond will depend upon rekindling the spirit of 1973.

Assisted migration—moving species by translocation

By **Patrick D. Shirey**[8] *and* **Gary A. Lamberti**[9]

Assisted migration is the intentional translocation of species outside of their recent range to mitigate environmental change, which could include climate change, impaired watersheds, or altered land use (*13*). Perhaps the most famous translocation within the United States is the snail darter (delisted in 2022)—which was moved outside of its historic range in the 1970s to mitigate Tellico Dam construction in the darter's habitat. Other examples include the Virginia roundleaf birch (agencies propagated and distributed seedlings to botanical gardens after the population dwindled to 40 trees), and the Tennessee coneflower (nurseries and botanical gardens helped propagate the species to reduce risk to wild populations and supplement the wild populations). Though the basic science and logic behind translocation are straightforward, the scientific evidence to suggest whether it overall does more good than harm, and if good, then how best to do it, has been unsettled. This challenge has led to calls for controlled experiments with adequate planning and monitoring to be included in management plans for imperiled species (*14*).

In the Endangered Species Act of 1973, Congress did not restrict translocation as a management tool. However, in 1984, at a time when the Reagan administration was concerned about imperiled species potentially restricting private property development, the USFWS placed a restriction on translocations such that experimental populations could not be introduced outside of a probable historic range unless the primary habitat of the species has been unsuitably and irreversibly altered or destroyed [49 FR 33893, 50 CFR §17.81(a) 1984] (*15*). One management challenge under this restriction is that the regulations did not define unsuitable and irreversible habitat destruction. However, this regulatory restriction only applied to plant species occurring on federal or state land; privately owned plants did not have such restrictions against movement unless being sold in interstate commerce, opening the door for citizen-initiated assisted migration of listed, imperiled plant species (*16*).

In 2010, we suggested that the USFWS revisit the experimental population restrictions because assisted migration could be a viable management option albeit with risks (*15*). In 2023, the USFWS changed the regulation to eliminate the historic range restriction (88 FR 42642), noting that establishing populations outside of a historical range is necessary to avoid extinction for species such as the Florida Key deer threatened by climate change, and the Guam rail and Guam kingfisher (sihek) threatened by the invasive brown tree snake. Under the 2023 rule, the agencies must demonstrate that the experimental population will further conservation of the species, and must monitor possible adverse effects to the ecosystem that may result from the experimental population being established outside of its historical range.

Though the experimental population regulatory changes were sensible measures to improve tools available to agency biologists, the risks of assisted migration warrant a precautionary approach that requires detailed planning prior to coordinated assisted migration of a species. This detailed planning includes updating older recovery plans (*17*) and addressing the problem of chronically underfunded species recovery efforts (*18*).

Harnessing economics for effective implementation

By **Amy W. Ando**[10]

Though the ESA precludes the use of economic analysis in making listing decisions, insights and tools from economics have helped to make management and policy related to the ESA more successful and trigger sweeping changes in many human behaviors including logging, development, and water use. For example, economics research has informed efforts to reduce perverse habitat destruction incentives created by the original ESA and helped to quantify the impacts, costs, and benefits of ESA protections (*19*). Because natural resource economics has powerful tools (both analytical theory and numerical optimization) for optimizing policy and management in the face of trade-offs, uncertainty, and human behavior, this discipline can contribute yet more to biodiversity conservation under the ESA in a world where habitats are complex and changing.

Economists are working with ecologists and scholars of water management on strategies to help species in complex aquatic habitats (*20*). Joint management of water resources and aquatic species can help to minimize the cost of protecting species; for example, when planning dam removal to improve salmon habitat and migration, considering hydropower benefits can help decision-makers choose sites for removal that minimize the social costs. And efforts to regulate water use to protect in-stream flows for species need to be careful not to regulate only one type of water use when users can shift to deplete other sources instead. Also, bioeconomic research can inform strategies to save migratory species (*21*). New

Whooping cranes in South Dakota take off during spring migration. Economics research can inform strategies to ensure availability of habitat during migration.

policies such as "pop-up" habitat modification (like flooding of rice fields) or permeability improvement (like taking down fences) during times that migratory species are passing through can draw upon economics to optimize the timing, location, and extent of temporary actions to maximize their net benefits to society. Economists can also help to clarify how the net benefits of a migratory species vary over its range, helping to set the stage for regional negotiations that ensure a species' survival is in the best interests of people throughout its entire range. Conservation plans for all species must account for habitat shifts that are happening because of climate change; a conservation portfolio approach to reserve site planning can efficiently help to ensure that species have supportive environments in an uncertain future (*22*).

Economics can also help move beyond emergency measures to save species that are on the brink of extinction. Ongoing research can help ESA policy-makers and managers to enhance efforts and institutions that encourage private land owners to engage in preemptive conservation that avoids the need for endangered species listing at all (*23*). For example, successful preemptive conservation is more likely to occur if action is taken to help coordinate multiple private landowners to avoid free-rider problems and to prompt conservation before the species is so endangered that success of preemption is costly and unlikely. Economics can inform strategic thinking about management strategies and policies once a species has been recovered enough to be taken off the list (*24*). For example, differentiating population requirements for a species across the states in its range can reduce the ongoing costs of supporting the species' survival, and ancillary policies such as compensation for direct and indirect damages from a species like the gray wolf can reduce private incentives to eradicate them.

Pushing boundaries with new interventions

By **Stephen Palumbi**[11] *and* **Michael Wara**[12]

Protecting the literal foundation of tropical reef ecosystems requires new interventions that push the boundaries of historic implementation of the ESA and will require careful exercise of agency discretion under the Act. At the same time, preservation of reef ecosystems can be viewed as part of a decades-long effort to shift ESA protections from a focus on individuals to species to whole ecosystems within the confines of the statute.

Originally ESA protections for corals, as for other taxa, focused on the need to conserve particular species and their habitats. Rapid decline of coral reefs owing to climate change–driven heatwaves has led to global efforts in coral protection and calls to restore reefs by growing corals in coastal nurseries. Yet these efforts rarely result in fully restored reefs, and many nursery-grown corals succumb to rising temperatures. A new strategy is to restore reefs with naturally occurring corals that exhibit resistance to heat damage (*25*). Breeding corals in aquaculture facilities for higher heat resistance, and hybridizing them with more heat-resistant species, are also underway. In addition, engineering corals by changing their symbionts or microbiome or through gene editing has been proposed and proof-of-concept research conducted.

Two coral species are fully protected under endangered species rules, and more are listed as threatened. How might coral interventions affect the protection of corals under the ESA (*26*)? Protecting and increasing species numbers in lab or zoo settings is in line with the ESA, as is adding individuals from different natural populations to enhance population diversity or adaptation (*26*). Adding new species may be more of a gray zone because they may supplant native corals under ESA protection, and thus may constitute a "take" under ESA regulation and require interagency consultation and permitting.

Breeding corals for higher heat tolerance in the lab through artificial selection may be similar to efforts to breed black-footed ferrets for disease resistance (*27*), a project underway with USFWS approval (though release of these animals has not happened yet). The van Oppen team in Australia took internal symbionts from corals into the lab (*28*) and evolved them over 10 years to be more resistant to high heat. They stripped corals of their regular symbionts and substituted the lab-evolved strains. A few colonies successfully integrated the lab-evolved symbionts and grew well under higher-temperature conditions. ESA protections currently regulate "infecting" endangered corals with manipulated symbionts, as well as placing them back out into the field (*26*).

Probably the most technically challenging of the possible interventions involves genetically engineering corals. Cleves and

PHOTO: GERRIT VYN/NPL/MINDEN PICTURES

colleagues (*29*) took a CRISPR injection rig to Australia for the few nights of coral spawning each year and injected thousands of eggs. Yet, such corals are not currently permitted to be released into the wild, and at this point there is no clear understanding of the genes that need to be altered to generate climate-resistant corals. In this case, if genes in the wild are found that confer climate protection, they can be used under the ESA. But creating those genes—even if it were possible—appears to be outside current ESA guidelines.

Both the environmental harm to corals and new approaches to saving coral reefs are advancing at an accelerating pace. For most of these interventions, permits for research or enhancement, incidental take, or interagency consultation mechanisms are built into the ESA system and can and should allow exploration of these new possibilities. An important opportunity for facilitating new conservation approaches could be the development of recovery plans for 15 Indo-Pacific coral species (*30*).

Many mechanisms within the ESA balance between protection and enhancement of populations. For the last half-century, the ESA has been fundamental in protecting species as they existed in the past. Attention must turn to adapting its implementation to preserve ecosystems for the future.

Learning to overcome barriers to adaptive management

By **Mark W. Schwartz[13]** *and* **Matthew A. Williamson[14]**

A core challenge for public agencies responsible for ESA implementation and enforcement is to clearly demonstrate success so as to be recognized by society as providing legitimate, effective governance. To be sure, species are recovering under the ESA. But how recovery funding drives that recovery is unclear. The USFWS has a ranking system to prioritize species, but recovery funding is poorly correlated with priority rank. Recovery plan actions for species are ranked, but to little effect. In addition, although federal agencies have adopted Adaptive Management, little effort is allocated to monitoring outcomes of actions (*31*).

Effectiveness and legitimacy of the ESA are fostered through transparency and clear links between expenditures, actions, and outcomes. Over the past 20 years, drawing on advances in decision science and computational algorithms, conservation practice has created a variety of frameworks for planning, decision-making, spatial prioritization, evidence use, and outcome evaluation (*32*). Despite demonstrated successes (*33*), use of these frameworks to manage federally listed endangered species remains the exception. Accelerating the recovery of endangered species requires increasing the capacity to coordinate and efficiently invest in priority actions targeted to specific objectives combined with monitoring, learning, reporting, and adjusting future actions (*31*).

If the ESA is to truly deliver on recovering endangered species, with strong credibility among the public, then an explicit, transparent rationale for resource allocation to achieve recovery objectives is vital. Recently revised public recovery documentation (Species Status Assessments, Recovery Plans, Recovery Implementation Strategy, and Implementation Action Tables) have improved planning and action tracking but fail to explicitly link actions to expected outcomes. Adaptive management is most effective when plans rest on a conceptual model that links actions to recovery objectives through some theory of change (*34*).

There are several barriers to strategic adaptive management of endangered species. First, and foremost, is that the lead ESA agencies, tasked with recovery planning and tracking, are minority financial contributors to recovery actions. In fiscal year 2020, for example, just 8.4% of the $1.25 billion of public funding spent on endangered species came from the USFWS. As a consequence, the USFWS plans, prioritizes, and tracks actions that are almost entirely not their own. With just a small fraction of the funds, the USFWS has limited capacity to direct resources to priority species, a situation exacerbated by congressional earmarks for special interest species. Within species, the USFWS not only lacks the capacity to direct funds, but uses a three-tiered priority rank that is not driven by decision tools to optimize outcomes.

Lacking the required financial resources to fully implement recovery actions, public agencies make difficult choices in funding actions, and critical monitoring and evaluation functions appear frequently left out. Inadequate monitoring and evaluation not only undermine the ability of agencies to justify their actions to the public, but also forego efficiencies to be gained through learning and improving. Better cross-agency coordination and collaboration is needed to make optimal use of limited resources and implement adaptive management. Interventions on behalf of endangered species are experiments from which we must learn (*35*).

Sustainable, trustworthy, human-technology partnership

By **Tanya Berger-Wolf[15,16], Sara Beery[17], David Rolnick[18,19], Justin Kitzes[20], David Thau[21], Devis Tuia[22], Daniel Rubenstein[23]**

Despite conservation successes, we are in the middle of a mass extinction without even knowing all that we are losing and how fast. To address the urgency and scale of these challenges, there has been an explosion of technology developed to collect data on biodiversity, and parallel advances of computational methods in data analysis, machine learning (ML), artificial intelligence (AI), and cyberinfrastructure. The goal is to fill the data gap and turn raw data into high-resolution information about living organisms, enabling scientific inquiry, conservation, and policy decisions (*36*).

For example, the National Oceanic and Atmospheric Administra-

[1]Indiana University Maurer School of Law, Bloomington, IN, USA. rfischma@indiana.edu [2]Vanderbilt University Law School, Nashville, TN, USA. [3]U.S. Fish and Wildlife Service, Fort Collins, CO, USA. brenna_forester@fws.gov [4]Department of Biological Sciences, Smith College, Northampton, MA, USA. [5]Northwest Fisheries Science Center, National Marine Fisheries Service, Seattle, WA, USA. [6]Director General, International Union for the Conservation of Nature (IUCN), Gland, Switzerland. [7]Executive Governor, International Council of Environmental Law (ICEL), New York, NY, USA. nrobinson@law.pace.edu [8]Department of Geology and Environmental Science, University of Pittsburgh, Pittsburgh, PA, USA. pds25@pitt.edu [9]Department of Biological Sciences, University of Notre Dame, Notre Dame, IN, USA. [10]Department of Agricultural, Environmental, and Development Economics, The Ohio State University, Columbus, OH, USA. ando.21@osu.edu [11]Department of Oceans and Department of Biology, Stanford University, Stanford, CA, USA. spalumbi@stanford.edu [12]Woods Institute for the Environment, Stanford University, Stanford, CA, USA. [13]Department of Environmental Science and Policy, University of California, Davis, CA, USA. mwschwartz@ucdavis.edu [14]Human-Environment Systems, Boise State University, Boise, ID, USA. [15]Departments of Computer Science and Engineering, Electrical and Computer Engineering, and Evolution, Ecology, and Organismal Biology, The Ohio State University, Columbus, OH, USA. berger-wolf.1@osu.edu [16]Wild Me, Portland, OR, USA. [17]Department of Electrical Engineering and Computer Science, Massachusetts Institute of Technology, Cambridge, MA, USA. [18]School of Computer Science, McGill University, Montreal, QC, Canada. [19]Mila-Quebec AI Institute, Montreal, QC, Canada. [20]Department of Biological Sciences, University of Pittsburgh, Pittsburgh, PA, USA. [21]World Wildlife Fund, San Francisco, CA, USA. [22]School of Architecture, Civil and Environmental Engineering, Ecole Polytechnique Fédérale de Lausanne (EPFL), Sion, Switzerland. [23]Department of Ecology and Evolutionary Biology, Princeton University, Princeton, NJ, USA. [24]Office of Fisheries & Wildlife Management, Eastern Band of Cherokee Indians, Cherokee, NC, USA. calehick@ebci-nsn.gov [25]Native American Fish and Wildlife Society, Northglenn, CO, USA. jthor@nafws.org [26]The Hastings Center, Garrison, NY, USA. kaebnickg@thehastingscenter.org [27]School for the Future of Innovation in Society, Arizona State University, Tempe, AZ, USA. [28]CITES Secretariat, Geneva, Switzerland. deleuil@cites.org

A field biologist adds scent to the ground to encourage animals to stop in front of a trail camera, a technology increasingly used to survey animal species.

PHOTO: ANTHONY SOUFFLE/STAR TRIBUNE/GETTY IMAGES

tion (NOAA) Advanced Sampling and Technology for Extinction Risk Reduction and Recovery (ASTER3) (*37*) program for fisheries' conservation uses aerial and submersible drones, acoustic sensors, satellite- and drone-based imaging, -omics, and AI/ML. The USFWS uses ML to track and count bird populations from aerial images, while the Bureau of Ocean and Energy Management tracks and counts whales using algorithms to identify individuals in photographs (*38*). States use motion-sensitive cameras and an ML image object detector (*39*) to survey animal species, and smartphone-enabled citizen scientists count insects, identify bird songs, and report millions of plant observations (*40*). Algorithms developed for deploying US Federal Air Marshals are now used to plan park rangers' routes and deter wildlife criminals (*41*). Techniques for planning robot paths are leveraged to prioritize areas for biodiversity conservation (*42*).

The technological shift has the potential to enable a more effective, affordable, highly automated, globally distributed, locally relevant, real-time biodiversity monitoring system, improving equity across taxa as well as geographic regions (*43*). Technology can change the scale of conservation efforts by expanding our understanding of habitats and communities and predicting how they might change under different protection plans.

Yet, technology comes with risks. The collected data are biased, missing large areas and many taxonomic groups. Lack of robust collaborations between conservation biologists and computational and AI experts slows the development of computational tools. Biased data and methods will distort evaluation and discovery. If not carefully used, relying on technology for nature observation can also distance humans from nature, severing an important personal connection needed to inspire the next generation of scientists and nature lovers.

Technology is expensive, and conservation is already underfunded, leading to inequities in access to tools, data, and computational resources, as well as the expertise needed to use them. Technology pulls funding away from other needs, not always with commensurate impact, with the focus too often on using technology for its own sake. Conservation needs buy-in and support from local communities who are directly affected by nature loss. However, technology can undermine community or individual data rights or be deployed in languages or with cultural norms not relevant locally. But when local communities are given agency in every part of the process, trusting and productive partnerships can be developed.

The same technologies that accelerate impact can also accelerate environmental and conservation risks. Computation can be energy and water intensive, and computing hardware uses rare metals and produces e-waste. Additionally, AI-enabled data-gathering tools may be used by nature criminals, and are already used extensively to aid oil and gas extraction.

To be useful, technology needs to be a sustainable and trustworthy partner. Ultimately, technology alone, even AI, will not save the planet's species. But neither will humans alone. Human and machine partnership for conservation is our best chance for success.

Adding tribal experience and removing inequity

By **Caleb R. Hickman**[24] *and* **Julie Thorstenson**[25]

Over millennia, tribes have learned to coexist with species on the American continent. Despite centuries of conflict with settler-colonial Americans, federally recognized tribes influence the management of nearly 140 million acres in the US. These lands feature diverse legal classifications offering protective status with regulatory burdens specific to tribes (*44*). Studies underscore the pivotal role of Indigenous stewardship, revealing higher biodiversity levels and more borders with protected areas compared to adjacent state lands (*44*). Indigenous-managed lands constitute only 2.6% of the US but overlap with 12% of Key Biodiversity Areas, underscoring their ecological importance (*44*).

Despite their crucial conservation role, tribes face considerable funding disparities compared to states. Tribes miss out on the annual federal aid of more than $1 billion allocated to states for conservation under the Wildlife Restoration Act (Pittman-Robertson) and the Sport Fish Restoration Act (Dingell-Johnson). In addition, the State Wildlife Grant (SWG) program, distributed on the basis of species and land area (which often lumps in tribal lands), allocated $1.2 billion over 20 years for nongame species conservation to every state. Tribes do not receive the SWG funds, but a similar fund for tribes is the extremely limited Tribal Wildlife Grant (TWG) program. The TWG program, funded with

The Shoshone-Bannock Tribes have worked to protect and restore the Snake River and endangered sockeye salmon.

PHOTO: MICHAEL QUINTON/MINDEN PICTURES

competitive awards and capped at $200,000 per project, has disbursed $105.6 million since 2002, yet only 25% of applications received funding (*44*). This results in capacity challenges, whereby tribes must juggle all taxa management (among other natural resources) while state agencies can hire specialized biological staff that focus on single taxon groups, and single species. Insufficient funds result in reduced conservation efforts, management sovereignty, and tribal lifeways.

Tribally held priorities can be overlooked when applying the ESA. We recommend applying Indigenous perspectives to the ESA as a way to avoid neocolonial American practices. Lamb *et al.* (*45*) recommend integrating food security and cultural relationships into species recovery plans. We see a need to revitalize traditional coexistence philosophies (*46*) while avoiding the "Ecological Indian" fallacy that overromanticizes the role of Indigenous people as historical stewards rather than modern practitioners (*47*). Without Indigenous coexistence philosophy in modern management, neocolonial influences may lead tribes to embrace market trade and industrial capitalism (*3*). Despite inquiries about the "in vogue" traditional ecological knowledge, tribes' philosophies often remain overlooked without direct federal oversight, which is an all too often paternalistic approach (*48*).

To achieve true species recovery for all, a shift in conservation philosophy is essential (*46*). Tribes, as sovereign nations, face a disproportionate burden compared to US citizen states, which is antithetical to the Secretarial Order 3206 that emphasizes cultural deference. A recent inclusive step occurred when President Biden's administration supported a memorandum on Tribal Consultation, which can include species conservation.

By recognizing the distinct challenges that tribes face, the scientific community can also play a vital role in reframing the ESA into a law for everyone. This equity can be realized when a coproduced form of conservation includes tribal knowledge systems and priorities from the beginning and shares resources throughout the process (*48*).

C.R.H. (ᎠᎾᏓᏍᏗ) is a citizen of the Cherokee Nation. J.T. is Lakota and a citizen of the Cheyenne River Sioux Nation.

Genome editing and deliberate extinction

By **Gregory E. Kaebnick[26], James P. Collins[27], Athmeya Jayaram[26]**

Advancing genome editing technologies, prominent among them synthetic gene drive systems, may lead to methods for suppressing or locally exterminating some species, or even driving them extinct. How that prospect accords with the ESA is an emerging policy issue with potentially profound ramifications for environmental, public health, and agricultural policy.

Effects of a gene drive system would depend on the design of the system, e.g., alleles targeted for change, diversity of a species' gene pool, and a species' population structure (*49*). For example, a drive that reduced female fertility in malaria-transmitting mosquitoes *Anopheles gambiae* could lead to substantial population decline on a regional scale, though modeling suggests that complete extinction is unlikely (*50*). Gene drive systems are also in development to eliminate invasive rodent populations that threaten other species on oceanic islands (*51*). Other candidate species include the New World screwworm, a blow fly causing considerable damage to livestock and posing a threat to humans, for which genes required for female development or fertility have been identified and could be targeted by gene drive (*52*).

Eliminating disease-carrying mosquitoes and screwworm appears to be permissible under the ESA, which exempts insect pest species that present "an overwhelming and overriding risk" to humans. The law's applicability to a widespread population decline of invasive rodent populations due to a gene-drive system is more ambiguous. ESA protections apply only after a species is listed as endangered, which typically requires evidence that the species has already declined. The ESA, therefore, may not apply to the prospective threat of a gene drive (*53*). Additionally, how genome editing would be considered in the listing process is not settled. The factors that trigger listing have generally been external threats to a species such as hunting and habitat change, not genetic alterations integrated into a species' gene pool.

But if the letter of the law needs clarification, the spirit of the ESA clearly places an extremely high value on species and rules out eradication in most cases. The exception made for insect pests shows, however, that some goals, such as preventing the enormous public health harms associated with some insects, might override that high value. Exactly which harms are overriding—and whether they are posed only by insects—are important questions. But, plainly, if the ESA is taken to heart, genetic interventions that could lead to a species' extinction should be evaluated very conservatively and would be acceptable only rarely.

Regulating trade toward global sustainable development

By **Thomas Deleuil**[28] *and* **Ying Zhao**[28]

A group of scientists and environmental managers in 1963 called for "an international convention on regulation of export, transit and import of rare or threatened wildlife species or their skins and trophies" as enshrined in a resolution of the IUCN (*54*). In 1973, based on a recommendation of the 1972 Stockholm Conference on the Human Environment, the United States hosted a Plenipotentiary Conference in Washington, DC, where the CITES was opened for signature. The US was the first signatory country to ratify the Convention, which came into force in 1975 (*55*).

CITES is an international legally binding agreement regulating billions of dollars of international trade in specimens of wild animals and plants. The two cardinal rules are that trade shall not be detrimental to the survival of the species and traded specimens must have been acquired legally (*56*).

Parties are required to adopt domestic legislation to ensure full implementation of CITES at the national level. In the US, the ESA is the domestic legislation for CITES. The USFWS acts as both the Management Authority and Scientific Authority for CITES, tasked with providing scientific advice, verifying the legality of specimens traded, issuing CITES permits and certificates, enforcing pertinent laws, and submitting trade reports, for example (*57*).

The ESA not only encompasses US international obligations under CITES but also imposes, in some cases, stricter domestic measures above CITES standards, including the protection of species that are not covered by the Convention. For instance, the ESA mandates the development of recovery plans for the conservation and survival of listed species when deemed necessary (*56*). Thus, the ESA also demonstrates the commitment of the US to the conservation of species.

Today, CITES has 184 signatory Parties and regulates trade in over 40,900 species. It is one of the most successful international environmental treaties concerned with nature conservation. Notably, no species listed under CITES has become extinct, and the US—through ESA—has played its part in this global effort. However, since the adoption of the Convention in 1973, societies have evolved and environmental threats have multiplied. Through ESA, the USFWS, Office of Law Enforcement, has also played and continues to play an important role in combating illegal wildlife trade, including online trade (*58*).

The pressure to regulate trade in and conservation of wild species is growing. In an increasingly complex world, as both CITES and ESA mark their 50th anniversaries, they are more relevant than ever to ensure that wild species are conserved for the benefit of people, planet, and prosperity to achieve the United Nations Sustainable Development Goals.

REFERENCES AND NOTES

1. D. Lueck, J. A. Michael, *J. Law Econ.* **46**, 27 (2003).
2. J. A. Smith, K. Brust, J. Skelton, J. R. Walters, *Condor* **120**, 223 (2018).
3. T. Dietz, E. Ostrom, P. C. Stern, *Science* **302**, 1907 (2003).
4. R. L. Fischman, V. J. Merestsky, M. P. Casteilli, *Yale J. Regul.* **38**, 976 (2021).
5. R. L. Fischman, J. B. Ruhl, *Conserv. Biol.* **30**, 268 (2016).
6. B. Forester, T. Lama, "The role of genomics in the future of ESA decision-making" in *The Codex of the Endangered Species Act, Volume II, The Next Fifty Years*, L. E. Baier, J. F. Organ, Eds. (Rowman and Littlefield, 2023), pp. 159–186.
7. W. C. Funk, B. R. Forester, S. J. Converse, C. Darst, S. Morey, *Conserv. Genet.* **20**, 115 (2019).
8. R. S. Waples *et al.*, *J. Hered.* **113**, 121 (2022).
9. M. Kardos *et al.*, *Nat. Ecol. Evol.* **7**, 675 (2023).
10. M. Kardos, *Proc. Natl. Acad. Sci. U.S.A.* **120**, e2316880120 (2023).
11. S. Hoban *et al.*, *Conserv. Lett.* **16**, e12953 (2023).
12. J. Barbara, Lausche, Weaving a Web of Environmental Law, Chapter 6, "The Making of CITES" (2008); https://www.iucnael.org/en/academy-publications/7-weaving-a-web-of-environmental-law.
13. J. S. McLachlan, J. J. Hellmann, M. W. Schwartz, *Conserv. Biol.* **21**, 297 (2007).
14. C. Sáenz-Romero *et al.*, *Can. J. For. Res.* **50**, 843 (2020).
15. P. D. Shirey, G. A. Lamberti, *Conserv. Lett.* **3**, 45 (2010).
16. P. D. Shirey, B. N. Kunycky, D. T. Chaloner, M. A. Brueseke, G. A. Lamberti, *Conserv. Lett.* **6**, 300 (2013).
17. P. D. Shirey, S. A. R. Colvin, L. H. Roulson, T. E. Bigford, *Fisheries* **47**, 256 (2022).
18. P. D. Shirey, S. A. R. Colvin, *Fisheries* **47**, 299 (2022).
19. C. Langpap, J. Kerkvliet, J. F. Shogren, *Rev. Environ. Econ. Policy* **12**, 69 (2018).
20. K. Kroetz, Y. Kuwayama, C. Vexler, *Rev. Environ. Econ. Policy* **14**, 194 (2020).
21. H. J. Albers *et al.*, *Rev. Environ. Econ. Policy* **17**, 111 (2023).
22. A. W. Ando, M. L. Mallory, *Proc. Natl. Acad. Sci. U.S.A.* **109**, 6484 (2012).
23. T. Treakle, R. Epanchin-Niell, G. D. Iacona, *Conserv. Biol.* **37**, e14104 (2023).
24. C. Sims, D. Aadland, D. Finnoff, J. Hochard, *Ecol. Econ.* **174**, 106656 (2020).
25. B. Cornwell *et al.*, *eLife* **10**, e64790 (2021).
26. NOAA Fisheries, Endangered Species Act Legal and Policy Review of Interventions to Increase the Persistence and Resilience of Coral Reefs (2020); https://www.fisheries.noaa.gov/resource/document/endangered-species-act-legal-and-policy-review-interventions-increase-persistence.
27. R. L. Sandler, L. Moses, S. M. Wisely, *Biol. Conserv.* **257**, 109118 (2021).
28. W. Y. Chan, L. Meyers, D. Rudd, S. H. Topa, M. J. van Oppen, *Glob. Change Biol.* **29**, 6945 (2023).
29. P. A. Cleves *et al.*, *Proc. Natl. Acad. Sci. U.S.A.* **117**, 28899 (2020).
30. NOAA Fisheries, 15 Indo-Pacific Coral Species Recovery Outline; https://www.fisheries.noaa.gov/resource/document/15-indo-pacific-coral-species-recovery-outline.
31. M. Evansen, A. Carter, J. Malcom, *Environ. Res. Lett.* **16**, 031001 (2021).
32. M. W. Schwartz *et al.*, *Conserv. Lett.* **11**, e12385 (2018).
33. B. G. Marcot, J. E. Lyons, D. C. Elbert, L. Todd, *Animals* **11**, 569 (2021).
34. L. A. Dietz, M. Brown, V. Swaminathan, *Am. J. Primatol.* **72**, 425 (2010).
35. P. J. Ferraro *et al.*, *Science* **381**, 735 (2023).
36. D. Tuia *et al.*, *Nat. Commun.* **13**, 792 (2022).
37. National Oceanic and Atmospheric Administration (NOAA) Fisheries, "Advanced Sampling and Technology for Extinction Risk Reduction and Recovery"; https://www.fisheries.noaa.gov/endangered-species-conservation/advanced-sampling-and-technology-extinction-risk-reduction-and.
38. D. Blount *et al.*, *Mamm. Biol.* **102**, 1005 (2022).
39. S. Beery, D. Morris, S. Yang, arXiv:1907.06772 (2019).
40. D. Fraisl *et al.*, *Nat. Rev. Methods Primers* **2**, 64 (2022).
41. F. Fang *et al.*, *Proc. AAAI Conf. Artif. Intell.* **30**, 3966 (2016).
42. D. Silvestro, S. Goria, T. Sterner, A. Antonelli, *Nat. Sustain.* **5**, 415 (2022).
43. GPAI, *Biodiversity & Artificial Intelligence, Opportunities and Recommendations, Report* (Global Partnership on AI, 2022).
44. J. Thorstenson, "Diversity and Complexity of Tribal Fish and Wildlife Programs" in *Wildlife Stewardship on Tribal Lands. Our Place Is in Our Soul*, S. Hoagland, S. Albert, Eds. (Johns Hopkins Univ. Press, 2023), pp. 12–21.
45. C. T. Lamb *et al.*, *Science* **380**, 694 (2023).
46. K. Anker, "Ecological jurisprudence and Indigenous relational ontologies Beyond the 'ecological Indian'?" in *From Environmental to Ecological Law*, K. Anker, P. D. Burdon, G. Garver, M. Maloney, C. Sbert, Eds. (Routledge, 2021), pp. 104–118.
47. S. Krech III, *Ecological Indian: Myth and History* (Norton, 1999).
48. C. R. Hickman, J. Thorstenson, A. Carlisle, S. J. Hoagland, S. Albert, "Research with Tribes: A Suggested Framework for the Co-Production of Knowledge" in *Wildlife Stewardship on Tribal Lands. Our Place*
49. NASEM, *Gene Drives on the Horizon: Advancing Science, Navigating Uncertainty, and Aligning Research with Public Values* (NASEM, 2016).
50. A. R. North, A. Burt, H. C. J. Godfray, *BMC Biol.* **18**, 98 (2020).
51. A. Birand *et al.*, *Mol. Ecol.* **31**, 1907 (2022).
52. M. J. Scott *et al.*, *Commun. Biol.* **3**, 424 (2020).
53. J. Monast, *North Carol. Law Rev.* **97**, 1329 (2019).
54. CITES, Official Newsletter of the Parties, Special Edition, 3 March 2003 – 30th Anniversary; https://cites.org/sites/default/files/eng/news/world/30special.pdf.
55. CITES, List of Contracting Parties: https://cites.org/eng/disc/parties/chronolo.php.
56. CITES Articles II, III, IV and V. See also, inter alia: P. A. Sheikh, E. H. Ward, The Endangered Species Act: Overview and Implementation. Congressional Research Service, 23 and 47-48 (4 March 2021); http://crsreports.congress.gov/product/pdf/R/R46677.
57. C. D. Daniel, Evaluating, *William Mary Environ Law Policy Rev.* **23**, 683 (1999).
58. CITES, Official Newsletter of the Parties, Issue 19; https://cites.org/eng/news/world/19/4.php.

ACKNOWLEDGMENTS

The findings and conclusions in the contribution from B.R.F., T.M.L., and M.K. are those of the authors and do not necessarily represent the views of the US Fish and Wildlife Service. G.E.K., J.C., and A.J. are supported by NSF award 2317702.

10.1126/science.adn3245

PERSPECTIVES

CLIMATOLOGY

Genetic insight on ice sheet history

Octopus DNA reveals timing of the most recent collapse of the West Antarctic Ice Sheet

By **A. Dutton**[1] and **R. M. DeConto**[2]

At the South Pole of Earth sits a landmass that has been home to a continent-sized ice sheet for the past 34 million years. Scientists have long been drawn to this icy expanse, initially to explore and discover, and later to study the evolution of the Antarctic continent, climate, and ice sheet. Despite decades of probing the region from the surface and from space, some important aspects of Antarctic history remain elusive. On page 1384 of this issue, Lau *et al.* (*1*) make headway to fill one such knowledge gap by reporting genetic evidence that two distinct populations of octopus were connected by a waterway across an area now completely covered by the ice sheet. This suggests that the West Antarctic Ice Sheet (WAIS) collapsed during a past warm period ~129,000 to 116,000 years ago, known as the Last Interglacial.

More than 50 years ago, glaciologist John Mercer was the first to deduce from sedimentary evidence that the WAIS melted away at some point during the Pleistocene (2.58 million to 11,700 years ago) (*2*). By leveraging independent evidence for sea levels that were several meters higher than present day during the Last Interglacial, Mercer hypothesized that the WAIS disintegrated during that warm period. Presciently, Mercer proposed that if that had indeed happened, then within 50 years, the disintegration of the WAIS would be imminent, leading to a globally averaged sea-level rise of about 5 m (*3*).

Although global mean sea surface temperature during the Last Interglacial was roughly the same as today (*4*), the Antarctic warmed to temperatures that were several degrees higher than present day (*5*). Future warming scenarios suggest that WAIS collapse could be triggered within several decades (*6*), if it has not already begun (*7*). This would bring about an estimated average 4 to 5 m of global sea-level rise (*8*), although the seas would rise higher in some places (such as the US east coast) relative to others because of changes in the gravity field associated with ice loss (*9*). Knowing the conditions under which the WAIS collapsed during the Last Interglacial should help pinpoint how and when such an event will unfold again under anthropogenically driven future warming, with enormous policy implications for global mitigation and adaptation efforts.

In the decades that followed Mercer's work, scientists set out to test his hypothesis in various ways. Some focused on looking for evidence within the Antarctic ice sheet itself (*10*) or within sediments off shore (*11*). Others searched further afield to combine estimates of total sea-level rise with existing estimates of Greenland melt volume to calculate the Antarctic contribution (by subtraction) (*12*). Modelers tried to discern how the Antarctic ice sheet would have responded to the Last Interglacial climate conditions (*6*). Using this multipronged approach, firmly centered on the geologic history, evidence has been mounting that the WAIS may have collapsed during the Last Interglacial. However, each study's findings have come with caveats. The general conclusion from much of this work is that the findings are largely circumstantial, with multiple possible interpretations.

In a pioneering study, Lau *et al.* bring an entirely different dataset to bear on the increasingly urgent question of whether or not the WAIS collapsed during the Last Interglacial. The study brings molecular biologists and geologists together to discern whether the genetic history of Turquet's octopus (*Pareledone turqueti*) could reveal the timing of when a waterway may have formed if the WAIS fully retreated. Although a disappearance of the WAIS would result in a massive inundation of coastal regions, it would simultaneously open up areas on the seafloor that are currently covered by ice, allowing Turquet's octopus to colonize new habitats and mix genes with populations that were formerly geographically isolated from each other.

Lau *et al.* focused on the modern populations of *P. turqueti* in the Amundsen, Ross, and Weddell Seas that are situated in the Southern Ocean off the coast of the WAIS. The authors determined that these populations are genetically distinct but have some admixture, indicating a potential historical trans–West Antarctic seaway (see the figure). Given the current ice sheet configuration, historical gene flow could only occur if connected by an interior waterway across regions of the WAIS that are currently grounded below sea level. Their genomic data analysis detected a historical gene flow from the Ross Sea to the Weddell Sea and vice versa. Specifically, the timing of this connection in their demographic model agrees with the timing of the Last

Ice sheet and octopus geography

Octopuses in the Amundsen, Ross, and Weddell Seas are isolated by today's ice sheet (left). If the vulnerable, marine-based sectors of the ice sheet retreated during the Last Interglacial (right), the resulting seaways would have allowed ancient connections between octopus populations compatible with genetic data.

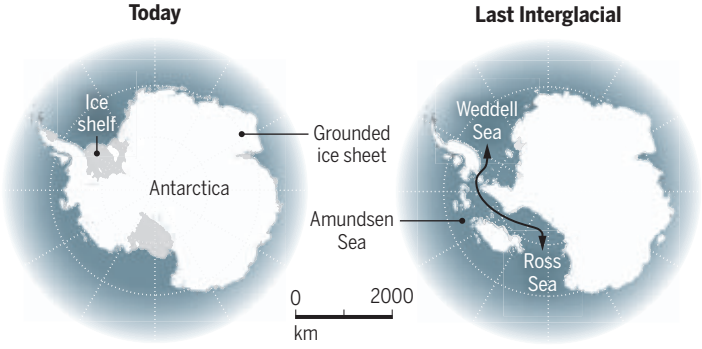

GRAPHIC: M. HERSHER/*SCIENCE*

[1]Department of Geoscience, University of Wisconsin–Madison, Madison, WI, USA. [2]Department of Earth, Geographic, and Climate Sciences, University of Massachusetts Amherst, Amherst, MA, USA. Email: dutton3@wisc.edu

Interglacial, implying WAIS retreat of the marine-based portions of the ice sheet. Whether or not this analysis withstands further scrutiny and the test of time, the implications of this result pose some intriguing questions, including whether this history will be repeated, given Earth's current temperature trajectory.

Answering this question requires resolving additional questions about the timing, nature, and conditions of past deterioration of the WAIS. What were the physical conditions that primed this sector of the ice sheet to retreat, and precisely when did it happen? If the WAIS retreated early in the Last Interglacial as some data suggest (*10*, *12*), was this event the consequence of changes in ocean currents, temperatures, and/or solid earth response that preceded the interglacial? If the trigger occurred just before the warm period, then perhaps the simplistic emphasis on how warm it got during the interglacial should not be a focus.

There are also questions about how quickly sea level rises as the WAIS disintegrates. Would it rise relatively slowly and gradually, drawn out over millennia, or would it rise in one or more rapid jumps as vulnerable sectors of the ice sheet retreat? Understanding the past nature of ice loss informs future sea-level rise projections, which are of fundamental importance for coastal planners.

The problem, perhaps, runs even deeper than these specific, scientific questions. The challenge in identifying a precise tipping point—and all the conditions thereof—is that the tipping point will likely not be apparent until it has been passed. Policy-makers will always have to make decisions in the face of uncertainty about the future, and this latest piece of evidence from octopus DNA stacks one more card on an already unstable house of cards. ■

REFERENCES AND NOTES

1. S. C. Y. Lau *et al.*, *Science* **382**, 1384 (2023).
2. J. H. Mercer, *Int. Assoc. Hydrol. Sci* **79**, 217 (1968).
3. J. H. Mercer, *Nature* **271**, 321 (1978).
4. J. S. Hoffman, P. U. Clark, A. C. Parnell, F. He, *Science* **355**, 276 (2017).
5. E. Capron, A. Govin, R. Feng, B. L. Otto-Bliesner, E. W. Wolff, *Quat. Sci. Rev.* **168**, 137 (2017).
6. R. M. DeConto *et al.*, *Nature* **593**, 83 (2021).
7. E. Rignot, J. Mouginot, M. Morlighem, H. Seroussi, B. Scheuchl, *Geophys. Res. Lett.* **41**, 3502 (2014).
8. L. Pan *et al.*, *Sci. Adv.* **7**, eabf7787 (2021).
9. J. X. Mitrovica, N. Gomez, P. U. Clark, *Science* **323**, 753 (2009).
10. C. S. M. Turney *et al.*, *Proc. Natl. Acad. Sci. U.S.A.* **117**, 3996 (2020).
11. R. McKay *et al.*, *Quat. Sci. Rev.* **34**, 93 (2012).
12. A. Dutton, J. M. Webster, D. Zwartz, K. Lambeck, B. Wohlfarth, *Quat. Sci. Rev.* **107**, 182 (2015).

10.1126/science.adm6957

SIGNALING

Deciphering downstream receptor signaling

Advancing drug discovery requires increasingly integrative structural biology approaches

By **Marta Filizola**[1] *and* **Jonathan A. Javitch**[2,3,4]

G protein–coupled receptors (GPCRs) are important cell-surface signaling proteins that are responsive to diverse extracellular stimuli and are key drug targets (*1*). Understanding how compounds activate GPCRs and modulate their interactions with intracellular proteins such as G proteins and β-arrestins is crucial for drug discovery because these proteins transduce signals to downstream effectors, triggering biological responses. This includes elucidating the molecular details behind the ability of the drug–GPCR complex to generate a functional response (efficacy) and the concentration of the drug required to produce half-maximal response (potency) (*2*). Although agonist binding to a GPCR triggers conformational rearrangements throughout the receptor and its transducer (*3*), the molecular mechanisms that govern ligand efficacy and potency are difficult to ascertain. On page 1378 of this issue, Heydenreich *et al.* (*4*) explored how individual amino acids in the prototypical G_s-coupled β_2-adrenergic receptor "interpret" information encoded in the atoms of its endogenous agonist, adrenaline, to drive its efficacy and potency.

"...the molecular mechanisms that govern ligand efficacy and potency are difficult to ascertain."

Traditionally, the quest to decipher GPCR signaling has focused on recording agonist-specific functional responses, but the molecular determinants and steps involved in these responses have largely remained obscure. Most pharmacological, structural, and mutational studies of GPCRs have focused on the ligand-binding pocket, the GPCR–transducer interface, or both. In a painstaking study spanning multiple domains of investigation, including alanine mutagenesis, a bioluminescence resonance energy transfer (BRET) functional assay, analysis of inactive and active crystallographic structures, computational data analysis, and evolutionary analysis, Heydenreich *et al.* have undertaken what they call an integrative approach to understand the GPCR communication network (that is, the allosteric pathway through which agonist binding is communicated from its binding site on the receptor to the GPCR–G protein interface). Changes on the receptor's surface or at distant allosteric sites can be just as impactful as those at the ligand-binding site or the receptor–transducer interface. Notably, the allosteric network of noncovalent contacts that they identify in the β_2-adrenergic receptor, a major drug target for the treatment of respiratory diseases and heart failure, involves pharmacologically important residues that contribute as drivers, modulators, passengers, and bystanders to the molecular and structural foundations of adrenaline's potency and efficacy.

Although distinct from key concepts of probability and information theory analyses that provide insights into the rules that govern information and uncertainty (*5*, *6*) in physics-based evaluations of the molecular dynamics of a system, the important residues identified by Heydenreich *et al.* can in principle be used to guide ligand design. This could enable the identification of chemical groups that can be modified to achieve desired signaling responses and eventually be tested iteratively and also explored in the context of other agonists. Notably, the observation that surface-exposed driver, modulator, and passenger residues identified with an endogenous ligand are also targeted by drugs acting as negative and positive allosteric modulators suggests that these sites should be prioritized in high-throughput virtual screening efforts for the discovery of new allosteric modulators.

[1]Department of Pharmacological Sciences, Icahn School of Medicine at Mount Sinai, New York, NY, USA. [2]Department of Psychiatry, Vagelos College of Physicians and Surgeons, Columbia University, New York, NY, USA. [3]Department of Molecular Pharmacology and Therapeutics, Vagelos College of Physicians and Surgeons, Columbia University, New York, NY, USA. [4]Division of Molecular Therapeutics, New York State Psychiatric Institute, New York, NY, USA.
Email: marta.filizola@mssm.edu

Evolutionary analyses indicate possible overlaps in closely related systems (*7*). The study of Heydenreich *et al.* concludes that the functional role of a residue cannot be predicted solely on the basis of evolutionary conservation. It is plausible that the residues and networks involved in the efficacy or potency resulting from ligand binding are distinct and nonoverlapping, varying with the specific ligand, GPCR, and/or intracellular partner subtypes.

Notably, a data analysis based on efficacy and potency measurements for a single ligand derived from a highly amplified assay, point mutations limited to substitution with alanine in a single receptor, and allosteric networks derived from the analysis of two static receptor conformations inevitably overlooks two critical aspects of GPCR signaling that have emerged in the past decade. These are pluridimensional efficacy, the ability of the GPCR to engage multiple G protein and non–G protein effectors; and biased agonism, which is the ability of the GPCR to preferentially engage one effector over another (*8*). Contrary to the traditional view of GPCR-mediated signal transduction as a linear pathway mediated by single GPCR–G protein complexes, it is now evident that the inherent conformational plasticity of the receptors is exploited by ligands inducing maximal stimulation (full agonism) or lower efficacy (partial agonism). These ligands stabilize receptor conformations that preferentially couple to and/or activate different G protein subtypes or non–G protein effectors, enabling different downstream signaling cascades that can result in either beneficial or adverse physiological effects.

"...changes in amino acids far from the ligand-binding site can substantially alter drug response and receptor signaling..."

The resulting functional selectivity can originate not only from ligand-specific conformational changes in the receptors but also in the G protein or non–G protein partners, as well as from the varying kinetics of the transducer's conformational dynamics and its association with and dissociation from the receptor (*9*). These aspects of GPCR signaling necessitate high-resolution spatiotemporal measurements of the stability, dynamics, and activation kinetics of the GPCR–transducer complex, which can be conflated in amplified assays such as the BRET functional assays used by Heydenreich *et al.* Readouts from these assays are time-averaged and represent an ensemble average of the receptor–G protein complex, interpreted through the lens of a steady-state impact on BRET between the G_s α and γ subunits. The conclusion of Heydenreich *et al.* that the pharmacological importance of a residue cannot be inferred merely from the extent of its conformational change during receptor activation, as determined from the analysis of only two high-resolution receptor–G protein complex structures, underscores that the system's dynamics cannot be ignored. These dynamics can be crucial for characterizing agonist-induced allosteric pathways that extend beyond the receptor and receptor-transducer interface into the transducer protein. This consideration should also account for the impact of different lipid environments on signaling, given the growing evidence that not only cholesterol, but also other cell membrane lipids such as anionic lipids, can influence both receptor activation and G protein coupling (*10, 11*).

The realization that changes in amino acids far from the ligand-binding site can substantially alter drug response and receptor signaling challenges both the pharmaceutical industry and academic researchers to rethink drug design strategies—to not just focus on hypotheses of chemical optimization derived from analyses of direct ligand–receptor interactions in the orthosteric binding site. Instead, it is necessary to explore the rich landscape of a receptor's molecular surface and its internal communication network, as indicated by the analyses of Heydenreich *et al.* In the future, such studies can be further enhanced by integrating computational and experimental measurements of ligand-specific conformational dynamics and activation kinetics in GPCR–transducer complexes to fully decipher the molecular basis of ligand efficacy and potency at GPCRs for the development of improved therapeutics. ■

REFERENCES AND NOTES

1. A. S. Hauser *et al.*, *Nat. Rev. Drug Discov.* **16**, 829 (2017).
2. R. R. Neubig, M. Spedding, T. Kenakin, A. Christopoulos, *Pharmacol. Rev.* **55**, 597 (2003).
3. X. Deupi, B. Kobilka, *Adv. Protein Chem.* **74**, 137 (2007).
4. F. M. Heydenreich *et al.*, *Science* **382**, adh1859 (2023).
5. T. Schreiber, *Phys. Rev. Lett.* **85**, 461 (2000).
6. C. E. Shannon, *Bell Syst. Tech. J.* **27**, 379 (1948).
7. O. Lichtarge, H. R. Bourne, F. E. Cohen, *J. Mol. Biol.* **257**, 342 (1996).
8. C. M. Costa-Neto, L. T. Parreiras-e-Silva, M. Bouvier, *Mol. Pharmacol.* **90**, 587 (2016).
9. S. R. J. Hoare *et al.*, *Front. Cell. Neurosci.* **15**, 814547 (2022).
10. N. Thakur *et al.*, *Nat. Commun.* **14**, 794 (2023).
11. H. Y. Yen *et al.*, *Nature* **559**, 423 (2018).

ACKNOWLEDGMENTS

The authors acknowledge funding from National Institutes of Health grants DA045473 (M.F.) and MH54137 (J.A.J.).

10.1126/science.adm8393

MATERIALS SCIENCE

Mimicking polar bear hairs in aerogel fibers

Encapsulated aerogel fibers offer thermal insulation, breathability, and strength

By **Zhizhi Sheng**[1] *and* **Xuetong Zhang**[1,2]

Aerogels have been considered as super thermal insulators since their invention in 1931. The successful adoption of aerogels, which are made by replacing the liquid in a gel with gas while maintaining a stable network, in NASA vehicles such as the Mars rover has inspired the use of aerogels in personal warming. But applications of aerogels in textiles have been limited by their insufficient moisture permeability. Aerogel fibers are being developed to address the trade-off between thermal insulation and moisture permeability. However, aerogel fibers presently lack the strength and flexibility necessary to allow weaving or knitting into a wearable fabric. On page 1379 of this issue, Wu *et al.* (*1*) report a feasible strategy to construct bioinspired knittable aerogel fibers with superb thermal insulation and mechanical robustness, which allows weaving into fabric with air permeability. This could instigate the development of advanced thermal textiles for personal warming.

Aerogel fibers can be obtained by spinning nanoscale building blocks (e.g., aramid nanofibers, silica nanoparticles, graphene nanosheets, and so on) in a spinning dope with sol-gel transition and subsequent special drying (*2*–*7*). By modulating the interactions between these building blocks, various aerogel fibers with desired mechanical properties can be achieved, making bending, knotting, twisting, and weaving possible (*8*). However, at the present time, aerogel fibers cannot be woven into large textiles because of their insufficient strength; they also cannot withstand

[1]Suzhou Institute of Nano-Tech and Nano-Bionics, Chinese Academy of Sciences, Suzhou, China. [2]Division of Surgery and Interventional Science, University College London, London, UK. Email: xtzhang2013@sinano.ac.cn

machine washing. Thus, they do not meet the requirements for modern textile applications. Wu *et al.* fabricated encapsulated aerogel fibers (EAFs) by mimicking the core-shell characteristic of polar bear hairs, which allows heat insulation in extremely cold environments in the Arctic. The EAFs are composed of a chitosan aerogel core that can trap air in the abundant air pockets (more than 90% porosity) and provide sufficient thermal insulation. The thermoplastic polyurethane (TPU) shell affords mechanical robustness (1000% tensile strain). The textile made from EAFs has a thermal conductivity of 26.9 ± 1.8 mW/m·K, outperforming wool, nylon, and polyester textiles. The EAF textile is only one-fifth as thick as down, which has a comparable thermal insulation performance. In −20°C, the EAF sweater produced by Wu *et al.* exhibited thermal protection superior to that of a down jacket, wool sweater, and cotton sweater.

Aerogel fibers are promising materials for next-generation thermal insulation textiles (*8*). For these fabrics, individual aerogel fibers can provide the best thermal insulation while the interfiber voids allow breathability (see the figure). The superiority of aerogel fibers in recent textile history is reflected in the following two key aspects: processing and performance. The traditional sol-gel transition is a slow and static process (*8*) that is difficult to couple with the fast, dynamic, and continuous spinning procedure used to make traditional textiles. To solve this, Wu *et al.* produced EAFs by freeze-spinning a precursor, which then undergoes a dynamic sol-gel transition followed by freeze-drying and coating-drying steps. These fibers are ready for use and do not require complicated postprocessing steps such as conventional yarn-spinning in textiles. As a result of this processing method, the sweater knitted with EAF fibers by Wu *et al.* costs less for source material but has the same warmth as down and also has excellent performance, including washability, dyeability, and flexibility. Importantly, the EAF fibers can also retain stable thermal insulation after more than 10,000 stretching and releasing cycles.

Compared with electrospun fibers and other traditional porous fibers, aerogel fibers have ultrahigh specific surface area and superhigh porosity. Thus, in addition to their use in textiles, aerogel fibers may be advantageous in adsorption, separation, optics, energy, and other applications (*4*, *5*, *9*–*11*). The existence of mesopores in aerogel fibers, together with the macropores formed by overlapping fibers, makes it possible to achieve both high sorption capacity and fast sorption kinetics. These abundant multiscale porosities are also helpful in solving the conflict between permeability and selectivity in membrane separation. Furthermore, the transparency of aerogel fibers can be tuned by rationalizing the size of nanoscale building blocks (e.g., silica nanoparticle size) for optical devices (*3*). Notably, the richness of nanopores in aerogel fibers could allow entrapping guest materials in these pore spaces, for instance, molecules, nanoparticles, and functional liquids stabilized by capillary forces (*2*, *4*, *12*–*14*), which will be useful for a myriad of applications. For example, the introduction of phase-change fluids in aerogel fibers achieves both thermal energy storage and photothermal or electrothermal responsiveness (*5*). Moreover, adjusting the interior nanopockets of aerogel fibers could yield materials with applications in environmental remediation and biomedical science, such as carbon dioxide capture (*13*) and efficient hemostasis (*15*).

Although aerogel fibers have witnessed tremendous progress, challenges exist regarding how to develop fast spinning technology and resolve the continuous fabrication that is necessary for mass production. It is crucial to understand spinning thermodynamics and kinetics to decouple the mismatch between the slow sol-gel transition rate and the fast spinning rate. At present, the wet spinning rate of aerogel fibers is around 20 m/min, which is much slower than the industrially available wet spinning (200 m/min), dry spinning (1500 m/min), and melt spinning (5000 m/min) of traditional fibers. Additionally, although continuous spinning and batch drying have been established for aerogel fibers [by Wu *et al.* and also see (*2*, *3*)], a feasible strategy to bridge the two processes to realize a fully continuous process remains elusive. To achieve whole continuous production of aerogel fibers, unraveling the mechanism of solvent removal during a dynamic rapid decompression is critical, accompanied by instrument capability. With the simultaneous advancement of materials and fabrication, aerogel fibers could have many potential applications. ■

Next-generation textiles with enhanced thermal insulation

Polar bear hairs are composed of a porous core surrounded by a dense shell, which provides heat insulation in extremely cold conditions. Mimicking the structure of these hairs by encapsulating an aerogel core in a thermoplastic polyurethane (TPU) shell confers mechanical robustness and superior thermal insulation. These encapsulated aerogel fibers (EAFs) can be woven, dyed, stretched, and washed, making them ideal for use in textiles; EAFs could also have other applications beyond personal warming.

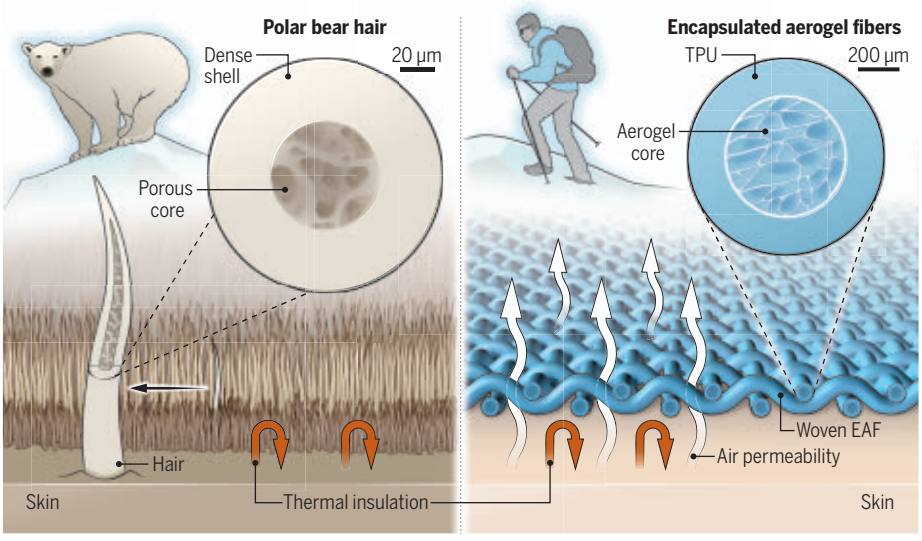

GRAPHIC: N. BURGESS/*SCIENCE*

REFERENCES AND NOTES

1. M. Wu *et al.*, *Science* **382**, 1379 (2023).
2. Z. Liu, J. Lyu, D. Fang, X. Zhang, *ACS Nano* **13**, 5703 (2019).
3. Y. Du *et al.*, *ACS Nano* **14**, 11919 (2020).
4. Y. Hou, Z. Sheng, C. Fu, J. Kong, X. Zhang, *Nat. Commun.* **13**, 1227 (2022).
5. G. Li, G. Hong, D. Dong, W. Song, X. Zhang, *Adv. Mater.* **30**, 1801754 (2018).
6. Y. Li, X. Zhang, *Adv. Funct. Mater.* **32**, 2107767 (2021).
7. X. Li, G. Dong, Z. Liu, X. Zhang, *ACS Nano* **15**, 4759 (2021).
8. Z. Sheng *et al.*, *Adv. Sci.* **10**, 2205762 (2023).
9. S. Zhao *et al.*, *Nature* **584**, 387 (2020).
10. A. E. Aliev *et al.*, *Science* **323**, 1575 (2009).
11. X. Xu *et al.*, *Science* **363**, 723 (2019).
12. Z. Sheng *et al.*, *Adv. Mater.* **33**, 2104851 (2021).
13. H. Jiang *et al.*, *Small* **19**, 2302627 (2023).
14. A. Geilen *et al.*, *Nat. Phy.* **19**, 1805 (2023).
15. X. Yang *et al.*, *Adv. Healthc. Mater.* **12**, 2201591 (2023).

10.1126/science.adm8388

NEUROLOGY

Neurosurgery elucidates somatic mutations

Surgical innovation is helping to identify roles for somatic mutations in brain disorders

By Eduardo A. Maury[1,2,3], Christopher A. Walsh[1,3,4], Kristopher T. Kahle[1,5,6,7]

Somatic variants are genomic alterations present in some cells of the body but not in others. In contrast to inherited germline variants, somatic variants are typically acquired during postzygotic cell divisions or from environmental factors. Somatic variants in a given tissue can also be highly dynamic, such as in the brain, where the number of clonal variants can change during aging and disease (*1*). Neuro-oncology has greatly benefited from the analyses of somatic mutations in tissue obtained from surgical biopsies or resections. Increased understanding of somatic mutations in brain tumors brought a revolution in prognostication and individualized treatments. Somatic mutations are now increasingly being implicated in neurological disorders beyond cancer, particularly in children with congenital brain and cerebrovascular diseases. Teams of neurosurgeons and scientists are performing gene sequencing on surgical brain samples from these patients—paving the way to expand understanding of nononcologic brain disease through the study of somatic mutations.

To date, most studies of somatic mutations in nononcologic neurological disease have relied on post-mortem brain samples or samples from other tissues, such as the blood. This is partly owing to the limited number of medically indicated approaches for obtaining brain tissue while the patient is alive and current clinical practice that frequently discards tissue during surgery because it is thought to be of limited diagnostic value. This lack of fresh brain tissue limits the sensitivity and specificity of somatic mutation detection because DNA and RNA quality can degrade post-mortem, and variants specific to brain cells might not be present in nonbrain tissue. In addition, blood, which is the most readily available tissue for sampling, can accumulate tissue-specific somatic mutations such as variants acquired through clonal hematopoiesis, which complicates the detection of somatic variants present in the nervous system.

Several recent studies have demonstrated the power of exploring somatic mutations directly from tissue collected in the operating room to gain insights into neurological disorders. These disorders include congenital focal cortical dysplastic syndromes such as focal cortical dysplasia (FCD) and hemimegalencephaly (HMG) (*2*–*4*). Clinically, patients with these conditions present with seizures refractory to pharmacological management and are diagnosed by use of brain imaging to detect lesions that disrupt the cortical layering of the brain. Lesion size can vary from subcentimeter in FCD to a whole hemisphere in HMG. The current treatment is radical surgical excision of the lesions, which puts the patient at high risk of morbidity, especially in the case of hemispherectomy to treat HMG.

Genetic causes of these conditions were initially difficult to identify because they only affected a subset of cells. Blood samples obtained from patients with FCD and HMG appear largely normal when analyzed with traditional sequencing approaches that capture germline variants. However, the development of next-generation sequencing technologies and bioinformatic pipelines has made it possible to identify somatic variants from neurosurgically resected samples. Using this approach, somatic mutations in the mechanistic target of rapamycin (*MTOR*) gene that increase mTOR pathway activity were identified as causative of these disorders. The mTOR pathway helps determine cell size and has been implicated in cancer. Larger lesions had a larger proportion of cells affected by the mutations (*4*, *5*). These genetic insights were brought about through collaborations between neurosurgeons and scientists and led to a new clinical classification system for FCD (*6*).

Inhibitors of the mTOR pathway now represent promising therapeutic approaches for patients with FCD and HMG. Small-molecule inhibitors used to treat cancer could in theory be used as monotherapies or adjuncts to surgical resection for the treatment of FCD or HMG. These inhibitors include sirolimus and evorolimus, which target mTOR directly, or duvelisib, and miransertib (ARQ-092), which target proteins that interact with mTOR. Encouragingly, treating patients with tuberous sclerosis and phosphatase and tensin homolog (PTEN) hamartoma tumor syndrome (both neurodevelopmental disorders) with evorolimus resulted in improved clinical outcomes in randomized clinical trials (*7*, *8*). Phase 2 clinical trials on the effect of evorolimus on FCD are currently underway in the United States (NCT02451696) and South Korea (NCT03198949). However, questions remain on the optimal inclusion criteria or treatment combinations for these studies.

More recently, somatic mutations have been implicated in mesial temporal lobe epilepsy, which is one of the most common forms of epilepsy and is often resistant to treatment with antiseizure medication. Whole-exome sequencing of 105 hippocampal samples from patients with this type of epilepsy who underwent surgical treatment revealed pathogenic somatic variants in protein tyrosine phosphatase nonreceptor type 11 (*PTPN11*), son of sevenless homolog 1 (*SOS1*), *KRAS*, *BRAF*, and neurofibromin 1 (*NF1*). These genes are all known or predicted to activate the mitogen-activated protein kinase (MAPK) signaling pathway, which is involved in cancer (*9*). Therefore, established anticancer agents targeting the MAPK pathway could be imagined as neurosurgical adjuncts or even a primary treatment option for this disorder.

Recent studies of somatic mutations in sporadic arteriovenous malformations (AVMs) revealed activating mutations in *KRAS* that can be therapeutically targeted (*10*). AVMs are vascular lesions present in the brain that cause hemorrhagic strokes by forming abnormal connections between arteries and veins, forming a nidus (tangle) of fragile blood vessels. Currently, surgery is the only treatment for this condition, but surgery is highly challenging, and complications such as massive bleeding occur frequently. Consequently, interventions carry high risk of morbidity for the patient and require specialized neurosurgical care, which is not readily available worldwide. In one study, therapeutically

[1]Division of Genetics and Genomics, Manton Center for Orphan Disease, Boston Children's Hospital, Boston, MA, USA. [2]Harvard/MIT MD-PhD Program, Harvard Medical School, Boston, MA, USA. [3]Program in Medical and Population Genetics, Broad Institute of MIT and Harvard, Cambridge, MA, USA. [4]Howard Hughes Medical Institute, Boston Children's Hospital, Boston, MA, USA. [5]Program in Neuroscience, Broad Institute of MIT and Harvard, Cambridge, MA, USA. [6]Department of Neurosurgery, Boston Children's Hospital, Boston, MA, USA. [7]Department of Neurosurgery, Massachusetts General Hospital, Boston, MA, USA. Email: kahle.kristopher@mgh.harvard.edu; christopher.walsh@childrens.harvard.edu

Somatic variation–informed neurosurgery and medical management

In the future, somatic mutation information could be used to direct neurosurgical and medical management of neurological disorders. Biopsies or surgical resection samples could be obtained and processed through next-generation sequencing to identify somatic variants. These variants could then be correlated with clinical data such as demographics, neurophysiology, neuroimaging, and medical history to expand research efforts and identify targeted therapies that could be used as monotherapy or adjuncts to surgery. This information could also be used for surgical planning if necessary.

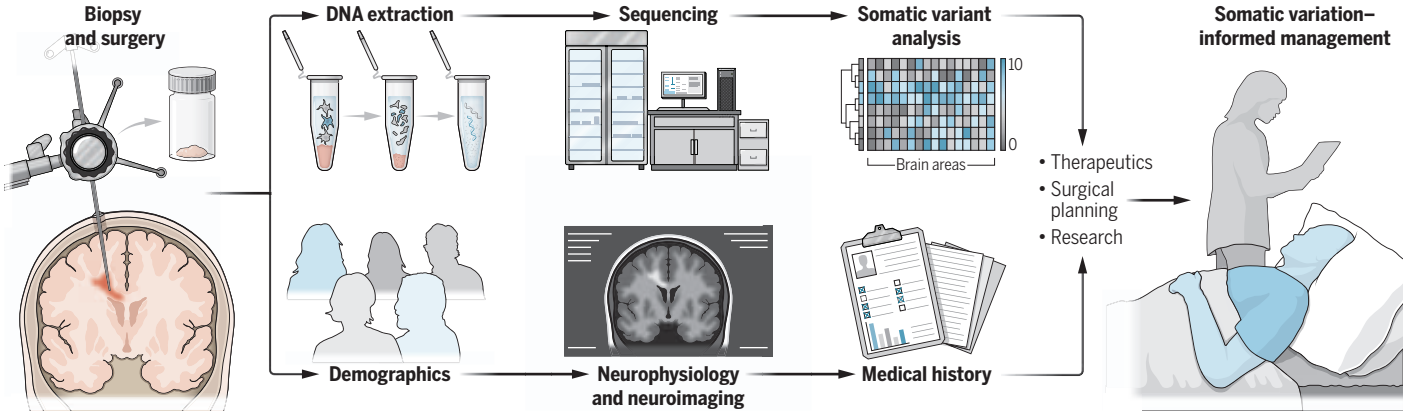

GRAPHIC: A. FISHER/*SCIENCE*

resected samples from 26 patients with AVMs were obtained, and whole-exome sequencing was used to identify somatic mutations present in at least 1% of cells. Using cell-sorting and digital droplet polymerase chain reaction–based sequencing, the study showed that pathogenic somatic mutations in *KRAS* were enriched in brain endothelial cells. Furthermore, application of MAPK kinase (MEK) and phosphatidylinositol 3-kinase (PI3K) inhibitors to cultured endothelial cells down-regulated the KRAS signaling pathway, demonstrating potential therapeutic efficacy for AVMs.

The full resection of pathological tissues can be difficult or unsafe, particularly in nononcologic disorders such as multifocal epilepsy and neurovascular disease. Therefore, to expand the study of somatic variants in neurological disease, innovative tissue sampling approaches are required. To overcome this challenge, neurosurgeons have started to create methods that permit tissue sampling during common procedures. These sampling approaches could then also be used to inform the pharmacological and surgical approaches that are used to treat the disease before attempting a full resection.

The standard diagnosis of a patient with treatment-resistant epilepsy involves the implantation of stereo-electroencephalography electrodes, which allow intracranial recordings of electrical activity, to identify the source of epileptogenic activity in the brain. In one study, DNA was obtained from the electrodes after they had been removed from the brain. Analysis of this DNA identified pathogenic somatic variants in the FCD-related genes *AKT3* and DEP domain containing 5, GATOR1 subcomplex subunit (*DEPDC5*). The brain regions carrying the highest fraction of cells with somatic mutations in these genes corresponded to the area of largest epileptogenic activity across individuals (*11*). This study highlights the great clinical potential of using electrodes to identify correlations between somatic genomic alterations and functional brain disruption. The approach could be extended to study how somatic variants and epileptic activity disrupt transcription: Highly epileptogenic regions could be compared with those with normal neuronal activity. More specific analyses for detecting somatic variants or designs of electrodes that optimize tissue sampling might provide higher-definition genomic maps of the brain.

Another promising approach is endovascular sampling of blood vessel lumens (*12*), although its application to somatic variant detection is yet to be explored. This approach makes use of diagnostic cerebral angiography, which involves the insertion of a catheter into the patient's vasculature and injection of dye to visualize blood vessel morphology. This procedure is commonly used in the diagnosis and staging of vascular pathologies from strokes to vascular malformations. A guidewire can accurately target a specific region of the lumen for sampling. In a study of patients with AVM, the gene expression profile of the lumen samples not only captured dysregulation in the expected MAPK pathway but also correlated well with the expression profile of the resected AVMs from these patients (*12*). This is a notable finding because this approach could allow for surgical planning based on the molecular profile of the vascular pathology and could be applied to any pathology for which diagnostic cerebral angiopathy is used. However, whether it could yield enough DNA for the detection of somatic variants remains an open question.

In addition to congenital or neurodevelopmental disorders, somatic mutations are being studied in neurodegeneration. A study in Alzheimer's disease performed single-cell whole-genome sequencing on neurons from post-mortem brain samples and found an increased rate of somatic mutations in neurons from individuals with Alzheimer's disease compared with controls. This increase was partly driven by higher amounts of oxidative damage to nucleotides (*13*). Some existing neurosurgical approaches are suited to sample tissue from individuals with neurodegenerative disorders—for example, using the tissue along the path of deep-brain stimulation electrodes in Parkinson's disease, or biopsies of the insertion site when implanting a ventricular shunt in a patient with normal-pressure hydrocephalus. However, these approaches have not yet been used for the detection of somatic mutations. Deep-brain stimulation is beginning to be used for the treatment of neuropsychiatric disorders, and the ability to sample brain tissue directly from this patient population represents an exciting new frontier in somatic mutation research.

To assess the somatic mutation landscape more fully across neurological disorders, it is vital to leverage consortia and biobanks to gather large numbers of surgically resected brain samples. Neurosurgeons and scientists from the Cleveland Clinic in the United States and the European Brain Bank Consortium were recently able to gather 474 neurosurgically resected brain samples from individuals with various forms of drug-resistant epilepsy. They performed

high-depth whole-exome sequencing to identify putative genes associated with epilepsy and to compare somatic mutation rates across disorders (*14*). The use of consortia could also help to obtain control tissue that is typically discarded—for example, intact blood vessels from resected lobectomies or nondiseased tissue from wide resections. Further efforts of consortia to bring neurosurgeons and scientists together have the potential to enhance understanding of these highly complex disorders (*15*).

The basic and translational research of somatic mutations in neurological disorders will require close collaborations across disciplines. From molecular biologists to bioinformaticians and clinicians, it is essential that there is an appreciation of the intricacies of the current treatment of these disorders. However, as the limits of what can be learned from post-mortem tissues are reached, it is critical that neurosurgeons lead innovation in tissue sampling and data analysis to maximize not only how much can be learned from patients but also how these findings can be effectively translated into better outcomes (see the figure). More imperative, training specialized neurosurgeon-scientists able to wield both classical neurosurgical micro-instruments as well as new tools, including "molecular scalpels" (pharmacotherapy or gene therapies) and the computational algorithms required to analyze these samples, will further catalyze the translation of somatic mutation research into benefits for patients. ■

REFERENCES AND NOTES

1. S. Bizzotto, *Front. Neurosci.* **17**, 1172469 (2023).
2. N. S. Sim *et al.*, *Acta Neuropathol.* **138**, 901 (2019).
3. S. Baldassari *et al.*, *Acta Neuropathol.* **138**, 885 (2019).
4. A. M. D'Gama *et al.*, *Cell Rep.* **21**, 3754 (2017).
5. J. H. Lee *et al.*, *Nat. Genet.* **44**, 941 (2012).
6. I. Najm *et al.*, *Epilepsia* **63**, 1899 (2022).
7. S. Srivastava *et al.*, *Hum. Mol. Genet.* **31**, 3393 (2022).
8. M. Li *et al.*, *Orphanet J. Rare Dis.* **14**, 39 (2019).
9. S. Khoshkhoo *et al.*, *JAMA Neurol.* **80**, 578 (2023).
10. S. I. Nikolaev *et al.*, *N. Engl. J. Med.* **378**, 250 (2018).
11. R. Checri *et al.*, *Brain Commun.* **5**, fcad174 (2023).
12. E. Winkler *et al.*, *Neurology* **98**, e1637 (2022).
13. M. B. Miller *et al.*, *Nature* **604**, 714 (2022).
14. J. A. López-Rivera *et al.*, *Brain* **146**, 1342 (2023).
15. C. Chung *et al.*, *Nat. Genet.* **55**, 209 (2023).

ACKNOWLEDGMENTS

E.A.M. is supported by the Harvard/MIT MD-PhD program (T32GM007753) and the Ruth L. Kirschstein NRSA F31 Fellowship (F31MH124292). C.A.W. was supported by grants from the NIH (R01-NS035129, R01NS032457, and R01AG070921), the Tan Yang Center for Autism Research, and by the Allen Frontiers Program. C.A.W. is an investigator of the Howard Hughes Medical Institute. K.T.K. was supported by the Yale-Rockefeller Centers for Mendelian Genomics; grants R01-NS109358, R01-NS111029, and R01-NS117609 from the National Institutes of Health; the Simons Foundation; March of Dimes; Hydrocephalus Association; and Rudi Schulte Research Institute. K.T.K. and C.A.W. have a US provisional patent (application no. 63/462,890) for the causal role of Ras/Raf/MAPK pathway overactivation in focal epilepsy pending (planned filing).

10.1126/science.adj2244

PSYCHOLOGY

Increasing policy support for reducing racial health disparities

Perceiving racial health disparities as unjust could catalyze or halt change

By **Allison Earl**[1] *and* **Veronica Derricks**[2]

In the United States, Black Americans experience disproportionately negative outcomes in domains as varied as wealth, employment, and health (*1*). However, efforts to obtain support for the policies necessary to tackle these disparities have had limited success, underscoring a critical need for effective interventions to change behavior. On page 1394 of this issue, Brown *et al.* (*2*) report that highlighting racial health disparities was more likely to prompt social media engagement and policy support compared with highlighting disparities in economic measures or belongingness (the feeling of being an accepted member of a group). The authors demonstrated that health disparities are catalyzing because health inequities contravene moral values that should never be violated and, consequently, evoke feelings of injustice. The premise is intriguing and could be used to increase policy support for reducing racial gaps.

Information about racial health disparities results in more social media engagement than information about other types of racial disparities.

PHOTO: PEOPLEIMAGES/ISTOCK.COM

Myriad factors contribute to racial disparities in health outcomes at both the interpersonal and structural levels. Interpersonally, clinicians often hold racial biases that influence clinical decision-making (e.g., chemotherapy or screening recommendations) (*3*) and behaviors (e.g., attempts at relationship building) (*4*). Structurally, policies can negatively affect Black Americans' access to and quality of health care (e.g., unequal allocation of resources, such as vaccines, and limited clinic locations and hours) (*5*). Policies that are ostensibly unrelated to health care also have widespread effects on health outcomes. For instance, economic and governmental institutions that restrict wealth for racially minoritized populations (e.g., charging higher interest rates when purchasing a home) can shape Black Americans' access to health care and transportation, insurance costs, and financial resources available for medical treatments (*6*).

Despite the persistence of health inequities, politicians, policy-makers, and the general public in the US have shown little interest in taking action to effectively mitigate these disparities and may actively work to maintain these gaps (e.g., continued efforts to repeal the Affordable Care Act and restrict Medicaid funding) (*7*). In their work, Brown *et al.* randomly assigned Americans to view information (messages and infographics) about racial disparities in health, economic factors, or belongingness in either experimental (online) or social media contexts. They found that information about health disparities increased perceived injustice, which enhanced social media engagement and support for policies to reduce disparities.

Given these findings, one temptation may be to frame all racial disparities in the context of their impact on health. Yet, decades of research, billions of dollars in funding, and

[1]Department of Psychology and Research Center for Group Dynamics at the Institute for Social Research, University of Michigan, Ann Arbor, MI, USA. [2]Department of Psychology, Indiana University, Indianapolis, IN, USA. Email: anearl@umich.edu

the National Institute on Minority Health and Health Disparities have been dedicated to reducing disparities in health outcomes. Although many outcomes have improved (e.g., disparities in cancer rates) (*3*), many disparities remain.

Brown *et al.*'s findings suggest that perceiving injustice is key for inspiring support for policies designed to ameliorate disparities. People are motivated to believe that they live in a just society, where individuals get what they deserve, and that society has created institutions that afford everyone fundamental human rights (*8*). However, perceiving injustice may not always prompt remediation; people may manage perceptions of injustice by deepening their commitment to systems that create and reinforce disparities at the expense of minoritized groups (*8*). For instance, a sample of mostly white Americans reported less support for economic- and health-related policies to manage COVID-19 when the policies explicitly mentioned that Black individuals would benefit (*9*).

People are also sensitive to social group membership and prefer to allocate resources to "people like me" at the expense of "people not like me" (*10*). For example, when faced with the notion that their racial group may lose social status, white Americans were more likely to endorse policies that favored their own group at the expense of other racial groups (*11*). White Americans may also dehumanize Black Americans so that the inequities are no longer perceived as unjust (*12*). To have the most impact, work aimed at implementing the findings from Brown *et al.* may need to consider that people are motivated to maintain the status quo and may react against perceived injustice by doubling down on the inequities instead of reducing them.

Brown *et al.* examined how people respond once confronted with injustice; however, people might be content to simply avoid confronting injustice altogether. For instance, white Americans would rather avoid racialized information than acknowledge racial advantages and disadvantages (*13*). Indeed, people prefer to ignore, derogate, or counterargue messages that challenge their current attitudes and behaviors rather than be persuaded by them (*14*). Unless someone is already engaging in egalitarian actions or has positive attitudes toward reducing racial gaps in outcomes, then they may be more likely to ignore any message about racial disparities rather than acting to remedy them.

It is also important to consider the perspective of audiences who are directly implicated by messages describing disparities. For example, receiving information that highlights racial disparities in HIV rates reduces Black Americans' attention to the information and lowers their trust in the information provider because such information raises concerns about being judged by one's racial identity (*15*). Thus, if interventions do not carefully consider the experiences that audiences are bringing with them, they may evoke disengagement and ironically exacerbate the problems that they are attempting to remedy.

Racial disparities in the US persist across many important domains. Brown *et al.* have taken up the call to address these disparities by designing and implementing a series of thought-provoking studies that highlight perceived injustice as a lever to motivate action on racial gaps. To foster policy support most successfully, researchers must take into account how audiences may respond to perceiving injustice. To build on Brown *et al.*'s galvanizing work, scholars could develop complementary interventions that address barriers that might arise when encountering messages highlighting injustice (e.g., people not wanting to engage with the messages or having little empathy for groups implicated by these disparities). This will allow the difficult but incredibly important work of reducing racial gaps to continue. ■

REFERENCES AND NOTES

1. N. Ndugga, S. Artiga, "How Recognizing Health Disparities for Black People is Important for Change" (Kaiser Family Foundation, 2023); https://www.kff.org/policy-watch/how-recognizing-health-disparities-for-black-people-is-important-for-change/.
2. R. M. Brown *et al.*, *Science* **382**, 1394 (2023).
3. M. Tong *et al.*, "Racial Disparities in Cancer Outcomes, Screening, and Treatment" (Kaiser Family Foundation, 2022); https://www.kff.org/racial-equity-and-health-policy/issue-brief/racial-disparities-in-cancer-outcomes-screening-and-treatment/.
4. M. J. Shen *et al.*, *J. Racial Ethn. Health Disparities* **5**, 117 (2018).
5. B. Starfield *et al.*, *Annu. Rev. Public Health* **33**, 89 (2012).
6. R. Rothstein, *The Color of Law: A Forgotten History of How Our Government Segregated America* (Liveright Publishing, 2017).
7. The White House, "Fact Sheet: The Congressional Republican Agenda: Repealing the Affordable Care Act and Slashing Medicaid" (The White House Statements and Releases, 2023); https://www.whitehouse.gov/briefing-room/statements-releases/2023/02/28/fact-sheet-the-congressional-republican-agenda-repealing-the-affordable-care-act-and-slashing-medicaid/.
8. J. T. Jost *et al.*, *Polit. Psychol.* **25**, 881 (2004).
9. A. Franks *et al.*, *Anal. Soc. Issues Public Policy* **22**, 130 (2022).
10. H. Tajfel, J. C. Turner, in *Political Psychology: Key Readings*, J. T. Jost, J. Sidanius, Eds. (Psychology Press, 2004), pp. 276–293.
11. M. A. Craig, J. A. Richeson, *Psychol. Sci.* **25**, 1189 (2014).
12. P. A. Goff *et al.*, *J. Pers. Soc. Psychol.* **94**, 292 (2008).
13. J. R. Schultz *et al.*, *Transl. Issues Psychol. Sci.* **1**, 392 (2015).
14. A. Earl, M. P. Hall, in *The Handbook of Attitudes, Volume 1: Basic Principles*, D. Albarracin, B. T. Johnson, Eds. (Routledge, 2018), pp. 377–403.
15. V. Derricks, A. Earl, *J. Commun.* **73**, 511 (2023).

ACKNOWLEDGMENTS

The authors thank D. Albarracin, S. Dal Cin, D. Dunning, D. Hertz, P. Ellsworth, E. Kross, N. Lewis, S. McClelland, H. Mehlman, M. Meyer, M. Rodriguez, R. Smallman, J. Smith, K. Sonneville, K. Takahashi, and L. White for feedback.

10.1126/science.adm7199

NEUROSCIENCE

An unexpected role for a glutamate receptor

γ-Aminobutyric acid acts on a glutamate receptor, evoking synaptic plasticity

By **Ian D. Coombs** *and* **Mark Farrant**

Ion channels activated by the neurotransmitter glutamate underlie excitatory signaling between neurons in the brain. In mammals, these ionotropic glutamate receptors (iGluRs) belong to three families formed from GluA, GluN, and GluK subunits, respectively: the α-amino-3-hydroxy-5-methyl-4-isoxazolepropionic acid (AMPA), *N*-methyl-D-aspartate (NMDA), and kainate receptors (*1*). By contrast, receptors of a fourth homologous iGluR family—the δ or GluD receptors—do not respond to glutamate. Despite sharing a similar architecture with other iGluRs, including a transmembrane pore, the question of whether GluD receptors pass current has been controversial (*2*, *3*). Instead, they are best known as synaptic organizing proteins (*2*, *4*). On page 1389 of this issue, Piot *et al.* (*5*) show that one GluD family member, GluD1, can bind the inhibitory neurotransmitter γ-aminobutyric acid (GABA) and trigger potentiation of GABA-mediated synaptic currents. This challenges the dogmatic distinction between glutamate and GABA receptors and identifies GluD1 as a regulator of inhibitory signaling.

The GluD family members, GluD1 and GluD2, can both be found at excitatory synapses. They connect, through adaptor proteins of the cerebellin family, to presynaptic adhesion molecules of the neurexin family, forming trans-synaptic complexes that play key roles in synapse assembly and activity-driven synaptic modifications (*6*). These roles were first identified for GluD2 at synapses made by granule cell parallel fibers onto Purkinje cells in the developing cerebellum, where the binding of D-serine, released by Bergmanglia, enables long-term depression of excitatory transmission by facilitating

Department of Neuroscience, Physiology, and Pharmacology, University College London, London, UK. Email: i.coombs@ucl.ac.uk; m.farrant@ucl.ac.uk

AMPA receptor internalization (*7*). GluD1 is similarly implicated in trans-synaptic interactions that have been shown to influence the formation of excitatory synapses (*8*) and the balance of AMPA receptor– and NMDA receptor–mediated signaling (*9*). However, distinct among iGluRs, GluD1 has also been found at GABA-releasing inhibitory synapses, specifically, at those between somatostatin-positive interneurons and cortical pyramidal neurons. GluD1 interactions with cerebellin and neurexin, together with the binding of D-serine or glycine, are proposed to trigger intracellular signals that regulate the assembly of the inhibitory postsynapse (*10*).

Prompted by these findings, Piot *et al.* investigated the action of GABA on GluD1 receptors. Using recombinant receptors expressed in African clawed frog (*Xenopus laevis)* oocytes, they recorded currents from consitutively open GluD1 and GluD2 "Lurcher" mutants (*11*). The authors found that the GluD1 currents were enhanced by both D-serine and GABA, which competed for the same binding site. GABA was as efficacious as D-serine, albeit with much lower potency. By contrast, GluD2 currents were inhibited by D-serine but unaffected by GABA, hinting at multiple functional differences between GluD1 and GluD2, at least in their Lurcher forms. Piot *et al.* visualized GABA binding to GluD1 using x-ray crystallography of isolated GluD1 ligand-binding domains, which established that key molecular determinants of the binding are shared by GABA and D-serine, consistent with the competitive actions observed. Of critical importance for their subsequent experiments, the authors also identified point mutations in GluD1 that were able to abolish GABA binding while leaving D-serine binding largely intact.

To address the question of whether GABA could signal through wild-type (non-Lurcher) GluD1 receptors at synapses, Piot *et al.* recorded from CA1 pyramidal neurons in acute hippocampal slices from mice and electrically stimulated the release of GABA from neurons in the stratum lacunosum-moleculare (where the dendrites of CA1 pyramidal neurons are located), which is a region of intense GluD1 expression. Bursts of high-frequency synaptic stimulation, or application of D-serine, enhanced the amplitude of inhibitory postsynaptic currents (IPSCs) mediated by type A GABA ($GABA_A$) receptors (see the figure). These effects were occluded by short hairpin RNA–based down-regulation of GluD1 expression. Moreover, by introducing GluD1 mutants that lacked specific signaling capabilities, the authors showed that GABA binding and cerebellin interactions were required for the enhancement of IPSC amplitude but the passage of ions through GluD1 channels was not.

It remains to be determined which of the four isoforms of cerebellin (*4*) participate in the inhibitory plasticity described by Piot *et al.* and whether this "non-ionotropic" effect of GluD1 requires cerebellin to be engaged with presynaptic neurexins. This is a key question. GABAergic interneurons are famously heterogeneous, and such interactions might be expected to determine the cellular specificity of the plasticity. Multiple distinct interneuron subtypes are found in, or bordering, the stratum lacunosum-moleculare, prominent among which are neurogliaform cells (*12*). These form atypical synapses and, unlike most other interneurons, their activation results in prolonged GABA elevations that reach relatively low peak concentrations. Given this, the apparent low affinity of GluD1 for GABA is particularly intriguing.

How has the iGluR gating machinery been adapted by GluD1 to produce an apparently non-ionotropic effect? Of note, calcium ions greatly decrease the potency of D-serine at GluD2-Lurcher receptors by stabilizing the receptor ligand-binding domains in a dimeric conformation (*13*), likely dictating whether ligand binding ultimately engages gating- or desensitization-like states. The GluD1 ligand-binding domain structures obtained by Piot *et al.* contain calcium ions bound at the dimer interface; whether the functional influence of these ions is similar to that seen with GluD2, and how this affects the synaptic action of GABA on GluD1, are important issues. Some of these questions might be addressed by using cryo–electron microscopy to visualize intact GluD1 receptors in the presence and absence of GABA and calcium ions.

Beyond the immediate mechanics of GluD1 "activation," it is not known which downstream effector proteins and signaling pathways are ultimately key to IPSC potentiation nor how this potentiation interacts with other forms of inhibitory plasticity. The low affinity of GABA, and, therefore, the presumed brevity of the GluD1 signal (even during high-frequency synaptic stimulation), suggests a tight linkage between GluD1 and its effector. An unbiased proteomic screen previously identified several potential GluD1 interacting proteins (*10*), but their roles in the newly described GABA-induced plasticity remain to be determined. It is interesting to note the recent recognition that alternative splicing can give rise to GluD1 isoforms with different carboxy-terminal cytoplasmic tails (*14*). This raises the possibility of different cohorts of GluD1 binding partners and thus the involvement of different signaling pathways that are potentially dependent on the type of synapse or developmental stage.

In humans, numerous variants of the gene encoding GluD1 (*GRID1*) have been identified. These copy number and missense variants are associated with several neurological conditions, including schizophrenia, autism, intellectual disability, and seizures (*15*). Whether the disruption of GluD1-dependent inhibitory plasticity plays any role in the effects of disease-associated *GRID1* variation is an important question for future study. ■

A new mediator of inhibitory plasticity

GluD1 receptors form trans-synaptic complexes that include cerebellins (CBLN) and neurexin (NRXN). At an inhibitory hippocampal synapse, GluD1 can bind γ-aminobutyric acid (GABA), causing the potentiation of type A GABA ($GABA_A$) receptor–mediated inhibitory postsynaptic currents (IPSCs). When GluD1 binds GABA (two of the four subunits are shown), it likely undergoes structural changes akin to those leading to gated and desensitized states in other ionotropic glutamate receptors, but the mechanism that leads to potentiated IPSCs is unknown.

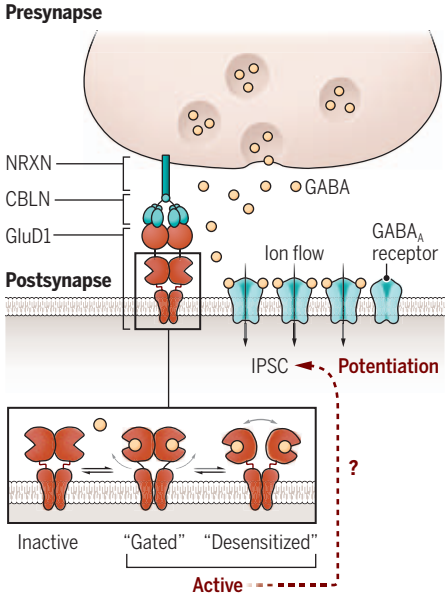

GRAPHIC: A. MASTIN/*SCIENCE*

REFERENCES AND NOTES

1. K. B. Hansen *et al.*, *Pharmacol. Rev.* **73**, 1469 (2021).
2. M. Yuzaki, A. R. Aricescu, *Trends Neurosci.* **40**, 138 (2017).
3. J. Kumar *et al*, *Biophys. J.* **122**, 2383 (2023).
4. T. C. Südhof, *Curr. Opin. Neurobiol.* **81**, 102727 (2023).
5. L. Piot *et al.*, *Science* **382**, 1389 (2023).
6. M. Fossati, C. Charrier, *Curr. Opin. Neurobiol.* **66**, 85 (2021).
7. W. Kakegawa *et al.*, *J. Physiol.* **584**, 89 (2007).
8. W. Tao *et al.*, *Proc. Natl. Acad. Sci. U.S.A.* **115**, E5373 (2018).
9. J. Dai *et al.*, *Nature* **595**, 261 (2021).
10. M. Fossati *et al.*, *Neuron* **104**, 1081 (2019).
11. L. P. Wollmuth *et al.*, *J. Neurosci.* **20**, 5973 (2000).
12. M. Capogna, *J. Physiol.* **589**, 1875 (2011).
13. K. B. Hansen *et al.*, *J. Neurosci.* **29**, 907 (2009).
14. R. Herbrechter *et al.*, *Cell. Mol. Life Sci.* **78**, 5605 (2021).
15. J. P. Allen *et al.*, *Hum. Mol. Genet.* 10.1093/hmg/ddad188 (2023).

ACKNOWLEDGMENTS

M.F. is supported by the Medical Research Council (MR/T002506/1) and the CureGRIN Foundation.

10.1126/science.adm6771

RETROSPECTIVE

Endel Tulving (1927–2023)

Explorer, innovator, and theorist of human memory

By **Roberto Cabeza**[1,2] *and* **Emrah Düzel**[3,4]

Endel Tulving, leader in the field of human memory research, died on 11 September. He was 96. Tulving pioneered the study of memory encoding and retrieval conditions and first distinguished episodic from semantic memory. His work with amnesic patients yielded insights into implicit memory, multiple memory systems, and the relationship between memory and consciousness. Tulving also embraced emerging functional neuroimaging techniques, elucidating the roles of frontal and parietal lobes in episodic memory.

Born on 26 May 1927 in Petseri, Estonia, Tulving moved to Germany at age 19 and to Canada in 1949. He earned his bachelor's and master's degrees in psychology from the University of Toronto in 1953 and 1954, respectively. After completing his PhD in experimental psychology at Harvard University in 1956, he joined the University of Toronto faculty. Except for a few years at Yale University, he remained there until he retired in 1992.

Joining the cognitive revolution, Tulving challenged the idea of memory as simple stimulus-response associations. In 1966, he showed that learners impose subjective organization onto new information. In 1973, he revealed the "encoding specificity principle": Retrieval cues' capacity to elicit memories depends on matching encoding conditions.

Distinguishing semantic memory (general knowledge of the world) and episodic memory (personally experienced unique events) was Tulving's most far-reaching contribution. When he proposed the idea in 1972, he stirred intense debate by upending the prevailing view that long-term memory was unitary. The episodic-semantic distinction has since influenced the fields of cognition, neuropsychology, cognitive neuroscience, and clinical research on, for instance, Alzheimer's disease and frontotemporal dementias.

In the mid-1970s, Tulving began conducting neuropsychological research on patients with brain injuries. Alongside his graduate student Daniel Schacter, he investigated the distinction between explicit (conscious) and implicit (unconscious) memory, finding in 1982 that recognition memory, like other explicit memory types, declines over time, but priming effects do not. This revelation and other evidence led him to propose a multiple memory systems theory including episodic, semantic, and implicit memory systems.

In 1985, Tulving associated memory forms with types of conscious awareness: procedural memory (skill learning) is "anoetic" (non-knowing), semantic memory is "noetic" (knowing), and episodic memory is "autonoetic" (self-knowing) awareness. He coined the term "mental time travel" to convey that autonoetic awareness is akin to reliving a past experience. These links to consciousness allowed Tulving to address memory tests' inability to isolate one type of memory. He introduced the remember/know paradigm, in which participants use subjective experience to distinguish between two components of recognition memory: recollection, which truly reflects episodic memory, and familiarity, which may reflect contributions of other memory systems. The remember/know paradigm has been widely used since, including in patient and functional neuroimaging studies.

PHOTO: KEITH BEATY/TORONTO STAR VIA GETTY IMAGES

After retirement, Tulving moved to the Rotman Research Institute of the Baycrest Centre in Toronto and became a visiting professor at the Center for Neuroscience and Department of Psychology at the University of California, Davis. One of the first memory researchers to adopt brain imaging technology, Tulving was intrigued by the possibility of determining whether episodic versus semantic memory, and autonoetic versus noetic awareness, are neurobiologically dissociable. In 1994, he used positron emission tomography (PET) studies to show the involvement of frontal and parietal regions in episodic memory. He also noticed that early PET studies revealed an intriguing regularity: Episodic encoding elicited activations mainly on the left prefrontal cortex, but retrieval engaged primarily right prefrontal regions. The right-lateralization of retrieval activity was linked to the mental state of episodic retrieval Tulving called "episodic retrieval mode," which was associated with sustained activity. Tulving's novelty-encoding hypothesis highlighted the neurobiological and motivational importance of novel events for forming new episodic memories. In the late 1990s, he realized that episodic memory allows mental time travel to one's future as well as past.

We and our collaborator Lars Nyberg were among Tulving's first postdoctoral students at Rotman. At weekly meetings, when postdocs presented ideas, Tulving's input was witty and sharp but always friendly. He celebrated our successes. During his frequent visits to the postdoc office, he would ask us about our latest discoveries or what we had learned from Mother Nature before telling us a dad joke. His humor also infused his scientific communication. During one lecture at an international conference, he had a student cross the stage dressed in a gorilla costume to make the point that novelty is key to making episodic memories endure. Indeed, we can still vividly recall this event 25 years later.

With his ability to communicate across disciplines and his openness to unfamiliar research fields, Tulving welcomed us into cross-disciplinary endeavors in episodic memory in nonhuman animals, clinical neurology, and psychiatry. Although at times he expressed annoyance when a grant or paper was rejected, he would immediately rally and try again. He and his wife, accomplished artist Ruth Mikkelsaar, enjoyed hosting us in their home, where we drank Manhattans and discussed wide-ranging topics and ideas.

Tulving's numerous honors and awards include memberships in multiple national academies and societies. He also received distinguished contribution awards from the American Psychological Association and the Association for Psychological Science and was made an Officer of the Order of Canada, the country's most prestigious civilian honor.

In addition to his pioneering contributions to the science of memory, Tulving will be remembered through the students whom he trained and guided. They continue to disseminate his ideas and to train their own students in the fundamental principles of memory function that he developed. ■

10.1126/science.adn2158

[1]Department of Psychology and Neuroscience, Duke University, Durham, NC, USA. [2]Department of Psychology, Humboldt University, Berlin, Germany. [3]Institute of Cognitive Neurology and Dementia Research, Otto von Guericke University, Magdeburg, Germany. [4]Institute of Cognitive Neuroscience, University College London, London, UK. Email: cabeza@duke.edu

BOOKS *et al.*

Data inflow and outflow are regulated differently by different jurisdictions, affecting what we see online.

POLICY

Data geopolitics

A group of scholars explore the implications of how governments control and restrict digital information

By **Dov Greenbaum**

In an era of escalating global polarization, when jurisdictions enforce data sovereignty, imposing governance or control over the data produced within their borders, "the news you see, the facts you see, and even the maps you see change depending on where you are," observes legal scholar Mark Lemley (*1*). And with the expanding role of artificial intelligence in society, constraints on access to the data on which such technologies are trained can have severe and systemic ramifications.

In their timely tome *Data Sovereignty*, editors Anupam Chander and Haochen Sun aim to provide a comprehensive understanding of this issue. The book is divided into four parts, covering digital sovereignty basics, the intersection of technologies and institutions with data sovereignty, trade regulations related to data flows, and issues specific to data localization.

A central challenge concerning the analysis of data sovereignty is the absence of a precise definition for the term. The editors assert that data sovereignty encompasses the data protection laws, competition laws, and security laws designed to control aspects of data both within and beyond a territory. They describe this concept, deemed both "necessary and dangerous," as the "exercise of control over the internet" serving as a protective barrier against both foreign states and corporations.

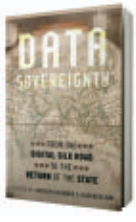

Data Sovereignty: From the Digital Silk Road to the Return of the State
Anupam Chander and Haochen Sun, Eds.
Oxford University Press, 2023. 408 pp.

Compared with its relatively positive reception in the Global North, data sovereignty is often perceived in the Global South as "the government hijacking the Internet to protect itself," write Chander and Sun. In acknowledging that data sovereignty is both a necessity for democratic government and a potential tool to "immunize oppression," they contend that digital sovereignty ought to be operated within a framework of checks and balances.

Governments are often motivated to invoke data sovereignty by at least three considerations: a desire to protect citizens from illegal content and from having their content illegally usurped, a desire to promote their jurisdiction's own technology, and a desire to control populations by limiting access to incoming and outgoing data streams. Throughout the book, many of the chapters look to the four most prominent stakeholders in the area of data sovereignty: China, the European Union, the United States, and global industry leaders.

Colloquially known as the "Great Firewall of China," Chinese infrastructure and regulation showcase extensive state control over the inflow and outflow of data. Additionally, exported Chinese internet infrastructure seeks to project this sovereignty worldwide. The European Union employs regulations to principally control foreign technology firms. In what has been called the "Brussels effect," the EU aims to use its regulatory oversight to expand its influence beyond its immediate territory.

Meanwhile, the United States projects soft power through "functional sovereignty" mediated by its dominant technology and social media companies. Within the US itself there has historically been minimal government control over data flow owing to the country's concentration of corporate powers, its expansive speech protections, the nature of its intellectual property laws, its relatively weak privacy laws, its ineffective domestic regulatory bodies, and the severe limitations placed on corporate regulation imposed by international groups.

Unencumbered by governance, private US corporations that make the market and manage data can thus also promote and censor information as they see fit, setting up what philosopher Luciano Floridi has referred to as a clash "between companies and states" (*2*). Growing recognition of this problem has led to bipartisan support for the idea that the internet ought to be more heavily regulated before it undermines democracy. Although the book mentions some of the legislative efforts that have been proposed, given the speed of change in this area, this analysis is already somewhat dated.

Individual citizens ought to also have control over their personal data ("self-sovereignty"). However, this control, when it is granted and ostensibly managed through consent and oversight, is frequently illusory because even seemingly insignificant bits of information can be used to deduce highly private details as a result of advances in data processing and artificial intelligence.

Ultimately, this volume provides an insightful exploration of data sovereignty, shedding light on the multifaceted challenges and opportunities that lie ahead in the evolving landscape of data governance. ■

The reviewer is at the Zvi Meitar Institute for Legal Implications of Emerging Technologies and Harry Radzyner Law School, Reichman University, Herzliya, Israel, and Department of Molecular Biophysics and Biochemistry, Yale University, New Haven, CT, USA.
Email: dov.greenbaum@aya.yale.edu

REFERENCES AND NOTES

1. M. A. Lemley, *Duke Law J.* **70**, 1397 (2021).
2. L. Floridi, *Philos. Technol.* **33**, 369 (2020).

10.1126/science.adm9960

PHOTO: OLEG BLOKHIN/ISTOCK PHOTO

SCIENCE AND SOCIETY

Making a digital dupe of Anderson Cooper

Two computer scientists discuss deepfakes and how they made a facsimile of the anchor

By **Jamie Dickman**

On 3 December 2023, CNN aired an episode of *The Whole Story with Anderson Cooper* that featured a computer–generated facsimile of Cooper. University of California, Berkeley, computer scientist Hany Farid and Stanford University undergraduate Maty Bohacek worked with CNN to create the virtual news anchor. The project began as an exercise in learning how deepfakes—digitally created likenesses—could be assembled, but the pair quickly realized that they had all the resources necessary to render a fully synthetic Cooper. They completed the project within the span of 2 months using primarily open-source software. The final product's realism has worrying implications for the trustworthiness of visual media and television, not to mention the livelihoods of onscreen performers, the latter of which has been a point of contention in recent Hollywood strikes.

"My lab here at Berkeley is not in the business of creating fakes," said Farid, a cybersecurity expert. "We're in the business of detecting them, and if you want to be in the business of detecting stuff, you've got to know how [it's] built." We spoke with Farid and Bohacek about the project and the broader phenomenon of generative artificial intelligence (AI). This interview has been edited for brevity and clarity.

Q: How did this project get started?

Farid: I did a piece with Donie O'Sullivan, who is a reporter for CNN and works on the Anderson Cooper show, where we cloned his [Donie's] voice and then we called his parents with this AI voice, and they couldn't tell.

We were screwing around cloning people's voices, and we cloned Anderson Cooper's voice. And at some point in that conversation, I said, "I think we might be getting close to having all the pieces we need to create a full-blown version of a virtual Anderson Cooper."

Computer scientists created a virtual likeness of Anderson Cooper, who is shown here at a 2016 Presidential Primary Debate.

PHOTO: SCOTT OLSON/GETTY IMAGES

Q: Can you walk me through how you create a video like this?

Farid: So, there are actually three parts: the text, the audio, and the video. They wouldn't let us generate a script for Anderson Cooper. That's not surprising, right? The guy's on national television. So, the first thing we're going to do is generate Anderson Cooper saying [the CNN script]. That's all open source code.

Bohacek: [To create the video, we need to] identify where the head is in the footage, and then re-render the lower area of the face, so that the mouth opens and closes in the way that the words are spoken in the audio. You need to do a little bit of tweaking here and there, but the problem with most of these technologies is that they're very low-res.

The second part is making it look sharper and enhancing the frames in the video that are already synced with the audio. We do some preprocessing, some postprocessing, but that's basically it.

Q: How much expertise or training would someone need to do this?

Bohacek: It was a lot of time and a lot of effort, but it was just putting the pieces together. I think that anyone with decent Python skills and the dedication could do that at some point.

Farid: I think right now you need somebody like Maty; he's got some good engineering skills and good coding skills. He's got years of programming skills. But here's the thing: About every 6 to 12 months, it gets twice as good, twice as cheap, and twice as easy to use. So, even if the average Joe can't do it today, they're going to eventually be able to do it.

Q: Are you concerned that someone could use what they've learned from the segment to create AI performers for nefarious reasons? What steps did you take to prevent this?

Farid: We went back and forth on "Should we publish how we did this?" We landed on "no." We're not going to tell people the series of things that we had to do to get this to really work because we felt like the downside outweighed the benefits. There was no real upside. I don't think it's like we know something that nobody will ever figure out. [But as] anybody who does cybersecurity will tell you: You find a vulnerability, you need to tell the world.

Q: What responsibilities do technologists have to ensure that this technology is deployed ethically?

Farid: Physicists, chemists, biologists—they've been dealing with this stuff forever. They have had time to think about the ethics of stem cell research, of cloning, of developing things that can be weaponized. Our community doesn't have that culture. That's why I think we are struggling a little bit.

If you look at the early days of the internet, it was very much this libertarian view that technology wants to be free and that regulation and government [should be] hands-off. And I think that's a spectacularly naïve way of thinking about the world. Yet, we do that with technology all the time because we have this disconnect between technology—bits, pixels, and bytes—and the physical world. There is no more online world and offline world; that distinction vanished a long time ago. ■

The interviewer is at the Medill School of Journalism, Northwestern University, Evanston, IL, USA, and was an intern in *Science*'s Editorial department in the summer of 2023. Email: jamiedickman1@gmail.com

10.1126/science.adl4197

Science Podcasts

AAAS

Hear the stories behind the latest news and research from *Science*.

LISTEN & SUBSCRIBE

NEW EPISODES EVERY THURSDAY

LETTERS

A man walks along a dried-up Zayandeh Rud River riverbed in Isfahan, Iran.

PHOTO: NURPHOTO VIA GETTY IMAGES

Edited by **Jennifer Sills**

Iran's Zayandeh Rud River basin in crisis

The Zayandeh Rud River, the largest river in Iran's central plateau (*1*), has held strategic importance for centuries because of its location. Although the river was added to Iran's natural heritage list in 2011 (*2*), for the past two decades, imprudent actions by the government and residents have led to environmental and management problems in the river's basin (*3*). Between 1998 and 2018, the Zayandeh Rud River's average flow decreased by 1 million cubic meters (*4*). Given that Iran, situated in a semiarid region, consistently grapples with water scarcity, the government should work to protect its most important river.

The Zayandeh Rud's precarious state has resulted from unsustainable water use in the region. Unauthorized upstream pump installations, particularly in the past decade, have led to indiscriminate water extraction by local residents, triggering water crises (*5*). Downstream, water-rich crops, expansive farming in unsuitable conditions, and the absence of modern agricultural technologies have intensified the problem (*6*). Meanwhile, water-intensive steel industries and oil refineries divert water resources. Water mismanagement, exacerbated by inadequate governance, a lack of monitoring, and a shortage of skilled professionals, has pushed the country to the brink of crisis.

Iran has breached its Ramsar Convention obligations (*7*) by allowing unauthorized water diversions and violating regulations that protect wetlands. These activities have caused 90% of the Zayandeh Rud to dry up (*8*). This extreme desiccation has resulted in the Gavkhooni wetland drying up, ecosystem disruption, soil degradation, and decreases in water and air quality (*9*).

Iran has taken some steps to protect the river and basin. The government established the Zayandeh Rud River Quality Protection Council (*10*) to prevent pollution and improve the management and water quality of the river, and it has enacted laws that require the fair distribution of water and outline a nine-point plan for basin restoration (*11*). However, these measures are inadequate. In alignment with environmental rights principles (*12*), addressing the challenges in the Zayandeh Rud water basin will involve prioritizing the environment, preventing illegal upstream harvesting, ensuring transparency in water usage across the basin, focusing on land use and integrated management, transitioning from traditional to modern and greenhouse agriculture, reforming water governance, and transferring high-demand water industries to other cities. Implementing these measures would effectively address the complex and critical situation in the Zayandeh Rud water basin.

Iman Salahshoori[1,2] and Majid Namayandeh Jorabchi[3]*
[1]Department of Polymer Processing, Iran Polymer and Petrochemical Institute, Tehran, Iran. [2]Department of Chemical Engineering, Science and Research Branch, Islamic Azad University, Tehran, Iran. [3]Leibniz Institute for Catalysis, Rostock, Germany.
*Corresponding author.
Email: majid.jorabchi@catalysis.de

REFERENCES AND NOTES

1. F. Molle, I. Ghazi, H. Murray-Rust, in *River Basin Trajectories: Societies, Environments and Development*, F. Molle, P. Wester, Eds. (CAB International, 2009), chap. 9.
2. M. Ebrahimnia, B. Jafari Bibalan, in *Reviving the Dying Giant: Integrated Water Resource Management in the Zayandeh Rud Catchment, Iran*, S. Mohajeri, L. Horlemann, Eds. (Springer International Publishing, Cham, 2017), pp. 11–31.
3. M. Zarepour Moshizi, A. Yousefi, A. M. Amini, P. Shojaei, *GeoJournal* **88**, 2121 (2023).
4. F. Saedi, A. Ahmadi, K. C. Abbaspour, *J. Wat. Clim. Change* **12**, 2068 (2021).
5. S. Eslamian *et al*., in *Reviving the Dying Giant: Integrated Water Resource Management in the Zayandeh Rud Catchment, Iran*, S. Mohajeri, L. Horlemann, Eds. (Springer International Publishing, Cham, 2017), pp. 201–217.
6. M. A. Torfe, M. Mirmohammad Sadeghi, S. Mohajeri, in *Reviving the Dying Giant: Integrated Water Resource Management in the Zayandeh Rud Catchment, Iran*, S. Mohajeri, L. Horlemann, Eds. (Springer International Publishing, Cham, 2017), pp. 33-47.
7. "Convention on wetlands of international importance especially as waterfowl habitat" (1971); https://www.ramsar.org/sites/default/files/documents/library/scan_certified_e.pdf.
8. S. Mohajeri *et al*., in *Integrated Water Resources Management: Concept, Research, and Implementation*, D. Borchardt, J. J. Bogardi, R. B. Ibisch, Eds. (Springer, Cham, 2016), pp. 603–627.
9. K. Madani, A. AghaKouchak, A. Mirchi, *Iran. Stud.* **49**, 997 (2016).
10. "By-laws of the Zayandeh Rood River Quality Protection Council" (2005) [in Farsi].
11. H. Murray-Rust, H. R. Salemi, P. Droogers, "Basin level water resources development, 1945–2010" (International Water Management Institute, 2004); https://EconPapers.repec.org/RePEc:iwt:bosers:h036062.
12. United Nations, "Mapping report" (2014); https://www.ohchr.org/en/special-procedures/sr-environment/mapping-report.

10.1126/science.adm8965

Restore the Yangtze River's floodplains

In 2020, China implemented a 10-year fishing ban in the Yangtze River, a substantial aquatic biodiversity conservation initiative (*1*). Although the ban has offered protection to Yangtze species, habitat destruction prevents China from maximizing its benefits (*2*). The loss of aquatic habitats, especially floodplains, is now a more substantial driver

of biodiversity loss in the Yangtze River than illegal hunting and overfishing (*3*).

Both fish stock and biodiversity have shown signs of recovery in the years since the ban took effect (*2*). In 2022, 25 fish species were collected that were not found in 2020, and overall fish density in the Yangtze River had increased by 20% (*4*). Populations of the iconic and endangered Yangtze finless porpoise (*Neophocaena asiaeorientalis asiaeorientalis*) have experienced an unprecedented increase from 1012 in 2017 to 1249 in 2022 (*4*).

Floodplains—seasonally inundated areas along the river and connected lakes—are invaluable seasonal breeding and spawning habitats for aquatic species (*5*), especially for the Yangtze finless porpoise (*6*). However, anthropogenic activities such as dam construction, urbanization, and agricultural expansion have led to rapid floodplain loss. Some floodplains have become permanently dry, some are now permanently underwater but inaccessible to breeding species, and some have been lost entirely through erosion. The area of seasonal floodplains in the main stem of the Yangtze River has shrunk to less than 3.3% of the floodplain area that existed in the 1970s (*7*, *8*). Maintaining the population size of fish in the Yangtze River requires a floodplain area of 14,400 km², but the total current area is only about 5500 km² (*9*). The construction and operation of cascading reservoirs in the upper reaches of the Yangtze River could further exacerbate the decline of Yangtze seasonal floodplains (*2*).

The 10-year fishing ban is an important step for the ecological restoration of the Yangtze River, but its effectiveness depends on the restoration of seasonal floodplains. In the middle and lower reaches of the Yangtze River, the central government has built embankments on each side, and local governments have built additional "sub"-embankments, as well as floodgates between the river and connected lakes. The function of sub-embankments and gates was to control flooding, but upstream dams and the primary embankment now serve this purpose. Demolishing the sub-embankments and gates would allow floodwaters to flow freely within the main embankments, which would restore the floodplains and eliminate human development activities without increasing the risk of flooding beyond the river. The Yangtze River Protection Law, the country's first legislation on a river basin, went into effect in early 2021. The river's shoreline is strictly protected under the law, laying the foundation for floodplain recovery (*10*).

Zhigang Mei[1], Kexiong Wang[1], Hao Du[2], Peilin Cheng[2]*, Ding Wang[1]*

[1]Key Laboratory of Aquatic Biodiversity and Conservation of the Chinese Academy of Sciences, Institute of Hydrobiology, Wuhan 430072, China. [2]Key Laboratory of Freshwater Biodiversity Conservation, Ministry of Agriculture of China, Yangtze River Fisheries Research Institute, Chinese Academy of Fishery Sciences, Wuhan 430223, China.
*Corresponding author. Email: wangd@ihb.ac.cn, chengpeilin@yfi.ac.cn

REFERENCES AND NOTES

1. State Council of the People's Republic of China, "10-year fishing ban starts in key waters of Yangtze River" (2021); https://english.www.gov.cn/news/topnews/202101/01/content_WS5fef1f0bc6d0f7257694313b.html.
2. H. Yang *et al.*, *Aquacult. Fish.* 10.1016/j.aaf.2023.06.004 (2023).
3. H. Wang *et al.*, *Innovation* **3**, 100235 (2022).
4. Ministry of Agriculture and Rural Affairs of the People's Republic of China, "Bulletin on aquatic biological resources and habitat status in the Yangtze River basin" (2022); http://www.moa.gov.cn/xw/zwdt/202310/t20231012_6438134.htm [in Chinese].
5. P. Keddy, *Wetland Ecology Principles and Conservation, Third Edition* (Cambridge University Press, 2023).
6. Z. Mei *et al.*, *Biol. Conserv.* **257**, 109132 (2021).
7. H.-Z. Wang, X.-Q. Liu, H.-J. Wang, *Acta Hydrobilog. Sin.* **43**, 157 (2019).
8. H. Z. h. Wang, X. u. Liu, H. a. Wang, *Am. Fish Soc. Symp.* **84**, 263 (2016).
9. X. Liu, H. Wang, *Divers. Distrib.* **16**, 932 (2010).
10. R. Li, W. Jin, *Ecol. Societ.* **28**, 32 (2023).

10.1126/science.adn0769

Pakistan's turtle species at risk of extinction

Pakistan's five species of marine turtles, eight species of freshwater turtles, and two species of land turtles face numerous threats (*1*). The Indian narrow-headed softshell turtle (*Chitra indica*) is listed as Endangered under Appendix II of the Convention on International Trade in Endangered Species (CITES) (*2*). Olive ridleys (*Lepidochelys olivacea*), once common, have not been observed nesting in Pakistan since 2004 (*1*). If Pakistan does not take steps to mitigate the risks to wild turtles, they could face imminent extinction.

Human activities have degraded turtle habitats. Unchecked urban growth and increasing pollution have led to habitat loss (*1*). Rapid coastal development has encroached on once pristine sea turtle nesting sites (*3*). Climate change also threatens turtle habitats through increasing temperatures and rising sea levels (*4*).

Fishing poses another threat to Pakistan's turtles. Approximately 30,000 sea turtles are accidentally entangled in tuna gillnets each year (*5*). Although most turtles in the region are herbivorous, and others feed on insects, crustaceans, and very small fish (*6*), some fishers kill turtles intentionally because they incorrectly believe that turtles prey on large fish (*7*).

The illegal turtle trade from Pakistan to China and East Asia has led to substantial decreases in wild turtle populations (*8*). Demand for turtles is driven by their cultural associations with luck and longevity (*9*). They are kept as pets and consumed as food and as components of traditional medicine. In 2015, five confiscated shipments included 1.9 tons of turtle body parts and 1345 live freshwater turtles (*10*).

Turtle conservation requires the collective efforts of governments, conservation groups, and local communities. Community-based initiatives, sustainable practices, and increased awareness about the impact of climate change and pollution on turtle habitats could mitigate further habitat loss. Because many turtles are found in surface waters (*11*), fishermen should switch from surface to subsurface gillnetting to reduce turtle entanglement. Educating the public about turtle conservation could reduce intentional culls.

Although exporting turtles is forbidden according to CITES (*12*), smuggling is enabled by lucrative rewards and Pakistan's weak laws and lenient penalties. To thwart trade, Pakistan must strictly enforce the CITES ban on turtle export and implement strict anti-wildlife trade measures. The government should install dogs at exit points to curb trade at airports and seaports by detecting the turtles' scent. Because Pakistan lacks reliable turtle data, the government should also conduct a systematic survey to lay the foundation for conservation and future research.

Shahid Ahmad and Wei Mao*
School of Ecology and Environment, Hainan University, Hainan 570228, China.
*Corresponding author.
Email: maowei@hainanu.edu.cn

REFERENCES AND NOTES

1. D. Khan, "Turtle Species in Pakistan are about to go extinct," *pro Pakistani* (2018); https://propakistani.pk/2018/05/24/turtle-species-in-pakistan-are-about-to-go-extinct.
2. A. Safi, M. Z. Khan, *J. Zool. Stud.* **1**, 31 (2014).
3. Government of Pakistan, Ministry of Climate Change, Mangroves for the Future, Pakistan, "A handbook on Pakistan's coastal and marine resources" (2016).
4. E. S. Poloczanska, C. J. Limpus, G. C. Hays, *Adv. Mar. Biol.* **56**, 151 (2009).
5. WWF–Pakistan, "Experts term development activities and pollution a major threat to sea turtles" (2022).
6. S. Yousaf, T. Mahmood, *Int. J. Agric. Biol.* **20**, 723 (2018).
7. B. Muzammal, "Policy and access: A story of marginalized fishing community in Pakistan" (2016).
8. A. Wahab, K. Saeed, M. Azam, S. Nasir, "Distribution and status of threatened species of freshwater turtles in selected areas of Indus River system," Zoological Survey of Pakistan (2012).
9. S. M. Cheung, D. Dudgeon, *Aquat. Conserv. Mar. Freshw. Ecosyst.* **16**, 751 (2006).
10. "Population of marine turtles declining," *Express Tribune* (2019).
11. M. G. Sarwar, F.-i. Abbas, I. A. Shahjehan, *J. Bioresour. Manag.* **2**, 8 (2015).
12. M. Rizvi, "Environment-Pakistan: Exports threaten freshwater turtle," *Environment Bulletin* (2000).

10.1126/science.adm7123

RESEARCH

IN *SCIENCE* JOURNALS

Edited by **Michael Funk**

Healing of injuries to the Achilles tendon, shown in a computed tomography image, involve increased growth of peripheral nerves.

PHOTO: K H FUNG/SCIENCE SOURCE

TENDINOPATHY

Tendon repair gets up its nerve

Tendons have peripheral nerve inputs for sensory feedback; however, the role of these nerves in tendon injury and repair remains unclear. Cherief *et al.* demonstrated that an increase in peripheral nerve growth occurs after Achilles tendon injury in mice. Experimental blockade of nerve growth resulted in decreased tendon healing and reduced expansion of tendon sheath progenitor cells. Human tendon tissue imaging and transcriptomics corroborated the relationship between nerve growth and tendon healing. Further, activating the nerve growth factor receptor TrkA enhanced nerve responses to tendon injury, boosted progenitor cell expansion, and improved metrics of tendon repair. —MEO

Sci. Transl. Med. (2023)
10.1126/scitranslmed.ade4619

ASTROCHEMISTRY

Ryugu PAHs formed in interstellar clouds

Astronomical observations show that polycyclic aromatic hydrocarbons (PAHs) are abundant and widespread in the interstellar medium. PAH molecules consist of several adjacent aromatic rings terminated by hydrogens. Zeichner *et al*. performed laboratory isotopic analysis of PAHs in samples of the asteroid Ryugu that were collected by the Hayabusa2 spacecraft. They found that two ^{13}C nuclei occurred in the same molecule more often than would be expected if ^{13}C were randomly incorporated into PAHs. This isotope fractionation effect occurred during formation at temperatures under 100 kelvin. The authors argue that at least some of the Ryugu PAHs must have formed in cold interstellar clouds and thus predate the Solar System. —KTS

Science, adg6304, this issue p. 1411

SUPERCONDUCTIVITY

Twisted superconductors

Twisted two-dimensional (2D) structures exhibit a wealth of interesting behaviors. Recently, the 2D materials used in such superlattices have largely been graphene and various transition metal dichalcogenides. However, cuprate superconductors can also be thought of as 2D materials, with the copper-oxide planes coupled to each other through Josephson coupling. Zhao *et al*. created high-quality twisted structures of a bismuth-based cuprate by cleaving a single exfoliated crystal and placing the two halves on top of each other at various angles. Near the twist angle of 45°, Josephson coupling was suppressed by the d-wave superconducting order parameter of the material. The researchers also observed a Josephson diode effect caused by the breaking of time reversal symmetry. —JS

Science, abl8371, this issue p. 1422

SOLAR CELLS

Optimizing nickel oxide transporters

Inverted perovskite solar cells have advantages in manufacturing, but their buried hole-transport layer (HTL) often limits power conversion efficiency (PCE). Yu *et al*. showed that treatment of a nickel oxide nanoparticle HTL with hydrogen peroxide made

the particles smaller and more uniform and also created Ni^{3+} surface groups that improved bonding to organic phosphonic acid self-assembled monolayers. A device with 25.2% certified PCE was fabricated and retained 85% of its initial efficiency after 500 hours of accelerated aging at 85°C. —PDS

Science, adj8858, this issue p. 1399

STRUCTURAL BIOLOGY

An asymmetric kinase complex

Mutations in leucine-rich repeat kinase 2 (LRRK2) are implicated in the development of Parkinson's disease, so this enzyme is a target for therapeutics currently in clinical trials. Zhu *et al*. determined the structures of LRRK2 bound to Rab29, a membrane-associated protein thought to target the kinase to specific organelles, and found that the resulting complexes adopted several oligomerization states. The largest complex included four copies of LRRK2 in two different conformations: one was similar to the inactive state seen previously and the other represented a proposed active state. Functional experiments and work with mutants provide insight into the structural features of this complex and may inspire new strategies for therapeutic inhibition. —MAF

Science, adi9926, this issue p. 1404

WEATHER FORECASTING

Fast and easy

The numerical models used to predict weather are large, complex, and computationally demanding; they also do not learn from past weather patterns. Lam *et al*. introduced a machine learning–based method that has been trained directly from reanalysis data of past atmospheric conditions. In this way, the authors were able to quickly predict hundreds of weather variables globally up to 10 days in advance and at high resolution. Their predictions were more accurate than those of traditional weather models in 90% of tested cases and displayed better severe event prediction for tropical cyclones, atmospheric rivers, and extreme temperatures. —HJS

Science, adi2336, this issue p. 1416

TEXTILES

Inspired by polar bears

Polar bears have fur that has a porous core encapsulated in a dense shell, a structure that keeps these animals warm and dry but is relatively lightweight. Wu *et al*. were inspired by this structure in developing an encapsulated aerogel fiber (see the Perspective by Sheng and Zhang). The synthetic fibers have mechanical properties that allow for weaving and knitting while at the same time being excellent thermal insulators. They can also be produced at scale with a simple two-step freeze-spinning and encapsulation process. —BG

Science, adj8013, this issue p. 1379; see also adm8388, p. 1358

FETAL IMMUNOLOGY

An immune atlas of developing human lungs

From birth, the airways provide protection against respiratory pathogens and inhaled toxins, but little is known about the early development of lung immune cells. Using single-cell transcriptomics, Barnes *et al.* characterized human embryonic and fetal immune cells in the developing lungs between 5 and 22 weeks after conception. All stages of B cell development were detected, suggesting that fetal lungs provide a local niche for B cell maturation. Myeloid cells were widespread, including near epithelial tips, and produced interleukin-1ß, which induced epithelial stem cell differentiation into basal cells within fetal lung organoids. This work provides an immune atlas of developing human lungs and suggests a role for fetal immune cells in guiding the development of the lung epithelium. —CO

Sci. Immunol. (2023) 10.1126/sciimmunol.adf9988

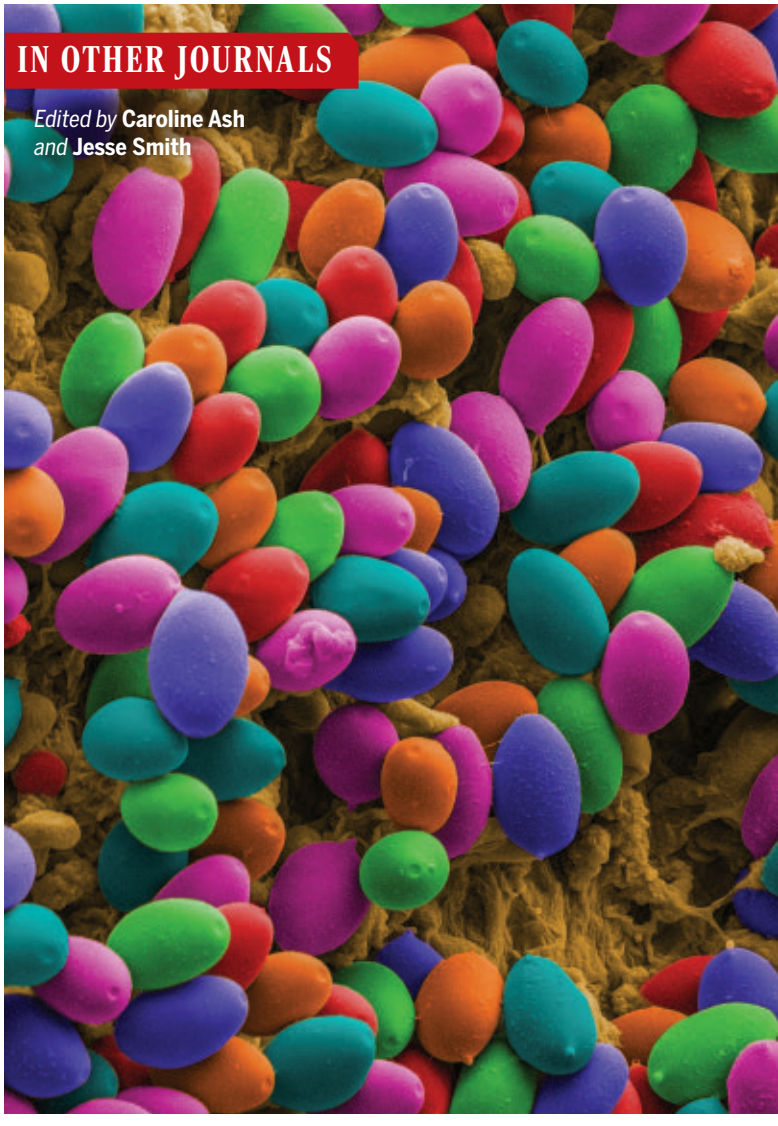

IN OTHER JOURNALS

Edited by **Caroline Ash** *and* **Jesse Smith**

ECONOMICS

It takes a neighborhood to raise a voter

Chyn and Haggag studied nearly 6000 children living in low-income public housing in Chicago. In one-third of them, their families had been forced to relocate when their buildings were slated for demolition during 1995 to 1998 and received government support to move to higher-income, lower-crime areas. Relocated children were 10% more likely to vote in general elections during 2008 to 2016 compared with their nonrelocated counterparts. Results were driven largely by females and by those who relocated at earlier ages (5 to 11 years old) and appear to be linked to increased education and earnings among those who relocated. —BW

Rev. Econ. Stat. (2023) 10.1162/rest_a_01207

NEUROSCIENCE

Tau moves vesicles

Neuronal communication relies on release of neurotransmitter-containing synaptic vesicles (SVs) from the presynaptic terminals. The different mobility of the two major types of SVs is critical for correct neuronal communication, but how this happens is unknown. Longfield *et al.* have found that the protein tau, known for its role in neurodegenerative diseases, controls the mobility of SVs. Tau molecules

PHOTO: TED KINSMAN/SCIENCE SOURCE

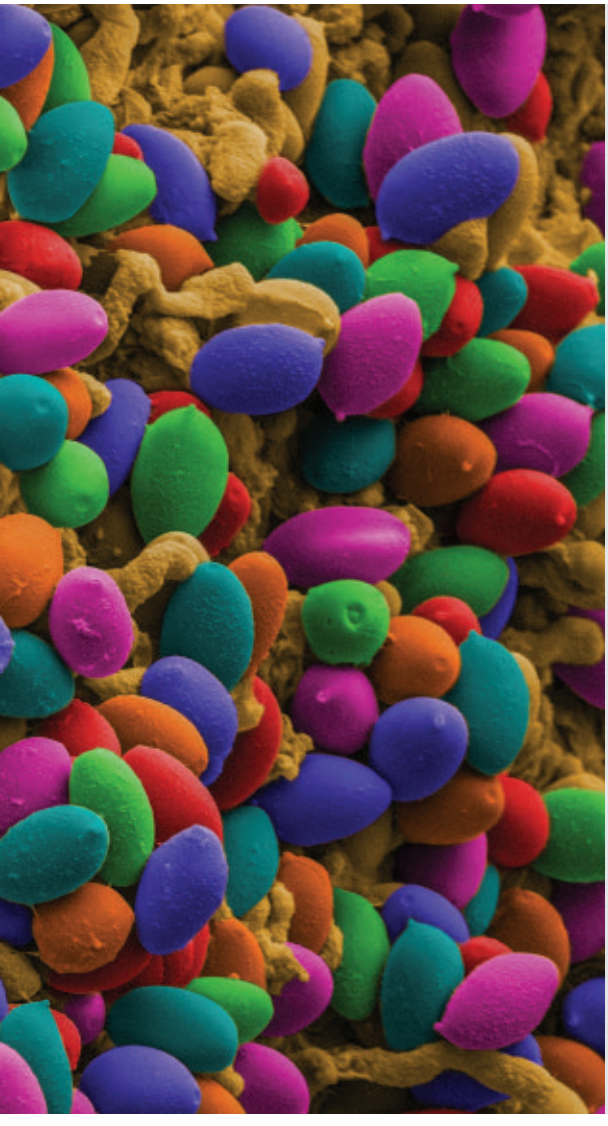

DOMESTICATION

What's that growing under the bed?

Mushrooms that produce the psychoactive compound psilocybin have been cultivated for decades, although the unlawful nature of their use has resulted in the origins of many strains being obscured. McTaggart *et al.* sequenced wild populations of *Psilocybe cubensis* in Australia and compared them with 86 sequenced commercial cultivars. *P. cubensis* seems to have been introduced to Australia with livestock in the 19th century, where it grew abundantly on dung and was accidentally foraged for food. Now, naturalized populations show far greater diversity compared with cultivars, which show evidence of genetic bottlenecks within the past 50 years and may not have sufficient fitness to thrive outside of cultivation. However, there is little evidence that domestication has improved the psychedelic effects of *P. cubensis*; rather, it has made them easier to grow in basements or under beds. Psilocybin now is finding legitimate uses for treating serious mental health disorders, and its cultivation is thus of considerable commercial interest. —CNS and CA

Curr. Biol. (2023)
10.1016/j.cub.2023.10.059

Spores of *P. cubensis* (seen here in "psychedelic" colors) have been collected for clandestine magic mushroom cultivation over the past 50 years.

form transient nanobiomolecular condensates at presynaptic terminals, which selectively regulates the mobility of SVs. Thus, tau dysregulation during neurodegeneration might affect SV mobility and impair synaptic transmission. —MMa

Nat.Commun. (2023)
10.1038/s41467-023-43130-4

SPECTROSCOPY

Accelerating photoreaction discovery

In recent years, efficient high-throughput screening methods have been developed that should substantially accelerate the rate of discoveries in various fields of organic chemistry. However, organic photochemistry lags due to challenges associated with excited-state chemical reactions. Bain *et al.* present a system for rapid screening of photochemical systems using transient absorption spectroscopy, as demonstrated using pyrimidine nucleosides. The proposed framework is general and can be extended to other excited-state spectroscopic techniques. It offers a promising experimental tool for photochemical reaction discovery, complementing recently proposed machine learning–based computational tools for modeling excited-state dynamics. —YS

J. Phys. Chem. Lett. (2023)
10.1021/acs.jpclett.3c02389

GENOMICS

Putting more omics together

Recent years have seen major advances in the amount of information that can be gleaned from genomic testing of tissue samples. Single-cell genomic methods were invented and then refined or combined into multi-omics analyses featuring different types of data. Yang *et al.* present the next advance in this progression, with a computational method called SpaTrio, which combines single-cell multi-omics with spatial data. This method is likely to yield valuable insights into several biological processes, as the authors demonstrate by examining tissues as different as those in the brain, liver, and breast, some in a healthy state and others in diseases such as steatosis or cancer. —YN

Cell Genom. (2023)
10.1016/j.xgen.2023.100446

GEOLOGY

Earth's early crustal water source

Archean cratons are what remains of the very first continents formed on Earth. However, forming these continents requires the proper chemistry and dynamics, with a water source in the mantle being one of the hardest problems to solve. Wu *et al.* hypothesize that a water-rich magma ocean may have overturned after the moon-forming impact, supplying sufficient water to the lithosphere to generate Earth's earliest continental crust. This hypothesis could resolve the question of the source of the water while also explaining other features of very early crustal growth. —BG

Geophys. Res. Lett. (2023)
10.1029/2023GL105178

MALARIA

One anchor to bind them all

Classically, malaria is diagnosed microscopically in blood samples. Despite its familiarity and size, malaria parasite cell biology is not well understood. Liffner *et al.* used ultrastructural expansion light microscopy to prepare physically enlarged samples in which immunofluorescent markers can be used to explore parasite anatomy. This technique revealed that during mitosis, developing organelles such as the rhoptries (specialist structures required for host cell invasion), Golgi, and prefission mitochondria anchor to the parasite's plasma membrane by means of the centriole plaque and its associated proteins. —CA

Elife (2023)
10.7554/eLife.88088.2

ALSO IN *SCIENCE* JOURNALS

Edited by **Michael Funk**

BITCOIN

Cryptocurrency skepticism

After El Salvador adopted the cryptocurrency bitcoin as legal tender, its government incentivized it with the Chivo Wallet app, a digital wallet backed by their central banking system. Despite major incentives, bitcoin was rarely adopted except among one privileged group: young, educated men with bank accounts. Compared with traditional banks, bitcoin offers improved privacy and transparency and rapid, inexpensive transactions. These are all features that economists assumed were desirable for Salvadorans because most are unbanked, need remittances, and can access Chivo Wallet because they usually own phones with Internet. However, Alvarez *et al*. found that Salvadorans' preference for tangible cash and, ironically, privacy and transparency fears impeded bitcoin adoption. Unless populations are financially literate and trust virtual currencies, policies incentivizing their adoption may fail. —EEU

Science, add2844, this issue p. 1375

NEUROSCIENCE

Glia and negative memory formation

Fruit flies can be taught to associate specific odors with painful electrical shocks. However, how these associative memories are formed and stored in their brains is not fully understood. Miyashita *et al*. unexpectedly discovered that ensheathing glia, the cells that wrap around the mushroom bodies and are the flies' main neural processing centers, release glutamate from synaptic vesicles. The glutamate released binds to NMDARs on mushroom body neurons and kainate receptors on dopaminergic neurons. NMDARs require both glutamate binding and simultaneous cellular depolarization to open. Functional imaging experiments demonstrated that NMDARs permit the transmission of shock information to the mushroom bodies only when flies are exposed to an odor and shock simultaneously, but not when flies are exposed to shocks alone. —PRS

Science, adf7429, this issue p. 1376

TRANSCRIPTION

Visualizing transcription initiation

In eukaryotic cells, general transcription factors (GTFs) support RNA polymerase (Pol) II to assemble a preinitiation complex on a core promoter, open double-stranded DNA, and start RNA synthesis. Chen *et al*. determined the structures of 16 de novo transcribing complexes, TC2 to TC17, containing nascent RNAs of 2 to 17 nucleotides, respectively. Connecting these structures revealed an abrupt transition from initially transcribing complexes (in TC2 to TC9, GTFs remained bound to the promoter and Pol II) to early elongation complexes (in TC10 to TC17, GTFs dissociated from the promoter). This transition was accompanied by remarkable conformational and compositional changes, including transcription bubble collapse and GTF dissociation, which allowed Pol II to escape the promoter for product RNA synthesis. —DJ

Science, adi5120, this issue p. 1377

SIGNAL TRANSDUCTION

Mapping receptor pharmacology

G protein–coupled receptors such as the beta-adrenergic receptor for adrenaline are key targets for therapeutic drug development. Heydenreich *et al*. undertook systematic mutation of each receptor residue to determine which are important for receptor signaling (see the Perspective by Filizola and Javitch). The authors evaluated the contribution of each residue to the fundamental pharmacological properties of efficacy and potency of the endogenous receptor ligand adrenaline and found that one-fifth of residues contributed to efficacy or potency of signaling by the receptor. Some mapped to sites of ligand or G protein binding, but more than two-thirds did not. The important sites appeared to work together in an allosteric network that led to structural changes and signaling responses. Such detailed information may help to guide the development of new ligands that produce the desired signaling responses. —LBR

Science, adh1859, this issue p. 1378; see also adm8393, p. 1357

CHEMISTRY AUTOMATION

A dye design loop

As chemists make increasing use of automated equipment and predictive synthesis algorithms, an autonomous research device is coming closer to realization. Koscher *et al*. developed a prototype platform for exploring the prospective dye-like properties of several polycyclic small-molecule classes. By combining machine learning–enabled planning and analysis with robotic reaction modules, the apparatus iteratively synthesizes variously substituted compounds to optimize their absorption properties, lipophilicity, and photo-oxidative stability. The authors elaborate on when and why human input still comes into play. —JSY

Science, adi1407, this issue p. 1374

SOCIAL DISPARITIES

How to motivate mitigation efforts

Racism in America is a system of oppression that produces and sustains racially unequal outcomes across education, the economy, health, incarceration, and other institutions. These intertwined institutions place Black Americans at a compounded disadvantage even in the absence of overt discrimination. An effective way to challenge systemic racism is through social movements or policies. However, Black-White disparities in some domains (e.g., poverty and alienation) may not mobilize resistance toward racism as much as disparities in other domains (e.g., health and physical harm), although all domains are pernicious and reinforce each other. Brown *et al*. found that threats to health or body (e.g., aggressive police encounters) spark outrage and motivate more action because they trigger morality concerns (see the Perspective by Earl and Derricks). Framing disparities to engage moral injustice feelings may better motivate policy reform to dismantle systemic racism. —EEU

Science, adh4262, this issue p.1394; see also adm7199, p. 1362

ICE SHEETS

Many-armed record of collapse

How the West Antarctic Ice Sheet (WAIS) responded to warmer climates in the geologic past has obvious relevance to our understanding of what its future could be as global temperatures rise due to human activities. Using genetic analyses of a type of circum-Antarctic octopus, *Pareledone turqueti*, Lau *et al*. showed that the WAIS collapsed completely during the last interglacial period, when global sea levels were 5 to 10 meters higher than today and global average temperatures were only about 1°C warmer (see the Perspective by Dutton and DeConto). The implication of this finding is that major WAIS collapse and the consequent rise in sea level could be caused even by the minimal

temperature rises projected for stringent climate change mitigation. —HJS

Science, ade0664, this issue p. 1384; see also adm6957, p. 1356

NEUROSCIENCE

Excitatory receptor type also inhibits

Glutamate delta receptors look like ionotropic glutamate channels but do not behave like classic neurotransmitter receptors because of their insensitivity to glutamate and inability to gate the ion channel pore upon ligand binding. Piot *et al*. found that GluD1, the least characterized member of this receptor family, instead binds GABA, the main inhibitory neurotransmitter in vertebrates (see the Perspective by Coombs and Farrant). GABA binds to the ligand-binding domain of GluD1 and drives conformational rearrangements in the receptor. GluD1 receptors localize at hippocampal GABAergic synapses, where they regulate the efficacy of GABAergic transmission. Activation of GluD1 receptors at hippocampal GABAergic synapses induces inhibitory synaptic plasticity. —PRS

Science, adf3406, this issue p. 1389; see also adm6771, p. 1363

DNA DAMAGE

Surviving DNA damage with IRAKs

The kinase IRAK1 promotes radiotherapy resistance in cancers. Li *et al*. found that this function of IRAK1 was independent of its regulation by innate immune receptor signaling. Double-stranded DNA breaks induced by radiation triggered IRAK4-dependent activation and nuclear translocation of IRAK1, which bound to and inhibited a pro-apoptotic complex, thereby supporting cell survival. This mechanism required the DNA damage response kinase ATR and Pellino family ubiquitin ligases. Disrupting the pathway sensitized p53-mutant zebrafish to radiation. —LKF

Sci. Signal. (2023) 10.1126/scisignal.adh3449

RESEARCH ARTICLE SUMMARY

CHEMISTRY AUTOMATION

Autonomous, multiproperty-driven molecular discovery: From predictions to measurements and back

Brent A. Koscher†, Richard B. Canty†, Matthew A. McDonald†, Kevin P. Greenman, Charles J. McGill, Camille L. Bilodeau, Wengong Jin, Haoyang Wu, Florence H. Vermeire, Brooke Jin, Travis Hart, Timothy Kulesza, Shih-Cheng Li, Tommi S. Jaakkola, Regina Barzilay, Rafael Gómez-Bombarelli, William H. Green, Klavs F. Jensen*

INTRODUCTION: The discovery of small molecules with desired functional properties is critical to advances in health, energy, and sustainability. The process is conducted through often slow, laborious, iterative design-make-test-analyze (DMTA) cycles. Emerging machine learning (ML) tools can generate new candidate molecules, predict their properties, and propose reaction pathways with computer-aided synthesis planning (CASP). Progress in chemical automation can enable chemical synthesis and characterization with minimal human intervention after a manual setup. For example, automated feedback-guided chemistry platforms have demonstrated chemical optimization within narrow, well-defined classes of reactions.

RATIONALE: Integrating ML generative algorithms, ML property prediction, CASP, robotics, and automated chemical synthesis, purification, and characterization into a DMTA workflow can lead to the development of autonomous chemical discovery platforms able to operate across varied chemical spaces without manual reconfiguration. An ideal property-focused discovery platform would propose and synthesize molecules to enrich ML generative and property models and ultimately discover top-performing molecules. In reality, it is necessary to exclude reactions that the available automation hardware cannot safely execute.

RESULTS: Toward autonomous discovery, we demonstrate an integrated DMTA cycle that iteratively proposes, realizes, and characterizes molecules to explore chemical spaces guided only by prediction tools. Four molecular scaffolds with potential applications as organic dyes serve as exploration case studies, whereas a fifth scaffold demonstrates the platform-exploiting refined ML models to optimize dye properties. Dye-like molecules constitute a compelling test case as fundamental properties are readily measurable and their realization involves multistep synthesis by a wide variety of chemical transformations. The platform automatically characterized three target properties—absorption maximum (λ_{max}), octanol-water partition coefficient ($\log K_{ow}$), and photooxidative stability ($\log k_{deg}$)—and used them to refine model predictions and inform future experiment selection.

A graph-completion generative model designs candidate molecules, which are evaluated with an ML model for each of the three properties. A CASP tool proposes multistep synthetic recipes, which are executed by an automated liquid handler, batch reactors, high-performance liquid chromatography (HPLC), and robotic arms. A plate reader measures absorption spectra, calibrated HPLC retention times provide water-octanol partition coefficients, and a simulated solar light source combined with the plate reader quantifies photooxidative degradation. The measured molecular properties are automatically fed back to retrain the property prediction models, completing one step of the automated DMTA cycle. Initially, the platform is highly uncertain about each scaffold (i.e., the ML prediction models have significant model errors), so it chooses to realize the simplest derivatives to anchor property predictions. Subsequent iterations favor more synthetically complex derivatives to fill gaps in the learned chemical space. Three iterations were sufficient for the ML model deviations to approach experimental uncertainty and enable exploitation. Human involvement was limited to setting and adjusting objectives, providing requested materials, and occasionally fixing unrecoverable errors such as clogging of the HPLC unit.

CONCLUSION: We have demonstrated a DMTA cycle that explores chemical space and exploits known chemical structures without manual experimentation. The platform proposed, synthesized, and characterized 303 unreported dye-like molecules spread across four exploration scaffolds and one exploitation scaffold. The integrated platform can explore unknown structure-property spaces by searching for structures with desired properties (hits) and can exploit characterized structure-property spaces by optimizing structures of promising candidates (leads). Further development of closed-loop integrated platforms promises to accelerate molecular discovery. ■

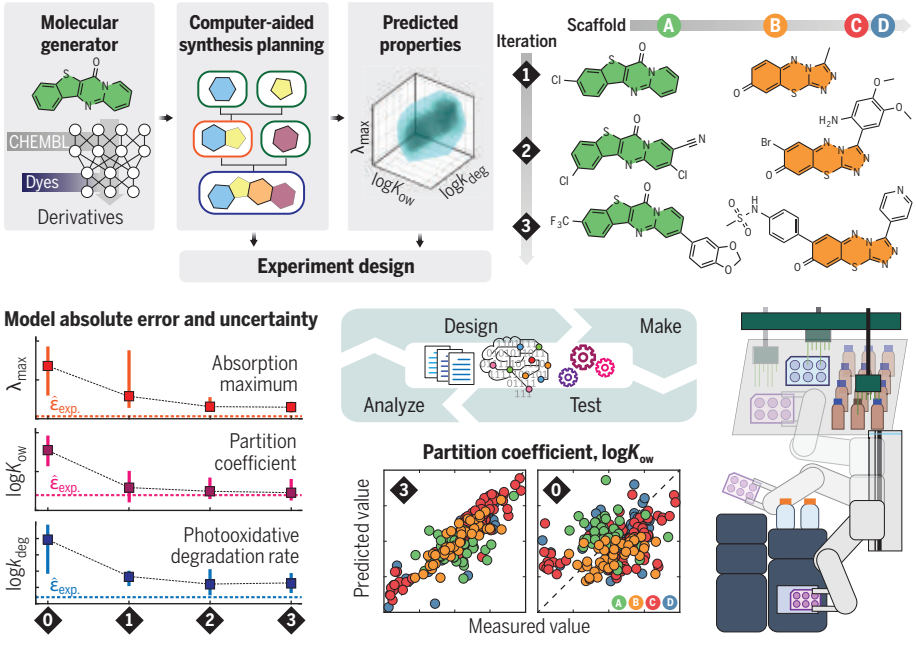

Autonomous molecular discovery. A suite of machine learning tools iteratively plans experiments to learn about a structure-property space defined by molecular dye scaffolds. $\hat{\varepsilon}_{exp.}$, mean experimental error.

The list of author affiliations is available in the full article online.
*Corresponding author. Email: kfjensen@mit.edu
†These authors contributed equally to this work.
Cite this article as B. Koscher *et al.*, *Science* **382**, eadi1407 (2023). DOI: 10.1126/science.adi1407

READ THE FULL ARTICLE AT
https://doi.org/10.1126/science.adi1407

RESEARCH ARTICLE

CHEMISTRY AUTOMATION

Autonomous, multiproperty-driven molecular discovery: From predictions to measurements and back

Brent A. Koscher[1]†, Richard B. Canty[1]†, Matthew A. McDonald[1]†, Kevin P. Greenman[1], Charles J. McGill[1], Camille L. Bilodeau[1], Wengong Jin[2], Haoyang Wu[1], Florence H. Vermeire[1], Brooke Jin[1], Travis Hart[1], Timothy Kulesza[1], Shih-Cheng Li[1], Tommi S. Jaakkola[3], Regina Barzilay[3], Rafael Gómez-Bombarelli[4], William H. Green[1], Klavs F. Jensen[1]*

A closed-loop, autonomous molecular discovery platform driven by integrated machine learning tools was developed to accelerate the design of molecules with desired properties. We demonstrated two case studies on dye-like molecules, targeting absorption wavelength, lipophilicity, and photooxidative stability. In the first study, the platform experimentally realized 294 unreported molecules across three automatic iterations of molecular design-make-test-analyze cycles while exploring the structure-function space of four rarely reported scaffolds. In each iteration, the property prediction models that guided exploration learned the structure-property space of diverse scaffold derivatives, which were realized with multistep syntheses and a variety of reactions. The second study exploited property models trained on the explored chemical space and previously reported molecules to discover nine top-performing molecules within a lightly explored structure-property space.

The efficient prediction, realization, and validation of small molecules, polymers, and materials with desirable functional properties is needed to accelerate advances in medicine (*1*, *2*), materials (*3*–*5*), and sustainability (*6*, *7*). This work focuses on organic small molecules that must manifest multiple distinct properties simultaneously, constraining molecular design and increasing structural complexity. Emerging predictive tools can quickly generate new candidate molecules (*8*–*13*), predict the performance of candidates (*11*, *14*–*16*), and propose practical reaction pathways (*17*–*21*); meanwhile, chemical automation can now dependably conduct experiments with minimal human intervention after an initial setup phase. Integrating generative algorithms, computer-aided synthesis planning (CASP), iteratively updated large datasets, and automated chemical synthesis, purification, and characterization for each step of the design-make-test-analyze (DMTA) cycle all into a single workflow could improve experiment efficiency and ultimately enable autonomous chemical discovery. Automated feedback-guided chemistry platforms have demonstrated molecular chemical discovery and optimization within narrow classes of reactions, performing iterative cross-coupling reactions (*8*, *22*), rediscovering reactivity (*23*), optimizing single reactions (*24*–*26*), and driving enzyme-assisted carbohydrate synthesis (*27*). Although these demonstrations highlight the potential of integrating predictive tools and chemical automation, their specialized implementations restrict the types of chemistry executed, the types of structures that can be realized, and notably, the chemical spaces that can be explored by these platforms.

Currently, there is a gap between the general nature of chemical prediction tools, retrosynthesis planning and property prediction, and the specialized nature of existing chemical automation platforms for the synthesis of small molecules. Closing this gap can lead to the development of autonomous chemical discovery platforms that can pivot between different discovery spaces without the need for manual reconfiguration. In the idealized case, a molecular property–focused discovery platform would propose and evaluate synthesizable molecules by using all known reactions to avoid constraints beyond those imposed by multiproperty spaces. This work narrows the gap by demonstrating an integrated platform to iteratively propose, realize, and validate molecules to explore chemical spaces guided only by prediction tools. In practice, a minimal set of reactions that cannot be safely executed by the selected automation hardware and engineering controls must be excluded. The platform integrates general chemical tools to automatically propose diverse molecules, plan synthetic pathways, execute multistep reaction pathways, purify target molecules, and characterize the performance of isolated molecules to learn about unfamiliar chemical spaces (Fig. 1A). By weighing potential challenges with each workflow in the DMTA cycle, the platform holistically evaluates the utility of a datapoint to the models against the experimental complexities required to realize a proposed molecule. Although this is analogous to how a trained chemist might approach chemical discovery, the autonomous platform can perform this evaluation on multiple properties and multiple experimental plans for thousands to millions of molecules simultaneously. As a result of this holistic consideration, the platform chooses unadorned structures to probe unexplored chemical spaces and builds more complex derivatives to optimize the properties of familiar spaces.

To initiate the automated DMTA cycle, candidate structures can be generated by using molecular generation workflows based on genetic algorithms (*8*, *9*), reinforcement learning (*10*–*12*), or conditional generation (*13*, *28*). Plausible pathways to realize candidates can be proposed by using retrosynthetic planning packages, such as ASKCOS (*17*, *18*), Synthia (*19*, *29*), IBM RXN (*20*), and AiZynthFinder (*21*). The properties of candidates can be predicted with quantitative structure-activity relationship models or statistical models such as Chemprop, a message-passing neural network (*16*). Molecules can be realized with advances in chemical automation such as reconfigurable high-throughput platforms (*18*, *24*, *30*) equipped with hardware to access diverse reaction conditions (*31*) and molecular property characterization (*7*, *32*). Such platforms have been used to discover novel chemical transformations (*32*, *33*), optimize reactions (*34*, *35*), and develop functional materials (*7*, *26*, *33*). This work integrates these tools to demonstrate a platform that can autonomously drive molecular discovery.

We demonstrated the platform (Fig. 1B) in two molecular discovery use cases for small molecule organic dyes: (i) exploration of unknown chemical spaces and (ii) exploitation of a known chemical space. The platform executes and automatically adjusts workflows as needed, with human intervention being limited to managerial (error recovery) and custodial (providing consumables) actions, both during and between iterations. A complete discussion on required human action is provided in the supplementary materials (SM8). Platform flexibility is crucial to execute multistep reaction pathways containing the breadth of reaction classes (Fig. 1C) needed to realize candidates covering the desired property space. We validated the platform's capabilities by targeting molecular dyes, a model system with diverse chemistry and complex molecular properties. During two case studies, the platform attempted over 3000 reactions, with more than 1000 yielding the predicted reaction product, completing multistep reaction pathways for 303 unreported molecules (i.e., without CAS

[1]Department of Chemical Engineering, Massachusetts Institute of Technology, Cambridge, MA, USA. [2]Broad Institute of MIT and Harvard, Cambridge, MA, USA. [3]Computer Science and Artificial Intelligence Laboratory, Massachusetts Institute of Technology, Cambridge, MA, USA. [4]Department of Materials Science and Engineering, Massachusetts Institute of Technology, Cambridge, MA, USA.
*Corresponding author. Email: kfjensen@mit.edu
†These authors contributed equally to this work.

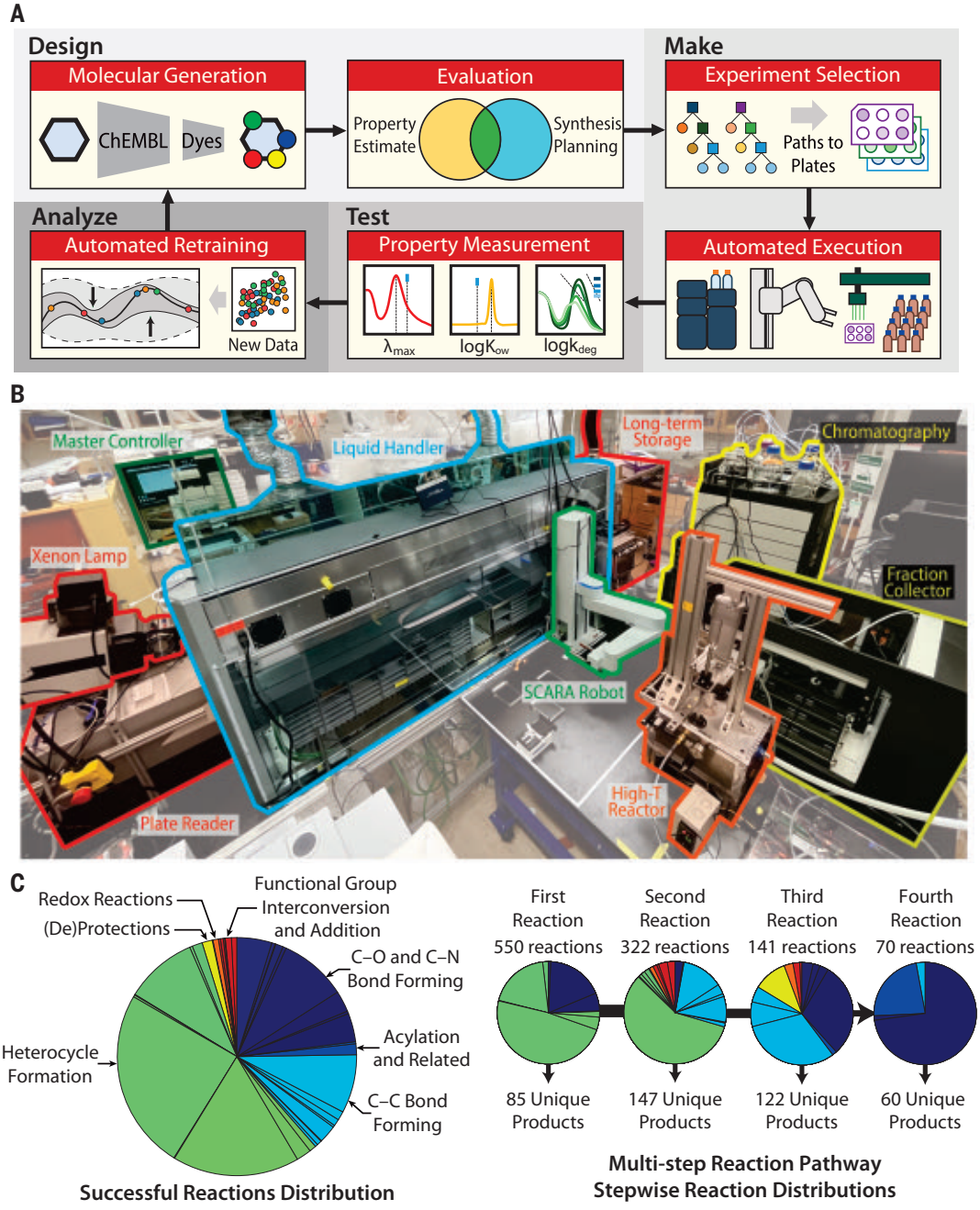

Fig. 1. Overview of the integrated platform and reactions predicted and successfully executed by the platform. (**A**) Illustrations of the key workflow components of the integrated platform and how each component fits into the DMTA cycle in which the properties tested are wavelength of maximum absorption (λ_{max}), octanol-water partition coefficient ($\log K_{ow}$), and rate of photooxidative degradation ($\log k_{deg}$). (**B**) Layout of the physical hardware of the experimental platform. (**C**) Stepwise breakdown of the classes of different reaction classes automatically executed by the platform during the exploration case study. The four smaller pie charts show the change in the reaction class distribution as a function of the reaction step number. Not all executed pathways have the same number of reactions, leading to fewer reactions at later step numbers. A detailed breakdown of the subreaction classes is given in fig. S5.

registry numbers prior to publication). For both case studies, the absorption maximum, partition coefficient, and photooxidative stability were the targeted properties, and the platform automatically measured and recorded each property to refine model predictions and inform future experiment selection.

Front-end predictions

The platform is tasked with either learning the properties of a chemical space of interest or realizing top-performing molecules within a chemical space containing existing examples. Before experiments can be executed, the platform must develop an experimental plan by proposing candidate structures, planning reaction pathways and reaction conditions, predicting candidate properties, and selecting candidates to realize (Fig. 1A, design). These prediction tasks are modular and can be exchanged to accommodate different objectives.

Candidate structures are proposed by using a hierarchical graph-completion model (*34*), which takes a molecule scaffold as input and completes the molecular graph with learned motifs, encoding and decoding full motifs at once rather than atom by atom. The model was first pretrained on ChEMBL (*35*) to learn general organic chemistry rules and then fine-tuned on a curated set of dye molecules (supplementary materials, SM2) to complete input scaffolds with diverse dye-like structural motifs. Graph completion proposes molecules spanning the multiproperty space of dye molecules and tends to generate more realistic and feasible structures compared with other molecular generation approaches (*8*–*13*, *28*). Graph completion also has the benefit of generating diverse derivatives while preserving the input scaffold, enabling exploration within a local chemical structure family. The technique adds common functional groups such as dialkylamino or cyano groups, whereas a graph-to-graph translation model we tested added polyene chains or boron inspired by high-performing cyanine

and BODIPY dyes, respectively, without conserving the central scaffold.

For each of the generated candidate molecules, multiple synthesis pathways are automatically planned and proposed by using ASKCOS (*17*, *18*), which makes template-based retrosynthesis recommendations with reaction templates extracted from large reaction databases. Reaction templates are iteratively applied in a tree search to propose reaction pathways that terminate at available reagents, connecting available starting materials, chemicals, and generated structures. A set of preferred-vendor chemical catalogs—containing SMILES, package sizes, vendor product IDs, and prices—and our in-lab inventory formed the set of reagents available to ASKCOS. Reaction pathways that do not terminate at available reagents within five reaction steps were discarded from consideration (supplementary materials, SM3). The majority of reaction pathways for generated molecules require multiple reactions, often from different reaction classes. By executing multistep reaction pathways, more of the multidimensional property space becomes accessible (Fig. 2A, volume), and moreover, there are more candidate options within the space (Fig. 2A, density). Single-step syntheses cover only 30% of the space accessible with five reaction steps and have 1000-fold fewer candidate options (Fig. 2A). In our property space of interest, molecules requiring more than five reaction steps did not further expand the volume of property space but did increase complexity and resource requirements. As a result, we set a limit of five reaction steps for the case studies presented, but other spaces may require more steps for adequate exploration.

Retrosynthesis planning also serves to determine which generated candidates are considered synthesizable. Depending on the heterocyclic scaffold, 10 to 20% of generated molecules return synthesis pathways terminating at buyable starting materials. Retrosynthesis planning is the most time intensive front-end prediction needed to create an experimental plan. Unrealistic molecules suggested by molecular generation are often filtered with synthesizability proxy metrics (*36*–*39*); however, commonly used metrics did not increase the quality of reaction planning (fig. S2), and therefore, they were not used to prefilter candidate structures during exploration. The continued development of more efficient methods to recommend candidates and pathways simultaneously would increase platform planning throughput (*39*).

Reaction conditions are recommended by ASKCOS by using a neural network model trained on a large set of literature reaction conditions (*40*). The recommendation of reaction conditions can be challenging as necessary reagents, catalysts, cocatalysts, solvents, and reaction temperature must be predicted simultaneously. To assist ASKCOS, we defined a set of rules for the 100 most popular chemical transformation templates (supplementary materials, SM3) against which ASKCOS predictions are checked. These rules identify common problems such as not recommending all required reagents for well-known reactions (e.g., recommendation of phosphorus ligand, base, solvent, and palladium source for cross-coupling reactions) or recommending outdated catalysts when improved catalysts are known. Reaction condition recommendations that did not match the predefined rules were automatically either corrected when a single required chemical was missing or removed from consideration when multiple issues were present. Although defining rules for known reactions can help fix some problematic recommendations, the continued development of reaction condition models is needed to increase the success rate of platform-executed reactions. Pathways containing a reaction without any valid recommended conditions are automatically discarded. The combination of reaction pathways and reaction conditions form experimental plans for each of the generated molecules (Fig. 2B).

For candidates with an experimental plan, their dye-like properties were predicted by using a set of Chemprop (*14*, *15*) property prediction models: wavelength of maximum absorption, partition coefficient, and photooxidative

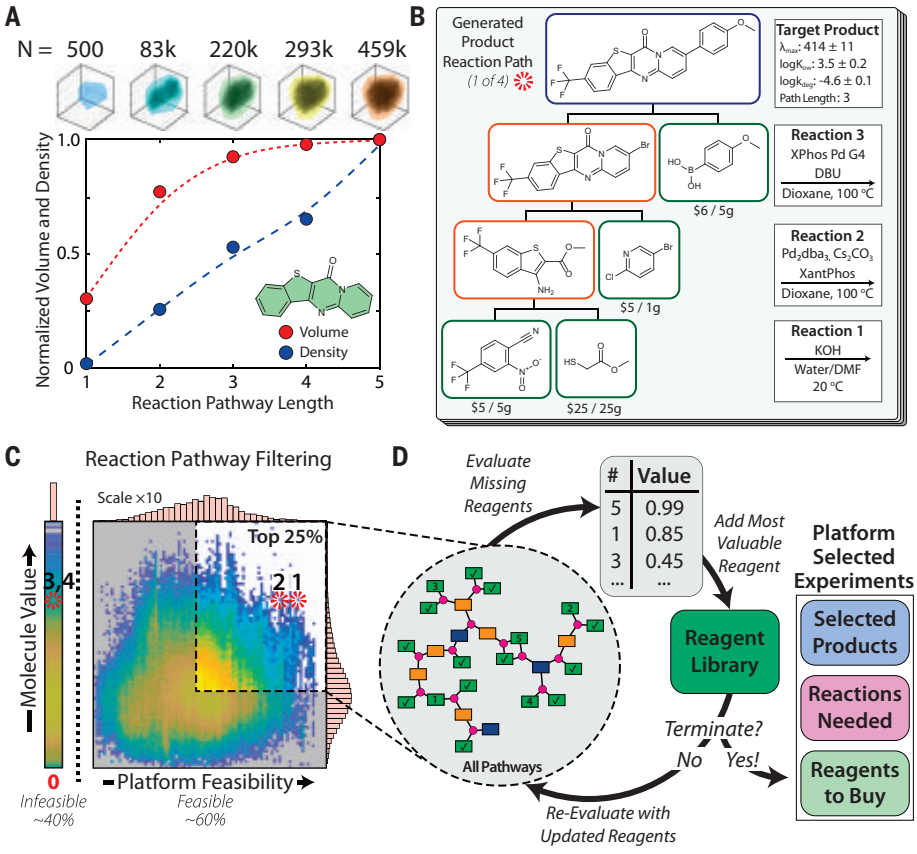

Fig. 2. Product and reaction pathway selection. (**A**) Property space (λ_{max}, logK_{ow}, and logk_{deg}) convex hull volume (red) and density of candidates (blue) for the BTPP scaffold shown in the exploration case study as a function of reaction pathway length. Dashed lines are splines provided as a guide to the eye. The convex hull volume at each pathway length has units of wavelength, logK_{ow}, and logk_{deg} normalized to the volume at a reaction pathway length of 5. The density is the similarly normalized number of candidates per unit of volume. (**B**) Example of an experimental plan to be scored, including the predicted property values (units of nanometers for λ_{max} and units of $\log_{10}(s^{-1})$ for logk_{deg}) and reaction pathways, and the top-ranked reaction context. The target candidate molecule had four experimental plans for consideration [red stars in (C)]. (**C**) Evaluation of experimental plan scores considering the platform feasibility of the proposed reaction pathway and candidate molecule value. The space is separated by infeasible (left) and feasible (right) candidate pathways. Candidates were deemed infeasible if they required platform-inaccessible reaction conditions or reagents. The color scale represents the density of candidates, increasing from low (blue) to high (yellow). (**D**) Decision cycle for additional reagents to buy by evaluating the products and reaction pathways they enable. Upon terminating, the platform has selected products to make, reactions to execute, and reagents to purchase. Reaction pathways connect buyable reactants (green) to intermediate products (orange) and target final products (blue).

degradation rate. Chemprop is lightweight and fast, so an ensemble of models can be automatically retrained from the whole dataset with each batch of experimental data (supplementary materials, SM4) (*14*–*16*, *41*). The ensemble variance is used as a proxy for model uncertainty to further inform molecule selection. Each of the models was initially trained on datasets of different sizes: 26,400 experimental absorption maxima from a compiled literature dataset (*42*), 23,500 experimental partition coefficient values also from a compiled literature dataset (*43*), and 85 experimental photooxidative degradation rates measured in house for a set of common molecular dyes (supplementary materials, SM11). Because of the small size of the third dataset, we used a random forest model implemented through Chemprop to predict photooxidative degradation rates (supplementary materials, SM4). On every iteration of the DMTA cycle, ensembles of models were trained with experimental data measured on realized molecules and the initial datasets. Subsequent rounds of property predictions were automatically made with the most recent property model version, and the predicted properties and uncertainties were used in conjunction with experimental plans to select the next iteration of candidates for experimental realization.

Selecting candidate molecules is challenging, as it involves a tradeoff between optimizing multiple properties and executing a successful synthesis. Additionally, both syntheses and properties are predictions from statistical models with varying uncertainty, which further complicates selection. For an input scaffold, there can be thousands of candidates, each with up to 10 pathways, and thousands of reagents to consider across all pathways. Reactions that require inaccessible conditions, require reagents without vendor information, or involve blacklisted reagents are automatically identified and removed from consideration. Two general categories of infeasible reactions are those requiring inaccessible reagents (no platform-known source or prohibitively expensive) and those involving platform-incompatible reaction conditions (reaction temperatures outside the range of 5° to 200°C or the use of reagents that cannot be safely handled by platform). Incompatible reagents include reactive gases (e.g., hydrogen and carbon monoxide), solid reagents that do not form solutions (e.g., alkali metals and metal powders.), and highly reactive reagents that require special handling to be used safely (such as organolithiums). The capabilities of the platform can be expanded by developing or purchasing special reactors, nitrogen-purged enclosures, and other engineering controls to safely handle these reagents. Despite 40% of proposed pathways being infeasible (Fig. 2C), the general nature of CASP implemented by ASKCOS means that there are usually proposed alternative pathways with accessible reactions, and only around 15% of candidates are removed from consideration.

The feasible candidate pathways are scored by their molecular value (the product of scaled prediction values and scaled ensemble variances) and relative platform feasibility (the product of inverse reagent cost, inverse pathway length, and compatibility of proposed reaction conditions with the well plate format) (supplementary materials, SM5). Only the highest scoring quartile of candidates are considered further (Fig. 2C). Any reagents required for the candidates that are not in the laboratory chemical inventory are rank ordered by the cumulative scores of the top 10 (exploration) or top one (exploitation) candidates that they are used to synthesize. The top-ranked reagent is added to the platform library and candidates that can be synthesized with the addition of the reagent are added to the selected products list. All remaining candidates are rescored and reagents reranked based on the updated library (Fig. 2D). The cycle of evaluation and selection is repeated until a predefined number of candidates are selected or the reagent budget is exhausted. Afterwards, the platform generates a document to prompt the operator to prepare stock solutions, specifying which vendors to purchase from and the minimum amount of material needed. The operator decides how to make stock solutions; solutions are prepared at high concentrations in solvents such as dimethylformamide, which would introduce 1 to 5% of stock solution solvent into the reaction, or at lower concentrations in volatile solvents such as chloroform, which would evaporate before the reaction begins. Completing this planning document serves as an optional managerial checkpoint for the operator to review the experiments to make sure that they will be safe.

Automation and experimental execution

Platform-selected reaction pathways are automatically translated (supplementary materials, SM6) into synthesis and characterization workflows to be executed in 96-well plates. Well plates offer ease of parallelization and sufficient material throughput (10 to 100 μmol scale) for multistep synthesis (*44*–*46*). The platform batches reactions into well plates on the basis of reaction temperature, reagent incompatibilities, and the order of reactions in multistep pathways. A finite sequence of temperatures that maximizes the number of selected pathways that can be completed is identified (Fig. 3A, plating), enabling multiple classes of reactions to be executed in the same well plate, and increasing throughput compared with the manual approach of grouping reactions by class alone. When this procedure leaves empty wells in a plate, the platform selects additional molecules that can be synthesized with the reagents in the platform library, increasing the use of the synthesis hardware and giving additional structures for property prediction model retraining with minimal additional experimental effort. Along with reaction execution tasks, high-level goal-oriented tasks to work up the reaction, analyze reaction outcomes, isolate target products, and characterize the isolated molecules are automatically generated, creating a series of platform jobs (Fig. 3A, organization). Four independent systems with different capabilities work simultaneously to accomplish these goal-oriented tasks while a master controller orchestrates tasks over a local network (Fig. 3A, experimental platform). Currently, the four systems are a liquid handler, a high-performance liquid chromatography (HPLC) with mass spectrometry instrument, a robotic arm, and a special processes unit that manages a storage carousel, a high-temperature reactor, a plate reader, and a photodegradation reactor.

Platform systems query two databases: a design database and a results database (supplementary materials, SM7). The design database tracks platform resources and is used by the platform systems to make real-time decisions on how to accomplish their assigned tasks. The results database manages experimental data and is used by the platform systems to record synthesis outcomes and molecular properties. The master controller schedules tasks to honor time constraints between tasks, adjusting to workflow changes made by the systems as needed (Fig. 3B). The occurrence of congestion on the platform necessitates additional rules for trafficking well plates between systems. Performance, a measure of platform efficiency (figs. S6 and S7; supplementary materials, SM7), is the percentage of well-based or plate-based operations, as appropriate, which did not generate an error requiring human intervention. For example, the HPLC analyzes the contents of every well, whereas the robotic arm moves an entire well plate at once, so their performances are evaluated per well and per plate, respectively. The performance of all systems exceeded 95% during the final 30 jobs for the exploration case study, which involved >1600 reactions (Fig. 3C) that were carried out across 910 hours of operations in a 5-month period. An analysis of the platform's performance is presented in the supplementary materials (SM7). It is important to note that although other high-throughput experimentation platforms can achieve higher throughputs (>1000 single-step reactions per day) for reaction condition screening, they do so for a narrow set of single-step reactions (e.g., C–C or C–N coupling) (*46*–*48*). The platform throughput is limited to ~200 reactions per day by HPLC analysis of reaction outcomes, but because of the wide scope of the workflows (prediction, execution, isolation, characterization, and model

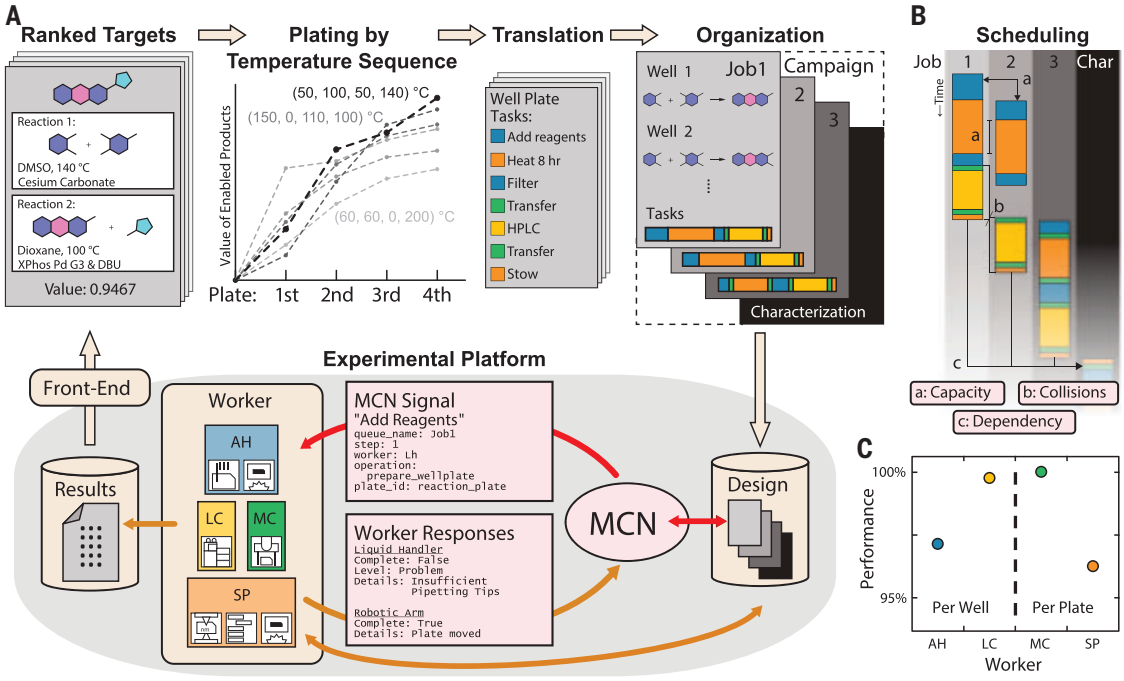

Fig. 3. Flow of information during experiment design, orchestration, execution, and data generation. (**A**) Platform-selected reactions from front-end predictions (Fig. 2) are batched into well plates, and the sequence of well plates with the highest value set of products is chosen (supplementary materials, SM5). Dashed lines are a guide to the eye to connect sequences of discrete temperatures. The well plate sequence is translated into a set of multistep goals and organized into lists of tasks for each well plate; the jobs are collated into a campaign and sent to the design database. The master control network (MCN) and databases mediate the flow of information from a campaign to the platform systems to the models for retraining. System legend: liquid handler and heater-shaker reactors (AH), blue; HPLC (LC), yellow; master controller and robotic arm (MC), green; plate reader, storage unit, and high-temperature and photodegradation reactors (SP), orange. (**B**) The initial scheduling of jobs in accordance with the scheduling algorithm: honoring (i) the capacity of a system to perform multiple tasks at once, (ii) the collision of resources between groups of tasks, and (iii) the dependencies between three synthesis jobs and a characterization job. (**C**) System performance (percent of steps not requiring human intervention) throughout the last 30 jobs of the exploration case study.

retraining), our realized throughput is lower and depends on the platform-selected chemistry. Other control architectures, such as those implemented in Chemputer (*49*, *50*) and ChemOS (*51*), were considered, but none supported parallel operation in well plates, work up and isolation, characterization, and the ability to modify workflows spontaneously. The described platform can perform multiple unrelated jobs in parallel and only requires human intervention for nonautomated error recovery and restocking (see "The role of the platform operator"; further detailed in supplementary materials, SM8).

To begin executing a job, the master controller checks that the first required system is available and that subsequent systems will have timely availability, ensuring that ongoing operations are not interrupted (Fig. 3B). Syntheses begin with reaction preparation in 96-well plates: The liquid handling robot finds the required reagents, dispenses them at appropriate volumes depending on stoichiometry and stock solution, and dispatches the reaction well plate to a reactor capable of the required reaction conditions [e.g., palladium-catalyzed reactions are sent to a nitrogen purged reactor; custom reactors are described in the supplementary materials (SM11)]. If the needed reagent is a product of a previous reaction, the volume dispensed is adjusted on the basis of the estimated reaction yield (supplementary materials, SM9). Reactions are run for 8 hours, which is excessive for faster reactions and inadequate for the most sluggish ones. Selecting an optimal duration for well plates containing many different reactions is not currently possible; quantitatively predicting kinetics for any proposed substrate, catalyst, and reagent combination is very challenging. How to predict more nuanced reaction conditions and durations for diverse reaction classes is an unsolved challenge that requires scalable predictions of chemical kinetics for complex molecules.

After executing reaction tasks, a series of automatically selected and executed work-up tasks process the crude products in preparation for ensuing reactions and HPLC analysis. Reactions with inorganic reagents such as carbonate or palladium complexes are extracted with chloroform and water in deep well plates, and all reactions are filtered through filter well plates. For intermediate products, a small sample (5 to 10%) of the filtered reaction is transferred to a new plate and diluted with dimethyl sulfoxide to dissolve the target products in a reverse-phase HPLC–compatible solvent. The reaction samples are transferred to the HPLC autosampler by the robotic arm and analyzed with a standardized water and acetonitrile gradient (supplementary materials, SM9). Reaction success was determined by identifying expected reaction product masses, and reaction yield was estimated from the HPLC chromatogram measured by the photodiode array detector. Operation and data export were automated through a vendor-supplied application-programming interface, and analysis occurred in real time (supplementary materials, SM9). For final products, the reaction outcome is analyzed in the same manner, but the majority of the filtered reaction is added to the HPLC analysis well plate. The retention time is used in a subsequent semipreparative HPLC run to isolate final products. The two-run method proved robust, but retention time prediction and real-time control of eluent composition could enable more efficient isolation without a prerequisite analytical run. Although not every product peak was baseline separated from by-products, our property assays capitalized on dye-molecule absorption of visible light, minimizing the influence of any ultraviolet-absorbing impurities on the property measurements. Although isolation of intermediate products is desirable, limitations of the current platform instruments make this impractical. Therefore, we used filtered intermediate reactions as feedstock for subsequent reactions, with around one-third of the multistep reaction pathways yielding the targeted final products. This success rate could be bolstered by preparative-scale HPLC purification but is not required to demonstrate autonomous molecular discovery. Given the limitations of small reaction scales and multistep reaction pathways, the operator must scale up reactions

and take NMR spectra off of the platform. Structural validation is a challenge for discovery-scale platforms but can be accomplished with NMR after interesting chemical spaces have been discovered.

For each property of interest, measurement and data processing protocols are defined beforehand (supplementary materials, SM9 and SM10) and are automatically applied to isolated products. Platform systems add measured data to the results database in real time for use when retraining the property prediction models. Absorption spectra are measured with a plate reader, partition coefficients are extracted from calibrated HPLC retention times, and photooxidative degradation rates are measured in a custom-built solar degradation device (supplementary materials, SM12). The device simulated sunlight at 10% solar intensity while periodically collecting absorption spectra in a plate reader; by quantifying the change in intensity of the pure sample spectrum deconvoluted from the measured spectrum, the rate of degradation could be extracted (supplementary materials, SM11). Additional properties can be measured with new hardware or workflows such as biological assays, and parallel implementation allows new hardware to work alongside existing hardware.

The role of the platform operator

Efforts toward realizing autonomous chemical discovery platforms have highlighted minimizing human intervention; however, human operators continue to have essential roles in the operation of these platforms. In this study, humans first need to set up platform goals and initialization operations (supplementary materials, SM8). During platform operation, operators oversee proposed experiments, help recover errors, and manage resources. One common source of platform errors requiring human intervention is hardware collision, which requires the operator to investigate the causes of the collision before reenabling the affected subsystems. These collisions arise from tight tolerances and robotic arm training drift that could be reduced by incorporating autocalibration equipment to preventively retrain positions. A particularly temperamental platform component is the HPLC, which requires an operator to bring it back online after errors such as clogged plumbing. Hardware or software solutions to improve robustness against common errors could be developed, such as analyzing which reactions lead to HPLC clogs and changing how those reactions are conducted. After set up, the platform proposes a series of experiments with operational plans. The operator may choose to review these proposed experiments to determine if they are safe to execute and whether they address the discovery goal well enough to invest platform time and resources; if not, the operator refines the goal or provides more tools to the platform. Afterwards, while the platform executes experiments, the operator is involved in platform resource management (keeping the platform stocked and purchasing and preparing stock material; supplementary materials, SM8). These managerial and custodial tasks are key factors that enable autonomous discovery and are often omitted when describing the operation of automated chemical platforms.

Despite progress, it is unlikely that human intervention will be completely removed from autonomous chemical discovery platforms in the near term and will continue to be a key point in ongoing conversations as autonomous platforms continue to advance. However, to assess autonomy in chemical discovery platforms (*52*, *53*), five items must ultimately be considered: (i) The scope and context of the discovery goal, (ii) the degree of choice afforded to the platform to accomplish the goal, (iii) the scale of real-time process-level feedback and adaptation, (iv) the manner in which experimental data informs future experiment design, and (v) the extent of platform automation. A detailed breakdown of these items is presented in the supplementary materials (SM8). As an illustrative comparison, specialized reaction optimization platforms are tasked to describe a reaction condition–yield landscape, but the scope of that discovery goal is narrow, and the experiment choices that can be made are highly constrained (adjustments to concentrations, temperatures, etc.) (*54*). These discovery tasks can be accomplished with fixed hardware configurations, minimal workflow flexibility, and can be guided by routine optimization algorithms. Although these platforms are self driving, their degree of autonomy is restricted to small, well-defined scopes and discovery goals. The platform we developed aims to explore general structure-property chemical spaces by leveraging the power of general machine learning predictive tools, only limited by safety considerations. As more chemistry is conducted by general-purpose autonomous discovery platforms, workflows and predictive models can be continually refined, further shifting the role of the operator toward supervision.

Exploration case study

Molecular exploration of chemical spaces beyond current datasets aims to identify productive spaces and determine whether molecules within those spaces have a set of desired properties. Property prediction models in these unexplored chemical spaces are uncertain because relevant training examples are not present to anchor predictions. To improve the property prediction models in these spaces, the platform first proposes a large number of candidates, then experimentally realizes several low-cost examples, and finally uses those examples to anchor future predictions. This approach allows the models to understand the chemical space with accessible chemistry and avoid investing excessive time and resources into synthetically complex, predicted high-performing molecules. With more accurate, anchored models, a further evaluation can narrow down the potential chemical space to a small number of hits for further exploration. This approach to molecular discovery is typical for identifying promising hit chemical spaces in hit-to-lead workflows.

To demonstrate molecular exploration, we prompted the platform to explore the properties of unexplored heterocyclic dye-like molecules. To find candidate scaffolds, we manually filtered ring structures with fewer than eight hits in the ZINC database (supplementary materials, SM1), as many molecular dye families are based around conserved, conjugated heterocyclic scaffolds (like xanthenes and coumarins). Cyclization reactions are critical to form heterocyclic structures but are challenging for retrosynthesis planners because multiple bonds form simultaneously (*55*). We manually inspected ASKCOS-recommended cyclization reactions for the ZINC hits to verify the ring-forming reaction templates and selected four heterocyclic structures to serve as exploration scaffolds (Fig. 4A). The graph-completion model automatically generated candidates by allowing any combination of C–H bonds on each scaffold to be functionalized (fig. S1). To explore the property space of these heterocyclic scaffolds, we prompted the platform to perform three rounds of molecular exploration. Beforehand, we provided a set of preferred-vendor chemical catalogs to the platform that, with the in-lab inventory, determined the domain of possible molecules. In each round, the platform considered property predictions, the practical constraints of reaction platform-feasibility, and reagent availability to select candidates to realize and characterize. Before starting subsequent rounds, the characterization data were used to update the property prediction models (discussion of the models follows in Fig. 5). The platform then used the retrained property models to drive a new iteration of the DMTA cycle.

Across the three rounds of exploration, the platform realized between 40 and 130 derivatives of each scaffold (Fig. 4A); the variation reflected differences in reaction fidelity. Recommended reaction pathways vary in length and retrosynthetic strategy, both between and within scaffolds. In some property space regions, the diversity and complexity required can be accessed by coupling commercial reagents together in single-step reactions. In other cases, starting materials with appropriate functional handles are available such that after forming the conserved heterocyclic scaffold, familiar reactions like palladium-catalyzed

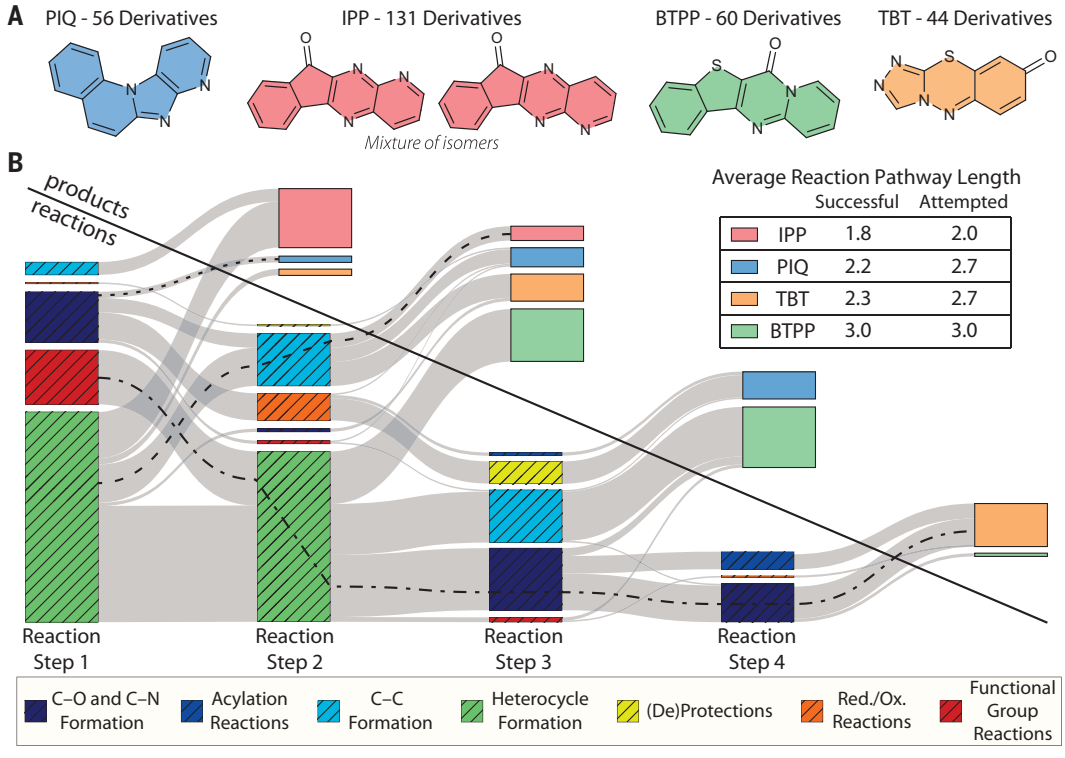

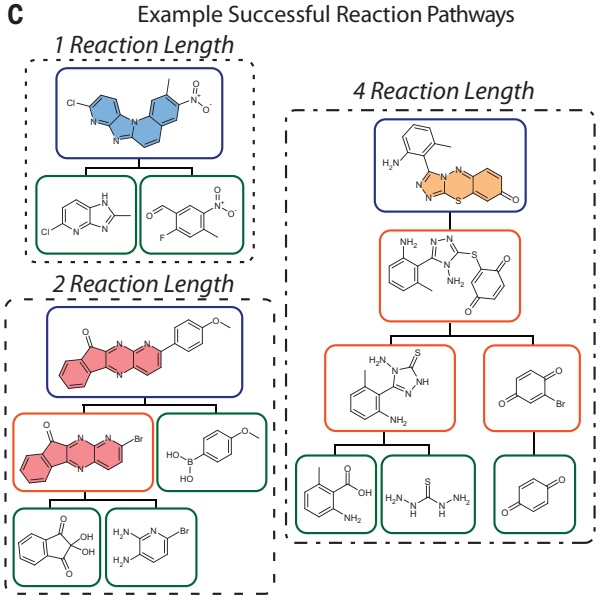

D Reaction Classes Selected

	IPP	PIQ	TBT	BTPP
C–O and C–N Formation	132/236	109/255	171/431	198/260
Acylation Reactions	0/12	10/39	16/46	5/13
C–C Formation	103/142	11/109	7/73	36/86
Heterocycle Formation	66/72	1/7	16/220	56/226
(De)Protections	2/8	0/1	6/6	---
Red./Ox. Reactions	4/8	4/46	---	---
Functional Group Reactions	47/141	11/73	20/234	23/86

Well Plate Numbers Used

Normal Well Plate	18	25	31	21
Filtration Plate	8	12	14	9
Deep Well Plate	17	14	18	6
Reactor Block Plate	4	6	4	5

Fig. 4. Chemistry predicted and attempted for the exploration case study. (**A**) Structures of the four scaffolds of interest explored by the platform: pyridoimidazoquinoline (PIQ), IPP, BTPP, and TBT. Shading color corresponds to the scaffold throughout the figure. (**B**) Diagram showing different products (solid bars, color coded by scaffold) synthesized by a variety of reaction types (hatched bars, color coded by reaction classification) and reaction pathway lengths. The sizes of the bars are proportional to the number of successful reactions and products. (**C**) Examples of successful reaction pathways for a derivative through a single-step pathway for the PIQ scaffold (dotted pathways), a two-step pathway for the IPP scaffold (dashed pathway), and a four-step pathway for the TBT scaffold (dash-dot pathway). An example of a successful three-step reaction pathway for the BTPP scaffold is shown in Fig. 2B. These example reaction pathways contain the cyclization strategy used to access each scaffold, as automatically planned by ASKCOS. Molecule box colors are the same as in Fig. 2. (**D**) The 37% overall reaction success rate broken down by class, scaffold, and number of attempts, and the number of well plates of different varieties needed to process those reactions.

cross couplings can be used to build the needed diversity and complexity. For more complex cases, reaction pathways begin by synthesizing reagents with appropriate functional handles before executing the critical cyclization reaction (Fig. 4B). When looking at the executed reaction pathways for each scaffold, the successful routes go through similar diversification strategies containing a key cyclization reaction (Fig. 4C). For each scaffold, a variety of reaction classes [based on the RXNO ontology (*56*)] were attempted to realize the automatically selected derivatives (Fig. 4D). The reaction success rate depends on the scaffold and reaction class. For example, a group of pathways that use a Friedel-Crafts acylation step were attempted for the indenopyridopyrazinone (IPP) derivatives (Fig. 4D), but the deactivated nature of the IPP scaffold prevented these reactions from succeeding. Such failure of chemistry did not halt the platform; rather, the reaction failure was recorded in the results database and dependent reaction pathways and characterizations were automatically disregarded in future operations. Varied reaction outcomes are often the result of insufficient specificity of reaction templates used in retrosynthesis planning or poor condition recommendations for uncommon reaction templates. Although outside of the scope of work presented, negative reaction outcomes could be used to improve retrosynthesis planning with each iteration. Similarly, successful cyclization reactions could be used to enhance model confidence when recommending those important reactions. Altogether, the platform selected 720 molecules to realize with an average pathway length of 2.6 reactions, requiring the platform to process 37 reaction

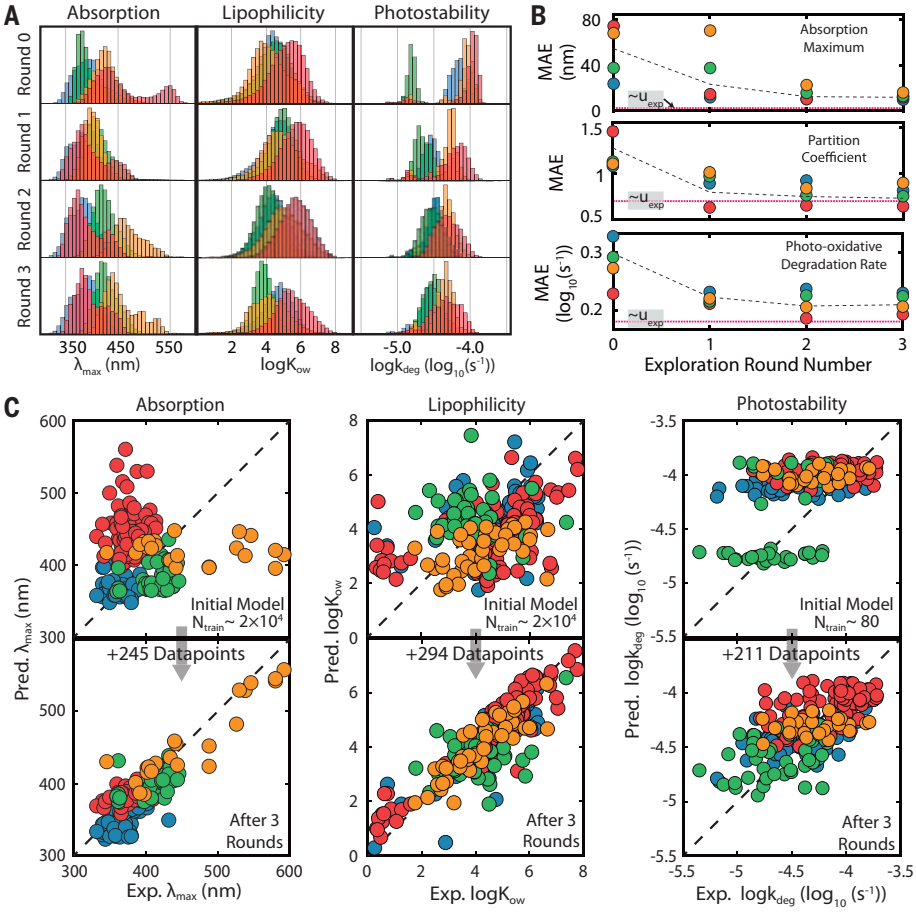

Fig. 5. Changes in property prediction models during iterative exploration. (**A**) Changes in the predicted property space with the general property model (Round 0) and following each round of exploration (Rounds 1 to 3). The shaded colors are based on scaffold coloring from Fig. 4 and apply to all subfigures. (**B**) Changes in the models' MAEs for each version of the λ_{max}, logK_{ow}, and logk_{deg} models evaluated by using cross-validation. Dashed black lines correspond to MAE values for all scaffolds combined. The experimental uncertainty (u_{exp}) is shown in each plot as a magenta dashed line. Exp., experimental; pred., predicted. (**C**) Comparison of predictions and experimental values for each of the property prediction models as initially trained and following three rounds of exploration. N_{train}, number of initial training molecules.

well plates and 181 additional well plates for workup and characterization (Fig. 4D), resulting in 294 previously unreported molecules being realized.

Property predictions for candidates made with initial property models (Fig. 5A, round 0) spanned a range of values and were relatively uncertain for the heterocyclic scaffolds of interest. These initial models were trained on datasets that were either extracted from literature or measured in house and contain no examples of the four scaffolds of interest. For exploration, the candidates that are most valuable are affordable, easy to synthesize, have properties that approach our target property space (redder absorbing, smaller partition coefficient, and photooxidatively stable), and have sizable prediction model ensemble variance (fig. S3 and supplementary materials, SM5). This approach favors diverse structures that move the derivatives' predicted properties toward the desired property space while providing information that will reduce the ensemble variance. As seen in Fig. 5, B and C, the absorption maximum, partition coefficient, and photooxidative degradation rates for the automatically realized and characterized molecules were substantially different from initial model predictions.

By iteratively and automatically realizing and measuring diverse derivatives, the platform learns about the structure-property space for the scaffolds of interest, improving the property prediction quality. Initial property prediction agreement with experimental values was subpar, with mean absolute errors (MAEs) of 52 nm for wavelength of maximum absorption, 1.3 for partition coefficient, and 0.30 $\log_{10}(s^{-1})$ for the rate of photooxidative degradation (Fig. 5B, round 0). The first round of exploration provided between 10 and 45 examples of each scaffold, depending on the complexity and success rate of the pathways for that scaffold. This handful of examples anchored the property models, shifting the predicted property space (Fig. 5A) and improving the models' MAEs (Fig. 5B), but the impact was not equal across properties or scaffolds. To investigate the impact of adding additional data, the platform performed two additional rounds of chemical exploration using the same candidate selection criteria but with updated property models and hence, candidate values, after each round. During three rounds of exploration—synthesizing 110, 110, and 90 molecules in the first, second, and third rounds, respectively—the property models improved for all scaffolds (Fig. 5, B and C), but the degree of improvement varied, and the impact of new data diminished for all property models with each round of exploration (Fig. 5B). For each property of interest, the number of experimental data points varied depending on the signal requirements for the assay. The partition coefficients were measured by using a calibrated retention time and were recorded for all identified products, resulting in 294 data points. Sufficient material had to be isolated to measure the absorption spectrum, and additional material was needed to measure the photooxidative degradation rate, resulting in 245 spectra and 211 first-order kinetic rate constants. Following the addition of the successful experimental data, the MAEs decreased to 11 nm, 0.7, and 0.21 $\log_{10}(s^{-1})$. For each of the scaffolds, the predicted property spaces (Fig. 5A) shifted toward ground-truth values as the property models learned about the structure-property spaces (Fig. 5, B and C), and for partition coefficients, the final MAE approached the limit imposed by experimental uncertainty.

Although the models' predictions improved for each scaffold, there was little change in predictive ability across general chemical spaces, demonstrating the local nature of these structure-property spaces. By verifying a handful of local experimental examples to anchor model predictions, candidate scaffolds that perform well can be more confidently considered for further examination. Initial property models both overpredicted [such as IPP absorption maxima or (triazolobenzothiadiazinone) TBT photooxidative degradation rate (Fig. 5)] and underpredicted [such as TBT or benzothienopyridopyrimidinone (BTPP) absorption maxima (Fig. 5)] the real performance of the candidate scaffolds depending on the local structure-property space. Despite a sizable number of datapoints from literature, the initial property models still did not extrapolate well to unexplored scaffolds. This exemplifies the challenge of relying only on generative and property-predicting models to guide molecular discovery, an ongoing challenge in untested chemical spaces.

Our platform overcomes this challenge by automatically designing and executing experiments with minimal human assistance, verifying interesting chemical spaces by first focusing on improving property-predicting models with relevant local examples before attempting complex and expensive molecular targets. For exploring these unknown chemical spaces, the ensemble variance appears to be a simple and effective metric to select regions about which the models are less confident for active learning campaigns. Looking more closely at each property, the absorption maximum and photooxidative stability predictions have larger ensemble variances than their corresponding experimental measurement variances, whereas the ensemble variances from the partition coefficient model prediction nearly match the experimental variances. As a result, as the accuracy of the partition coefficient model improves, its precision decreases (measured as ensemble variance), whereas for the other two models, accuracy and precision improve together. Although ensemble variance is a straightforward value to calculate and understand, as a new chemical space is explored, ensemble variance becomes a less efficient guide for properties with appreciable experimental error.

Exploitation case study

Property-predicting models can be exploited to realize potential top-performing molecules in chemical spaces containing preexisting data. Model exploitation naturally follows molecular exploration and is analogous to hit identification moving to lead optimization. Exploitation can be achieved on the same integrated platform as exploration by reweighting how candidates are valued. Predicted top performers are typically more synthetically complex and expensive, so rather than realizing several low-cost candidates, only a few confidently predicted top performers are selected.

To demonstrate model exploitation, we chose to optimize benzophenothiazinone (BPT) (Fig. 6A), a promising scaffold with sufficient cyclization yield and good model agreements in test experiments (fig. S15), a modest number of existing data points providing opportunity to discover new molecules, and structural similarities to other common dye families. We updated the property models with three examples of the scaffold to represent the promising hit and prompted the platform to discover lead molecules that simultaneously maximized absorption wavelengths, minimized partition coefficients, and minimized photodegradation rates (Fig. 6B). Although it is tempting to consider predicted property values alone when evaluating candidates (Fig. 6C), molecular generation is known to propose unusual structures (*39*) that may be outside the scope of property prediction models and have unrealistic predicted values. By considering model ensemble variance, synthetic accessibility score (*36*), and total reagent cost during candidate selection, the influence of out-of-scope structures can be minimized (Fig. 6C), thus valuing realistic candidates more highly and shifting values away from the optima idealistically defined by properties alone (Fig. 6B and fig. S4). The relative importance of these additional considerations can be weighted depending on acceptable tolerances to unusual chemical structures and prediction uncertainties in the candidate space.

The reaction pathways for the generated BPT derivatives all contain an established cyclization reaction involving the condensation of a halogenated naphthoquinone and a substituted 2-aminobenzenethiol (Fig. 6A). Several C–H sites on BPT were not accessible within a feasible number of reactions or from purchasable chemicals (Fig. 6A). From the generated derivatives, the platform automatically selected 14 of the highest-valued derivatives (Fig. 6B) to be realized, a selection of which are shown in Fig. 6C (remaining structures in SM13). Because of the air sensitivity of 2-aminobenzenethiol derivatives, the platform failed to realize some candidates that were attempted (fig. S13). For the nine candidates that were successfully realized and characterized, the predicted absorption maxima (MAE, 11 nm) and photooxidative degradation rate (0.4 log units) showed good agreement with experimental values, whereas the partition coefficient was consistently underpredicted by 2 log units. The performance of the BPT scaffold is appealing and could warrant continued investigation: It is structurally similar to phenoxazine dyes such as Nile blue, which was investigated for targeted delivery of photogenerated singlet oxygen (*57*) but is >10-fold more photooxidatively stable. Moreover, the molecules are fluorescent (fig. S9), suggesting the family might have additional photochemical activity to explore.

On inspection, the modest agreement of the partition coefficient values is not unexpected, as the derivatives that were selected by the platform all contain a primary aromatic amine. Although amine-containing derivatives can offer improved properties over amine-free derivatives, the prediction of their partition coefficients is challenging because their pK_a values (where K_a is the acid dissociation constant) can span a wide range, with charged species partitioning more into the aqueous phase. The partition coefficient model was not trained on enough aromatic amines to learn that the pK_a of 1-amino-BPT is too low for the derivatives to be ionized at the measured conditions. In practice, the partition coefficient of bioactive molecules is improved by introducing sulfonate groups that have sufficiently low pK_a values to be fully ionized in aqueous media. However, for our chemical space and properties of interest, amines strongly improve absorption maximum and photooxidative stability, whereas sulfonates only improve the partition coefficient. Because the importance of our properties of interest were equally weighted, the platform selected amine derivatives, improving two properties and modestly improving

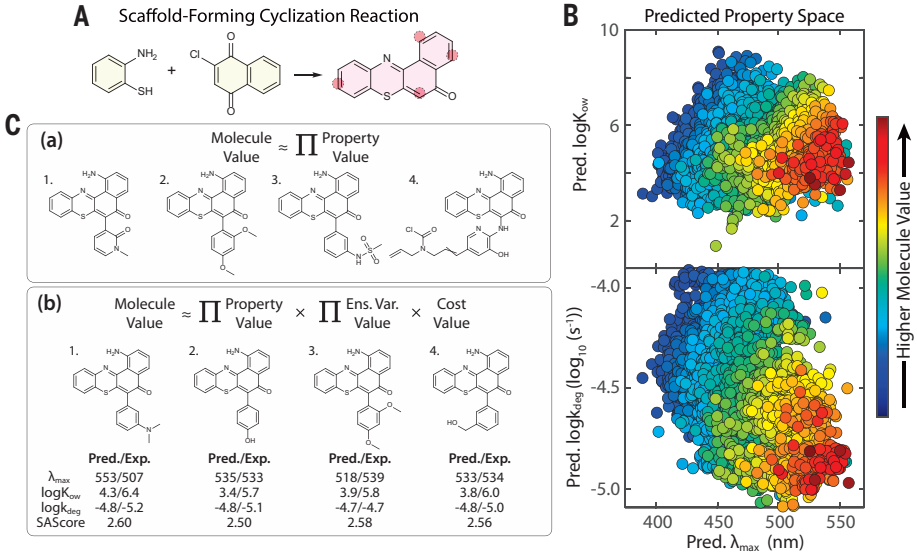

Fig. 6. Model exploitation case study. (**A**) Key cyclization reaction needed to access the ring-containing scaffold examined in the exploitation case study. Sites that were accessible with commercially available reagents in fewer than five reaction steps are highlighted in red. (**B**) Predicted property space of the generated candidates for logK_{ow} versus λ_{max} (top) and logk_{deg} versus λ_{max} (bottom). The color of each point reflects the candidate value in the exploitation workflow. (**C**) Two approaches to valuing candidates: (a) Idealistically considering only the predicted property values and (b) considering the predicted property value, ensemble variances (Ens. Var.), and cost. The top four most valuable molecules are shown for each valuation method.

the third. To maximize the improvement of the least improved property, a different selection function is needed, such as nondominated sorted or dynamic property weighting (*58*). Additionally, as the number of properties to consider grows, introducing property weightings will be advantageous to prioritize more critical properties, making new selection functions more desirable.

Conclusions

Discovery of molecules with targeted properties has historically been driven by manual experimentation, chemists' intuition, and an understanding of mechanisms and first principles. We have co-opted recently developed tools that assist chemists with the DMTA cycle to automatically explore chemical space and exploit known chemical structures. In the classic approach to the molecular discovery cycle, a hit molecule is altered to understand structure-function relationships; the platform we demonstrate does this without manual experimentation. The platform proposed, synthesized, and characterized 303 unreported dye-like molecules spread across four exploration scaffolds and one exploitation scaffold. The same integrated platform was able to both explore unknown structure-property spaces by searching for hit structures and exploit known structure-property spaces by optimizing lead structures. By the final rounds of operation, a typical job might encounter a single fault requiring operator intervention while preparing, executing, working up, and analyzing a well plate of up to 96 reactions (over the course of >1600 reactions). Although we present a general autonomous chemical discovery platform, there are areas in which autonomy can be further developed. There are cases in which human intervention can be further reduced by implementing existing, though often costly and less accessible equipment across the platform, such as commercial devices to dispense powders and prepare stock solutions. Additionally, the robust prediction of product distributions, by-products, and the corresponding solubilities in different environments would enable improved predictive purification and preemptive identification of potential experimental issues; however, these models do not exist. Reinforcement learning could also be used to develop a variety of workflows (*59*) that could help develop new operations or refine existing workflows, introducing a new dimension of platform adaptability for future versions of autonomous chemical discovery platforms.

Dye-like molecules represent a compelling property space and chemical space to explore and exploit; multistep syntheses applying a variety of chemical transformations are needed to access structures with a range of properties. The modular architecture of the integrated platform we demonstrated allows additional modules and workflows to be added as needed for different properties, such as biological activity, without impacting existing platform capabilities. Future iterations of the platform will benefit from improvements in predictive capabilities, particularly reaction fidelity, condition recommendation, and molecular generation, as well as analytical tools such as structural elucidation by means of HPLC or standalone detectors. The ongoing development of closed-loop integrated platforms is a promising path to continue accelerating molecular discovery.

Materials and methods

The following discussion summarizes the user workflow for an example scaffold (BTPP derivative from Fig. 2B). A more detailed description of autonomous candidate generation, candidate property evaluation and synthesis planning, model retraining, and all platform operations, including chemical handling, reaction preparation, execution, workup, and analysis, and product property analysis can be found in the provided supplementary materials.

Workflow initiation and platform operation (by a human operator)

The DMTA cycle must be instantiated by an operator who provides three configuration files to enable the workflow to run autonomously: (i) a set of Chemprop model parameters detailing each model's training, initial/literature data, and a specific goal for each property (maximize, minimize, or target a specific value), (ii) a scaffold from which to generate candidate molecules—in this work scaffolds were checked to ensure each had few literature precedents for discovery in unmapped chemical spaces—and (iii) a catalog of materials that can be handled by the automated synthesis machinery with associated costs and total budget. After starting the DMTA cycle, the operator must support the autonomous workflow by providing materials requested by the platform. Most requests entail providing chemicals not already in the platform library or not present in sufficient quantity; typically, such a request is fulfilled by refilling a solvent vessel or providing a stock solution in a septum-capped vial, either a 2-mL HPLC vial or 20-mL scintillation vial. Occasionally the platform may request restocking of consumable labware, such as well plates, lids, pipette tips, etc., but these are stored on-platform in sufficient quantity for multiple rounds of the DMTA cycle. When fulfilling requests, the operator enters identities and locations for labware and volumes and concentration for solutions into a platform-generated spreadsheet for easy updating of the platform library. Platform requests are made immediately before starting uninterruptible tasks, as scheduling and predicting material needs across multiple parallel and mutable jobs is impractical. Therefore, for the platform to run at capacity, an operator is required to monitor the system. On rare occasions, the operator may need to rectify an error such as a robotic collision; these events are almost always traced back to human error, such as placing a piece of labware in the wrong location but could be addressed with additional computer vision and advanced automated inventories, for example.

Chemprop model construction

Models for predicting molecule properties were all built using Chemprop, a software package available at https://github.com/chemprop/chemprop. For the larger dataset sizes of the absorption maximum and partition coefficient models, predictions were made using message-passing neural networks (MPNN) followed by conventional feed-forward networks. For small dataset sizes, random forest (RF) models have comparable or better performance than MPNNs. Therefore, the photooxidative degradation rate model was implemented with a RF within the Chemprop environment. Uncertainty was estimated with the variance of predictions from an ensemble of Chemprop models. Models were hyperparameter optimized before beginning the discovery campaign (training parameters can be found in table S2). Chemprop automatically implements the different model architectures, ensembling for uncertainty estimation, and hyperparameter optimization. To demonstrate the rate of discovery, either 10-fold or leave-one-out cross-validation was performed (depending on the number of new data points), although in operation, validation is not required as newly synthesized molecules will not be in the training data.

Candidate generation, reaction planning, and experiment selection

Methods for candidate generation, reaction planning, and experiment selection are covered in the main text (Front-end predictions) and supplementary materials (SM1 to SM6).

Reaction Execution and Workup

To achieve the desired reaction throughput, reactions were run in parallel in 96-well plates. All well plates were prepared with a Tecan Freedom Evo 200 liquid handler equipped with a liquid-handling (LiHa) arm, a multichannel arm (MCA), and a robotic manipulator (RoMa) arm that pipette individually addressed wells, pipette 96 wells in parallel, and move well plates, respectively. Additionally, workflows were developed for the RoMa to assemble and disassemble devices on the liquid handler bed, such as the Te-VacS microplate filtration system. Reaction groups taking place between 4° and 120°C were run on a

Inheho Teleshake or Thermoshake on the Tecan Evo bed. To accommodate the dilution and decrease in material with each step in a multistep synthesis, the platform multiplies the single step concentration (generally about 15 μmol) by the number of subsequent steps, so the first reaction in a three-step reaction would be prepared at 45 μmol, the second step at 30 μmol, and the final step at the desired 15 μmol. For air- and water-sensitive reaction groups, reactions were run on a dedicated Teleshake with a removable cover (by the RoMa) that has (replaceable) septa over each well and is constantly purged with nitrogen (supplementary materials, SM12), allowing pipetting into wells and heating to reaction temperatures with minimal exposure to air. For well plate compatibility, reactions taking place below 80°C were run in polypropylene well plates (1.8 mL working volume) while those above 80°C were run in Paradox aluminum well plates with glass inserts (0.8 mL working volume). A separate Precise Flex 400 collaborative robotic arm outside of the liquid handler was used to transfer well plates and resources between systems. Reactions beyond 120°C were run in a custom-made oven (supplementary materials, SM12) purged with nitrogen and sealed by means of an electric linear actuator uniformly pressing a fluorinated polymer film over an aluminum well plate with glass inserts (Para-dox Plate).

Crude reaction workup used the liquid handler to perform both extraction and filtration. For extraction, the target product is dissolved in chloroform and water is used to extract water-soluble impurities and salts. Use of chloroform ensures that the organic phase is on the bottom of the well and allows use of the MCA to extract all 96 wells at once without concern about the location of the boundary between the phases. Additionally, as chloroform is easily evaporated away with mild heating it is used to transfer material between wells, allowing the material to be redissolved in the predicted solvent. This is especially useful during filtration, which uses 96-well polypropylene filter well plates (0.45 μm) with the Te-VacS microplate filtration system to collect filtrate from each well. Filtration is required to prevent disruptions to HPLC operation. The reverse-phase HPLC system (water/acetonitrile gradient) cannot handle chloroform, so after filtration, an aliquot of the product is dissolved in dimethyl sulfoxide and the chloroform is evaporated.

HPLC was performed with a Shimadzu Nexera series system equipped with a photodiode array and mass spectrometer detectors and a well plate compatible autosampler. The mass spectrometer was used to identify target products, which were isolated as (nearly) pure material by collecting the product peak with a well plate compatible fraction collector. With a semipreparative HPLC column, enough material could be collected to assay the new molecules' properties of interest. As with the Tecan Evo, all operations of the Shimadzu Nexera were automated and coordinated by the master control network (supplementary materials, SM7).

Property Assays: Absorption maximum, partition coefficient, and photooxidative stability

Partition coefficients were determined with a calibrated HPLC retention time method (calibration and fitting data are presented in supplementary materials, SM10) based on an initial screen of 30 common molecules using the same gradient used for analytic screening. Absorption spectra were measured with a Tecan Spark plate reader. Sample well plates were loaded into and unloaded from the Spark by the RoMa. Spectral measurements were exported, and the raw and background-subtracted spectra were submitted to the experimental results database (control integration and data processing details can be found in supplementary materials, SM11). Photooxidative stability was measured with the Spark in conjunction with a custom-built reactor attached to the Spark on its second door. The reactor was purged with heated air (40°C) and utilized a forklift to hold the well plate under constant illumination, broad spectrum light from a xenon arc lamp (42 mW/m^2 average intensity). Periodically, the plate would be transferred back to the Spark for absorption spectra measurements. Using cumulative exposure time and estimated pristine compound spectrum tracking through spectral deconvolution (supplementary materials, SM11), a first-order degradation rate constant was determined for each sample.

Automated model retraining

Model retraining is automatically triggered after either a set period of time has elapsed or the platform completes a chemical discovery campaign. New data are appended to the initial training data and an ensemble of models is trained according to the configuration file, originally configured during the initial Chemprop model construction. Given the relatively small increase to the dataset from each round of discovery campaign, hyperparameters were not re-optimized when retraining the models, maintaining fast model retraining times. Additionally, high-performance computing resources through MIT SuperCloud for rapid model retraining and the updated models were returned to the prediction pipeline to start the next chemical discovery campaign.

REFERENCES AND NOTES

1. K. R. Campos *et al*., The importance of synthetic chemistry in the pharmaceutical industry. *Science* **363**, eaat0805 (2019). doi: 10.1126/science.aat0805
2. T. Dimitrov, C. Kreisbeck, J. S. Becker, A. Aspuru-Guzik, S. K. Saikin, Autonomous Molecular Design: Then and Now. *ACS Appl. Mater. Interfaces* **11**, 24825–24836 (2019). doi: 10.1021/acsami.9b01226; pmid: 30908004
3. M. Abolhasani, E. Kumacheva, The rise of self-driving labs in chemical and materials sciences. *Nat. Synth.* **2**, 483–492 (2023). doi: 10.1038/s44160-022-00231-0
4. E. Stach *et al*., Autonomous experimentation systems for materials development: A community perspective. *Matter* **4**, 2702–2726 (2021). doi: 10.1016/j.matt.2021.06.036
5. B. P. MacLeod, F. G. L. Parlane, A. K. Brown, J. E. Hein, C. P. Berlinguette, Flexible automation accelerates materials discovery. *Nat. Mater.* **21**, 722–726 (2022). doi: 10.1038/s41563-021-01156-3; pmid: 34907322
6. J. Peng *et al*., Human- and machine-centred designs of molecules and materials for sustainability and decarbonization. *Nat. Rev. Mater.* **7**, 991–1009 (2022). doi: 10.1038/s41578-022-00466-5
7. S. Langner *et al*., Beyond Ternary OPV: High-Throughput Experimentation and Self-Driving Laboratories Optimize Multicomponent Systems. *Adv. Mater.* **32**, e1907801 (2020). doi: 10.1002/adma.201907801; pmid: 32049386
8. E.-W. Lameijer, T. Bäck, J. N. Kok, A. P. Ijzerman, Evolutionary Algorithms in Drug Design. *Nat. Comput.* **4**, 177–243 (2005). doi: 10.1007/s11047-004-5237-8
9. Y. Kwon, S. Kang, Y.-S. Choi, I. Kim, Evolutionary design of molecules based on deep learning and a genetic algorithm. *Sci. Rep.* **11**, 17304 (2021). doi: 10.1038/s41598-021-96812-8; pmid: 34453086
10. M. Popova, O. Isayev, A. Tropsha, Deep reinforcement learning for de novo drug design. *Sci. Adv.* **4**, eaap7885 (2018). doi: 10.1126/sciadv.aap7885; pmid: 30050984
11. Z. Zhou, S. Kearnes, L. Li, R. N. Zare, P. Riley, Optimization of Molecules via Deep Reinforcement Learning. *Sci. Rep.* **9**, 10752 (2019). doi: 10.1038/s41598-019-47148-x; pmid: 31341196
12. S. K. Gottipati *et al*., Learning To Navigate The Synthetically Accessible Chemical Space Using Reinforcement Learning, *Proceedings of the 37th International Conference on Machine Learning*, July 13 to 18 2020, 3668–3679 (PMLR, vol. 119, 2020).
13. S. Kang, K. Cho, Conditional Molecular Design with Deep Generative Models. *J. Chem. Inf. Model.* **59**, 43–52 (2019). doi: 10.1021/acs.jcim.8b00263; pmid: 30016587
14. Chemprop: Molecular Property Prediction; https://github.com/chemprop/chemprop.
15. E. Heid *et al*., Chemprop: A Machine Learning Package for Chemical Property Prediction. ChemRxiv [Preprint] (2023); https://doi.org/10.26434/chemrxiv-2023-3zcfl-v2.
16. K. Yang *et al*., Analyzing Learned Molecular Representations for Property Prediction. *J. Chem. Inf. Model.* **59**, 3370–3388 (2019). doi: 10.1021/acs.jcim.9b00237; pmid: 31361484
17. ASKCOS; https://github.com/ASKCOS/.
18. C. W. Coley *et al*., A robotic platform for flow synthesis of organic compounds informed by AI planning. *Science* **365**, eaax1566 (2019). doi: 10.1126/science.aax1566; pmid: 31395756
19. T. Klucznik *et al*., Efficient Syntheses of Diverse, Medicinally Relevant Targets Planned by Computer and Executed in the Laboratory. *Chem* **4**, 522–532 (2018). doi: 10.1016/j.chempr.2018.02.002
20. P. Schwaller *et al*., Predicting retrosynthetic pathways using transformer-based models and a hyper-graph exploration strategy. *Chem. Sci.* **11**, 3316–3325 (2020). doi: 10.1039/C9SC05704H; pmid: 34122839
21. S. Genheden *et al*., AiZynthFinder: A fast, robust and flexible open-source software for retrosynthetic planning. *J. Cheminform.* **12**, 70 (2020). doi: 10.1186/s13321-020-00472-1; pmid: 33292482
22. J. Li *et al*., Synthesis of many different types of organic small molecules using one automated process. *Science* **347**, 1221–1226 (2015). doi: 10.1126/science.aaa5414; pmid: 25766227
23. S. H. M Mehr, D. Caramelli, L. Cronin, Digitizing chemical discovery with a Bayesian explorer for interpreting reactivity data. *Proc. Natl. Acad. Sci. U.S.A.* **120**, e2220045120 (2023). doi: 10.1073/pnas.2220045120; pmid: 37068251
24. A. C. Bédard *et al*., Reconfigurable system for automated optimization of diverse chemical reactions. *Science* **361**, 1220–1225 (2018). doi: 10.1126/science.aat0650; pmid: 30237351
25. A. M. K. Nambiar *et al*., Bayesian Optimization of Computer-Proposed Multistep Synthetic Routes on an Automated Robotic Flow Platform. *ACS Cent. Sci.* **8**, 825–836 (2022). doi: 10.1021/acscentsci.2c00207; pmid: 35756374
26. B. P. MacLeod *et al*., Self-driving laboratory for accelerated discovery of thin-film materials. *Sci. Adv.* **6**, eaaz8867 (2020). doi: 10.1126/sciadv.aaz8867; pmid: 32426501

27. T. Li *et al*., An automated platform for the enzyme-mediated assembly of complex oligosaccharides. *Nat. Chem.* **11**, 229–236 (2019). doi: 10.1038/s41557-019-0219-8; pmid: 30792508
28. P. C. Kotsias *et al*., Direct steering of de novo molecular generation with descriptor conditional recurrent neural networks. *Nat. Mach. Intell.* **2**, 254–265 (2020). doi: 10.1038/s42256-020-0174-5
29. B. Mikulak-Klucznik *et al*., Computational planning of the synthesis of complex natural products. *Nature* **588**, 83–88 (2020). doi: 10.1038/s41586-020-2855-y; pmid: 33049755
30. S. Steiner *et al*., Organic synthesis in a modular robotic system driven by a chemical programming language. *Science* **363**, eaav2211 (2019). doi: 10.1126/science.aav2211; pmid: 30498165
31. S. H. M. Mehr, M. Craven, A. I. Leonov, G. Keenan, L. Cronin, A universal system for digitization and automatic execution of the chemical synthesis literature. *Science* **370**, 101–108 (2020). doi: 10.1126/science.abc2986; pmid: 33004517
32. G. Pizzuto, J. De Berardinis, L. Longley, H. Fakhruldeen, A. I. Cooper, SOLIS: Autonomous Solubility Screening using Deep Neural Networks, *Proceedings of the International Joint Conference on Neural Networks*, 18 to 23 July 2022, (IEEE, 2022). doi: 10.1109/IJCNN55064.2022.9892533
33. B. Burger *et al*., A mobile robotic chemist. *Nature* **583**, 237–241 (2020). doi: 10.1038/s41586-020-2442-2; pmid: 32641813
34. W. Jin, R. Barzilay, T. Jaakkola, Hierarchical Generation of Molecular Graphs using Structural Motifs, *ICML'20: Proceedings of the 37th International Conference on Machine Learning*, July 2020, 4839–4848 (PMLR, 2020).
35. A. Gaulton *et al*., ChEMBL: A large-scale bioactivity database for drug discovery. *Nucleic Acids Res.* **40** (D1), D1100–D1107 (2012). doi: 10.1093/nar/gkr777; pmid: 21948594
36. P. Ertl, A. Schuffenhauer, Estimation of synthetic accessibility score of drug-like molecules based on molecular complexity and fragment contributions. *J. Cheminform.* **1**, 8 (2009). doi: 10.1186/1758-2946-1-8; pmid: 20298526
37. C. W. Coley, L. Rogers, W. H. Green, K. F. Jensen, SCScore: Synthetic Complexity Learned from a Reaction Corpus. *J. Chem. Inf. Model.* **58**, 252–261 (2018). doi: 10.1021/acs.jcim.7b00622; pmid: 29309147
38. A. Thakkar, V. Chadimová, E. J. Bjerrum, O. Engkvist, J.-L. Reymond, Retrosynthetic accessibility score (RAscore) - rapid machine learned synthesizability classification from AI driven retrosynthetic planning. *Chem. Sci.* **12**, 3339–3349 (2021). doi: 10.1039/D0SC05401A; pmid: 34164104
39. W. Gao, C. W. Coley, The Synthesizability of Molecules Proposed by Generative Models. *J. Chem. Inf. Model.* **60**, 5714–5723 (2020). doi: 10.1021/acs.jcim.0c00174; pmid: 32250616
40. H. Gao *et al*., Using Machine Learning To Predict Suitable Conditions for Organic Reactions. *ACS Cent. Sci.* **4**, 1465–1476 (2018). doi: 10.1021/acscentsci.8b00357; pmid: 30555898
41. G. Scalia, C. A. Grambow, B. Pernici, Y. P. Li, W. H. Green, Evaluating Scalable Uncertainty Estimation Methods for Deep Learning-Based Molecular Property Prediction. *J. Chem. Inf. Model.* **60**, 2697–2717 (2020). doi: 10.1021/acs.jcim.9b00975; pmid: 32243154
42. J. F. Joung, M. Han, M. Jeong, S. Park, Experimental database of optical properties of organic compounds. *Sci. Data* **7**, 295 (2020). doi: 10.1038/s41597-020-00634-8; pmid: 32901041
43. Y. Chung *et al*., Group Contribution and Machine Learning Approaches to Predict Abraham Solute Parameters, Solvation Free Energy, and Solvation Enthalpy. *J. Chem. Inf. Model.* **62**, 433–446 (2022). doi: 10.1021/acs.jcim.1c01103; pmid: 35044781
44. L. Gao *et al*., 'Chemistry at the speed of sound': Automated 1536-well nanoscale synthesis of 16 scaffolds in parallel. *Green Chem.* **25**, 1380–1394 (2023). doi: 10.1039/D2GC04312B; pmid: 36824604
45. A. Osipyan *et al*., Automated, Accelerated Nanoscale Synthesis of Iminopyrrolidines. *Angew. Chem. Int. Ed.* **59**, 12423–12427 (2020). doi: 10.1002/ange.202000887; pmid: 32048418
46. S. W. Krska, D. A. DiRocco, S. D. Dreher, M. Shevlin, The Evolution of Chemical High-Throughput Experimentation To Address Challenging Problems in Pharmaceutical Synthesis. *Acc. Chem. Res.* **50**, 2976–2985 (2017). doi: 10.1021/acs.accounts.7b00428; pmid: 29172435
47. A. C. Sun *et al*., A droplet microfluidic platform for high-throughput photochemical reaction discovery. *Nat. Commun.* **11**, 6202 (2020). doi: 10.1038/s41467-020-19926-z; pmid: 33273454
48. A. Bellomo *et al*., Rapid catalyst identification for the synthesis of the pyrimidinone core of HIV integrase inhibitors. *Angew. Chem. Int. Ed.* **51**, 6912–6915 (2012). doi: 10.1002/anie.201201720; pmid: 22689502
49. P. S. Gromski, J. M. Granda, L. Cronin, Universal Chemical Synthesis and Discovery with 'The Chemputer'. *Trends Chem.* **2**, 4–12 (2020). doi: 10.1016/j.trechm.2019.07.004
50. A. J. S. Hammer, A. I. Leonov, N. L. Bell, L. Cronin, Chemputation and the Standardization of Chemical Informatics. *JACS Au* **1**, 1572–1587 (2021). doi: 10.1021/jacsau.1c00303; pmid: 34723260
51. L. M. Roch *et al*., ChemOS: An orchestration software to democratize autonomous discovery. *PLOS ONE* **15**, e0229862 (2020). doi: 10.1371/journal.pone.0229862; pmid: 32298284
52. S. Lo *et al*., Review of Low-cost Self-driving Laboratories: The "Frugal Twin" Concept (2023; https://chemrxiv.org/engage/chemrxiv/article-details/64f94d43dd1a73847f598050).
53. R. B. Canty, B. A. Koscher, M. A. McDonald, K. F. Jensen, Integrating autonomy into automated research platforms. *Digit. Discov.* **2**, 1259–1268 (2023). doi: 10.1039/D3DD00135K
54. N. H. Angello *et al*., Closed-loop optimization of general reaction conditions for heteroaryl Suzuki-Miyaura coupling. *Science* **378**, 399–405 (2022). doi: 10.1126/science.adc8743
55. Y. Mo *et al*., Evaluating and clustering retrosynthesis pathways with learned strategy. *Chem. Sci.* **12**, 1469–1478 (2020). doi: 10.1039/D0SC05078D; pmid: 34163910
56. RXNO, reaction ontologies; https://github.com/rsc-ontologies/rxno.
57. M. Li *et al*., Near-Infrared Light-Initiated Molecular Superoxide Radical Generator: Rejuvenating Photodynamic Therapy against Hypoxic Tumors. *J. Am. Chem. Soc.* **140**, 14851–14859 (2018). doi: 10.1021/jacs.8b08658; pmid: 30362735
58. J. C. Fromer, C. W. Coley, Computer-aided multi-objective optimization in small molecule discovery. *Patterns (N. Y.)* **4**, 100678 (2023). doi: 10.1016/j.patter.2023.100678; pmid: 36873904
59. A. A. Volk *et al*., AlphaFlow: Autonomous discovery and optimization of multi-step chemistry using a self-driven fluidic lab guided by reinforcement learning. *Nat. Commun.* **14**, 1403 (2023). doi: 10.1038/s41467-023-37139-y; pmid: 36918561
60. B. A. Koscher, R. B. Canty, M. A. McDonald, K. F. Jensen, Autonomous, multi-property-driven molecular discovery: from predictions to measurements and back. Zenodo (2023), doi: 10.5281/zenodo.10037800
61. B. A. Koscher, R. B. Canty, M. A. McDonald, K. F. Jensen, Code for: Autonomous, multi-property-driven molecular discovery: from predictions to measurements and back. Zenodo (2023), doi: 10.5281/zenodo.10083815

ACKNOWLEDGMENTS

The authors thank the Shimadzu Innovation Center for their creation of the application programming interface which allowed programmatic control of the HPLC-MS and fraction collector. The authors thank the ASKCOS development team, particularly M. Liu, M. Murnin, M. Fortunato, and T. Struble for help with ASKCOS and the ASKCOS API. The authors acknowledge the MIT SuperCloud and Lincoln Laboratory Supercomputing Center for providing high-performance computing resources that have contributed to the research results reported within this report. The authors thank R. Alrufayi for help gathering the rules for implementation of reaction condition recommendations correction and P. Tumkur for developing Arduino code and the custom circuit board for the high-temperature thermal reactor. The authors thank A. Croke for help scaling up reaction workup. **Funding:** DARPA Accelerated Molecular Discovery (AMD) program under contract HR00111920025 and the MIT Consortium, Machine Learning for Pharmaceutical Discovery and Synthesis consortium (MLPDS). K.P.G. was supported by the National Science Foundation Graduate Research Fellowship Program under grant no. 1745302. **Author contributions:** Design, development, and supervised construction of the platform: B.A.K., R.B.C., M.A.M, and K.F.J.; Development, maintenance, and assembly of the robotic platform: B.J., T.H., and T.K.; Development and implementation of platform control and automation software: B.A.K., R.B.C., and M.A.M.; Design and development of property prediction models: K.P.G., C.J.M., H.W., F.H.V., and S.-C.L.; Development of automated property-prediction model retraining: K.P.G. and C.J.M.; Advisement on the development of property prediction models: R.G.-B. and W.H.G.; Design and development of graph-completion model: C.L.B. and W.J.; Advisement on the development of graph-completion model: T.S.J., R.B., and K.F.J.; Development of chemistry and assays and performance of experiments: B.A.K., R.B.C., and M.A.M.; Interpretation of results: all authors; Writing: B.A.K., R.B.C., and M.A.M.; Editing: all authors; Conceptualization, supervision of the project, and funding acquisition: T.S.J., R.B., R.G.-B., W.H.G., and K.F.J. **Competing interests:** The authors declare no competing interests. **Data and materials availability:** All data and code used in this study are freely available in the main text, supplementary materials, GitHub (https://github.com/RBCanty/MIT_AMD_Platform), and through Zenodo (*60, 61*), with the exception of the Shimadzu HPLC API, data from the CAS Content Collection, and Tecan Spark API, which are proprietary and unable to be publicly shared. For information on the Shimadzu API, contact the Shimadzu US Innovation Center (Columbia, MD; https://www.shimadzu.com/an/news-events/collabo/sicadl.html#lab01). For information on accessing the CAS Content Collection, contact the CAS Customer Center (https://www.cas.org/cas-data/cas-reactions). For information on the Tecan Spark API, contact your local Tecan Service Representative (https://www.tecan.com/contact-us).

License information: Copyright © 2023 the authors, some rights reserved; exclusive licensee American Association for the Advancement of Science. No claim to original US government works. https://www.science.org/about/science-licenses-journal-article-reuse

SUPPLEMENTARY MATERIALS

science.org/doi/10.1126/science.adi1407
Materials and Methods
Supplementary Text
Figs. S1 to S17
Tables S1 to S5
References (*62*–*76*)

Submitted 5 April 2023; accepted 9 November 2023
10.1126/science.adi1407

RESEARCH ARTICLE SUMMARY

BITCOIN

Are cryptocurrencies currencies? Bitcoin as legal tender in El Salvador

Fernando Alvarez*, David Argente*, Diana Van Patten*

INTRODUCTION: The introduction of digital currencies is perhaps the most important development in monetary economics in the past decade. However, a currency's defining role is to serve as a medium of exchange, and cryptocurrencies have yet to be widely adopted as such. This study leverages a unique quasinatural experiment that can shed light on the reasons behind this lack of adoption. El Salvador became the first country to make bitcoin legal tender; not only must bitcoin be accepted as a means of payment for taxes and debts, but also businesses are required to accept bitcoin as a medium of exchange. The government also launched an app called "Chivo Wallet," which allows users to digitally trade both bitcoins and US dollars (USD, the official currency in El Salvador) without paying transaction fees, and provided major adoption incentives such as a large bonus for downloaders. Moreover, the pandemic provided an additional incentive to adopt touchless payments; if bitcoin has a chance to be used as a medium of exchange, then this setting gave the cryptocurrency a prime opportunity. Furthermore, the study of Chivo Wallet, a digital currency backed by a central bank, is informative to the debate surrounding central bank digital currencies (CBDCs).

RATIONALE: We conducted a nationally representative face-to-face survey involving 1800 households in El Salvador and complemented its results with an analysis using all transactions identified as involving Chivo Wallet leveraging data from the blockchain. We explored whether Chivo Wallet and bitcoin were adopted after the government's "Big Push," what factors deterred adoption by individuals and firms, and what insights can be obtained from blockchain data. We also analyzed the broader lessons learned from this example.

RESULTS: We found that bitcoin was not widely used as a medium of exchange and usage of Chivo Wallet was low. Most downloads took place just as the app was launched. Since then, adoption and remittances using Chivo Wallet have been decreasing over time. These results suggest that it is unlikely that the usage of bitcoin and Chivo Wallet will increase. Privacy and transparency concerns appear to be key barriers to adoption. We also documented that this technology involves a large initial adoption cost, has benefits that significantly increase as more people use it, and faces resistance from firms in terms of its adoption. These findings are relevant for countries studying the viability of CBDCs and of crypto as a currency. Further, our survey sheds light on how it is the already wealthy and banked who use crypto, which stands in stark contrast with recurrent hypotheses claiming that the use of crypto may particularly help the poor and unbanked. An analysis relying on all blockchain transaction–level data from Chivo allowed us to validate and better understand our survey results and provided new insights on the dynamics of the use of Chivo Wallet.

CONCLUSION: Despite bitcoin's legal tender status and the large incentives to promote Chivo Wallet in El Salvador, the cryptocurrency was not adopted at large as a medium of exchange, and digital payments were scarce and concentrated. These findings are informative about the intrinsic value of cryptocurrencies as means of payments and about the scope of CBDCs in developing countries. ■

The list of author affiliations is available in the full article online.
*Corresponding author. Email: f-alvarez1@uchicago.edu (F.A.); david.argente@yale.edu (D.A.); diana.vanpatten@yale.edu (D.V.P.)
Cite this article as F. Alvarez *et al.*, *Science* **382**, eadd2844 (2023). DOI: 10.1126/science.add2844

READ THE FULL ARTICLE AT
https://doi.org/10.1126/science.add2844

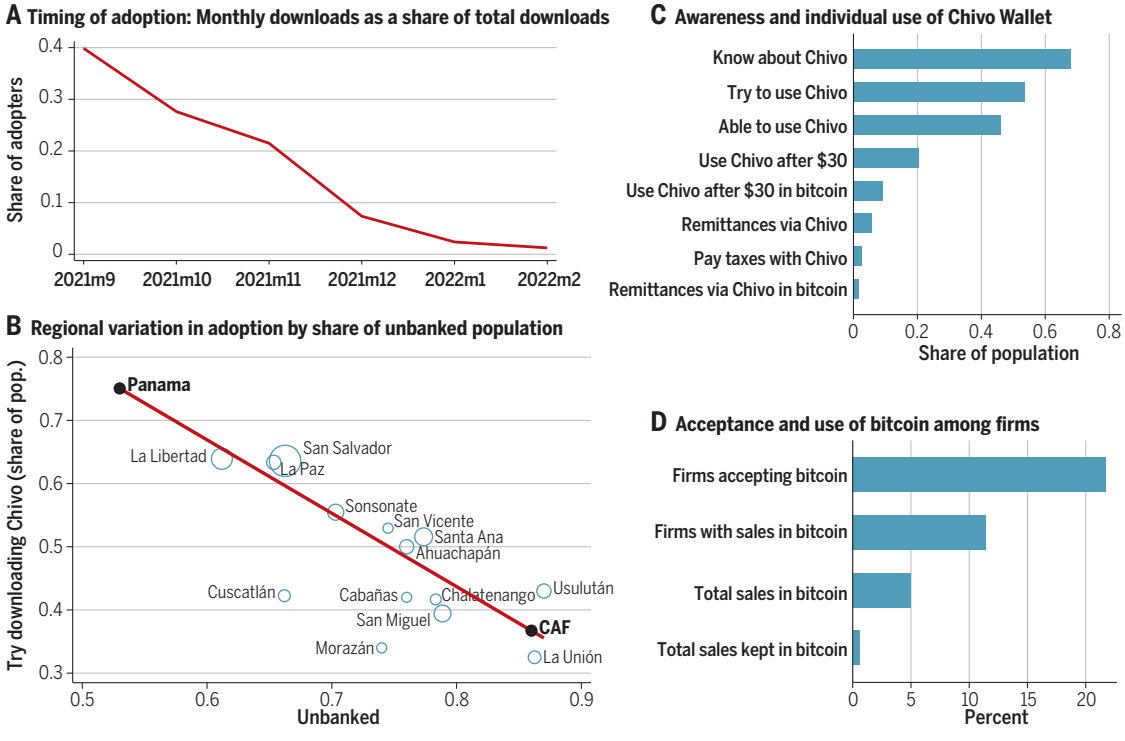

Adoption of Chivo Wallet in El Salvador. (**A**) Dynamics of Chivo Wallet downloads and (**B**) regional variations in adoption across El Salvadoran regions by shares of unbanked. (**C** and **D**) Summary of the survey's results on adoption by individuals and firms, respectively.

RESEARCH ARTICLE

BITCOIN

Are cryptocurrencies currencies? Bitcoin as legal tender in El Salvador

Fernando Alvarez[1]*, David Argente[2]*, Diana Van Patten[2]*

A currency's essential feature is to be a medium of exchange. This study explores the potential of cryptocurrencies to be used in daily transactions in El Salvador, the first country to make bitcoin legal tender. The government's "big push" introduced "Chivo Wallet," a digital wallet sharing features with Central Bank Digital Currencies (CBDCs), with perks to use it for trading bitcoins and US dollars. Through a nationally representative, face-to-face survey of 1800 households and blockchain data encompassing all Chivo Wallet transactions, we document a pattern of low and decreasing usage of digital payments and bitcoin. Privacy and security concerns are key adoption barriers, which speaks to a policy debate on crypto and CBDCs with anonymity at its core. Additionally, we estimate Chivo Wallet's adoption cost and complementarities among adopters.

In its first form money is simply any commodity … which any person will readily receive, and which, therefore, every person desires to have by him in greater or less quantity, in order that he may have the means of procuring necessaries of life at any time.
– William Stanley Jevons

The introduction of digital currencies in general, and of cryptocurrencies in particular, is perhaps the most important development in monetary economics in the past decade. Cryptocurrencies such as bitcoin differ markedly from traditional banks. Bitcoin relies on cryptography for security and operates on a decentralized network with verifiable transactions, contrasting with centralized banks governed by regulations. For the unbanked and those reliant on remittances, bitcoin presents a potential solution by enabling financial transactions, bridging the gap left by traditional banking systems. However, a currency's key and defining role is to serve as a medium of exchange (*1*, *2*), and cryptocurrencies have yet to be widely adopted for this purpose (*3*).

This study leverages a unique quasinatural experiment that can shed light on the reasons behind bitcoin's lack of adoption. On 7 September 2021, El Salvador became the first country to make bitcoin legal tender through the "Bitcoin Law." A legal tender refers to a form of payment that is recognized by law as valid for settling financial obligations within a particular jurisdiction. According to the Bitcoin Law, not only must bitcoin be accepted as a means of payment for taxes and outstanding debts, but also all businesses are required to accept bitcoin as a medium of exchange for all transactions (*4*). The Salvadoran government also launched an app called "Chivo Wallet," a custodial wallet app that allows users to digitally trade both bitcoins and US dollars (USD) without paying any transaction fees. The government also provided major adoption incentives, such as a large bonus for downloaders that could potentially solve the coordination failure, and also subsidized fees. Moreover, the COVID-19 pandemic provided an additional incentive to adopt touchless payment methods. If bitcoin has a chance to be used in transactions as a medium of exchange, then this setting gave the cryptocurrency a prime opportunity.

Furthermore, central banks are considering alternatives to enter the era of digital payments. Nine of 10 central banks are exploring central bank digital currencies (CBDCs), and more than half are developing them or running concrete experiments (*5*). A retail CBDC, a digital currency backed by a central bank with legal tender status, shares many features with a fast payment system such as Chivo Wallet. Moreover, because Chivo Wallet allows for payments both in bitcoins and in USD, an analysis of its implementation is informative to the debate surrounding CBDCs, and a comparison between bitcoin and USD usage within the app is informative about the use of crypto in particular.

Situating the current study and key contributions

Unique monetary episodes can provide valuable insights into the workings of the economy and inform future policy-making. Sargent's seminal work on hyperinflations is a prime example of this research tradition (*6*). Our study of the Salvadorean experience follows in this tradition by studying an unprecedented monetary experiment in which bitcoin became legal tender and digital currency started being traded through Chivo Wallet. Our examination shows that the designation of bitcoin as legal tender does not imply that it becomes a general medium of exchange as defined by previous work, i.e., an object "which is habitually, and without hesitation, taken by anybody in exchange for any commodity" (*7*). Important references in the literature argue that "acceptability" makes an object more likely to become a medium of exchange and can be influenced by government policies (*2*, *8*, *9*), and that the state can give a currency value by allowing the public to use it to pay taxes (*1*, *10*–*13*). We contribute to this long-standing work by documenting that accepting a digital currency to pay for taxes is not a sufficient condition for it to become widely accepted.

Our work also contributes to the study of cryptocurrencies. Empirically, the literature has focused on the risks faced by individuals (*14*, *15*), arbitrage opportunities and price manipulation (*16*, *17*), bitcoin network participants (*18*, *19*), bitcoin's price fluctuations (*3*, *62*), the determinants of asset pricing (*20*), and developing the notion that bitcoin seems to function more like a speculative investment than a bona fide currency (*3*). Our results provide insights on the characteristics of adopters and the bottlenecks of adoption in a setting where incentives to adopt are high, fees are subsidized, and we have measurable variation in determinants such as income and financial literacy. This study is also related to the growing theoretical literature on cryptocurrencies, which has built models stressing the network effects of its adoption (*18*, *21*, *22*) and the cost of its production (*23*, *24*). Complementary to these studies, our work quantifies the fixed costs of adoption along with the network effects.

Further, through the study of Chivo Wallet payments in USD, we address the literature on CBDCs, in which empirical evidence is scarce (*25*) (*26*). As in the case of Chivo Wallet, recent policy briefs argue that CBDCs should not be bearer instruments (*27*). This is the case, for instance, for China's CBDC (*28*), and is also the case of Chivo Wallet. Moreover, whereas Chivo Wallet is not backed by a central bank, it is backed by the government and is not required to be linked to a bank account, just as would be the case with a CBDC. Our work highlights several challenges to the implementation of CBDCs, such as the role of privacy and transparency concerns, while suggesting there is a role for policies that incentivize adoption given the presence of strong complementarities among adopters. More broadly, our study relates to work on the adoption of payment methods beyond cash (*29*–*32*).

[1]Kenneth C. Griffin Department of Economics, University of Chicago, Chicago, IL 60637, USA. [2]School of Management, Yale University, New Haven, CT 06511, USA.
*Corresponding author. Email: f-alvarez1@uchicago.edu (F.A.); david.argente@yale.edu (D.A.); diana.vanpatten@yale.edu (D.V.P.)

Research questions

RQ 1: Were Chivo Wallet and bitcoin actually adopted after the government's "big push"?
RQ 2: What factors deterred the adoption of Chivo Wallet and bitcoin by individuals?
RQ 3: What other broader lessons can be drawn from this experiment?
RQ 4: What were the drivers of adoption by firms?
RQ 5: What insights can be obtained from blockchain data?

Methods

The context

El Salvador has been the stage for several monetary experiments. In 2001, the USD became legal tender and the country's only official currency (*33*). Later, on 7 September 2021, El Salvador became the first country to make bitcoin legal tender through the Bitcoin Law. Although there might be many reasons behind the decision, when the policy was announced, the president stated that it would generate jobs, provide financial inclusion, and facilitate sending remittances (*34*). In addition, bitcoin was seen as a mechanism to introduce people into financial services. For context, only one-third of the Salvadorian adult population had a bank account at a financial institution in 2017 (*35*). Moreover, our survey's background questions show that in El Salvador, most transactions are paid in cash; in fact, >50% of people only use cash, >70% of adults are unbanked, and almost 90% of them do not use mobile banking, as reported in fig. S7 (*36*). We found that 64.6% of Salvadorans have access to a mobile phone with internet, a prerequisite to adopt Chivo Wallet (*37*).

The Bitcoin Law

The first article of the Bitcoin Law describes its main objective and endows bitcoin with a legal tender status (*38*). It also makes bitcoin a unit of account within the country and, according to the theory of chartalism, endows it with value by accepting it as a means of payment for tax purposes. The Bitcoin Law also goes beyond the usual provisions of a legal tender, making bitcoin a medium of exchange of mandatory acceptance nationwide. Article 7 reads: "Every economic agent must accept bitcoin as payment when offered to him by whoever acquires a good or service." Another relevant article of the law is related to how bitcoin usage will be implemented in the country. In particular, Article 8 mandates the government to provide the means to conduct transactions using bitcoin. How was the adoption of bitcoin facilitated and promoted by the state? The government's answer was "Chivo Wallet" (*39*).

The Chivo Wallet app

Just as bitcoin became legal tender, the government launched Chivo Wallet and an educational campaign on how to use it. This digital wallet allows users to convert bitcoins into USD and vice versa without a fee and to send or receive either currency (*40*). As shown in fig. S4, payments are made through the application by entering the recipient's identification number or phone number and the payment amount (*41*). The app can also be used to pay at local establishments, is compatible with other bitcoin on-chain and Lightning wallets, and connects with El Salvador's banking system to deposit or withdraw USD from a bank account (*42*). Chivo Wallet can be used by registered Salvadorans even if they reside abroad to facilitate sending remittances potentially faster and at a lower cost than alternative services. Chivo Wallet also has a version intended for firms, which allows them to charge their clients and pay taxes. It does not provide users with the key to their bitcoin, which makes it a "custodial" wallet in which transactions are not anonymous; users are required to enter their personal information after downloading the app, just as in the case of several CBDCs (*27*, *28*).

Adoption incentives

Usage of bitcoin in El Salvador is related to Chivo Wallet's adoption, and as an adoption incentive, citizens who downloaded the app could receive a $30 bitcoin bonus from the government, which is a substantial amount in this Central American country with a GDP per capita of $4131 (*43*). These $30 bonuses were automatically deposited in their wallets; however, the money could not be withdrawn as cash before first being transferred to another Chivo Wallet because the bonus was intended to promote bitcoin usage. As another government incentive, users could get a significant discount on gasoline if they paid using Chivo Wallet (*44*). Moreover, transactions in bitcoin usually involve substantial fees. For instance, bitcoin ATM fees can range from 5% to over 20%, with an average of about 8.5%, and transactions in bitcoin reached a fee of >$60 USD per transaction in April 2021 and an average value of $1.8 USD in February 2022. Transactions in bitcoin and conversions from bitcoins to USD using Chivo Wallet and cash withdrawals at Chivo Wallet ATMs do not incur any fees. This can be interpreted as an additional government subsidy. In El Salvador, payments of public salaries and pensions remain in USD. Allowing for these payments to be in bitcoins could have provided another adoption incentive (*45*).

Bitcoin in other countries

The lack of access to banking services and infrastructure increases the potential of digital payments to promote financial inclusion. Consistent with this, most of the top 20 countries in the 2021 Global Crypto Adoption Index are emerging economies. The Central African Republic (CAF) was the second country, after El Salvador, to make bitcoin legal tender in April 2022, the same month in which Panama approved its own Crypto Law (*46*). High-income countries have not been absent from the crypto stage. For instance, an Arizona senator proposed a bill to make bitcoin legal tender in that state in January 2022 (*47*).

Measures

In the midst of a growing interest to promote digital currencies among monetary authorities, El Salvador offers a rare opportunity to learn about the potential of cryptocurrencies to become a widely used payment method. However, access to data poses a challenge because El Salvador's government reveals only selected information (*48*). To overcome this challenge, we conducted surveys to generate data that would be otherwise unobtainable. This allowed us to measure the adoption of respondents based on their characteristics, focusing not only on downloads but also on usage.

The survey was face-to-face, nationally representative, and spanned 1800 households during February 2022 (*49*), leading to results with a 95% confidence interval and a 1.94% margin of error. Respondents were all >18 years old, as this is a prerequisite to be eligible to use Chivo Wallet. The national survey was conducted in partnership with CID-Gallup (*50*). Interviewers were trained a week in advance to conduct the survey, and we implemented a pilot interviewing 50 people to ensure that survey questions were clear. Our sample validation can be found in table S2; the sample almost exactly matches total population shares in terms of gender, age, districts, and education levels.

The sample is also representative in terms of bank account ownership (*51*). The national-scale and face-to-face nature of the survey posed a challenge compared with an internet or phone survey. However, both features are important in our setting. First, understanding adoption patterns requires a sample that includes small cities and rural areas; focusing on main population centers may bias results. Second, because bitcoin's adoption through Chivo Wallet requires access to both a cell phone and an internet connection, a survey by phone or internet, which relies on respondents having access to either communication method would mechanically underestimate adoption costs. Finally, the face-to-face format of our survey preserves data quality while allowing us to conduct a longer survey with more detailed questions than would be feasible through the phone or internet (*52*). The survey measures sociodemographic variables, knowledge about Chivo Wallet, downloads of the app, and usage both in bitcoins

and USD. We include details on the specific questions in the supplementary materials, section D.

We complement our survey results with an analysis using all transactions identified as involving Chivo Wallet, leveraging data from the blockchain, a distributed public ledger. We not only studied overall volumes transacted through Chivo Wallet, but separately analyzed the patterns of deposits and withdrawals, and identified consistencies between the survey outcomes and the blockchain results.

Results

RQ 1: Were Chivo Wallet and bitcoin actually adopted after the government's "big push"?

Awareness

We found that 68% of potential users knew about the app's existence. Most of those who were aware of the app learned about it through social media, followed by television and radio, news, and friends and family, as summarized by fig. S8. Almost 78% of those who were aware of the app had tried to download it. Most downloads happened just as Chivo Wallet was launched. Figure 1A shows that 40% of all downloads occurred in September 2021 and there were virtually no downloads in 2022. The latter suggests that our survey was already capturing the most relevant share of adopters of this digital wallet.

In terms of heterogeneity, we found that banked, educated, and young men were more likely to know about Chivo Wallet (table S3), as were people who owned a cell phone with internet. Moreover, conditional on knowing about Chivo Wallet, these characteristics also make a person more likely to try to adopt it, as documented in Table 1 (*53*). People with these demographics also tended to download the app on their own without help (table S4). These findings suggest that the introduction of Chivo Wallet mainly provided an additional means of payment among those already banked instead of stimulating more financial inclusion among the unbanked.

Not all users agreed with the widespread use of Chivo Wallet. Individuals who agreed tended to own a mobile phone with internet, and were younger and male. Columns 1 to 3 in table S5 show that people who agreed with the use of Chivo Wallet were 0.3 percentage points more likely to download the app, and columns 4 to 6 show that individuals who were less likely to agree also tended to be those who needed help installing the app.

Reasons to download Chivo Wallet

The key incentive for downloading the app was the $30 bonus, which is equivalent to 0.7% of annual income per capita. Other reasons deemed as the most important were the contactless nature of the payment method in the midst of the pandemic and the potential to receive remittances; fig. S11 summarizes all reasons regarded as most important.

Chivo Wallet usage by households

Most respondents spent their $30 bonus to pay for expenses in bitcoins, and almost 20% of those who downloaded the app had not yet used their bonus (*54*). However, most users did not keep using Chivo Wallet after spending their bonus. Table 2 presents descriptive statistics on Chivo Wallet's usage among those who downloaded it and who reported using the app after spending the bonus. A salient feature of people who downloaded Chivo Wallet and kept using it after spending their bonus is that they were more likely to be young, educated, male, banked, and much more likely (26%) to be using other digital wallets in addition to Chivo Wallet to conduct transfers (*55*). Distance to a Chivo Wallet ATM and facing issues with the app, however, were not good predictors of whether the user remained active, suggesting that these were not the binding barriers to sustain usage (*56*).

More than half of these "active users" had not made a cash withdrawal from a Chivo Wallet ATM, although the mean number of withdrawals was 2.59, given the presence of extreme values in the right tail (*57*). The number of payments and transfers received or sent was also largely driven by very active users in the right tail. Deposits in USD is the only statistic in which users in the 25th percentile have a nonzero value. We can conclude that active Chivo Wallet users transact in USD more than bitcoins, because the average amount of payments and transfers, sent or received, was consistently larger in USD.

Regional variation

Figure 1B shows important regional variation in the probability of downloading Chivo Wallet depending on the share of unbanked population in each department. It also benchmarks the CAF, the second country to make bitcoin legal tender, and Panama, which enacted a crypto law in April 2022, with respect to departments in El Salvador given our estimates and their share of unbanked. Figures S18 and S19 also show regional differences in adoption and

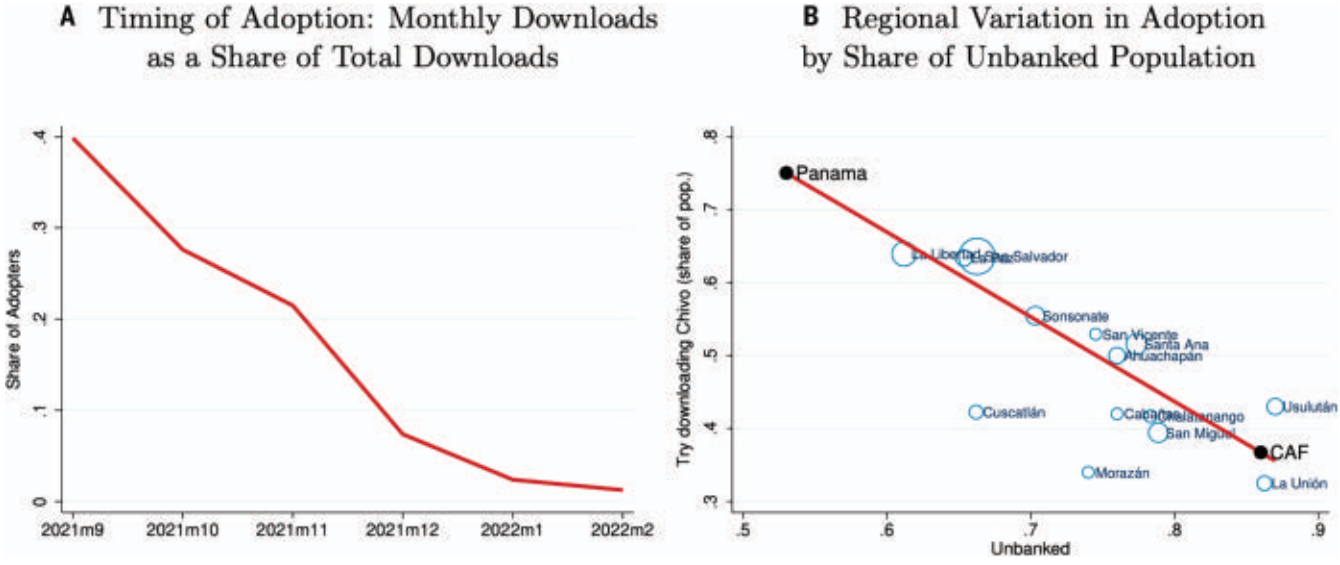

Fig. 1. Chivo Wallet's adoption. (**A**) Timing of adoption: Monthly downloads. (**B**) Regional variation in adoption as a share of total downloads by share of unbanked population. (A) shows the month in which each user in our sample downloaded Chivo Wallet as a share of total downloads. (B) shows the relationship between the share of people who have tried to use Chivo Wallet and the fraction of people who do not have access to a bank account in El Salvador, by department. (B) also includes, for comparison, the shares of unbanked in Panama and the CAF.

Table 1. Adoption of Chivo Wallet. The dependent variable was "have you tried to download Chivo Wallet?"

	(1)	(2)	(3)	(4)
Cell phone with internet	0.1085***			0.0757**
	(0.036)			(0.035)
Unbanked		−0.1132***		−0.0815***
		(0.023)		(0.026)
Years of schooling				
Middle school			0.0849***	0.0676**
			(0.023)	(0.024)
High school+			0.1168***	0.0832**
			(0.029)	(0.036)
Age				
Age 25 to 34			−0.0236	−0.0241*
			(0.014)	(0.013)
Age 35 to 44			−0.0480	−0.0473
			(0.032)	(0.032)
Age 45 to 54			−0.0969*	−0.0888*
			(0.045)	(0.041)
Age 55+			−0.1349***	−0.1238***
			(0.029)	(0.028)
Gender				
Female			−0.0292	−0.0089
			(0.021)	(0.020)
Single			−0.0567**	−0.0528**
			(0.023)	(0.023)
Observations	1224	1224	1224	1224
R^2	0.023	0.019	0.041	0.055
Department	Yes	Yes	Yes	Yes

The sample only includes respondents who knew about the existence of Chivo Wallet. Results in this table rely on a linear probability model. Results are robust to other specifications, in particular, columns (1) and (3) of table S12 show the marginal effects under a logit model. The regression includes department fixed effects, and each of the controls is obtained from survey questions on whether a person owns a financial instrument (unbanked), years of schooling, age, gender, and marital status. Standard errors are clustered by department.

awareness about Chivo Wallet depending both on the average income and the share of unbanked per "department," with departments being similar to counties. Regions with higher levels of development tended to be more active using Chivo Wallet. The share of users who continued using the application after spending the $30 USD bonus in departments such as San Salvador and La Libertad, which have the highest income per capita in the country, was twice as large as in departments with low income per capita, such as Usulután and Chalatenango (*58*). Similarly, departments with a larger share of unbanked population had as little as half the adoption levels as departments in which most of the population had access to banking services.

Along similar lines, assuming that the implementation of a digital wallet is similar in other contexts, our estimates allow us to explore how other features of adoption would manifest in other countries, which could prove valuable to policy makers. Given our estimates, in the CAF, only 37 to 45% of the population would have been aware of the app's existence, 8 to 14% would continue using the app given similar adoption incentives as in El Salvador, and <2% would use the app for remittances. In the case of Panama, income per capita is higher than in El Salvador, as is access to banking services. We estimate that >95% of the adult population in Panama would be aware of the technology, between 30 and 56% would continue using it after spending the adoption incentives, and 10 to 30% would use it for remittances. The last two estimates are cut in half when considering payments in bitcoins in either country.

Role of taxes and remittances

By law, bitcoin can be used to pay taxes. Chartalism implies that endowing a currency with the power to pay taxes gives it value as a means of exchange. However, only 5% of Salvadorans have paid taxes using Chivo Wallet. Moreover, in El Salvador, some households receive >60% of their income from remittances, as summarized in fig. S15. Chivo Wallet is not widely used to receive remittances from abroad; only 3% (8%) of people have received remittances in bitcoins (USD) using the app. This finding aligns with reports from the Central Reserve Bank of El Salvador, which found that only 1.45% of remittances were received through digital wallets in March 2022, and provides external validation to our survey (*59*).

RQ 2: What factors deterred the adoption of Chivo Wallet and bitcoin by individuals?

Chivo Wallet adoption deterrents

More than 21% of respondents knew about Chivo Wallet but did not try to download it. The reasons not to download it are summarized in fig. S13A. The most important reason was that users preferred to use cash. The second most relevant reason not to download Chivo Wallet were trust issues: Respondents did not trust the system or bitcoin itself (*60*). Privacy and security are at the heart of the debate around CBDCs and bitcoin. Concerns regarding lack of anonymity and secure transactions could then explain, at least partially, the main two reasons not to download the app, because cash is an anonymous payment method (*61*). The next most frequent reason mentioned was not owning a phone with internet, followed by the technology being complicated. In sixth place, Salvadorans mentioned technical difficulties using the app; fig. S14 summarizes the main reported problems.

Bitcoin adoption deterrents

Figure S13B reports the main reasons why individuals do not use bitcoin. For >50% of respondents, the main reason not to use bitcoin was that they did not understand it nor trust it. Although the volatility of bitcoin has potential as a deterrent (*62*), trust and transparency seem to be more salient than uncertainty, because bitcoin's volatility was mentioned by <10% of respondents. If volatility were the main deterrent from using Chivo Wallet, then we should then see people downloading the app and transacting in USD, which are very stable; however, this was not the case, as explained in the previous paragraph.

Taking stock

Figure 2A summarizes results from our first two research questions. We documented that more than two-thirds of Salvadorans were aware that Chivo Wallet exists. However, not all of those who knew about the app have tried to download it; just over half of all respondents did so. The main reason not to download Chivo Wallet was that individuals prefer to pay in cash, followed by mistrust; these motifs may be related to privacy concerns. The main reason that they downloaded the app was to use the $30 bonus offered by the government, but less than half of those who were able to download Chivo Wallet, 20% of adult citizens, continued to use it after spending the bonus and they mostly used it to transact in USD, not in bitcoins.

Table 2. Descriptive statistics: Active Chivo Wallet users.

	(1) Mean	(2) SD	(3) 10th	(4) 25th	(5) Median	(6) 75th	(7) 90th
ATM withdrawals	2.5	8.7	0	0	0	2	4
Average amount of ATM withdrawals (in USD)	54.9	65.6	10	20	30	60	120
Payments/transfers sent in bitcoins	2.3	7.8	0	0	0	2	5
Payments/transfers sent in USD	9.2	24.8	0	0	1	5	20
Average amount of payments/transfers sent in bitcoin (in USD)	32.5	38.2	3	10	20	42.5	80
Average amount of payments/transfers sent in dollars (in USD)	39.6	47.1	7	12	20	50	100
Payments/transfers received in bitcoins	2.1	7	0	0	0	1	4
Payments/transfers received in USD	6.2	18	0	0	0	2	15
Average amount of payments/transfers received in bitcoin (in USD)	51.3	77	2	10	25	55	100
Average amount of payments/transfers received in dollars (in USD)	55.3	78.9	5	15	30	70	120
Deposits in bitcoins	1.31	3.9	0	0	0	1	2.5
Deposits in USD	4.4	13.8	0	0	1	2	10

The table shows distribution of responses to the questions: (i) How many times per month do you withdraw money from Chivo Wallet ATMs?; (ii) What is the average amount of your ATM withdrawals?; (iii) How many payments or transfers do you perform per month using Chivo Wallet in bitcoins or in USD?; (iv) What is the average amount of your payments or transfers in bitcoins or in USD?; (v) How many payments or transfers did you receive per month using Chivo Wallet in bitcoins or in USD?; (vi) What is the average amount of your payments or transfers you received in bitcoins or in USD?; and (vii) How many times have you deposited money to your Chivo Wallet in bitcoins or in USD? We divided the number of deposits by the months a person was active in Chivo Wallet to convert them to a monthly variable and rounded the values to the closest integer. The sample includes those who kept using Chivo Wallet after spending their $30 bonus (20.6% of respondents). We dropped observations above the 99th percentile to avoid extreme outliers.

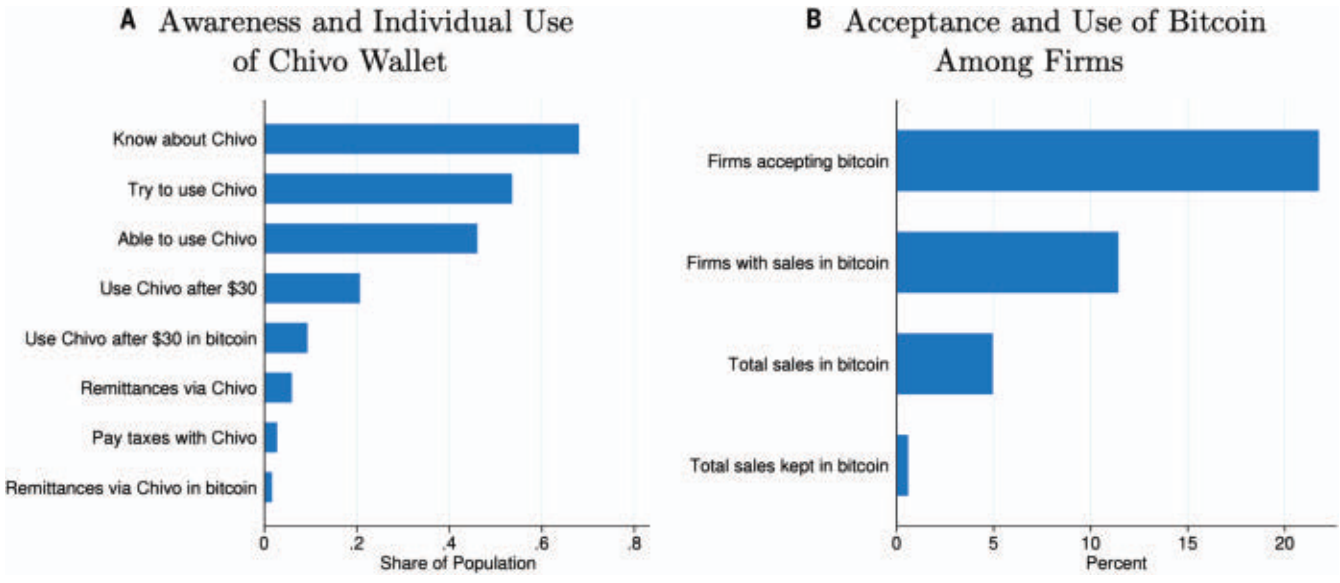

Fig. 2. Taking stock. (**A**) Awareness and individual use. (**B**) Acceptance and use of bitcoin with Chivo Wallet among firms. (A) shows shares with respect to the entire sample, so it is subject to a 1.94% margin of error. In (B), the top two bars show percentages with respect to all surveyed owners and employees who knew about payment methods at the firm. The bottom two bars show percentages with respect to total sales.

Moreover, most individuals who used Chivo Wallet after spending the bonus did not engage with the app intensively; the median user reported no ATM withdrawals and no payments, sent or received, in bitcoin in a given month. To put this in perspective, the median number of daily transactions per person across means of payments was between 1.3 and 1.4 in several countries (*63*), and Chivo Wallet's developer indicates that there are 0.001 to 0.003 daily transactions per adult (*64*). Further, we did not find evidence of Chivo Wallet being used to pay for taxes or to send remittances at a substantial scale. Figure S20 replicates Fig. 2A for the share of the banked and unbanked population, respectively.

Overall, we have documented that bitcoin is not being widely used as a medium of exchange and that Chivo Wallet's usage is low in El Salvador. The latter stands despite the "big push" exerted by the government, which involved endowing bitcoin with legal tender status through the Bitcoin Law, the $30 bonus, gas discounts, and no fees, and despite the pandemic's incentive to use touchless payment methods.

RQ 3: What other broader lessons can be drawn from this experiment?

Complementarities

For some technologies, the benefit of adopting increases as more people adopt (*65*). Arguably, such complementarities, also called network externalities, are an inherent feature of digital payment methods and give a potential role for policy to improve allocations (*66*). Thus, we can draw broad lessons applicable to other payment technologies from the analysis of Chivo Wallet. We found evidence of complementarities, both in the decision to adopt the app and on how intensively people used it, as reported in the supplementary materials, section C.

Adoption and variable costs

We leveraged the familiarity with the $30 introductory bonus and asked two questions to estimate the distribution of (self-reported)

adoption costs. The first question was: "How large does the bonus need to be to convince you to download Chivo Wallet?," which was directed to people who had not downloaded the app, but knew about it (14.5% of respondents). The second question was: "What is the minimum bonus that would have convinced you to download Chivo Wallet?," which was directed to people who had downloaded the app (53.5% of respondents). Table S7 displays our results. Although the mean reported value was $30, the median user would have accepted $20 USD, and there were people in the 10th percentile who would have adopted it even without a bonus. The adoption cost was larger for individuals with certain demographics: Unbanked respondents reported $6.9 USD higher cost than those who were banked, people without a cellphone with internet reported a $8.6 USD higher cost than those with one, it was $2.9 USD costlier for households with only elementary education to adopt compared with those with education beyond elementary, and finally, women reported a $8.9 USD higher cost than men.

Chivo Wallet allows users to withdraw cash from Chivo Wallet ATMs and convert bitcoin into USD without a fee. However, outside of Chivo Wallet, most providers charge significant fees. Table S8 shows the maximum reported willingness to pay to withdraw $100 USD at a Chivo Wallet ATM was $3.3 USD on average. This amount is less than half of the mean fee to purchase cash at bitcoin ATMs outside of El Salvador. Moreover, the median respondent was willing to pay only $1 USD. These findings suggest that Chivo Wallet users would not engage in cash withdrawals if they faced nonsubsidized fees. Table S8 also reports that the average willingness to pay to convert bitcoins into USD was $2.9 USD, and the median user would be willing to pay only $0.05 USD. These amounts are much smaller than any transaction cost of exchanges, indicating that Chivo Wallet would not be used in the absence of the subsidies.

Impact on usage of other payment methods

If users adopt Chivo Wallet, then they might substitute it for other payment methods such as cash and cards. We found some evidence consistent with this substitution. We documented that 10% of users who downloaded Chivo Wallet decreased their use of cash and 11% reduced their use of debit cards (*67*). The government also offered a discount of ~8% per gallon for gas purchases with Chivo Wallet, which allowed us to measure the elasticity of substitution, which measures how easily people switch between Chivo Wallet and other payment methods, as detailed in the supplementary materials, section C. Although the sample size is small, the estimated elasticities of substitution are positive and large, which suggests that the welfare costs of policies disincentivizing other payment methods (such as cash) are lower if digital payments are available.

RQ 4: What were the drivers of adoption by firms?

The Bitcoin Law states that all economic agents must accept bitcoin, but this does not necessarily translate into all firms effectively doing so (*68*). To study the extent to which firms accepted bitcoin, we relied on a subset of respondents who identified themselves as owners of firms or as employees who knew about the payment methods accepted by their employer, who then answered a series of questions about their business. Results are summarized in Fig. 2B.

First, we documented that whereas almost all firms accepted cash, slightly over 20% accepted bitcoin (*69*). Among those that did accept bitcoin, 75% started accepting it just as the law was enacted. Only 11.4% of firms had positive sales in bitcoin. This estimate aligns with results from two independent surveys targeting firms of all sizes and across sectors (*70*). Further, our survey indicates that 81% of firms accepting bitcoin have not seen a change in their sales since starting to accept it, and whereas the median firm made no sales in bitcoin, 4.9% of all sales were paid in bitcoin through Chivo Wallet, mainly to large firms. These estimates align with those by two independent local surveys (*71*).

Second, we documented that firms accepting bitcoin were mostly large and in the fifth quintile of the firm size distribution (*72*). These large firms were also more likely to accept cards. Third, most firms reporting sales in bitcoin converted them into USD: 71% converted sales into USD and then withdrew them as cash, 17% converted sales into USD and kept them in Chivo Wallet, and only 12% of firms stored their sales in bitcoin within Chivo Wallet. Finally, we found that 11% of firms have increased prices since bitcoin became legal tender, which is consistent with the hypothesis that firms might be transferring costs related to the cryptocurrency (e.g., volatility) to customers (*73*).

RQ 5: What insights can be obtained from blockchain data?

So far, our conclusions discussed have been drawn from the survey data that we collected. This section leverages that all bitcoin transactions are recorded on the blockchain, a distributed public ledger, to analyze Chivo Wallet's activity based on actual transaction data. This exercise allowed us to validate and better understand our survey results. The analysis using transaction-level data for all of Chivo Wallet's transactions on the blockchain also provides new insights into how bitcoin transactions are carried out in El Salvador and by whom. Data sources are detailed in the supplementary materials, section E.

It is important to understand which Chivo Wallet transactions would surface in the blockchain and which ones would not. As of today, verifying a bitcoin transaction on the blockchain is both costly and takes several hours (*74*). Given this constraint, many wallets that use bitcoin for relatively small payments do not verify all transactions on the blockchain. Instead, they are custodial wallets and rely on a clearing house. Chivo Wallet is no exception; therefore, transactions from one Chivo Wallet to another one, in general, would not register on the blockchain. Transactions between different addresses owned by Chivo Wallet as an entity do appear on the blockchain, and we label them as internal transactions (*75*). Transactions from Chivo Wallet to external crypto wallets also surface in the public ledger. These would include, for example, payments from tourists visiting El Salvador and paying in bitcoin from their foreign wallets.

According to our data, as of 3 November 2022, Chivo Wallet was associated with 142,148 addresses, which were involved in 425,514 transactions and a total of 3,424 bitcoins deposited into Chivo Wallet. These are all the transactions that can be identified as involving Chivo Wallet either as a buyer or a seller of bitcoin. Figure 3 summarizes some of the observed dynamics. As shown in Fig. 3A, the total transactions in bitcoins, expressed in USD, reached their peak between October and December 2021 and decreased significantly thereafter. The latter is consistent with the results of our survey, which document high activity within the first months of Chivo Wallet's operation and a sharp decrease thereafter.

Figure 3A shows all activity, whereas Fig. 3B considers only external transactions and decomposes them as total deposits into and withdrawals from Chivo Wallet (*76*). First, the co-movement between both types of external transactions was substantial. Second, an analysis of the average size of each type of transaction, reported in fig. S24, shows that deposits were composed by many small and relatively frequent transactions; for example, these could be transactions from tourists visiting El Salvador to use bitcoin or residents from El Salvador who had bitcoin in other wallets (*77*). Their active behavior resembles the one by the right tail of Chivo Wallet users who were extremely active, as documented in table S6. The magnitude of inflows of bitcoin in the survey and on the blockchain data also align. According to our survey, between $221,000 and $334,000 USD flowed into Chivo Wallet per day, whereas according to blockchain data, this amount was ~$245,000 USD per day (*78*). Third, a joint analysis of Fig. 3B and fig. S24 shows that withdrawals (i.e., sales of bitcoin by Chivo Wallet) tended to be large and happen rarely, and in synchrony, with the pace of accumulated deposits. This pattern suggests that withdrawals

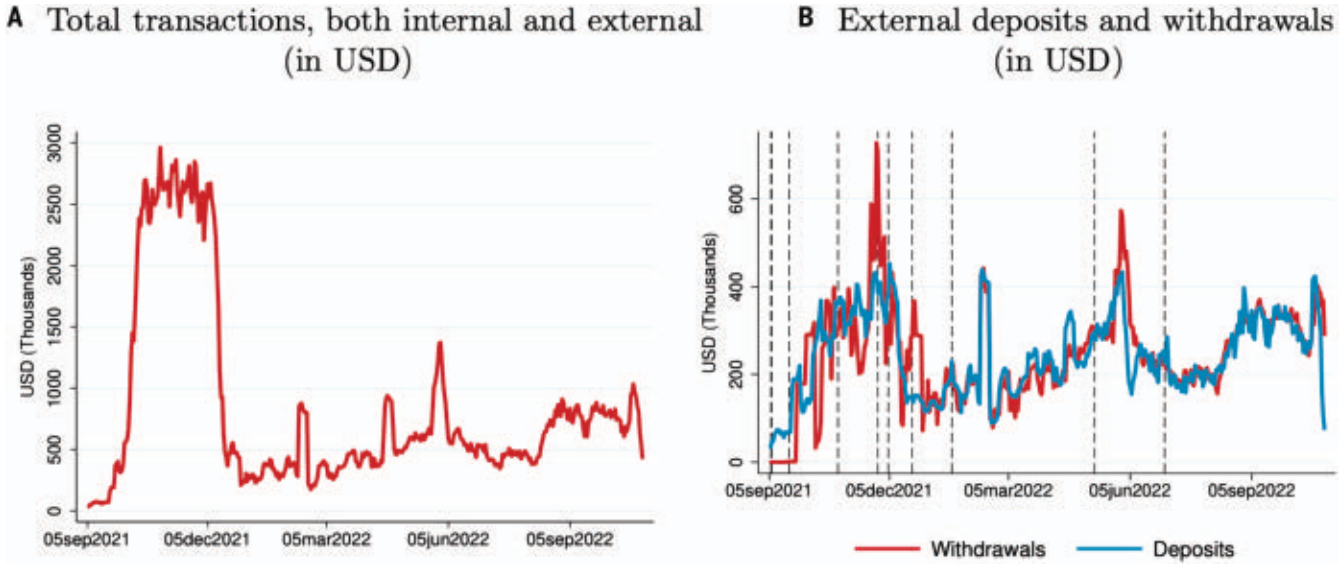

Fig. 3. Chivo Wallet's blockchain transactions. (**A**) Total transactions, both internal and external. (**B**) External deposits and withdrawals (in USD). (A) shows the total number of transactions in Chivo Wallet, including internal transactions and external withdrawals and deposits in USD. We converted bitcoin's value into USD because otherwise the patterns would also reflect bitcoin's price changes, which were substantial in this period. (B) shows the dynamics of external withdrawals and deposits. The vertical dashed lines date moments when El Salvador's government announced a bitcoin purchase.

occured as part of Chivo Wallet's bitcoin inventory management, such that Chivo Wallet accumulated balances of bitcoin to lower the transaction cost of selling them. This behavior is consistent with the almost zero net accumulation of bitcoin within the wallet shown in fig. S25. This behavior resembles the one displayed by firms in El Salvador, which tended to convert all of the bitcoin they received into USD almost immediately. Finally, the data verify that trading volumes in Chivo Wallet are uncorrelated with bitcoin prices; thus, Chivo Wallet trading volumes seem to be driven by idiosyncratic reasons rather than by bitcoin market prices; section E of the supplementary materials provides more details on this relationship.

Discussion

Following the tradition of studying unique monetary episodes to inform policymaking, our analysis of the Salvadorean experience with bitcoin as legal tender offers valuable insights into the complexities of the adoption of cryptocurrencies as a medium of exchange and the implementation of CBDCs. El Salvador's government provided a "big push" to incentivize the use of digital payments and bitcoin, including a large sign-up bonus and subsidized fees. Bitcoin is not only endowed with legal tender status, allowing the currency to be used to pay taxes and debts, but also must be accepted by any economic agent by law. Monetary theories such as chartalism suggest that these conditions should be sufficient for bitcoin to become a medium of exchange.

However, our results show that, despite all incentives and the enhanced attractiveness of contactless payments in the midst of the pandemic, bitcoin is being not widely used as a medium of exchange and usage of Chivo Wallet is low. Most downloads took place just as Chivo Wallet was launched. Since then, adoption and levels of remittances through Chivo Wallet have been decreasing over time. These results suggest that it is unlikely that usage of bitcoin and Chivo Wallet will increase. Our empirical results challenge the implications of chartalism.

Privacy and transparency concerns appear to be key barriers to adoption; unexpectedly, these are the two concerns that decentralized currencies such as crypto aim to address. Moreover, we document that this payment technology involves a large initial adoption cost, has benefits that significantly increase as more people use it (i.e., complementarities), and faces resistance from firms in terms of its adoption. Our findings lay out the challenges faced by digital payments and cryptocurrencies to become widely accepted, and are relevant for countries studying the viability of CBDCs and of crypto as a currency. Moreover, our survey work using a representative sample sheds light on how it is the already wealthy and banked who use crypto, which stands in stark contrast with recurrent hypotheses claiming that the use of crypto may help the poor and unbanked the most.

There is substantial heterogeneity across demographic groups in the likelihood of adopting and using bitcoin as a means of payment. The reasons that young, educated men are more likely to use bitcoin for transactions remain an open question. One hypothesis is that this group has higher financial literacy. We found that, even conditional on access to financial services and education, young men were still more likely to use bitcoin. However, financial literacy encompasses several other areas of knowledge that are not captured by these controls. An alternative hypothesis is that young, educated men have a higher propensity to adopt new technologies in general. The literature on payment methods has documented that young individuals have a greater propensity to adopt means of payment beyond cash, such as cards (*87*). Nevertheless, further research is necessary to causally identify the factors contributing to the observed heterogeneity across demographic groups. An analysis relying on all blockchain transaction-level data from Chivo Wallet allowed us to validate and better understand our survey results and is a unique opportunity to provide new insights on the dynamics of Chivo Wallet's activity. The latter is valuable because the app is a unique exchange in that it can also be used as means of payment by law.

Furthermore, the results carry policy implications for other countries. A study of this experience is informative in drawing broader lessons on the likelihood of success of CBDCs and cryptocurrencies in contexts outside of El Salvador. Assuming that the implementation of a digital wallet is similar in other contexts, our estimates allow us to explore what would be the adoption of the technology in other countries, which can prove valuable to policy makers. Two interesting cases are the CAF, which recently made bitcoin legal tender and has a stable local currency, as well as Panama, which also enacted a Crypto Law and where the USD is the official currency, as in El Salvador. El Salvador falls in between these

countries in terms of both income per capita and access to banking services (*79*). The introduction of a cryptocurrency could lead to outcomes different from the ones we documented in countries where the local currency is unstable and there are restrictions on capital mobility, such as Argentina and Turkey. Thus, an analysis of these contexts may offer fertile ground for future research to explore.

Overall, we conclude that despite bitcoin's legal tender status and the large incentives to promote Chivo Wallet, the cryptocurrency is not adopted at large by the population as a medium of exchange and digital payments are scarce and concentrated. These findings are informative about the intrinsic value of cryptocurrencies as means of payments, as viewed in the larger context of monetary models in economics and about the scope of CBDCs in developing countries.

REFERENCES AND NOTES

1. W. Jevons, *Money and the Mechanism of Exchange, The International Scientifie Series* (D. Appleton, 1875).
2. N. Kiyotaki, R. Wright, Acceptability, means of payment, and media of exchange. *Fed. Reserve Bank Minneap. Q. Rev.* **16**, 18 (1992). doi: 10.21034/qr.1632
3. D. Yermack, *Handbook of Digital Currency* (Elsevier, 2015), pp. 31–43. doi: 10.1016/B978-0-12-802117-0.00002-3
4. Although a means of payment is an object used to make purchases and settle debts, the concept of medium of exchange is broader; it is an object that is taken in exchange for something to then be exchanged for something else, without the "prerequisite" of an existing debt (*8*).
5. A. Kosse, I. Mattei, "Gaining momentum: Results of the 2021 BIS survey on central bank digital currencies" (Bank for International Settlements, 2022); https://www.bis.org/publ/bppdf/bispap125.htm.
6. T. J. Sargent, in: *Inflation: Causes and Effects*, R. E. Hall, Ed. (Univ. of Chicago Press, 1982), pp. 41–98.
7. K. Wicksell, "Money and credit," in *Lectures on Political Economy*, K. Wicksell, Ed. (Routledge, 1906).
8. N. Kiyotaki, R. Wright, On money as a medium of exchange. *J. Polit. Econ.* **97**, 927–954 (1989). doi: 10.1086/261634
9. S. R. Aiyagari, N. Wallace, Government transaction policy, the medium of exchange, and welfare. *J. Econ. Theory* **74**, 1–18 (1997). doi: 10.1006/jeth.1996.2250
10. A. Smith, *An Inquiry into the Nature and Causes of the Wealth of Nations* (McMaster University Archive for the History of Economic Thought, 1776).
11. E. Cannan, P. H. Wicksteed, The common sense of political economy, including a study of the human basis of economic law. *Econ. J. (Lond.)* **20**, 394 (1910). doi: 10.2307/2221031
12. R. M. Starr, The price of money in a pure exchange monetary economy with taxation. *Econometrica* **42**, 45 (1974). doi: 10.2307/1913684
13. For instance, Adam Smith describes that "A prince who should enact that a certain proportion of his taxes should be paid in paper money of a certain kind might thereby give a certain value to this paper money" (*10*).
14. D. Duffie, "Digital currencies and fast payment systems: Disruption is coming," paper presented at the Asian Monetary Policy Forum, 31 May 2019, Sentosa, Singapore.
15. N. Borri, Conditional tail-risk in cryptocurrency markets. *J. Empir. Finance* **50**, 1–19 (2019). doi: 10.1016/j.jempfin.2018.11.002
16. I. Makarov, A. Schoar, Trading and arbitrage in cryptocurrency markets. *J. Financ. Econ.* **135**, 293–319 (2020). doi: 10.1016/j.jfineco.2019.07.001
17. J. M. Griffin, A. Shams, Is bitcoin really untethered? *J. Finance* **75**, 1913–1964 (2020). doi: 10.1111/jofi.12903
18. L. W. Cong, Y. Li, N. Wang, Token-based platform finance. *J. Financ. Econ.* **144**, 972–991 (2022). doi: 10.1016/j.jfineco.2021.10.002
19. I. Makarov, A. Schoar, "Blockchain analysis of the bitcoin market" (Tech. Rep., National Bureau of Economic Research, 2021); http://dx.doi.org/10.2139/ssrn.3942181.
20. Y. Liu, A. Tsyvinski, Risks and returns of cryptocurrency. *Rev. Financ. Stud.* **34**, 2689–2727 (2020). doi: 10.1093/rfs/hhaa113
21. E. Pagnotta, A. Buraschi, "An equilibrium valuation of bitcoin and decentralized network assets" (Tech. Rep., Social Science Research Network Electronic Journal, 2018); http://dx.doi.org/10.2139/ssrn.3142022.
22. B. Biais, A. Menkveld, C. Casamatta, C. Bisi'ere, M. Bouvard, "Equilibrium bitcoin pricing" (Tech. Rep., Social Science Research Network Electronic Journal, 2019); http://dx.doi.org/10.2139/ssrn.3261063.
23. L. W. Cong, Z. He, J. Li, Decentralized mining in centralized pools. *Rev. Financ. Stud.* **34**, 1191–1235 (2021). doi: 10.1093/rfs/hhaa040
24. M. Sockin, W. Xiong, "A model of cryptocurrencies" (Working Paper 26816, National Bureau of Economic Research, 2020); https://www.nber.org/papers/w26816.
25. R. Auer *et al.*, Central bank digital currencies: Motives, economic implications, and the research frontier. *Annu. Rev. Econ.* **14**, 697–721 (2022). doi: 10.1146/annurev-economics-051420-020324
26. Detailed literature reviews on CBDCs can be found in (*80*) and (*25*).
27. D. Duffie, K. Mathieson, D. Pilav, "Central bank digital currency: Principles for technical implementation" (Tech. Rep., Social Science Research Network Electronic Journal, 2021); http://dx.doi.org/10.2139/ssrn.3837669.
28. D. Duffie, "Can China conquer crypto?" *Foreign Affairs*, 22 April 2022.
29. T. Suri, Mobile money. *Annu. Rev. Econ.* **9**, 497–520 (2017). doi: 10.1146/annurev-economics-063016-103638
30. R. Borzekowski, K. K. Elizabeth, A. Shaista, Consumers' use of debit cards: Patterns, preferences, and price response. *J. Money Credit Bank.* **40**, 149–172 (2008). doi: 10.1111/j.1538-4616.2008.00107.x
31. B. Yang, A. T. Ching, Dynamics of consumer adoption of financial innovation: The case of ATM cards. *Manage. Sci.* **60**, 903–922 (2014). doi: 10.1287/mnsc.2013.1792
32. The app that we studied differs in important aspects from other mobile payment technologies. First, it was launched and sponsored by the central government and allows for payments both in a cryptocurrency and in the local currency (USD); thus, it shares features with CBDCs. Second, the app was launched nationwide along with generous incentives to adopt and no fees, which allows us to provide statistics on the distribution of adoption costs while isolating the fees' impact. Our work also relates to recent work studying the degree of substitutability between payment methods (*81*–*84*). We quantified the degree of substitutability between mobile payments and other payment methods and found it to be larger than the substitutability between cash and cards.
33. The former currency is no longer circulated; therefore, prices, accounts, and transactions were converted into USD (*85*).
34. For instance, in terms of job generation, as a way to encourage investments from bitcoin entrepreneurs, the government offered permanent residency to anyone who spends three bitcoin in the country and explained that, since bitcoin is legal tender, foreigners would not have to pay capital gains tax in El Salvador on profits made if bitcoin's value goes up. Moreover, remittances make up 22% of El Salvador's GDP, and bitcoin could potentially be a channel to send these remittances while paying lower fees.
35. Consejo Nacional de Inclusión y Educación Financiera, "Politica nacional de inclusion financiera para El Salvador (PNIF-SLV)" (BCR, 2021); https://www.bcr.gob.sv/bcrsite/uploaded/content/category/387473516.pdf.
36. More details on financial inclusion in El Salvador are provided in table S1.
37. We collected data on access to a cell phone with internet ourselves, because information on cell phone and internet access was only available for each one separately in household surveys. Fig. S9 and Fig. 10 provide details on these measures separately and other demographics relying on survey data.
38. Article 1 reads: "The purpose of this law is to regulate bitcoin as unrestricted legal tender with liberating power, unlimited in any transaction, and to any title that public or private natural or legal persons require carrying out."
39. In El Salvador, "chivo" is a slang term meaning "cool."
40. El Salvador established a trust fund, which is known to have a limit of $150 million, to allow for the automatic conversion of bitcoin into USD without fees. Official details on the trust fund or Salvadoran bitcoin purchases have not been disclosed. Hitherto, the only sources of information have been the president's Twitter posts, which indicate that the country had acquired approximately ,800 bitcoin as of April 2022.
41. Users can withdraw USD from their wallet either by doing a transfer from their bank account or by withdrawing cash from a Chivo Wallet ATM without a fee. As of September 2021, there were 200 Chivo Wallet ATMs in El Salvador (see figs. S5 and S6), and 51 in the US. Similarly, users can load money into their wallets through an official website using a credit or debit card or with cash through Chivo Wallet ATMs. Although funds remain in Chivo Wallet, they represent a claim to either USD or bitcoins, which is not uncommon in payment platforms. In other words, both USD and bitcoins are a parallel digital asset with a fixed exchange rate. In Chivo Wallet, the price of bitcoin is adjusted in real time to its market price. For instance, a customer could pay a firm or another user the USD price of an item in bitcoins, and the app would use the real-time exchange rate to charge her.
42. The Lightning Network is a protocol that uses temporary payment channelsoperating off-chain. After a channel is closed, payments are validated on the blockchain.
43. World Bank, "GDP per capita (current US$)" (2020); https://data.worldbank.org/indicator/NY.GDP.PCAP.CD.
44. Major gas stations dropped the gallon price by $0.20 for customers who paid with Chivo Wallet between September and October, and another drop of $0.30 per gallon was announced in November.
45. For instance, during the 2001–2002 Argentinean crisis, several provinces introduced low- denomination bonds ("quasi money") and used them to pay wages and other inputs (*86*). It is worth noting that El Salvador is relatively small and is therefore a bitcoin price-taker; indeed, fig. S3 shows there were no large changes in the (global) price of bitcoin after the Bitcoin Law or Chivo Wallet's launching. Thus, the experiment speaks about whether bitcoin is used as a means of payment given the above-described incentives despite the fact that it has a given resale value.
46. Panama and CAF are benchmarked against regions in El Salvador in Fig. 1B.
47. Bill SB 1341 was introduced by state Sen. Wendy Rogers.
48. Most information comes from the president's Twitter account. We tried, unsuccessfully, to contact multiple government entities, including Chivo Wallet customer service, El Salvador's Superintendency of the Financial System, Central Bank, and Casa Presidencial, to receive more quantitative information.
49. In terms of the timing of the survey, information was collected across several weeks always including weekends; weekends were important in reaching a representative sample of profiles.
50. CID-Gallup has been conducting surveys in Latin America for >40 years. It has an office in El Salvador that periodically conducts large-scale surveys.
51. Total population shares match the General Directorate of Statistics and Censuses' 2021 projections.
52. Approximate survey length was 27 min. To obtain candid responses, respondents were guaranteed confidentiality and notified that the survey aimed to inform academic research.
53. Table 1 relies on a linear probability model. Results are robust to other specifications, in particular, columns (1) and (3) of table S12 show the marginal effects under a logit model.
54. According to Chivo Wallet's regulations, users must spend their bonus in bitcoins to incentivize its usage. Some people found ways to circumvent this restriction; for instance, sending the bonus to a family member and asking her to withdraw the money from a Chivo Wallet ATM.
55. These findings regarding the prominence of young adoption is consistent with (*87*).
56. Table S6 shows no evidence of technical issues with the app being a concern by constructing a dummy equal to one if the user faced problems using the app.
57. Figs. S5 and S6 show Chivo Wallet ATM locations. Fig. S12 displays mean distances to a Chivo Wallet ATM across population shares.
58. In general, extending income adoption relations requires caution, as countries with higher income, such as Panama, may have higher adoption of digital payments (e.g., card or mobile) and, thus, lower incentives to adopt a Chivo Wallet type of service (*88*). However, the adoption of digital payments in Panama was similar to that in El Salvador; in Panama, 13.3% of people over 15 years of age report having borrowed from a financial institution or used a credit card, whereas 11.5% is the corresponding percentage in El Salvador. Moreover, in both countries, 6.5% of people over 15 years of age have made a payment using their mobile phone or internet according to the World Bank's G20 Financial Inclusion Indicators.
59. Fig. S2 reports official monthly data on remittances in bitcoins, and fig. S17 summarizes our results.

60. Mistrust is also the main reason not to agree with the use of Chivo Wallet (fig. S16).
61. Note that, in the US, apps to trade bitcoin are required to gather information on the identity of the trader, so bitcoin is not associated with anonymity in the US, just as in El Salvador's case.
62. D. G. Baur, K. Hong, A. D. Lee, Bitcoin: Medium of exchange or speculative assets? *J. Int. Financ. Mark. Inst. Money* **54**, 177–189 (2018). doi: 10.1016/j.intfin.2017.12.004
63. J. Bagnall *et al*., "Consumer cash usage: A cross-country comparison with payment diary survey data" (Tech. Rep., Social Science Research Network Electronic Journal, 2014); http://dx.doi.org/10.2139/ssrn.2436365.
64. Source: "Chivo Wallet registra un promedio de 6,000 transacciones por d´ıa, segu´n experto argentino," Diario El Mundo, November 2021. Estimate obtained based on an adult population of 4.3 million.
65. F. Alvarez, D. Argente, F. Lippi, E. M´endez, D. Van Patten, "Strategic complementarities in a dynamic model of technology adoption: P2P digital payments" (Working Paper 31280, National Bureau of Economic Research, 2023); https://doi.org/10.3386/w31280.
66. The diffusion of many technologies is also shaped by learning; this mechanism, however, does not necessarily create an externality or room for policy interventions to improve outcomes.
67. More details are reported in fig. S21.
68. Businesses that refuse to accept bitcoin are operating in violation of local regulations and exposed to sanctions under the Consumer Protection Law; our survey points to enforcement on firm adoption being imperfect.
69. The share that accepts cards is only a little over 25%. Even among firms that accept bitcoin, prices were quoted in USD and the Chivo Wallet app provided real-time bitcoin equivalents.
70. First, a survey ran by the Salvadoran Foundation for Economic and Social Development (FU- SADES) toward the end of 2021 indicates that 10% of businesses have made sales in bitcoin ("Institutional Position N.106," FUSADES, December 2021). Second, the Chamber of Commerce and Industry of El Salvador (Camarasal) conducted a survey in February 2022 reporting that 13.9% of businesses have made sales in bitcoin ("First Business Survey 2022," Camarasal, March 2022).
71. The Chamber of Commerce and Industry of El Salvador reports a similar estimate of firms that have not changed their sales, and (91.7%) the Salvadoran Foundation for Economic and Social Development estimates that the share of sales paid in bitcoin is between 1 and 5%.
72. Table S9 shows results robust to controlling for the sector of the firm. Findings are very similar if only including responses from the firm's owner or from an employee who reports to work in sales.
73. Fig. S22 shows (i) a summary of the results on prices from the consumer's perspective (21% have encountered higher prices at some businesses) and (ii) the full distribution of shares of sales in bitcoin across firms. Fig. S23 summarizes findings on firms.
74. Although it can be verified faster, this extra speed incurs an additional cost.
75. Although one entity can own several addresses, these are not transactions between Chivo Wallets owned by individuals.
76. Thus, this figure considers transactions that involve an address that can be identified as Chivo Wallet and another address.
77. The fees paid for these deposits tended to be higher closer to Chivo Wallet's launch (see fig. S26), which would be consistent with more urgency from bitcoiners trying to pay for goods and services when Chivo Wallet's hype was at its peak. Throughout the period, fees for deposits into Chivo Wallet tended to be higher than those paid for withdrawals, which also points to more urgency on the deposits' front compared with withdrawals. The data indicate that Chivo Wallet mostly transacted with well-known exchanges; the main one being Binance (12% of all the volume transacted), followed by Bitso, OKX, and Coinbase.
78. Flows from the blockchain data have a standard deviation of 184,300. To calculate these flows using our survey, we focused on inflows of bitcoin into Chivo Wallet from other wallets, because these are the transactions recorded on the blockchain. Thus, our population of interest consists of individuals who have deposited bitcoin into Chivo Wallet and have transferred bitcoins to wallets other than Chivo Wallet, ~2% of the adult population of El Salvador. For this sample, we computed total deposits per day as the difference between the total amount sent per day and the total amount received per day in the app, including transactions in both USD and bitcoins, because convertibility across currencies is free within the app. To estimate the total deposits in bitcoins per day, we multiplied total deposits times the share of deposits in bitcoins (17.3%).
79. The CAF has an income per capita of ~$418 USD and Panama of approximately $12,172 USD, and as in El Salvador, the alternative to bitcoin is a stable currency. Approximately 13.7% of the population in the CAF has access to a bank account, whereas in Panama this number is ~46.5% (Fig. 1B).
80. F. Carapella, J. Flemming, "Central bank digital currency: A literature review" (Tech. Rep., Social Science Research Network Electronic Journal, 2020); https://doi.org/10.17016/2380-7172.2790.
81. A. Deviatov, N. Wallace, Optimal inflation in a model of inside money. *Rev. Econ. Dyn.* **17**, 287–293 (2014). doi: 10.1016/j.red.2013.06.003
82. F. Alvarez, F. Lippi, Cash burns: An inventory model with a cash-credit choice. *J. Monet. Econ.* **90**, 99–112 (2017). doi: 10.1016/j.jmoneco.2017.07.001
83. F. Alvarez, D. Argente, On the effects of the availability of means of payments: The case of Uber. *Q. J. Econ.* **137**, 1737–1789 (2022). doi: 10.1093/qje/qjac008
84. F. Alvarez, D. Argente, "Consumer surplus of alternative payment methods: Paying Uber with cash" (Working Paper 28133, National Bureau of Economic Research, 2022); http://dx.doi.org/10.2139/ssrn.3462480.
85. A. J. Swiston, "Official dollarization as a monetary regime: Its effects on El Salvador" (Working Paper 2011/129, International Monetary Fund, 2008); https://ssrn.com/abstract=1864432.
86. G. B. Gorton, E. W. Tallman, *Fighting Financial Crises: Learning from the Past* (Univ. of Chicago Press, 2018). doi: 10.7208/chicago/9780226479651.001.0001
87. M. Brown, N. Hentschel, H. Mettler, H. Stix, The convenience of electronic payments and consumer cash demand: Causal evidence from the staggered introduction of contactless debit cards" (Research Paper 2020/02, University of St. Gallen School of Finance, 2022); http://dx.doi.org/10.2139/ssrn.3582388.
88. Z. Wang, P. Han, "Technology adoption and leapfrogging: Racing for mobile payments" (Working Paper 21-5, Federal Reserve Bank of Richmond, 2021); http://dx.doi.org/10.21144/wp21-05.
89. S. Meiklejohn *et al*., "A fistful of bitcoins: Characterizing payments among men with no names," in *Proceedings of the 2013 Conference on Internet Measurement Conference (IMC '13)*, Barcelona, Spain, 23 to 25 October 2013 (Association for Computing Machinery, 2013), pp. 127–140; https://doi.org/10.1145/2504730.2504747.
90. D. Ermilov, M. Panov, Y. Yanovich, "Automatic bitcoin address clustering," in *2017 16th IEEE International Conference on Machine Learning and Applications (ICMLA)*, Cancún, Mexico, 18 to 21 December 2017 (IEEE, 2017), pp. 461–466; https://doi.org/10.1109/ICMLA.2017.0-118.
91. S. Foley, J. R. Karlsen, T. J. Putnins, Sex, drugs, and bitcoin: How much illegal activity is financed through cryptocurrencies? *Rev. Financ. Stud.* **32**, 1798–1853 (2019). doi: 10.1093/rfs/hhz015
92. Data and code for: F. Alvarez, D. Argente, D. Van Patten, Are cryptocurrencies currencies? Bitcoin as legal tender in El Salvador, Dryad (2023); https://doi.org/10.5061/dryad.z8w9ghxjm.

ACKNOWLEDGMENTS

We thank M. Bassetto, M. Brown, D. Duffie, M. Golosov, K. Huynh, C. Monnet, A. Neumeyer, D. Niepelt, A. Schoar, H. Uhlig, N. Wallace, and Z. Wang for helpful comments and discussions. **Funding:** The authors used funding from their own universities, which at the time the project was conducted were: University of Chicago (F.A.), The Pennsylvania State University (D.A.), and Yale University (D.V.P.). **Author contributions:** Conceptualization: F.A., D.A., D.V.P.; Funding acquisition: F.A., D.A., D.V.P.; Investigation: F.A., D.A., D.V.P.; Methodology: F.A., D.A., D.V.P.; Writing – original draft: F.A., D.A., D.V.P.; Writing – review and editing: F.A., D.A., D.V.P. **Competing interests:** The authors declare no competing interests. **Data and materials availability:** Data and code for this study have been deposited at Dryad (*92*). **License information:**

Copyright © 2023 the authors, some rights reserved; exclusive licensee American Association for the Advancement of Science. No claim to original US government works. https://www.science.org/about/science-licenses-journal-article-reuse

SUPPLEMENTARY MATERIALS

science.org/doi/10.1126/science.add2844
Supplementary Text
Figs. S1 to S27
Tables S1 to S13
References (*93*–*96*)

Submitted 1 June 2022; resubmitted 23 April 2023
Accepted 7 November 2023
10.1126/science.add2844

Your Legacy to Science

AN ESTATE GIFT TO THE
AMERICAN ASSOCIATION FOR THE ADVANCEMENT OF SCIENCE

Since 1848, our founding year, the American Association for the Advancement of Science (AAAS) has been deeply committed to advancing science, engineering and innovation around the world for the benefit of all people.

By making AAAS a beneficiary of your will, trust, retirement plan or life insurance policy, you become a member of our 1848 Society, joining Thomas Edison, Alexander Graham Bell and the many distinguished individuals whose vision led to the creation of AAAS and our world-renowned journal, *Science*, so many years ago.

Unlike many of its peers, *Science* is not for-profit. Your estate gift would provide long-term financial stability and durable annual income that will support operations and competitive innovation for years to come. **This support is vital.**

"As a teacher and instructor, I bear responsibility for the younger generations. If you have extra resources, concentrate them on organizations, like AAAS, that are doing work for all."

—Prof. Elisabeth Ervin-Blankenheim, 1848 Society member

If you intend to include AAAS in your estate plans, provide this information to your lawyer or financial adviser:

Legal Name: American Association for the Advancement of Science
Federal Tax ID Number: 53-0196568
Address: 1200 New York Avenue, NW, Washington, DC 20005

If you would like more information on making an estate gift to AAAS, cut out and return the form below or send an email to philanthropy@aaas.org. Additional details are also available online at **www.aaas.org/1848Society**.

1848 SOCIETY
AAAS

cut here

Yes, I would like more information about joining the AAAS 1848 Society.

PLEASE CONTACT ME AT:

Name: _____

Address: _____

City: _____ State: _____ Zip code: _____ Country: _____

Email: _____ Phone: _____

RETURN THIS FORM TO:
AAAS Office of Philanthropy and Strategic Partnerships • 1200 New York Avenue, NW • Washington, DC 20005 USA

RESEARCH ARTICLE SUMMARY

NEUROSCIENCE

Glia transmit negative valence information during aversive learning in *Drosophila*

Tomoyuki Miyashita, Kanako Murakami, Emi Kikuchi, Kyouko Ofusa, Kyohei Mikami, Kentaro Endo, Takaaki Miyaji, Sawako Moriyama, Kotaro Konno, Hinako Muratani, Yoshinori Moriyama, Masahiko Watanabe, Junjiro Horiuchi, Minoru Saitoe*

INTRODUCTION: During *Drosophila* aversive olfactory conditioning, flies are exposed simultaneously to an odor and aversive electrical shocks. Flies learn to associate the odor with the aversive stimulus and subsequently avoid the odor. Learning and memory of this association requires a brain region known as the mushroom bodies (MBs). Odor information is conveyed to the MBs by cholinergic projection neurons, which originate in the antennal lobes and synapse onto the dendrites of MB neurons. However, the cells and pathways that convey aversive shock information to the MBs have been uncertain. Activation of dopaminergic (DA) pathways that innervate the axons of MB neurons can bypass the requirement for aversive stimulation during conditioning, suggesting that DA may convey this information. On the other hand, dopamine is required for memory reinforcement and synaptic plasticity, complex functions that should occur after the transmission of aversive shock information to the MBs. Recent ex vivo imaging studies have suggested that glutamate (Glu) binding to *N*-methyl-D-aspartate (NMDA)–type Glu receptors (NMDARs) on MB neurons conveys shock information to the MBs, while DA functions subsequently to induce plasticity and reinforce associative memories.

RATIONALE: NMDARs are expressed abundantly on the MBs and are required for forming associative memories. However, presynaptic Glu terminals—identified by expression of the vesicular Glu transporter (VGLUT), which transports Glu into synaptic vesicles—are extremely sparse in the MBs. This suggested that unidentified Glu terminals expressing an uncharacterized VGLUT may play a role in the transmission of shock information to the MBs and subsequent memory formation.

RESULTS: We identified a previously unknown DVGLUT, DVGLUT2, through sequence homology and verified that it functions as a Glu transporter. DVGLUT2 is not expressed in neurons but instead is associated with vesicle-like structures in ensheathing glia (EG), which surround neuropil structures, including the MBs. Aversive electrical stimulation induces rapid Ca^{2+} transients in EG, vesicular exocytosis, and Glu release. Although EG surround all lobes of the MBs similarly, Glu release only occurs in select MB compartments. Other aversive stimuli, including bitter taste and noxious heat stimuli, also induce Glu release from EG in similar patterns. Blocking exocytosis from EG during conditioning impairs aversive learning, whereas artificial activation of EG can replace aversive stimuli during conditioning. Glu released from EG binds to NMDARs on MB neurons and kainate receptors (KARs) on DA neurons. Because of the Mg^{2+} block mechanism of NMDARs, Glu binding on its own is unable to induce Ca^{2+} influx into MB neurons. However, coincidental activation of MB neurons by both odors and aversive stimuli during aversive conditioning is sufficient to remove Mg^{2+} block and induce NMDAR-mediated Ca^{2+} influx, resulting in synergistic activation of MB neurons by odors and shocks. Glu binding to KARs is sufficient to induce Ca^{2+} influx into DA neurons and DA release onto MB neurons, but this release is not required for aversive learning after normal odor-shock paired conditioning. Instead, KAR-dependent DA release is required to prevent aberrant learning when shock onset precedes odor onset during backward conditioning.

CONCLUSION: Our results are consistent with a model in which shock information transmitted from EG bifurcates into two pathways. One pathway consists of Glu release onto NMDARs on MB neurons, and the second pathway induces the release of DA from DA neurons upon aversive but not neutral or appetitive stimulation. Glu released onto MB neurons works synergistically with odor signals and is required for learning, whereas Glu released onto DA neurons prevents inappropriate learning in situations in which an odor cannot be used to predict shocks. Overall, our data suggest that vesicle release of Glu from EG serves to transmit aversive information to higher-order brain areas and also functions to separate aversive sensory information from reinforcement signals during the formation of associative memories. ■

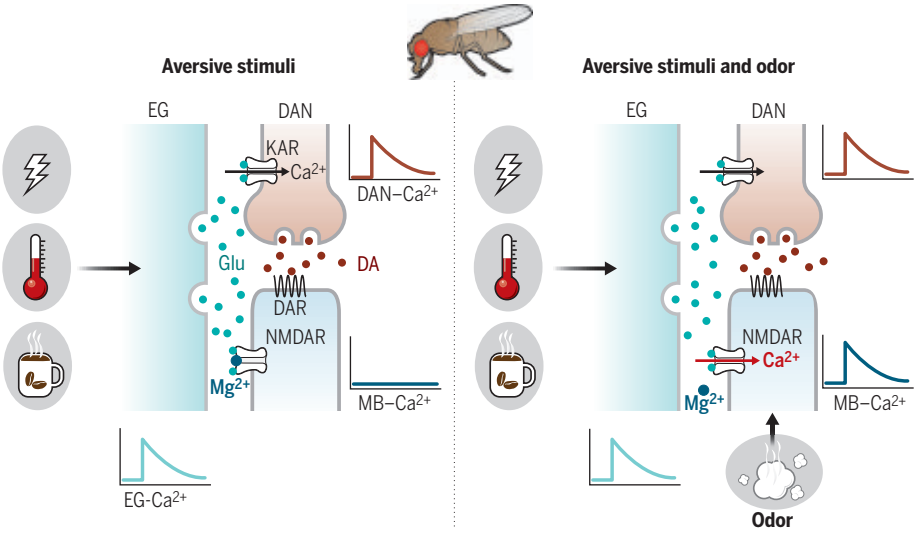

Ensheathing glia transmit aversive information. Aversive stimuli induce vesicular exocytosis from EG and release of Glu onto KAR on dopaminergic neurons (DANs) and NMDARs on MB neurons. (**Left**) When aversive stimuli are unpaired, Mg^{2+} block prevents Ca^{2+} influx. (**Right**) When paired with odors, odor-dependent depolarization removes Mg^{2+} block, allowing Ca^{2+} influx into appropriate MB neurons.

The list of author affiliations is available in the full article online.
*Corresponding author. Email: saito-mn@igakuken.or.jp
Cite this article as T. Miyashita *et al.*, *Science* **382**, eadf7429 (2023). DOI: 10.1126/science.adf7429

READ THE FULL ARTICLE AT
https://doi.org/10.1126/science.adf7429

RESEARCH ARTICLE

NEUROSCIENCE

Glia transmit negative valence information during aversive learning in *Drosophila*

Tomoyuki Miyashita[1], Kanako Murakami[1,2], Emi Kikuchi[1], Kyouko Ofusa[1], Kyohei Mikami[3], Kentaro Endo[3], Takaaki Miyaji[4,5], Sawako Moriyama[6], Kotaro Konno[7], Hinako Muratani[1,8], Yoshinori Moriyama[6], Masahiko Watanabe[7], Junjiro Horiuchi[3], Minoru Saitoe[1,3]*

During *Drosophila* aversive olfactory conditioning, aversive shock information needs to be transmitted to the mushroom bodies (MBs) to associate with odor information. We report that aversive information is transmitted by ensheathing glia (EG) that surround the MBs. Shock induces vesicular exocytosis of glutamate from EG. Blocking exocytosis impairs aversive learning, whereas activation of EG can replace aversive stimuli during conditioning. Glutamate released from EG binds to *N*-methyl-D-aspartate receptors in the MBs, but because of Mg^{2+} block, Ca^{2+} influx occurs only when flies are simultaneously exposed to an odor. Vesicular exocytosis from EG also induces shock-associated dopamine release, which plays a role in preventing formation of inappropriate associations. These results demonstrate that vesicular glutamate released from EG transmits negative valence information required for associative learning.

In *Drosophila* aversive olfactory conditioning, flies are simultaneously exposed to an odor and aversive electrical shocks. Flies learn to associate the odor [the conditioned stimulus (CS)] with the shocks [the unconditioned stimulus (US)] and subsequently avoid the odor. This association is formed and stored in the mushroom bodies (MBs). Odor information is delivered to the MBs from the antennal lobes by cholinergic projection neurons that synapse onto MB neuron dendrites located in the calyces. However, the cells and transmitters that deliver US information to the MBs have been unclear. Prevailing models propose that US information is transmitted by dopaminergic neurons (DANs) (*1*–*3*), but recent ex vivo imaging studies have suggested that US information may be transmitted to *N*-methyl-D-aspartate receptors (NMDARs) in the MBs by glutamatergic (Glu) neurons (*4*, *5*). However, *Drosophila* vesicular glutamate transporter (DVGLUT) staining is largely absent in the MBs, even though NMDARs are abundantly expressed in the MBs (*6*–*9*). This suggested that uncharacterized glutamatergic cells expressing a previously unidentified DVGLUT may transmit aversive information to the MBs.

[1]Learning and Memory Project, Tokyo Metropolitan Institute of Medical Science, Tokyo 156-8506, Japan. [2]Department of Biological Science, Graduate School of Science, Tokyo Metropolitan University, Tokyo 192-0397, Japan. [3]Center for Basic Technology Research, Tokyo Metropolitan Institute of Medical Science, Tokyo 156-8506, Japan. [4]Department of Molecular Membrane Biology, Faculty of Pharmaceutical Sciences, Okayama University, Okayama 700-8530, Japan. [5]Department of Genomics and Proteomics, Advanced Science Research Center, Okayama University, Okayama 700-8530, Japan. [6]Division of Endocrinology and Metabolism, Department of Internal Medicine, School of Medicine, Kurume University, Fukuoka 830-0011, Japan. [7]Department of Anatomy, Faculty of Medicine, Hokkaido University, Hokkaido 060-8368, Japan. [8]Department of Engineering Science, Graduate School of Informatics and Engineering, The University of Electro-Communications, Tokyo 182-8585, Japan.
*Corresponding author. Email: saito-mn@igakuken.or.jp

Results

DVGLUT2 is expressed in ensheathing glia

We performed BLAST (Basic Local Alignment Search Tool) searches and identified CG4288 on the basis of its homology to mammalian VGLUTs. CG4288 had been previously reported as a potential DVGLUT (*10*), and its amino acid sequence is highly homologous to sequences of mouse VGLUT1-3 (figs. S1 and S2A). Notably, CG4288 possesses 12 transmembrane domains similar to those of other VGLUTs and conserved arginine (R) and glutamine (E) residues in transmembrane domain 4 that are required for Glu transport (*11*). To determine whether CG4288 functions as a vesicular Glu transporter, we inserted recombinant protein into artificial lipid membrane vesicles and measured the incorporation of ^{3}H-labeled Glu in these vesicles (*12*). [^{3}H]-Glu was incorporated into CG4288-containing proteoliposomes in the presence of valinomycin, a K^+ ionophore that generates an electrochemical gradient required for VGLUT activity. This incorporation was suppressed by the VGLUT blocker, EvansBlue, or by the addition of excess unlabeled Glu (fig. S2B), verifying that CG4288 encodes a previously unidentified DVGLUT. Thus, we designated the previously characterized DVGLUT encoded by CG9887 as DVGLUT1, and our newly characterized DVGLUT encoded by CG4288 as DVGLUT2.

To determine where DVGLUT2 is located in the brain, we generated an antibody to DVGLUT2 (fig. S3A) and performed immunofluorescence analyses. We did not find DVGLUT2 in the MB lobes (Fig. 1A). Instead, we found it in structures reminiscent of ensheathing glia (EG), which surround neuropil structures including the MBs and the central complex. EG can be identified by using an EG GAL4 driver, NP6520 (*13*, *14*), and a UAS_{GAL}-GFP reporter. GFP (green fluorescent protein) expression cleanly overlapped with the DVGLUT2 signal (Fig. 1B and fig. S3B). GFP expression from NP6520 was not affected when we suppressed GAL4 activity in neurons using pan-neuronal Elav-GAL80, whereas expression was abolished when we suppressed GAL4 activity in glia using pan-glial Repo-GAL80 (Fig. 1C). Expression of DVGLUT2 transcripts significantly decreased when two different DVGLUT2–RNA interference (RNAi) transgenes (330461 and 104145) were expressed from a glial Repo-GAL4 driver but not from a Elav-GAL4 driver (fig. S3C), further supporting the idea that DVGLUT2 is expressed specifically in glia. As previously reported (*14*), EG extend processes into MB lobes, where they are seen to divide MB compartments (Fig. 1C, arrowheads).

Because DVGLUT2 has the ability to transport Glu into vesicles, we next examined whether we could identify synaptic vesicle (SV)–like structures in EG using electron microscopy. EG can be distinguished from MB structures by their higher electron densities (*15*). Consistent with immunofluorescence analyses, we found that EG processes invade MB lobes (Fig. 1D and fig. S3D). We further detected SV-like structures in both MB lobes, and in EG structures close to MB lobes. Using electron microscopy and immunogold labeling, we confirmed that DVGLUT2 is associated with SV-like structures in EG (Fig. 1E and fig. S3E). The diameter of SV-like structures detected in EG with electron microscopy and DVGLUT2-positive vesicles labeled with immunogold were statistically indistinguishable from the diameter of SVs observed in MB neurons (fig. S3F).

Vesicular exocytosis from EG is required for olfactory aversive conditioning

To analyze the importance of DVGLUT2 in olfactory aversive conditioning, we used the TARGET (*16*) and Gene-Switch (*17*) systems to suppress DVGLUT2 in EG. Aversive learning was disrupted when DVGLUT2 was suppressed in adult glia but not in adult neurons (Fig. 2A and fig. S4A). Glial cells in the adult brain include cortex glia, astrocyte-like glia, and EG (*14*, *18*). Olfactory aversive conditioning was impaired when DVGLUT2 was suppressed in EG but not in cortex or astrocyte-like glia (Fig. 2B). To further determine whether vesicle exocytosis from EG is required for aversive

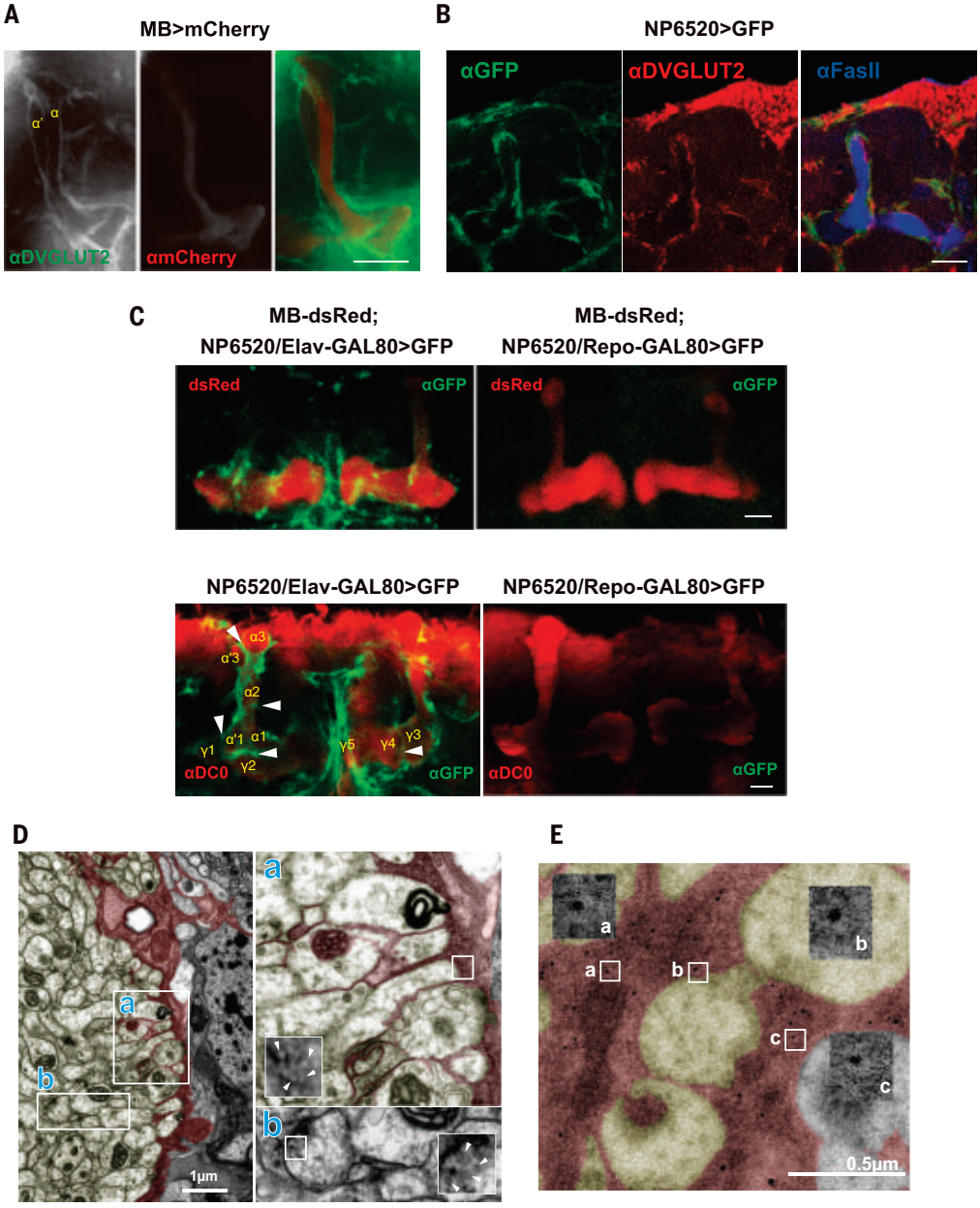

Fig. 1. DVGLUT2 is found in EG. (**A**) Immunohistochemistry using antibody to DVGLUT (αDVGLUT2). The MB lobes were visualized by expressing mCherry from the MB-LexA driver. The α and α′ lobes of the MBs are labeled. (**B**) DVGLUT2 localizes to EG. GFP was expressed from the NP6520 driver. The MB lobes were labeled using anti-Fas II antibodies. (**C**) NP6520 does not drive expression in neurons. (Left) GFP expression from the NP6520 driver was not affected by Elav-Gal80, whereas (right) it was abolished by Repo-Gal80. The MB lobes were labeled by means of dsRed or anti-PKA antibodies. GFP expressed from NP6520 seems to delineate MB compartments (arrowheads). Scale bars, (A) to (C) 10 μm. (**D**) Electron micrograph of EG bordering the MB. EG are colored magenta. Magnified images of the regions (a and b) encompassed by the white rectangles at left are shown at right. (Insets) Further magnified images of the regions encompassed by white rectangles at right. Vesicle-like structures in EG are indicated by arrowheads in (a), and SVs in neuronal synapses are indicated by arrowheads in (b). (**E**) Immunoelectron micrograph of EG. Immunogold-labeled αDVGLUT2 is found on the vesicle-like structures. Regions encompassed by white squares are magnified in the insets.

learning, we expressed a temperature-sensitive dynamin mutant, shi^{ts} (*19*), in EG (EG>shi^{ts}). Dynamin is required for SV recycling, and expression of shi^{ts} is used to abolish synaptic output from neurons at restrictive temperatures (*19*, *20*). Aversive olfactory learning scores were significantly impaired in these flies when they were trained at restrictive temperature (30°C) and tested at permissive temperature (18°C), but not when they were trained at the permissive temperature and tested at the restrictive temperature (Fig. 2C and fig. S4, B and C). These results indicate that vesicle recycling in EG is required during aversive learning when electric shocks are used as the US. EG>shi^{ts} at 30°C produced a larger learning impairment than suppressing DVGLUT2 (EG>DVGLUT2-RI). This suggests that either glial suppression of DVGLUT2 is less efficient than shi^{ts}-dependent inhibition of vesicle cycling, or that other transmitters in addition to Glu may be released from EG vesicles to affect learning.

Denatonium is a bitter compound that can also be used as an aversive stimulus during aversive memory conditioning (*21*). Aversive memory formation by using denatonium as the US was also severely impaired in EG>shi^{ts} flies at restrictive temperature, whereas appetitive memory formation by using sucrose as the reward was unaffected (Fig. 2, D and E), indicating that EG transmit aversive, but not appetitive, information to the MBs.

Aversive stimuli induce vesicle exocytosis and Glu release from EG

To determine whether aversive stimuli induce vesicle exocytosis from EG onto MB lobes, we performed syb–GRASP (GFP reconstitution across synaptic partners) experiments (*22*) in which functional GFP is only reconstituted upon vesicular release from EG at the MBs. We generated transgenic flies expressing synaptobrevin fused to GFP exons 1 to 10 (syb-spGFP1-10) in EG and its GRASP partner, mouse CD8, fused to GFP exon 11 (mCD8-spGFP11) in the MBs. In these flies, syb-spGFP1-10 is transported to the cell surface of EG upon vesicle fusion, and functional GFP is reconstructed when vesicle fusion occurs in the vicinity of mCD8-spGFP11

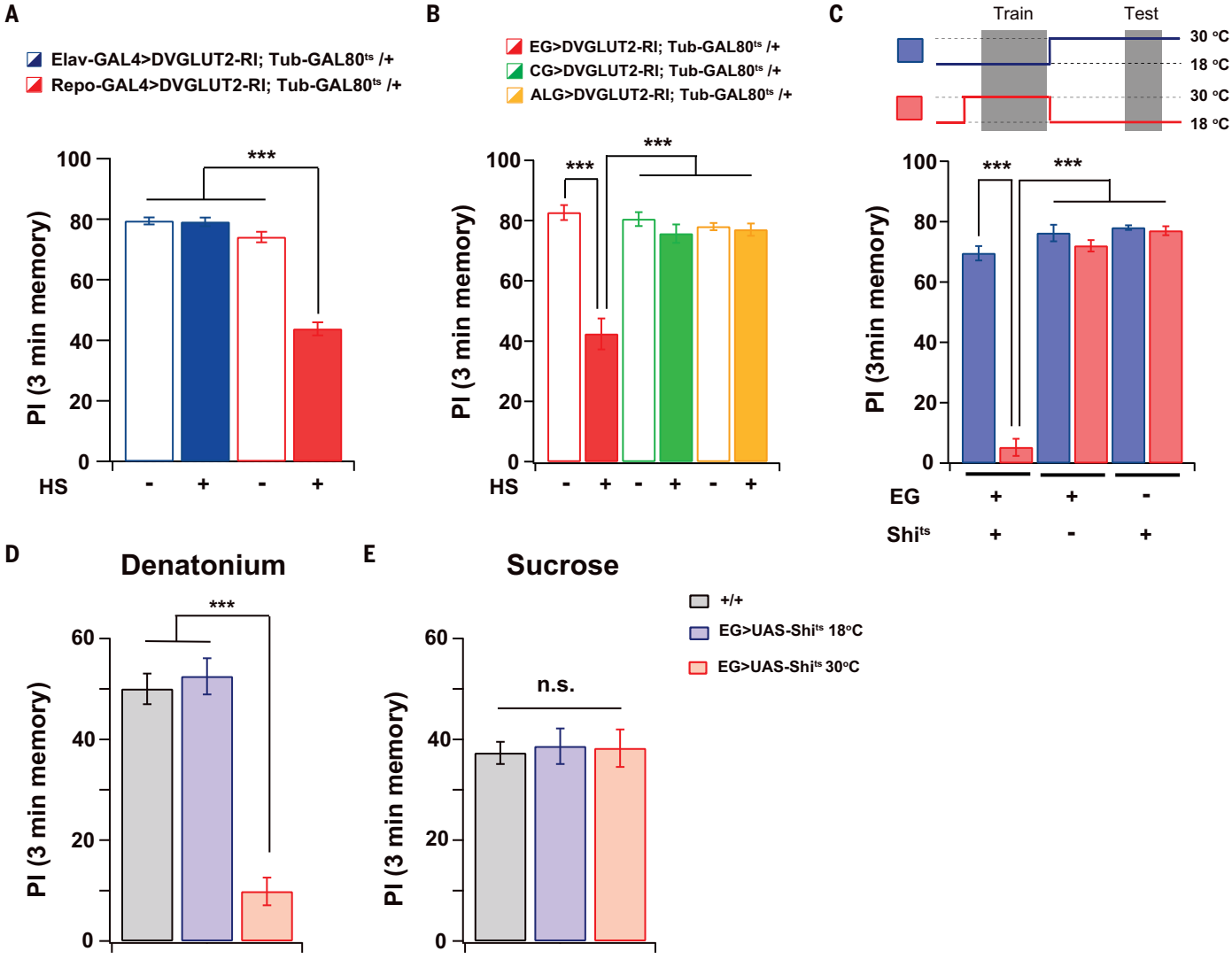

Fig. 2. Vesicular exocytosis from EG is required for aversive memory formation. (**A**) Reducing expression of DVGLUT2 in glia but not neurons disrupts olfactory aversive conditioning. During conditioning, flies are exposed to an odor (the CS+ or shock-paired odor) for 1 min while simultaneously being electrically shocked every 5 s. Flies are next exposed to a second odor (the CS−, or unpaired odor) for 1 min in the absence of shocks. Memory acquisition is measured 3 min after conditioning by having the flies choose between the two odors. A performance index (PI) is calculated by subtracting the percentage of flies that choose the shock-paired odor from the percentage that choose the unpaired odor. A higher PI is correlated with greater memory. DVGLUT2 was suppressed in adult flies at the restrictive temperature (+HS). (**B**) DVGLUT2 is required acutely in EG during olfactory aversive conditioning. DVGLUT2 was suppressed acutely in EG, cortex glia (CG), and astrocyte-like glia (ALG). (**C**) Blocking vesicular exocytosis from EG during conditioning impairs aversive memory formation. (**D**) Blocking vesicular exocytosis from EG during conditioning impairs aversive memory formation with denatonium. (**E**) Blocking vesicular exocytosis from EG during conditioning does not affect appetitive memory formation with sucrose. ***$P < 0.001$.

expressed in the MBs. No GFP signals were observed in these flies in the naïve state or after odor presentation alone. However, signals were observed after shock alone or after simultaneous shock-odor presentation during aversive olfactory conditioning (Fig. 3A). Although EG surround all MB lobes, GFP signals were not observed in all lobes homogeneously but instead observed specifically in the peduncle, γ1, γ5, α2, β1, β′1, and β′2 compartments of the MB lobes (Fig. 3, B and C). We observed similar but not identical GFP signal patterns when the transgenic flies were exposed to denatonium or to noxious heat but not when they were fed sugar rewards (fig. S4D).

To detect vesicle exocytosis from EG in real time, we generated transgenic flies that express a DVGLUT2::pHluorin fusion protein in EG (Fig. 3D) and examined fluorescence changes in EG that contact the horizontal lobes of the MBs. Consistent with syb-GRASP results, we observed vesicular exocytosis from EG in γ1, γ5, and β′1, β′2 compartments in response to shock presentation (Fig. 3E and fig. S5A). Because of the orientation of the fly and the angle of the brain in our in vivo setup, we could not observe the peduncles, α2, and β1 compartments, which also showed vesicular exocytosis in syb-GRASP experiments.

Next, to determine whether vesicular release is associated with increases in EG intracellular Ca^{2+}, we used transgenic flies expressing syt-GCaMP, a fusion protein of synaptotagmin and GCaMP (*23*), in EG. Shock, but not odor, presentation induced Ca^{2+} responses in EG surrounding MB lobes in a

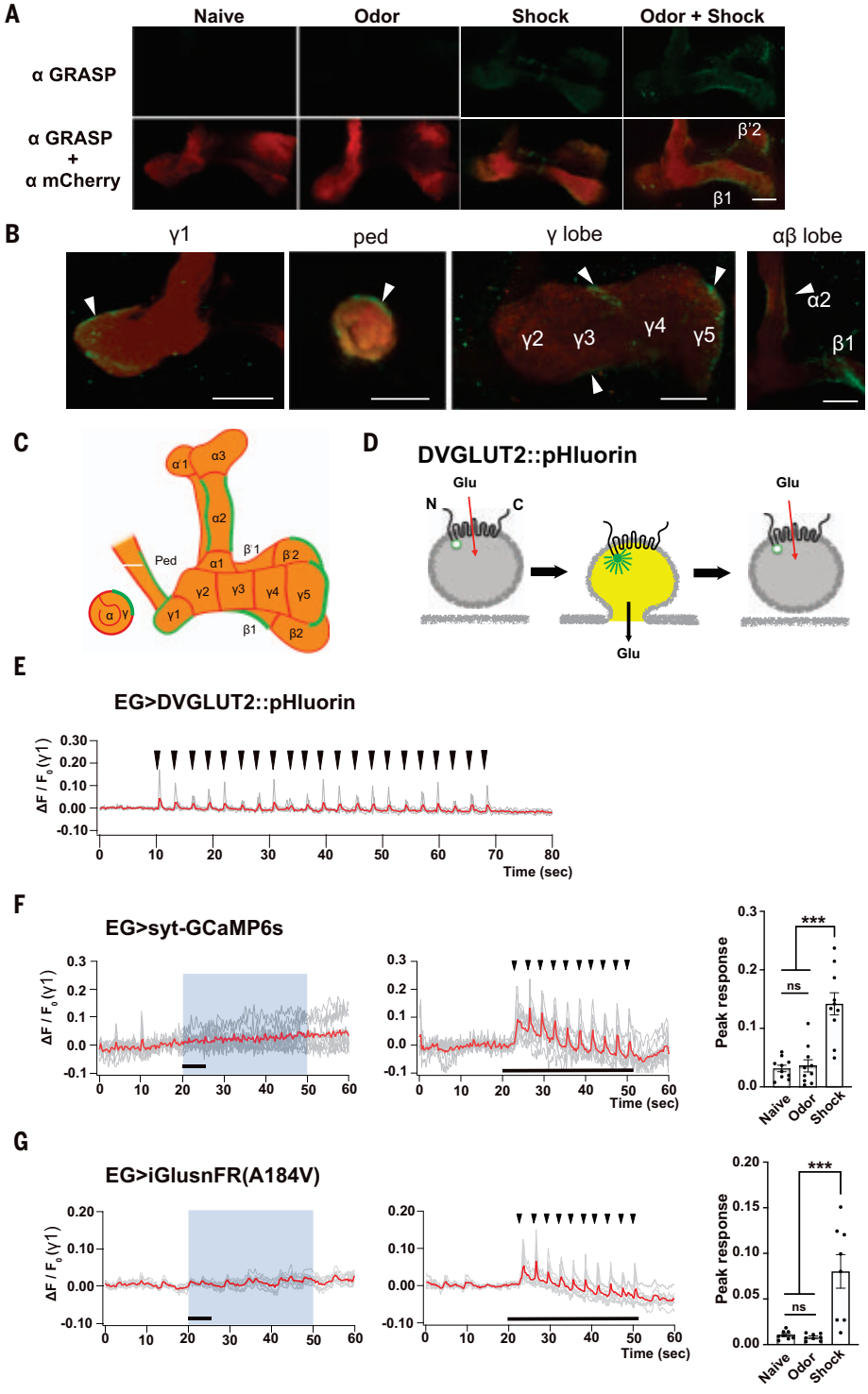

Fig. 3. Electrical shocks induce vesicle exocytosis from EG. (**A**) GRASP signals (reconstruction of GFP from component parts) in naïve, odor-stimulated, shock-stimulated, and odor and shock-stimulated EG>syb-spGFP$_{1\text{-}10}$; MB>mCD8-spGFP$_{11}$ flies. (**B**) Magnified GRASP signals. Arrowheads indicate GFP signals at junctures between compartments. (**C**) Schematic diagram showing the location of shock-induced GRASP signals. (**D**) Schematic diagram of vesicle exocytosis monitored by means of DVGLUT2::pHluorin. (**E**) Vesicular exocytosis from EG in the MB γ1 compartment in response to electric shocks. Triangles indicate electrical shocks in this and subsequent figures. All functional imaging was performed at 20 mM Mg^{2+} concentrations in this study unless otherwise mentioned. (**F**) Ca^{2+} responses in EG bordering the γ1 compartment during odor and shock presentation. The light blue band in Figs. 3 to 6 indicates odor (3-octanol) presentation. Peak responses were determined for the period indicated by the black bars. 3-Octanol was used as the odor in this study unless otherwise mentioned. (**G**) Glu release from EG in the γ1 compartment during odor and shock presentation. Scale bars,e 10 μm. The time windows used to determine peak responses are shown as black bars. ***P < 0.001.

pattern similar to what we observed for vesicular exocytosis (Fig. 3F and fig. S5B). Furthermore, denatonium treatment, but not sugar treatment, induced Ca^{2+} responses in EG (fig. S4E). When we next measured Glu release from EG by expressing the Glu sensor iGlusnFR(A184V) (*24*) in EG, we again found a pattern of increase in Glu signals from EG that paralleled Ca^{2+} and vesicular exocytosis signals (Fig. 3G and fig. S5C).

EG transmits aversive signals to the MBs

To next examine MB Ca^{2+} responses during electrical shock presentation, we expressed syt-GCaMP in the MBs. Although odor exposure evoked significant Ca^{2+} responses in the MBs, we did not observe Ca^{2+} responses in any MB compartments upon shock presentation (Fig. 4A and fig. S6A). We verified that Glu was released onto MB lobes in response to electrical shocks and denatonium but not to odors and sugar (Fig. 4B and fig. S6B). Patterns of Glu release onto MB compartments paralleled patterns of Glu release from EG upon electrical shocks.

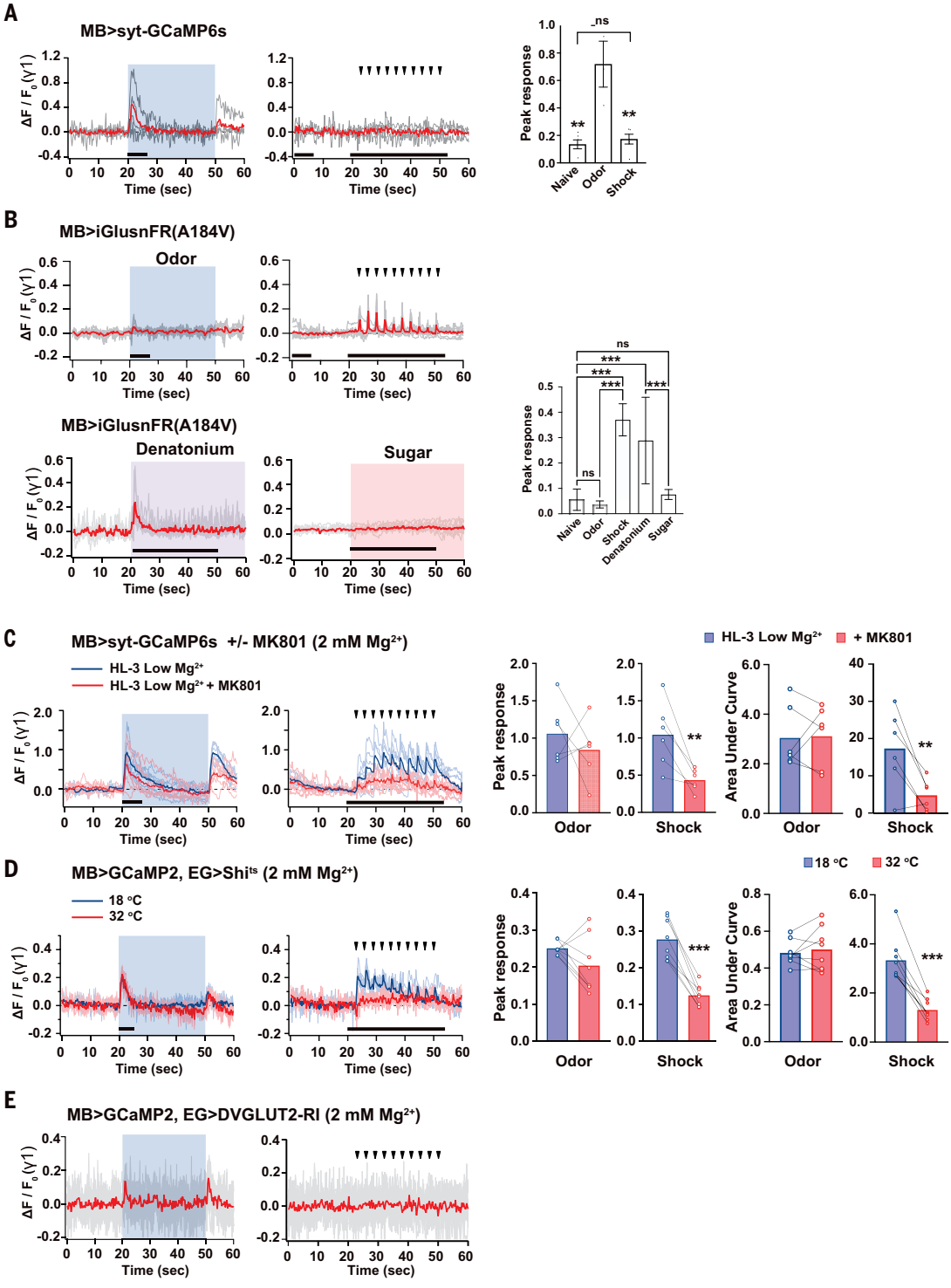

Fig. 4. EG transmit aversive signals to the MBs. (**A**) Ca^{2+} responses in the γ1 compartment of naïve, odor-stimulated, or shock-stimulated flies. (**B**) Glu release measured in the MB γ1 compartment upon odor, shock, denatonium, and sugar presentation. (**C**) Ca^{2+} responses in the γ1 compartment at 2 mM Mg^{2+}. Peak responses and areas under curves were measured during the period indicated with black bars. (**D**) Shock-induced Ca^{2+} responses at 2 mM Mg^{2+} were abolished by blocking EG vesicular exocytosis. (**E**) Shock-induced Ca^{2+} responses at 2 mM Mg^{2+} were abolished when DVGLUT2 was suppressed in EG. $^{**}P < 0.01$; $^{***}P < 0.001$.

Why were Ca^{2+} responses not observed in the MBs even though Glu was released onto the MBs upon electrical shock? Aversive somatosensory information is conveyed by ascending fiber of the ventral nerve cord (AFV), and previous ex vivo imaging studies suggest that AFV-evoked MB responses are mediated by NMDARs (*4*, *5*). Because of Mg^{2+} block, Glu binding on its own is unable to activate NMDARs at resting membrane potentials. Instead, activation requires both Glu binding as well as postsynaptic depolarization to release Mg^{2+} ions that block the channel pore (*25*, *26*). The concentration of extracellular Mg^{2+} in the fly brain is around 20 mM (*27*), and Mg^{2+} concentrations higher than 10 mM are sufficient to cause Mg^{2+} block (*8*). When we reduced the extracellular Mg^{2+} concentration to 2 mM, we found significant Ca^{2+} responses in the MBs upon electrical shocks, and these responses were suppressed by the NMDAR inhibitor MK801 (Fig. 4C and fig. S6C). To determine whether shock-evoked MB responses at low Mg^{2+} concentrations are caused by vesicular exocytosis from EG, we

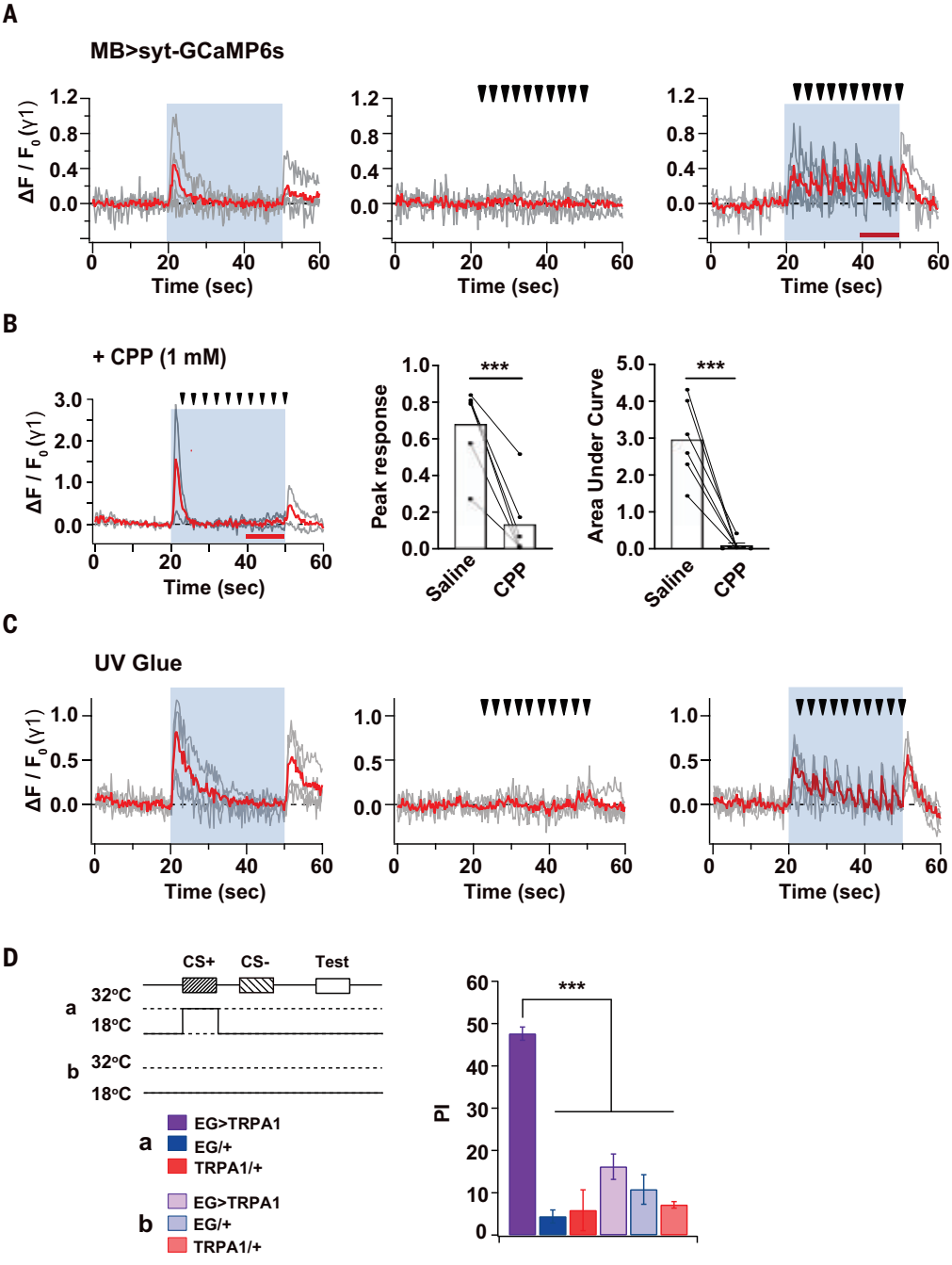

Fig. 5. Odor inputs gate the transmission of shock information to the MBs. (**A**) Ca^{2+} responses in the γ1 compartment during odor, shock, and simultaneous odor and shock presentation. (**B**) The NMDAR blocker CPP abolishes shock-dependent Ca^{2+} responses in the MBs during simultaneous odor and shock presentation. (**C**) Ca^{2+} responses in the MBs in which observation windows were sealed with transparent glue in the absence of added buffers. (**D**) Artificial activation of EG can replace aversive stimuli during aversive conditioning. PI scores measure the flies' preference for the CS− odor compared with the CS+ odor. ***$P < 0.001$.

examined MB Ca^{2+} responses in transgenic flies expressing GCaMP in the MBs and shi^{ts} in EG at 2 mM Mg^{2+} conditions (Fig. 4D). Whereas both shock- and odor-evoked Ca^{2+} responses were observed at permissive temperature (18°C), shock-evoked but not odor-evoked responses were abolished at restrictive temperature (32°C). Moreover, when DVGUT2 was suppressed in EG, again shock-evoked but not odor-evoked Ca^{2+} responses were extinguished (Fig. 4E).

Although syb-GRASP data suggest that vesicular exocytosis from EG occurred predominantly at the outer border of γ1, γ4, γ5, β'1, and β'2 compartments, Glu responses were observed throughout each of these compartments (fig. S7).

Integration of aversive information into the MBs is gated by coincident odor input

We next examined whether depolarization of MB neurons by odor presentation is sufficient to remove Mg^{2+} block and permit the transmission of shock information to the MBs. When flies were exposed to an odor in the absence of electric shocks, we observed Ca^{2+} responses in the MBs. When flies were exposed to shocks in the absence of odors, we observed no MB Ca^{2+} responses. However, when we exposed flies to odor and shocks simultaneously, we observed a synergistic effect in which previously missing shock responses were observed added to odor responses (Fig. 5A and fig. S8A). Shock-associated Ca^{2+} influx during coincident odor shock inputs were suppressed by the NMDAR blocker CPP (carboxypiperazin-4-yl-propyl-1-phosphonic acid) (Fig. 5B).

Although we found that shock inputs in the absence of odor inputs are prevented from being transmitted to the MBs at 20 mM Mg^{2+} concentrations, other physiological and functional imaging studies used lower Mg^{2+} concentrations

and did not observe this effect. Thus, to determine whether our observed gating mechanism occurs in the absence of externally added buffer, we performed experiments in which we opened the fly head capsule and filled it with transparent glue that was hardened by ultraviolet (UV) irradiation in the absence of added buffers (*28*, *29*). Similar to our observations of when we filled head capsules with buffer containing 20 mM Mg^{2+}, we observed Ca^{2+} responses in the MB upon odor presentation, but not shock presentation alone. We further observed shock-associated Ca^{2+} responses during simultaneous odor shock presentation (Fig. 5C and fig. S8B), again indicating that shock information is only transmitted to MB neurons that have been depolarized by odor inputs.

Because EG convey aversive information to the MBs, we examined whether artificial activation of EG can replace aversive stimuli during conditioning. We used transgenic EG>TRPA1 flies expressing the temperature-sensitive cation channel dTRPA1 (*30*) in EG and observed increased Ca^{2+} responses when dTRPA1 channels were activated by temperature shifts to 32°C (fig. S9A). When we performed syb-GRASP experiments in these flies, similar to denatonium, heat, and electrical shock presentation we observed reconstituted GFP signals in the peduncle and γ1 of the MB lobes at 32°C, indicating that vesicular exocytosis from EG to MB neurons occurs upon activation of dTRPA1 in EG (fig. S9B). After exposing these flies to two odors—the first (CS+) at 32°C to activate dTRPA1, and the second (CS–) at 18°C, at which TRPA1 channels are inactive—we observed that flies displayed a subsequent strong avoidance to the CS+ odor (Fig. 5D), demonstrating that artificial activation of EG can bypass the requirements for aversive stimulation during aversive memory formation.

EG also transmit aversive signals to DANs

Electrical shocks induce Ca^{2+} influx in the axon terminals of DANs and dopamine (DA) release onto MBs (*31*–*34*). However, the neural mechanism that causes shock-associated DA release remains unclear. To examine whether vesicular exocytosis from EG also transmits aversive information to DANs to regulate DA release, we used transgenic flies expressing shi^{ts} in EG and a DA sensor in the MBs and measured DA release onto γ1. At the permissive temperature, we observed DA release onto γ1 after both shock and odor presentation. At the restrictive temperature, shock-associated DA release was abolished, whereas odor-associated DA release was unaffected, indicating that vesicular release from EG is required specifically for shock-dependent DA release onto γ1 (Fig. 6A). We also observed Ca^{2+} responses in DAN axon terminals in the γ1 compartment in response to odor presentation and shock presentation. Again, shock-associated responses were abolished at the restrictive temperature in EG>shi^{ts} flies, demonstrating that both Ca^{2+} responses and DA release from DANs depend on EG signaling (Fig. 6B). Further, shock-associated but not odor-associated Ca^{2+} responses were extinguished by CNQX (6-cyano-7-nitroquinoxaline-2,3-dione), an inhibitor of AMPA and kainate-type Glu receptors (Fig. 6C). Consistent with this, when we suppressed the expression of kainate receptors in the DANs, Ca^{2+} responses associated with shock presentation but not odor presentation were significantly suppressed (Fig. 6D). To examine whether DA activity may also be required for shock-associated EG responses, we expressed a shi^{ts} transgene in DA neurons but did not observe any differences in shock-associated Ca^{2+} responses in EG at restrictive or permissive temperatures (Fig. 6E). Thus, EG function upstream to both MBs and DANs during transmission of aversive information. Glu released from EG binds to and activates kainate receptors on DANs, whereas an independent mechanism activates DANs during odor exposure.

We next examined whether EG-mediated DA release is involved in associative learning. Unexpectedly, when we suppressed kainate receptors in DANs, we found that aversive learning (3-min memory) and long-lasting 7-hour memory were normal (Fig. 6F). In contrast to conventional forward conditioning, backward conditioning—in which the onset of the US occurs before CS exposure—does not normally form associative memory. We found that suppression of kainate receptors in DANs caused flies to form significant 3-min memory after backward conditioning (Fig. 6G). These results suggest that direct transmission of aversive information to DANs through kainate receptors is not required for normal memory but instead functions to prevent formation of inappropriate associations in situations in which the CS does not serve as a predictor of the US.

Discussion

Glia are known to regulate neural and synaptic plasticity and play a critical role in regulating behavioral changes (*35*–*39*). Our data indicate that glia can further function to directly transmit aversive sensory information to higher-order brain areas and separate aversive sensory information from reinforcement signals during the formation of associative memories. Previously, DA had been proposed to both transmit aversive information to the MBs and reinforce associations (*33*, *40*–*43*). However, our data indicate that EG Glu pathways that mediate transmission of aversive information are distinct and function upstream of DA pathways that reinforce associations (*32*, *44*, *45*). Aversive stimuli induce increases in Ca^{2+} concentrations, vesicular exocytosis, and release of glutamate from EG. Blocking vesicular cycling or suppressing glutamate transporter activity in EG disrupts memory, whereas artificial activation of EG can replace aversive stimulation to induce associative memory formation.

Because associations can be formed with many different odors, aversive Glu signals are likely to be sent to many MB axons. However, plasticity should only occur at select locations where coincident odor and aversive information converge (*46*). NMDARs have been proposed to function as coincidence detectors that regulate Hebbian plasticity because they require both depolarization to remove Mg^{2+} block and Glu binding to be activated (*47*, *48*). Our results are consistent with this idea. Glutamate released from EG on its own is unable to induce Ca^{2+} influx into mushroom body neurons at physiological Mg^{2+} concentrations but is able to do so in low-Mg^{2+} conditions or when mushroom body neurons are coincidently activated by odors. Furthermore, suppressing NMDARs in the mushroom bodies impairs aversive learning (*5*). Altogether, our results indicate that odor-dependent depolarization removes Mg^{2+} block of NMDARs, which allows glutamate released by EG to activate NMDARs in appropriate neurons for formation of odor-specific memories.

Glutamate released by EG also induces Ca^{2+} activity and DA release through activation of kainate-type glutamate receptors on DANs. Unexpectedly, however, direct transmission of aversive information from EG to kainate receptors on DANs is not necessary for forming associations. Instead, our data suggest that transmission of aversive information to DANs prevents associations from forming in situations in which the CS cannot be used to predict the US. Thus, kainate receptor-dependent DA release in the absence of odors prevents the formation of inappropriate associations, whereas DA released upon coincident odor or shock stimulation of postsynaptic MB neurons through an independent mechanism reinforces associations. Previous studies have proposed mechanisms that allow postsynaptic mushroom body neurons to induce local DA release. Cervantes-Sandoval *et al.* (*49*) describe reciprocal synapses formed between mushroom body neurons and DA neurons where DANs receive cholinergic input from MB neurons, and ex vivo studies suggest that coincidentally activated MB neurons generate carbon monoxide that functions as a retrograde messenger to induce local DA release from presynaptic terminals (*45*, *50*). We hypothesize that both or either of these mechanisms may reinforce association in coincidentally activated MB neurons (fig. S10).

Although EG cover the entire MB neuropil, aversive stimuli do not cause EG to release glutamate to all MB compartments equally. Instead, vesicular exocytosis and glutamate release occur prominently in the peduncle,

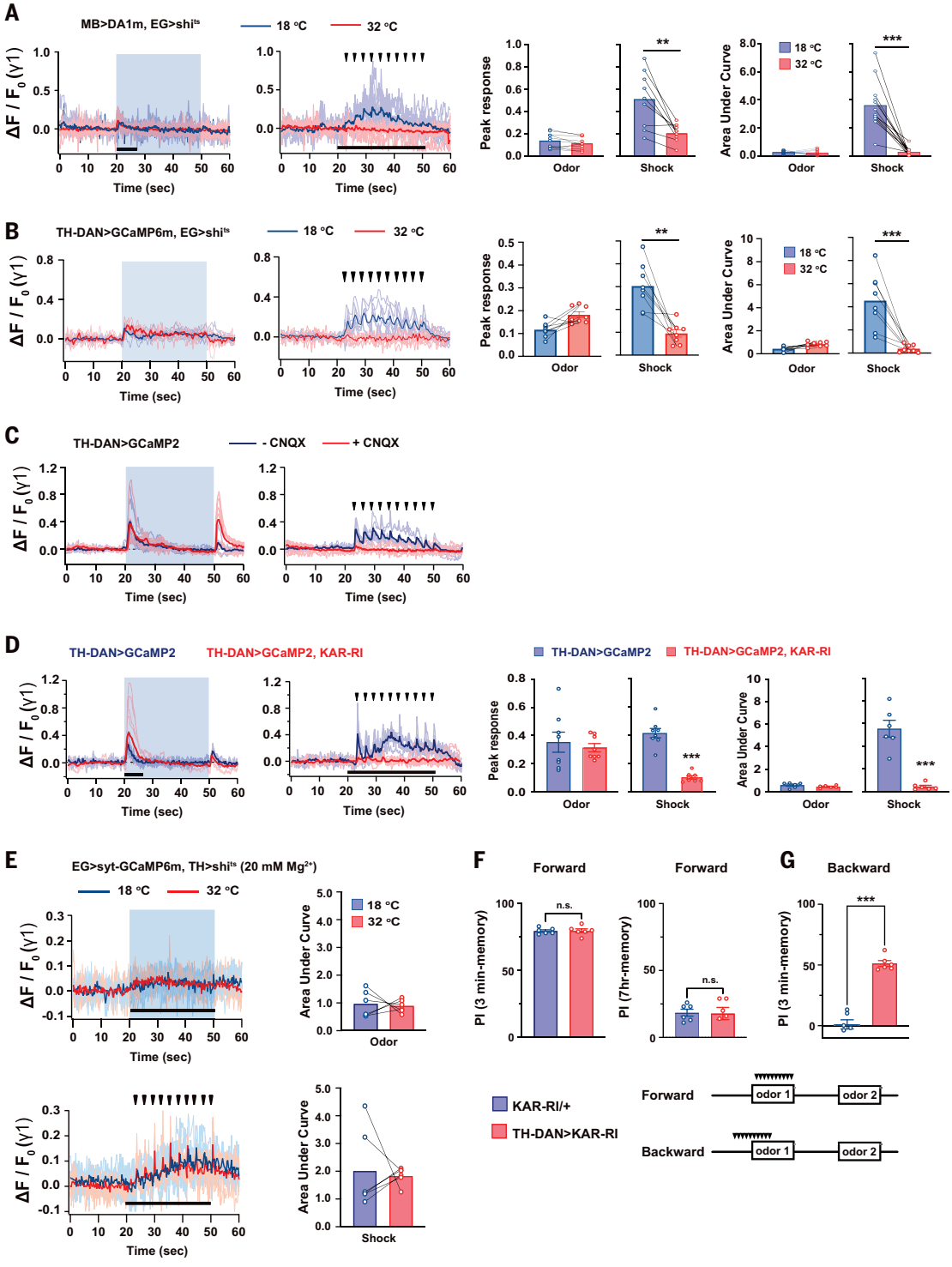

Fig. 6. EG regulates DA release upon shock presentation. (**A** and **B**) Blocking exocytosis from EG abolished shock-induced but not odor-induced DA release (A) and Ca^{2+} responses in DANs (B). (**C**) CNQX abolished shock-induced but not odor-induced Ca^{2+} responses in DANs. (**D**) Suppression of kainate receptors (KAR-RI) abolished shock-induced Ca^{2+} responses in DANs. (**E**) Blocking vesicular exocytosis from DANs did not affect Ca^{2+} responses in EG. (**F**) Three min of memory and 7 hours of memory after conventional forward conditioning were unaffected by suppressing kainate receptors in DANs. (**G**) Significant 3 min memory was formed after backward conditioning in TH-DNA>KAR-RI flies. $^{**}P < 0.01$; $^{***}P < 0.001$.

γ1, and γ5 compartments with little to no release in compartments such as γ3. These data are consistent with models assigning different valences to different MB compartments (*23*, *51*). In mammalian astrocytes, different activation pathways are known to produce distinct microdomain activity (*52*). Our current data support the idea that physiological and functionally relevant information is precisely arranged and processed in spatially different subclasses and subdomains of astrocytes (*53*–*55*).

Methods summary

Cloning DVGLUT2 cDNA

DVGLUT2 (CG4288) was amplified by means of polymerase chain reaction (PCR) by using the following primers: 5′-GGGGACAAGTTGTGTCAAAAGCAGCTTCCAAGCAGTTCGGATTCCAGT-3′, and 5′-GGGGACCACTTTGTACAAGAAAGCTGGGTCGACACAATGGTGCGCATATC-3′, and cloned into pDONR221 (Thermo Fisher Scientific).

Fly strains and generation of UAS-DVGLUT2::pHluorin flies

A *w* Canton-S line, *w*(*CS10*), was used as our wild-type line, and all transgenic lines used in our experiments were outcrossed to *w*(*CS10*)

at least six times (*56*). DVGLUT2::pHluorin was generated by inserting pHluorin into the first SV loop of DVGLUT2 as previously described for mammalian VGLUT2::pHluorin (*57*).

Immunoblotting and immunohistochemistry

Antibodies to DVGLUT2 peptide were generated in rabbits against the C-terminal sequence of DVGLUT2, CQLTQTAGFVNSGAELKD, and affinity purified. Antibodies were used for immunoblotting at 2.8 μg/ml and immunohistochemistry at 6.9 μg/ml. For synaptic-GRASP experiments, reconstituted GFP was detected by using antibody to GRASP (Sigma-Aldrich).

For electrical shock presentation, flies were placed in the electrical grid chamber and received 1.5-s pulses of 60-V electrical shocks for 1 min at 0.2 Hz. For aversive bitter taste presentation, flies were starved for 16 hours in vials containing Whatman paper saturated with water. Starved flies were then placed in vials containing Whatman paper saturated with 10 mM denatonium for 1 min. For reward sucrose presentation, starved flies were placed in vials containing Whatman paper with 2 M sucrose for 2 min. For noxious heat presentation, flies were placed in glass vials and immersed in a 42°C water bath for 1 min.

Glu uptake assays

The expression vector DVGLUT2/pET-28a(+) was constructed and transformed into *Escherichia coli* C43 (DE3) cells according to previously described protocols (*12*). Purified DVGLUT2 was reconstituted into proteoliposomes by using the freeze-thaw method, and L-Glu uptake was assayed using the gel-permeation procedure (*58*).

Electron microscopy

Fly brains were fixed with 2% paraformaldehyde (PFA) 0.1 M cacodylate buffer, pH 7.3 (CB) containing 2.5% glutaraldehyde and 15% saturated picric acid, postfixed with 2% osmium tetroxide in 0.1 M CB, and stained with 50% saturated uranyl acetate in 50% ethanol. Samples were dehydrated, polymerized in epoxy resin (EPON 812, TAAB), sectioned into coronal serial semithin sections (4 μm thickness), and stained with toluidine blue. Sections were embedded on glass microscope slides and polymerized in epoxy resin. A total of 40 to 60 ultrathin serial sections (50 to 80 nm thickness) were cut, stained with uranyl acetate and lead citrate, and observed under a transmission electron microscope (JEM-1400, JEOL, and H-7650, HITACHI).

Immunoelectron microscopy

Brains were fixed with 4% PFA in 0.1 M phosphate buffer containing 0.1% glutaraldehyde and 15% saturated picric acid, blocked with 10% Normal goat serum/0.05% NaN_3/PBST (phosphate buffered saline with Tween20), and incubated with rabbit antibody to DVGLUT2 peptide at 2.8 μg/ml. Samples were then incubated with colloidal gold [1:100, EM goat anti-rabbit immunoglobulin G (IgG), 20 nm, BB International) and enhanced by using a silver enhance kit (AURION R-Gent SE-EM, Aurion). Post-fixations were conducted with 1% osmium tetroxide in 0.1 M phosphate buffer, followed by dehydration in a graded series of ethanol and propylene oxide. Samples were embedded in epoxy resin (EPON 812, TAAB). Ultrathin sections were observed under a transmission electron microscope (JEM-1400, JEOL).

Quantification of Transcripts

Transcripts were quantified by means of real-time PCR (CFX96 C1000, Bio-Rad) as described previously (*59*).

Behavioral assays

Standard single-cycle aversive olfactory conditioning was performed as previously described (*56*, *60*). Two odors [3-octanol (OCT) and 4-methylcyclohexanol (MCH)] were used as CS. For conditioning with electrical shocks, the US of electrical shocks was paired with one of the odors and consisted of 1.5-s pulses of 60-V dc electric shocks. For conditioning with denatonium, flies were exposed to the CS+ odor in a training vial containing 10 mM denatonium for 1 min and then transferred to a training vial containing water, where they were exposed to the CS– odor for 1 min. To test for memory retention, flies were placed at the choice point of a T-maze in which they were exposed simultaneously to the CS+ (previously paired with the US) and CS– (unpaired with the US). A performance index (PI) was calculated by subtracting the percentage of flies that chose the CS+ from the percentage that chose the CS–. Peripheral control experiments, including odor acuity and shock reactivity assays, were performed as described previously (*56*, *60*).

For appetitive conditioning with sucrose, flies were first exposed to the CS– odor for 2 min and then transferred to a training vial containing 2 mM sucrose, where they were exposed to the CS+ odor for 2 min. Flies were tested as described above, and PIs were calculated by subtracting the percentage of flies that chose the CS– odor from the percentage that chose the CS+ odor.

For temperature shift experiments, flies were transferred to a room at 30°C 5 min before providing sensory stimuli, loaded into a preheated training chamber, and exposed to the CS+ odor for 1 min. Flies were then immediately transferred to a 20°C room, loaded into a 20°C training chamber, and exposed to the CS– odor for 1 min.

Functional imaging

Flies were immobilized in an imaging chamber, and the parietal cuticle was removed with a syringe needle to expose the brain. A recording solution [70 mM NaCl, 5 mM KCl, 10 mM $NaHCO_3$, 5 mM Hepes (pH 7.1), 5 mM Treharose, 115 mM Sucrose, 1.5 mM $CaCl_2$ and 20 mM $MgCl_2$] was used to cover the brain. For low-Mg^{2+} recording solution, 2 mM $MgCl_2$ was used instead of 20 mM. For functional imaging in the absence of added buffer, exposed brains were immediately covered with UV Curing Optical Adhesives (NOA68, Thorlabs) as described previously (*28*, *29*). For olfactory aversive conditioning, 60-V, 100-ms pulses of electric shock were applied to flies through a 50-kΩ resistor every 3 s while CS+ odor was pumped through the imaging chamber at 200 ml/min for 30 s.

Fluorescent images were captured at 4 Hz by use of a confocal microscope system. F_0 was calculated as the mean fluorescence intensity during the 10 s immediately before stimulation, and ΔF was defined as the difference between the F values at each time point. $\Delta F/F_0$ for DVGLUT2::pHluorin (vesicular exocytosis) and DA1m (DA responses) were measured similarly to measurements of $\Delta F/F_0$ for GCaMP (Ca^{2+} responses). To quantify stimulation-induced fluorescent changes, $\Delta F/F_0$ in the absence of stimulation was subtracted from $\Delta F/F_0$ at indicated time points during and after stimulation. MK-801 (Tocris), CPP (Tocris), and CNQX (Tocris) were used at a concentration of 100 μM, 1 mM, and 200 μM, respectively.

Statistics

All data in bar and line graphs are expressed as means ± SEMs; $n = 6$ to 12 independent assays for all data. Student's t test was used to evaluate the statistical significance between two data sets. For multiple comparisons, one-way or two-way analysis of variance was used, followed by post hoc analyses by use of Prism software (GraphPad Software) or XLtoolbox (Free Software Foundation). Statistical significance was indicated as $^*P < 0.05$, $^{**}P < 0.01$, and $^{***}P < 0.001$ and not significant for $P > 0.05$.

REFERENCES AND NOTES

1. M. Adel, L. C. Griffith, The role of dopamine in associative learning in *Drosophila*: An updated unified model. *Neurosci. Bull.* **37**, 831–852 (2021). doi: 10.1007/s12264-021-00665-0; pmid: 33779893
2. Y. Aso, G. M. Rubin, Dopaminergic neurons write and update memories with cell-type-specific rules. *eLife* **5**, e16135 (2016). doi: 10.7554/eLife.16135; pmid: 27441388
3. A. C. Keene, S. Waddell, Drosophila memory: Dopamine signals punishment? *Curr. Biol.* **15**, R932–R934 (2005). doi: 10.1016/j.cub.2005.10.058; pmid: 16303554
4. K. Ueno, S. Naganos, Y. Hirano, J. Horiuchi, M. Saitoe, Long-term enhancement of synaptic transmission between antennal lobe and mushroom body in cultured Drosophila brain. *J. Physiol.* **591**, 287–302 (2013). doi: 10.1113/jphysiol.2012.242909; pmid: 23027817
5. K. Ueno *et al.*, Coincident postsynaptic activity gates presynaptic dopamine release to induce plasticity in *Drosophila* mushroom bodies. *eLife* **6**, e21076 (2017). doi: 10.7554/eLife.21076; pmid: 28117664
6. R. W. Daniels, M. V. Gelfand, C. A. Collins, A. DiAntonio, Visualizing glutamatergic cell bodies and synapses in

Drosophila larval and adult CNS. *J. Comp. Neurol.* **508**, 131–152 (2008). doi: 10.1002/cne.21670; pmid: 18302156
7. S. Kondo *et al*., Neurochemical organization of the *Drosophila* brain visualized by endogenously tagged neurotransmitter receptors. *Cell Rep.* **30**, 284–297.e5 (2020). doi: 10.1016/j.celrep.2019.12.018; pmid: 31914394
8. T. Miyashita *et al*., Mg(2+) block of Drosophila NMDA receptors is required for long-term memory formation and CREB-dependent gene expression. *Neuron* **74**, 887–898 (2012). doi: 10.1016/j.neuron.2012.03.039; pmid: 22681692
9. S. Xia *et al*., NMDA receptors mediate olfactory learning and memory in Drosophila. *Curr. Biol.* **15**, 603–615 (2005). doi: 10.1016/j.cub.2005.02.059; pmid: 15823532
10. R. W. Daniels *et al*., Increased expression of the *Drosophila* vesicular glutamate transporter leads to excess glutamate release and a compensatory decrease in quantal content. *J. Neurosci.* **24**, 10466–10474 (2004). doi: 10.1523/JNEUROSCI.3001-04.2004; pmid: 15548661
11. N. Juge, Y. Yoshida, S. Yatsushiro, H. Omote, Y. Moriyama, Vesicular glutamate transporter contains two independent transport machineries. *J. Biol. Chem.* **281**, 39499–39506 (2006). doi: 10.1074/jbc.M607670200; pmid: 17046815
12. S. Leviatan, K. Sawada, Y. Moriyama, N. Nelson, Combinatorial method for overexpression of membrane proteins in *Escherichia coli*. *J. Biol. Chem.* **285**, 23548–23556 (2010). doi: 10.1074/jbc.M110.125492; pmid: 20525689
13. T. Awasaki, S. L. Lai, K. Ito, T. Lee, Organization and postembryonic development of glial cells in the adult central brain of *Drosophila*. *J. Neurosci.* **28**, 13742–13753 (2008). doi: 10.1523/JNEUROSCI.4844-08.2008; pmid: 19091965
14. M. C. Kremer, C. Jung, S. Batelli, G. M. Rubin, U. Gaul, The glia of the adult *Drosophila* nervous system. *Glia* **65**, 606–638 (2017). doi: 10.1002/glia.23115; pmid: 28133822
15. S. Y. Takemura *et al*., A connectome of a learning and memory center in the adult *Drosophila* brain. *eLife* **6**, e26975 (2017). doi: 10.7554/eLife.26975; pmid: 28718765
16. S. E. McGuire, Z. Mao, R. L. Davis, Spatiotemporal gene expression targeting with the TARGET and gene-switch systems in *Drosophila*. *Sci. STKE* **2004**, pl6 (2004). doi: 10.1126/stke.2202004pl6; pmid: 14970377
17. Z. Mao, G. Roman, L. Zong, R. L. Davis, Pharmacogenetic rescue in time and space of the rutabaga memory impairment by using Gene-Switch. *Proc. Natl. Acad. Sci. U.S.A.* **101**, 198–203 (2004). doi: 10.1073/pnas.0306128101; pmid: 14684832
18. T. Awasaki, T. Lee, New tools for the analysis of glial cell biology in *Drosophila*. *Glia* **59**, 1377–1386 (2011). doi: 10.1002/glia.21133; pmid: 21305614
19. T. Kitamoto, Conditional modification of behavior in *Drosophila* by targeted expression of a temperature-sensitive shibire allele in defined neurons. *J. Neurobiol.* **47**, 81–92 (2001). doi: 10.1002/neu.1018; pmid: 11291099
20. J. Dubnau, L. Grady, T. Kitamoto, T. Tully, Disruption of neurotransmission in *Drosophila* mushroom body blocks retrieval but not acquisition of memory. *Nature* **411**, 476–480 (2001). doi: 10.1038/35078077; pmid: 11373680
21. Y. D. Chen, S. J. Park, R. M. Joseph, W. W. Ja, A. A. Dahanukar, Combinatorial pharyngeal taste coding for feeding avoidance in adult *Drosophila*. *Cell Rep.* **29**, 961–973.e4 (2019). doi: 10.1016/j.celrep.2019.09.036; pmid: 31644916
22. L. J. Macpherson *et al*., Dynamic labelling of neural connections in multiple colours by trans-synaptic fluorescence complementation. *Nat. Commun.* **6**, 10024 (2015). doi: 10.1038/ncomms10024; pmid: 26635273
23. R. Cohn, I. Morantte, V. Ruta, Coordinated and compartmentalized neuromodulation shapes sensory processing in *Drosophila*. *Cell* **163**, 1742–1755 (2015). doi: 10.1016/j.cell.2015.11.019; pmid: 26687359
24. J. S. Marvin *et al*., Stability, affinity, and chromatic variants of the glutamate sensor iGluSnFR. *Nat. Methods* **15**, 936–939 (2018). doi: 10.1038/s41592-018-0171-3; pmid: 30377363
25. M. L. Mayer, G. L. Westbrook, P. B. Guthrie, Voltage-dependent block by Mg^{2+} of NMDA responses in spinal cord neurones. *Nature* **309**, 261–263 (1984). doi: 10.1038/309261a0; pmid: 6325946
26. L. Nowak, P. Bregestovski, P. Ascher, A. Herbet, A. Prochiantz, Magnesium gates glutamate-activated channels in mouse central neurones. *Nature* **307**, 462–465 (1984). doi: 10.1038/307462a0; pmid: 6320006
27. D. Raccuglia *et al*., Network-specific synchronization of electrical slow-wave oscillations regulates sleep drive in *Drosophila*. *Curr. Biol.* **29**, 3611–3621.e3 (2019). doi: 10.1016/j.cub.2019.08.070; pmid: 31630955
28. D. Grover, T. Katsuki, R. J. Greenspan, Flyception: Imaging brain activity in freely walking fruit flies. *Nat. Methods* **13**, 569–572 (2016). doi: 10.1038/nmeth.3866; pmid: 27183441
29. C. Huang *et al*., Long-term optical brain imaging in live adult fruit flies. *Nat. Commun.* **9**, 872 (2018). doi: 10.1038/s41467-018-02873-1; pmid: 29491443
30. F. N. Hamada *et al*., An internal thermal sensor controlling temperature preference in *Drosophila*. *Nature* **454**, 217–220 (2008). doi: 10.1038/nature07001; pmid: 18548007
31. T. Riemensperger, T. Völler, P. Stock, E. Buchner, A. Fiala, Punishment prediction by dopaminergic neurons in *Drosophila*. *Curr. Biol.* **15**, 1953–1960 (2005). doi: 10.1016/j.cub.2005.09.042; pmid: 16271874
32. S. Waddell, Dopamine reveals neural circuit mechanisms of fly memory. *Trends Neurosci.* **33**, 457–464 (2010). doi: 10.1016/j.tins.2010.07.001; pmid: 20701984
33. S. Waddell, Reinforcement signalling in *Drosophila*; dopamine does it all after all. *Curr. Opin. Neurobiol.* **23**, 324–329 (2013). doi: 10.1016/j.conb.2013.01.005; pmid: 23391527
34. F. Sun *et al*., A genetically encoded fluorescent sensor enables rapid and specific detection of dopamine in flies, fish, and mice. *Cell* **174**, 481–496.e19 (2018). doi: 10.1016/j.cell.2018.06.042; pmid: 30007419
35. M. Martin-Fernandez *et al*., Synapse-specific astrocyte gating of amygdala-related behavior. *Nat. Neurosci.* **20**, 1540–1548 (2017). doi: 10.1038/nn.4649; pmid: 28945222
36. A. Adamsky *et al*., Astrocytic Activation generates de novo neuronal potentiation and memory enhancement. *Cell* **174**, 59–71.e14 (2018). doi: 10.1016/j.cell.2018.05.002; pmid: 29804835
37. D. Yamazaki *et al*., Glial dysfunction causes age-related memory impairment in Drosophila. *Neuron* **84**, 753–763 (2014). doi: 10.1016/j.neuron.2014.09.039; pmid: 25447741
38. Z. Ma, T. Stork, D. E. Bergles, M. R. Freeman, Neuromodulators signal through astrocytes to alter neural circuit activity and behaviour. *Nature* **539**, 428–432 (2016). doi: 10.1038/nature20145; pmid: 27828941
39. A. Kol *et al*., Astrocytes contribute to remote memory formation by modulating hippocampal-cortical communication during learning. *Nat. Neurosci.* **23**, 1229–1239 (2020). doi: 10.1038/s41593-020-0679-6; pmid: 32747787
40. Y. Aso *et al*., Specific dopaminergic neurons for the formation of labile aversive memory. *Curr. Biol.* **20**, 1445–1451 (2010). doi: 10.1016/j.cub.2010.06.048; pmid: 20637624
41. A. Claridge-Chang *et al*., Writing memories with light-addressable reinforcement circuitry. *Cell* **139**, 405–415 (2009). doi: 10.1016/j.cell.2009.08.034; pmid: 19837039
42. M. Heisenberg, Mushroom body memoir: From maps to models. *Nat. Rev. Neurosci.* **4**, 266–275 (2003). doi: 10.1038/nrn1074; pmid: 12671643
43. Y. Aso *et al*., Three dopamine pathways induce aversive odor memories with different stability. *PLOS Genet.* **8**, e1002768 (2012). doi: 10.1371/journal.pgen.1002768; pmid: 22807684
44. J. Horiuchi, Recurrent loops: Incorporating prediction error and semantic/episodic theories into Drosophila associative memory models. *Genes Brain Behav.* **18**, e12567 (2019). doi: 10.1111/gbb.12567; pmid: 30891930
45. M. Saitoe, S. Naganos, T. Miyashita, M. Matsuno, K. Ueno, A non-canonical on-demand dopaminergic transmission underlying olfactory aversive learning. *Neurosci. Res.* **178**, 1–9 (2022). doi: 10.1016/j.neures.2021.12.008; pmid: 34973292
46. R. A. Campbell *et al*., Imaging a population code for odor identity in the *Drosophila* mushroom body. *J. Neurosci.* **33**, 10568–10581 (2013). doi: 10.1523/JNEUROSCI.0682-12.2013; pmid: 23785169
47. T. V. Bliss, G. L. Collingridge, A synaptic model of memory: Long-term potentiation in the hippocampus. *Nature* **361**, 31–39 (1993). doi: 10.1038/361031a0; pmid: 8421494
48. J. Z. Tsien, Linking Hebb's coincidence-detection to memory formation. *Curr. Opin. Neurobiol.* **10**, 266–273 (2000). doi: 10.1016/S0959-4388(00)00070-2; pmid: 10753792
49. I. Cervantes-Sandoval, A. Phan, M. Chakraborty, R. L. Davis, Reciprocal synapses between mushroom body and dopamine neurons form a positive feedback loop required for learning. *eLife* **6**, e23789 (2017). doi: 10.7554/eLife.23789; pmid: 28489528
50. K. Ueno *et al*., Carbon monoxide, a retrograde messenger generated in postsynaptic mushroom body neurons, evokes noncanonical dopamine release. *J. Neurosci.* **40**, 3533–3548 (2020). doi: 10.1523/JNEUROSCI.2378-19.2020; pmid: 32253360
51. Y. Aso *et al*., The neuronal architecture of the mushroom body provides a logic for associative learning. *eLife* **3**, e04577 (2014). doi: 10.7554/eLife.04577; pmid: 25535793
52. A. Agarwal *et al*., Transient opening of the mitochondrial permeability transition pore induces microdomain calcium transients in astrocyte processes. *Neuron* **93**, 587–605.e7 (2017). doi: 10.1016/j.neuron.2016.12.034; pmid: 28132831
53. S. Curreli, J. Bonato, S. Romanzi, S. Panzeri, T. Fellin, Complementary encoding of spatial information in hippocampal astrocytes. *PLOS Biol.* **20**, e3001530 (2022). doi: 10.1371/journal.pbio.3001530; pmid: 35239646
54. N. Bazargani, D. Attwell, Astrocyte calcium signaling: The third wave. *Nat. Neurosci.* **19**, 182–189 (2016). doi: 10.1038/nn.4201; pmid: 26814587
55. R. de Ceglia *et al*., Specialized astrocytes mediate glutamatergic gliotransmission in the CNS. *Nature* **622**, 120–129 (2023). doi: 10.1038/s41586-023-06502-w; pmid: 37674083
56. T. Tamura *et al*., Aging specifically impairs amnesiac-dependent memory in *Drosophila*. *Neuron* **40**, 1003–1011 (2003). doi: 10.1016/S0896-6273(03)00732-3; pmid: 14659098
57. S. M. Voglmaier *et al*., Distinct endocytic pathways control the rate and extent of synaptic vesicle protein recycling. *Neuron* **51**, 71–84 (2006). doi: 10.1016/j.neuron.2006.05.027; pmid: 16815333
58. N. Juge *et al*., Metabolic control of vesicular glutamate transport and release. *Neuron* **68**, 99–112 (2010). doi: 10.1016/j.neuron.2010.09.002; pmid: 20920794
59. T. Miyashita, E. Kikuchi, J. Horiuchi, M. Saitoe, Long-term memory engram cells are established by c-Fos/CREB transcriptional cycling. *Cell Rep.* **25**, 2716–2728.e3 (2018). doi: 10.1016/j.celrep.2018.11.022; pmid: 30517860
60. T. Tully, W. G. Quinn, Classical conditioning and retention in normal and mutant Drosophila melanogaster. *J. Comp. Physiol. A* **157**, 263–277 (1985). doi: 10.1007/BF01350033; pmid: 3939242

ACKNOWLEDGMENTS

We thank A. Rallis and S. Sweeny for *elav-Gal80* flies; T. Awasaki for Repo-Gal80 NP6520, NP2222, and NP1243 flies; T. Sakai for syt-GRASP flies; and Y. Li for DA1m flies. We thank T. Tabata, C. Yokoyama, and members of the Learning and Memory Project for critical discussions and comments for manuscript preparation. **Funding:** Grants awarded to M.S. are a Grant-in-Aid for Scientific Research in Innovative Areas "Memory dynamism" (MEXT KAKENHI, JP25115006), a Grant-in-Aid for Scientific Research (A) (JSPS KAKENHI, JP19H02013), and Takeda Science Foundation Grant. Grants awarded to T.Miyas. are a Grant-in-Aid for Scientific Research (C) (JSPS KAKENHI, JP17K07070) and a Grant-in-Aid for Scientific Research in Innovative Areas "Glia decoding" (MEXT KAKENHI, JP21H05642). **Author contributions:** Conceptualization and design: M.S. and T.Miyas. Behavioral experiments: T.Miyas., K.Mu., H.M., and E.K. Immunoblotting and immunohistochemistry: T.Miyas., E.K., and K.O. Functional imaging: T.Miyas. DVGLUT2::pHluorin generation: T.Miyas., E.K., and K.O.. Glu uptake assays: T.Miyaj., S.M., and Y.M. Electron microscopy: K.Mi., K.E., K.K., and M.W. Data analysis, manuscript writing, and editing: T.Miyas., J.H., and M.S. **Competing interests:** The authors declare that they have no competing interests. **Data and materials availability:** All data are available in the main text or the supplementary materials. All constructs and fly lines developed in this study are available upon request. **License information:** Copyright © 2023 the authors, some rights reserved; exclusive licensee American Association for the Advancement of Science. No claim to original US government works. https://www.science.org/about/science-licenses-journal-article-reuse

SUPPLEMENTARY MATERIALS

science.org/doi/10.1126/science.adf7429
Materials and Methods
Figs. S1 to S10
Table S1
References (*61*–*63*)
MDAR Reproducibility Checklist

Submitted 10 November 2022; accepted 20 October 2023
10.1126/science.adf7429

RESEARCH ARTICLE SUMMARY

TRANSCRIPTION

Structural visualization of transcription initiation in action

Xizi Chen†, Weida Liu†, Qianmin Wang†, Xinxin Wang†, Yulei Ren, Xuechun Qu, Wanjun Li, Yanhui Xu*

INTRODUCTION: To achieve sophisticated transcription regulation, eukaryotic RNA polymerase II (Pol II) does not open the core promoter by itself and requires general transcription factors (GTFs) (~38 polypeptides in total) to assemble a preinitiation complex (PIC). The PIC then sequentially transforms into an open-promoter PIC complex (OC), an initially transcribing complex (ITC), and an early elongation complex (EEC). Previous studies reported that notable functional and compositional changes occurred during these processes. However, the underlying molecular mechanisms remain largely elusive.

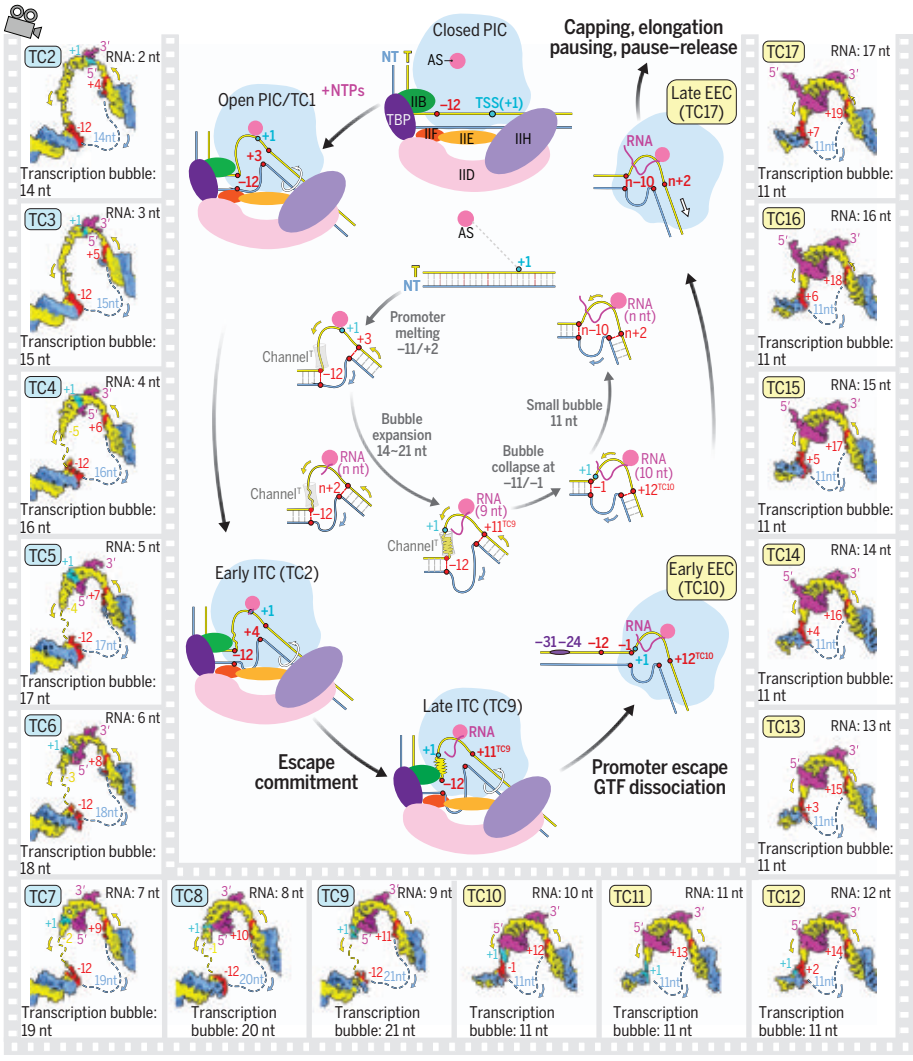
Closed PIC
Capping, elongation pausing, pause–release
Open PIC/TC1
+NTPs
Late EEC (TC17)
Promoter melting −11/+2
Bubble expansion 14–21 nt
Small bubble 11 nt
Bubble collapse at −11/−1
Early ITC (TC2)
Early EEC (TC10)
Late ITC (TC9)
Escape commitment
Promoter escape GTF dissociation
TC2 RNA: 2 nt Transcription bubble: 14 nt
TC3 RNA: 3 nt Transcription bubble: 15 nt
TC4 RNA: 4 nt Transcription bubble: 16 nt
TC5 RNA: 5 nt Transcription bubble: 17 nt
TC6 RNA: 6 nt Transcription bubble: 18 nt
TC7 RNA: 7 nt Transcription bubble: 19 nt
TC8 RNA: 8 nt Transcription bubble: 20 nt
TC9 RNA: 9 nt Transcription bubble: 21 nt
TC10 RNA: 10 nt Transcription bubble: 11 nt
TC11 RNA: 11 nt Transcription bubble: 11 nt
TC12 RNA: 12 nt Transcription bubble: 11 nt
TC13 RNA: 13 nt Transcription bubble: 11 nt
TC14 RNA: 14 nt Transcription bubble: 11 nt
TC15 RNA: 15 nt Transcription bubble: 11 nt
TC16 RNA: 16 nt Transcription bubble: 11 nt
TC17 RNA: 17 nt Transcription bubble: 11 nt

Schematic model of transcription initiation. Cryo-EM maps of nucleic acids are shown around the perimeter. Schematic models of representative complexes and nucleic acids are shown in the outer and inner rings of the central area, respectively. Functional states of Pol II and the transcription bubble are indicated. Directions of DNA translocation are indicated with arrows. IIB, IID, IIE, IIF, and IIH are transcription factors TFIIB, TFIID, TFIIE, TFIIF, and TFIIH, respectively. AS, active site of Pol II; NT, nontemplate strand; T, template strand; TBP, TATA box binding protein.

RATIONALE: We reconstituted the de novo transcribing complexes (TC2 to TC17) with Pol II halted on G-less promoters when nascent RNAs reach 2 to 17 nucleotides (nt) in length, respectively. We determined the cryo–electron microscopy (cryo-EM) structures and recapitulated the dynamic processes of transcription initiation by connecting structures of the PIC (Protein Data Bank ID 7EGB) and 16 TC complexes.

RESULTS: Structural analyses reveal marked complex reorganizations. Starting from the PIC, the GTF TFIIH couples the energy of adenosine triphosphate (ATP) hydrolysis to translocate the downstream promoter to Pol II, resulting in an OC that contains a transcription bubble of ~13 nt with the transcription start site (TSS) positioned at the active site. The OC then transforms into the ITC (TC2 to TC9), during which the upstream promoter and GTFs remain bound to Pol II, and thus the transcription bubble expands from 14 to 21 nt within the active center. The melted template strand guides the synthesis of nascent RNA, which increases its association with Pol II as it grows from 2 to 9 nt, which is correlated with a transition from abortive transcription to escape commitment. The differences between TC9 and TC10 reveal a sharp ITC-EEC transition and suggest that nucleoside triphosphate (NTP)–driven RNA-DNA translocation and template-strand accumulation in a nearly sealed channel may balloon out the channel, resulting in GTF dissociation, bubble collapse, and promoter escape. The structures of TC10 to TC17 reveal EEC conformation, indicating that Pol II escapes the initiation region and proceeds on the promoter, followed by pausing, RNA capping, pause-release, and productive elongation.

CONCLUSION: GTFs help Pol II open the core promoter through multiple interactions, which also create an obstacle to the escape of Pol II from the promoter and therefore must eventually be disrupted. Our study provides structural visualization of transcription initiation in action for understanding why and how transcription machinery undergoes such notable changes. ■

The list of author affiliations is available in the full article online.
*Corresponding author. Email: xuyh@fudan.edu.cn
†These authors contributed equally to this work.
Cite this article as X. Chen *et al.*, *Science* **382**, eadi5120 (2023). DOI: 10.1126/science.adi5120

READ THE FULL ARTICLE AT
https://doi.org/10.1126/science.adi5120

RESEARCH ARTICLE

TRANSCRIPTION

Structural visualization of transcription initiation in action

Xizi Chen[1,2]†, Weida Liu[1]†, Qianmin Wang[1]†, Xinxin Wang[1]†, Yulei Ren[1], Xuechun Qu[1], Wanjun Li[1], Yanhui Xu[1,2]*

Transcription initiation is a complex process, and its mechanism is incompletely understood. We determined the structures of de novo transcribing complexes TC2 to TC17 with RNA polymerase II halted on G-less promoters when nascent RNAs reach 2 to 17 nucleotides in length, respectively. Connecting these structures generated a movie and a working model. As initially synthesized RNA grows, general transcription factors (GTFs) remain bound to the promoter and the transcription bubble expands. Nucleoside triphosphate (NTP)–driven RNA-DNA translocation and template-strand accumulation in a nearly sealed channel may promote the transition from initially transcribing complexes (ITCs) (TC2 to TC9) to early elongation complexes (EECs) (TC10 to TC17). Our study shows dynamic processes of transcription initiation and reveals why ITCs require GTFs and bubble expansion for initial RNA synthesis, whereas EECs need GTF dissociation from the promoter and bubble collapse for promoter escape.

In eukaryotic cells, core promoters are made up of ~100 base pairs (bp), including elements that direct preinitiation complex (PIC) assembly and span the transcription start sites (TSSs) (*1*–*3*). Transcription initiation starts with the assembly of a PIC that consists of RNA polymerase II (Pol II) and general transcription factors (GTFs), including TFIIA, TFIIB, TFIID, TFIIE, TFIIF, and TFIIH (*4*–*6*). TFIID recognizes the core promoter through TATA box binding protein (TBP) and TBP-associated factors (TAFs) and recruits Pol II and other GTFs to assemble a closed-promoter PIC complex (CC). Adenosine triphosphate (ATP) hydrolysis of TFIIH results in the translocation of the downstream promoter to the Pol II active center. The PIC transforms into an open-promoter PIC complex (OC), which contains a transcription bubble with the template strand inserted into the Pol II active site to guide the synthesis of nascent RNA. Earlier structural studies revealed mechanisms of nucleoside triphosphate (NTP)–driven RNA growth and RNA-DNA translocation (*7*–*13*) as well as PIC assembly and promoter opening (*14*–*24*).

Extensive biochemical studies have shown marked functional and compositional changes at the early stage of transcription initiation. Briefly, an initially transcribing complex (ITC) is formed when RNA synthesis starts, and abortive initiation can be observed when RNAs are 2 or 3 nucleotides (nt) in length (*25*–*28*). Escape commitment has been proposed to occur when RNA reaches 4 nt long (*29*–*33*). When RNA is 7 to 10 nt long, the transcription bubble expands up to 17 or 18 nt, followed by an abrupt bubble collapse (*33*–*37*). Pol II will eventually break its contact with GTFs, escape from the promoter, and form an early elongation complex (EEC) (*38*, *39*). Although structures of reconstituted ITCs have been reported (*40*–*46*), these complexes were not started from a PIC but instead were assembled on artificial RNA-DNA hybrids that were formed by a mismatched transcription bubble in which the template strand paired with a synthetic complementary RNA. A recent study captured a structure of a yeast (*Saccharomyces cerevisiae*) backtracked ITC complex that started from a PIC (*47*). However, transcription initiation in yeast and mammals differs in various aspects. For example, yeast polymerase undergoes TSS scanning on the promoter for up to a hundred nucleotides (*48*, *49*), which does not occur in mammals.

Reported structures to date provide fragmented glimpses of complexes that have varying compositions and different promoters. The present understanding of de novo transcription initiation in mammals, including GTF dissociation, bubble expansion and abrupt collapse, and the ITC-EEC transition, is limited by inconsistencies across various experimental contexts and the lack of continuously captured structures of transcribing complexes in action. Despite decades of biochemical and structural studies, the underlying molecular mechanisms of these processes remain largely elusive.

[1]Fudan University Shanghai Cancer Center, Institutes of Biomedical Sciences, New Cornerstone Science Laboratory, State Key Laboratory of Genetic Engineering, Department of Biochemistry and Biophysics, School of Life Sciences, Shanghai Key Laboratory of Radiation Oncology, and Shanghai Key Laboratory of Medical Epigenetics, Shanghai Medical College of Fudan University, Shanghai 200032, China. [2]The International Co-laboratory of Medical Epigenetics and Metabolism, Ministry of Science and Technology, China, Department of Systems Biology for Medicine, School of Basic Medical Sciences, Shanghai Medical College of Fudan University, Shanghai 200032, China.
*Corresponding author. Email: xuyh@fudan.edu.cn
†These authors contributed equally to this work.

Results

In vitro reconstitution of de novo transcription initiation

To investigate de novo transcription initiation, we synthesized a series of modified super core promoters (SCPs) (Fig. 1A and data S1). Each promoter consists of an upstream TATA box, downstream TFIID-binding elements, and a G-less cassette between the putative TSS and a GG dinucleotide at varying positions on the nontemplate strand. The promoters are termed SCP^{nG}, with "n" denoting the G-stop position relative to the TSS, at which Pol II should stall if guanosine triphosphate (GTP) is not provided in the reaction. Mammalian Pol II and human GTFs were purified as previously described (*15*, *16*) (fig. S1A). The reactions of de novo transcription initiation were respectively performed on SCP^{3G} to SCP^{17G} promoters in the presence of ATP, uridine triphosphate (UTP), [α-^{32}P]-UTP, cytidine triphosphate (CTP), and chain-terminating 3′-*O*-methylguanosine-5′-triphosphate ($^{3'\text{-OM}}$GTP). Note that reaction on SCP^{2G} was not performed because the generated AG dinucleotide would lack a radioactive U nucleotide and would not be able to be detected.

The reaction on each SCP^{nG} promoter resulted in a predominant G-stop RNA of the expected length (Fig. 1B; fig. S1, B to E; and supplementary text). Reaction on SCP^{3G} generated the highest level of G-stop RNAs among all the reactions, and reactions on SCP^{4G} to SCP^{6G} generated much more abundant G-stop RNAs compared with the reactions on SCP^{7G} to SCP^{17G}. This suggests that short (3 to 6 nt) "dead-end" G-stop products are unstable and dissociate more frequently from the halted Pol II, which allows for multiple cycles of transcription initiation. RNA products longer than 6 nt remain stably bound to Pol II for up to one round of initiation.

We observed two short RNA products of ~2 to 4 nt in length (Fig. 1B; fig. S1, B to E; and supplementary text). The RNA products at the lower position largely accumulated in the presence of TFIIS (fig. S1D), which suggests that these short RNAs were derived from backtracked complexes, in which nascent RNAs backtracked to the active site by several nucleotides followed by RNA cleavage. A time-course reaction on SCP^{17G} showed an accumulation of RNAs at a position above the cleaved RNAs (fig. S1D), which suggests that these RNAs are abortive products that have dissociated from the transcribing complexes. Reactions on SCP^{nG} and G-less–containing adenovirus major late (AdML)$^{9G/10G}$ promoters under similar conditions generated similar heterogeneous RNA products that resulted from abortive transcription, cleaved RNAs from backtracked complexes, alternative TSS selection, and readthrough transcription (Fig. 1B and fig. S1, B to E). This result generally agrees with earlier in vitro transcription reactions on the AdML promoter (*26*–*28*, *33*) and

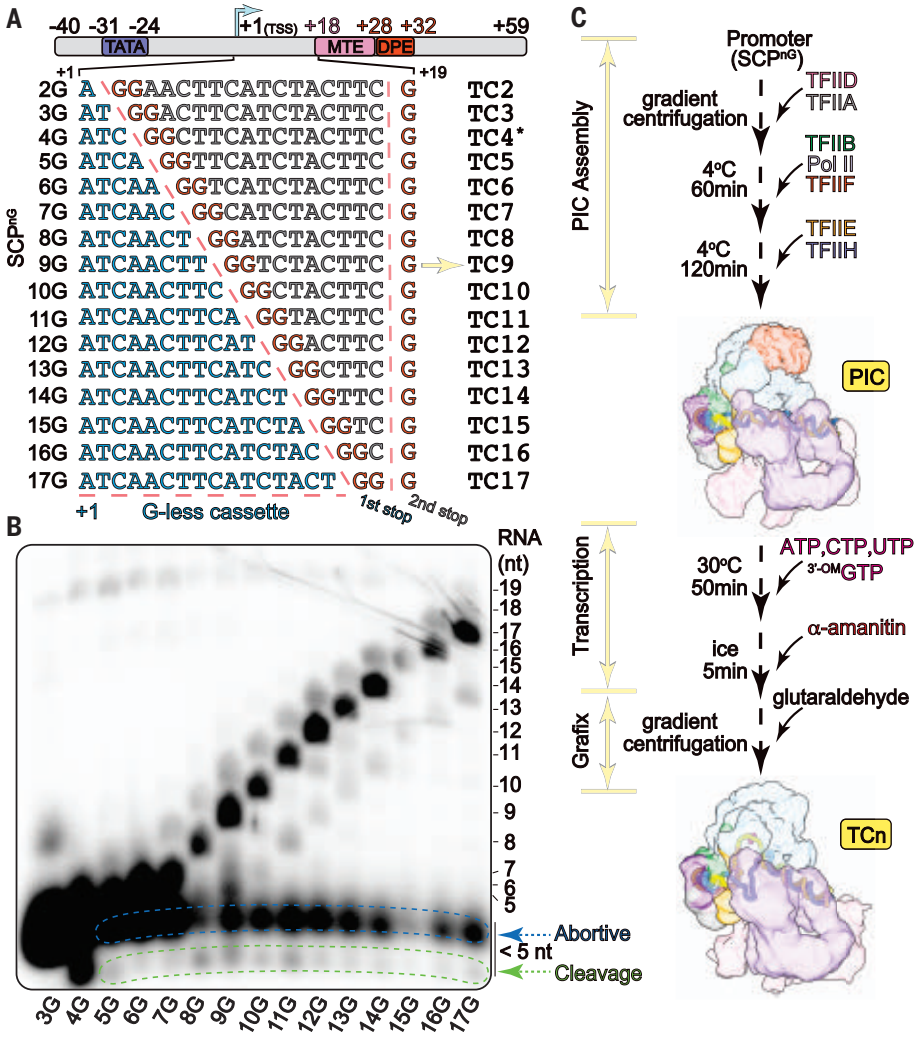

Fig. 1. In vitro reconstitution of de novo transcribing complexes. (**A**) Schematic diagram of SCP^{nG} promoters. The numbers above the promoter represent the positions relative to the TSS (+1). The GG dinucleotide at position "n" and the G nucleotide at +19 provide the first and second (if readthrough occurs) G-stop sites for Pol II. TCn represents the assembled transcribing complex on the indicated SCP^{nG} promoter. The asterisk indicates that TC4 on SCP^{4G} was used for the transcription assay and TC4 on SCP^{4G} mutant promoter was used for the structural study (fig. S1 and supplementary text). (**B**) In vitro transcription initiation assay. RNA products from one of the two independent experiments were visualized by autoradiography. The positions of abortive RNA and cleaved RNA from backtracked complexes are indicated. (**C**) Schematic diagram of the assembly of transcribing complexes. Transparent cryo-EM maps of the PIC and a representative TC show the changes in the promoter that is embedded within the complexes.

reported RNA heterogeneity in transcription initiation (*50*–*52*).

Structure determination

To visualize transcription initiation in action, we used SCP^{2G} to SCP^{17G} promoters to assemble de novo transcribing complexes termed TC2 to TC17, respectively (Fig. 1C). TC2 represents an ITC that forms the first RNA phosphodiester bond. TC17 was chosen as the last complex because a nascent RNA longer than 17 nt emerges from Pol II (*53*). TC4 was assembled on a SCP^{4G} mutant promoter that generated a better-resolved structure (see supplementary text). For each complex assembly, we first assembled a PIC on an SCP^{nG} promoter as previously described (*15*, *16*). We then added ATP, CTP, UTP, and $^{3'\text{-OM}}$GTP to start transcription initiation, which was followed by the addition of the mushroom toxin α-amanitin to inhibit the leaky activity of chain elongation. The reaction products were subjected to gradient fixation and cryo–electron microscopy (cryo-EM) structure determination (fig. S2 and data S2 to S4).

These transcribing complexes showed marked structural heterogeneity (fig. S2, data S2 to S4, and supplementary text), consistent with results from our in vitro assay (Fig. 1B and fig. S1, B to E) and earlier observations (*30*, *54*–*56*). However, RNA heterogeneity in the reactions does not necessarily correlate precisely with complex heterogeneity for structural studies because the latter represents a snapshot of the reaction at a specific point in time. For example, we found neither abortive complexes nor backtracked complexes in our cryo-EM data processing, likely owing to the following reason. Cryo-EM samples were prepared by freezing reaction products 50 min after the addition of NTP. DNA translocation and RNA synthesis were further inhibited by the addition of $^{3'\text{-OM}}$GTP and α-amanitin. By contrast, abortive and backtracked complexes were transient and unlikely to accumulate in the reactions. Even though small quantities of these complexes might exist in the samples, minor differences in nucleic acids were not sufficient to distinguish them from TC complexes in cryo-EM three-dimensional (3D) classification.

To obtain structures at high resolution, we collected a large amount of data (580,409 images in total) with a 300-kV Titan Krios G3 microscope over ~110 days. Cryo-EM 3D classification and comparison defined particles that were used for the reconstruction of the TC2 to TC17 complexes (summarized in data S4). Cryo-EM maps of most of the complexes revealed Pol II at a resolution of 2.7 to 3.3 Å and well-ordered RNA-DNA hybrids in the active center (fig. S3 and data S2). Nucleic acids, Pol II, and TFIIF were modeled in all the complexes. Other GTFs were modeled by docking the structure templates into the cryo-EM maps of TC2 to TC9 but were not modeled in TC10 to TC17 because of high flexibility.

Overall structures of ITCs and EECs

Dynamic processes of transcription initiation can be recapitulated by connecting structures of the PIC (*16*) and the transcribing complexes from TC2 to TC17 (Fig. 2A, Movie 1, and movie S1). As detailed later in the text and in Figs. 3 to 6, TC2 to TC9 represent ITCs correlated with abortive transcription and escape commitment. TC10 to TC17 represent EECs correlated with promoter escape. The differences between TC9 and TC10 suggest a sharp transition from the ITC to the EEC that is correlated with bubble collapse and GTF dissociation.

Structures of TC2 to TC9 reveal a similar overall architecture of the ITC (Fig. 2, A to C; fig. S4; movies S2 to S4; and supplementary text). Similar to what occurs in the PIC (*16*), GTFs remain bound to Pol II and the TATA box is bent by TBP. The following promoter region at −23 to −12 (−23/−12) is stabilized by the TFIIB N-terminal core domain (B-core-N), the TFIIB linker (B-linker), the TFIIF winged-helix domain (WH^{TFIIF}), and the Pol II protrusion. The upstream edge of the transcription bubble remains fixed at position −12 throughout TC2 to TC9. By contrast, the downstream edge of the transcription bubble is located at position n+2 in the TCn complex, which is

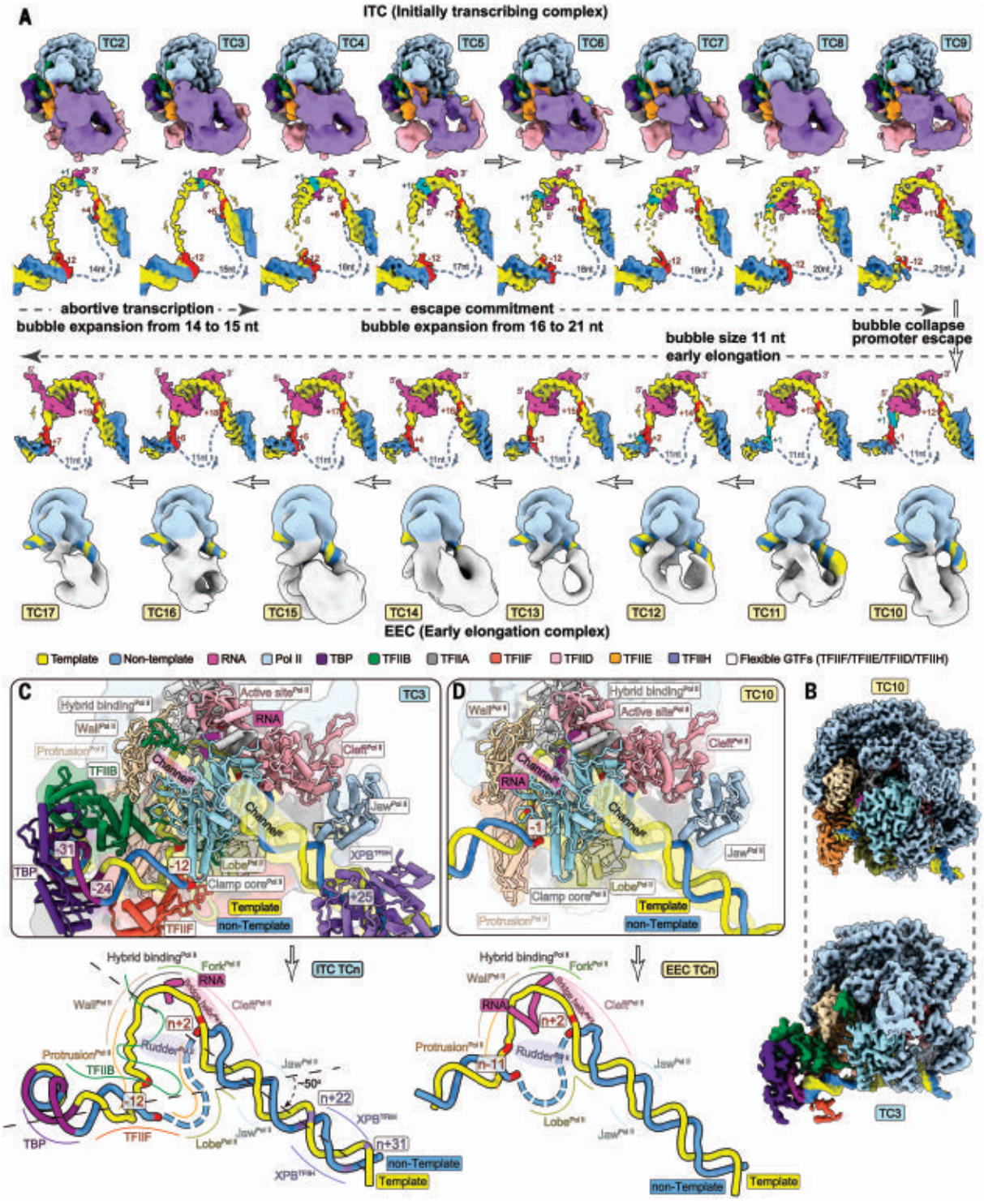

Fig. 2. Structures of the ITC and EEC. (**A**) Overall cryo-EM maps of TCn complexes and close-up views of nucleic acids. The color scheme is indicated at the bottom of the panel. The directions of strand translocation are indicated with arrows. The middle arrows indicate the functional states of Pol II and the transcription bubble. (**B**) Locally refined cryo-EM maps of Pol II, including Pol II, nucleic acids, and closely bound GTFs, in representative ITC and EEC complexes. (**C** and **D**) Close-up views of ITC (C) and EEC (D) structural models show protein-promoter interactions (top) and promoter conformations (bottom).

indicative of the continuous insertion of the downstream promoter into the active center. The promoter downstream of n+2 remains a straight double helix and is tilted by ~50° relative to the upstream duplex. The downstream promoter at n+2/n+11 inserts into the open DNA entry channel (channel^{E}). TFIIH binds the downstream promoter at n+22/n+31, consistent with its role early in transcription initiation (*25*, *57*–*61*), which is dependent on the downstream promoter regions (*62*). Nascent RNA pairs with the template strand to form an RNA-DNA hybrid in the active center.

Cryo-EM maps of TC10 to TC17 show similar organization of the EEC (Fig. 2, A, B, and D;

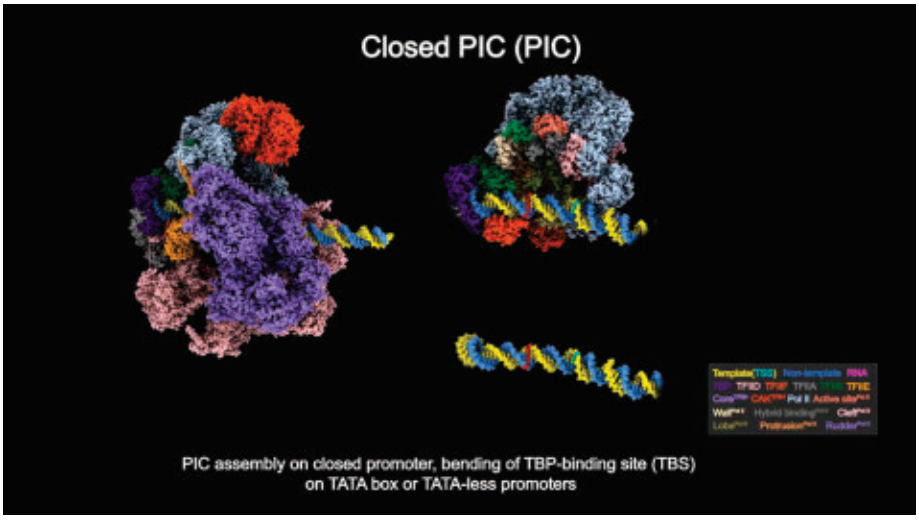

Movie 1. A movie of transcription initiation. The movie was generated by connecting structures of the PIC (*16*) and TC2 to TC17 and shows the movements of Pol II relative to the upstream promoter. The image on the left shows the full complex. The images at the upper right show an omitted structure and a cross-sectional view of the complex. The image at the bottom right shows nucleic acids. The color scheme is also shown at the bottom right. Brief descriptions of each state are included at the bottom of the screen.

fig. S5; and movies S2 to S4). The RNA-DNA hybrid was well stabilized within the Pol II activity center, and a weak density of flanking RNA was observed in an open RNA exit channel (channel^{R}). The flanking upstream and downstream double-stranded promoter regions are flexible owing to the lack of stabilization by GTFs, which nearly dissociate from the promoter (Fig. 2B and fig. S5A). The TFIIF dimerization module and TFIIE remain bound to Pol II. The remaining GTFs, including TFIID (with TBP), TFIIA, TFIIB, and TFIIH, are either completely dissociated from or flexibly tethered to Pol II through the associations of TFIIF, TFIIE, and/or the exposed promoter elements. The flexibility of GTFs in the EEC may also explain seemingly inconsistent observations of GTFs on transcribing complexes, which vary under different experimental conditions (*38*, *39*, *63*–*65*). Thus, Pol II is no longer restrained by the upstream promoter-bound GTFs and is free to move forward and escape the promoter. Here, GTF dissociation refers to a dissociation from the promoter but not from Pol II.

The transition from the PIC to the early ITC

Compared to the PIC (*16*), the ITC shows the following structural differences (Fig. 3, Movie 1, fig. S6, and movie S1): The downstream promoter is tilted by ~30° relative to that of the PIC, leading to slight displacement and rotation of the TFIIH core module and the TFIIH-associated TFIID away from Pol II. The cyclin-dependent kinase (CDK) activating kinase (CAK) module of TFIIH was not observed, in agreement with the requirement that the TFIIH core be in a proper position for loading CAK to Pol II (*16*). The Pol II active center is occupied by the melted promoter, and the ITC exhibits a slight expansion in the direction of the DNA axis while becoming more compact in the vertical direction (as in Fig. 3B). TBP, the B-core-N, and the Pol II protrusion are slightly displaced toward the upstream direction, whereas the Pol II lobe moves toward the downstream direction. The clamp head and clamp helices move toward the lobe by up to 11 Å. The clamp-associated rudder and B-linker are more ordered and may contribute to stabilizing the melted promoter. These domains and motifs would generate steric clashes with a closed promoter, which suggests their roles in maintaining the promoter in an open conformation.

Early-stage transcription initiation is recapitulated by connecting structures from the PIC to TC3 (Figs. 3C and 6, Movie 1, and movie S1). Because Pol II by itself does not appear to efficiently open linear promoter DNA, the DNA translocase XPB of TFIIH couples the energy of ATP hydrolysis to rotation and translocation of the downstream promoter to Pol II, resulting in promoter melting and displacement of the TSS by ~45 Å. The downstream promoter inserts into Pol II by translocation of ~16 bp, as measured by the displacement of the Pol II jaw-contacting point of the promoter, which is +5 in the PIC and +20 in TC3. This suggests an estimated insertion of 13 or 14 bp during the transition from the PIC to the OC. TFIIH-generated torque for promoter melting would be counteracted by rotation and translocation of the upstream promoter if it were not restrained otherwise by Pol II–bound B-core-N, TBP, and WH^{TFIIF}. Thus, extensive interactions among promoter, Pol II, and GTFs provide an integrated framework to open the promoter and maintain the open conformation. After OC formation, the melted template strand guides Pol II to synthesize the first phosphodiester bond of nascent RNA, followed by cycles of nucleotide addition, RNA chain extension, and RNA-DNA hybrid translocation (*66*, *67*).

TFIIH is required for efficient transcription initiation

TFIIH is required for transcription initiation (*58*, *61*) but may be dispensable for promoter opening or transcription initiation under certain experimental contexts (*24*, *68*–*70*). To test the effect of TFIIH in transcription initiation, we performed an in vitro transcription assay on representative templates (SCP^{4G}, SCP^{9G}, SCP^{10G}, and SCP^{17G}) in the presence and absence of TFIIH individually (fig. S1E). TFIIH supported the generation of G-stop RNAs, whereas the reactions in the absence of TFIIH showed largely decreased amounts of G-stop RNAs. Thus, TFIIH is essential for efficient in vitro transcription initiation. Transcription initiation did occur in the absence of TFIIH, albeit much less efficiently. The results may reconcile earlier studies that appeared to be controversial and suggest a context-dependent effect of TFIIH on transcription.

The absence of TFIIH led to only a slight decrease in the level of abortive RNAs, in sharp contrast to the largely decreased level of G-stop RNAs, which is indicative of an increase in the abortive/productive ratio (fig. S1E). Such an incremental abortive/productive ratio suggests that TFIIH may not only facilitate promoter opening but also prevent bubble reannealing (leading to RNA dissociation) in the early stage of transcription initiation. In the absence of TFIIH, nascent RNAs are more inclined to dissociate from Pol II to become abortive RNAs rather than productive RNAs. This observation agrees with the proposed function of TFIIH in pumping the downstream promoter to the active site, potentially aiding the formation and stabilization of the transcription bubble (*25*, *57*–*62*). This phenomenon also accounts for the discrepancy between eukaryotic Pol II, which exhibits a much lower abortive/productive ratio, and bacterial RNA polymerase (RNAP), which has no TFIIH equivalent and is characterized by a high abortive/productive ratio (*71*, *72*).

RNA-DNA hybrid stability is correlated with abortive transcription, escape commitment, and promoter escape

Throughout all the structures, Pol II adopts a posttranslocation state with $^{3'\text{-OM}}$GMP at the 3′ end of the RNA paired with the first downstream cytosine at position +n of the template strand (Fig. 4, A and B; figs. S7 and S8; and supplementary text). At the nucleotide addition (A) site, a free $^{3'\text{-OM}}$GTP pairs with the second downstream cytosine at position n+1 of the template strand. The melted template strand exhibits a helical fold with phosphate

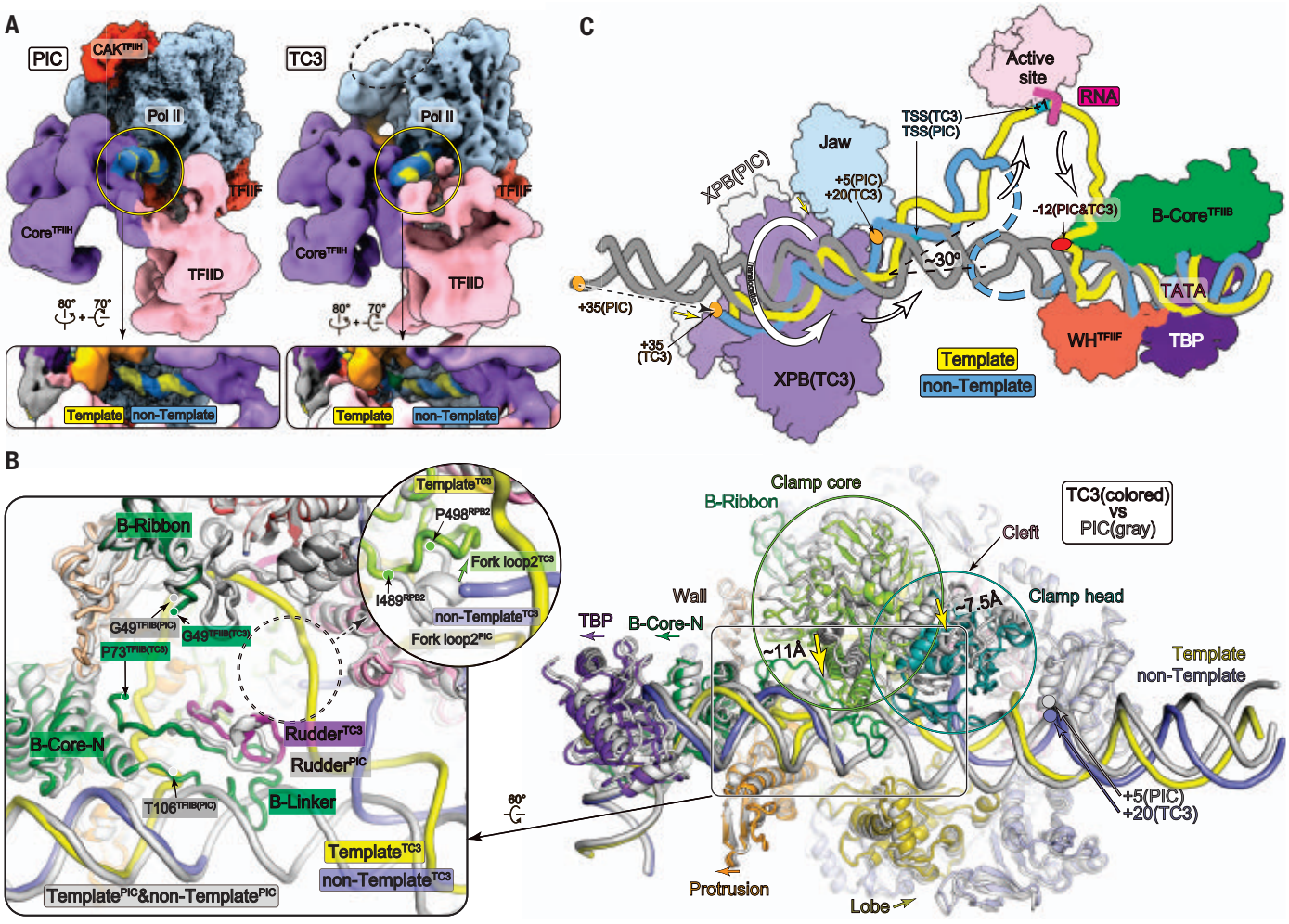

Fig. 3. The transition from the PIC to the early ITC. (**A**) Cryo-EM maps of the PIC (*16*) (top left) and a representative early ITC (TC3) (top right) shown with Pol II in a similar orientation. Close-up views of the promoters in the closed (bottom left) and open (bottom right) conformations are also shown. CAK is positioned on the Pol II surface in the PIC but is absent in TC3, as indicated by the white dashed oval. Although TC2 is almost identical to TC3, it has a less-stable RNA and thus was not used for comparison. (**B**) Superimposition of the PIC and TC3 structures with conformational differences indicated by arrows, from PIC to TC3 (right). Close-up views of the differences are shown on the left. The circular close-up view shows fork loop 2 near the active site, which moves toward the bridge helix to avoid a clash with the melted nontemplate strand. (**C**) A model of the PIC-ITC transition, with molecular motions indicated with arrows. The closed promoter and XPB subunit in the PIC are colored gray. Molecules in the ITC are colored as indicated. Single-letter abbreviations for the amino acid residues are as follows: G,Gly; I, Ile; P, Pro; and T, Thr.

backbone packing against a positively charged path of the active center cleft. In TCn structures, the RNA-DNA hybrids within the active center adopt a conformation similar to that of the elongation complex (EC) (fig. S8, B and C). Conformational variations exist at the single-stranded template strand outside of the active center and the 5′ flanking nucleotides of nascent RNA, which are flexible owing to the lack of stabilization.

RNA density is weak in TC2 and TC3 (Figs. 2A and 4B and movie S4), consistent with extensive abortive transcription on the SCP^{3G} promoter (Fig. 1B and fig. S1B). The short dead-end RNAs are prone to dissociate from the halted Pol II as a result of less stabilization by the template strand and Pol II. RNA dissociation may allow the unpaired template strand to retreat and guide a new cycle of RNA synthesis.

As the length of the RNA increases in complexes TC4 to TC9, cryo-EM maps of the RNA-DNA hybrid tend to be better resolved (Figs. 2A and 4B and movie S4), which is indicative of a metastable RNA-DNA hybrid correlated with escape commitment and a marked decrease in abortive initiation (*29*–*33*) (Fig. 1B and fig. S1B). Longer RNA makes more contact with the template strand and the Pol II active center cleft, which is rich in positively charged residues. We did not observe conformational differences in the Pol II active centers of TC2 to TC9. Thus, the transition from abortive transcription to escape commitment may result from an increase in RNA length rather than the proposed conformational changes of the transcribing complex (*31*).

TC10 to TC17 structures reveal well-ordered 10-bp RNA-DNA hybrids in the active center similar to those of EC structures (*11*, *73*), consistent with a stable RNA binding and promoter escape (Fig. 2A, figs. S5 and S8, and movie S4). The nascent RNA protrudes out of the active center, winds through the open channel^{R}, and touches the Pol II dock (fig. S5C). Cryo-EM maps show the growth of RNA in TC10 to TC13 (fig. S5F). However, only 13 nt could be visualized in TC14 to TC17, and the 5′ flanking nucleotides were flexible owing to the lack of stabilization.

The B-finger touches the 5′ end of nascent RNA in the early ITC

Cryo-EM maps of the early ITC show a putative TFIIB finger (B-finger, residues 50 to 72,

also known as B-reader) in the Pol II active center (Fig. 4, B and C; and fig. S9), which has been biochemically detected (*74*, *75*) and structurally observed (*24*, *40*, *43*–*46*). The B-finger of TC3 contacts the template strand at position −2/−3 and touches the 5′ end of nascent RNA, showing an insertion in the active center deeper than that of the previously reported structures (*40*, *43*–*46*). The B-finger in TC2 to TC6 is more separated from the active site and less stable as the RNA chain grows and is invisible in TC7 to TC9, which suggests a gradual

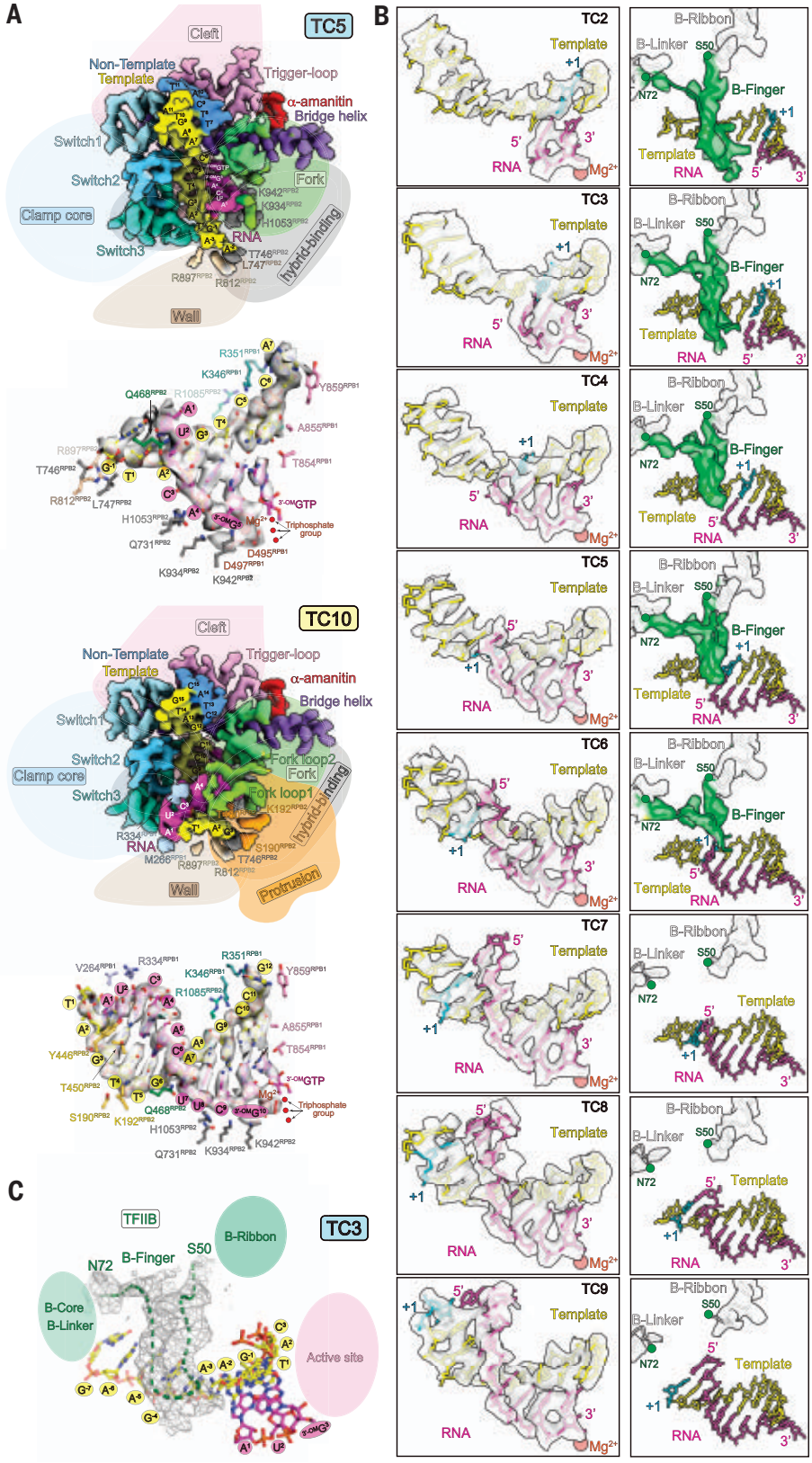

Fig. 4. RNA-DNA hybrid and the B-finger in the active center. (**A**) Cryo-EM maps of the active center of TC5 and TC10, which are representative ITC and EEC complexes, respectively. Because the active center is deeply buried, surrounding modules are simplified as background. Close-up views show RNA-DNA hybrid and Pol II residues that contribute to hybrid stabilization. Nucleic acids of the template strand and nascent RNA are numbered relative to the TSS. (**B**) Transparent cryo-EM maps of the RNA-DNA hybrid (left) and B-finger (right) in TC2 to TC9. Cryo-EM maps of the B-ribbon and B-linker are shown to mark the B-finger boundaries [residues Ser^{50} (S50) and Asn^{72} (N72)] that remain similarly positioned throughout TC2 to TC9. The structural model of the B-finger was not built, and a putative trace is shown instead. Cryo-EM density of the B-finger is more upwardly positioned from TC2 to TC6 and is invisible in TC7 to TC9. (**C**) Cryo-EM map of the B-finger and structural model of the RNA-DNA hybrid in TC3. Single-letter abbreviations for the amino acid residues are as follows: A, Ala; D, Asp; H, His; K, Lys; L, Leu; M, Met; Q, Gln; R, Arg; S, Ser; T, Thr; V, Val; and Y, Tyr.

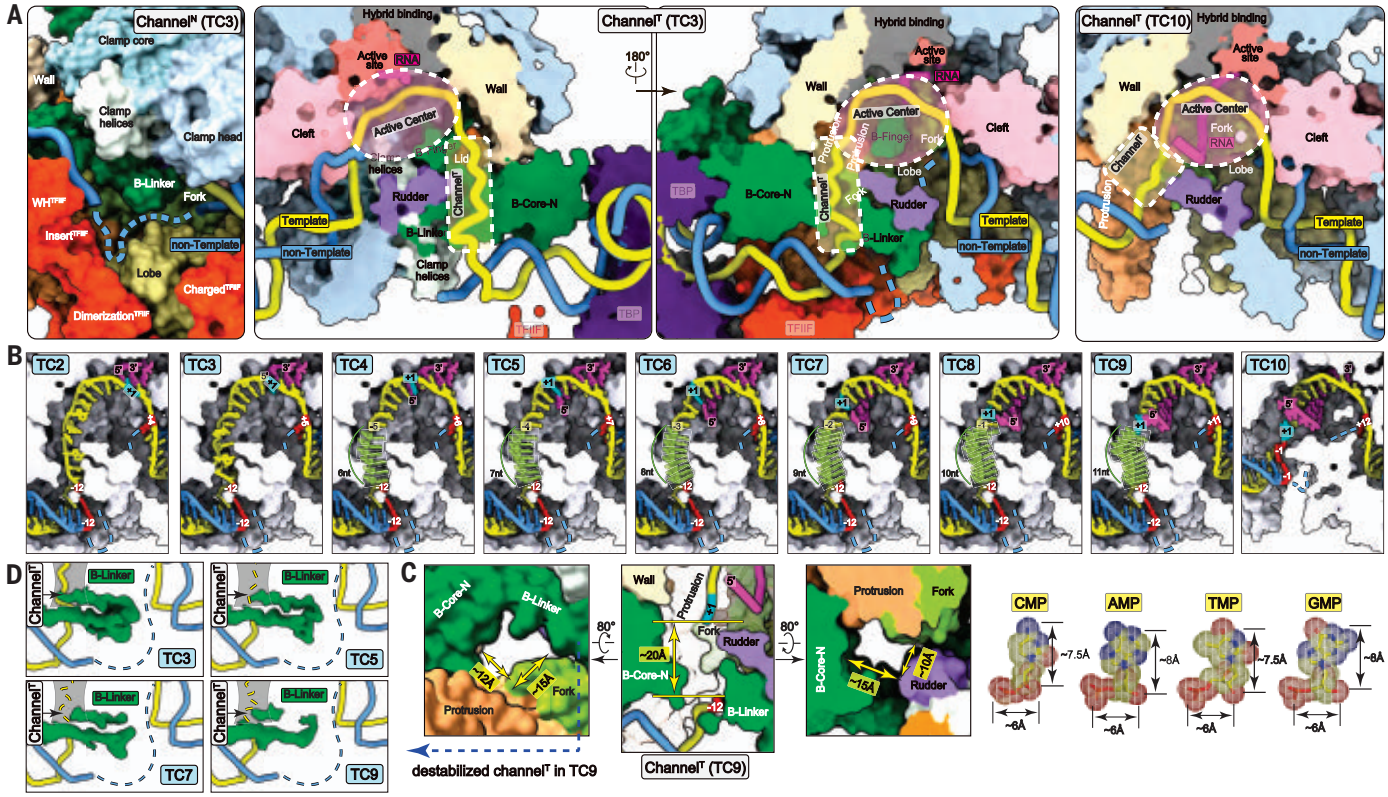

Fig. 5. Template strand accumulation in channel^T and the ITC-EEC transition. (**A**) Cross-sectional views of the open channel^N of TC3 (left), the narrow channel^T of TC3 in two different views (middle), and the expended channel^T of TC10 (right). Proteins and nucleic acids are shown in surface and cartoon representations, respectively. The active center and channel^T are circled by white dashed lines. The invisible regions of the nontemplate strand are shown as dashed lines. (**B**) Cross-sectional views of channel^T in TC2 to TC10 for comparison. DNA and RNA are shown in stick representation. The channel^T is narrow in TC2 to TC9 and largely expanded in TC10. Accumulation of the disordered template strand in channel^T of the ITC (TC4 to TC9) is diagramed with green transparent nucleic acids. Each nontemplate strand is shown as a dashed line, and channel^N is covered in this view. Cryo-EM maps of nucleic acids are shown in fig. S10C. (**C**) Estimated dimensions of channel^T and nucleotides for comparison. Channel^T is shown in three different views. The blue dashed arrow indicates the position of the B-linker in (D). (**D**) Destabilization of the B-linker at the gate of channel^T in TC9. Cryo-EM maps of the B-linker of TC3, TC5, TC7, and TC9 are shown in comparable contour levels and are colored in green.

retreat out of the active center. As evidenced by its reported effects on transcription activity and TSS selection (including TSS scanning in yeast) (*35*, *52*, *76*–*80*), the placement of the B-finger in the early ITC suggests its supportive role in efficient initiation and promoting the stability of early ITCs.

Exit channels of the template and nontemplate strands

The melted template and nontemplate strands occupy otherwise empty channels, termed channel^T and channel^N, respectively (Fig. 5 and fig. S10). As exemplified by TC3 and TC17 structures, the weak but noticeable density of the nontemplate strand winds over an open channel^N formed by the Pol II lobe, clamp, and protrusion, which is generally similar to that of the Pol II EC (*11*, *73*) and the Pol III pretermination complex (*81*). Consistent with the architecture of the open channel^N, the melted nontemplate strand is highly flexible and less restricted. This is a conserved feature in eukaryotic Pol II and differs from bacterial RNAP, in which the σ factor restrains the nontemplate strand and regulates transcription initiation (*82*, *83*).

The cross-sectional view of the ITC shows that the active center merges with the narrow channel^T formed by the B-core-N, the B-linker, and the Pol II active center cleft, hybrid binding, protrusion, rudder, lid, wall, and clamp helices (Fig. 5, A and B; and fig. S10C). The channel^T is nearly sealed, with two ends capped by the RNA-DNA hybrid and the upstream DNA duplex. The narrow channel^T may support the placement of the template strand in the active center that is necessary for RNA synthesis in the early ITC. Compared with the empty channel^T of the PIC, the DNA-occupied channel^T of the ITC is slightly enlarged by the displacement of Pol II protrusion and B-core-N (Fig. 3B), which suggests an adjustable size based on the molecules inside.

In the EEC, TFIIB is invisible and the channel^T is no longer sealed and serves as a wide and short extension of the active center (Fig. 5, A and B; and fig. S10C). The expended channel^T is similar to that of the Pol II EC (*11*, *73*) (fig. S5E). The transcription bubble is maintained in a fixed length of 11 nt, with the upstream (n–10) and downstream (n+2) edges stabilized by the Pol II rudder and bridge helix, respectively (Figs. 2, A and C, and 5; and fig. S4).

The transition from the ITC to the EEC is correlated with GTF dissociation, bubble collapse, and promoter escape

Comparison of the TC9 and TC10 structures with Pol II superimposed suggests considerable conformational changes in the ITC-EEC transition (Figs. 2 and 6, Movie 1, fig. S11, and movie S1). In TC10, the channel^T is largely expanded, and extensive contacts between GTFs and Pol II are lost. The template and nontemplate strands at −11/−1 collapse into a straight DNA duplex that merges with the upstream promoter. Pol II is more separated from the TATA box, which is likely unbent because Pol II and TFIIB are necessary for stable promoter bending (*16*). When the upstream promoter is superimposed as a fixed reference, Pol II undergoes considerable rotation and displacement by

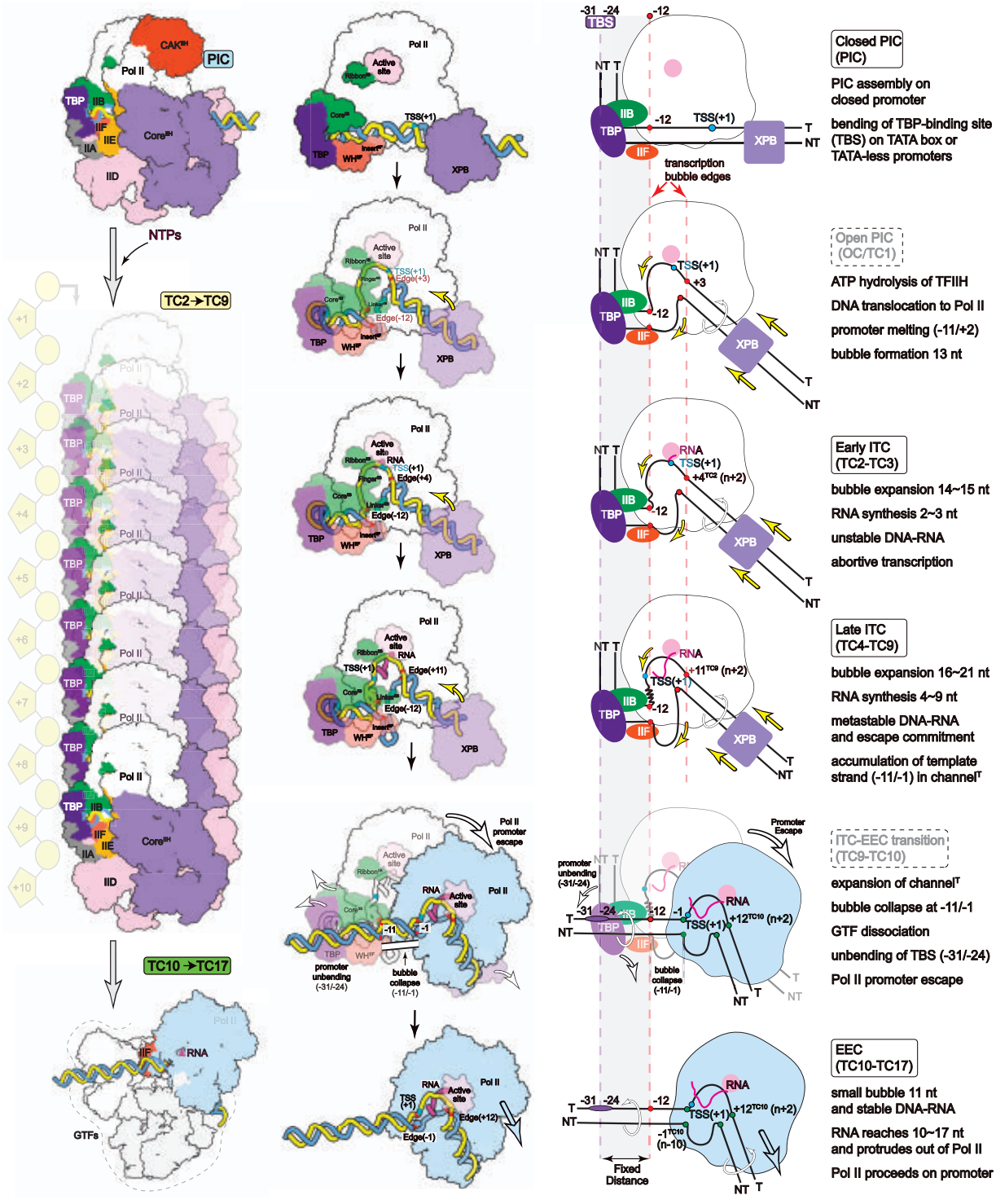

Fig. 6. A working model of transcription initiation. The transitions from the PIC (*16*) to the ITC and to the EEC are shown in cryo-EM maps of full complexes (left), simplified complexes (middle), and schematic models (right) with short descriptions. T and NT represent template and nontemplate strands, respectively. TBS represents the TBP-binding sites on TATA box and TATA-less promoters. The complexes from top to bottom are shown with the upstream promoter aligned to indicate a transcribing Pol II relative to the promoter. The open PIC and ITC-EEC transition schematics indicate proposed states by connecting the related structures.

~110 Å, which suggests that a process of promoter escape occurred on an active gene. As a result, Pol II proceeds on the promoter and the complex turns into an EEC.

The above result generally agrees with earlier biochemical studies that are not fully consistent with each other. For example, by detecting changes in the transcription bubble, complex stability, or dissociation of GTFs (mainly TFIIB), previous studies showed that the functional transition occurs when RNA reaches 7 (*35*), 8 (*34*), 9 (*37*), 10 (*33*), 7 or 9 (*38*), 12 or 13 (*63*), or more than 9 or 10 nt (*36*, *57*). This apparent discrepancy may result from the heterogeneity of transcription initiation, variations in promoters and experimental contexts, and limitations of the detection method (see supplementary text).

To test the ITC-EEC transition on another promoter, we assembled TC9 and TC10 on the AdML^{9G} and AdML^{10G} promoters, respectively, and determined cryo-EM structures (fig. S12 and data S2 to S4). The two structures are similar to their counterparts on the SCP^{9G} and SCP^{10G} promoters, respectively, which suggests a common point of conformational transition. Thus, comparing TC9 and TC10 structures in a similar experimental context may serve as a framework to unite previous studies and provide structural insights into the dynamic processes of the ITC-EEC transition, a rate-limiting step in transcription initiation (*30*, *32*, *34*).

GTFs remain associated with the early EEC, and TFIID dissociates from the late EEC

Cryo-EM maps of the EEC show the density of the Pol II-associated TFIIF and TFIIE (fig. S5B). As previously reported, TFIIE and TFIIF in the EEC are incompatible with DRB sensitivity-inducing factor (DSIF) in a paused elongation complex (PEC) (*84*) and an elongation factor super elongation complex (SEC) in SEC-Pol II complex (*85*). Thus, the retained TFIIE and TFIIF may function not only in supporting initiation but also in preventing the negative effects of pausing and elongation factors before the transition from the EEC to the PEC or the productive EC.

To investigate whether other GTFs dissociate from transcribing complexes, we assembled complexes of TC3 (early ITC), TC9 (late ITC), TC10 (early EEC), and TC17 (late EEC), followed by glycerol gradient ultracentrifugation (fig. S13A). Peak fractions (as in cryo-EM sample preparation) of each complex were subjected to Western blotting using antibodies against representative Pol II and GTF subunits, including RPB2 (Pol II subunit), TFIIB, TAF1 and TBP (two TFIID subunits), TFIIEβ, TFIIFα, and XPB (TFIIH subunit). All the GTFs maintained their association with both the early ITC and the late ITC in consistent stoichiometry. TFIID partially dissociated from the early EEC, whereas other GTFs remained in a stable association. In the fractions of the late EEC, TAF1 and TBP of TFIID were nearly undetectable, and there appeared to be a reduction in the levels of TFIIB, TFIIF, TFIIE, and TFIIH.

The above results agree with our structural observation and provide complementary insights into GTFs in transcribing complexes (fig. S13B). TFIID seems to bind the exposed downstream promoter elements (DPEs) (positions 28 to 32) in TC10, which become buried within Pol II channel^{E} and inaccessible to TFIID in TC17. TFIID in the apo form may bind TBP and inhibit its binding to the promoter (*16*, *86*, *87*). TFIIH may tether with Pol II through the binding of TFIIE and TFIID. TFIIB may disengage from Pol II while maintaining partial connections with TBP, TFIIF, or the TFIIB-recognition element (BRE) of the upstream promoter. The presence of GTFs within the EEC could potentially vary across different promoters owing to differences in GTF-binding elements. Their retention may be regulated by elongation factors, Mediator, CTD phosphorylation, or chromatin. Nevertheless, the GTFs that are associated with the EEC in peripheral positions might not contribute to the transcription reaction.

Template-strand accumulation in channel^{T} and NTP-driven translocation may promote the ITC-EEC transition

The ITC-EEC transition may result from relative motion between nucleic acids and Pol II, a process of RNA-DNA translocation that is coupled to NTP loading, pyrophosphate release, and conformational changes of the bridge helix and trigger loop (*7*, *8*, *13*, *66*, *67*). We next investigated the correlation between RNA-DNA translocation and the ITC-EEC transition. Cryo-EM maps of TC2 and TC3 revealed the continuous density of template strands of 14 and 15 nt in length, respectively, spanning the upstream and downstream edges of the transcription bubble (Figs. 2A and 5B and fig. S10C). However, in TC4 to TC9, although the template strand becomes longer, only ~10 nt within the active center could be modeled, whereas 6 to 11 nt (in TC4 to TC9, respectively) outside of the active center are invisible. The disordered template strand does not appear to squeeze out of the nearly sealed channel^{T}, and its flexibility suggests nonspecific placement of the unpaired nucleotides in channel^{T}. In TC9, the Pol II active center is occupied by the 9-bp RNA-DNA duplex, and the 11-nt single-stranded template strand (and potentially with the B-finger) is likely accumulated in the channel^{T}. The irregular channel^{T} exhibits a volume of ~10 Å by 15 Å by 20 Å and may not accommodate single-stranded DNA longer than 11 nt (Fig. 5C).

The above analysis suggests a template stand–scrunching mechanism for the transition from the ITC to the EEC (Fig. 5B, Movie 1, fig. S10C, and movie S1). In the late ITC, RNA chain extension and RNA-DNA translocation lead to the accumulation of the template strand in the narrow channel^{T}. The addition of one more nucleotide to the RNA chain and NTP-driven RNA-DNA translocation may provide a final push to balloon out the channel^{T}. Because Pol II remains rigid, the B-linker and B-core-N dissociate from Pol II to release the accumulated template strand.

In support of this hypothesis, an earlier study showed a decrease in the complex stability on the AdML^{6G} to AdML^{9G} promoters (*35*). Cryo-EM density of the B-linker at the gate of channel^{T} is continuous in TC3 and TC5 but becomes less ordered and disconnected in TC7 and TC9, which indicates the destabilization of channel^{T} (Fig. 5D). Moreover, TFIIB dissociates from Pol II before RNA reaches 10 nt in length (*38*, *39*). Previous studies in yeast Pol II have proposed that steric clashes between RNA and the B-ribbon may lead to TFIIB dissociation (*44*, *46*). This is not likely the case in mammals because RNA shorter than 12 nt does not reach the B-ribbon (fig. S5D).

More supporting evidence comes from a comparison of the mammalian ITC structures with the structure of the yeast ITC on a G-less promoter (G is at +26) (*47*) (fig. S6 and supplementary text). The yeast ITC structure represents a backtracked complex containing a 5-nt nascent RNA in the active center. The structure shows a partially open channel^{T}, which may allow the template strand of more than a hundred nucleotides to thread out of the complex for TSS scanning. The differences in channel^{T} (sealed versus open) and the template strand (which is melted within the catalytic pocket by up to 21 nt in the mammalian ITC versus threaded out of the catalytic pocket by more than a hundred nucleotides in yeast ITC) highlight the regulatory role of channel^{T} in potentially controlling bubble size in mammals and suggest distinct underlying mechanisms of transcription initiation in mammals and yeast (*48*, *49*).

Comparison with transcription initiation in bacteria

Our proposed mechanism of transcription initiation in mammals is generally similar to the well-characterized transcription initiation by bacterial RNAP, which forms CC, OC, ITC, and EC complexes and undergoes promoter opening, bubble expansion, bubble collapse, and promoter escape through a DNA-scrunching mechanism (*88*–*91*). The bacterial σ factor, which is functionally equivalent to eukaryotic GTFs, associates with RNAP and stabilizes the upstream promoter in the ITC. During promoter escape, the σ factor is forced to dissociate from RNAP by the scrunched DNA in the transcription bubble (*92*) and by the compressed σ-finger because of RNA growth (*93*–*95*). Distinct from what occurs in the mammalian system, the bacterial σ factor recognizes the single-stranded non-template DNA and contributes to promoter escape (*82*, *83*) that is substantially variable dependent on the types of promoters (*71*, *72*).

Discussion

Studies over the past three decades have established that there are functional transitions during eukaryotic transcription initiation. However, understanding this process at the molecular level has been a long-standing challenge because of the difficulty in obtaining de novo transcribing complexes, which are highly dynamic and heterogeneous (*30*, *54*–*56*). Our work reconciles earlier studies and provides structural visualization of transcription initiation in action (Fig. 6, Movie 1, and movie S1). As detailed above, the transition from the PIC to the early ITC involves promoter melting, transcription bubble formation, nascent RNA synthesis, and abortive transcription. From the early ITC to the late ITC, the transcription bubble expands and RNA

is more stable within Pol II, which is correlated with escape commitment. From the late ITC to the EEC, the complex undergoes abrupt transitions, including channel^{T} expansion, GTF dissociation, bubble collapse, and promoter escape.

The proposed model may be applicable to Pol II–mediated transcription initiation on TATA-less promoters, which account for most core promoters (*1*). TATA-less promoters tend to exhibit lower transcriptional activity than TATA box promoters and often result in heterogeneous TSSs, limiting their usage in biochemical and structural studies. Our previous study showed that during PIC assembly, TFIID supports TBP to load and bend the upstream promoter region, termed the TBP-binding site (TBS), regardless of whether it contains a TATA box or not (*16*). PIC complexes assembled on the TATA box and TATA-less promoters adopt similar organizations, which suggests a general mechanism of transcription initiation. Although the selection of a TSS is fine-tuned by the surrounding sequences and the inherent heterogeneity (*50*–*52*), transcription seems to be started ~31 bp downstream of the TBS (*35*, *48*), which is primarily determined by the site of PIC assembly, which is dependent on promoter sequence and chromatin organization (*1*, *14*).

Our study also provides a structural basis for understanding why transcription initiation undergoes such notable changes. To avoid promiscuous transcription, Pol II by itself could neither find a target promoter nor open a promoter to initiate RNA synthesis. This is why GTFs are necessary for promoter recognition and transcription initiation. However, the stability that results from the multiple interactions among GTFs, Pol II, and the promoter also creates an obstacle for Pol II to escape the promoter and therefore must eventually be disrupted. The modular organization of the PIC and the ITC is well suited to achieve this purpose. In the early ITC, the active center and channel^{T} can accommodate the template strand and allow for bubble expansion and initial RNA synthesis. In the late ITC, the RNA-DNA hybrid is stable and long enough to support NTP-driven translocation and disruption of the GTF–Pol II–promoter contacts. In the EEC, the peripherally positioned GTFs would not restrain Pol II on the promoter. Therefore, coordinated changes of the GTFs and the transcription bubble support a functional transition from the ITC, which requires GTFs and promoter opening for initial RNA synthesis, to the EEC, which requires GTF dissociation and bubble collapse for promoter escape and stable RNA production.

Materials and methods

Cryo-EM sample preparation

Pol II was isolated from *Sus scrofa* thymus, and *Homo sapiens* TFIID, TFIIA, TFIIB, TFIIF, TFIIE, and TFIIH were prepared as previously described (*15*, *16*). Promoter sequences (SCP^{nG} and AdML$^{9G/10G}$) are listed in data S1. The promoter DNA was generated by annealing the template strand with equimolar amounts of single-stranded nontemplate DNA at a final concentration of 50 μM in water. The annealing reaction was carried out at 95°C for 10 min and gradually cooled down to 25°C within 2 hours.

To prepare each TC complex, the purified PIC components of 300 pmol of TFIID, 1500 pmol of TFIIA, and 450 pmol of promoter DNA (SCP^{nG} and AdML$^{9G/10G}$) were mixed at 4°C for 2 hours in a 150-μl mixture containing 25 mM HEPES-KOH pH 7.9, 100 mM KCl, 6 mM $MgCl_2$, 2 mM DTT, and 5% (v/v) glycerol. After incubation, the mixture was subjected to glycerol gradient ultracentrifugation. The gradient was generated from equal volumes of a 10% glycerol solution [10% (w/v) glycerol, 30 mM HEPES-KOH pH 7.9, 50 mM KCl, 6 mM $MgCl_2$, 2 mM DTT] and a 50% glycerol solution [50% (w/v) glycerol, 30 mM HEPES-KOH pH 7.9, 50 mM KCl, 6 mM $MgCl_2$, 2 mM DTT] with a BioComp Gradient Master 108 (BioComp Instruments). The ultrafiltration was performed using a swinging bucket rotor SW60Ti (Beckman) at 36,000 rpm for 14 hours at 4°C. Peak fractions containing promoter DNA-TFIID-TFIIA were pooled and concentrated to ~1.5 mg/ml. Subsequently, the 100 pmol of preassembled promoter DNA-TFIID-TFIIA was mixed with 500 pmol of TFIIB, 110 pmol of Pol II, and 160 pmol of TFIIF at 4°C for 1 hour in a 150-μl mixture containing 25 mM HEPES-KOH pH 7.9, 75 mM KCl, 6 mM $MgCl_2$, 2 mM DTT, and 5% (v/v) glycerol. Next, 300 pmol of TFIIE and 200 pmol of TFIIH were added to the mixture, and it was further incubated for 2 hours to assemble the PIC complex. After the incubation, 15 μl of 20× NTP mix [containing 40 mM ATP, 40 mM CTP, 40 mM UTP, 2 mM 3′-*O*-methylguanosine-5′-triphosphate (APExBIO)] was added to the 285 μl of PIC mixture to initiate the transcription reaction. The reactions were carried out for 50 min at 30°C and then quenched by adding 0.5 μl of 0.4 mM α-amanitin, followed by GraFix (*96*). For Grafix, the glycerol gradient was prepared using a low buffer containing 15% (v/v) glycerol, 30 mM HEPES-KOH pH 7.9, 100 mM KCl, 2 mM $MgCl_2$, 10 μM $ZnCl_2$, and 2 mM DTT and a high buffer containing 35% (v/v) glycerol, 30 mM HEPES-KOH pH 7.9, 100 mM KCl, 2 mM $MgCl_2$, 10 μM $ZnCl_2$, 2 mM DTT, and 0.01% glutaraldehyde. The samples were centrifuged at 38,000 rpm at 4°C for 14 hours using an SW41 Ti rotor (Beckman Coulter). Subsequently, fractions containing cross-linked complexes were quenched with 50 mM Tris pH 7.4 (25°C). The peak fractions were assessed by negative-stain EM. Fractions of interest were pooled, concentrated, and subjected to buffer exchange into a buffer containing 30 mM HEPES-KOH pH 7.9, 100 mM KCl, 2 mM $MgCl_2$, 10 μM $ZnCl_2$, 2 mM DTT, and 0.8% (v/v) glycerol using a 100-kDa cut-off centrifugation filter unit (Amicon Ultra). For each assembly step, the samples were monitored by SDS-PAGE and visualized by Coomassie blue staining. TC3, TC9, TC10, and TC17 were assembled and subjected to glycerol gradient ultracentrifugation without cross-linking, and peak fractions (as in the cryo-EM sample) of each complex were subjected to Western blotting using the indicated antibodies (anti-TAF1 antibody: A303-505A, Bethyl; anti-RPB2 antibody: A5928, ABclonal; anti-XPB antibody:10580-1-AP, Proteintech; anti-TFIIFα antibody: 10093-2-AP, Proteintech; anti-TBP antibody: A2192, ABclonal; anti-TFIIEβ antibody: A305-054A, Bethyl; and anti-TFIIB antibody: A1708, ABclonal).

For cryo-EM grid preparation, 3 μl of the sample at a concentration of ~0.2 μM was applied to freshly glow-discharged Quantifoil R1.2/1.3 Au holey carbon grids. After incubation of 5 s at a temperature of 4°C and a humidity of 100%, the grids were blotted for 0.5 to 1.0 s in Vitrobot Mark IV (Thermo Fisher Scientific), plunge-frozen in liquid ethane, and stored at liquid nitrogen temperature. The grids were prepared in the H_2/O_2 mixture for 15 s using a Gatan 950 Solarus plasma cleaning system with a power of 5 W. The ø 55/20-mm blotting paper is made by TED PELLA and used for plunge freezing.

In vitro transcription initiation assay

The transcription reaction was conducted by mixing 0.4 pmol of promoter DNA, 0.5 pmol of TFIID, 1.5 pmol of TFIIA, 1.5 pmol of TFIIB, 1 pmol of RNA Pol II, 1.5 pmol of TFIIF, 1.5 pmol of TFIIE, and 0.8 pmol of TFIIH in an 18.8-μl reaction mixture containing 25 mM HEPES-KOH pH 7.9, 50 mM KCl, 5 mM $MgCl_2$, 1 mM DTT, 10% (v/v) glycerol, 200μg/mL bovine serum albumin (BSA), and 8 units of RiboLock RNase Inhibitor (Thermo Fisher Scientific). The mixture was incubated at 25°C for 30 min. After the incubation, reactions were initiated by the addition of 1 μl of 20× NTP mix containing 1.2 mM ATP, 0.2 mM CTP, 0.02 mM UTP, 2.4 mM 3′-*O*-methylguanosine-5′-triphosphate (APExBIO), and 0.2 μl of 10 mCi/ml [α-^{32}P]-UTP (Perkin Elmer). The transcription reactions were carried out for 50 min at 30°C and stopped by heating the reaction mixture to 68°C for 3 min. In the time-course assay, the reactions were stopped at time intervals of 5, 10, 30, and 50 min. Subsequently, after cooling on ice, the reaction mixtures were treated with 1 μl of calf intestinal alkaline phosphatase (CIAP) (20 U/μl, Thermo Fisher Scientific) at 37°C for 30 min. The RNA products were analyzed by 23% urea polyacrylamide gels, and the autoradiograph was obtained by storage-phosphor scanning (Typhoon; Cytiva).

Cryo-EM data collection and image processing

Detailed parameters of data collection and image processing are shown in data S2 and S3 and summarized in data S4. A brief description is provided below, and fig. S2 shows the

data collection and image processing of TC5 and TC10, two representative complexes.

The cryo-EM grids were loaded onto a Titan Krios transmission electron microscope (Thermo Fisher Scientific) operated at 300 kV for data collection. The cryo-EM images were automatically recorded by a post-GIF Gatan K3 Summit direct electron detector in the super-resolution counting mode using Serial-EM with a nominal magnification of 64,000× in the EFTEM mode, which yielded a super-resolution pixel size of 0.667 Å on the image plane, and with defocus values ranging from −1.5 to −2.5 μm. Each micrograph stack was dose-fractionated to 40 frames with an exposure rate of 21 e^- $pixel^{-1}$ s^{-1}, a total electron exposure of ~50 e^- $Å^{-2}$, and a total exposure time of 4.2 s.

For TC5 and TC10 complexes, 49,009/58,688 ("/" separates parameters in TC5 and TC10) micrographs were collected for further processing. Drift and beam-induced motion correction were applied on the super-resolution movie stacks using MotionCor2 (*97*) and binned twofold to a calibrated pixel size of 1.334Å $pixel^{-1}$. The defocus values were estimated by Gctf (*98*) from summed images without dose weighting. Other procedures of cryo-EM data processing were performed within RELION v3.1 (*99*, *100*) and cryoSPARC v3 (*101*) using the dose-weighted micrographs. Particles of 28,786,688/33,235,621 were picked by reference autopicking in RELION using high-resolution Pol II map [Electron Microscopy Data Bank (EMDB) ID 3218] as a 3D reference, 0.05 picking threshold, and 180 minimum interparticle distance, with other parameters set to default, and were subjected to reference-free 2D classification using a mask diameter of 420 Å, iterations of 30, Tau2Fudge factor of 2, classes of 200, e-step of −1 Å, and ignore CTFs until first peak (Yes) (other parameters were set to default). Particles of 19,288,625/21,463,872 were selected from good 2D classes for 3D classification in RELION.

All the 3D classification and 3D autorefine in RELION used an initial low-pass filter of 40 Å, Tau2Fudge factor of 4, iterations of 160, classes of 9, and e-step of −1 Å (other parameters were set to default). Particles of 12,743,286/12,467,838 were selected from 3D classes using a mask diameter of 420 Å. The yielded particles were applied for subtraction with a Pol II mask. The subtracted particles were applied for 3D classification using a mask diameter of 280 Å to get the ITC and EEC conformations, respectively. The particles of the ITC and EEC were used for refinement in cryoSPARC Local Refinement, yielding a reconstruction at 2.98 Å/2.82 Å resolution for Pol II (including the bound nucleic acids). All the refinement of Pol II has been subjected to CTF refinement, postprocessing, and Bayesian polishing in RELION. The subtracted particles of Pol II in ITC and EEC conformation were reverted to original particles, followed by 3D classification to obtain overall maps of ITCs and EECs. The overall maps were refined with a box size of 200 pixels and a down-sampled pixel size of 2.668 Å.

All reported resolutions are based on the gold-standard Fourier shell correlation (FSC) = 0.143 criterion. The gold-standard FSC curves were corrected for the effects of a soft mask with high-resolution noise substitution. We also used the 3D FSC server to evaluate our maps. All the visualization and evaluation of the 3D volume map were performed using UCSF Chimera (*102*), and the local resolution variations were calculated using cryoSPARC.

Model building and structure refinement

The overall cryo-EM maps and locally refined maps of all samples were used for model building. The structures of the mammalian PIC complex [Protein Data Bank (PDB) ID 7EGB] (*15*) and mammalian elongation complex (PDB ID 5FLM) (*11*) were used as initial structural templates. For ITC complexes, structural modules of Pol II and GTFs were individually docked into the cryo-EM maps by rigid-body fitting using UCSF Chimera. For EEC complexes, Pol II and TFIIF were docked into the cryo-EM maps, whereas other GTFs were not built because the density did not support confident model docking. The structural models were manually adjusted in COOT (*103*).

Overfitting of the model was monitored by refining the model in one of the two half maps from the gold-standard refinement approach and testing the refined model against the other map. The structural models (except the flexibly docked TFIIE, TFIIH, and TFIID) were evaluated using Phenix real-space refine and MolProbity (*104*) using resolution at 6.5 Å for the ITC and 3.5 Å for the EEC and constraints of rotamer, Ramachandran, and secondary structure. Map and model representations in the figures and movies were prepared by PyMOL (*105*), UCSF Chimera, or UCSF ChimeraX (*102*).

REFERENCES AND NOTES

1. V. Haberle, A. Stark, Eukaryotic core promoters and the functional basis of transcription initiation. *Nat. Rev. Mol. Cell Biol.* **19**, 621–637 (2018). doi: 10.1038/s41580-018-0028-8; pmid: 29946135
2. D. S. Luse, Promoter clearance by RNA polymerase II. *Biochim. Biophys. Acta* **1829**, 63–68 (2013). doi: 10.1016/j.bbagrm.2012.08.010; pmid: 22982364
3. A. Saunders, L. J. Core, J. T. Lis, Breaking barriers to transcription elongation. *Nat. Rev. Mol. Cell Biol.* **7**, 557–567 (2006). doi: 10.1038/nrm1981; pmid: 16936696
4. R. G. Roeder, The role of general initiation factors in transcription by RNA polymerase II. *Trends Biochem. Sci.* **21**, 327–335 (1996). doi: 10.1016/0968-0004(96)10050-5; pmid: 8870495
5. L. Zawel, D. Reinberg, Initiation of transcription by RNA polymerase II: A multi-step process. *Prog. Nucleic Acid Res. Mol. Biol.* **44**, 67–108 (1993). doi: 10.1016/S0079-6603(08)60217-2; pmid: 8434126
6. M. C. Thomas, C. M. Chiang, The general transcription machinery and general cofactors. *Crit. Rev. Biochem. Mol. Biol.* **41**, 105–178 (2006). doi: 10.1080/10409230600648736; pmid: 16858867
7. A. L. Gnatt, P. Cramer, J. Fu, D. A. Bushnell, R. D. Kornberg, Structural basis of transcription: An RNA polymerase II elongation complex at 3.3 Å resolution. *Science* **292**, 1876–1882 (2001). doi: 10.1126/science.1059495; pmid: 11313499
8. D. Wang, D. A. Bushnell, K. D. Westover, C. D. Kaplan, R. D. Kornberg, Structural basis of transcription: Role of the trigger loop in substrate specificity and catalysis. *Cell* **127**, 941–954 (2006). doi: 10.1016/j.cell.2006.11.023; pmid: 17129781
9. K. D. Westover, D. A. Bushnell, R. D. Kornberg, Structural basis of transcription: Nucleotide selection by rotation in the RNA polymerase II active center. *Cell* **119**, 481–489 (2004). doi: 10.1016/j.cell.2004.10.016; pmid: 15537538
10. K. D. Westover, D. A. Bushnell, R. D. Kornberg, Structural basis of transcription: Separation of RNA from DNA by RNA polymerase II. *Science* **303**, 1014–1016 (2004). doi: 10.1126/science.1090839; pmid: 14963331
11. C. Bernecky, F. Herzog, W. Baumeister, J. M. Plitzko, P. Cramer, Structure of transcribing mammalian RNA polymerase II. *Nature* **529**, 551–554 (2016). doi: 10.1038/nature16482; pmid: 26789250
12. A. C. Cheung, P. Cramer, Structural basis of RNA polymerase II backtracking, arrest and reactivation. *Nature* **471**, 249–253 (2011). doi: 10.1038/nature09785; pmid: 21346759
13. P. Cramer, D. A. Bushnell, R. D. Kornberg, Structural basis of transcription: RNA polymerase II at 2.8 Ångstrom resolution. *Science* **292**, 1863–1876 (2001). doi: 10.1126/science.1059493; pmid: 11313498
14. X. Chen *et al*., Structures of +1 nucleosome–bound PIC-Mediator complex. *Science* **378**, 62–68 (2022). doi: 10.1126/science.abn8131; pmid: 36201575
15. X. Chen *et al*., Structures of the human Mediator and Mediator-bound preinitiation complex. *Science* **372**, eabg0635 (2021). doi: 10.1126/science.abg0635; pmid: 33958484
16. X. Chen *et al*., Structural insights into preinitiation complex assembly on core promoters. *Science* **372**, eaba8490 (2021). doi: 10.1126/science.aba8490; pmid: 33795473
17. S. Schilbach, S. Aibara, C. Dienemann, F. Grabbe, P. Cramer, Structure of RNA polymerase II pre-initiation complex at 2.9 Å defines initial DNA opening. *Cell* **184**, 4064–4072.e28 (2021). doi: 10.1016/j.cell.2021.05.012; pmid: 34133942
18. S. Rengachari, S. Schilbach, S. Aibara, C. Dienemann, P. Cramer, Structure of the human Mediator-RNA polymerase II pre-initiation complex. *Nature* **594**, 129–133 (2021). doi: 10.1038/s41586-021-03555-7; pmid: 33902108
19. S. Aibara, S. Schilbach, P. Cramer, Structures of mammalian RNA polymerase II pre-initiation complexes. *Nature* **594**, 124–128 (2021). doi: 10.1038/s41586-021-03554-8; pmid: 33902107
20. R. Abdella *et al*., Structure of the human Mediator-bound transcription preinitiation complex. *Science* **372**, 52–56 (2021). doi: 10.1126/science.abg3074; pmid: 33707221
21. S. Schilbach *et al*., Structures of transcription pre-initiation complex with TFIIH and Mediator. *Nature* **551**, 204–209 (2017). doi: 10.1038/nature24282; pmid: 29088706
22. Y. He, J. Fang, D. J. Taatjes, E. Nogales, Structural visualization of key steps in human transcription initiation. *Nature* **495**, 481–486 (2013). doi: 10.1038/nature11991; pmid: 23446344
23. P. J. Robinson *et al*., Structure of a complete Mediator-RNA polymerase II pre-initiation complex. *Cell* **166**, 1411–1422.e16 (2016). doi: 10.1016/j.cell.2016.08.050; pmid: 27610567
24. S. Rengachari *et al*., Structural basis of SNAPc-dependent snRNA transcription initiation by RNA polymerase II. *Nat. Struct. Mol. Biol.* **29**, 1159–1169 (2022). doi: 10.1038/s41594-022-00857-w; pmid: 36424526
25. F. C. Holstege, P. C. van der Vliet, H. T. Timmers, Opening of an RNA polymerase II promoter occurs in two distinct steps and requires the basal transcription factors IIE and IIH. *EMBO J.* **15**, 1666–1677 (1996). doi: 10.1002/j.1460-2075.1996.tb00512.x; pmid: 8612591
26. H. Cai, D. S. Luse, Transcription initiation by RNA polymerase II in vitro. Properties of preinitiation, initiation, and elongation complexes. *J. Biol. Chem.* **262**, 298–304 (1987). doi: 10.1016/S0021-9258(19)75926-2; pmid: 2432061
27. D. S. Luse, G. A. Jacob, Abortive initiation by RNA polymerase II in vitro at the adenovirus 2 major late promoter. *J. Biol. Chem.* **262**, 14990–14997 (1987). doi: 10.1016/S0021-9258(18)48127-6; pmid: 3667620
28. D. S. Luse, T. Kochel, E. D. Kuempel, J. A. Coppola, H. Cai, Transcription initiation by RNA polymerase II in vitro. At least two nucleotides must be added to form a stable ternary complex. *J. Biol. Chem.* **262**, 289–297 (1987). doi: 10.1016/S0021-9258(19)75925-0; pmid: 2432060
29. H. A. Ferguson, J. F. Kugel, J. A. Goodrich, Kinetic and mechanistic analysis of the RNA polymerase II transcrption

reaction at the human interleukin-2 promoter. *J. Mol. Biol.* **314**, 993–1006 (2001). doi: 10.1006/jmbi.2000.5215; pmid: 11743717
30. J. F. Kugel, J. A. Goodrich, Promoter escape limits the rate of RNA polymerase II transcription and is enhanced by TFIIE, TFIIH, and ATP on negatively supercoiled DNA. *Proc. Natl. Acad. Sci. U.S.A.* **95**, 9232–9237 (1998). doi: 10.1073/pnas.95.16.9232; pmid: 9689063
31. J. F. Kugel, J. A. Goodrich, Translocation after synthesis of a four-nucleotide RNA commits RNA polymerase II to promoter escape. *Mol. Cell. Biol.* **22**, 762–773 (2002). doi: 10.1128/MCB.22.3.762-773.2002; pmid: 11784853
32. J. F. Kugel, J. A. Goodrich, A kinetic model for the early steps of RNA synthesis by human RNA polymerase II. *J. Biol. Chem.* **275**, 40483–40491 (2000). doi: 10.1074/jbc.M006401200; pmid: 10982810
33. F. C. Holstege, U. Fiedler, H. T. Timmers, Three transitions in the RNA polymerase II transcription complex during initiation. *EMBO J.* **16**, 7468–7480 (1997). doi: 10.1093/emboj/16.24.7468; pmid: 9405375
34. A. R. Hieb, S. Baran, J. A. Goodrich, J. F. Kugel, An 8 nt RNA triggers a rate-limiting shift of RNA polymerase II complexes into elongation. *EMBO J.* **25**, 3100–3109 (2006). doi: 10.1038/sj.emboj.7601197; pmid: 16778763
35. M. Pal, A. S. Ponticelli, D. S. Luse, The role of the transcription bubble and TFIIB in promoter clearance by RNA polymerase II. *Mol. Cell* **19**, 101–110 (2005). doi: 10.1016/j.molcel.2005.05.024; pmid: 15989968
36. J. A. Coppola, D. S. Luse, Purification and characterization of ternary complexes containing accurately initiated RNA polymerase II and less than 20 nucleotides of RNA. *J. Mol. Biol.* **178**, 415–437 (1984). doi: 10.1016/0022-2836(84)90151-7; pmid: 6492155
37. M. Pal, D. S. Luse, The initiation-elongation transition: Lateral mobility of RNA in RNA polymerase II complexes is greatly reduced at +8/+9 and absent by +23. *Proc. Natl. Acad. Sci. U.S.A.* **100**, 5700–5705 (2003). doi: 10.1073/pnas.1037057100; pmid: 12719526
38. E. Ly, A. E. Powell, J. A. Goodrich, J. F. Kugel, Release of human TFIIB from actively transcribing complexes is triggered upon synthesis of 7- and 9-nt RNAs. *J. Mol. Biol.* **432**, 4049–4060 (2020). doi: 10.1016/j.jmb.2020.05.005; pmid: 32417370
39. L. Zawel, K. P. Kumar, D. Reinberg, Recycling of the general transcription factors during RNA polymerase II transcription. *Genes Dev.* **9**, 1479–1490 (1995). doi: 10.1101/gad.9.12.1479; pmid: 7601352
40. X. Liu, D. A. Bushnell, D. Wang, G. Calero, R. D. Kornberg, Structure of an RNA polymerase II-TFIIB complex and the transcription initiation mechanism. *Science* **327**, 206–209 (2010). doi: 10.1126/science.1182015; pmid: 19965383
41. X. Liu, D. A. Bushnell, D. A. Silva, X. Huang, R. D. Kornberg, Initiation complex structure and promoter proofreading. *Science* **333**, 633–637 (2011). doi: 10.1126/science.1206629; pmid: 21798951
42. A. C. Cheung, S. Sainsbury, P. Cramer, Structural basis of initial RNA polymerase II transcription. *EMBO J.* **30**, 4755–4763 (2011). doi: 10.1038/emboj.2011.396; pmid: 22056778
43. Y. He *et al*., Near-atomic resolution visualization of human transcription promoter opening. *Nature* **533**, 359–365 (2016). doi: 10.1038/nature17970; pmid: 27193682
44. S. Sainsbury, J. Niesser, P. Cramer, Structure and function of the initially transcribing RNA polymerase II-TFIIB complex. *Nature* **493**, 437–440 (2013). doi: 10.1038/nature11715; pmid: 23151482
45. D. A. Bushnell, K. D. Westover, R. E. Davis, R. D. Kornberg, Structural basis of transcription: An RNA polymerase II-TFIIB cocrystal at 4.5 angstroms. *Science* **303**, 983–988 (2004). doi: 10.1126/science.1090838; pmid: 14963322
46. D. Kostrewa *et al*., RNA polymerase II-TFIIB structure and mechanism of transcription initiation. *Nature* **462**, 323–330 (2009). doi: 10.1038/nature08548; pmid: 19820686
47. C. Yang *et al*., Structural visualization of de novo transcription initiation by *Saccharomyces cerevisiae* RNA polymerase II. *Mol. Cell* **82**, 660–676.e9 (2022). doi: 10.1016/j.molcel.2021.12.020; pmid: 35051353
48. C. Giardina, J. T. Lis, DNA melting on yeast RNA polymerase II promoters. *Science* **261**, 759–762 (1993). doi: 10.1126/science.8342041; pmid: 8342041
49. F. M. Fazal, C. A. Meng, K. Murakami, R. D. Kornberg, S. M. Block, Real-time observation of the initiation of RNA polymerase II transcription. *Nature* **525**, 274–277 (2015). doi: 10.1038/nature14882; pmid: 26331540
50. L. Vo ngoc, C. J. Cassidy, C. Y. Huang, S. H. Duttke, J. T. Kadonaga, The human initiator is a distinct and abundant element that is precisely positioned in focused core promoters. *Genes Dev.* **31**, 6–11 (2017). doi: 10.1101/gad.293837.116; pmid: 28108474
51. M. Pal, D. S. Luse, Strong natural pausing by RNA polymerase II within 10 bases of transcription start may result in repeated slippage and reextension of the nascent RNA. *Mol. Cell. Biol.* **22**, 30–40 (2002). doi: 10.1128/MCB.22.1.30-40.2002; pmid: 11739720
52. J. A. Fairley, R. Evans, N. A. Hawkes, S. G. Roberts, Core promoter-dependent TFIIB conformation and a role for TFIIB conformation in transcription start site selection. *Mol. Cell. Biol.* **22**, 6697–6705 (2002). doi: 10.1128/MCB.22.19.6697-6705.2002; pmid: 12215527
53. W. Gu, M. Wind, D. Reines, Increased accommodation of nascent RNA in a product site on RNA polymerase II during arrest. *Proc. Natl. Acad. Sci. U.S.A.* **93**, 6935–6940 (1996). doi: 10.1073/pnas.93.14.6935; pmid: 8692922
54. R. T. Kamakaka, C. M. Tyree, J. T. Kadonaga, Accurate and efficient RNA polymerase II transcription with a soluble nuclear fraction derived from *Drosophila* embryos. *Proc. Natl. Acad. Sci. U.S.A.* **88**, 1024–1028 (1991). doi: 10.1073/pnas.88.3.1024; pmid: 1992453
55. J. T. Kadonaga, Assembly and disassembly of the *Drosophila* RNA polymerase II complex during transcription. *J. Biol. Chem.* **265**, 2624–2631 (1990). doi: 10.1016/S0021-9258(19)39847-3; pmid: 1689291
56. A. E. Horn, J. F. Kugel, J. A. Goodrich, Single molecule microscopy reveals mechanistic insight into RNA polymerase II preinitiation complex assembly and transcriptional activity. *Nucleic Acids Res.* **44**, 7132–7143 (2016). doi: 10.1093/nar/gkw321; pmid: 27112574
57. A. Dvir, R. C. Conaway, J. W. Conaway, Promoter escape by RNA polymerase II. A role for an ATP cofactor in suppression of arrest by polymerase at promoter-proximal sites. *J. Biol. Chem.* **271**, 23352–23356 (1996). doi: 10.1074/jbc.271.38.23352; pmid: 8798537
58. T. K. Kim, R. H. Ebright, D. Reinberg, Mechanism of ATP-dependent promoter melting by transcription factor IIH. *Science* **288**, 1418–1421 (2000). doi: 10.1126/science.288.5470.1418; pmid: 10827951
59. M. Douziech *et al*., Mechanism of promoter melting by the xeroderma pigmentosum complementation group B helicase of transcription factor IIH revealed by protein-DNA photo-cross-linking. *Mol. Cell. Biol.* **20**, 8168–8177 (2000). doi: 10.1128/MCB.20.21.8168-8177.2000; pmid: 11027286
60. A. Dvir, R. C. Conaway, J. W. Conaway, A role for TFIIH in controlling the activity of early RNA polymerase II elongation complexes. *Proc. Natl. Acad. Sci. U.S.A.* **94**, 9006–9010 (1997). doi: 10.1073/pnas.94.17.9006; pmid: 9256425
61. J. A. Goodrich, R. Tjian, Transcription factors IIE and IIH and ATP hydrolysis direct promoter clearance by RNA polymerase II. *Cell* **77**, 145–156 (1994). doi: 10.1016/0092-8674(94)90242-9; pmid: 8156590
62. L. Spangler, X. Wang, J. W. Conaway, R. C. Conaway, A. Dvir, TFIIH action in transcription initiation and promoter escape requires distinct regions of downstream promoter DNA. *Proc. Natl. Acad. Sci. U.S.A.* **98**, 5544–5549 (2001). doi: 10.1073/pnas.101004498; pmid: 11331764
63. P. Čabart, A. Újvári, M. Pal, D. S. Luse, Transcription factor TFIIF is not required for initiation by RNA polymerase II, but it is essential to stabilize transcription factor TFIIB in early elongation complexes. *Proc. Natl. Acad. Sci. U.S.A.* **108**, 15786–15791 (2011). doi: 10.1073/pnas.1104591108; pmid: 21896726
64. R. Fujiwara, N. Damodaren, J. E. Wilusz, K. Murakami, The capping enzyme facilitates promoter escape and assembly of a follow-on preinitiation complex for reinitiation. *Proc. Natl. Acad. Sci. U.S.A.* **116**, 22573–22582 (2019). doi: 10.1073/pnas.1905449116; pmid: 31591205
65. N. Yudkovsky, J. A. Ranish, S. Hahn, A transcription reinitiation intermediate that is stabilized by activator. *Nature* **408**, 225–229 (2000). doi: 10.1038/35041603; pmid: 11089979
66. F. W. Martinez-Rucobo, P. Cramer, Structural basis of transcription elongation. *Biochim. Biophys. Acta* **1829**, 9–19 (2013). doi: 10.1016/j.bbagrm.2012.09.002; pmid: 22982352
67. M. Kireeva, M. Kashlev, Z. F. Burton, Translocation by multi-subunit RNA polymerases. *Biochim. Biophys. Acta* **1799**, 389–401 (2010). doi: 10.1016/j.bbagrm.2010.01.007; pmid: 20097318
68. S. Alekseev *et al*., Transcription without XPB establishes a unified helicase-independent mechanism of promoter opening in eukaryotic gene expression. *Mol. Cell* **65**, 504–514.e4 (2017). doi: 10.1016/j.molcel.2017.01.012; pmid: 28157507
69. C. Plaschka *et al*., Transcription initiation complex structures elucidate DNA opening. *Nature* **533**, 353–358 (2016). doi: 10.1038/nature17990; pmid: 27193681
70. J. F. Santana, G. S. Collins, M. Parida, D. S. Luse, D. H. Price, Differential dependencies of human RNA polymerase II promoters on TBP, TAF1, TFIIB and XPB. *Nucleic Acids Res.* **50**, 9127–9148 (2022). doi: 10.1093/nar/gkac678; pmid: 35947745
71. L. M. Hsu, N. V. Vo, C. M. Kane, M. J. Chamberlin, In vitro studies of transcript initiation by *Escherichia coli* RNA polymerase. 1. RNA chain initiation, abortive initiation, and promoter escape at three bacteriophage promoters. *Biochemistry* **42**, 3777–3786 (2003). doi: 10.1021/bi026954e; pmid: 12667069
72. K. L. Henderson *et al*., Mechanism of transcription initiation and promoter escape by *E. coli* RNA polymerase. *Proc. Natl. Acad. Sci. U.S.A.* **114**, E3032–E3040 (2017). doi: 10.1073/pnas.1618675114; pmid: 28348246
73. X. Liu, L. Farnung, C. Wigge, P. Cramer, Cryo-EM structure of a mammalian RNA polymerase II elongation complex inhibited by α-amanitin. *J. Biol. Chem.* **293**, 7189–7194 (2018). doi: 10.1074/jbc.RA118.002545; pmid: 29550768
74. M. J. Bick, S. Malik, A. Mustaev, S. A. Darst, TFIIB is only ~9 Å away from the 5′-end of a trimeric RNA primer in a functional RNA polymerase II preinitiation complex. *PLOS ONE* **10**, e0119007 (2015). doi: 10.1371/journal.pone.0119007; pmid: 25774659
75. H. T. Chen, S. Hahn, Mapping the location of TFIIB within the RNA polymerase II transcription preinitiation complex: A model for the structure of the PIC. *Cell* **119**, 169–180 (2004). doi: 10.1016/j.cell.2004.09.028; pmid: 15479635
76. B. S. Chen, M. Hampsey, Functional interaction between TFIIB and the Rpb2 subunit of RNA polymerase II: Implications for the mechanism of transcription initiation. *Mol. Cell. Biol.* **24**, 3983–3991 (2004). doi: 10.1128/MCB.24.9.3983-3991.2004; pmid: 15082791
77. E. J. Cho, S. Buratowski, Evidence that transcription factor IIB is required for a post-assembly step in transcription initiation. *J. Biol. Chem.* **274**, 25807–25813 (1999). doi: 10.1074/jbc.274.36.25807; pmid: 10464320
78. T. S. Pardee, C. S. Bangur, A. S. Ponticelli, The N-terminal region of yeast TFIIB contains two adjacent functional domains involved in stable RNA polymerase II binding and transcription start site selection. *J. Biol. Chem.* **273**, 17859–17864 (1998). doi: 10.1074/jbc.273.28.17859; pmid: 9651390
79. N. A. Hawkes, S. G. Roberts, The role of human TFIIB in transcription start site selection in vitro and in vivo. *J. Biol. Chem.* **274**, 14337–14343 (1999). doi: 10.1074/jbc.274.20.14337; pmid: 10318856
80. K. Tran, J. D. Gralla, Control of the timing of promoter escape and RNA catalysis by the transcription factor IIb fingertip. *J. Biol. Chem.* **283**, 15665–15671 (2008). doi: 10.1074/jbc.M801439200; pmid: 18411280
81. H. Hou *et al*., Structural insights into RNA polymerase III-mediated transcription termination through trapping poly-deoxythymidine. *Nat. Commun.* **12**, 6135 (2021). doi: 10.1038/s41467-021-26402-9; pmid: 34675218
82. A. Feklistov, S. A. Darst, Structural basis for promoter-10 element recognition by the bacterial RNA polymerase σ subunit. *Cell* **147**, 1257–1269 (2011). doi: 10.1016/j.cell.2011.10.041; pmid: 22136875
83. Y. Zhang *et al*., Structural basis of transcription initiation. *Science* **338**, 1076–1080 (2012). doi: 10.1126/science.1227786; pmid: 23086998
84. S. M. Vos, L. Farnung, H. Urlaub, P. Cramer, Structure of paused transcription complex Pol II-DSIF-NELF. *Nature* **560**, 601–606 (2018). doi: 10.1038/s41586-018-0442-2; pmid: 30135580
85. Y. Chen *et al*., Allosteric transcription stimulation by RNA polymerase II super elongation complex. *Mol. Cell* **81**, 3386–3399.e10 (2021). doi: 10.1016/j.molcel.2021.06.019; pmid: 34265249

86. T. Kokubo, S. Yamashita, M. Horikoshi, R. G. Roeder, Y. Nakatani, Interaction between the N-terminal domain of the 230-kDa subunit and the TATA box-binding subunit of TFIID negatively regulates TATA-box binding. *Proc. Natl. Acad. Sci. U.S.A.* **91**, 3520–3524 (1994). doi: 10.1073/pnas.91.9.3520; pmid: 8170939
87. A. B. Patel *et al*., Structure of human TFIID and mechanism of TBP loading onto promoter DNA. *Science* **362**, eaau8872 (2018). doi: 10.1126/science.aau8872; pmid: 30442764
88. J. Chen, H. Boyaci, E. A. Campbell, Diverse and unified mechanisms of transcription initiation in bacteria. *Nat. Rev. Microbiol.* **19**, 95–109 (2021). doi: 10.1038/s41579-020-00450-2; pmid: 33122819
89. Y. Liu *et al*., Structural and mechanistic basis of reiterative transcription initiation. *Proc. Natl. Acad. Sci. U.S.A.* **119**, e2115746119 (2022). doi: 10.1073/pnas.2115746119; pmid: 35082149
90. A. Revyakin, C. Liu, R. H. Ebright, T. R. Strick, Abortive initiation and productive initiation by RNA polymerase involve DNA scrunching. *Science* **314**, 1139–1143 (2006). doi: 10.1126/science.1131398; pmid: 17110577
91. A. N. Kapanidis *et al*., Initial transcription by RNA polymerase proceeds through a DNA-scrunching mechanism. *Science* **314**, 1144–1147 (2006). doi: 10.1126/science.1131399; pmid: 17110578
92. J. T. Winkelman *et al*., Crosslink mapping at amino acid-base resolution reveals the path of scrunched DNA in initial transcribing complexes. *Mol. Cell* **59**, 768–780 (2015). doi: 10.1016/j.molcel.2015.06.037; pmid: 26257284
93. L. Li, V. Molodtsov, W. Lin, R. H. Ebright, Y. Zhang, RNA extension drives a stepwise displacement of an initiation-factor structural module in initial transcription. *Proc. Natl. Acad. Sci. U.S.A.* **117**, 5801–5809 (2020). doi: 10.1073/pnas.1920747117; pmid: 32127479
94. S. Samanta, C. T. Martin, Insights into the mechanism of initial transcription in *Escherichia coli* RNA polymerase. *J. Biol. Chem.* **288**, 31993–32003 (2013). doi: 10.1074/jbc.M113.497669; pmid: 24047893
95. D. Pupov, I. Kuzin, I. Bass, A. Kulbachinskiy, Distinct functions of the RNA polymerase σ subunit region 3.2 in RNA priming and promoter escape. *Nucleic Acids Res.* **42**, 4494–4504 (2014). doi: 10.1093/nar/gkt1384; pmid: 24452800
96. B. Kastner *et al*., GraFix: Sample preparation for single-particle electron cryomicroscopy. *Nat. Methods* **5**, 53–55 (2008). doi: 10.1038/nmeth1139; pmid: 18157137
97. S. Q. Zheng *et al*., MotionCor2: Anisotropic correction of beam-induced motion for improved cryo-electron microscopy. *Nat. Methods* **14**, 331–332 (2017). doi: 10.1038/nmeth.4193; pmid: 28250466
98. K. Zhang, Gctf: Real-time CTF determination and correction. *J. Struct. Biol.* **193**, 1–12 (2016). doi: 10.1016/j.jsb.2015.11.003; pmid: 26592709
99. S. H. Scheres, RELION: Implementation of a Bayesian approach to cryo-EM structure determination. *J. Struct. Biol.* **180**, 519–530 (2012). doi: 10.1016/j.jsb.2012.09.006; pmid: 23000701
100. D. Kimanius, B. O. Forsberg, S. H. Scheres, E. Lindahl, Accelerated cryo-EM structure determination with parallelisation using GPUs in RELION-2. *eLife* **5**, e18722 (2016). doi: 10.7554/eLife.18722; pmid: 27845625
101. A. Punjani, J. L. Rubinstein, D. J. Fleet, M. A. Brubaker, cryoSPARC: Algorithms for rapid unsupervised cryo-EM structure determination. *Nat. Methods* **14**, 290–296 (2017). doi: 10.1038/nmeth.4169; pmid: 28165473
102. E. F. Pettersen *et al*., UCSF Chimera—A visualization system for exploratory research and analysis. *J. Comput. Chem.* **25**, 1605–1612 (2004). doi: 10.1002/jcc.20084; pmid: 15264254
103. P. Emsley, K. Cowtan, Coot: Model-building tools for molecular graphics. *Acta Crystallogr. D Biol. Crystallogr.* **60**, 2126–2132 (2004). doi: 10.1107/S0907444904019158; pmid: 15572765
104. V. B. Chen *et al*., MolProbity: All-atom structure validation for macromolecular crystallography. *Acta Crystallogr. D Biol. Crystallogr.* **66**, 12–21 (2010). doi: 10.1107/S0907444909042073; pmid: 20057044
105. W. L. DeLano, The PyMOL Molecular Graphics System (2002); http://www.pymol.org.

ACKNOWLEDGMENTS

We thank Y. Zhang and H. Zhang for their help with the transcription initiation assay and the Center of Cryo-Electron Microscopy at Fudan University for their support with cryo-EM data collection. **Funding:** This work was supported by grants from the National Key R&D Program of China (2021YFA1300100 and 2022YFA1303200), the National Natural Science Foundation of China (32271242, 32030055, 31830107, and 31821002), the Basic Research Special Zone Plan of Shanghai (22TQ020), the XPLORER Prize (Y.X.), the New Cornerstone Investigator Program (Y.X.), the Shanghai Oriental Scholar Distinguished Professor Project (X.C.), and the Young Elite Scientists Sponsorship Program by CAST (X.C.). **Author contributions:** X.C. and X.W. prepared the samples with the help of X.Q. and Wa.L.; We.L. and Q.W. performed the cryo-EM analyses and model building with the help of Y.R.; X.C. and Y.X. designed the experiments, analyzed the data, and wrote the manuscript; and Y.X. supervised the project. **Competing interests:** The authors declare no competing interests. **Data and materials availability:** The cryo-EM maps and coordinates have been deposited to the Electron Microscopy Data Bank (EMDB) and Protein Data Bank (PDB). The transcribing complexes include TC2 (EMD-37395, PDB ID 8WAK), TC3 (EMD-37396, PDB ID 8WAL), TC4 (EMD-37398, PDB ID 8WAN), TC5 (EMD-37399, PDB ID 8WAO), TC6 (EMD-37400, PDB ID 8WAP), TC7 (EMD-37401, PDB ID 8WAQ), TC8 (EMD-37402, PDB ID 8WAR), TC9 (EMD-37403, PDB ID 8WAS), TC10 (EMD-37404, PDB ID 8WAT), TC11 (EMD-37405, PDB ID 8WAU), TC12 (EMD-37406, PDB ID 8WAV), TC13 (EMD-37407, PDB ID 8WAW), TC14 (EMD-37408, PDB ID 8WAX), TC15 (EMD-37409, PDB ID 8WAY), TC16 (EMD-37410, PDB ID 8WAZ), TC17 (EMD-37411, PDB ID 8WB0), TC9 on AdML^{9G} (EMD-37412), and TC10 on AdML^{10G} (EMD-37413). **License information:** Copyright © 2023 the authors, some rights reserved; exclusive licensee American Association for the Advancement of Science. No claim to original US government works. https://www.science.org/about/science-licenses-journal-article-reuse

SUPPLEMENTARY MATERIALS

science.org/doi/10.1126/science.adi5120
Supplementary Text
Figs. S1 to S13
References (*106*, *107*)
MDAR Reproducibility Checklist
Movies S1 to S4
Data S1 to S4

Submitted 1 May 2023; accepted 11 November 2023
10.1126/science.adi5120

Pushing the Boundaries of Knowledge

As AAAS's first multidisciplinary, open access journal, *Science Advances* publishes research that reflects the selectivity of high impact, innovative research you expect from the *Science* family of journals, published in an open access format to serve a vast and growing global audience. Check out the latest findings or learn how to submit your research: **ScienceAdvances.org**

Science Advances
AAAS

GOLD OPEN ACCESS, DIGITAL, AND FREE TO ALL READERS

RESEARCH ARTICLE SUMMARY

SIGNAL TRANSDUCTION

Molecular determinants of ligand efficacy and potency in GPCR signaling

Franziska M. Heydenreich*, Maria Marti-Solano†, Manbir Sandhu†, Brian K. Kobilka*, Michel Bouvier*, M. Madan Babu*

INTRODUCTION: Heterotrimeric guanine nucleotide–binding protein (G protein)–coupled receptors (GPCRs) bind extracellular ligands to modulate intracellular signaling responses. Two fundamental properties of ligand-receptor-signaling systems are efficacy (the maximum achievable response) and potency (the ligand concentration required to produce the half-maximal response). Although efficacy and potency have been measured for numerous ligand-receptor-signaling systems for several decades, the molecular determinants and principles governing these pharmacological properties remain a mystery.

RATIONALE: Understanding how each receptor residue contributes to efficacy and potency can aid in designing drugs to elicit desired signaling responses. Using the adrenaline–β2 adrenergic receptor (β2AR)–Gα_s system, we perturbed the side chain of each of the receptor's 412 residues and determined the impact on efficacy and potency. By developing a data science framework that integrates pharmacological and structural data, we contextualized ligand-induced structural changes and revealed the principles of efficacy and potency.

RESULTS: Only 20% of the β2AR residues contribute to the receptor's pharmacological properties. One-third of those pharmacologically relevant residues map to ligand- or G protein–binding sites or to evolutionarily conserved motifs; the other two-thirds are distributed throughout the receptor. All ligand-binding residues are important for signaling but show differential contributions to efficacy and potency, which indicates that specific contacts between ligand and receptor could be modulated to fine-tune pharmacological properties. By contrast, only one-third of the receptor residues that contact the G protein contribute to pharmacology, which indicates that these positions tolerate mutations and provides an explanation for the evolvability of G protein selectivity.

We integrated structural data about active and inactive receptor conformations with pharmacological measurements. Not all residues that undergo structural change are pharmacologically important, and several pharmacologically important residues do not undergo structural change upon activation. We categorized all receptor residues into four classes: Driver and passenger residues mediate active state–specific contacts, and, whereas drivers affect pharmacology when mutated, passengers do not. Modulator and bystander residues do not mediate active state–specific contacts, but modulators affect pharmacology when mutated, whereas bystanders do not.

We uncovered an allosteric network of active state–specific contacts mediated by driver residues from the ligand-binding pocket to the G protein–binding interface, thereby identifying structural changes that are pharmacologically relevant. Modulator residues are located near the allosteric network and functional sites. Surface-exposed driver, modulator, and passenger residues represent key allosteric sites and potential targets for the development of new allosteric ligands. Analysis of human polymorphisms and the conservation of residues across species revealed that passenger, modulator, and driver residues are under increasing selection pressure compared with bystander residues in this receptor.

CONCLUSION: Our work reveals how a GPCR decodes and translates the information encoded in a ligand to mediate a distinct signaling response. We anticipate that the application of this data science framework will enable the design of orthosteric and allosteric molecules that can elicit defined signaling responses. ■

The list of author affiliations is available in the full article online.
*Corresponding author. Email: franziska.heydenreich@pharmazie.uni-marburg.de (F.M.H.); kobilka@stanford.edu (B.K.K.); michel.bouvier@umontreal.ca (M.B.); madan.babu@stjude.org (M.M.B.)
†These authors contributed equally to this work.
Cite this article as F. M. Heydenreich *et al.*, *Science* **382**, eadh1859 (2023). DOI: 10.1126/science.adh1859

READ THE FULL ARTICLE AT
https://doi.org/10.1126/science.adh1859

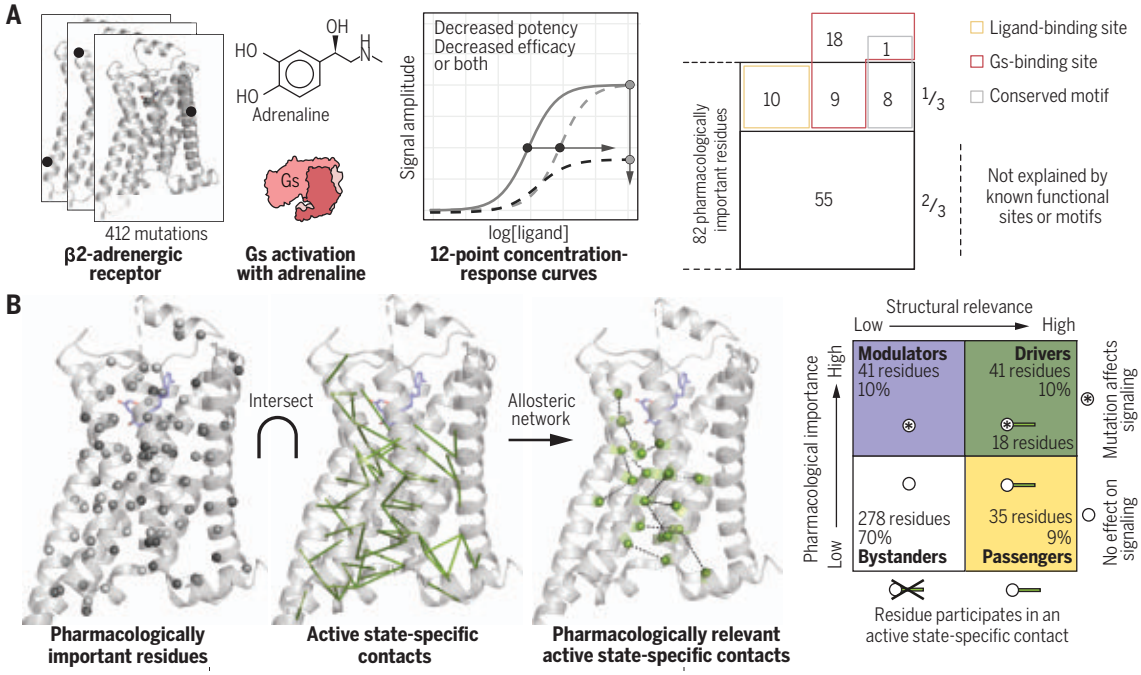

Determinants and molecular origins of efficacy and potency in a ligand-receptor-signaling system. (**A** and **B**) By developing a data science framework that integrates experimental values of adrenaline-stimulated Gs signaling for 412 mutants of the β2AR (A) and data on structural changes upon ligand-induced receptor activation (B), we reveal the determinants and the allosteric network governing ligand efficacy and potency in this prototypical GPCR system.

RESEARCH ARTICLE

SIGNAL TRANSDUCTION

Molecular determinants of ligand efficacy and potency in GPCR signaling

Franziska M. Heydenreich[1,2,3]*†, Maria Marti-Solano[2,4]‡, Manbir Sandhu[5]‡, Brian K. Kobilka[1]*, Michel Bouvier[3]*, M. Madan Babu[2,5]*

Heterotrimeric guanine nucleotide–binding protein (G protein)–coupled receptors (GPCRs) bind to extracellular ligands and drugs and modulate intracellular responses through conformational changes. Despite their importance as drug targets, the molecular origins of pharmacological properties such as efficacy (maximum signaling response) and potency (the ligand concentration at half-maximal response) remain poorly understood for any ligand-receptor-signaling system. We used the prototypical adrenaline–β2 adrenergic receptor–G protein system to reveal how specific receptor residues decode and translate the information encoded in a ligand to mediate a signaling response. We present a data science framework to integrate pharmacological and structural data to uncover structural changes and allosteric networks relevant for ligand pharmacology. These methods can be tailored to study any ligand-receptor-signaling system, and the principles open possibilities for designing orthosteric and allosteric compounds with defined signaling properties.

Heterotrimeric guanine nucleotide–binding protein (G protein)–coupled receptors (GPCRs) constitute a major family of membrane proteins that respond to diverse extracellular ligands, including photons, small molecules, neurotransmitters, and hormones (*1*–*5*). In humans, more than 500 endogenous ligands (*6*) act on 800 GPCRs and regulate key aspects of human biology (*7*, *8*). As a result of their capacity to modulate human physiology, GPCRs are targets of about one-third of all US Food and Drug Administration (FDA)–approved drugs for various diseases (*9*). Ligand binding to a GPCR induces conformational changes that enable modulation of downstream signaling responses (*10*). During that process, the ligand shifts the conformational equilibrium of the receptor toward a more active or inactive state, depending on whether it is an agonist, antagonist, or inverse agonist (*11*, *12*). The conformational states associated with agonist binding strongly increase the likelihood of a signaling response (e.g., G protein activation). This agonist capacity to promote signaling has been classically quantified by two fundamental pharmacological parameters: efficacy and potency (*13*), which can be determined by monitoring the receptor signaling response at various ligand concentrations (concentration-response curves). Efficacy relates to the maximum amplitude of a signaling response, whereas potency refers to the agonist concentration at which signaling reaches the half-maximal response. Endogenous agonist efficacy and potency are within a physiologically relevant range as a result of evolutionary selection pressure on the tertiary structure of GPCRs. Thus, understanding how the ligand interacts with the receptor to modulate the signaling response is paramount to rationalizing the link between endogenous ligand properties and receptor sequence and structure, which can aid in designing drugs that engage specific receptor residues to elicit distinct signaling responses in a disease context.

Numerous structural studies have revealed the importance of the movement of specific transmembrane helices as a key feature that is associated with receptor activation upon ligand binding (*14*–*16*). Furthermore, changes in the size of the ligand-binding cavity have been associated with high-affinity ligand binding and the strength of the signaling response (*17*). Extensive mutagenesis studies have identified residues along the receptor sequence that are important for modulating downstream signaling activity (*18*, *19*). Despite the thorough pharmacological, structural, and mutational characterization of numerous ligand-GPCR pairs over the years, we do not yet fully understand how specific residues of the receptor decode and translate the information that is encoded in the ligand atoms to mediate a distinct intracellular signaling response (i.e., the molecular origins of efficacy and potency). For instance, in the well-studied adrenaline–β2 adrenergic receptor (β2AR)–Gs signaling system, it is unclear whether all residues that contact the ligand or the G protein (fig. S1) are important for adrenaline's efficacy and potency toward Gs and whether all residues that are involved in structural changes during activation are important for signaling (fig. S1). If not, it would be helpful to identify the residues that help convert ligand binding into a signaling response and how they contribute to the efficacy and potency response of the ligand at the receptor.

To systematically infer how ligand atoms are decoded by the receptor sequence and structure to modulate downstream signaling response, one needs to perturb the side chain of every receptor residue, reliably measure the impact on efficacy and potency for a signaling response, and contextualize the structural changes of the receptor residue with its pharmacological importance. We used β2AR, a well-studied, prototypical family A GPCR that mediates the fight-or-flight response when activated by its endogenous agonist adrenaline (epinephrine) and signals through the G protein Gs. By developing a data science framework that integrates (i) experimentally measured values of adrenaline-stimulated Gs signaling upon systematically perturbing the side chain of every residue in β2AR and (ii) data on structural changes associated with agonist binding, receptor activation, and Gs coupling (Fig. 1), we reveal the molecular origins and principles that govern ligand efficacy and potency in this prototypical GPCR signaling system.

BRET-based biosensors allow in-depth pharmacological profiling of receptor mutants

We perturbed the side chain of each of the 412 residues in the receptor by mutating the residue to alanine, or glycine if the native amino acid was alanine, because both types of substitutions are well tolerated in the long, membrane-spanning α helices (*20*) of a GPCR. For each mutant, we then evaluated its adrenaline-stimulated Gs signaling profile in a live-cell assay with a bioluminescence resonance energy transfer (BRET)–based biosensor (*21*, *22*) (fig. S2 and Materials and methods). The biosensor reports on the distance between the Gα and Gγ subunits of the heterotrimeric G protein; this distance increases upon receptor activation as a result of conformational changes in the α subunit and its dissociation from the βγ subunits, leading to a decrease of resonance energy transfer between the donor and acceptor that are fused to the α and γ subunit, respectively. Each assay was performed as 12-point concentration-response curves in biological triplicates (Fig. 1,

[1]Department of Molecular and Cellular Physiology, Stanford University School of Medicine, Stanford, CA, USA. [2]MRC Laboratory of Molecular Biology, Cambridge, UK. [3]Department of Biochemistry and Molecular Medicine, Institute for Research in Immunology and Cancer, Université de Montréal, Montreal, QC, Canada. [4]Department of Pharmacology, University of Cambridge, Cambridge, UK. [5]Department of Structural Biology and Center of Excellence for Data-Driven Discovery, St. Jude Children's Research Hospital, Memphis, TN, USA.
***Corresponding author. Email: franziska.heydenreich@pharmazie.uni-marburg.de (F.M.H.); kobilka@stanford.edu (B.K.K.); michel.bouvier@umontreal.ca (M.B.); madan.babu@stjude.org (M.M.B.)**
†Present address: Department of Pharmaceutical Chemistry, University of Marburg, Marburg, Germany.
‡These authors contributed equally to this work.

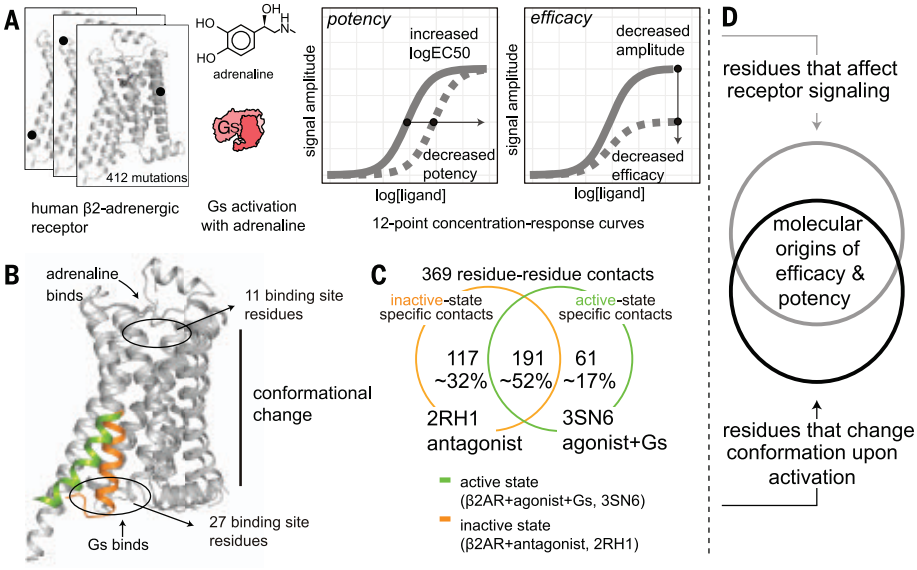

Fig. 1. An approach to integrate pharmacological and structural data to reveal the molecular determinants of efficacy and potency. (**A**) Every residue of a receptor is mutated, and key pharmacological properties of the adrenaline-β2AR-Gs signaling system are determined experimentally. (**B** and **C**) Active- and inactive-state structures of receptors are analyzed as networks of noncovalent contacts between residues to infer contacts that are specific for the active and/or inactive state. (**D**) These data are integrated using a data science approach to discover the molecular determinants and the underlying allosteric network governing efficacy and potency.

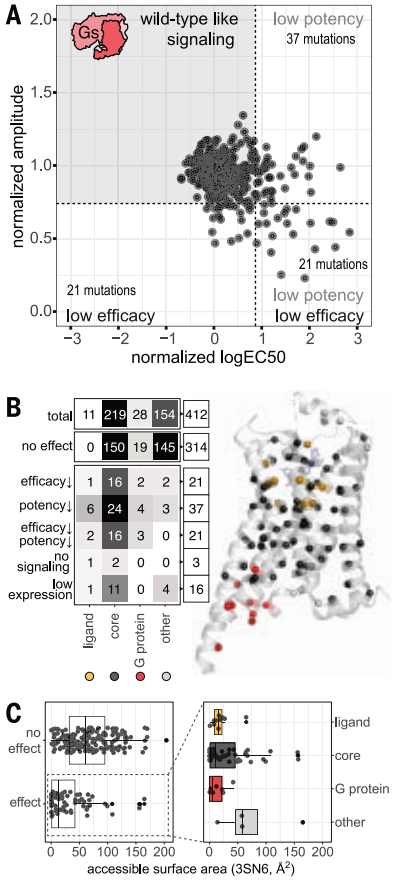

Fig. 2. Receptor positions that affect efficacy or potency upon mutation. (**A**) Overview of potency (normalized $logEC_{50}$) and efficacy (normalized signal amplitude) of all β2AR mutations. Cutoffs are shown as dashed lines (Materials and methods). (**B**) Distribution of residues by functional relevance and their effect on efficacy and potency (Materials and methods). Ligand-binding pocket and G protein–binding site include residues within 4 Å of adrenaline (PDB ID: 4LDO) or Gs (PDB ID: 3SN6), respectively. (**C**) Accessible surface area of residues, grouped by whether a mutation affects signaling (effect) or not (no effect). For residues where signaling was affected by mutation, the location of mutations in the ligand-binding site, in the core, in the G protein–binding site, or in none of the above (other) is indicated.

top panel, and Materials and methods) to quantify the signal amplitude (efficacy) and the log mean effective concentration ($logEC_{50}$) (potency) of the adrenaline-stimulated G protein activation (fig. S2 and Materials and methods). Because a mutation may affect receptor abundance and low cell-surface abundance could negatively influence the signaling, we also evaluated the abundance of all mutants by cell-surface enzyme-linked immunosorbent assay (ELISA) (fig. S3, A to C, and Materials and methods). We performed measurements on cells expressing wild-type β2AR or no receptor as controls. In total, we obtained more than 16,000 signaling data points; the pharmacological properties for agonist-induced Gs activation for each mutant are reported in table S1. For subsequent analyses of these data, we used the GPCRdb numbering scheme (*23*), a system based on Ballesteros-Weinstein numbering (*24*), wherein the first number in the superscript refers to the helix or loop, and the second number refers to the position relative to the most conserved residue (numbered 50) in that helix [e.g., $L124^{3x43}$, which is 7 residues before the most conserved residue in transmembrane helix 3 (TM3)].

One-fifth of the positions in β2AR are important for adrenaline efficacy, potency, or both

For 16 receptor positions, side chain perturbation severely affected cell-surface abundance (<25% of wild-type level; Materials and methods). These mutants were excluded from further analysis because we could not reliably determine whether the observed reduction in signaling resulted from altered function, reduced abundance, or both (fig. S3, A to C). Many of these positions are highly conserved and are likely important for protein folding, receptor biogenesis, and transport to the cell membrane (fig. S3, D to H). The remaining 396 mutants had cell-surface abundance that allowed reliable estimation of pharmacological parameters and were therefore considered for further analysis (abundance >25% of the wild-type β2AR; Materials and methods). Most of the single-point mutations (~80%; at 314 positions) did not negatively affect Gs signaling, and ~20% (at 82 positions) had an impact on signaling. Of these 82, 21 primarily reduced efficacy, 37 primarily reduced potency, 21 reduced both potency and efficacy, and 3 resulted in no measurable signal (Fig. 2, A and B).

Mapping these positions on the secondary structure elements of the receptor showed that TM5 was enriched in mutations that affected potency only, whereas TM3 was enriched in mutations that affected efficacy only. The mutations that affected efficacy and potency simultaneously were distributed across the different transmembrane helices (fig. S4, A to D). Although some of the identified positions overlap with functional residues in the ligand-binding pocket and the G protein–binding interface, several positions mapped to other parts of the receptor, including residues on the receptor surface, with the highest density mapping to the receptor core (Fig. 2, B and C). These findings collectively indicate that the efficacy and potency of this endogenous agonist at this receptor are likely governed by a subset of receptor positions (~20%) that are not just restricted to known functional sites but are also distributed in different parts of the structure. These receptor positions thus decode and translate ligand binding into a signaling response and are, hence, pharmacological determinants for this ligand-receptor-signaling system.

Receptor residue–ligand atom contacts contribute differentially to efficacy and potency

We investigated how each ligand-contacting residue contributes to efficacy and potency. For this, we first identified all receptor residues that contact adrenaline using a distance cutoff [Protein Data Bank (PDB) ID: 4LDO (*25*)] (Fig. 3A and Materials and methods) and the ligand atoms that they contact by constructing a receptor residue–ligand atom contact matrix (Fig. 3B). Although mutants of all 10 of the 11 adrenaline-contacting residues that expressed well negatively affected the signaling response, they had distinct effects on efficacy and potency (Y316^{7x42}A markedly decreased receptor abundance; fig. S3). Mutations in around half of the positions (6 of 10) affected potency only, one affected efficacy only, two affected both efficacy and potency when mutated, and D113^{3x32}A completely abolished signaling. D113^{3x32} is critical for agonist binding in β2AR (*26*, *27*) and other aminergic receptors because it contacts the positively charged amine group, which is a common feature of endogenous agonists for monoamine receptors. When this information was mapped onto the ligand-binding pocket (Fig. 3C), it was obvious that the ligand-contacting residues that affect potency only upon mutation group together on one side of the receptor involving TM3, TM5, and TM6, whereas those that affect both efficacy and potency upon mutation group together on the other side of the receptor, largely involving TM6 and TM7. The ligand-contacting residue that affected efficacy only is in TM3 and is deeply buried in the binding pocket. These results indicate that each receptor residue that contacts the ligand contributes differentially to the overall pharmacological response. Of the 159 Å^2 of receptor surface area occupied by the ligand, 20% (31.5 Å^2) appears to be important for both efficacy and potency, 6% (9 Å^2) for efficacy only, and 59% (93 Å^2) for potency only. Thus, the pharmacological parameters of a ligand at a receptor seem to emerge from the differential contribution of each receptor residue to the overall efficacy and potency in response to a ligand.

From the ligand perspective, the distance-based contact map shows that some adrenaline atoms are in close proximity to residues that only affect potency when mutated (the oxygen atoms in the hydroxyl groups and the aromatic carbon C3; Fig. 3B). The map also shows that the aromatic atoms C1, C2, C5, and C6 are in close proximity to residues that affect potency only, efficacy only, or both when mutated. The remaining ligand atoms make extensive contact with two residues that affect both efficacy and potency when mutated, including the N312^{7x38} and the key D113^{3x32} (O3, C7, C8, N1, and C9). These findings reveal the existence of spatially clustered groups of adrenaline atoms that mediate contact with specific receptor residues to preferentially affect efficacy and/or potency responses in receptor signaling. An implication of this observation is that chemical modifications of these atoms that can mediate contacts with specific receptor residues might allow a more targeted ligand modification to alter the efficacy or potency of Gs activation. This can be seen from the receptor residue–ligand atom contact matrix for the β2-adrenergic ligand salmeterol (fig. S5). Together, these results indicate that, although all ligand-contacting residues are important for receptor signaling, distinct receptor residues and specific chemical groups on the ligand contribute differentially to efficacy and potency responses. Thus, although efficacy

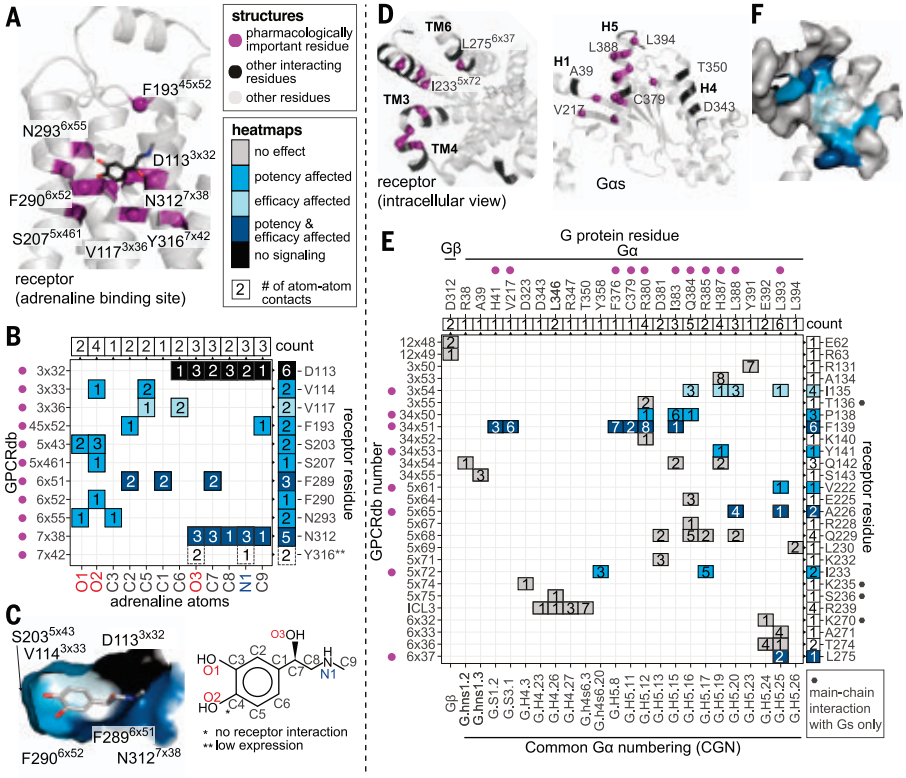

Fig. 3. Effect of mutations in the ligand- and G protein–binding sites. (**A**) View of the ligand-binding site; positions are labeled with residue number and GPCRdb number in superscript. Pharmacologically important residues (according to cutoff values; see Materials and methods) are indicated in violet. The following are not labeled for clarity: V114^{3x33}, S203^{5x43}, and F289^{6x51}. (**B**) Receptor residue–ligand atom contact plot with the ligand atoms on the *x* axis and the receptor's GPCRdb and residue numbers on the *y* axis. The number of noncovalent contacts between a receptor residue and ligand atom is shown in each square of the heatmap. The chemical structure of adrenaline below the heatmap indicates the labeling of adrenaline atoms used for the *x* axis. Box colors in the heatmap refer to the pharmacological effect of the mutation [efficacy affected (light blue), potency affected (ocean blue), both efficacy and potency affected (dark blue), or no measurable signaling (black)]. The number of receptor residues contacted by each ligand atom and the number of ligand atoms contacted by each receptor residue are indicated in boxes at the top and right-hand side of the heatmap, respectively. (**C**) Surface view of the ligand-binding site, where the surface of each receptor residue is colored by the effect that its mutation had on signaling. (**D**) Views of the G protein–binding site on the receptor and the Gs protein. Positions are labeled with residue number and with GPCRdb numbers. Pharmacologically important residues are indicated in violet, and other interacting residues are marked in black. (**E**) Receptor–G protein residue contact plot based on the structure of β2AR in complex with heterotrimeric Gs (PDB ID: 3SN6). G protein residues are shown on the *x* axis and the receptor residues on the *y* axis. The receptor residues that contact the G protein through a receptor main chain contact only are marked with a dark gray hexagon on the right side of the matrix. The number of noncovalent contacts between a receptor residue and a G protein residue are mentioned in each square of the heatmap. Boxes are colored as in (B). The CGN number is provided on the *x* axis. The number of contacting residues by the receptor and the G protein are shown on the top and right-hand side of the heatmap. Residue T68 is not included because it is a contact that is observed only in the structure of β2AR with Gs peptide (PDB ID: 6E67). (**F**) Surface view of the G protein–binding site colored by mutational effect, with helix 5 shown as cartoon. Single-letter abbreviations for the amino acid residues are as follows: A, Ala; C, Cys; D, Asp; E, Glu; F, Phe; G, Gly; H, His; I, Ile; K, Lys; L, Leu; M, Met; N, Asn; P, Pro; Q, Gln; R, Arg; S, Ser; T, Thr; V, Val; W, Trp; and Y, Tyr.

and potency are measured as a general ligand property at a receptor, they arise from a collection of receptor residue–ligand atom noncovalent contacts, each of which contributes differentially to pharmacological properties in downstream signaling response.

Only one-third of the G protein–contacting residues are important for efficacy and potency

From the structures of the β2AR-Gs complex (PDB IDs: 3SN6 and 6E67), we observed that 27 receptor residues make 49 noncovalent contacts with 24 G protein residues (Fig. 3, D to F, and Materials and methods). Only one-third (9 of 27) of the receptor interface residues showed an effect on G protein activation when mutated. This is in stark contrast to the ligand-binding residues, where all positions were important for receptor signaling (Fig. 3B). Of the positions in the G protein–binding site, four affected potency only, two affected efficacy only, and three affected both when mutated. From the G protein perspective, key conserved residues that undergo conformational changes during receptor binding [e.g., H5.12,15,16,19,20,25, S3.1, and S1.2 in the common G protein numbering (CGN) scheme (*28*)] mediate extensive contacts with receptor residues that affected efficacy, potency, or both when mutated (*28*, *29*). Collectively, these results reveal that there is a subset of receptor-interface residues that translate ligand potency and efficacy into G protein activation at the receptor–G protein interface. A large fraction of receptor residues that contact the G protein can be mutated to alanine with little effect on efficacy or potency and are thus evolvable. The latter findings imply that upon gene duplication and divergence, receptors can tolerate certain types of mutations at the G protein–binding interface without losing their capacity for signal transduction. Such a structure-to-function architecture may provide an additional explanation as to why GPCRs could evolve by gene duplication and acquire new G protein selectivity (*30*, *31*).

Conserved motifs only explain a fraction of residues important for signaling

Of all the positions that had an influence on ligand efficacy and potency, only a fraction (19 of 82 residues; 24%) were in the ligand-binding and G protein–binding sites. A detailed analysis of the key motif residues of GPCRs, as well as the most highly conserved positions (x50 positions in each helix) (Materials and methods), accounted for an additional eight residues (10%) (fig. S6). Key sequence and structural motifs with known functional roles include CWxP, PIF, NPxxY, and DRY (where each uppercase letter is an amino acid residue, and each "x" represents any amino acid). However, two-thirds of the pharmacologically important residues (55 of 82 residues) do not map to known functional sites or motifs and are hence not readily interpretable. These positions most likely represent receptor- or receptor family–specific switches or allosteric conduits that contribute to translating ligand binding into signaling.

Structural changes alone do not specify the pharmacological importance of a residue

Because key structural changes have been extensively described as a hallmark of receptor activation (*14*, *16*, *32*, *33*), we investigated how those structural changes are associated with pharmacologically important residues. We calculated how much each residue moved during activation by computing the distance between the α-carbon atoms of each residue in the inactive (highest-resolution structure, 2.4 Å; PDB ID: 2RH1) and active, G protein–bound state (highest-resolution structure, 3.2 Å; PDB ID: 3SN6). The distribution of the distance moved by each residue is skewed to the right, where in ~8% of the cases, the α-carbon atom moved more than 4 Å (22 residues; fig. S1B). Of these, only seven were pharmacologically important and affected efficacy or potency when mutated, whereas the rest had no impact on downstream signaling (Fig. 4, A and B). Furthermore, comparing the set of residues that were pharmacologically important with those that were not revealed that an approximately equal proportion between the two sets appeared to undergo a structural change (i.e., move >4 Å). Finally, an analysis of dihedral angles in the active and inactive states also revealed no association between the extent of change in the dihedral angle and pharmacological importance of a residue (fig. S7). These findings collectively suggest that it is not possible to infer the pharmacological importance of a residue just from the extent of structural change (translation or rotation) during receptor activation.

Because the formation or breaking of noncovalent contacts during activation comprises both translational (distance) and rotational

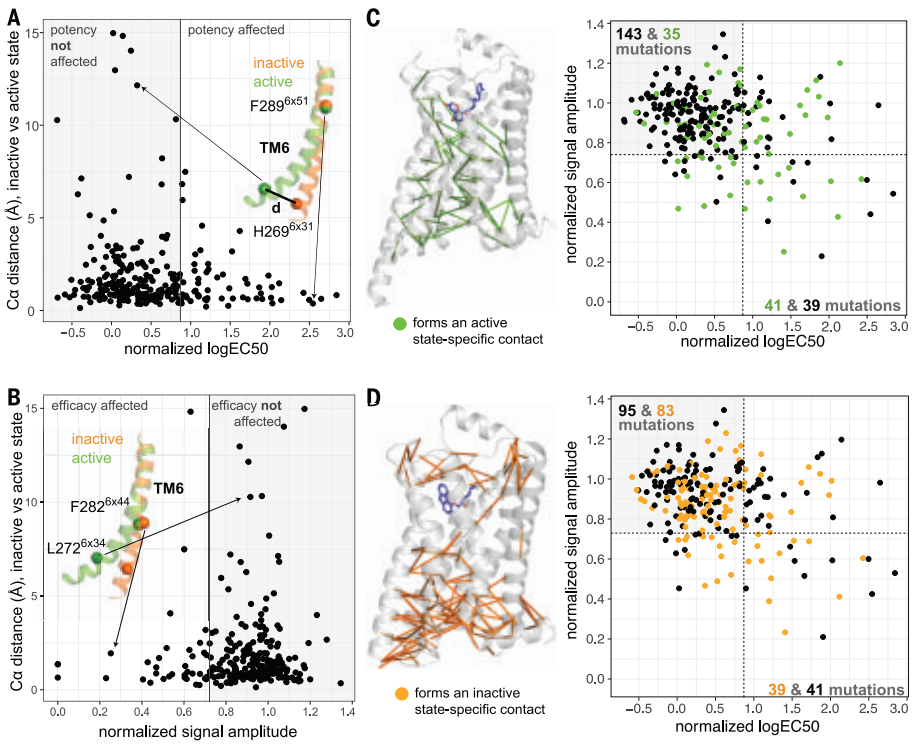

Fig. 4. Structural changes and pharmacological importance of residues. (**A**) Distance between Cα atoms in the inactive state (PDB ID: 2RH1) versus the active, G protein–bound state (PDB ID: 3SN6) plotted against normalized Gs $logEC_{50}$ of the alanine or glycine mutant in that position. White and gray areas indicate residues with potency affected and not affected, respectively, upon mutation. (**B**) Distance between Cα atoms plotted against normalized Gs signal amplitude. White and gray areas indicate residues with efficacy affected and not affected, respectively, upon mutation. (**C**) Active state–specific contacts (Materials and methods) are shown on the active, G protein–bound receptor structure. Potency and efficacy values for all mutants are plotted (except those with low abundance and those for which no signaling was detected). Mutants are colored green if the mutated residue is involved in an active state–specific contact and black if it is not. White areas indicate residues with efficacy, potency, or both affected, and the gray area indicates those that were not affected upon mutation. Numbers in the plots denote the number of residues in each category (black or green). (**D**) Inactive state–specific contacts on the inactive-state structure. A mutant (data point in the plot) is colored orange if the residue is involved in an inactive state–specific contact and black if it is not. White and gray areas of the graph are defined as in (C).

(dihedral angle) changes to different extents, we focused on residues that make active state–specific contacts or break inactive state–specific contacts to assess whether they can inform pharmacological importance (Fig. 4, C and D; Materials and methods; and table S2). Considering those two categories, the formation of an active state–specific contact by a residue showed a higher association with pharmacological importance. For instance, ~50% (41 of 80 residues with structural data) of residues that are pharmacologically important participated in an active state–specific contact, whereas only 20% (35 of 178) of the pharmacologically unimportant residues did. This effect was not observed for inactive state–specific contacts, for which ~50% (39 of 80) of pharmacologically important residues with structural data and 47% (83 of 178) of unimportant residues participated in an inactive state–specific contact. These findings indicate that systematic integration of mutational effects and structural analyses considering active state–specific residue contacts may help identify and characterize the subset of pharmacologically important residues that undergo a structural change in this ligand-receptor system. Notably, it can explain which of the structural changes that happen during activation are relevant for ligand efficacy and potency at the receptor.

Linking structural changes with pharmacological importance reveals new roles for residues

To identify the structural changes relevant for efficacy and potency, we devised an approach to integrate the experimentally determined pharmacological parameters with the active state–specific contacts (Fig. 5A and Materials and methods). We first classified every residue as pharmacologically important (if it affects efficacy, potency, or both when mutated) or

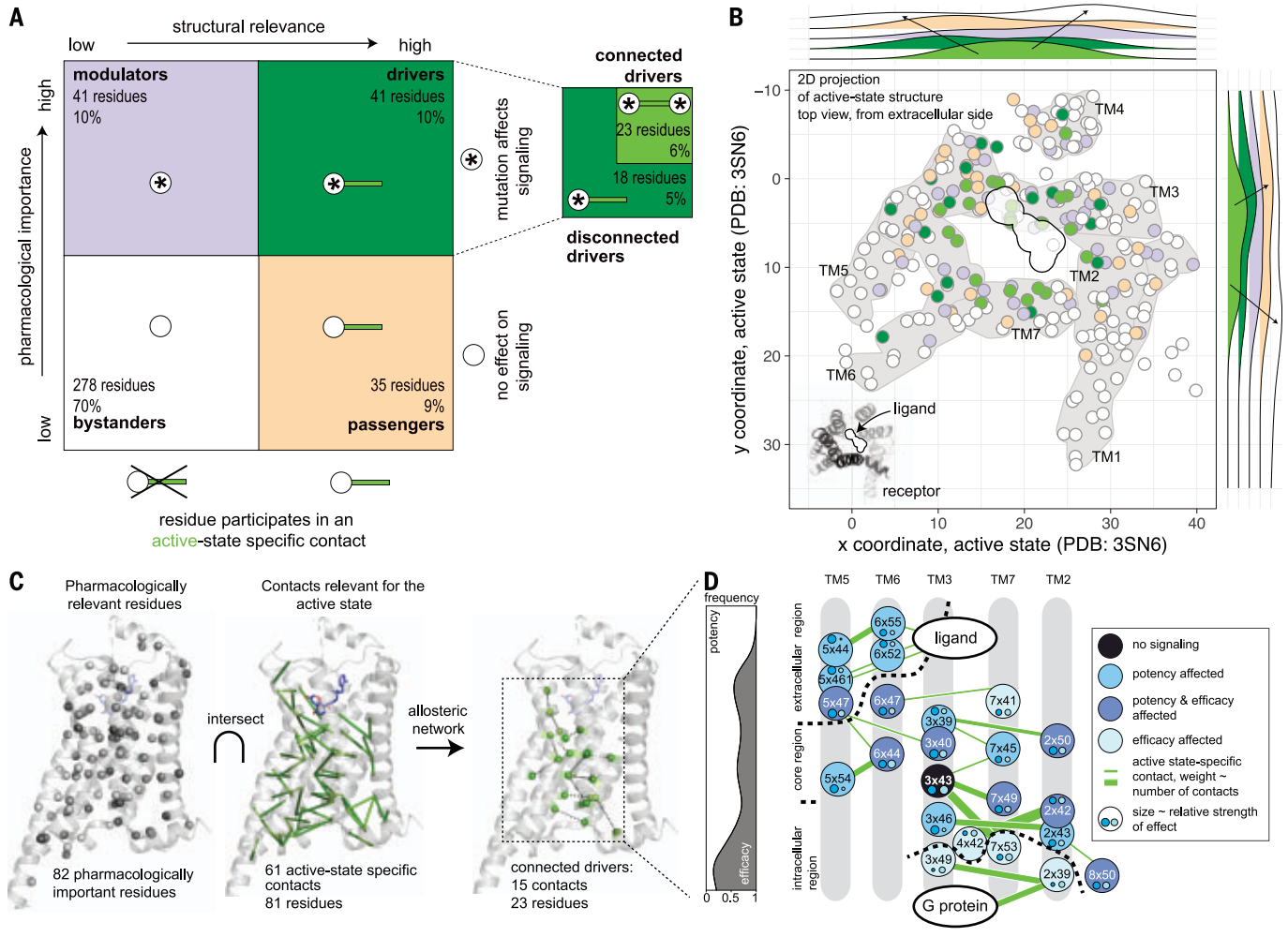

Fig. 5. The allosteric contact network for efficacy and potency as determined by structure and pharmacology. (**A**) Classification of residues according to their pharmacological importance (whether a mutation affected signaling or not) and structural relevance (whether a residue forms an active state–specific contact or not) into four main classes: bystanders (white), passengers (wheat), modulators (slate), and drivers (green), the latter of which is subdivided into connected drivers (driver residues connected to other driver residues) and unconnected driver residues (Materials and methods). (**B**) Position of residues classified by their participation in active state–specific contacts and their importance for pharmacology on a two-dimensional (2D) top-view projection of the active, G protein–bound structure of the β2AR (PDB ID: 3SN6). Frequency of residues along the *x* and *y* axes of the receptor (plane parallel to the membrane) is shown on the distributions outside. Arrows denote the direction of the peaks of the distribution for the residue classes. Driver residues tend to be in the center, whereas bystander residues tend to be at the periphery. (**C**) Integration of pharmacologically important residues and the residues contributing to newly established contacts in the active-state structure yields the allosteric network for efficacy and potency (see main text). (**D**) Residues forming the allosteric networks for efficacy and potency are represented as a cartoon, colored by the effect of the mutation. The graph (left) depicts the frequency of potency versus efficacy effects for residues in the network, projected on the axis running along the extra- to intracellular side. Small circles and their sizes (scaled to the relative strength of effect) within each residue indicate the magnitude and effect on potency and efficacy. Edge thickness in the network corresponds to the number of contacts, ranging from 1 to 5.

not pharmacologically important (if it has no effect on either efficacy or potency). We then stratified according to whether a residue forms an active state–specific contact or not (i.e., whether it is structurally important or not). On the basis of these two properties, we defined four classes of residues: (i) driver residues that mediate an active state–specific contact and affect pharmacology (41 residues), (ii) modulator residues that do not form an active state–specific contact but are important for pharmacology (41 residues), (iii) passenger residues that mediate an active state–specific contact but are not important for pharmacology (35 residues), and (iv) bystander residues that neither mediate active state–specific contacts nor affect pharmacology when mutated (278 residues) (Materials and methods and Fig. 5A). Thus, the pharmacologically important residues are either drivers or modulators (82 mutations that affect pharmacology), and the structurally important residues are either drivers or passengers (76 residues that mediate an active state–specific contact). As a general pattern, driver residues tend to be close to the central axis going through the receptor and perpendicular to the membrane, whereas modulator and passenger residues are located further away from this axis, in proximity with solvent or membrane-exposed positions (Fig. 5B). These observations prompted us to investigate the existence of a network of pharmacologically relevant active state–specific residue contacts mediated by driver residues and further understand the role of modulator residues for signal transduction.

A subset of residues driving efficacy and potency form an allosteric contact network

Of the 41 driver residues, 23 form 15 active state–specific noncovalent contacts to other driver residues with a shared pharmacological effect (connected drivers) (Materials and methods). This allosteric network of active state–specific contacts mediated by driver residues allowed us to describe how potency and efficacy signals are transmitted across the receptor structure at the residue level through coordinated structural rearrangements (Fig. 5C and fig. S8). The network involving connected drivers started extracellularly in TM5 and TM6 and formed several contacts between TM5 and TM6, including with F282^{6x44} of the PIF motif (*34*, *35*) (Fig. 5D), before reaching TM3 in the receptor core. TM3 further connected to TM7 and the most conserved residue in TM2, D79^{2x50} (*26*), which is part of the allosteric sodium-binding motif (*36*) (Fig. 5D). Finally, the network reached residues in the intracellular region, including D130^{3x49} and Y326^{7x53} of the conserved DRY and NPxxY motifs in TM3 and TM7, respectively (Fig. 5D). Potency-affecting driver residues in the network were enriched at the extracellular side of the receptor involving TM5 and TM6 (total of 9 residues; Fig. 5D), and efficacy-affecting driver residues were enriched at the intracellular side of the receptor in TM7, TM2, and TM3 (total of 5 residues; Fig. 5D). Driver residues in the allosteric network that affected both efficacy and potency were enriched in the center of the receptor, connecting to potency-only and efficacy-only residues (9 residues; Fig. 5D). This raises the question as to how ligand binding to the receptor initiates and transmits information through the allosteric network to modulate downstream signaling.

Key contact-rewiring events initiate and transmit information to mediate signaling

To understand how information is transmitted in the adrenaline-β2AR-Gs signaling system, we analyzed the relation between the ligand- and G protein–binding residues and the allosteric network. Focusing on the ligand-receptor interface, the allosteric contact network included three residues directly located in the ligand-binding site (N293^{6x55}, F290^{6x52}, and S207^{5x461}; all affected potency only when mutated); the other eight ligand-binding residues do not form active state–specific contacts. This highlights the existence of residues in the ligand-binding pocket that directly participate in the allosteric network. It also highlights the distinct roles mediated by the ligand-contacting residues on the receptor: although several residues stabilize ligand-receptor interactions, a subset of three driver residues that also contact the ligand likely initiate the allosteric changes during receptor activation (Fig. 5 and fig. S9). The latter set of three residues makes more extensive contact with other receptor residues compared with adrenaline. By contrast, ligand-binding residues that do not mediate active state–specific contacts (e.g., modulator residues D113^{3x32} and N312^{7x38}) make substantial contacts with adrenaline and fewer contacts with other receptor residues (fig. S9). Thus, some receptor and ligand atom contacts might contribute to the affinity of ligand binding, whereas others might have a more direct role in triggering the allosteric network to transmit the signaling response, perhaps through initiating a structural change and stabilizing a particular receptor conformation.

Focusing on the G protein–binding residues, of the nine that affected efficacy or potency when mutated (Materials and methods), one residue (driver residue T68^{2x39}) is part of the allosteric network. Although T68 does not mediate a contact in the receptor–heterotrimeric G protein complex structure, it does form a contact with Gs in the receptor-Gs peptide complex structure (*37*), which may represent an intermediate state in complex formation. Furthermore, L275^{6x37} (a disconnected driver that affects efficacy when mutated) mediates contact with a conserved residue on the G protein [H5.25; CGN scheme (*28*)]. L275^{6x37} is held in place through an inactive state–specific contact with I127^{3x46}. Upon receptor activation, this inactive state–specific contact is broken, allowing 6x37 to contact the G protein and 3x46 to mediate an active state–specific contact with Y326^{7x53} (*38*). Notably, this noncovalent contact is between a residue that affects potency only (3x46) and one that affects efficacy only (7x53). Thus, the G protein–binding residues that affect efficacy and potency when mutated can be classified into those that directly interact with the G protein and those that are part of or are connected to the allosteric network (fig. S10). Together, these observations highlight the importance of key rewiring events in the allosteric network involving the switch from the inactive state–specific contacts to active state–specific contacts upon ligand binding and G protein engagement for signal transduction (Fig. 5D and fig. S10). It also highlights that as functionally relevant intermediate state conformations are structurally characterized, the roles of some of the residues identified can be interpreted in more mechanistic detail.

Modulator residues near the allosteric network and functional sites modulate pharmacology

Of the 82 residues that were important for efficacy or potency, the role of two-thirds (54 of 82 residues; 41 are driver and 13 are modulators) could be explained as either involved in ligand or G protein binding, conserved motif residues, or driver residues forming the allosteric network or that mediate active state–specific contacts (fig. S11). We then investigated the role of the remaining one-third of the residues that are pharmacologically important (28 of 82 residues) and categorized them according to their likely function (fig. S11; these are the remaining 28 of the 41 modulator residues). Of those, the function of 10 residues may be explained by their ability to directly contact and perhaps stabilize a residue in the ligand-binding pocket or by being in the putative ligand entry pathway. Another six residues mediate noncovalent contacts with a driver residue (network modifier), and the function of seven modulators may be explained by lipid interaction. The roles for the remaining five residues were less clear (table S1, explanation column). We analyzed conformations of the active and inactive states, but a deeper understanding of the role of modulator residues can be obtained through the investigation of intermediate conformational states, by considering the role of structured water molecules in stabilizing or mediating conformational transitions, or through the analyses of data describing receptor dynamics (*39*, *40*). Taken together, these results identify and describe how residues around the allosteric network

and functional sites may modulate ligand efficacy and potency in β2AR.

Surface-exposed driver, modulator, and passenger residues represent key allosteric sites

Some of the pharmacologically important positions mapped to surface-exposed sites that were not part of the orthosteric ligand-binding site or the G protein–binding interface (Fig. 2C). The identification of pharmacologically important residues that lie on the receptor surface suggested possible structural sites for modulating receptor signaling that could be targeted by natural allosteric molecules (*41*, *42*). To test whether lipids, such as cholesterol, exert effects allosterically by binding to such sites and altering signaling, we analyzed structures of receptors in complex with cholesterol (Materials and methods and fig. S12). Cholesterol bound to a site containing three modulator and three passenger residues on the receptor surface. Thus, surface-exposed pharmacologically important residues might be targeted by synthetic allosteric ligands. In line with this idea, an analysis of the structure of the receptor in complex with the negative allosteric modulator (NAM) AS408 revealed that its binding interface contained two amino acids, I214^{5x53} (driver) and C125^{3x44} (modulator), that are important for receptor signaling and three passenger residues, all of which are surface exposed (Fig. 6, A and B, and Materials and methods; 7 residues contact the NAM). Similarly, an analysis of the structure of the receptor in complex with the positive allosteric modulator (PAM) 6FA showed that it bound to a different exposed surface containing the driver residue, D130^{3x49}, which is important for receptor signaling (Fig. 6, A to C). Five of the nine residues in the PAM binding site were passengers—i.e., residues that mediate active state–specific contacts but that do not affect efficacy or potency when mutated (Fig. 6, A to C). Passenger residues were significantly overrepresented (compared with random expectation) in both PAM and NAM binding sites, even when the N and C termini were excluded from the test ($P = 1.5 \times 10^{-3}$; hypergeometric test).

These results show that allosteric modulators, which were discovered through screening efforts, tend to bind surface-exposed sites that contain driver, modulator, and passenger residues rather than the more prevalent bystander residues (i.e., residues that do not mediate active state–specific contacts and are not important for pharmacology). Although the active state–specific contacts mediated by the passenger residues might minimize entropic cost by stabilizing a specific receptor conformation, thereby energetically favoring allosteric ligand binding, the perturbation of the driver or modulator residues at such sites might affect the allosteric network and hence mediate the positive or negative cooperativity at the orthosteric ligand-binding site. In other words, a combination of (i) conformational stabilization of the active or inactive state by the allosteric ligand through interactions with passenger residues and (ii) perturbation of the allosteric network through interactions with surface-exposed modulator or driver residues might contribute to the property of the allosteric ligand. An important implication

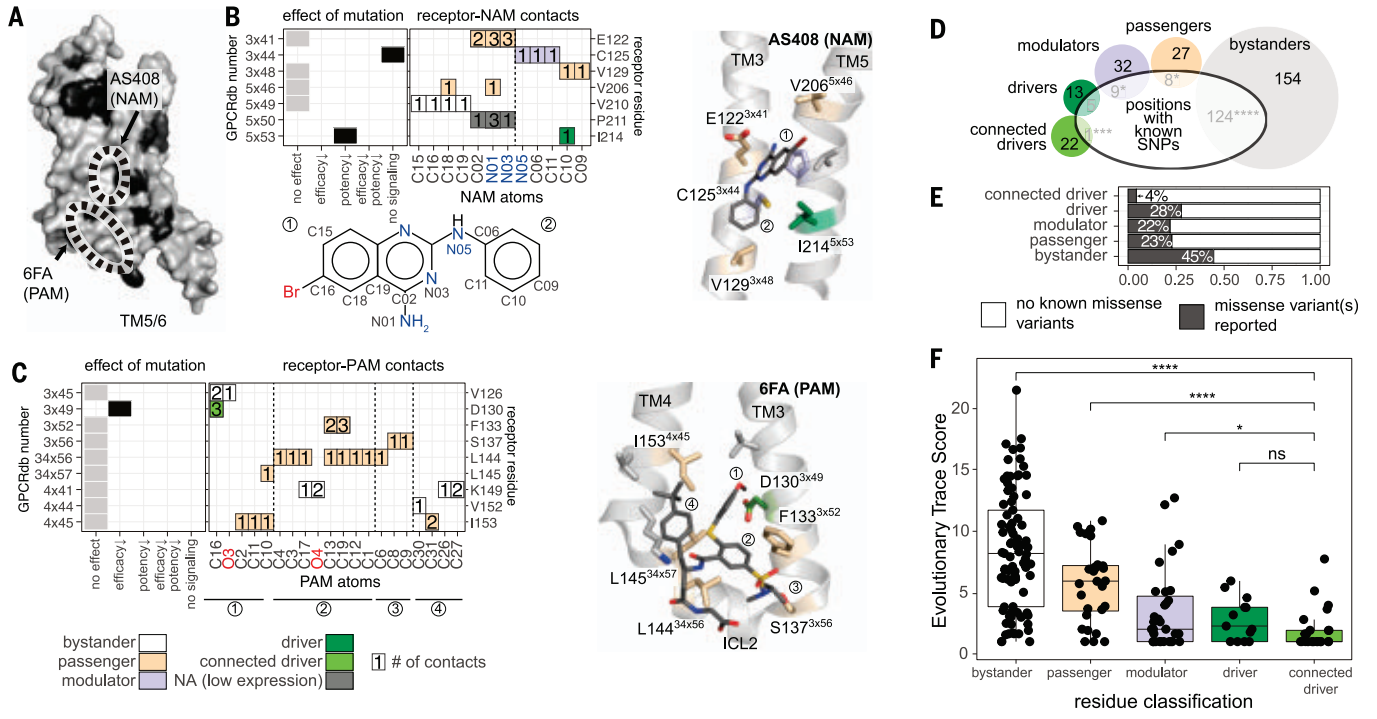

Fig. 6. Allosteric sites, evolutionary conservation, and natural variation. (**A**) Surface-exposed, pharmacologically important residues are shown in black on the β2AR (PDB ID: 3SN6). (**B**) Effect of mutations in the binding site for AS408, a NAM, receptor residue–ligand atom contact plot, and structural view. The contact plot shows the number of contacts between receptor residues (*y* axis) and NAM atoms (*x* axis). Colors for the receptor-NAM contacts in the plot refer to the classification of the residues as in Fig. 5. The chemical formula of the allosteric modulator below the heatmap indicates the labeling of NAM atoms used for the *x* axis of the contact plot. (**C**) Effect of mutations in the binding site for 6FA, a PAM, receptor residue–ligand atom contact plot, and structural view. The contact plot shows the number of contacts between receptor residues (*y* axis) and PAM atoms (*x* axis). Colors for the receptor-PAM contacts in the plot refer to the classification of the residues as in Fig. 5. The circled numbers below the *x* axis refer to different parts of the modulator and are mapped on the structure view for reference. (**D**) The number of residues with known SNPs for each class. (**E**) Percentage of residues for which at least one SNP has been reported by class. Significant differences from the expected frequency by chance are indicated according to a hypergeometric test (*$P \le 0.05$; **$P \le 0.01$; ***$P \le 0.001$; ****$P \le 0.0001$; ns, not significant). (**F**) Adrenergic receptor ET score for the different residue classes. Groups were compared using a Wilcoxon test (*$P \le 0.05$; **$P \le 0.01$; ***$P \le 0.001$; ****$P \le 0.0001$; ns, not significant). Driver refers to the subset that is in the disconnected driver group.

of this observation is that the discovery of such surface-exposed driver, modulator, and passenger residues through the integration of pharmacological and structural data (in the presence of orthosteric ligands and the absence of allosteric compounds) may reveal sites that could be targeted for development of new allosteric ligands.

Passenger, modulator, and driver residues are under higher evolutionary selection pressure

To assess the importance of the residues relevant for pharmacology and/or active-state conformation, we analyzed data on natural genetic variation from the human population. An analysis of the genome sequence data from more than 140,000 individuals available through the gnomAD database (*43*) revealed a notable pattern in the distribution of single-nucleotide polymorphisms (SNPs) according to the different residue categories (Fig. 6, D and E). Bystander residues harbored a larger number of positions with SNPs compared with what is expected by chance. Passenger and modulator residues contained fewer positions with SNPs than expected by chance. The allosteric network mediated by the connected driver residues had the lowest number of positions harboring SNPs in the human population, which indicates that these residues were under the strongest selection pressure (Fig. 6, D and E, and Materials and methods). Thus, driver, modulator, and passenger residues appear to be under differential selection pressure compared with bystander residues of this receptor in the human population, which is consistent with the importance of the residue categories.

To assess the importance of the residues across orthologs of adrenergic receptors from different species, we performed an analysis of evolutionary trace (ET) scores in the context of our residue classification (i.e., driver, modulator, passenger, and bystander). ET is a phylogenetic method that identifies functionally important positions in protein families. Low ET scores indicate positions that are highly conserved across homologs. Depending on how the alignments are constructed, residues with low ET scores can also represent positions that are conserved in a subfamily-specific manner (*44*–*46*). Driver residues were the most conserved followed by modulator, passenger, and bystander residues (Fig. 6F). Not all highly conserved residues were pharmacologically or structurally important; hence, the role of a residue cannot be predicted from evolutionary conservation alone. These findings reveal that categorizing residues on the basis of structural and pharmacological importance can reveal category-specific associations of positions under purifying selection within the adrenergic receptors, aminergic receptors, as well as the entire family of class A GPCRs (Fig. 6F and fig. S13).

Mapping of the ET scores (adrenergic GPCRs) onto the allosteric networks revealed that driver residues with the lowest ET scores were at the center of the network in the receptor core, including all of the network residues in TM3 and TM7 (fig. S13). By contrast, the network positions with the lowest conservation (i.e., higher variability; ET scores > 3rd quartile, higher than 75% of the values) were either close to the ligand-binding site or in the intracellular region (fig. S13). These positions are more tolerant to mutations and may evolve or have evolved to recognize new ligands or different G proteins (fig. S13). This suggests that although a major part of the residues constituting the allosteric network is conserved within adrenergic GPCRs, key positions that interface with the ligand or G protein that are necessarily receptor-specific tend to be more variable. The uncoupling of ligand- and G protein–binding sites might have facilitated the evolution of GPCRs to respond to chemically diverse ligands and to couple to different G proteins. Collectively, the observations on human genetics and evolutionary data, which are independent of the approaches that we used to identify the residue classes, represent further evidence to support the model of the residues that govern the molecular origins of efficacy and potency in this signaling system.

Discussion

Ligand efficacy and potency at a receptor are the key pharmacological parameters used to describe ligand-mediated receptor signaling. Although it is widely established that agonist binding activates the receptor and mediates structural rearrangements, ultimately resulting in a signaling response, we do not fully understand the molecular origins of this process and how each amino acid in the receptor decodes the information encoded in ligand atoms and collectively translates this into the emergence of efficacy and potency. We designed an integrative approach, combining pharmacological, structural, computational, and evolutionary analyses at a per-residue level, that revealed how receptors decode the information on the ligand atoms, mediate a series of structural changes through an allosteric network, and ultimately influence G protein binding and the downstream signaling response.

One-fifth of all residues in β2AR were important for adrenaline efficacy and potency for Gs signaling. Although some residues mapped to functionally important sites, such as ligand-binding, G protein–binding, and conserved motif residues, more than two-thirds of the pharmacologically important residues mapped to other sites on the receptor, including those on the receptor surface. A conceptual framework that combined structural and pharmacological data helped us to propose potential roles for the receptor residues and allowed us to distinguish key, pharmacologically important structural changes from those that are less pharmacologically relevant. This framework resulted in the identification of an allosteric network of noncovalent contacts (based on active state–specific structural changes) that are mediated by pharmacologically important residues from the extracellular to the intracellular side. Our classification of residues into drivers, modulators, passengers, and bystanders provides a rational framework to explain the molecular and structural origins of potency and efficacy.

The exact nature of the pharmacologically and structurally important residues, as well as the allosteric network, likely depends on the choice of ligand, receptor, and effector. We expect considerable overlap for closely related systems based on the evolutionary analyses, but it is likely that the residues and the network will consist of nonoverlapping receptor positions that depend on the specific ligand and the effector, including the G protein subtype.

In addition to revealing such networks, the detailed analysis of ligand atom contacts with receptor residues presented in this work can help us to better understand the role of individual atoms in eliciting a pharmacological response. It can also aid in ligand design by enabling the identification of chemical groups that can be modified to achieve a desired signaling response. Our observation that surface-exposed driver, modulator, and passenger residues identified using the endogenous ligand are contacted by NAMs and PAMs suggests that such sites should be prioritized in high-throughput virtual screening efforts for the discovery of potential allosteric modulators.

Apart from revealing general principles, the approach and the findings presented here can help us understand how disrupting and engineering parts of the network could alter receptor output, thereby facilitating the design of receptors with desired signaling properties (*47*). It could also help us understand how changes in receptor residues, such as SNPs or disease-related mutations, could influence signaling responses to endogenous agonists or GPCR drugs. The framework developed in this work should enable the investigation of such questions for diverse ligand-receptor-signaling systems by leveraging high-throughput approaches, such as deep mutational scanning, to pharmacologically characterize mutations and the increasing availability of new structures of ligand-receptor-signaling protein complexes. Furthermore, the framework to classify residues on the basis of pharmacological and structural relevance can be applied to any functional readout and property describing conformational change. In this manner, the approach can be extended to biological systems beyond GPCRs.

Materials and methods

Experimental methods

DNA constructs and mutagenesis

The design of the human β2AR construct was based on the commercially available pSNAPf -ADRβ2 Control Plasmid (NEB) coding sequence, which consist of a N-terminal signal sequence, the SNAP-tag, and the receptor sequence. A BamHI restriction site was added between the SNAP tag and the receptor sequence, the receptor sequence was codon optimized. The wild-type receptor amino acid at position 16 was arginine. The two most common alleles at position 16 are arginine and glycine (as defined by the 1000 Genomes Project). The SNAP-β2AR was cloned into pcDNA3.1. BRET-based biosensor constructs for Gαs, Gβ1, and Gγ1 subunits were in pcDNA3.1. The Gs biosensor consisted of RlucII-Gαs, where Renilla luciferase (RlucII) was inserted after amino acid 67, unmodified human Gβ1, and GFP10-Gγ1.

β2AR mutants for positions 2 to 412 were generated as described (*48*). Amino acids other than alanine were replaced by alanine, and native alanines were replaced with glycines. Briefly, primers were designed using the custom-made software AAScan (*49*) (available at https://github.com/dmitryveprintsev/AAScan) and ordered from Integrated DNA Technologies (IDT) as 500 pmol DNA oligos in 96-well plates. The primer sequences are available in table S3. Forward and reverse mutagenesis primers were used in separate polymerase chain reaction (PCR) reactions together with one primer each, which annealed in the ampicillin resistance gene (CTCTTACTGTCATGCCATCCGTAAGATGC and GCATCTTACGGATGGCATGACAGTAAGAG). PCRs were run as touchdown PCRs in 20 μl final volume. Resulting half-vector fragments were combined, digested with 0.5 μl DpnI (NEB) for 1 hour, cleaned up using ZR-96 DNA Clean & Concentrator-5 (Zymo Research), assembled by Gibson assembly using HiFi DNA assembly Master Mix (NEB) at 45°C for 1 hour (*50*) and transformed using Mix & Go competent cells (Zymo Research). The resulting colonies were cultured in 5 ml LB medium in 24-well plates overnight. The DNA was purified using Qiaprep 96 Plus kits (Qiagen) and sent for sequencing (Bio Basic Inc. or in-house). Sequences were analyzed using custom software MutantChecker (available at https://github.com/dmitryveprintsev/AAScan). Mutants that were not successfully generated as described were cloned using an alternative method: pcDNA3.1 was digested with NheI and XhoI (NEB), the β2AR coding sequence was amplified in two PCRs, each using one of the mutagenesis primers and either T7long or BGH primer (CGAAATTAATACGACTCACTATAGGGAGACCCAAGCTGG and TAGAAGGCACAGTCGAGG), which anneal upstream and downstream of the coding sequence, respectively. The two fragments were combined, digested using DpnI, and cleaned up as described above. The clean fragments were assembled with digested, cleaned pcDNA3.1 using HiFi DNA assembly Master Mix (NEB).

Cell-culture and BRET-based signaling assays

Adherent HEK-293 SL cells (a gift from S. Laporte) were cultured in Dulbecco's minimum essential medium (DMEM) with 4.5 g/l glucose, L-glutamine, supplemented with 10% newborn calf serum (NCS) (Wisent BioProducts, Canada) and 1x penicillin-streptomycin (PS) (100X, Wisent BioProducts, Canada) at 37°C with 5% CO_2. For transfections, DMEM without phenol red was used. Cells were transiently transfected using linear 25 kDa polyethyleneimine (PEI) (Polysciences Inc., Canada, no. 23966) in a 3:1 ratio with DNA. Per condition, a total of 1 μg DNA was used to transfect 240,000 cells in 1.2 ml in suspension. The DNA mix consisted of 100 ng receptor DNA, combined with 75 ng Gαs-RlucII, 200 ng GFP10-Gγ1, and 100 ng Gβ1 plasmid DNAs; finally, 525 ng salmon sperm DNA (ssDNA) was added to bring the total amount of DNA to 1000 ng total in a volume of 100 μl. DNA was then combined with diluted PEI in phosphate-buffered saline (PBS) and added to the cells. Cells were seeded at 20,000 cells per well into Cellstar PS 96-well cell culture plates (Greiner Bio-One, Germany) and incubated for 2 days at 37°C, 5% CO_2. A Fluent780 liquid handler equipped with an MCA 96-well head (Tecan) and a Multidrop Combi (Thermo), each installed in a class II biosafety cabinet were used to aid with transfections.

Before measurement, the medium was removed from the 96-well plates followed by the addition of Tyrode's buffer (137 mM NaCl, 0.9 mM KCl, 1 mM $MgCl_2$, 11.9 mM $NaHCO_3$, 3.6 mM NaH_2PO_4, 25 mM Hepes, 5.5 mM glucose, 1 mM $CaCl_2$, pH 7.4) and incubated for at least 30 min at 37°C. Plates were treated with ligand or vehicle (buffer control) for 10 min before measurement and with coelenterazine 400a (Nanolight Technology) at 5 μM final 5 min before measurement. Ligand concentrations used were: 31.6 nM ($10^{-8.5}$ M) to 3.16 mM ($10^{-3.5}$M) in half-log steps, diluted in vehicle, plus vehicle itself. Coelenterazine 400 a was prepared with 1% Pluronic F-127 in Tyrode's buffer to increase solubility. Adrenaline was prepared in 0.01 M HCl to increase stability, the low pH was buffered by Tyrode's buffer upon addition of ligand to the cells. The stability of adrenaline in the above aqueous solution was confirmed by comparing the signaling responses obtained immediately after ligand preparation, after 3 hours, 6 hours 20 min, 8 hours 40 min, and 11 hours. The BRET signal was read using a Synergy Neo (Biotek) equipped with dual photomultiplier tubes (PMTs) (emission: 410 nm and 515 nm, gain 150 for each PMT and 1.2 s integration time). BRET was measured on an integrated platform with a Biomek NX liquid handler equipped with a 96-well head (Beckman, used for ligand addition), a multidrop combi (Thermo, luciferase substrate addition), an automated CO_2 incubator Cytomat 6001 (Thermo, plate storage before experiment and during incubation), a barcode reader and Synergy Neo plate reader (Biotek). Ligand dilutions were kept at 4°C with the aid of a Peltier element. All signaling experiments were run in three biological replicates by default. In those cases where very low luciferase counts for multiple plates were observed, indicative of a failing transfection, all transfections and measurements of the day were repeated. All transfections and measurements for the days where an instrument failure led to a premature stop of the robotic system were repeated. BRET data for transfections with very low luciferase counts were completely removed during the data analysis (see manual curation).

All signaling experiments were carried out in at least biological triplicates, wild-type and mock-transfection controls were repeated six times per measurement day.

Cell-surface ELISA

HEK-293 SL cells were transfected using PEI as above and seeded into poly-L-lysine coated 96-well plates (Greiner BioOne, Germany) and incubated for 2 days at 37°C 5% CO_2. Each well was washed with 200 μl PBS, the cells were then treated with 50 μl 3% paraformaldehyde per well for 10 min. Each well was washed as follows: Three washes with wash buffer total (PBS + 0.5% BSA); for the last wash step, the cells were incubated with wash buffer for 10 min. Primary rabbit anti-SNAP antibody (GenScript, USA) was added at 0.25 μg/ml in 50 μl and incubated for 1 hour at room temperature (RT), followed by three wash steps as described above. The cells were incubated with secondary anti-rabbit HRP antibody (GE Healthcare) diluted 1:1000 for 1 hour. Again, the cells were washed three times with wash buffer and then three times with PBS. Per well, 100 μl SigmaFast solution was added, the plates were incubated at RT in the dark. Reactions were stopped by the addition of 25 μl 3M HCl. 100 μl of the resulting solution was transferred to a new transparent 96-well plate, and the optical density was read at 492 nm using a Tecan GENios Plus microplate reader. Cell-surface ELISAs were carried out in three biological replicates with internal quadruplicates. Each plate contained wild-type and mock-transfected cells as controls.

Analysis of biosensor signal dependence on cell-surface expression

Twelve different amounts of wild-type receptor DNA were combined with constant amounts

of biosensor DNA and transfected into HEK293 cells as described above. The amounts of wild-type receptor DNA were 0.05, 0.1, 0.2, 0.5, 1, 2, 5, 10, 20, 50, 150 and 200 ng. Two days after transfection, the cell-surface expression level and Gs biosensor BRET signal were determined for each transfection. Cell-surface expression in percent of the level obtained for a 100 ng wild-type receptor DNA transfection (the standard used for signaling experiments as described above) was then plotted against Gs biosensor signal amplitude and Gs biosensor $logEC_{50}$ (fig. S3, A and B). All experiments were repeated in three to four biological replicates.

Computational methods and data analysis

Processing of signaling data

The BRET data were processed using BRET2DTF and DataFitter custom software (Dmitry Veprintsev; https://github.com/dbv123w/DataFitter). All biological replicates of concentration-response curves were separately fitted to a Hill equation using a Hill slope of 1 to determine the agonist concentration at the half-maximal signal response ($logEC_{50}$) as well as the pretransition and posttransition baselines (may also be referred to as top and bottom). All concentration-response curves were visually inspected. We removed complete repeats (i.e., all 12 data points) in those cases where the experiment had obviously failed due to a transfection that did not work (see explanation in "Cell-culture and BRET-based signaling assays" section above) or where data could not be fitted reliably due to noise. In the whole mutant dataset of 1324 concentration-response curves (number excludes controls), 42 single replicate curves were excluded. In addition, replicates for seven mutations showed no measurable signaling (see table S1, curation column set to 2). Data could be fitted starting at ~20% of wild-type amplitude, corresponding to ~0.015 difference between the pre- and posttransition baselines in raw BRET (where raw BRET = GFP/RlucII signal). In total, after these curation steps, quadruplicates for 77 mutants, triplicates for 306 mutants, and duplicates for 29 mutants were retained. No single data points were removed in any case.

The results from data fitting were read into R (RStudio 1.3.959 to 2022.07.1 and R 4.0.0 to 4.2.1) and processed using custom scripts. The following packages were used: tidyverse (especially dplyr, ggplot2, purrr, tibble, tidyr, forcats, and stringr), plotly, MASS, reshape, reshape2, ggrepel, patchwork, ggpubr, bio3d (*51*), and openxlsx.

The data were read in, reformatted, averaged, annotated (addition of GPCRdb number, expression level, amino acid number, mutation), filtered based on the results of manual curation, normalized, and visualized in R. We checked the dataset for outliers, day-to-day variation and trends, the effect of expression level on signaling response, and baseline signal variation. We compared the BRET signal for mock transfections where ssDNA was used instead of receptor DNA with mutant pretransition baselines to assess possible changes in constitutive activity. Based on the variability of wild-type pretransition baselines we decided not to interpret changes in mutant pretransition baselines. Although we were not able to measure changes in constitutive activity reliably, this does not mean that none of the mutants affect constitutive activity. Measured mutant amplitudes were normalized to the wild type using the most recently measured wild-type dataset to correct for day-to-day variation and variation during the day, whereas mutant $logEC_{50}$ values were normalized to the mean $logEC_{50}$ obtained for the wild type. The normalization did not correct for expression level because the dependence of the signal was minor for receptor expressing to at least 25% of wild-type level (fig. S3, A and B). The measured $logEC_{50}$ and amplitude values were also used to interpret 22 receptor positions in Hauser *et al.* (*15*) and Hedderich *et al.* (*42*). The typical error of an ELISA was much larger than the error of a BRET experiment, at least in our experience; such a correction would therefore have rather lowered the confidence in the results. Cutoffs were applied to the normalized, and curated data, resulting in discretization. Once normalized, the wild-type data were centered around a normalized amplitude of 1 and a normalized $logEC_{50}$ of 0. Cutoffs were chosen so that none of the 57 wild-type concentration-response curves (measured on different days and batches) were classified as not wild-type–like. For the normalized amplitude, the cutoff was <0.74 (this corresponds to two wild-type standard deviations). For the normalized $logEC_{50}$, the cutoff was >0.87, this corresponds to a 7.4-fold change.

Our cutoff for a gain of function would be >1.28 for the normalized amplitude and <−0.71 for the normalized $logEC_{50}$ (cutoffs were applied to nonrounded values; table S1 values are displayed to two decimal precision). Because we were interested in identifying those positions whose mutation impairs signaling, the one mutation that increased efficacy was not explicitly considered in our analyses.

Graphs and illustrations were generated in R (ggplot2), Adobe Illustrator CS6 and CC and Affinity Designer 2. For display in figures, concentration-response curves were fitted in R using the package drc. The raw BRET values were fitted to obtain the BRET value for the pretransition baseline. Subsequently, the data were normalized using the pretransition baseline and the wild-type signal amplitude, resulting in a normalized BRET response where 0% and 100% correspond to the wild-type response. For fitting of the normalized data, the LL.4 function was used, the slope was fixed to 1, and the pretransition baseline was fixed to 0.

Residue-residue contacts

Residue-residue contacts were obtained from the Protein Contacts Atlas (http://pca.mbgroup.bio/index.html) (*52*). Two residues are listed as a contact if the distance between the two atoms minus their van der Waals radii equals 0.5 Å or less, corresponding to a maximum distance of ~4.2 Å. Text files downloaded from Protein Contacts Atlas containing residue-residue contacts were read into R and cleaned. We then fortified the tables with additional information [secondary structure elements (SSEs) and GPCRdb numbers for each amino acid], filtered the contact tables to exclude main chain–main chain contacts, and include contacts between two different SSEs only. The contacts were filtered to include only those residues resolved in both crystal structures used for the comparison, 2RH1 and 3SN6. In the inactive and in the active G protein–bound structures of the β2AR, 282 and 285 residues form 1275 and 1233 residue-residue contacts, respectively. To focus on residue contacts that contribute to large domain motions instead of local rearrangements during activation, we excluded contacts formed exclusively between backbone atoms and contacts within the same secondary structure element (i.e., contacts formed within a single helix). This reduced the number of residue-residue contacts to 117 contacts that are only present in the inactive state; 61 contacts that are only present in the active, G protein–bound state; and 191 contacts that are present in both the active and inactive states. Contacts are listed in table S2.

Definition of the ligand- and G protein–binding sites

Definitions of the ligand-binding site and the G protein–binding site were based on the structures of β2AR with adrenaline and an engineered nanobody (PDB ID: 4LDO) (*25*), in complex with heterotrimeric G protein and Gs peptide (3SN6 and 6E67) (*14*, *37*). All residues within 4 Å of adrenaline were classified as part of the ligand-binding site, the residues were verified using LigPlot+ v.2.2 and literature data (*26*, *53*–*56*). Using PyMOL 2.5.2, all residues within 4 Å of G protein or Gs peptide were determined and classified as residues in the G protein–binding site. Additionally, this residue selection was confirmed by atom-atom contacts from the Protein Contact Atlas. Residues in the ligand and G protein–binding site, respectively, are marked in table S1.

Residue classification

We defined driver and modulator residues as those residues that affect Gs signaling upon

mutation (see above for cutoffs). Additionally, disconnected drivers participate in an active state–specific contact, and connected driver residues form an active state–specific contact to another driver residue. In addition, both connected driver residues need to negatively affect potency, or both need to affect efficacy. That is, if the mutation at one driver residue affected potency and the mutation at the interacting driver residue affected efficacy they were classified as disconnected drivers due to a mismatch in effects. Passenger and bystander residues were defined as those residues that do not affect Gs signaling upon mutation. Additionally, passenger residues must form at least one active state–specific contact. Residues not forming such contacts and not affecting Gs signaling upon mutation were classified as bystanders. Hierarchically, we defined (i) connected drivers as the structurally and pharmacologically most important residues, followed by (ii) disconnected drivers and (iii) modulators that are pharmacologically important but do not mediate active state–specific contact, (iv) passenger residues which mediate active state–specific contact(s) but do not affect pharmacology, and finally (v) bystanders, which are not involved in forming an active state–specific contact and do not affect pharmacology. The allosteric network consisted of 15 residue-residue contacts (33 atom-atom contacts) between 23 residues. Of the 33 atom-atom contacts, 26 were side chain–side chain contacts and 7 were main chain–side chain contacts.

ET analysis

We used ET analysis to identify β2AR residues with evolutionarily encoded functional roles at the cross section of the network of pharmacologically important residue positions. ET scores were obtained from the Lichtarge Lab ET webserver (http://evolution.lichtargelab.org/gpcr). We compared the conservation of amino acids at the level of the adrenergic receptor subfamily ["Adrenoceptor (118)"], amine receptors ["All_amine (547)"], and class A ("ClassA_5105") GPCRs. For each phylogenetic comparison, the lower ET scores at a residue position represent high conservation of specific amino acids at the position within the phylogenetic class. We compared the enrichment of low ET score positions among the residues found in the driver, modulator, passenger, and bystander categories. Groups were compared using a Wilcoxon test (*$P \leq 0.05$; **$P \leq 0.01$; ***$P \leq 0.001$; ****$P \leq 0.0001$; ns, not significant).

Extraction of structure features

To calculate the distance between Cα atoms of each residue in the inactive versus the active state, we used the highest-resolution inactive-state structure (PDB ID: 2RH1) and the only available G protein complex structure at the time of performing this analysis (PDB ID: 3SN6) of the β2AR, aligned the two structures in PyMOL and exported the new coordinates. The PDB files were read into R using the package bio3d, followed by extraction of the x, y, and z coordinates for each structure and the calculation of distance as

$$\text{distance} = \sqrt{(x_{\text{active}} - x_{\text{inactive}})^2 + (y_{\text{active}} - y_{\text{inactive}})^2 + (z_{\text{active}} - z_{\text{inactive}})^2}$$

Likewise, we extracted the dihedral angles for each residue in the above structures using bio3d. The difference in the angles ϕ, ψ, and ω between the active and inactive state was calculated as

$$\Delta\phi = (\phi_{\text{active}} - \phi_{\text{inactive}} + 180)\%360 - 180$$

Calculation of accessible surface area

Accessible surface area was calculated using dssp (https://swift.cmbi.umcn.nl/gv/dssp/) (*57*, *58*), and values are provided in table S1. In addition, we calculated the accessible surface area of the adrenaline-binding site with and without the ligand present using MDTraj (https://www.mdtraj.org) and GROMACS (https://www.gromacs.org/).

Analysis of SNP data

SNP data for ADRB2 was retrieved from the Genome Aggregation Database (gnomAD, https://gnomad.broadinstitute.org/, version gnomAD v2.1.1). The data were analyzed using custom scripts with functions from the tidyverse (especially readr, dplyr, and ggplot2), and the packages janitor, rebus, and stats. Statistical over- and underrepresentation of SNPs in driver, modulator, passenger, and bystander positions were calculated using a hypergeometric test.

REFERENCES AND NOTES

1. M. Audet, M. Bouvier, Restructuring G-protein- coupled receptor activation. *Cell* **151**, 14–23 (2012). doi: 10.1016/j.cell.2012.09.003; pmid: 23021212
2. C. G. Tate, G. F. X. Schertler, Engineering G protein-coupled receptors to facilitate their structure determination. *Curr. Opin. Struct. Biol.* **19**, 386–395 (2009). doi: 10.1016/j.sbi.2009.07.004; pmid: 19682887
3. D. M. Rosenbaum, S. G. F. Rasmussen, B. K. Kobilka, The structure and function of G-protein-coupled receptors. *Nature* **459**, 356–363 (2009). doi: 10.1038/nature08144; pmid: 19458711
4. A. J. Venkatakrishnan *et al*., Molecular signatures of G-protein-coupled receptors. *Nature* **494**, 185–194 (2013). doi: 10.1038/nature11896; pmid: 23407534
5. G. Thiel, A. Kaufmann, O. G. Rössler, G-protein-coupled designer receptors – New chemical-genetic tools for signal transduction research. *Biol. Chem.* **394**, 1615–1622 (2013). doi: 10.1515/hsz-2013-0164; pmid: 23893685
6. J. F. Armstrong *et al*., The IUPHAR/BPS Guide to PHARMACOLOGY in 2020: Extending immunopharmacology content and introducing the IUPHAR/MMV Guide to MALARIA PHARMACOLOGY. *Nucleic Acids Res.* **48**, D1006–D1021 (2020). doi: 10.1093/nar/gkz951; pmid: 31691834
7. M. J. Marinissen, J. S. Gutkind, G-protein-coupled receptors and signaling networks: Emerging paradigms. *Trends Pharmacol. Sci.* **22**, 368–376 (2001). doi: 10.1016/S0165-6147(00)01678-3; pmid: 11431032
8. T. Schöneberg, I. Liebscher, Mutations in G Protein–Coupled Receptors: Mechanisms, Pathophysiology and Potential Therapeutic Approaches. *Pharmacol. Rev.* **73**, 89–119 (2021). doi: 10.1124/pharmrev.120.000011; pmid: 33219147
9. A. S. Hauser, M. M. Attwood, M. Rask-Andersen, H. B. Schiöth, D. E. Gloriam, Trends in GPCR drug discovery: New agents, targets and indications. *Nat. Rev. Drug Discov.* **16**, 829–842 (2017). doi: 10.1038/nrd.2017.178; pmid: 29075003
10. L. M. Wingler *et al*., Angiotensin Analogs with Divergent Bias Stabilize Distinct Receptor Conformations. *Cell* **176**, 468–478.e11 (2019). doi: 10.1016/j.cell.2018.12.005; pmid: 30639099
11. X. Deupi, B. Kobilka, Activation of G protein–coupled receptors. *Adv. Protein Chem.* **74**, 137–166 (2007). doi: 10.1016/S0065-3233(07)74004-4; pmid: 17854657
12. M. Audet, M. Bouvier, Insights into signaling from the β_2-adrenergic receptor structure. *Nat. Chem. Biol.* **4**, 397–403 (2008). doi: 10.1038/nchembio.97; pmid: 18560432
13. R. R. Neubig, M. Spedding, T. Kenakin, A. Christopoulos, International Union of Pharmacology Committee on Receptor Nomenclature and Drug Classification. XXXVIII. Update on terms and symbols in quantitative pharmacology. *Pharmacol. Rev.* **55**, 597–606 (2003). doi: 10.1124/pr.55.4.4; pmid: 14657418
14. S. G. Rasmussen *et al*., Crystal structure of the β_2 adrenergic receptor–Gs protein complex. *Nature* **477**, 549–555 (2011). doi: 10.1038/nature10361; pmid: 21772288
15. A. S. Hauser *et al*., GPCR activation mechanisms across classes and macro/microscales. *Nat. Struct. Mol. Biol.* **28**, 879–888 (2021). doi: 10.1038/s41594-021-00674-7; pmid: 34759375
16. G. G. Gregorio *et al*., Single-molecule analysis of ligand efficacy in β_2AR–G-protein activation. *Nature* **547**, 68–73 (2017). doi: 10.1038/nature22354; pmid: 28607487
17. T. Warne, P. C. Edwards, A. S. Doré, A. G. W. Leslie, C. G. Tate, Molecular basis for high-affinity agonist binding in GPCRs. *Science* **364**, 775–778 (2019). doi: 10.1126/science.aau5595; pmid: 31072904
18. E. M. Jones *et al*., Structural and functional characterization of G protein–coupled receptors with deep mutational scanning. *eLife* **9**, e54895 (2020). doi: 10.7554/eLife.54895; pmid: 33084570
19. M. P. Wescott *et al*., Signal transmission through the CXC chemokine receptor 4 (CXCR4) transmembrane helices. *Proc. Natl. Acad. Sci. U.S.A.* **113**, 9928–9933 (2016). doi: 10.1073/pnas.1601278113; pmid: 27543332
20. M. Eilers, A. B. Patel, W. Liu, S. O. Smith, Comparison of helix interactions in membrane and soluble α-bundle proteins. *Biophys. J.* **82**, 2720–2736 (2002). doi: 10.1016/S0006-3495(02)75613-0; pmid: 11964258
21. C. Galés *et al*., Probing the activation-promoted structural rearrangements in preassembled receptor–G protein complexes. *Nat. Struct. Mol. Biol.* **13**, 778–786 (2006). doi: 10.1038/nsmb1134; pmid: 16906158
22. C. Galés *et al*., Real-time monitoring of receptor and G-protein interactions in living cells. *Nat. Methods* **2**, 177–184 (2005). doi: 10.1038/nmeth743; pmid: 15782186
23. V. Isberg *et al*., Generic GPCR residue numbers – Aligning topology maps while minding the gaps. *Trends Pharmacol. Sci.* **36**, 22–31 (2015). doi: 10.1016/j.tips.2014.11.001; pmid: 25541108
24. J. A. Ballesteros, H. Weinstein, in *Methods in Neurosciences*, S. C. Sealfon, Ed. (Academic Press, 1995), pp. 366–428.
25. A. M. Ring *et al*., Adrenaline-activated structure of β_2-adrenoceptor stabilized by an engineered nanobody. *Nature* **502**, 575–579 (2013). doi: 10.1038/nature12572; pmid: 24056936
26. C. D. Strader *et al*., Conserved aspartic acid residues 79 and 113 of the β-adrenergic receptor have different roles in receptor function. *J. Biol. Chem.* **263**, 10267–10271 (1988). doi: 10.1016/S0021-9258(19)81509-0; pmid: 2899076
27. C. D. Strader, I. S. Sigal, R. A. F. Dixon, Structural basis of β-adrenergic receptor function. *FASEB J.* **3**, 1825–1832 (1989). doi: 10.1096/fasebj.3.7.2541037; pmid: 2541037
28. T. Flock *et al*., Universal allosteric mechanism for Gα activation by GPCRs. *Nature* **524**, 173–179 (2015). doi: 10.1038/nature14663; pmid: 26147082
29. D. Sun *et al*., Probing $G\alpha_{i1}$ protein activation at single–amino acid resolution. *Nat. Struct. Mol. Biol.* **22**, 686–694 (2015). doi: 10.1038/nsmb.3070; pmid: 26258638

30. T. Flock *et al*., Selectivity determinants of GPCR–G-protein binding. *Nature* **545**, 317–322 (2017). doi: 10.1038/nature22070; pmid: 28489817
31. M. Sandhu *et al*., Dynamic spatiotemporal determinants modulate GPCR:G protein coupling selectivity and promiscuity. *Nat. Commun.* **13**, 7428 (2022). doi: 10.1038/s41467-022-34055-5; pmid: 36460632
32. A. Manglik *et al*., Structural Insights into the Dynamic Process of β_2-Adrenergic Receptor Signaling. *Cell* **161**, 1101–1111 (2015). doi: 10.1016/j.cell.2015.04.043; pmid: 25981665
33. G. Swaminath *et al*., Sequential binding of agonists to the β_2 adrenoceptor: Kinetic evidence for intermediate conformational states. *J. Biol. Chem.* **279**, 686–691 (2004). doi: 10.1074/jbc.M310888200; pmid: 14559905
34. S. Chen *et al*., Mutation of a single TMVI residue, Phe^{282}, in the β_2-adrenergic receptor results in structurally distinct activated receptor conformations. *Biochemistry* **41**, 6045–6053 (2002). doi: 10.1021/bi012189c; pmid: 11993999
35. A.-M. Schönegge *et al*., Evolutionary action and structural basis of the allosteric switch controlling β_2AR functional selectivity. *Nat. Commun.* **8**, 2169 (2017). doi: 10.1038/s41467-017-02257-x; pmid: 29255305
36. V. Katritch *et al*., Allosteric sodium in class A GPCR signaling. *Trends Biochem. Sci.* **39**, 233–244 (2014). doi: 10.1016/j.tibs.2014.03.002; pmid: 24767681
37. X. Liu *et al*., Structural Insights into the Process of GPCR-G Protein Complex Formation. *Cell* **177**, 1243–1251.e12 (2019). doi: 10.1016/j.cell.2019.04.021; pmid: 31080070
38. A. J. Venkatakrishnan *et al*., Diverse activation pathways in class A GPCRs converge near the G-protein-coupling region. *Nature* **536**, 484–487 (2016). doi: 10.1038/nature19107; pmid: 27525504
39. A. J. Venkatakrishnan *et al*., Diverse GPCRs exhibit conserved water networks for stabilization and activation. *Proc. Natl. Acad. Sci. U.S.A.* **116**, 3288–3293 (2019). doi: 10.1073/pnas.1809251116; pmid: 30728297
40. N. R. Latorraca, A. J. Venkatakrishnan, R. O. Dror, GPCR Dynamics: Structures in Motion. *Chem. Rev.* **117**, 139–155 (2017). doi: 10.1021/acs.chemrev.6b00177; pmid: 27622975
41. D. M. Thal, A. Glukhova, P. M. Sexton, A. Christopoulos, Structural insights into G-protein-coupled receptor allostery. *Nature* **559**, 45–53 (2018). doi: 10.1038/s41586-018-0259-z; pmid: 29973731
42. J. B. Hedderich *et al*., The pocketome of G-protein-coupled receptors reveals previously untargeted allosteric sites. *Nat. Commun.* **13**, 2567 (2022). doi: 10.1038/s41467-022-29609-6; pmid: 35538063
43. K. J. Karczewski *et al*., The mutational constraint spectrum quantified from variation in 141,456 humans. *Nature* **581**, 434–443 (2020). doi: 10.1038/s41586-020-2308-7; pmid: 32461654
44. S. Madabushi *et al*., Evolutionary trace of G protein-coupled receptors reveals clusters of residues that determine global and class-specific functions. *J. Biol. Chem.* **279**, 8126–8132 (2004). doi: 10.1074/jbc.M312671200; pmid: 14660595
45. O. Lichtarge, H. R. Bourne, F. E. Cohen, An evolutionary trace method defines binding surfaces common to protein families. *J. Mol. Biol.* **257**, 342–358 (1996). doi: 10.1006/jmbi.1996.0167; pmid: 8609628
46. B. Selçuk, I. Erol, S. Durdağı, O. Adebali, Evolutionary association of receptor-wide amino acids with G protein–coupling selectivity in aminergic GPCRs. *Life Sci. Alliance* **5**, e202201439 (2022). doi: 10.26508/lsa.202201439; pmid: 35613896
47. K. M. Chen, D. Keri, P. Barth, Computational design of G Protein-Coupled Receptor allosteric signal transductions. *Nat. Chem. Biol.* **16**, 77–86 (2020). doi: 10.1038/s41589-019-0407-2; pmid: 31792443
48. F. M. Heydenreich *et al*., High-throughput mutagenesis using a two-fragment PCR approach. *Sci. Rep.* **7**, 6787 (2017). doi: 10.1038/s41598-017-07010-4; pmid: 28754896
49. D. Sun *et al*., AAscan, PCRdesign and MutantChecker: A suite of programs for primer design and sequence analysis for high-throughput scanning mutagenesis. *PLOS ONE* **8**, e78878 (2013). doi: 10.1371/journal.pone.0078878; pmid: 24205336
50. B. Paetzold, C. Carolis, T. Ferrar, L. Serrano, M. Lluch-Senar, *In situ* overlap and sequence synthesis during DNA assembly. *ACS Synth. Biol.* **2**, 750–755 (2013). doi: 10.1021/sb400067v; pmid: 24161008
51. B. J. Grant, A. P. C. Rodrigues, K. M. ElSawy, J. A. McCammon, L. S. D. Caves, Bio3d: An R package for the comparative analysis of protein structures. *Bioinformatics* **22**, 2695–2696 (2006). doi: 10.1093/bioinformatics/btl461; pmid: 16940322
52. M. Kayikci *et al*., Visualization and analysis of non-covalent contacts using the Protein Contacts Atlas. *Nat. Struct. Mol. Biol.* **25**, 185–194 (2018). doi: 10.1038/s41594-017-0019-z; pmid: 29335563
53. C. D. Strader *et al*., Identification of residues required for ligand binding to the beta-adrenergic receptor. *Proc. Natl. Acad. Sci. U.S.A.* **84**, 4384–4388 (1987). doi: 10.1073/pnas.84.13.4384; pmid: 2885836
54. C. Ambrosio, P. Molinari, S. Cotecchia, T. Costa, Catechol-binding serines of β_2-adrenergic receptors control the equilibrium between active and inactive receptor states. *Mol. Pharmacol.* **57**, 198–210 (2000). pmid: 10617695
55. R. Del Carmine, P. Molinari, M. Sbraccia, C. Ambrosio, T. Costa, "Induced-fit" mechanism for catecholamine binding to the β_2-adrenergic receptor. *Mol. Pharmacol.* **66**, 356–363 (2004). doi: 10.1124/mol.66.2.356; pmid: 15266027
56. G. Liapakis *et al*., The forgotten serine: A critical role for $Ser\text{-}203^{5.42}$ in ligand binding to and activation of the β_2-adrenergic receptor. *J. Biol. Chem.* **275**, 37779–37788 (2000). doi: 10.1074/jbc.M002092200; pmid: 10964911
57. W. Kabsch, C. Sander, Dictionary of protein secondary structure: Pattern recognition of hydrogen-bonded and geometrical features. *Biopolymers* **22**, 2577–2637 (1983). doi: 10.1002/bip.360221211; pmid: 6667333
58. W. G. Touw *et al*., A series of PDB-related databanks for everyday needs. *Nucleic Acids Res.* **43**, D364–D368 (2015). doi: 10.1093/nar/gku1028; pmid: 25352545
59. J. Patel, F. Heydenreich, mb-group/DeterminantsSignalingGPCR: DeterminantsSignalingGPCR, version v1.0, Zenodo (2023); https://doi.org/10.5281/zenodo.8349361

ACKNOWLEDGMENTS

We thank I. Chen, N. Gough, K. Nemec, E. Park, N. Casajuana-Martin, B. Plouffe, and J. Janetzko for their constructive comments on the manuscript as well as D. Malinverni for discussions. We thank B. Sejdiu for help with ASA calculations and J. Patel for help with the GitHub repository. We thank members of the Kobilka and Babu groups for constructive feedback on this work. **Funding:** This study was supported by Marie Skłodowska-Curie Individual Fellowships from the European Union's Horizon 2020 research and innovation program under grant agreement nos. 844622 and 832620 (F.M.H. and M.M.-S.); the American Lebanese Syrian Associated Charities (ALSAC) (M.M.B. and M.S.); American Heart Association grant no. 19POST34380839 (F.M.H.); National Institutes of Health grant R01NS028471 (B.K.K.); Canadian Institute of Health Research grant FDN no. 148431 (M.B.); UK Medical Research Council grant no. MC_U105185859 (M.M.B. and M.M.-S.); Royal Society University Research Fellowship URF\R1\221205 (M.M.-S.); Isaac Newton Trust grants [22.23(d)] (M.M.-S.); and the Wellcome Trust Institutional Strategic Support Fund (M.M.-S.). M.B. holds a Canada Research Chair in Signal Transduction and Molecular Pharmacology. B.K.K. is a Chan Zuckerberg Biohub Investigator. M.M.B. holds the St. Jude Endowed Chair in Biological Data Science. **Author contributions:** Conceptualization: F.M.H., B.K.K., M.B., and M.M.B. Methodology: F.M.H., M.B., M.M.B., and B.K.K. Formal analysis: F.M.H. Investigation: F.M.H., M.M.-S., and M.S. Project administration: F.M.H. Visualization: F.M.H. Software: F.M.H. Funding acquisition: F.M.H., M.M.-S., B.K.K., M.B., and M.M.B. Supervision: B.K.K., M.B., and M.M.B. Writing – original draft: F.M.H., M.M.-S., M.S., and M.M.B. Writing – review & editing: F.M.H., M.M.-S., M.S., B.K.K., M.B., and M.M.B. **Competing interests:** M.B. is the chairman of the scientific advisory board of Domain Therapeutics, a biotech company to which the BRET-based sensor used in this study was licensed for commercial use. B.K.K. is a cofounder and consultant for ConfometRx. The authors declare no other competing interests. **Data and materials availability:** The datasets generated during and/or analyzed during the current study are available in table S1 and table S2. The sequences of the primers used for mutagenesis are listed in table S3. All data are available in the main text or the supplementary materials; code can be accessed at Zenodo (59) or Github (https://github.com/mb-group/DeterminantsSignalingGPCR). Constructs from the alanine scanning library are available upon request to F.M.H. The BRET-based biosensor is available upon request to M.B. for academic, noncommercial studies through regular material transfer agreements.

License information: Copyright © 2023 the authors, some rights reserved; exclusive licensee American Association for the Advancement of Science. No claim to original US government works. https://www.science.org/about/science-licenses-journal-article-reuse

SUPPLEMENTARY MATERIALS

science.org/doi/10.1126/science.adh1859
Figs. S1 to S13
Tables S1 to S3
MDAR Reproducibility Checklist

Submitted 12 April 2023; accepted 7 November 2023
10.1126/science.adh1859

RESEARCH ARTICLES

TEXTILES

Biomimetic, knittable aerogel fiber for thermal insulation textile

Mingrui Wu[1], Ziyu Shao[1], Nifang Zhao[2], Rongzhen Zhang[1], Guodong Yuan[1], Lulu Tian[1], Zibei Zhang[1], Weiwei Gao[3]*, Hao Bai[1,2]*

Aerogels have been considered as an ideal material for thermal insulation. Unfortunately, their application in textiles is greatly limited by their fragility and poor processability. We overcame these issues by encapsulating the aerogel fiber with a stretchable layer, mimicking the core-shell structure of polar bear hair. Despite its high internal porosity over 90%, our fiber is stretchable up to 1000% strain, which is greatly improved compared with that of traditional aerogel fibers (~2% strain). In addition to its washability and dyeability, our fiber is mechanically robust, retaining its stable thermal insulation property after 10,000 stretching cycles (100% strain). A sweater knitted with our fiber was only one-fifth as thick as down, with similar performance. Our strategy for this fiber provides rich possibilities for developing multifunctional aerogel fibers and textiles.

Aerogels are recognized as the best thermal insulation material for their high porosity and extremely low thermal conductivity (*1*–*4*). Since their invention in the 1930s, aerogels have been applied in a wide spectrum of engineering fields, such as green buildings (*5*), energy storage devices (*6*), catalyst carriers (*7*), environmental treatment (*8*), and others. Unfortunately, the application of aerogels in thermal insulation textiles have been greatly limited because of their fragility and poor processability, which usually inevitably yields irreversible structural collapse and, therefore, loss of thermal insulation performance during the practical application of the textile. Although there have been a few attempts to mix aerogels into woven (*9*) or nonwoven (*10*) fabrics, the application of aerogels in thermal insulation textiles is still severely limited owing to either poor processability at high doping content or inefficient thermal insulation at low content (*11*, *12*). Aside from doping or coating aerogels to textiles, efforts were also made to directly develop aerogel fibers with excellent thermal insulation property (*13*). For example, over the last decade, many aerogel fibers made with silica (*14*), graphene (*15*, *16*), carbon nanotube (*17*), titanium oxide (*18*), and cellulose (*19*, *20*) have been prepared through various methods, including wet spinning (*21*), reaction spinning (*22*), and sol-gel confined transition (*23*). Although some of these recently developed aerogel fibers have achieved better mechanical properties (*24*, *25*), they still have insufficient strength and flexibility for weaving or knitting into textiles, especially at a large area (*26*, *27*). Moreover, these aerogel fibers are not machine washable and easily lose their thermal insulation capability underwater or in a humid environment. Therefore, designing and fabricating knittable and weavable aerogel fibers with excellent thermal insulation performance and multifunctionality remains a challenge.

Many animals have evolved special furs to survive in the extremely cold environments (*28*–*30*). As a prime example, polar bear hair exhibits a distinct core-shell structure (*31*–*33*). The hollow core with high porosity effectively traps air and provides excellent thermal insulation performance (*31*), and the dense shell provides efficient mechanical protection (about 300 MPa and 35% in tensile strength and strain, respectively) (*34*, *35*). As a result, people have long been fascinated by the capability of polar bear hair to insulate heat in the Arctic. Mimicking the strategies of the polar bear hair represents a feasible way to develop robust thermal insulation materials, especially fibers and textiles (*36*–*39*).

We encapsulated aerogel fibers with a thin, stretchable layer without severely sacrificing the thermal insulation property. The encapsulated aerogel fiber (EAF) is knittable and simultaneously achieves both thermal insulation and mechanical robustness by mimicking the core-shell structure of the polar bear hair. We continuously fabricated our EAFs using a facile two-step method in which aligned porous aerogel fibers are obtained through freeze-spinning (*36*, *40*–*42*), followed by a coating-drying step. We chose thermoplastic polyurethane (TPU) for the encapsulation layer because of its high mechanical strength and stretchability (*43*). Our EAF has a high internal porosity of over 90% (measured by Mercury Porosimetry) while exhibiting a large tensile strength of around 7.3 to 12.7 MPa (capable of lifting a 500-g weight with a single fiber). In addition, the EAF shows super stretchability of around 1000 to 1600% strain, nearly three orders of magnitude improved compared with traditional aerogel fiber (usually around 2% strain). The mechanical properties make our fibers suitable for knitting and weaving. A sweater knitted with our fibers is only around one-fifth as thick as down for the same warmth and has excellent washability and dyeability. With its simplicity and scalability, our work provides a feasible strategy to fabricate robust, super stretchable, and multifunctional aerogel fibers, which are fundamental for the development of thermal insulation textiles toward applications in extreme environments.

Biomimetic principle and fabrication of EAF

Polar bear hairs have a porous core and dense shell structure to prevent heat loss (Fig. 1A) (*32*, *44*). These structural features decouple the thermal insulation function and mechanical strength of the hair, which provided the inspiration for our design and preparation of the synthetic fibers (*45*). With plenty of pores tens of micrometers in size, the polar bear hair captures a large volume of stationary air, which effectively suppresses both thermal conduction and convection. The aligned porous walls substantially reduce the number of thermal conductive paths and provide a multireflective effect for strong infrared (IR) reflectance, which are both beneficial for efficient thermal insulation (*1*, *36*). The dense shell protects the porous cores, making the hair waterproof and insensitive to humid air, which are the main reasons for the loss of thermal insulation property in typical aerogel materials.

We designed an encapsulated aerogel fiber with similar thermal insulation mechanisms (Fig. 1B) and developed a facile two-step fabrication route to mimic the core-shell structure (Fig. 1C). First, we obtained aerogel fibers by freeze-spinning (*36*). We performed the freeze-spinning by using a well-dispersed polymer solution, which we extruded through a cold region, to generate a continuous stable ice fiber, which we collected using a motor. By controlling the extruding speed and the temperature of the cold source, we could adjust the porous structure within the aerogel fiber. Subsequently, the collected frozen fiber was freeze dried to retain the lamellar porous structure within the fiber (*46*–*48*). Finally, the aerogel fiber was coated with TPU solution and dried by coating-drying equipment, yielding the encapsulated aerogel fiber with the biomimetic core-shell structure. The as-prepared EAF exhibits similar core-shell microstructure compared to the polar bear hair, as we show with

[1]State Key Laboratory of Chemical Engineering, College of Chemical and Biological Engineering, Zhejiang University, Hangzhou 310058, China. [2]Institute of Zhejiang University-Quzhou, Quzhou 324000, China. [3]MOE Key Laboratory of Macromolecular Synthesis and Functionalization, Department of Polymer Science and Engineering, Zhejiang University, Hangzhou 310058, China.
*Corresponding author. Email: hbai@zju.edu.cn (H.B.); wwgao@zju.edu.cn (W.G.)

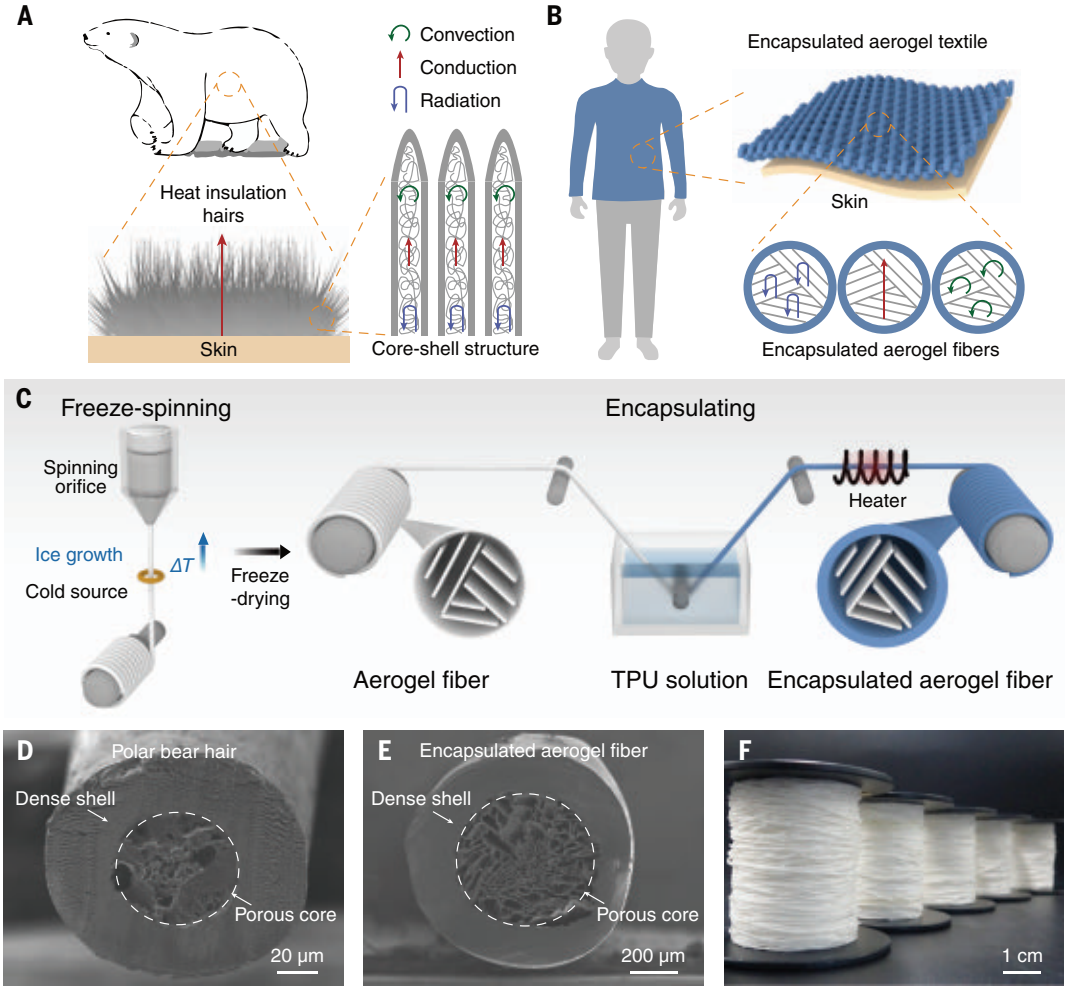

Fig. 1. Design and fabrication of encapsulated aerogel fiber. (**A** and **B**) Schematic illustration of thermal insulation principles of the (A) polar bear hairs and (B) our EAFs. (**C**) EAFs are prepared by freeze-spinning followed by a coating-drying step. (**D** and **E**) SEM images of a (D) polar bear hair and (E) EAF. (**F**) Optical images of as-prepared fiber reels showing the potential of large-scale fabrication.

scanning electron microscopy (SEM) images (Fig. 1, D and E). Through this facile approach, we realized various EAFs with a wide range of shell thickness and pore size at a large scale (Fig. 1F).

Thermal insulation and mechanical properties of EAF

The encapsulating layer has opposite effects on the fiber properties. The thicker layer provides stronger fibers yet reduces their thermal insulation efficiency (*49*). Therefore, we optimized the thickness of the encapsulating layer to ensure that the EAF achieved both excellent thermal insulation and mechanical strength. We show a series of SEM images exhibiting fibers coated with TPU at various thicknesses: 0, ~30, ~80, and ~140 μm (Fig. 2, A to D, respectively). We controlled the shell thickness by altering the viscosity of the coating solution and varying the coating times (fig. S1A). We compared these fibers with various encapsulating layer thicknesses for their thermal insulation performance by placing them on the same hot stage. We collected a series of IR images at varying stage temperatures from −20 to 80°C, showing two typical images (fig. S1B) when the stage temperature was −20 and 80°C, respectively. We measured the temperatures of the fiber surface and the stage on the basis of the IR images, which were taken when the surface temperature was stable, and the ambient temperature was kept at around 20°C during the measurement. We summarize the corresponding temperature difference ($|\Delta T|$) between the stage and the fiber surface in fig. S1C. As we expected, the thermal insulation performance of the aerogel fiber decreased with a thicker encapsulating layer. The $|\Delta T|$ of a single fiber (fig. S1C) is lower than that of a textile because the thinner fiber is more easily affected by its surroundings. The aligned pores provide a multireflective effect for strong IR reflectance, which greatly reduces thermal radiation (fig. S2). In terms of mechanical properties, the aerogel fiber became highly robust and stretchable after the inclusion of the dense encapsulating layer. The tensile strength of the fibers increased from 2.3 to 12.7 MPa, with shell thickness varying from 0 to 140 μm (Fig. 2E), whereas their elongations increased from 24 to 1600%. Although the core structure of our EAF might fracture during stretching, the encapsulating layer remained continuous, which ensured the integrity of EAF's structure and the stability of its function. The EAF with a diameter of 500 μm could even lift a 500-g weight (Fig. 2F). We summarize the variation of tensile strength and thermal insulation properties in respect to the encapsulating layer thickness in Fig. 2G. We clearly show that the addition of the encapsulating layer can substantially increase the mechanical performance of the aerogel fiber yet maintain thermal insulation properties. Therefore, we set the encapsulating layer to around 80 μm for the aerogel fiber 600 μm in diameter of to ensure both excellent thermal insulation and mechanical performances.

Multifunction of EAF

The encapsulating layer not only provides the aerogel fiber enough strength, but also protection for its thermal insulation property under cyclic stretching. The dense and intact encapsulated layer allows the EAF to fully recover after being stretched to even 1000% strain, with no change in its length (Fig. 3, A and B). In daily wearing, the fibers are subjected to cyclic stretching and radial compression, which are difficult requirements for conventional aerogel fibers. We investigated the thermal

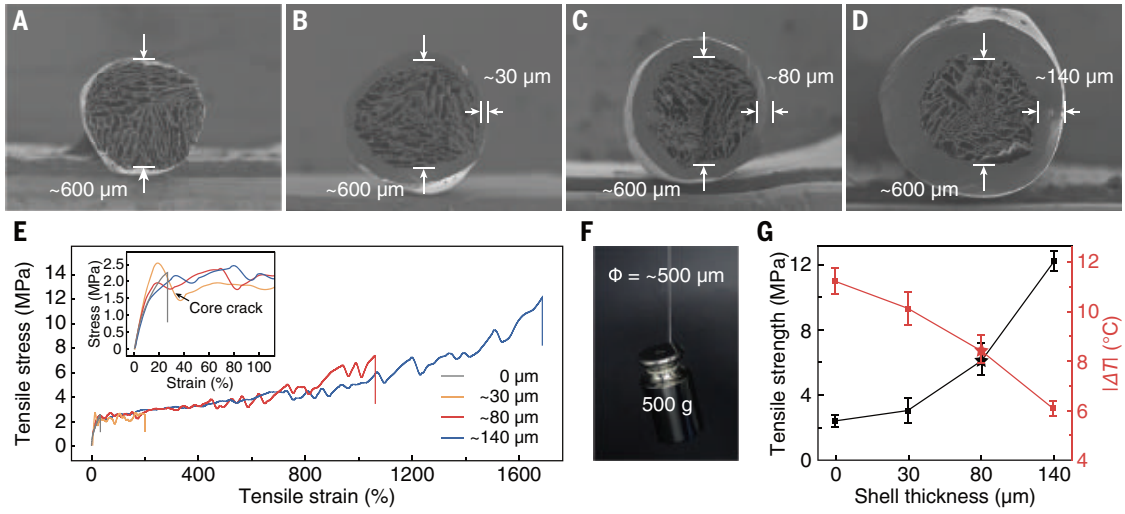

Fig. 2. Microstructure of EAFs with controllable shell thickness and characterization on their thermal and mechanical properties. (**A** to **D**) Radial cross-sectional SEM images showing the porous core with a diameter of 600 μm and the dense shell with a thickness of (A) 0, (B) ~30, (C) ~80, and (D) ~140 μm, respectively. (**E**) Tensile strain curves indicating both the enhanced strength (~12.7 MPa) and elongation (~1600%) of EAFs with a shell thickness of ~140 μm. (**F**) Photograph of a single EAF with a tensile load of 500 g, indicating its high strength. Φ, diameter of EAF. (**G**) As the shell thickness increased, the average tensile strength increased from 2.3 to 12.7 MPa, and $|\Delta T|$ between the fiber surface and the hot stage (~80°C) decreased from 10.8 to 6.2°C. Error bars indicate the standard deviation from five different samples.

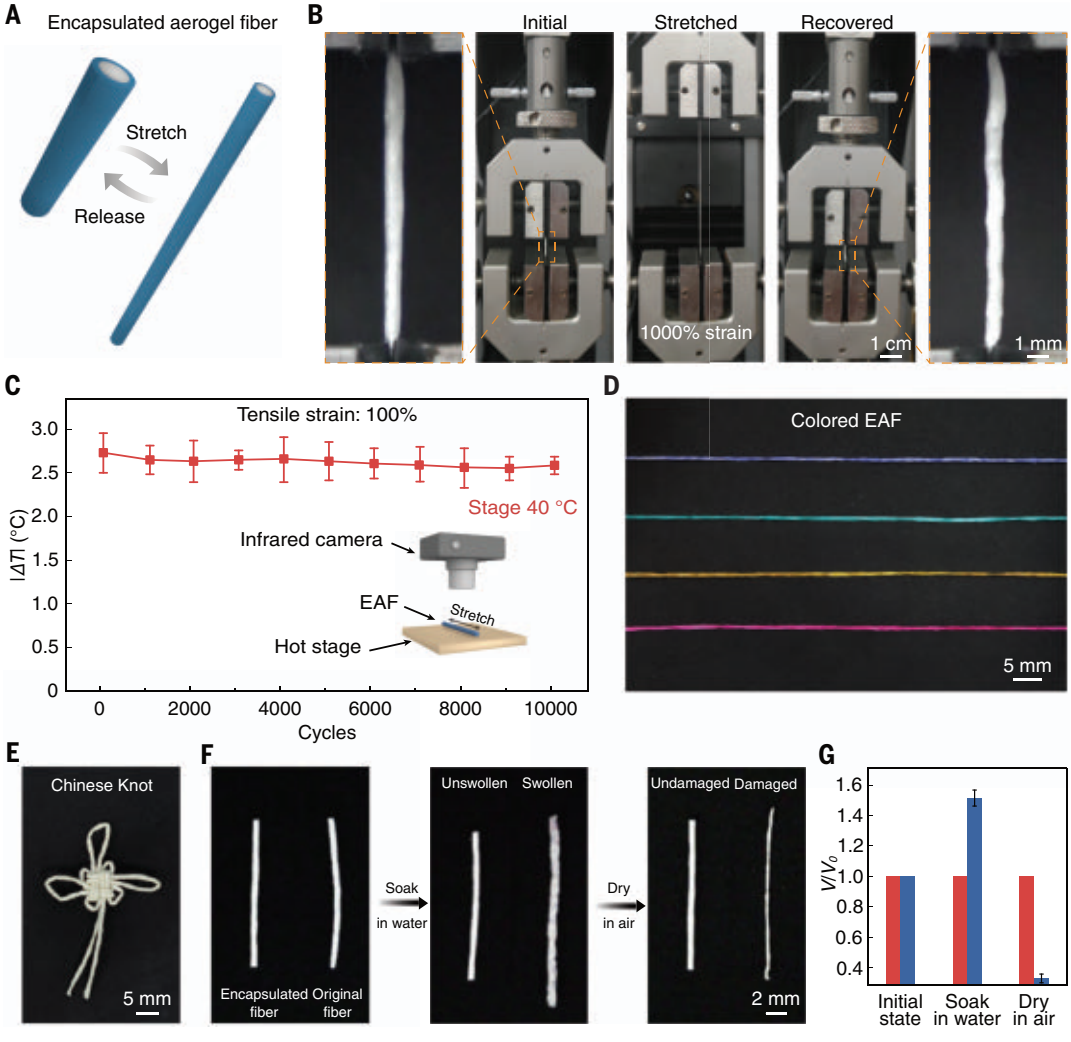

Fig. 3. Thermal insulation stability, waterproofness, flexibility, and dyeability of EAF. (**A**) Schematic diagram of the stretching and relaxation process of EAF. (**B**) Optical images of EAF when stretched from 0 to 1000% strain. (**C**) $|\Delta T|$ between the fiber surface and the hot stage (~40°C) was measured and plotted after recovery from various tensile cycles at 100% strain, illustrating the stable thermal insulation performance. (**D**) Optical image of the colorful EAFs, illustrating the dyeability. (**E**) The Chinese knot knitted with EAF, indicating the flexibility of the fiber. (**F**) Optical images comparing the morphologic change of the encapsulated and uncoated original aerogel fibers after soaking in water and drying in air, demonstrating the waterproofness of EAF. (**G**) Fiber volumetric change of both EAF and uncoated original aerogel fiber before and after soaking in water and after drying in air (V/V_0). Error bars indicate the standard deviation from three different samples.

insulation performance of the EAF after cyclic stretching by measuring the balanced temperature difference between the fiber surface and background hot stage (40°C) (Fig. 3C). The thermal insulation of our EAF was extremely stable with $|\Delta T|$ steady at around 2.7°C even after 10,000 stretching cycles at 100% strain, which indicates the property's retention even with daily wear. We attribute this stable thermal insulation performance to the robust encapsulating layer, which ensures the integrity of the fiber. Aside from stretching, our EAF is also recoverable from radial compression over 40% strain (fig. S3). These results indicate that by introducing the encapsulating layer, our EAF has both thermal insulation and mechanical robustness.

Additionally, we prepared colorful EAFs by adding various dyes into the spinning solutions during freeze-spinning (Fig. 3D). Aside from protection during stretching, the transparent, encapsulating TPU layer effectively prevents the colorful aerogel fibers from fading or damage by friction (*21*). With high flexibility (bending stiffness, 17 to 63×10^{-5} cN·cm^2), our EAF is knittable, as we demonstrated by making a Chinese knot (Fig. 3E). Moreover, the encapsulating layer also provides our fiber with excellent waterproofing. Unlike traditional materials such as silica aerogel, cotton, and down, which easily lose their thermal insulation function because of the filling of water in their porous structures in humid or underwater environments, our EAFs are intrinsically waterproof. As we demonstrated (Fig. 3F), the aerogel fiber made with chitosan was hydrophilic (fig. S4); it swelled easily in water within 10 s and shrunk with severe microstructure collapse after drying (fig. S5). In the fiber volumetric changing test, we used the ratio of volume after soaking and drying to the initial volume (V/V_0) to evaluate the waterproofness, where V_0 is the initial volume of the fiber and V is volume under the corresponding environments. The change in volume caused by this structural change was very large. After soaking in water, the AF expanded to 153% and shrank to 27% after drying (Fig. 3G) when compared with its original state. By contrast, our EAF remained intact both in water and after drying, with no obvious

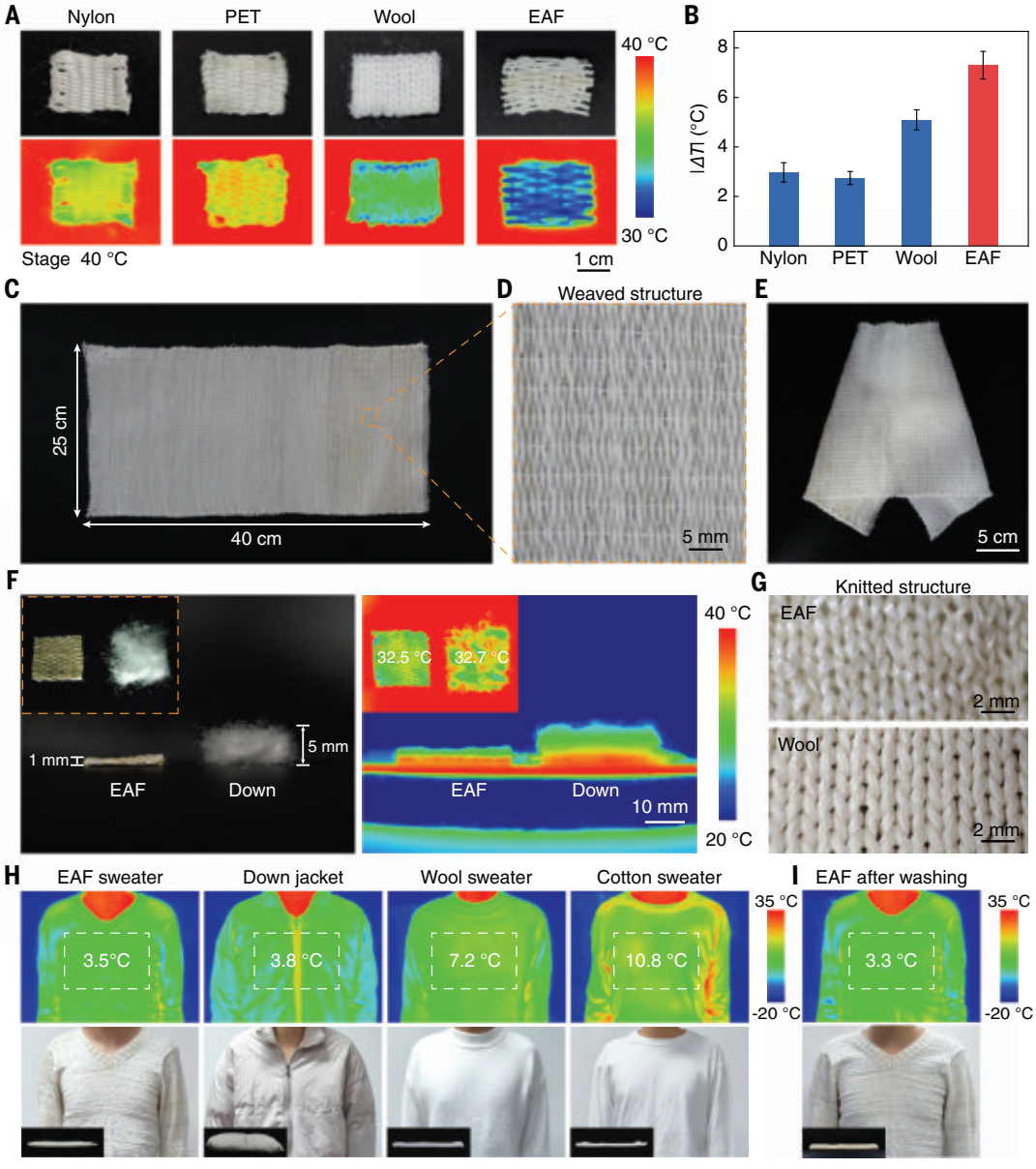

Fig. 4. The woven and knitted aerogel textiles with outstanding thermal insulating ability. (**A**) Optical and IR images of commercial and EAF textiles on a stage of 40°C. From left to right, the types of the textiles are nylon, PET, wool, and EAF, respectively. (**B**) The average $|\Delta T|$ between fiber surface and stage for the four textiles in (A). Error bars indicate the standard deviation from three different samples. (**C**) Optical image of a 40 × 25 cm EAF textile fabricated on a rapier loom, indicating the potential of large-scale production. (**D**) The enlarged view of the textile in (C), showing the detail of the woven structure. (**E**) Optical image showing the folded shape of the flexible textile in (C). (**F**) Optical and IR images of ~1-mm-thick encapsulated aerogel textile and ~5-mm-thick down with the same thermal insulation performance at a stage of 40°C. (**G**) A detailed comparison of the knitted structure of EAF and wool, demonstrating the excellent machinability of EAF. (**H**) A volunteer wearing our EAF textile, down jacket, and wool and cotton sweaters in a cold environment of −20°C. The surface temperatures of these textiles are measured to be 3.5°, 3.8°, 7.2°, and 10.8°C, respectively, by averaging the temperature in the labeled areas. Black boxes contain side views of the folded garments. The EAF sweater and down jacket have a thickness difference of more than five times. (**I**) IR image showing that our EAF sweater maintained its thermal insulation property at −20°C after washing, indicating its excellent washability.

change of the microstructure inside the fiber and volume (Fig. 3G and fig. S6).

Thermal insulation textile based on EAF

On the basis of their excellent flexibility and strength, we further wove EAFs into aerogel textiles. We compared the textile woven with EAFs with nylon, polyester (PET, polyethylene terephthalate), and wool textiles of similar thickness by placing them on the same hot stage (Fig. 4A and table S1). Accordingly, we took a series of IR images when the stage temperature was stabilized at 40°C. The higher $|\Delta T|$ of our EAF textile indicated better thermal insulation performance (Fig. 4B). We measured the thermal conductivity of our EAF textile using the steady-state method (supplementary materials) (*50*). The thermal conductivity of our textile (26.9 ± 1.8 mW/m·K) was much lower than that of nylon (91.2 ± 1.6 mW/m·K), PET (98.3 ± 1.9 mW/m·K), and wool (38.9 ± 1.1 mW/m·K) (table S1). Moreover, we further wove our EAFs into a 40 × 25 cm textile using an industrial rapier loom (Fig. 4C). This reflects the potential of producing scalable thermal insulation textiles with our EAFs, which has been a major hurdle restricting the development of traditional aerogel fibers. An enlarged view of the thermal insulation textile (Fig. 4D) shows a typical plain-woven structure without defects, indicating that our EAFs can resist the shearing and stretching during weaving. The resulting textile is also flexible enough to be folded or bent into various shapes (Fig. 4E and fig. S7), which is also crucial for comfortable wearing.

Down is a common material for warm clothing because of its excellent thermal insulation. We compared the thermal insulation property of our textile with down by placing them on the same hot stage. When they showed similar performance in thermal insulation, as indicated by IR images (Fig. 4F), the EAF textile was only around one-fifth as thick as the down. Using traditional knitting techniques, we made a sweater out of our EAFs with the same knitted structure as wool yarn (Fig. 4G). Additionally, we tested the thermal insulation property of our sweater in a cold environment of −20°C. Our biomimetic textile with largely reduced thickness, as shown in the inset optical images, shows superior thermal insulation efficiency than traditional down jackets and wool and cotton sweaters, as indicated by the outer temperature measured from the labeled areas (3.5°, 3.8°, 7.2°, and 10.8°C, respectively) in Fig. 4H.

Additionally, our textile is also washable owing to the encapsulating layer. After washing with a commercial washing machine, we did not observe any obvious change in the appearance (Fig. 4, H and I). More notably, the thermal insulation performance of our sweater does not degrade, as indicated by the IR image in Fig. 4I. The outer temperatures before and after washing were 3.5° and 3.3°C, respectively, in a −20°C environment. All the data shown above demonstrate that the textile woven with our EAFs excellently combines thermal insulation, mechanical strength, flexibility, knittability, dyeability, and waterproofness, which are all crucial for the development of next-generation thermal insulation textiles.

Conclusions

We tackled the long-standing hurdle for the practical application of fragile aerogel in robust thermal insulation textiles. Drastically different from traditional strategies of doping or coating aerogel in the textile, we used a biomimetic approach in which thermal and mechanical properties of the aerogel fiber were separately designed. We achieved this by developing a relatively strong polymeric aerogel fiber with lamellar pores and then encapsulating it with a stretchable rubber layer. With an encapsulated layer only about 80 μm thick, the tensile strain of our encapsulated aerogel fiber was greatly increased more than 500 times compared with traditional aerogel fibers. More notably, the EAF could endure more than 10,000 loading-unloading stretching cycles with extreme stability for thermal insulation, indicating its remarkable durability. Because of the protection of the encapsulating layer, the EAFs are suitable for weaving and knitting, which are essential for large-scale preparation. A thin sweater made of our biomimetic fiber is only around one-fifth as thick as a down jacket for the same warmth. Additionally, our textile also exhibits excellent flexibility, washability, and dyeability, which are all crucial for practical applications of the textile. Such textiles feature excellent thermal insulation and multifunction and have great potential in areas such as military uniforms and space suits in extremely cold environments (*51*). Beyond this proof-of-concept work, our research highlights a different strategy for biomimetic design of multifunctional fibers and textiles, which are required for various emerging applications such as wearable electronics and personal thermal management.

REFERENCES AND NOTES

1. B. Wicklein *et al*., *Nat. Nanotechnol.* **10**, 277–283 (2015).
2. E. Cuce, P. M. Cuce, C. J. Wood, S. B. Riffat, *Renew. Sustain. Energy Rev.* **34**, 273–299 (2014).
3. Y. Si, J. Yu, X. Tang, J. Ge, B. Ding, *Nat. Commun.* **5**, 5802 (2014).
4. J. Zhang *et al*., *Adv. Mater.* **35**, e2300813 (2023).
5. C. Xu *et al*., *Nanomicro Lett.* **15**, 64 (2023).
6. J. Yang *et al*., *Small* **15**, e1902826 (2019).
7. B. Cai, A. Eychmüller, *Adv. Mater.* **31**, e1804881 (2019).
8. J. Zhao *et al*., *Molecules* **28**, 3541 (2023).
9. J. Wang, *Integr. Ferroelectr.* **189**, 36–43 (2018).
10. Z. Li *et al*., *Mater. Des.* **99**, 349–355 (2016).
11. W. Ma *et al*., *Chem. Soc. Rev.* **50**, 7009–7061 (2021).
12. Y. Wang, J. Ren, C. Ye, Y. Pei, S. Ling, *Nanomicro Lett.* **13**, 72 (2021).
13. Z. Sheng *et al*., *Adv. Sci. (Weinh.)* **10**, e2205762 (2023).
14. S. Meng, J. Zhang, W. P. Chen, X. P. Wang, M. F. Zhu, *Microporous Mesoporous Mater.* **273**, 294–296 (2019).
15. Z. Xu, Y. Zhang, P. Li, C. Gao, *ACS Nano* **6**, 7103–7113 (2012).
16. G. Li, G. Hong, D. Dong, W. Song, X. Zhang, *Adv. Mater.* **30**, e1801754 (2018).
17. Y. Li *et al*., *Nanoscale* **10**, 9360–9368 (2018).
18. Y. N. Jin, M. F. Wu, G. H. Zhao, M. F. Li, *Chem. Eng. J.* **168**, 1248–1255 (2011).
19. J. Zhou, Y. Hsieh, *Nano Energy* **68**, 104305 (2020).
20. M. Song, J. Jiang, H. Qin, X. Ren, F. Jiang, *ACS Appl. Mater. Interfaces* **12**, 45363–45372 (2020).
21. Z. Liu, J. Lyu, D. Fang, X. Zhang, *ACS Nano* **13**, 5703–5711 (2019).
22. Y. Du *et al*., *ACS Nano* **14**, 11919–11928 (2020).
23. X. Li, G. Dong, Z. Liu, X. Zhang, *ACS Nano* **15**, 4759–4768 (2021).
24. Z. Liu *et al*., *ACS Nano* **16**, 15237–15248 (2022).
25. Z. Liu *et al*., *ACS Nano* **17**, 18411–18420 (2023).
26. S. Zeng *et al*., *Science* **373**, 692–696 (2021).
27. M. Chen *et al*., *Nat. Commun.* **13**, 7097 (2022).
28. P. Bao *et al*., *BMC Genomics* **21**, 355 (2020).
29. C. Cuyler, N. A. Oritsland, *Rangifer* **22**, 133–142 (2002).
30. R. Kuhn, W. Meyer, *Zoolog. Sci.* **27**, 826–829 (2010).
31. D. M. Lavigne, N. A. Oritsland, *Nature* **251**, 218–219 (1974).
32. T. Stegmaier, M. Linke, H. Planck, *Philos. Trans. A Math. Phys. Eng. Sci.* **367**, 1749–1758 (2009).
33. H. Li *et al*., *ACS Appl. Mater. Interfaces* **14**, 29302–29314 (2022).
34. Z. P. Xu *et al*., *Engineering (Beijing)* **14**, 100–112 (2022).
35. Y. J. Wang *et al*., *Chem. Eng. J.* **390**, 124623 (2020).
36. Y. Cui, H. Gong, Y. Wang, D. Li, H. Bai, *Adv. Mater.* **30**, e1706807 (2018).
37. Z. Y. Shao, Y. J. Wang, H. Bai, *Chem. Eng. J.* **397**, 125441 (2020).
38. A. Du *et al*., *Chem. Mater.* **30**, 6849–6857 (2018).
39. J. Wu *et al*., *ACS Appl. Mater. Interfaces* **12**, 19015–19022 (2020).
40. S. Deville, E. Saiz, R. K. Nalla, A. P. Tomsia, *Science* **311**, 515–518 (2006).
41. H. Bai, Y. Chen, B. Delattre, A. P. Tomsia, R. O. Ritchie, *Sci. Adv.* **1**, e1500849 (2015).
42. M. Li, X. G. Dai, W. W. Gao, H. Bai, *Acc. Mater. Res.* **3**, 1173–1185 (2022).
43. M. Choi *et al*., *Adv. Funct. Mater.* **31**, 2101511 (2021).
44. A. August *et al*., *Energy* **168**, 1017–1030 (2019).
45. U. G. K. Wegst, H. Bai, E. Saiz, A. P. Tomsia, R. O. Ritchie, *Nat. Mater.* **14**, 23–36 (2015).
46. G. Du *et al*., *Nat. Commun.* **10**, 800 (2019).
47. Z. Xu, M. Wu, W. Gao, H. Bai, *Sci. Adv.* **8**, eabo0946 (2022).
48. M. Li, N. F. Zhao, M. N. Wang, X. G. Dai, H. Bai, *Adv. Funct. Mater.* **32**, 2205309 (2022).
49. J. W. Zhou *et al*., *Joule* **6**, 2358–2371 (2022).
50. X. Xu *et al*., *Science* **363**, 723–727 (2019).
51. X. C. Bu, H. Bai, *Chem. Res. Chin. Univ.* **39**, 19–29 (2023).

ACKNOWLEDGMENTS

The authors thank L. Zhong, M. Li, and Y. Li at Zhejiang University for assistance with the test in cold environment; N. Zheng at the State Key Laboratory of Chemical Engineering; Zhejiang University for assistance with SEM measurements; and G. Xu at Zhejiang Sci-Tech University for assistance with textile weaving. **Funding:** This work was supported by the National Natural Science Foundation of China (nos. 22075244 and 51722306), the Research Funds of Institute of Zhejiang University-Quzhou (no. IZQ2022RCZX018), and the Fundamental Research Funds for the Central Universities (2021FZZX001-17). **Author contributions:** H.B. and W.G conceived the idea, designed the experiments, and supervised the research project. M.W. conducted the experiments. H.B., W.G., and M.W. analyzed the data and wrote the paper. All authors contributed to the experiments and discussion of the manuscript. **Competing interests:** The authors declare no competing interests. **Data and materials availability:** All data are available in the main text or the supplementary materials.

License information: Copyright © 2023 the authors, some rights reserved; exclusive licensee American Association for the Advancement of Science. No claim to original US government works. https://www.science.org/about/science-licenses-journal-article-reuse

SUPPLEMENTARY MATERIALS

science.org/doi/10.1126/science.adj8013
Materials and Methods
Supplementary Text
Figs. S1 to S7
Table S1

Submitted 17 July 2023; accepted 6 November 2023
10.1126/science.adj8013

ICE SHEETS

Genomic evidence for West Antarctic Ice Sheet collapse during the Last Interglacial

Sally C. Y. Lau[1,2]*, Nerida G. Wilson[3,4,5], Nicholas R. Golledge[6], Tim R. Naish[6], Phillip C. Watts[7], Catarina N. S. Silva[1,8], Ira R. Cooke[9], A. Louise Allcock[10], Felix C. Mark[11], Katrin Linse[12], Jan M. Strugnell[1,2]

The marine-based West Antarctic Ice Sheet (WAIS) is considered vulnerable to irreversible collapse under future climate trajectories, and its tipping point may lie within the mitigated warming scenarios of 1.5° to 2°C of the United Nations Paris Agreement. Knowledge of ice loss during similarly warm past climates could resolve this uncertainty, including the Last Interglacial when global sea levels were 5 to 10 meters higher than today and global average temperatures were 0.5° to 1.5°C warmer than preindustrial levels. Using a panel of genome-wide, single-nucleotide polymorphisms of a circum-Antarctic octopus, we show persistent, historic signals of gene flow only possible with complete WAIS collapse. Our results provide the first empirical evidence that the tipping point of WAIS loss could be reached even under stringent climate mitigation scenarios.

Climate change continues to cause unprecedented warming to Earth's system (*1*). The consequences of warming are leading to rapid changes in Antarctica, including Antarctic Ice Sheet mass loss, with global impacts (*1*). A major uncertainty in global mean sea level (GMSL) rise projections lies in the potential instability of the West Antarctic Ice Sheet (WAIS) (*2*). The marine-based WAIS has lost 159 ± 8 gigatons of ice mass per year between 1979 and 2017 (*3*) and will continue to be a major contributor to GMSL rise under all CO_2 emission scenarios (*4*). It is unclear whether the WAIS is vulnerable to rapid ice loss or even full collapse as a result of poor understanding of future changes and processes that influence ice sheet dynamics (*2*). WAIS collapse could raise global sea level by ~3.3 to 5 m (*5*, *6*), with direct consequences that include human displacement and global loss of ecosystems in coastal areas (*1*).

It is well understood from geological reconstructions that there were interglacial peaks (super interglacials) during periods of the Pleistocene that experienced warmer temperatures (+~0.5° to 1.5°C) and higher GMSL (up to +10 m) than present (*4*). These super interglacials include Marine Isotope Stages (MIS) 31, 11, and 5e, which occurred at approximately ~1.08 to 1.05 Ma, ~424 to 395 ka and ~129 to 116 ka, respectively (*4*). During MIS 31, the Southern Ocean sea surface temperature may have reached +5° ± 1.2°C above present during summer months (*7*). During MIS 11, global mean surface temperature (GMST) was 0.5° ± 1.6°C with GMSL 6 to 13 m higher than present and similarly during MIS 5e (the last interglacial), GMST was +0.5° to 1.5°C with GMSL 5 to 10 m higher than present (*4*). To date, there is no empirical evidence to indicate whether the WAIS has completely collapsed at any time in the three million years since the Pliocene (*8*, *9*). Inferring WAIS configurations during late Pleistocene super interglacial periods could therefore inform the sensitivity of Antarctic ice sheet response to climate change. So far, analyses of ice proximal marine drill core records show evidence of WAIS retreat during the late Pleistocene interglacials, but the exact timing (*10*) and extent (*9*, *11*) of any WAIS collapse remain ambiguous. Existing ice sheet models have yielded conflicting WAIS reconstructions during these periods, ranging from no collapse (*12*) to partial (*13*) or full collapse (*14*, *15*). Knowledge of how the WAIS was configured during super interglacials in the geological past is urgently needed to constrain future sea level rise projections (*2*). Novel approaches such as population genomics can serve as empirical proxies of past changes to the Antarctic Ice Sheet, detected through signals of historic gene flow among currently separated populations of marine organisms (*16*).

A complete past collapse of the WAIS would have opened the trans–West Antarctic seaways linking the present-day Weddell Sea (WS), Amundsen Sea (AS), and Ross Sea (RS) (*16*). Such seaways would have allowed marine benthic organisms to occupy the opened straits and disperse across them, thus leaving genetic signatures of this past connectivity in the genomes of their descendent, extant populations (*16*) (hereafter seaway populations). As the WAIS reformed, these organisms would be isolated again within the WS, AS, and RS basins, with any subsequent connectivity only possible around the continental margin. Although there is some support for existence of trans-Antarctic seaways based on species assemblage data at macroevolutionary scales (*17*–*20*) or low-resolution genetic data (*21*–*24*), all these studies lack power and/or spatial coverage to distinguish between past dispersal through trans–West Antarctic seaways or from contemporary circumpolar ocean currents. Importantly, these previous studies cannot be used for accurate demographic modeling to identify the likely timing of any collapse of the WAIS.

Collection of benthic species from the Southern Ocean is logistically challenging and regions such as AS and East Antarctica (EA) are difficult to access. Existing samples are typically characterized by DNA degradation due to long-term storage in collections at room temperature. We used a target capture approach that sequenced genome-wide, single nucleotide polymorphism (SNP) data in the circum-Antarctic benthic octopus, *Pareledone turqueti*, incorporating rare samples from AS and EA, collected over 33 years. Our approach enabled a comprehensive sampling strategy to robustly date and test for the presence of past trans–West Antarctic seaways using biological data as proxies.

We sequenced genome-wide SNPs derived from double-digest restriction site–associated DNA (ddRAD) (*25*) loci from 96 *P. turqueti* individuals collected from around the Southern Ocean (Fig. 1A). The dataset presents a circum-Antarctic overview of the species' genetic patterns, which record the contemporary connectivity driven by oceanic currents—mainly the Antarctic circumpolar current (ACC; clockwise) and the Antarctic Slope Current (ASC; counterclockwise) (Fig. 1, A and B), as well as any historical connectivity that would be associated with past trans–West Antarctic seaways. We used a reduced SNP dataset (one SNP per locus) to analyze population structure, which included 5188 unlinked SNPs. Complementary analyses (Structure, TreeMix) suggest that the population genomic variation of *P. turqueti* is characterized by geographically structured populations across the Southern Ocean (Fig. 1C and figs. S1 and S2). This makes it an appropriate species to test for the presence of trans–West Antarctic seaways as signals of historical WAIS collapse in highly admixed species would likely be masked by contemporary gene flow signatures (*16*). *Pareledone turqueti* can disperse through benthic crawling as adults and hatchlings [inferred from large egg size (maximum oocyte length 19.8 mm) and small number of eggs per clutch

[1]Centre for Sustainable Tropical Fisheries and Aquaculture and College of Science and Engineering, James Cook University, Townsville, Qld, Australia. [2]Securing Antarctica's Environmental Future, James Cook University, Townsville, Qld, Australia. [3]Collections & Research, Western Australian Museum, Welshpool, WA, Australia. [4]School of Biological Sciences, University of Western Australia, Perth, WA, Australia. [5]Securing Antarctica's Environmental Future, Western Australian Museum, Welshpool, WA, Australia. [6]Antarctic Research Centre, Victoria University of Wellington, Wellington, New Zealand. [7]Department of Biological and Environmental Science, University of Jyväskylä, Jyväskylä, Finland. [8]Centre for Functional Ecology - Science for People & the Planet (CFE), Associate Laboratory TERRA, Department of Life Sciences, University of Coimbra, Portugal. [9]Centre for Tropical Bioinformatics and Molecular Biology, James Cook University, Townsville, Qld, Australia. [10]School of Natural Sciences and Ryan Institute, University of Galway, Galway, Ireland. [11]Alfred Wegener Institute, Helmholtz Centre for Polar and Marine Research, Bremerhaven, Germany. [12]British Antarctic Survey, Cambridge, UK.
*Corresponding author. Email: cheukying.lau@jcu.edu.au

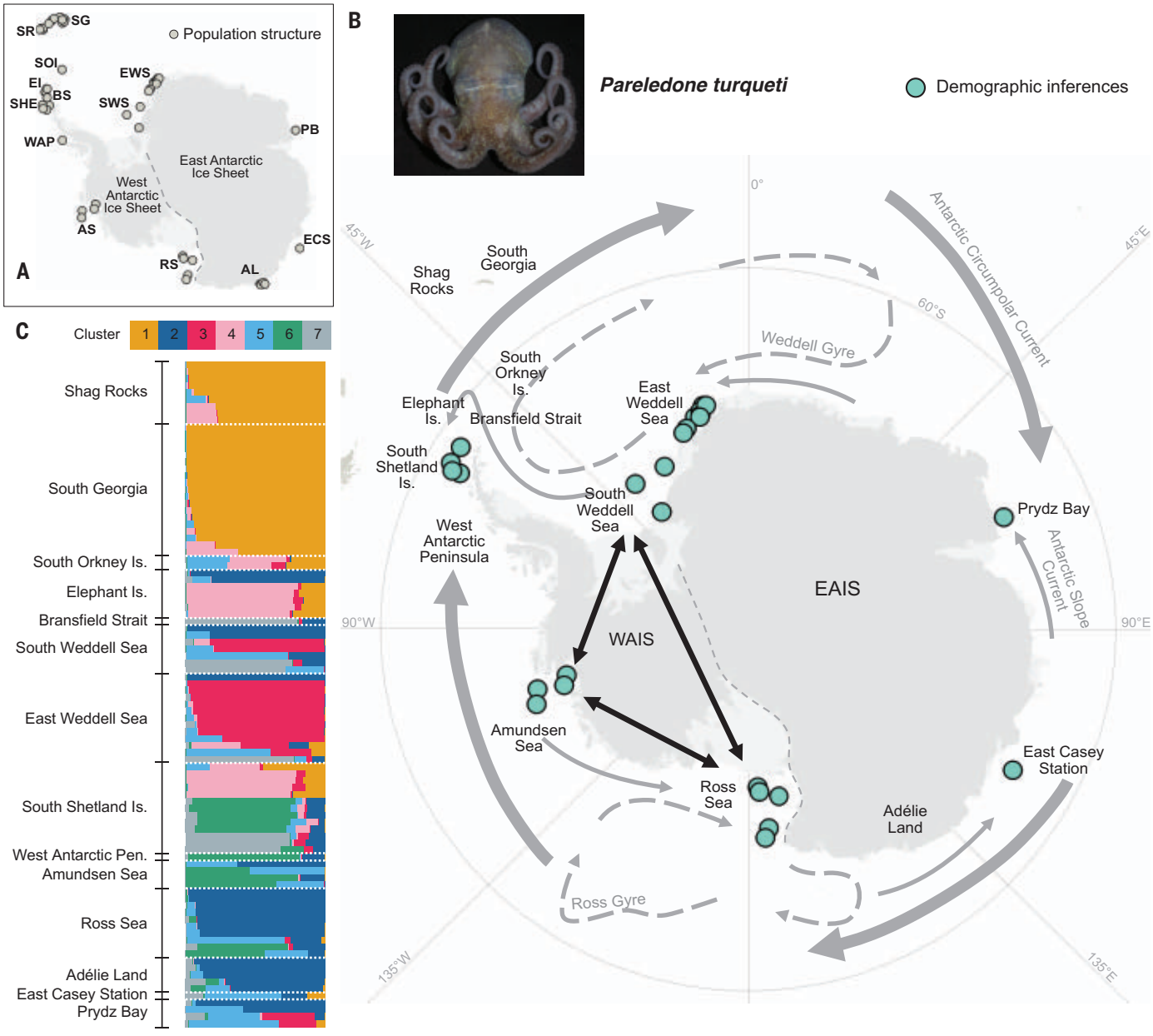

Fig. 1. Sample locations of *P. turqueti* with Structure analyses. (**A**) Samples used for analyses of population structure. Abbreviations: Shag Rocks, SR; South Georgia, SG; South Orkney Is., SOI; Elephant Is., EI; Bransfield Strait, BS; South Shetland Is., SHE; West Antarctic Peninsula, WAP; South and East Weddell Sea, S- and E-WS, respectively; Amundsen Sea, AS; Ross Sea, RS; Adélie Land, AL; East Casey Station, ECS; Prydz Bay, PB. (**B**) Samples used for admixture analyses and demographic modeling (collectively demographic inferences) to test for the existence of trans–West Antarctic seaways. Map includes the directionalities of the major contemporary circumpolar currents and regional currents in the Southern Ocean. Black arrows indicate connectivity pathways through trans–West Antarctic seaways that would result from WAIS collapse. Direct connectivity between WS-AS or AS-RS would indicate partial WAIS collapse, and direct connectivity between WS-AS-RS or WS-RS would indicate complete WAIS collapse. [Photo credit of *P. turqueti* specimen: E. M. Jorgensen] (**C**) Clustering analysis using Structure inferred $K = 7$ for *P. turqueti* (5188-SNP dataset). Each horizontal bar represents an individual sample, bars are grouped by geographical locations, and colors within each bar correspond to the proportion of each genetic cluster in the individual.

(n = 22 to 66)] (*26*, *27*). It has also been suggested that long-distance dispersal in *P. turqueti* may be achieved, at least occasionally, through adults or egg masses rafting on floating substrates, or that their benthic egg masses could become dislodged and disperse through the currents (*23*), although no direct evidence yet supports this.

In *P. turqueti*, long-distance connectivity linking East and West Antarctica is detected across the Antarctic continental shelf and Antarctic islands (Fig. 1C), likely indicating dispersal that reflects contemporary circumpolar currents, as found in other Southern Ocean benthic taxa (*28*). If the genomic data of *P. turqueti* can only be explained by serial circumpolar colonization around the Antarctic continent, then observed and expected heterozygosity would decrease as geographical distance increases. However, the observed data does not support this scenario (fig. S3 and table S1). Admixture is also observed between individuals from RS and AS with some individuals from WS (Fig. 1C), indicating a potential signature of trans–West

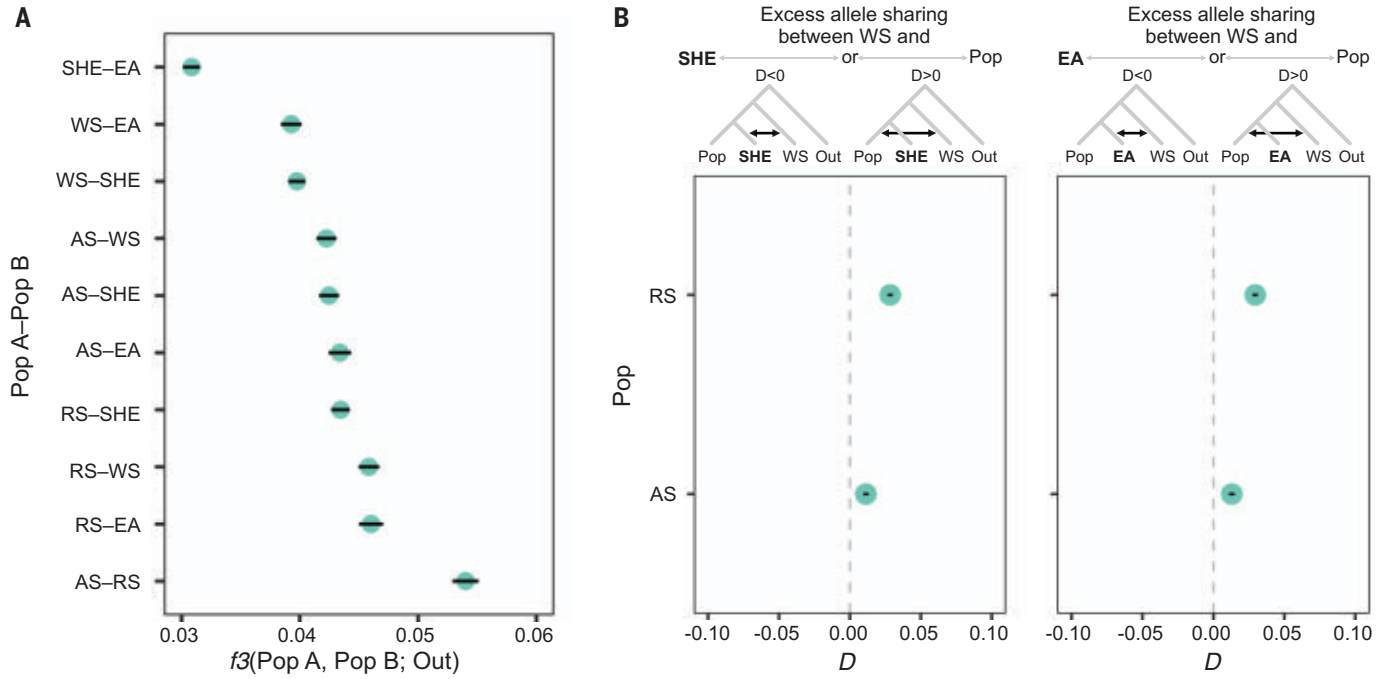

Fig. 2. Evidence of distinct allele frequency correlations between Amundsen Sea, Weddell Sea, and Ross Sea, as well as contemporary gene flow in *P. turqueti*. Error bars (black horizontal lines) indicate standard errors; filled circles indicate significant (Z-score values > 3 or < −3); Out, outgroup population, which includes Shag Rocks and South Georgia (samples combined). Data includes a 120,857-SNP dataset. Abbreviations: Weddell Sea (WS), South Shetland Islands (SHE), Amundsen Sea (AS), Ross Sea (RS), East Antarctica (EA). (**A**) Outgroup-f_3-statistics between pairs of populations. As f_3 value increases, more derived allele frequency is shared between the pairs of populations. (**B**) *D*-statistic (in the form of BABA-ABBA) examines patterns of allele sharing across four populations and indicates whether there is excess allele sharing between distinct populations. (Left) *D*-statistic is presented in the form of *D*(Pop, SHE, WS, Out), which examines whether there is excess allele sharing between SHE and WS (*D*<0; ABBA) or Pop and WS (*D*>0; BABA). (Right) *D*-statistic is presented in the form of *D*(Pop, EA, WS, Out), which examines whether there is excess allele sharing between EA and WS (*D*<0; ABBA) or Pop and WS (*D*>0; BABA).

Antarctic seaways. Supporting this concept, population differentiation analysis shows limited genetic divergence between WS-RS relative to other localities that are adjacent to each other (fig. S4).

Focusing on populations most informative of whether the WAIS collapsed in the past, we first examined whether there was distinct admixture between WS-AS-RS with respect to South Shetland Islands (SHE) and East Antarctica (EA) (including Prydz Bay and East Casey Station) samples using 120,857 SNPs (Fig. 1B). SHE and EA are known to be influenced by both the ACC and ASC (*29*) but are peripheral to the putative historical trans–West Antarctic connectivity; as such, these are ideal locations that can separate patterns of present-day connectivity around the WAIS and East Antarctic Ice Sheet (EAIS) from persistent, historical signals of gene flow.

We examined allele frequency correlations across WS, AS, and RS with respect to SHE and EA. The *D*-statistic (*30*) explores the patterns of allele sharing across four populations to test for evidence of admixture between populations of interest. The outgroup-f_3-statistic (*31*) explores the amount of derived allele frequency that is shared between pairs of populations relative to an outgroup population. The presence of admixture linked to trans–West Antarctic connectivity would result in high f_3 values as well as evidence of excess allele sharing (*D*>0) between WS-AS-RS. In *P. turqueti*, the highest f_3 values are detected between AS–RS, followed by RS–EA and RS–WS (Fig. 2A), thus indicating recent common ancestry across seaway populations as well as between RS and EA populations that are adjacent to each other. When SHE is treated as the sister lineage to AS/RS and WS [*D*(AS/RS, SHE, WS, outgroup)], there is excess allele sharing between AS/RS and WS (Fig. 2B). When EA is treated as a sister lineage to AS/RS and WS [*D*(AS/RA, EA, WS, outgroup)], excess allele sharing is also observed between AS/RS and WS (Fig. 2B). If circumpolar currents (ASC and ACC) were the only factors that have influenced gene flow patterns in *P. turqueti*, then low f_3 values would be observed between WS-RS as they are situated on the opposite side of West Antarctica, and excess allele sharing (*D*) would also be observed between WS-SHE and WS-EA as they are geographically adjacent. However, these results confirmed that in *P. turqueti* there are unexpected and significant allele frequency correlations among AS-RS-WS, despite also considering the locations situated between them around the WAIS (SHE) and EAIS (EA). Such observed admixture patterns are congruent with historical seaway connectivity in a species that is characterized by geographically structured populations.

A site frequency spectrum (SFS)–based, coalescent demographic modeling framework (fastsimcoal) (*32*) was used to test the hypothesis of whether historical trans-Antarctic seaways existed, with populations subsequently influenced by contemporary circumpolar gene flow. For demographic modeling, we included samples from WS, AS, RS, and EA with 163,335 SNPs in *P. turqueti*. We employed a hierarchical approach to test for WAIS collapse scenarios while incorporating modern circumpolar gene flow in the models (figs. S5 and S6). Step 1 compared contrasting scenarios of past WAIS configurations with circumpolar gene flow following the directionality of the ACC (clockwise). The models incorporated WS, EA, RS, and AS experiencing continuous circumpolar gene flow since population divergence. Under these scenarios, after population divergence WS, AS, and RS experienced no, partial, or complete connectivity, followed by modern ACC gene flow linking between WS, EA, RS, and AS. Limited differentiation was found between competing scenarios (no, partial, or complete connectivity) at step 1 (figs. S7 and S8). Therefore, at step 2

model complexity was increased to model more ecologically realistic scenarios, with circumpolar gene flow following both directionalities of the ACC and ASC (counterclockwise) for all scenarios (figs. S9 and S10). At step 3, unmodeled ancestral size change was further considered to distinguish competing models from the previous step.

The observed SFSs were statistically best explained by the scenario of a complete historical WAIS collapse (Fig. 3A and figs. S11 and S12), followed by modern circumpolar gene flow linked to ACC and ASC. The ancestral lineage of WS, AS, RS, and EA populations experienced an expansion followed by a bottleneck (Fig. 3A and table S2). During the mid-Pliocene, which ended ~3 million years ago [95% confidence interval (CI) between 3.6 and 3.5 million years ago (Mya)], the best model supports WS, AS, RS, and EA continental shelf locations splitting into four populations with direct asymmetric gene flow detected between WS-AS-RS. This suggests that ancient seaways were likely opened across the WAIS, which directly linked the present-day WS, AS, and RS, and could only be facilitated by WAIS collapse during past interglacials. The start of the historical, direct WS-AS-RS connectivity began ~3.6 to 3.0 Mya, which supports geological evidence of historical WAIS collapses during the Pliocene (*8*, *9*). The signature of direct WS-AS-RS connectivity ceased between 139 and 54 ka (based on 95% CI; Fig. 3A), which is in accordance with the end of the Last Interglacial.

Considering the estimated confidence intervals, the cessation of direct gene flow between WS-AS-RS could only be associated to the most recent interglacial MIS 5e (129 to 116 ka) because the prior super interglacial (MIS 11; ~424 to 395 ka)—which would also enable such direct connectivity—is far outside of the upper uncertainty bound of the connectivity. The maximum likelihood value of the direct WS-AS-RS connectivity was dated to 87 ka; the time lag between 87 ka and the time of MIS 5e (129 to 116 ka) can be explained at least in part by the time it takes for complete trans–West Antarctic migration to influence allele frequencies in a benthic direct developing octopus. Finally, contemporary circumpolar gene flow began after 87 ka, following the directions of the ACC and ASC, which generally reflects the influence of ongoing circumpolar currents on gene flow of Southern Ocean benthic taxa, in particular the ACC (*28*). For example, the high migration rates observed from WS→EA and RS→AS reflect the strength of ACC relative to ASC. To support the logic that populations were split from the same ancestral population, we considered the alternative tree topologies of diverse three-population models involving WS, RS and EA, or SHE (figs. S13 and S14). In all cases, recent, shared ancestry between RS and WS is not an alternative explanation

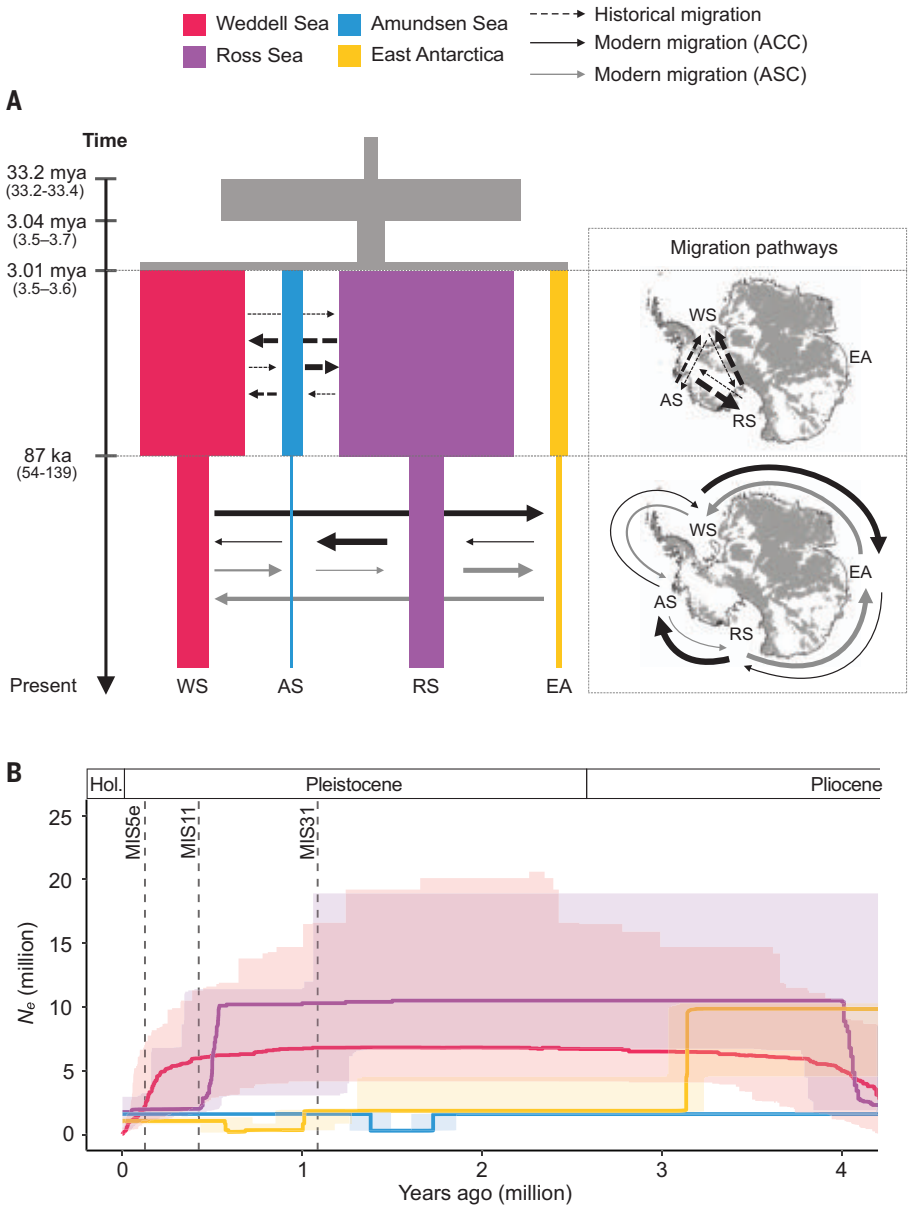

Fig. 3. Best-supported demographic model for *P. turqueti* indicating that signatures of complete historical WAIS collapse began during the mid-Pliocene and continued until the end of MIS 5e, supplemented by a StairwayPlot that indicates past changes in population size. (**A**) Maximum likelihood model for *P. turqueti* including the Amundsen Sea (AS), Ross Sea (RS), Weddell Sea (WS) and East Antarctica (EA) populations, as well as direct historical gene flow (3 Mya to 87 ka) between WS, AS, and RS and modern gene flow (87 to 0 ka) around the Antarctic continental shelf following the directionality of the Antarctic Circumpolar Current (ACC; clockwise), and the Antarctic Slope Current (ASC; counterclockwise). Maximized parameter estimates are visualized. The associated 95% confidence intervals (CI) are in brackets and reported in Table S2. Time of the events modeled are shown on the left. The width of the bars is proportional to the effective population size of the population. Arrows indicate migration (forward in time), with the width of the arrows proportional to the number of migrants per generation (2Nm). The migration pathways, based on modeled migration directions (forward in time), are also visualized on a map of Antarctica. Map shows subglacial bed elevation >0 m above present-day sea level and is extracted from Bedmap2 (*40*). Data includes a 163,335-SNP dataset. (**B**) *StairwayPlot* reconstruction of past changes in effective population size over time in *P. turqueti* in the last ~4 Mya. Line indicates median and shaded area indicates 2.5 and 97.5% confidence limits. Data includes a 191,024 SNP-dataset. Dashed vertical lines represent timing of MIS 5e (~125 ka), MIS 11 (~424 ka), and MIS 31 (~1.08 Mya). Abbreviations: Holocene, Hol.

for the observed data (tables S3 and S4), with consistent outcomes supporting historic direct gene flow between WS-RS ending around the Last Interglacial. The implication is that the conclusion of WAIS collapse is robust to the model assumption of a split from the same ancestral population.

One of the biggest challenges of inferring demographic events in the late Pleistocene include whether the species experienced a severe bottleneck (i.e., sharp reduction in N_e) in the recent past that eroded genomic history. For example, if the WAIS had collapsed in the late Pleistocene, large areas of newly ice-free habitats (where the WAIS existed previously) would have become available for benthic fauna to disperse and colonize. During the subsequent glacial maximum, as the AIS expanded across the Antarctic continental shelf, the marine shelf habitats would likely be reduced to small, isolated pockets of in situ ice-free refugia (*33*). Such changes in habitat availability would likely lead to severe population bottlenecks and subsequent genetic drift (*33*). As a result, a recent severe bottleneck could lead to loss of alleles and increased coalescence rate and events only dating back to the time of most recent bottleneck (*34*) (i.e., LGM at ~20 ka in *P. turqueti*). Demographic models detected events prior to LGM in *P. turqueti*, suggesting this species did not experience population bottlenecks in the recent past as severe as might be expected for a Southern Ocean benthic species.

We searched for signals of population size fluctuation prior to the LGM in *P. turqueti* using StairwayPlot (*35*), an SFS-based model-free method. We found that the demographic changes dated by StairwayPlot generally correspond with the dating of gene flow changes by fastsimcoal. Pronounced demographic changes (observed from Fig. 3B) were detected in the RS and WS populations at ~435 ka and ~200 ka, respectively. These timings coincide with the glacial stage MIS 12 and the relatively cool interglacial of MIS 7, both of which were subsequently followed by periods of peak warmth during MIS 11 and MIS 5e respectively. In species with population structure, population decline at a particular timepoint in StairwayPlot corresponds to signals of demographic change such as changes in population structure and migration rate (*36*). In the case of *P. turqueti*, the population decline detected in RS around MIS 11 and in WS around MIS 5e corresponds to demographic change likely associated with WAIS collapse. In the fastsimcoal model (Fig. 3A), the population decline detected across all populations after the Last Interglacial also corresponds to the widely accepted hypothesis that there would be limited in situ ice-free refugia on the Antarctic continental shelf during the LGM, leading to population bottlenecks in benthic species that could only survive on the shelf (*33*) (i.e., the case for *P. turqueti*) (*23*). These patterns suggest that recent super interglacials and the LGM likely strongly influenced species demography, particularly in populations associated with the signatures of WAIS collapse.

Estimation of past changes in population size with StairwayPlot indicated that those in the AS and EA were relatively stable since 3 Mya whereas fastsimcoal indicated size changes in these populations; such discordances are likely due to method-specific sensitivity in populations with low sample size in regions where it is challenging to collect biological samples ($n \leq 5$ in AS and EA). Overall, the timing of demographic events detected by independent inferences also corroborates the timings of major glacial-interglacial fluctuations in the Pliocene and the late Pleistocene, as well as events dated using independent markers (mitochondrial data) (*23*). Therefore, the dating of WAIS collapse, as seen through the genomic data of *P. turqueti* appears to be robust and unconfounded by noise.

Our demographic modeling approach was specifically designed to test whether trans–West Antarctic seaways existed in the past that could be detected with simple contrasting models. The best-supported demographic model was able to characterize an overview of the historical, direct WS-AS-RS connectivity linked to WAIS collapses through the Pliocene and as late as MIS 5e. Although additional periods of seaway closure occurred during other geological periods between 3 Mya and MIS 5e, our analyses are focused on dating the most recent gene flow linked to historical WAIS collapse. The evolutionary history of *P. turqueti* is highly complex and populations would have experienced specific demographic changes associated with each glacial-interglacial cycle throughout the Quaternary. We did not sequentially reconstruct their past changes in population size and connectivity patterns to avoid over-parameterization. Signatures of recent events are more clearly encoded in allele frequencies. We utilized a target capture approach that can sequence reduced representation genomic data in samples with DNA degradation. Our reduced representation SNP dataset has the power to reflect recent major events dated to around MIS 5e, MIS 11, and the Pliocene. Regardless of the overall challenge of demographic modeling for Southern Ocean species, signatures of a complete WAIS collapse, last detected at around the MIS 5e, were clear in *P. turqueti*.

We provide empirical evidence indicating that the genomic signatures of marine-based sectors WAIS collapse were present during the Last Interglacial (MIS 5e), when GMST was 0.5° to 1.5°C warmer than the preindustrial. Future WAIS collapse on centennial timescales is considered to be a low likelihood process (*4*); however, in recent trajectories estimated for temperature rise, such as for the most optimistic emission scenario Shared Socio-economic Pathway (SSP) 1-1.9, air temperature is projected to reach +1.2° to 1.7°C by 2100 (very likely range) (*4*). Moreover, Antarctic Ice Sheet models simulating the response to Intergovernmental Panel on Climate Change (IPCC) emissions scenarios (*15*, *37*) show that a threshold is crossed when warming is above SSP2-2.6 (the Paris climate target) whereby ice shelves are lost and marine-based sectors of WAIS undergo self-reinforcing melting due to marine ice sheet instability processes. This study provides empirical evidence indicating that the WAIS collapsed when the global mean temperature was similar to that of today, suggesting that the tipping point of future WAIS collapse is close. Future global sea level rise projections should consider the irreversible collapse of the WAIS and some marine sectors of the EAIS (*38*), which will commit the planet to multimeter GMSL over the coming centuries and millennium if global warming exceeds +1.5° to 2°C above preindustrial levels (*1*, *8*, *39*).

REFERENCES AND NOTES

1. IPCC, Climate Change 2021: The Physical Science Basis. Contribution of Working Group I to the Sixth Assessment Report of the Intergovernmental Panel on Climate Change (Cambridge Univ. Press, 2021).
2. F. Pattyn, M. Morlighem, *Science* **367**, 1331–1335 (2020).
3. E. Rignot *et al*., *Proc. Natl. Acad. Sci. U.S.A.* **116**, 1095–1103 (2019).
4. B. Fox-Kemper *et al*., in *Climate Change 2021: The Physical Science Basis. Contribution of Working Group I to the Sixth Assessment Report of the Intergovernmental Panel on Climate Change* (Cambridge Univ. Press, 2021), chap. 9.
5. D. G. Vaughan, *Clim. Change* **91**, 65–79 (2008).
6. J. L. Bamber, R. E. M. Riva, B. L. A. Vermeersen, A. M. LeBrocq, *Science* **324**, 901–903 (2009).
7. C. Beltran *et al*., *Quat. Sci. Rev.* **228**, 106069 (2020).
8. G. R. Grant *et al*., *Nature* **574**, 237–241 (2019).
9. T. Naish *et al*., *Nature* **458**, 322–328 (2009).
10. R. P. Scherer *et al*., *Geophys. Res. Lett.* **35**, 2007GL032254 (2008).
11. R. McKay *et al*., *Quat. Sci. Rev.* **34**, 93–112 (2012).
12. M. D. Holloway *et al*., *Nat. Commun.* **7**, 12293 (2016).
13. N. R. Golledge *et al*., *Geophys. Res. Lett.* **48**, e2021GL094513 (2021).
14. E. J. Steig *et al*., *Geophys. Res. Lett.* **42**, 4862–4868 (2015).
15. R. M. DeConto, D. Pollard, *Nature* **531**, 591–597 (2016).
16. J. M. Strugnell, J. B. Pedro, N. G. Wilson, *Quat. Sci. Rev.* **179**, 153–157 (2018).
17. K. Linse, H. J. Griffiths, D. K. A. Barnes, A. Clarke, *Deep Sea Res 2 Top Stud Oceanogr.* **53**, 985–1008 (2006).
18. D. K. A. Barnes, C. D. Hillenbrand, *Glob. Change Biol.* **16**, 3297–3303 (2010).
19. D. G. Vaughan, D. K. A. Barnes, P. T. Fretwell, R. G. Bingham, *Geochemistry, Geophys Geosystems*. **12**, Q10004 (2011).
20. C. Moreau *et al*., *Ecol. Evol.* **9**, 8465–8478 (2019).
21. C. Held, J. W. Wägele, *Sci. Mar.* **69**, 175–181 (2005).
22. K. Linse, T. Cope, A.-N. Lörz, C. Sands, *Polar Biol.* **30**, 1059–1068 (2007).
23. J. M. Strugnell, P. C. Watts, P. J. Smith, A. L. Allcock, *Mol. Ecol.* **21**, 2775–2787 (2012).
24. G. E. Collins *et al*., *Proc. Natl. Acad. Sci. U.S.A.* **117**, 22293–22302 (2020).
25. B. K. Peterson, J. N. Weber, E. H. Kay, H. S. Fisher, H. E. Hoekstra, *PLOS ONE* **7**, e37135 (2012).
26. S. V. Boletzky, *Antarct. Sci.* **6**, 139–142 (2004).
27. I. M. Barratt, M. P. Johnson, M. A. Collins, A. L. Allcock, *Polar Biol.* **31**, 583–594 (2008).
28. A. Riesgo, S. Taboada, C. Avila, *Mar. Genomics* **23**, 1–13 (2015).
29. A. F. Thompson, A. L. Stewart, P. Spence, K. J. Heywood, *Rev. Geophys.* **56**, 741–770 (2018).
30. E. Y. Durand, N. Patterson, D. Reich, M. Slatkin, *Mol. Biol. Evol.* **28**, 2239–2252 (2011).

31. M. Raghavan *et al*., *Nature* **505**, 87–91 (2014).
32. L. Excoffier, I. Dupanloup, E. Huerta-Sánchez, V. C. Sousa, M. Foll, *PLOS Genet.* **9**, e1003905 (2013).
33. A. L. Allcock, J. M. Strugnell, *Trends Ecol. Evol.* **27**, 520–528 (2012).
34. L. M. Gattepaille, M. Jakobsson, M. G. Blum, *Heredity* **110**, 409–419 (2013).
35. X. Liu, Y.-X. Fu, *Nat. Genet.* **47**, 555–559 (2015).
36. P. Lesturgie, S. Planes, S. Mona, *Mol. Ecol. Resour.* **22**, 554–566 (2022).
37. N. R. Golledge *et al*., *Nature* **526**, 421–425 (2015).
38. M. O. Patterson *et al*., *Nat. Geosci.* **7**, 841–847 (2014).
39. R. M. DeConto *et al*., *Nature* **593**, 83–89 (2021).
40. P. Fretwell *et al*., *Cryosphere* **7**, 375–393 (2013).

ACKNOWLEDGMENTS

We thank the Australian Antarctic Division (AAD), Alfred Wegener Institute for Polar and Marine Research (AWI), British Antarctic Survey (BAS), Museum Victoria (MV), National Institute of Water and Atmospheric Research (NIWA), and G. Jackson for assistance and samples for genetic analysis. We are grateful to T. Jernfors (University of Jyväskylä) for sequencing assistance. **Funding:** This work was supported by the following: Australian Research Council (ARC) Discovery grant DP190101347 (to J.M.S., N.G.W., N.R.G., and T.R.N.); New Zealand Ministry of Business, Innovation and Employment through the Antarctic Science Platform (ANTA1801) (to N.R.G. and T.R.N.); Thomas Davies Research grant (Australian Academy of Science) (to J.M.S.); David Pearse bequest, Antarctic Science Bursary, Antarctic PhD student support grant (Antarctic Science Foundation), and Australasian eResearch Organisations (AeRO) Cloud Grant (to S.C.Y.L.); CoSyst grant (to J.M.S. and P.C.W.); Academy of Finland grant 305532 (to P.C.W.); Australian Research Council (ARC) SRIEAS Grant SR200100005 Securing Antarctica's Environmental Future; Scientific Committee on Antarctic Research (SCAR) INSTANT program. **Author contributions:** Conceptualization: N.G.W., N.R.G., T.R.N., and J.M.S. Methodology: S.C.Y.L., N.G.W., C.N.S.S., and J.M.S. Investigation: S.C.Y.L. Formal Analysis: S.C.Y.L. and I.R.C. Visualization: S.C.Y.L. Funding acquisition: S.C.Y.L., N.G.W., N.R.G., T.R.N., P.C.W., and J.M.S. Resources: P.C.W., A.L.A., F.C.M., and K.L. Supervision: N.G.W., C.N.S.S., J.M.S. Writing – original draft: S.C.Y.L. Writing – review and editing: S.C.Y.L., N.G.W., N.R.G., T.R.N., P.C.W., C.N.S.S., I.R.C., A.L.A., F.C.M., K.L., and J.M.S. **Competing interests:** Authors declare that they have no competing interests. **Data and materials availability:** The ddRADseq data of Southern Ocean octopus generated for target capture bait design is deposited on National Centre for Biotechnology Information (NCBI) under the BioProject PRJNA853080, with Sequence Read Archive (SRA) accessions SRR19893055–SRR19893494. The target capture of ddRAD loci data in *Pareledone turqueti* is deposited under the BioProject PRJNA853871, with SRA accessions SRR19892485–SRR19892582. The draft partial genome of *P. turqueti* is available for download from https://www.marine-omics.net/resources/. All software used for data analyses in this study is publicly available. Detailed methods including scripts and command used to perform all analyses are provided at https://github.com/sallycylau/WAIS_turqueti. **License information:** Copyright © 2023 the authors, some rights reserved; exclusive licensee American Association for the Advancement of Science. No claim to original US government works. https://www.sciencemag.org/about/science-licenses-journal-article-reuse

SUPPLEMENTARY MATERIALS

science.org/doi/10.1126/science.ade0664
Materials and Methods
Supplementary Text
Figs. S1 to S26
Tables S1 to S13
Data S1 and S2
References (*41*–*96*)

Submitted 22 July 2022; accepted 30 October 2023
10.1126/science.ade0664

NEUROSCIENCE

GluD1 binds GABA and controls inhibitory plasticity

Laura Piot[1], Christina Heroven[2]†‡, Simon Bossi[1]†, Joseph Zamith[1], Tomas Malinauskas[3], Chris Johnson[2], Doris Wennagel[1], David Stroebel[1], Cécile Charrier[1], A. Radu Aricescu[2]*, Laetitia Mony[1]*, Pierre Paoletti[1]*

Fast synaptic neurotransmission in the vertebrate central nervous system relies primarily on ionotropic glutamate receptors (iGluRs), which drive neuronal excitation, and type A γ-aminobutyric acid receptors ($GABA_A$Rs), which are responsible for neuronal inhibition. However, the GluD1 receptor, an iGluR family member, is present at both excitatory and inhibitory synapses. Whether and how GluD1 activation may affect inhibitory neurotransmission is unknown. In this work, by using a combination of biochemical, structural, and functional analyses, we demonstrate that GluD1 binds GABA, a previously unknown feature of iGluRs. GluD1 activation produces long-lasting enhancement of GABAergic synaptic currents in the adult mouse hippocampus through a non-ionotropic mechanism that is dependent on trans-synaptic anchoring. The identification of GluD1 as a GABA receptor that controls inhibitory synaptic plasticity challenges the classical dichotomy between glutamatergic and GABAergic receptors.

Most excitatory neurotransmission in the central nervous system is mediated by the ionotropic glutamate receptor (iGluR) family members, which are classified as AMPA (GluA1 to 4), *N*-methyl-D-aspartate (NMDA) (GluN1, GluN2A to D, and GluN3A and B), kainate (GluK1 to 5), and delta (GluD1 and D2) receptors (*1*). At a typical excitatory synapse, glutamate released in the synaptic cleft binds postsynaptic iGluRs and drives opening of their cation-conductive ion channel, which results in membrane depolarization. Although structurally related (*2*), GluD1 and GluD2 receptors depart from other iGluRs by their insensitivity to glutamate and inability to gate the ion channel pore upon ligand binding (*3*, *4*). Instead, GluD receptors are thought to exert their physiological function by binding D-serine (or glycine) (*5*–*7*) and through metabotropic (i.e., non-ionotropic) signaling (*4*, *8*) [although ionotropic GluD signaling that is dependent on G protein–coupled receptors has also been suggested (*9*)]. This mechanism is best characterized for GluD2 receptors. Postsynaptic GluD2 binds cerebellin-1, a "molecular bridge" attached to presynaptic membrane proteins from the neurexin family, to form tripartite complexes that span the synaptic cleft and are involved in synapse formation, maintenance, and plasticity (*4*, *10*–*13*). Although GluD1 can also form triads with cerebellins and neurexins (*8*, *14*), relatively little is known about GluD1 signaling and its functional roles. Expressed throughout the forebrain (*15*–*17*), GluD1 receptors participate in excitatory synaptogenesis (*18*, *19*) and regulate the balance between AMPA and NMDA receptors (*20*). GluD1 also specifies the formation of inhibitory synapses in the neocortex (*21*–*24*).

[1]Institut de Biologie de l'ENS (IBENS), Ecole Normale Supérieure, Université PSL, CNRS, INSERM, F-75005 Paris, France. [2]MRC Laboratory of Molecular Biology, Cambridge CB2 0QH, UK. [3]Division of Structural Biology, Wellcome Centre for Human Genetics, University of Oxford, Oxford OX3 7BN, UK.
***Corresponding author. Email: radu@mrc-lmb.cam.ac.uk (A.R.A.); laetitia.mony@ens.psl.eu (L.M.); pierre.paoletti@ens.psl.eu (P.P.)**
†These authors contributed equally to this work.
‡Present address: CAMS Oxford Institute, University of Oxford, Oxford OX3 7BN, UK.

Results

GluD1 receptors bind GABA

Intrigued by the presence of GluD1 receptors at inhibitory postsynaptic sites (*23*, *24*), which is unparalleled among iGluRs, we investigated the ligand-binding profile and activation of GluD1 receptors. Because agonist binding does not elicit currents in delta receptors, we first introduced in GluD1 the "Lurcher" A654T (Ala^{654}→Thr) mutation, which renders GluD2 receptors constitutively active (*25*, *26*). After the expression of GluD1-A654T mutant receptors into *Xenopus* oocytes, small but reliable constitutive inward currents were observed (fig. S1, A and B). Application of D-serine or glycine potentiated these currents (fig. S1, B and C), which contrasts with the current inhibition observed on GluD2-Lurcher receptors (fig. S2, A to C) (*5*, *27*). Because GluD1-A654T constitutive currents were small, we inserted an additional mutation, C645I (Cys^{645}→Ile), to match the equivalent GluD2 M3 pore segment (fig. S1D). This double mutant GluD1-A654T-C645I, named GluD1-Lurcher hereafter, yielded larger constitutive currents (fig. S1E) that were also potentiated by D-serine and glycine (Fig. 1, A to C) while displaying almost no sensitivity to glutamate (Fig. 1C and fig. S3, A to C). Agonist dose-response curves on GluD1-Lurcher revealed D-serine potency in the high micromolar range [median effective concentration (EC_{50}) of 320 ± 10 μM (n = 13 to 17 cells); Fig. 1C and table S1], similar to that measured on GluD2-Lurcher receptors [median inhibitory concentration (IC_{50}) of 260 ± 10 μM (n = 5 or 6 cells); fig. S2,

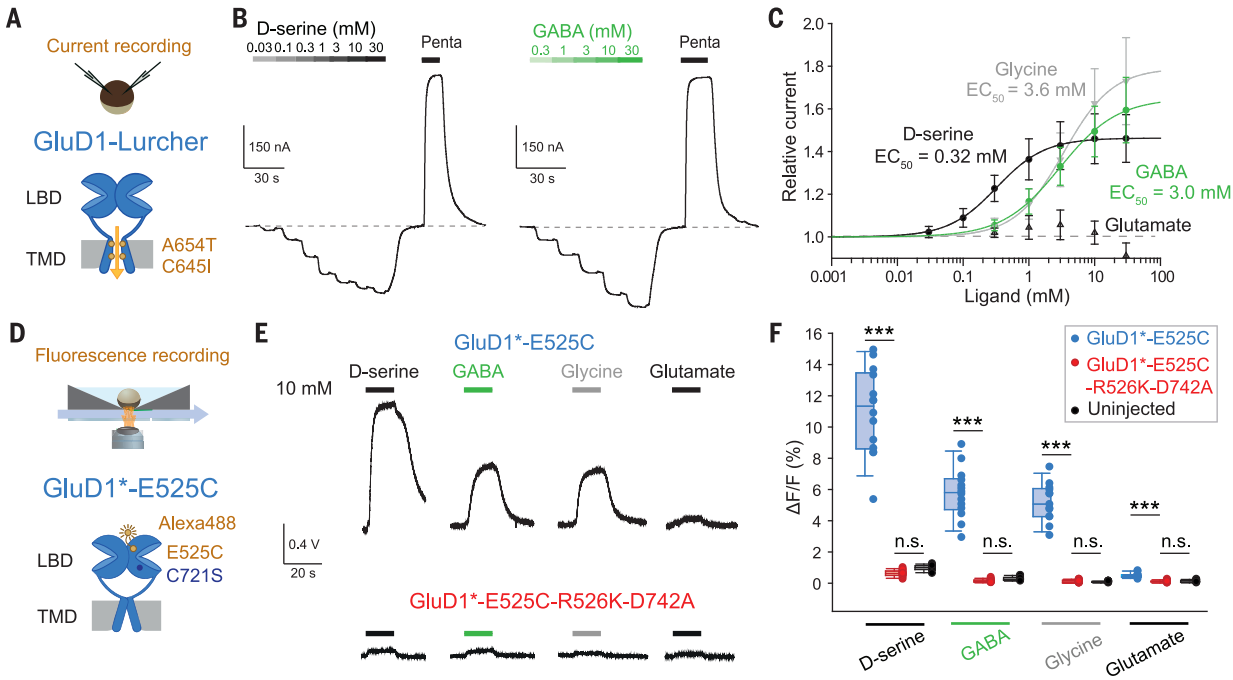

Fig. 1. GABA binds and triggers conformational changes at GluD1 receptors. (**A**) Schematic of the two-electrode voltage clamp technique performed on *Xenopus* oocytes that express GluD1-Lurcher receptors. TMD, transmembrane domain. (**B**) D-serine and GABA potentiate GluD1-Lurcher constitutive currents. The pore blocker pentamidine (Penta, 100 μM) was used to estimate the amount of constitutive current. Dashed lines represent the constitutive Lurcher currents. (**C**) Dose-response curves for GABA, D-serine, glycine, and glutamate on GluD1-Lurcher receptors. Values and sample numbers are provided in table S1. Error bars indicate SD. (**D**) Schematic of VCF performed on *Xenopus* oocytes that express GluD1*-E525C labeled with Alexa488-maleimide. GluD1* is the receptor containing the C721S mutation (Cys^{721}→Ser). (**E**) VCF signals of GluD1*-E525C and GluD1*-E525C-R526K-D742A receptors upon application of D-serine, glycine, GABA, and glutamate (10 mM each). R526K, Arg^{526}→Lys; D742A, Asp^{742}→Ala. (**F**) ΔF amplitudes triggered by 10-mM ligand application on oocytes that express either GluD1*-E525C or GluD1*-E525C-R526K-D742A receptors and on non-injected oocytes. The center line represents the median, box limits are upper and lower quartiles, and whiskers are minimum and maximum values. Values and sample numbers are listed in table S5. ***$P < 0.001$, and n.s. is not significant (Dunn's post hoc test). Detailed replicate numbers and the full statistical analysis are provided in table S6.

A to C, and (*5*, *27*, *28*)]. Glycine sensitivity appeared rightward shifted, in the low millimolar range [EC_{50} of 3.4 ± 0.2 mM (n = 9 cells); Fig. 1C and table S1], reminiscent of the glycine sensitivity of GluD2-Lurcher receptors [IC_{50} = 0.75 ± 0.05 mM (n = 10 cells); fig. S2C]. We then tested the ability of GluD1 receptors to sense γ-aminobutyric acid (GABA). GABA robustly potentiated GluD1-Lurcher currents with an apparent affinity in the low millimolar range [EC_{50} = 3.0 ± 0.2 mM (n = 15 to 17 cells)], lower than that of D-serine but similar to that of glycine, and with equal efficacy (Fig. 1, B and C; see also fig. S1, B and C, and table S1). This GABA effect was displaced by D-serine (fig. S3, D to F). By contrast, GABA was essentially ineffective on GluD2-Lurcher receptors, producing modest current inhibition and limited D-serine displacement only at high concentrations (fig. S2, D to F). Mutating conserved iGluR agonist-binding residues (*1*) in the GluD1 ligand-binding domain (LBD) fully abolished responses to GABA (figs. S2, G to I, and S3, G to I), revealing the primary role of the GluD1 LBD in GABA sensing. Application of GABA (10 mM) onto NMDA (fig. S4, A to D) and AMPA (fig. S4, E to H) receptors triggered negligible effects, which is consistent with insensitivity to GABA.

We next aimed to confirm these observations in GluD1 receptors devoid of the Lurcher mutations. We used voltage clamp fluorometry (VCF), a technique that enables detection of ligand (or voltage)–induced conformational changes in membrane proteins (*29*). We designed a series of GluD1 receptors with cysteines engineered at various positions in the LBDs for attachment of the environment-sensitive fluorescent probe Alexa488 and screened for potential VCF fluorescence changes (ΔFs) upon ligand addition (Fig. 1D). Several positions yielded robust ΔFs upon D-serine (or glycine) application. Position E525 (E, Glu) in the structurally sensitive D1-D1 dimer interface (*27*) produced particularly strong signals (table S2). We verified that the E525C (Glu^{525}→Cys) mutation and the fluorescent probe attachment had minimal effects on the properties of the receptor (fig. S5). Application of GABA on labeled GluD1-E525C receptors also triggered marked ΔFs, which revealed the ability of GABA to bind and elicit conformational changes at (non-Lurcher) GluD1 receptors (Fig. 1, D to F, and fig. S6, A to C). Glutamate application had hardly any effect (Fig. 1, E and F). No fluorescent signals were detected upon D-serine, glycine, or GABA addition onto binding-deficient GluD1 receptors (Fig. 1, E and F, and fig. S6, D to F), which demonstrates that ligand binding at the GluD1 LBD is the critical initial molecular event. VCF-based dose-response curves showed agonist apparent affinities in the sub- to low-millimolar range, with GABA sensitivity similar to that of glycine but lower than that of D-serine (fig. S6, B and C), which thus corroborates results obtained on GluD1 Lurcher receptors. Thermal shift assay and isothermal titration calorimetry (ITC) experiments on isolated LBDs confirmed direct binding of GABA (and D-serine, but not glutamate) to the GluD1 LBD with a binding affinity of 2 mM (Fig. 2, A and B; fig. S7, A and B; and table S3), which is consistent with our results on full-length GluD1 receptors. Conversely, GluD2 LBDs bound D-serine but not GABA (fig. S7, C to F). Therefore, GABA appears to be an active ligand at GluD1, but not GluD2, receptors.

Structure of the GABA binding site

To understand how GluD1 interacts with GABA, we determined the crystal structure of the GluD1

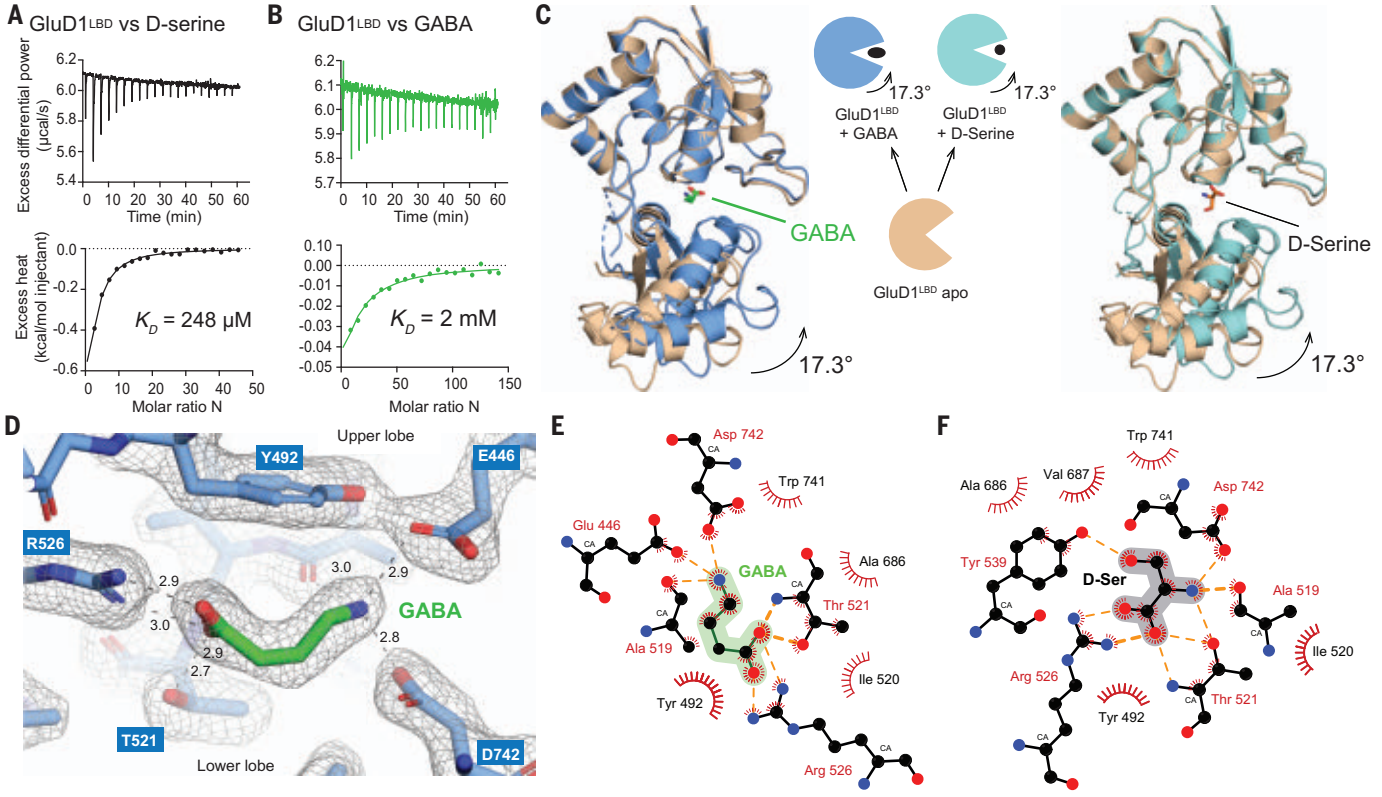

Fig. 2. Structures of the GABA-GluD1 and D-serine–GluD1 LBD complexes. (**A** and **B**) ITC analysis of D-serine (A) and GABA (B) binding to the isolated GluD1 LBD; values are listed in table S3. K_D, dissociation constant. (**C**) X-ray crystal structures of the GluD1 LBD in complex with GABA (left, blue) and D-serine (right, cyan) superimposed with the apo GluD1 LBD structure (tan). The extent of GluD1 LBD clamshell closure upon ligand binding is indicated. (**D**) Close-up view of the GABA binding site, which shows the 2mFo-DFc electron density map contoured at 1.0σ. Distances (in Å) between interacting atoms are indicated. (**E** and **F**) LigPlot diagrams of the GluD1-GABA (E) and GluD1–D-serine (F) complexes. CA, α-carbon atom.

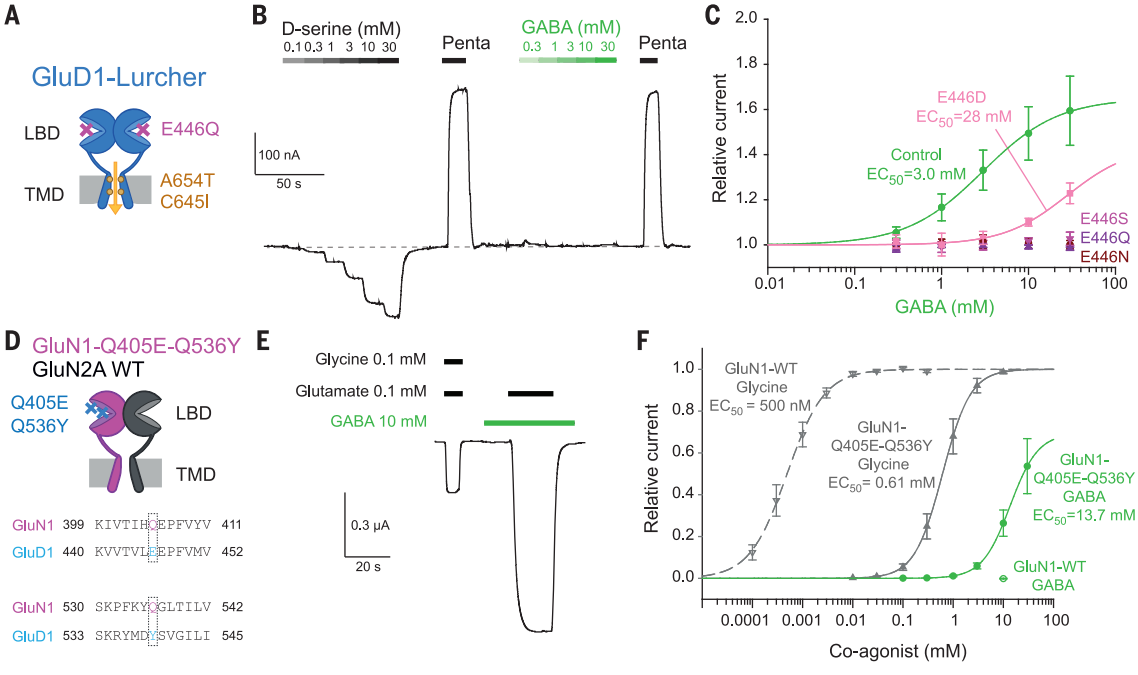

Fig. 3. Molecular determinants of GABA recognition by GluD1 receptors. (**A**) Schematic of a GluD1-Lurcher receptor that harbors the E446Q (Glu^{446}→Gln) mutation. (**B**) The E446Q mutation eliminates the sensitivity of GluD1-Lurcher to GABA but not to D-serine. Dashed lines represent the constitutive Lurcher currents. (**C**) GABA dose-response curves of various GluD1-Lurcher-E446 mutants. Error bars indicate SD. (**D**) A schematic of the GluN1-Q405E-Q536Y/GluN2A NMDA receptor mutant is shown at the top. An alignment of the GluD1 and GluN1 LBD sequences is shown at the bottom. Q405E, Gln^{405}→Glu; Q536Y, Gln^{536}→Tyr. (**E**) Mutations Q405E and Q536Y in the GluN1 LBD confer GABA sensitivity to GluN1/GluN2A NMDA receptors. Current traces elicited by successive applications of glutamate plus glycine, GABA alone, and glutamate plus GABA are shown. (**F**) GABA and glycine (coagonist) dose-response curves (in 1 mM glutamate) of GluN1-Q405E-Q536Y/GluN2A and wild-type (WT) GluN1/GluN2A receptors. The latter receptors are insensitive to GABA (10 mM). Error bars indicate SD. Values and sample numbers are provided in table S1.

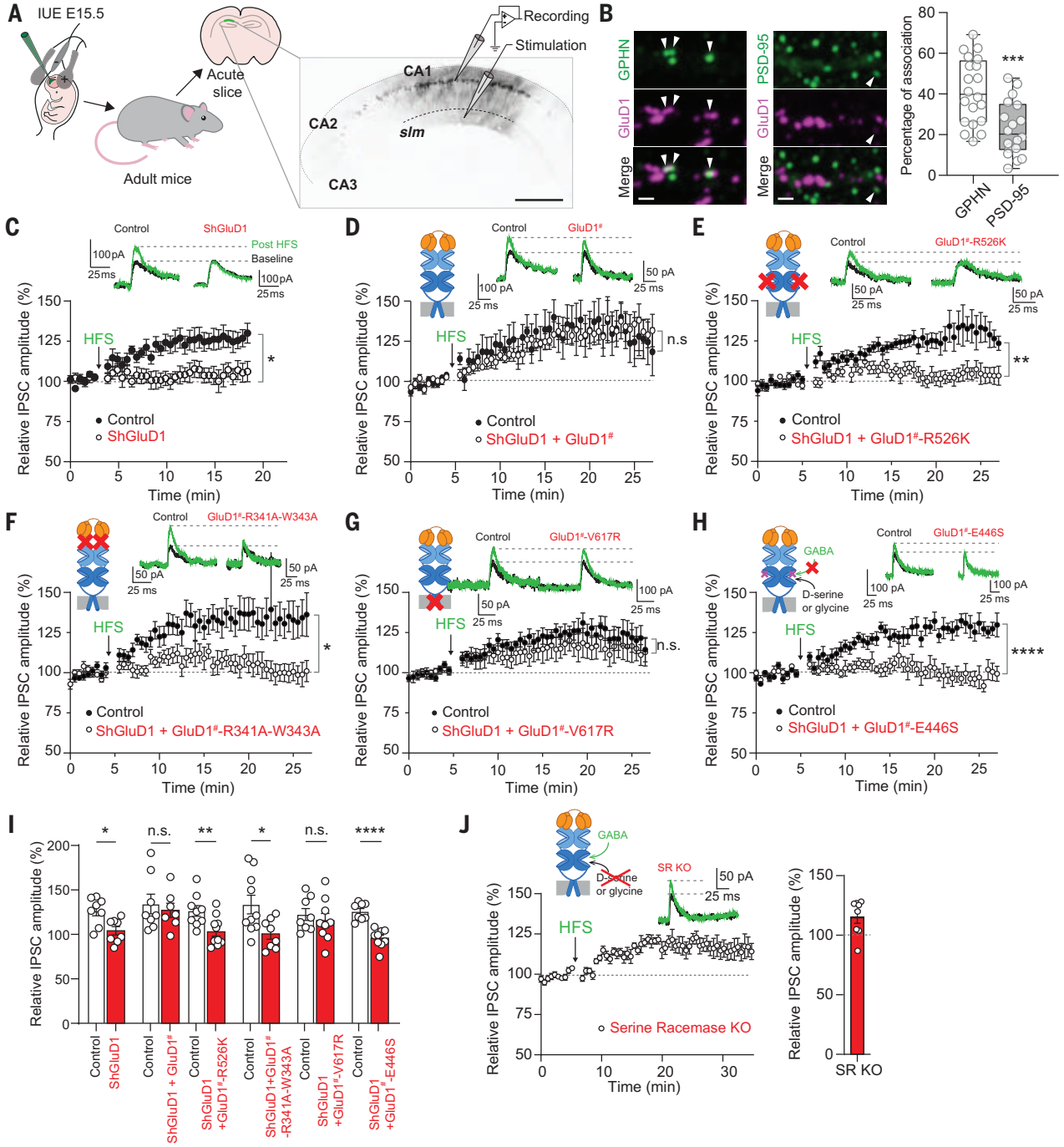

Fig. 4. GluD1 receptors mediate GABAergic synaptic plasticity. (**A**) A schematic of in utero electroporation (IUE) for cell-specific labeling and manipulation of GluD1 expression in the mouse hippocampus performed at embryonic day 15.5 (E15.5) is shown on the left. A confocal image of the hippocampus of a P21 mouse electroporated with tdTomato that shows selective targeting of CA1 pyramidal neurons is shown on the right. Imaging and whole-cell patch-clamp recordings were performed at CA1 synapses in the SLM, a region enriched in GluD1 receptors (*15*–*17*). Scale bar, 0.5 mm. (**B**) GluD1 preferentially associates with inhibitory SLM synapses. Colocalization images are shown on the left. The white arrowheads highlight the association between GluD1 and the indicated synaptic markers. A quantification is shown on the right. The center line represents the median, box limits are upper and lower quartiles, and whiskers are minimum and maximum values. For gephyrin (GPHN), $n = 20$ dendrites, and for postsynaptic density protein 95 (PSD-95), $n = 18$ dendrites; ***$P < 0.001$ (two-sided unpaired Student's t test). Scale bars, 2 μm. (**C**) HFS potentiates IPSCs in control neurons but not in neurons that express short hairpin RNA downregulating GluD1 expression (ShGluD1). For each condition, $n = 8$ cells. Representative IPSC traces before (black) and after (green) HFS are shown at the top. (**D**) Molecular replacement experiments. Reexpression of WT GluD1 rescues HFS-induced plasticity. $n = 7$ cells for control, and $n = 8$ cells for ShGluD1 plus GluD1# (the # indicates the shRNA-resistant GluD1 construct). (**E** to **H**) Ligand binding–deficient (E) ($n = 9$ cells versus $n = 10$ cells for control) and cerebellin binding–deficient (F) ($n = 8$ cells versus $n = 10$ cells for control) GluD1 receptors do not rescue HFS-induced inhibitory plasticity in neurons in which GluD1 is knocked down, but ion channel flux–deficient (G) ($n = 9$ cells versus $n = 8$ cells for control) GluD1 receptors do. GluD1-E446S (H), which allows binding of glycine and D-serine but not of GABA, does not rescue HFS plasticity ($n = 9$ cells versus $n = 8$ cells for control). R341A, Arg^{341}→Ala; V617R, Val^{617}→Arg; W343A, Trp^{343}→Ala. (**I**) Pooled data of molecular replacement experimental

results on HFS-induced IPSC amplitude. The control group is nonelectroporated neurons from the same electroporated mouse. (**J**) HFS-induced inhibitory plasticity is present in serine racemase knockout (SR KO) mice (n = 8 cells) (left). A quantification of HFS-induced plasticity in SR KO mice is shown on the right. Error bars indicate SEM. Detailed replicate numbers and the full statistical analysis are provided in in table S6. For (C) to (I), $*P < 0.05$, $**P < 0.01$, $***P < 0.0001$, and n.s. is not significant (two-sided Mann-Whitney test); error bars indicate SEM.

LBD–GABA complex using x-ray crystallography (Fig. 2, C and D; fig. S8, A and B; and table S4). The GluD1 LBD–GABA complex formed well-ordered crystals that diffracted to 1.9-Å resolution, which allowed for the unambiguous identification of GABA electron density (Fig. 2D). GABA binds the central LBD interlobe cleft and, typical of iGluR agonists (*1*, *30*), forms multiple interactions with both the upper and lower lobes (Fig. 2, D and E). In particular, the guanidinium group of GluD1-R526 (R, Arg) engages in a bidentate salt bridge with the carboxyl group of GABA, whereas the γ-amino group forms a dual electrostatic interaction with the carboxylates of GluD1-E446 (upper lobe) and GluD1-D742 (lower lobe) (D, Asp). Disrupting these interactions prevented GABA action on GluD1 receptors (fig. S3, G to I). Thus, charged interactions that include the strictly conserved bond between the arginine side chain of LBD helix D and the ligand α-carboxylate (*1*, *30*) are major anchors for GABA binding on GluD1. In addition, three aromatic tyrosine (Y) residues line the GABA binding pocket, including GluD1-Y492, which acts as a lid on top of the GABA molecule (Fig. 2, D and E). For comparison, we also solved the structure of the GluD1 LBD in the apo state and in the presence of D-serine (Fig. 2C; fig. S8, C to H; and table S4). The apo GluD1 LBD crystal form contained three dimers in the asymmetric unit and displayed open cleft conformations (Fig. 2C and fig. S9, A to C), which is reminiscent of other apo iGluR LBD structures (*1*, *30*). By contrast, the GABA-bound GluD1 LBD crystallized as an asymmetric dimer, in which LBDs adopt closed-cleft conformations, albeit the closure angles differed between the two protomers (17.3° and 10.5°, respectively, relative to chain E of the apo state; Fig. 2C and fig. S8, A to C). The GluD1 LBD–D-serine complex crystal diffracted to 1.63-Å resolution and contained one homodimer per asymmetric unit (table S4). Only one monomer had D-serine bound, and it adopted a closed-cleft conformation identical to that observed with GABA (closure of 17.3° relative to chain E of the apo state; fig. S8, D to F). The D-serine interactions with GluD1 LBD lobes again involve both ionic and hydrogen bonding (Fig. 2F and fig. S8F). Overall, the ligand-binding pose is notably similar to that described for D-serine bound to the GluD2 receptor LBD (*5*, *31*) (fig. S8).

Molecular determinants of GABA selectivity

To examine the molecular basis of GluD1 GABA binding and selectivity, we performed structure-based mutagenesis experiments. Substituting the LBD upper lobe residue E446 to Ser (S), Gln (Q), or Asp (N) abolished GABA effects on GluD1-Lurcher currents, but D-serine remained active (Fig. 3, A to C, and fig. S10). The more conservative E446D (Glu^{446}→Asp) mutant was not as discriminating and retained sensitivity to both ligands, although with reduced affinity (Fig. 3C, fig. S10, and table S1). These results are consistent with E446 making ionic interactions with GABA but not D-serine, which thus identifies E446 as pivotal for GABA recognition by GluD1. The importance of this residue as a key GABA anchor was reinforced by gain-of-function experiments performed on (GABA-insensitive) NMDA receptors. In the glycine-binding GluN1 subunit, the equivalent residue of GluD1-E446 is a glutamine (Q405) (Fig. 3D and fig. S11). Introduction of the single-point mutation Q405E (Gln^{405}→Glu) into the GluN1 LBD allowed direct activation of GluN1/GluN2A NMDA receptors by coapplication of glutamate and GABA (in replacement of glycine; fig. S12, A to C). The gating efficacy of GABA at NMDA receptors was further enhanced by introducing a second mutation in GluN1 [mutant GluN1-Q405E-Q536Y (Gln^{536}→Tyr)] to better mimic the GluD1 GABA binding environment (Fig. 3, D and E, and fig. S12C). On GluN1-Q405E-Q536Y/GluN2A receptors, the efficacy of GABA as a coagonist reached >50% of that of glycine (Fig. 3F), which points to E446 and Y539 as critical determinants of GABA recognition in GluD1 receptors. E446 and Y539 are conserved in GluD2 receptors (fig. S11), which suggests that other GluD1 determinants contribute to GABA selectivity among delta receptors.

GABA binding to GluD1 controls inhibitory synaptic strength

We then assessed the impact of GluD1 activation on synaptic transmission at mature GABAergic synapses. We focused on the stratum lacunosum-moleculare (SLM) of the mouse hippocampus, a region highly enriched in GluD1 receptors (*15*–*17*) (Fig. 4A). Confocal microscopy imaging revealed that GluD1 preferentially accumulates at inhibitory synapses rather than at excitatory synapses (Fig. 4B), as previously observed in distal dendrites of cortical pyramidal neurons (*23*, *24*). We recorded GABAergic inhibitory postsynaptic currents (IPSCs) from CA1 pyramidal cells while performing electrical stimulations in the SLM (fig. S13A). Application of the GluD1 agonist D-serine potentiated the IPSC amplitudes [EC_{50} of 180 ± 0.05 μM (n = 5 to 16 cells); fig. S13, B to D]. The continuous inclusion of D-aminophosphovalerate (D-APV) in these experiments ruled out a direct activation of NMDA receptors by D-serine as an underlying mechanism. Application of 5,7-dichlorokynurenic acid (DCKA), a ligand that, like D-serine, binds iGluR glycine sites (*7*) and potentiates GluD1-Lurcher receptors (fig. S14), also produced robust enhancement of IPSC amplitude (fig. S13E). Short hairpin RNA (shRNA)–based down-regulation of GluD1 expression following hippocampus-targeted in utero electroporation eliminated the D-serine– and DCKA-induced potentiation (fig. S13, B and E). It furthermore decreased the density of SLM inhibitory synapses (fig. S13F), as previously shown in the cortex (*23*). This indicates both developmental and acute effects of GluD1 signaling on GABAergic transmission at SLM CA1 synapses. We next induced short bursts of high-frequency stimulation (HFS) to promote the release of endogenous GABA from presynaptic inhibitory terminals (*32*). After HFS, IPSC amplitude increased by ~30% in control neurons but not in neurons in which GluD1 was knocked down, an effect that persisted throughout the recording (15 min; Fig. 4C) and likely involved a postsynaptic mechanism (fig. S13G). A molecular replacement strategy with mutant GluD1 receptors deficient in distinct signaling modalities (*23*) revealed that ligand binding and interaction with the extracellular scaffolding protein cerebellin, but not ion flux through GluD1 channels, are required for GluD1 to mediate enhancement of inhibitory neurotransmission (Fig. 4, D to I, and fig. S13H). Preventing binding of GABA, but not of D-serine or glycine, with the GluD1-E446S (Glu^{446}→Ser) mutant abolished HFS-induced plasticity (Fig. 4, H and I), whereas inhibitory plasticity was conserved in mice deficient in D-serine signaling (*33*) (Fig. 4J). Thus, activation of GluD1 receptors at SLM CA1 hippocampal GABAergic synapses induces prolonged potentiation of inhibitory synaptic strength through a non-ionotropic GABA-induced mechanism that relies on trans-synaptic anchoring.

Discussion

Our study unveils that, in the SLM of the mouse hippocampus, GluD1 receptors operate at GABAergic synapses as receptors that bind GABA and control inhibitory synaptic plasticity. We propose that synaptically released GABA, together with cerebellin, binds to and triggers conformational changes of postsynaptic GluD1 receptors, which activates intracellular signaling pathways, leading to an increase in the number and/or activity of type A GABA receptors ($GABA_A$Rs). This GluD1-driven mechanism of inhibitory plasticity, which is embedded in the inhibitory synapse itself, departs from previously described mechanisms of inhibitory plasticity that commonly rely on cross-talk with neighboring excitatory (glutamatergic) synapses (*34*). By

contrast, the non-ionotropic, trans-synaptic, and ligand-induced mechanism echoes the GluD2-induced plasticity at glutamatergic parallel fiber–Purkinje cell synapses in the cerebellum, where GluD2 activation by extracellular D-serine regulates AMPA receptor content (*4*, *6*, *35*, *36*). The high (10 mM) concentrations of neurotransmitter reached at fast chemical synapses after vesicular release (*37*–*39*) indicate substantial activation of GluD1 receptors by GABA despite their relatively low affinity for this agonist. The detailed mechanisms that couple GluD1 activation to the modulation of $GABA_AR$ activity, however, remain to be deciphered. The question of whether this previously unknown form of GABAergic synaptic plasticity interacts with other forms of inhibitory plasticity (*34*) also remains open. Because GluD1 receptors are broadly expressed in the forebrain (*15*–*17*), including at inhibitory synapses in the neocortex (*23*), GABA signaling through GluD1 receptors likely represents a general mechanism that extends the computational rules of inhibitory plasticity with consequences on neuronal circuit function.

In humans, GluD1 mutations are associated with susceptibility to autism and schizophrenia (*4*, *40*) as well as major depressive disorders (*41*). With their dual ability to reside at excitatory and inhibitory synapses, GluD1 receptors are not only specially equipped to act as powerful regulators of synaptic circuits but are also vulnerable nodes of excitation-inhibition imbalance during neuropsychiatric disorders. In that context, our finding that GluD1 receptors are molecular machines with hybrid features—functionally GABAergic but structurally glutamatergic—opens fresh perspectives on GluD1-targeted neuropharmacology.

REFERENCES AND NOTES

1. K. B. Hansen *et al*., *Pharmacol. Rev.* **73**, 298–487 (2021).
2. A. P. Burada, R. Vinnakota, J. Kumar, *Nat. Struct. Mol. Biol.* **27**, 84–91 (2020).
3. S. M. Schmid, S. Kott, C. Sager, T. Huelsken, M. Hollmann, *Proc. Natl. Acad. Sci. U.S.A.* **106**, 10320–10325 (2009).
4. M. Yuzaki, A. R. Aricescu, *Trends Neurosci.* **40**, 138–150 (2017).
5. P. Naur *et al*., *Proc. Natl. Acad. Sci. U.S.A.* **104**, 14116–14121 (2007).
6. W. Kakegawa *et al*., *Nat. Neurosci.* **14**, 603–611 (2011).
7. D. Stroebel, L. Mony, P. Paoletti, *Neuropharmacology* **193**, 108631 (2021).
8. M. Fossati, C. Charrier, *Curr. Opin. Neurobiol.* **66**, 85–92 (2021).
9. A. P. Burada, R. Vinnakota, B. Lambolez, L. Tricoire, J. Kumar, *Neuropharmacology* **196**, 108683 (2021).
10. T. Uemura *et al*., *Cell* **141**, 1068–1079 (2010).
11. K. Matsuda *et al*., *Science* **328**, 363–368 (2010).
12. J. Elegheert *et al*., *Science* **353**, 295–299 (2016).
13. J. Dai, K. Liakath-Ali, S. R. Golf, T. C. Südhof, *eLife* **11**, e78649 (2022).
14. P. C. Andrews, S. M. Dravid, *Neuropharmacology* **192**, 108587 (2021).
15. K. Konno *et al*., *J. Neurosci.* **34**, 7412–7424 (2014).
16. R. Hepp *et al*., *Brain Struct. Funct.* **220**, 2797–2815 (2015).
17. C. Nakamoto *et al*., *J. Comp. Neurol.* **528**, 1003–1027 (2020).
18. S. C. Gupta *et al*., *Neuropharmacology* **93**, 274–284 (2015).
19. W. Tao, J. Díaz-Alonso, N. Sheng, R. A. Nicoll, *Proc. Natl. Acad. Sci. U.S.A.* **115**, E5373–E5381 (2018).
20. J. Dai, C. Patzke, K. Liakath-Ali, E. Seigneur, T. C. Südhof, *Nature* **595**, 261–265 (2021).
21. K. Ryu, M. Yokoyama, M. Yamashita, T. Hirano, *Biochem. Biophys. Res. Commun.* **417**, 157–161 (2012).
22. M. Yasumura *et al*., *J. Neurochem.* **121**, 705–716 (2012).
23. M. Fossati *et al*., *Neuron* **104**, 1081–1094.e7 (2019).
24. E. Favuzzi *et al*., *Science* **363**, 413–417 (2019).
25. J. Zuo *et al*., *Nature* **388**, 769–773 (1997).
26. L. P. Wollmuth *et al*., *J. Neurosci.* **20**, 5973–5980 (2000).
27. K. B. Hansen *et al*., *J. Neurosci.* **29**, 907–917 (2009).
28. D. Tapken *et al*., *Sci. Rep.* **7**, 46145 (2017).
29. L. M. Mannuzzu, M. M. Moronne, E. Y. Isacoff, *Science* **271**, 213–216 (1996).
30. J. Pøhlsgaard, K. Frydenvang, U. Madsen, J. S. Kastrup, *Neuropharmacology* **60**, 135–150 (2011).
31. A. S. Kristensen *et al*., *Mol. Pharmacol.* **89**, 253–262 (2016).
32. Y. Komatsu, *J. Neurosci.* **14**, 6488–6499 (1994).
33. A. C. Basu *et al*., *Mol. Psychiatry* **14**, 719–727 (2009).
34. C. Q. Chiu, A. Barberis, M. J. Higley, *Nat. Rev. Neurosci.* **20**, 272–281 (2019).
35. W. Kakegawa, K. Kohda, M. Yuzaki, *J. Physiol.* **584**, 89–96 (2007).
36. K. Kohda *et al*., *Proc. Natl. Acad. Sci. U.S.A.* **110**, E948–E957 (2013).
37. B. Barbour, M. Häusser, *Trends Neurosci.* **20**, 377–384 (1997).
38. J. D. Clements, R. A. Lester, G. Tong, C. E. Jahr, G. L. Westbrook, *Science* **258**, 1498–1501 (1992).
39. A. Reiner, J. Levitz, *Neuron* **98**, 1080–1098 (2018).
40. A. J. Griswold *et al*., *Hum. Mol. Genet.* **21**, 3513–3523 (2012).
41. P. Muglia *et al*., *Mol. Psychiatry* **15**, 589–601 (2010).

ACKNOWLEDGMENTS

We thank L. Tricoire [Institute of Biology Paris Seine (IBPS), Sorbonne Université, Paris, France] for the gift of the GluD1 and GluD2 plasmids, D. B. Arnold (University of Southern California, USA) for plasmids available through Addgene, D. Bellini and F. Gorrec [MRC Laboratory of Molecular Biology (MRC-LMB), UK] for access to the crystallization facility and x-ray data collection, and J. Grimmett and T. Darling (MRC-LMB, UK) for support with scientific computing. We thank P.-J. Corringer (Institut Pasteur, Paris, France), S. Pless (University of Copenhagen, Denmark), and members of their teams for helpful discussions and advice on VCF, as well as the Institut de Biologie de l'École Normale Supérieure (IBENS) FabLab for help with 3D printing of the VCF perfusion chamber. We also thank N. Rebola [Institut du Cerveau (ICM), Paris] for the serine racemase knockout mice. **Funding:** This work was supported by the French government (Investissements d'Avenir ANR-10-LABX-54 MEMOLIFE and ANR-11-IDEX-0001-02 PSL* Research University), Sorbonne University (fellowships to L.P.), the Fondation pour la Recherche Médicale (FRM) (fellowship no. FDT202012010605 to L.P.), the European Research Council (ERC Advanced Grant no. 693021 to P.P. and ERC Starting Grant no. 803704 to C.C.), and the UK Medical Research Council (grants MR/L009609/1 and MC UP 1201/15 to A.R.A.). **Author contributions:** Experiments on *Xenopus* oocytes (two-electrode voltage clamp and VCF): L.P.; VCF set-up building and operation: L.M. and L.P.; Crystallography experiments analysis and design: C.H., T.M., and A.R.A.; Biochemical experiments (ITC) analysis and design: C.J. and C.H.; In utero electroporation experiments and design, confocal imaging, and analysis: J.Z. and C.C.; Western blot experiments: D.W.; Brain slice electrophysiological experiments: S.B.; Study design and data analysis: L.M., D.S., P.P.; Writing – original draft, review, and editing: L.P., C.C., A.R.A., L.M., P.P. **Competing interests:** A.R.A. is an employee of BioNTech UK Ltd. and has equity interests in BioNTech SE. All other authors declare that they have no competing interests. **Data and materials availability:** All data are available in the main text or the supplementary materials. Structure factors and coordinates of apo, D-serine–bound, and GABA-bound GluD1 LBDs were deposited in the Protein Data Bank (PDB) under IDs 8BLJ, 8BN2, and 8BN5, respectively. **License information:** Copyright © 2023 the authors, some rights reserved; exclusive licensee American Association for the Advancement of Science. No claim to original US government works. https://www.science.org/about/science-licenses-journal-article-reuse

SUPPLEMENTARY MATERIALS

science.org/doi/10.1126/science.adf3406
Materials and Methods
Figs. S1 to S14
Tables S1 to S6
References (*42*–*69*)
MDAR Reproducibility Checklist

Submitted 20 November 2022; accepted 25 October 2023
Published online 7 December 2023
10.1126/science.adf3406

SOCIAL DISPARITIES

Highlighting health consequences of racial disparities sparks support for action

Riana M. Brown[1]*†, Pia Dietze[2]*†, Maureen A. Craig[3,4]

Racial disparities arise across many vital areas of American life, including employment, health, and interpersonal treatment. For example, one in three Black children lives in poverty (versus one in nine white children), and, on average, Black Americans live four fewer years compared with white Americans. Which disparity is more likely to spark reduction efforts? We find that highlighting disparities in health-related (versus economic) outcomes spurs greater social media engagement and support for disparity-mitigating policy. Further, reading about racial health disparities elicits greater support for action (e.g., protesting) compared with economic- or belonging-based disparities. This occurs in part because people view health disparities as violating morally sacred values, which enhances perceived injustice. This work elucidates which manifestations of racial inequality are most likely to prompt Americans to action.

Movements pursuing social change are often sparked and sustained by specific events reaching mainstream consciousness. But which types of events are most likely to garner attention and support for social change? In 2014, for example, the majority-Black city of Flint, Michigan, came into the national spotlight when citizens confronted officials over lead leaching in the city's water supply (*1*). As another example, the Black Lives Matter (BLM) movement was sparked by the killing of Trayvon Martin, and BLM protests often rekindle after subsequent

[1]Annenberg Public Policy Center and Department of Psychology, University of Pennsylvania, Philadelphia, PA, USA. [2]Department of Psychological Science, University of California Irvine, Irvine, CA, USA. [3]Department of Psychology and Neuroscience, Duke University, Durham, NC, USA. [4]Department of Psychology, New York University, New York, NY, USA.
***Corresponding author. Email: riana.brown@appc.upenn.edu (R.M.B.); pdietze@uci.edu (P.D.)**
†These authors contributed equally to this work.

lives are lost. Although brain damage from lead exposure, disproportionate use of force, and deaths understandably draw attention, the systemic nature of racial inequality in the United States means that discrimination and disparities facing Black Americans are not siloed to threats to life and limb or, more generally, the domain of physical health (*2*). For example, Flint could have instead captured America's attention because of its high poverty rates that eventually made it the most impoverished US city (*3*); yet, it was notably a health-related event that sparked outrage. In this work, we empirically investigate how and why racial disparities in specific domains—economics (e.g., employment), health (e.g., access to hospitals), and feelings of belonging (e.g., interpersonal treatment)—differentially influence support for mitigating action.

People support action against situations that they perceive as unjust or unfair (*4*–*6*). This has been found across a variety of social issues, including inequality based on race (*7*–*9*), gender (*10*), and social class (*11*, *12*). Whereas past work has documented that a wide array of issues can elicit injustice perceptions and support for action, no empirical work (to our knowledge) has tested the relative mobilizing potency of different domains within the same group-based inequality. Our research provides this vital test to assess how and why exposure to different manifestations of racial inequality may specifically spark engagement to mitigate this pressing social issue.

Disparities between social groups occur in a variety of important life domains. Our work focuses on racial inequalities in domains that social scientists regard as vital to well-being and life fulfillment: health, economics, and belonging (*13*–*15*). Health-related disparities occur when social groups differ in their exposure to violence or other forms of physical dangers, disease, or injury or when physiological needs are insufficiently met (*16*). For example, Black American communities have less access to nutritious and healthy foods (*17*), have fewer hospitals and pharmacies (*18*–*20*), and experience more physical violence by police [racial disparities in police violence are now considered and addressed as a public health issue (*21*)]. Economic disparities, by contrast, reflect group differences in access to wealth, income, jobs, and resources (*22*). As examples of economic-based racial inequality, Black Americans, on average, attend lower-funded schools, which leads to lower future salaries (*23*); experience greater difficulty acquiring jobs and promotions (*24*, *25*); and have less accrued family wealth and lower homeownership rates (*18*, *26*). Finally, belonging-based disparities involve group differences in experiencing positive or negative interpersonal treatment (*27*). For instance, Black Americans, on average, face more discipline and suspensions in schools (*28*, *29*), experience alienation with the police (*30*), and feel unwelcome and treated with suspicion in shops and public areas (*31*, *32*). This research investigates the extent to which Americans support efforts to reduce racial disparities in these three life domains.

We posit that health disparities may be viewed as particularly pernicious because issues related to health and medical care—broadly,

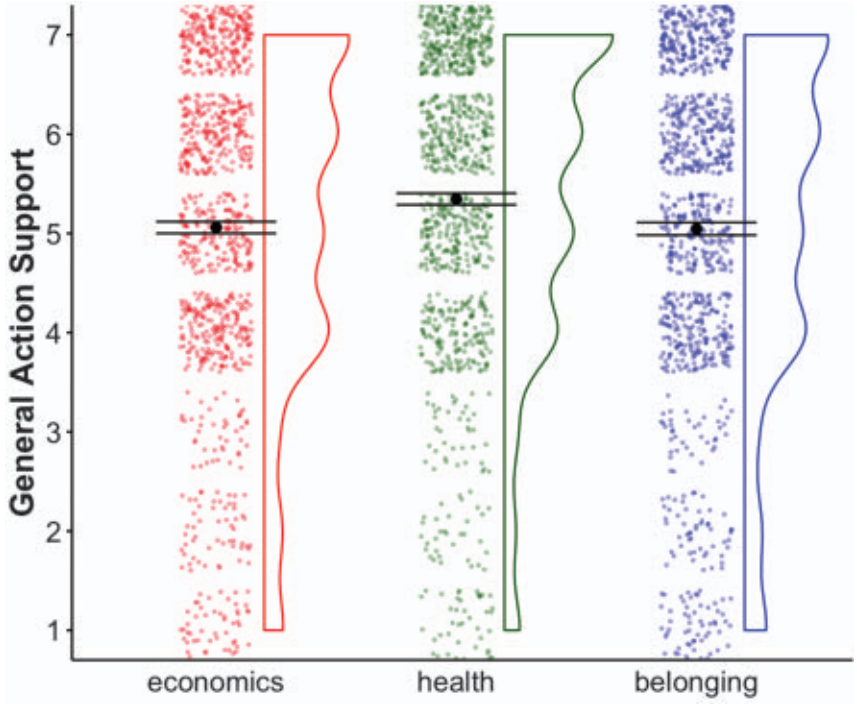

Fig. 1. Raincloud plot with jittered data for participants' general action support for different disparity domains (economic condition, health condition, and belonging condition) in study 1b. Error bars represent 95% CIs around the means (large black dots). Smaller dots indicate individual participant scores. The "cloud" areas reflect the data distributions.

DASP Lab
Sponsored
Health-based disparities between Black and White Americans involve experiencing greater physical danger or being denied access to physiological needs.
NYU.QUALTRICS.COM
Health-based Disparities Persist in America
Qualtrics makes sophisticated research simple a...
Learn more
DASP Lab
Sponsored
Economic-based disparities between Black and White Americans involve experiencing greater financial insecurity or being denied access to financial means.
NYU.QUALTRICS.COM
Economic-Based Disparities Persist in America
Learn more

Fig. 2. The health-based and economic-based ads used in study 2. Facebook users (N = 24,952) were randomly assigned to view one of the two ads (health-based ad or economic-based ad) embedded in their news feed, marked as sponsored content.

CREDIT: DASP LAB. FACEBOOK, 11 TO 12 MAY 2022; IMAGE BY ERHUI1979/GETTY IMAGES

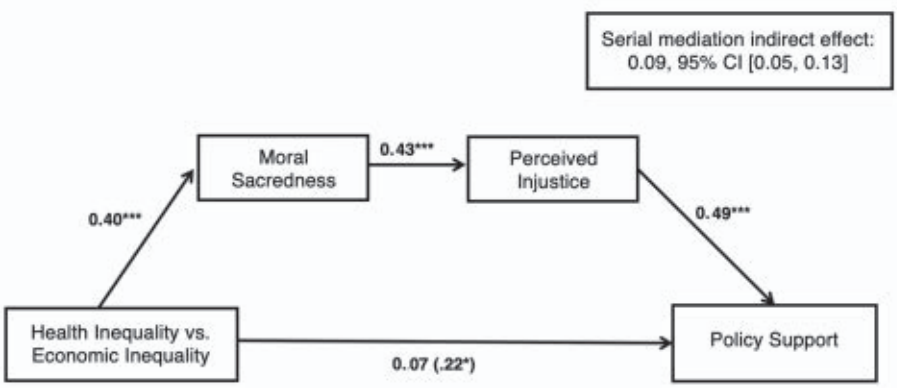

Fig. 3. Study 3 serial process model of the indirect effect of disparity condition (health versus economic) on policy support through moral sacredness affecting perceived injustice (with 10,000 bootstrap samples). The value in parentheses represents the total effect before the inclusion of the mediators. *P < 0.05; **P < 0.01; ***P < 0.001.

the protection of human life—are considered sacred moral values (*33*–*38*). Sacred moral values have "infinite or transcendental significance that precludes comparisons [and] trade-offs" [(*38*), p. 853]. In addition, they are often considered fundamental or core values (*39*). In support of this notion, in Maslow's classic hierarchy and past empirical work, health-relevant physiological needs are considered to be more fundamental compared with belonging-based or economic needs (*13*, *14*, *40*, *41*).

When something is sacred, it is treated as morally imperative to protect relative to non-sacred, secular concerns, such as economic issues [e.g., access to money (*33*, *37*–*39*, *42*)]. When a sacred moral value is violated, people report feeling outraged at the moral violation, seek to punish the violator, and act against the violation (*38*). Thus, the more fundamental need for health should be perceived as more morally sacred compared with less fundamental needs of economics and belonging and, as such, should be perceived as more unjust if violated. In turn, we predict that, on average, people will seek to alleviate health disparities over economic or belonging disparities.

We tested this hypothesis in four studies, using diverse methodologies and including three mostly white samples (study 1a, study 4a, and study 4b), a targeted sample with equal numbers of white and Black Americans (study 1b), a sample of social media users (study 2), and a nationally representative sample (study 3). We operationalize support for action against inequality in several different ways: support for individually enacted collective action (e.g., attending protests; study 1), institutional change (i.e., policy support; studies 3 and 4), and actual social media engagement (study 2). All study materials are provided in the supplementary materials, and all data and syntax are provided here. All studies followed ethical guidelines and were Institutional Review Board (IRB) approved.

Study 1

In a within-subjects experimental design, two samples (study 1a: N = 191 subjects, 73% white; study 1b, preregistered at https://aspredicted.org/qf39d.pdf: N = 337, 50% white, 50% Black) (*43*) of US citizens read nine examples of racial disparities, three each from the domains of health (e.g., "Black American communities have less access to hospitals, pharmacies, and medical care compared with white American communities"), economics (e.g., "Black American communities experience lower homeownership rates, leading to less wealth compared with white Americans"), and belonging (e.g., "Black Americans feel less welcome in shops and public spaces compared with white Americans") (see the supplementary materials for all items). After each example, participants reported whether the disparity was unjust or fair [reverse-coded; 2 items; r values within each domain ranged from 0.62 to 0.64 (study 1a) and 0.83 to 0.85 (study 1b)]. Participants also indicated their agreement (from 1, indicating strongly disagree, to 7, indicating strongly agree) that they "personally want to take action to reduce the given disparity" (general action). In study 1b, participants additionally indicated how likely (from 1, extremely unlikely, to 7, extremely likely) they were to engage in specific actions: donating, engaging in a protest, and sharing information on social media to reduce the disparity (concrete actions, 3 items; α values within each domain ranged from 0.82 to 0.87).

Results of study 1

To assess the effects of domain (study 1a and study 1b) and participant race (study 1b), we conducted multilevel models with disparity domain (study 1a and study 1b) and participant race (study 1b) as fixed effects and example type and participant as random effects. As predicted and preregistered (study 1b), both samples (Fig. 1) revealed significant effects of disparity domain on support for action [study 1a: F(2, 1524) = 8.10, P < 0.001; study 1b, general action: F(2, 2690) = 40.52, P < 0.001; study 1b, concrete actions: F(2, 2690) = 55.85, P < 0.001]. Participants reported greater support for addressing disparities in health compared with either economics [study 1a: β = 0.08, t(1524.02) = 3.18, P = 0.001; study 1b, general action: β = 0.17, t(2692.00) = 7.64, P < 0.001; study 1b, concrete actions: β = 0.12, t(2692.00) = 7.08, P < 0.001] or belonging [study 1a: β = 0.10, t(1524.02) = 3.77, P < 0.001; study 1b, general action: β = 0.17, t(2692.00) = 7.98, P < 0.001; study 1b, concrete actions: β = 0.18, t(2692.00) = 10.32, P < 0.001]. There were no differences in support for general action between the economic and belonging disparities (β values < 0.02, P > 0.510); however, participants reported greater support for concrete actions (e.g., protesting) to reduce economic- compared with belonging-based disparities [study 1b: β = 0.06, t(2692.00) = 3.24, P = 0.001].

In study 1b, we tested for moderation by participant group membership (white versus Black Americans), but only the disparity domain main effect and a main effect of participant race consistently emerged: Black Americans overall supported addressing all disparities more than white Americans, both in general [F(1, 335) = 12.39, P < 0.001] and for concrete actions [e.g., protests; F(1, 335.01) = 15.73, P < 0.001]. Overall, these results reveal that both white and Black Americans expressed more support for reducing health disparities compared with other disparities (see the supplementary materials for descriptive statistics and additional analyses).

As preregistered (study 1b), greater support for action to reduce health (compared with either economic or belonging) disparities was mediated by perceptions of injustice [study 1b: indirect effects > 0.02; 95% confidence intervals (CIs), (0.010, 0.048)] (see the supplementary materials for comprehensive results). Thus, across two ways of operationalizing support for action and among participants belonging to both socially advantaged and disadvantaged racial groups, study 1 provides consistent evidence that white and Black Americans support reducing health-based racial disparities more than economics- and belonging-based disparities. This heightened support for action is, in part, because of perceptions that health disparities are more unjust.

Study 2

To generalize the findings of study 1 to an ecologically valid context, study 2 (preregistered at https://aspredicted.org/g6dd4.pdf) experimentally tested which disparity domain garners more engagement on social media. Given that the health and economic disparities elicited the most and second-most support

for mitigation in study 1, we directly compare these domains for a conservative test. We created two versions of a sponsored advertisement on Facebook [see (*12*) for similar methodology]. Each ad presented a headline about racial inequality—one about health, the other about economic disparities—followed by a brief description of the issue (Fig. 2). We preregistered our hypothesis that the health disparities ad would garner more social media engagement compared with the economic disparities ad.

Results of study 2

We ran a split test (randomized experiment) to assess which ad was more engaging over 24 hours [see (*12*) for details on this metric]. As predicted, the health ad "won": It was more engaged with, reached more users, and was more cost-effective. The health ad reached 1156 (9.7%) more people compared with the economic ad and had a 95% chance of outperforming the economic ad in a replication. This finding reveals that even abstract information about racial health disparities—versus the specific examples used in study 1—elicits greater engagement with the issue in an ecologically valid setting.

Study 3

For study 3 (preregistered at https://aspredicted.org/j5rc9.pdf), we conceptually replicate studies 1 and 2 using a new outcome (policy support), and we measure a possible precursory mechanism—perceived violations of moral sacredness—which is hypothesized to spur injustice perceptions. A nationally representative sample of 1550 US residents (*44*) viewed a short infographic highlighting health-, economic-, or belonging-based racial disparities. Then, all participants reported on their agreement (from 1, strongly disagree, to 7, strongly agree) of how unjust ("these disparities are unjust") and morally sacred (2 items, $r = 0.48$; e.g., "these racial disparities involve issues or values that should never be violated") the issue was as well as their support for general policies to reduce it (2 items, $r = 0.77$, e.g.; "politicians need to prioritize creating policies that reduce these racial disparities") (see the supplementary materials for all items).

Results of study 3

An analysis of variance (ANOVA) (see the supplementary materials for descriptive statistics) revealed a marginal main effect of disparity domain on policy support [$F(2, 1547) = 2.75$, $P = 0.064$, $\eta_p^2 = 0.01$]. As predicted, planned contrasts revealed that participants exposed to health disparities supported mitigating policies more than those exposed to economic disparities [$\beta = 0.14$, $t(1547) = 2.32$, $P = 0.020$]. There were no differences in policy support between the economic and belonging conditions ($\beta = -0.09$, $P = 0.150$) nor, unexpectedly, between the belonging and health conditions ($\beta = 0.05$, $P = 0.378$). Additionally, we found support for the preregistered serial mediation model: Highlighting health (versus economic) disparities elicited support for mitigating policies as a result of perceptions that the issue is morally sacred, which, in turn, induced perceived injustice [95% CI, (0.05, 0.13); Fig. 3]. As such, with a nationally representative sample, study 3 finds support that health-based disparities (versus economic disparities) are seen as a violation of moral sacredness and are thus unjust, which evokes more policy support.

Study 4

Although we find greater support for the mitigation of health-based racial disparities compared with economic disparities (studies 1 to 3), it is possible that people reveal this preference because they view the solutions to address health-based disparities as less costly than the solutions to address economic disparities. Because we assessed general policy support in study 3, participants considering health disparities (versus economic disparities) might have conceived of different policies to address each issue. For example, solutions to combat racial health disparities, such as increasing access to healthcare in specific communities, might be perceived as less costly for the advantaged group and therefore less zero-sum; by contrast, frequently discussed solutions to address racial economic disparities, such as redistributing financial resources, may seem costly. We aimed to address this alternative explanation in study 4. Specifically, we tested whether our result regarding policy support—that people show greater support for policy solutions aimed to address racial health (versus economic) inequality—replicates when assessing support for a concrete policy that is consistent across conditions and is costly for everyone.

Additionally, we aimed to extend the potential applicability of our findings in study 4. The social determinants of health approach, endorsed by the Centers for Disease Control and Prevention, the World Health Organization (*45*), and other public health agencies (*45*), contends that fiscal economic policy is key to the mitigation of health inequality (*46*). As such, we assess support for a specific fiscal policy in study 4.

In two samples, study 4a ($N = 490$, 76% white) and study 4b (preregistered at https://aspredicted.org/qc7jv.pdf; $N = 1088$, 74% white), US citizens indicated their support (from 1, strongly oppose, to 7, strongly support) for the same fiscal federal policy—increasing taxes by 0.5% for all Americans. Crucially, participants were randomly assigned to one of two conditions in which they either read that this policy would help to reduce health-based or economic-based racial disparities.

Results of study 4

Across samples, as predicted and preregistered (study 4b), participants who read that a 0.5% tax increase for all Americans would go to reducing health-based disparities supported the increase more than those informed that the same tax increase would go to reducing economic-based disparities [study 4a: $t(488) = 2.35$, $P = 0.019$, $d = 0.21$; study 4b: $t(1086) = 4.02$, $P < 0.001$, $d = 0.24$] (*47*). This finding reveals that Americans express relatively more support for increasing taxes if the tax increase is aimed at mitigating health (versus economic) inequality, even if the proposed policy is held constant across conditions, is very concrete (versus general policy support in study 3), and affects all Americans.

Discussion

Across four studies (with six experiments), exposure to health disparities spurred greater support for taking action compared with economic (studies 1 to 4) or belonging-based disparities (studies 1a and 1b). Health disparities also garnered more social media engagement (study 2), support for general policies (study 3), and support for a specific fiscal policy (study 4) compared with economic disparities. These effects appear driven, at least in part, by perceptions that racial disparities in health outcomes violate a sacred moral value (study 3) and are more unjust (studies 1 and 3).

Notably, domains of social inequality are clearly highly interrelated; disparities in one domain may coincide with or even generate disparities in other domains. Consider the issue of underfunded public schools in majority-Black US neighborhoods: An economic issue—lack of public funding—contributes to schools providing nutrient-deficient lunches disproportionately to Black children. Despite their interconnected nature, our experiments demonstrate that highlighting the health consequences, in particular, will likely garner more support to address the issue than if the economic precursor is made salient. Even when the solution is economic or fiscal in nature (i.e., tax increases), people report more support for a policy that addresses health compared with economic issues.

This work provides evidence of the relative potency of health-related disparity information; however, this information is not a panacea. Research reveals that white Americans are less likely to support action to mitigate a health issue (e.g., COVID-19) if they are informed that the health issue exacerbates racial disparities compared with if racial disparities are not mentioned [(*48*); also see (*49*)]. Consistent with this work, participants' average levels of support in our studies suggest hesitance in taking concrete actions or enacting specific policies to reduce racial inequality (participants, on average, were neutral or in opposition to concrete action

and policy). Nevertheless, this research reveals that racial health disparities are among the most likely to garner support and that other race-based disparities are even less likely to mobilize Americans.

We also found a different pattern of results regarding comparisons between health and belonging disparities. In study 1, participants supported addressing health disparities more than belonging disparities, whereas study 3 did not find this. Although speculative, it could be that the change in operationalizations of support (individual action versus policy support) or experimental materials (mentioning "basic interpersonal needs") may account for this discrepancy.

The present research also has limitations that should be addressed in future inquiries. First, the current experiments focus exclusively on disparities between Black and white Americans. Although we would expect that our results would replicate for different dimensions of inequality (e.g., gender or class), different disparity domains (e.g., misapplications of the law, disparities in political representation), as well as disparities between other racial groups (e.g., white and Hispanic Americans), future research is needed to test this. Additionally, we did not target other racial minority groups (e.g., Asian Americans or Hispanic Americans) in recruitment. Thus, we cannot conclude how other racial minorities react to Black-white disparities. Future work can examine how different disparities may help or hinder intra-minority coalitions.

Second, although we focus on sacred moral values as a mediator, we do not consider this the only mechanism. It is likely that additional mechanisms contribute to responses to health (versus economic or belonging) disparities. For example, people may place more blame on victims of economic outcomes compared with health outcomes because of meritocratic worldviews (*50*). Alternatively, people may perceive health outcomes as more severe or urgent compared with outcomes in other inequality domains. Future studies should delve into additional possible mechanisms.

Overall, the present research represents a large-scale investigation of which forms of racial disparities spur support for action to reduce racial inequality (and one explanation as to why). Research across social science considers how activists and leaders of social movements galvanize involvement by tactically choosing how to present or frame an issue (*51*). Thus, the results of the present research could be informative for policy-makers, leaders of social movements, and citizens seeking to reduce racial inequality. Given that the United Nations pledged to reduce inequality within and among countries by 2030 and called for individuals to join the fight (*52*), this work can help us understand why violations of physical needs and safety can be powerful determinants of civilian movements for change.

REFERENCES AND NOTES

1. M. Smith, J. Bosman, M. Davery, "Flint's water crisis started 5 years ago. It's not over," *New York Times*, 25 April 2019; https://www.nytimes.com/2019/04/25/us/flint-water-crisis.html.
2. S. N. Bleich *et al*., *Health Serv. Res.* **54**, 1399–1408 (2019).
3. J. Mack, "Flint and Detroit among nation's top 5 poorest cities, new census data shows," *MLive*, 26 September 2019; https://www.mlive.com/news/2019/09/flint-and-detroit-among-nations-top-5-poorest-cities-new-census-data-shows.html.
4. J. Jetten, A. Iyer, N. R. Branscombe, A. Zhang, *Eur. Rev. Soc. Psychol.* **24**, 194–224 (2013).
5. M. van Zomeren, *Soc. Personal. Psychol. Compass* **7**, 378–388 (2013).
6. M. van Zomeren, T. Postmes, R. Spears, *Psychol. Bull.* **134**, 504–535 (2008).
7. H. P. Selvanathan, P. Techakesari, L. R. Tropp, F. K. Barlow, *Group Process. Intergroup Relat.* **21**, 893–912 (2018).
8. T. L. Stewart, I. M. Latu, N. R. Branscombe, N. L. Phillips, H. Ted Denney, *J. Soc. Issues* **68**, 11–27 (2012).
9. T. L. Dover, *Group Process. Intergroup Relat.* **25**, 746–767 (2022).
10. B. Doosje, N. R. Branscombe, R. Spears, A. S. Manstead, *J. Pers. Soc. Psychol.* **75**, 872–886 (1998).
11. R. M. Chow, J. Galak, *Psychol. Sci.* **23**, 1467–1469 (2012).
12. P. Dietze, M. A. Craig, *Nat. Hum. Behav.* **5**, 349–360 (2021).
13. A. H. Maslow, *Psychol. Rev.* **50**, 370–396 (1943).
14. E. Diener, E. Suh, *Soc. Indic. Res.* **40**, 189–216 (1997).
15. J. P. Ruger, *Lancet* **364**, 1075–1080 (2004).
16. Centers for Disease Control and Prevention, "Community Health and Program Services (CHAPS): Health Disparities Among Racial/Ethnic Populations" (US Department of Health and Human Services, 2008).
17. E. C. Gearan, K. Monzella, L. Jennings, M. K. Fox, *Nutrients* **12**, 3891 (2020).
18. E. Badger, "Redlining: Still a thing," *Washington Post*, 28 May 2015; https://www.washingtonpost.com/news/wonk/wp/2015/05/28/evidence-that-banks-still-deny-black-borrowers-just-as-they-did-50-years-ago/.
19. A. Johnson "Lack of health services and transportation impede access to vaccine in communities of color," *Washington Post*, 13 February 2021; https://www.washingtonpost.com/health/2021/02/13/covid-racial-ethnic-disparities/.
20. R. Ray, "Why are Blacks dying at higher rates from COVID-19?" (Brookings, 2020); https://www.brookings.edu/articles/why-are-blacks-dying-at-higher-rates-from-covid-19/.
21. J. E. DeVylder, D. M. Anglin, L. Bowleg, L. Fedina, B. G. Link, *Annu. Rev. Clin. Psychol.* **18**, 527–552 (2022).
22. American Psychological Association, "Economic inequality" (2022); https://www.apa.org/topics/economic-inequality.
23. M. García, "Poor black children are much more likely to attend high-poverty schools than poor white children" (Economic Policy Institute, 2017); https://www.epi.org/publication/poor-black-children-are-much-more-likely-to-attend-high-poverty-schools-than-poor-white-children/.
24. E. Patten, "Racial, gender wage gaps persist in U.S. despite some progress" (Pew Research Center, 2016); https://www.pewresearch.org/short-reads/2016/07/01/racial-gender-wage-gaps-persist-in-u-s-despite-some-progress/.
25. V. Wilson, W. Darity Jr., "Understanding black-white disparities in labor market outcomes requires models that account for persistent discrimination and unequal bargaining power" (Economic Policy Institute, 2022); https://www.epi.org/unequalpower/publications/understanding-black-white-disparities-in-labor-market-outcomes/.
26. R. Manduca, *Sociol. Sci.* **5**, 182–205 (2018).
27. R. F. Baumeister, M. R. Leary, *Psychol. Bull.* **117**, 497–529 (1995).
28. J. Kinsler, *Econ. Educ. Rev.* **30**, 1370–1383 (2011).
29. J. A. Okonofua, G. M. Walton, J. L. Eberhardt, *Perspect. Psychol. Sci.* **11**, 381–398 (2016).
30. M. Masterson, "Black teens report alienation, fear, in dealings with the police" (WTTW News, 2016); https://news.wttw.com/2016/11/25/black-teens-report-alienation-fear-dealings-police.
31. E. Anderson, *Sociol. Race Ethn.* **1**, 10–21 (2015).
32. J. Lee, *Work Occup.* **27**, 353–376 (2000).
33. J. Baron, M. Spranca, *Organ. Behav. Hum. Decis. Process.* **70**, 1–16 (1997).
34. G. S. Berns *et al*., *Phil. Trans. R. Soc. B* **367**, 754–762 (2012).
35. J. Graham, J. Haidt, in *The Social Psychology of Morality: Exploring the Causes of Good and Evil*, P. Shaver, M. Mikulincer, Eds. (APA Books, 2012), pp. 11–31.
36. P. Rozin, S. Wolf, *Judgm. Decis. Mak.* **3**, 325–334 (2008).
37. R. L. Ruttan, L. F. Nordgren, *J. Pers. Soc. Psychol.* **121**, 1223–1240 (2021).
38. P. E. Tetlock, O. V. Kristel, S. B. Elson, M. C. Green, J. S. Lerner, *J. Pers. Soc. Psychol.* **78**, 853–870 (2000).
39. P. E. Tetlock, *Trends Cogn. Sci.* **7**, 320–324 (2003).
40. A. H. Maslow, *Motivation and Personality* (Harper & Row Publishers, ed. 3, 1987).
41. E. W. Mathes, *J. Humanist. Psychol.* **21**, 69–72 (1981).
42. I. Ritov, J. Baron, *Organ. Behav. Hum. Decis. Process.* **79**, 79–94 (1999).
43. This is the final sample size after removing participants with incomplete responses. Initially, study 1a had 200 participants and study 1b had 343 participants. Results remain consistent if we retain participants with incomplete responses.
44. This is the final sample size after removing participants with incomplete responses. Initially, study 3 had 1607 participants. Results remain consistent if we retain participants with incomplete responses.
45. Centers for Disease Control and Prevention, "Social Determinates of Health at the CDC" (2022); https://www.cdc.gov/about/sdoh/index.html#:~:text=They%20are%20the%20conditions%20in,climate%20change%2C%20and%20political%20systems.
46. N. E. Adler, M. M. Glymour, J. Fielding, *JAMA* **316**, 1641–1642 (2016).
47. In study 4b, we preregistered one other policy (allocation of the federal budget). This item did not yield significant results (see the supplementary materials for detailed descriptions of all items and analyses).
48. A. L. Skinner-Dorkenoo *et al*., *Soc. Sci. Med.* **301**, 114951 (*2022*).
49. C. A. Miller, C. L. Wilkins, C. de Paula Couto, J. Farias, J. A. Lisnek, *Soc. Sci. Med.* **320**, 115712 (2023).
50. J. R. Kluegel, E. R. Smith, *Beliefs About Inequality: Americans' Views of What Is and What Ought To Be* (Routledge, 2017).
51. R. D. Benford, D. A. Snow, *Annu. Rev. Sociol.* **26**, 611–639 (2000).
52. Department of Economic and Social Affairs, "World Social Report 2020: Inequality in a Rapidly Changing World" (United Nations, 2020); https://www.un.org/development/desa/dspd/wp-content/uploads/sites/22/2020/02/World-Social-Report2020-FullReport.pdf.
53. R. M. Brown, P. Dietze, M. A. Craig, Highlighting health consequences of racial disparities sparks support for action, dataset, *Dryad* (2023); https://doi.org/10.5061/dryad.cz8w9gj8t.

ACKNOWLEDGMENTS

We thank the TESS program for aid in study 3. **Funding:** This study was supported by National Science Foundation grant NSF-BCS-2046842 (M.A.C.). **Author contributions:** Conceptualization: R.M.B., P.D., and M.A.C. Methodology: R.M.B., P.D., and M.A.C. Investigation: R.M.B. and P.D. Visualization: R.M.B. Funding acquisition: M.A.C. Project administration: R.M.B. and P.D. Supervision: P.D. and M.A.C. Writing – original draft: R.M.B. and P.D. Writing – review & editing: R.M.B., P.D., and M.A.C. **Competing interests:** The authors declare that they have no competing interests. **Data and materials availability:** All study materials are provided in the supplementary materials, and all data and syntax are provided at Dyrad (*53*). All studies followed ethical guidelines and were IRB approved (study 1, IRB-FY2018-1870; study 2, IRB-FY2018-2070; and studies 3 and 4, IRB-1700). **License information:** Copyright © 2023 the authors, some rights reserved; exclusive licensee American Association for the Advancement of Science. No claim to original US government works. https://www.science.org/about/science-licenses-journal-article-reuse

SUPPLEMENTARY MATERIALS

science.org/doi/10.1126/science.adh4262
Materials and Methods
Supplementary Text
Figs. S1 to S3
Tables S1 to S5
Study Materials
References (*54*, *55*)
MDAR Reproducibility Checklist

Submitted 2 March 2023; resubmitted 18 August 2023
Accepted 15 November 2023
10.1126/science.adh4262

SOLAR CELLS

Homogenized NiO_x nanoparticles for improved hole transport in inverted perovskite solar cells

Shiqi Yu[1,2]†, Zhuang Xiong[1,2]†, Haitao Zhou[1,2], Qian Zhang[1,2], Zhenhan Wang[1,2], Fei Ma[1,2], Zihan Qu[1,2], Yang Zhao[1,2], Xinbo Chu[1,2], Xingwang Zhang[1,2], Jingbi You[1,2]*

The power conversion efficiency (PCE) of inverted perovskite solar cells (PSCs) is still lagging behind that of conventional PSCs, in part because of inefficient carrier transport and poor morphology of hole transport layers (HTLs). We optimized self-assembly of [4-(3,6-dimethyl-9H-carbazol-9-yl)butyl]phosphonic acid (Me-4PACz) onto nickel oxide (NiO_x) nanoparticles as an HTL through treatment with hydrogen peroxide, which created a more uniform dispersion of nanoparticles with high conductivity attributed to the formation of Ni^{3+} as well as surface hydroxyl groups for bonding. A 25.2% certified PCE for a mask size of 0.074 square centimeters was obtained. This device maintained 85.4% of the initial PCE after 1000 hours of stabilized power output operation under 1 sun light irradiation at about 50°C and 85.1% of the initial PCE after 500 hours of accelerated aging at 85°C. We obtained a PCE of 21.0% for a minimodule with an aperture area of 14.65 square centimeters.

Metal halide perovskite solar cells (PSCs) with inverted (p-i-n) structures have achieved certificated power conversion efficiencies (PCEs) as high as 24% and have better long-term stability under light and heat stresses compared with the more efficient n-i-p structures (*1*–*4*). Organic materials such as poly[bis(4-phenyl)(2,4,6-trimethylphenyl)amine] (PTAA), which are often used as hole transport layers (HTLs), suffer from low conductivity, hydrophobicity, and energy-level mismatch (*5*–*7*).

Recently, self-assembled molecules (SAMs) such as [4-(3,6-dimethyl-9H-carbazol-9-yl)butyl] phosphonic acid (Me-4PACz) and [2-(3,6-dimethoxy-9H-carbazol-9-yl)ethyl]phosphonic acid (MeO-2PACz) have been successfully used in PSCs as HTLs to achieve inspiring PCEs (*8*, *9*). However, SAM bonding with transparent conductive oxide substrates such as indium tin oxide (ITO) and fluoride-doped tin oxide (FTO) may not be strong enough to create a homogeneous distribution on the substrate needed to avoid a broad device-performance distribution (*8*, *10*). Several recent studies showed that p-type nickel oxide (NiO_x) could form stronger chemical bonding with the SAM layer compared with ITO or FTO, help to deposit homogeneous SAM (*10*–*12*), and deliver better device performance and reproducibility (*13*, *14*).

A high-quality p-type NiO_x HTL needs to be compact to ensure better SAM deposition quality and reduce interface recombination, and also need to be highly conductive for better charge transfer. We developed a simple dopant-free method to modulate the NiO_x nanoparticle (NP) solution by adding H_2O_2 solvent. Incorporation of H_2O_2 improved the dispersion of NiO_x NPs and avoided particle aggregation that would inhibit full coverage of the transparent conductive oxide (TCO) substrate. This approach also increased the ratio of Ni^{3+} in NiO_x and formed NiOOH, a stable component that also has high conductivity. The Me-4PACz SAM that formed homogeneously on the modulated NiO_x surface was more favorable for the growth of the perovskite and deposition of uniform large-area films by reducing the contact angle, which improved charge extraction and lowered leakage currents. As a result, the modulated NiO_x combined with SAM bilayer–based devices exhibited an efficiency of 25.5% (Newport certified stabilized efficiency: 25.2%), and the 0.1-cm^2 devices retained 85.4 and 85.1% of the initial efficiency after 1000 hours of operation under AM1.5G light illumination at 50°C and 500 hours of continuous thermal stress at 85°C, respectively. In addition, a large-area device of 14.65 cm^2 had a PCE of 21%.

[1]Key Laboratory of Semiconductor Materials Science, Institute of Semiconductors, Chinese Academy of Sciences, Beijing 100083, P. R. China. [2]Center of Materials Science and Optoelectronics Engineering, University of Chinese Academy of Sciences, Beijing 100049, P. R. China.
*Corresponding author. Email: jyou@semi.ac.cn
†These authors contributed equally to this work.

HTL layer synthesis and characterization

We observed that H_2O_2 could interact with commercial NiO_x NPs (nominal size 10 nm) and improve the dispersion in aqueous solvent (figs. S1 and S2). High-resolution transmission electron microscopy showed that the control NiO_x NPs aggregated and their typical size was >10 nm (Fig. 1A). After H_2O_2 addition, the aggregation was suppressed and the single particle size also decreased to ~5 nm (Fig. 1B). Dynamic light scattering confirmed that the statistically average dispersion NP size decreased from 12 to 9 nm after H_2O_2 treatment, with a much narrower particle size distribution (Fig. 1C). The formation of hydrated NiO_x through reaction with H_2O_2 likely inhibited NiO_x NP aggregation, enhanced dispersion, and decreased the NP size (*15*).

The effect of the NP size and dispersion distribution on the growth of NiO_x films was reflected in the morphologies of the NiO_x films deposited on the FTO substrate. The H_2O_2-modulated NiO_x film was more compact and uniform compared with the control sample. Cross-sectional scanning electron microscopy (SEM) images (fig. S3) revealed that the modulated NiO_x film was dense and conformal. Cross-sectional transmission electron microscopy and energy dispersive spectroscopy mapping results (fig. S4) further confirmed this finding. The root-mean-square roughness of the NiO_x film was reduced from 4.4 to 3.2 and to 2.9 nm after adding 20 and 40 mol% H_2O_2, respectively (fig. S5). The improvement of the NiO_x morphology was expected to reduce the leakage current and recombination when combined with SAMapplied as HTLs in perovskite devices.

X-ray photoelectron spectroscopy (XPS) was performed to investigate the chemical states of the deposited NiO_x thin film. For the NiO_x film, with and without H_2O_2 modulation, the Ni 2p spectrum showed peaks at 857.1, 855.8, and 854.1 eV, representing the Ni^{4+}, Ni^{3+}, and Ni^{2+} species, respectively (Fig. 1, D and E) (*16*). Usually, Ni^{3+} originates from the Ni vacancies and mainly distributes in the grain boundaries of nonstoichiometric oxygen-rich NiO_x (*17*, *18*), which is beneficial for hole transport. As illustrated in the Ni 2p spectrum, the increase in the ratio of Ni^{3+} from 31.3 to 38.3% was evidence for the generation of Ni vacancies in the H_2O_2-modulated sample. In the oxygen 1s spectrum (fig. S6), we assigned peaks at binding energies of 529.5, 531.0, 532.2, and 533.2 eV to the NiO, hydroxide (–OH), Ni^{3+}–O, and Ni^{4+}–O, respectively (*16*). The ratio of –OH decreased from 29.6 to 22.4% in the H_2O_2-modulated sample. Conversely, the ratio of Ni^{3+}–O increased from 11.2 to 18.35%, likely caused by the transition from $Ni(OH)_2$ to NiOOH in H_2O_2-modulated NiO_x film. The presence of NiOOH not only improved the conductivity of NiO_x films (*19*), but also provided more surface hydroxyl groups for SAM bonding (*20*).

Both Fourier transform infrared (FTIR) and Raman spectroscopy further verified the conversion from $Ni(OH)_2$ to NiOOH. The FTIR absorption peaks at 410 and 500 cm^{-1} in the control NiO_x film, which we attributed to the bending vibration modes of γ(Ni-OH) and δ(Ni-OH), respectively (*21*, *22*), were absent in the H_2O_2-modulated NiO_x sample, indicating that the reaction $Ni(OH)_2$ occurred inside the treated film (Fig. 1F). In the Raman spectrum (fig. S7), the intensity of 2LO (1075 cm^{-1}) was suppressed in the H_2O_2-modulated NiO_x. The intensity of 2LO is inversely proportional to the concentration of Ni^{3+} inside NiO_x (*23*), so this result is consistent with increased density of Ni^{3+} in the H_2O_2-modulated samples.

Conductive-mode atomic force microscopy results also indicated that the conductivity of NiO_x increased substantially after modulation

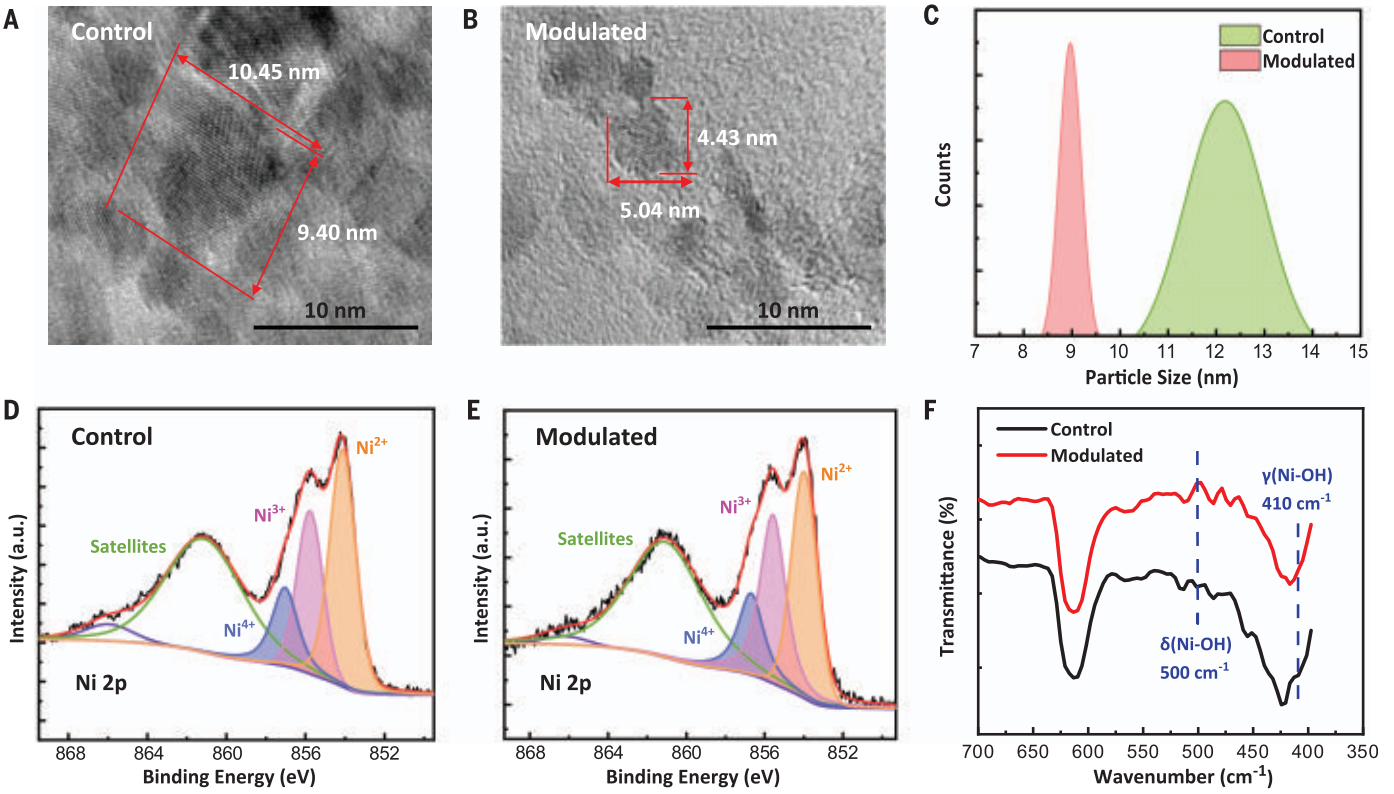

Fig. 1. Characterization of the NiO_x nanoparticles. (**A** and **B**) High-resolution transmission electron microscopy images of the control and modulated NiO_x nanoparticles, respectively. (**C**) Size distribution of control and modulated NiO_x nanoparticles in solvent, which was measured by dynamic light scattering. (**D** and **E**) XPS spectra of Ni 2p core levels for control and H_2O_2-modulated NiO_x films, respectively. (**F**) FTIR spectra of control and modulated NiO_x nanoparticles in the 400 to 700 cm^{-1} wavenumber region.

(fig. S8). For the NiO_x film mobility, it increased from 2.24×10^{-4} to 2.03×10^{-3} $cm^2\ V^{-1}\ s^{-1}$ after treatment based on space-charge-limited current measurement (fig. S9) (*24*). Both the control and modulated NiO_x were able to retain their original electrical properties after aging at 85°C for 100 hours (fig. S10).

Kevin probe microscopy (KPFM) was used to measure the surface potential distribution of Me-4PACz on the different substrates (FTO, FTO/control NiO_x, and FTO/modulated NiO_x, respectively; Fig. 2, A to C). The line profile comparison of KPFM is depicted in Fig. 2, D to F. Although Me-4PACz could cover most of the FTO substrate, some inhomogeneous regions were present. The SAM layer coverage was more uniform after inserting a NiO_x buffer layer, which could be caused by bonding between the phosphoric acid group and surface hydroxyl groups of the NiO_x through strong P-O···Ni or P=O···Ni bonds (*20*). As expected, Me-4PACz was almost fully uniformly assembled on the FTO/modulated NiO_x substrates, indicating that the condensed and uniform NiO_x layer with more surface hydroxyl groups provided a better site for the growth of a high-quality SAM layer.

XPS confirmed improved chemical absorption of SAM layer on the NiO_x substrates (Fig. 2, G to I). For the SAMs deposited on the FTO substrate, the P $2p_{1/2}$ and $2p_{3/2}$ core energy level was observed at 133.9 and 133.1 eV, respectively, indicative of Me-4PACz binding (*25*). The presence of an Sn 4s peak at 138.9 eV indicated incomplete coverage of the FTO surface. After inserting the NiO_x layer, the P 2p peak integrated intensity increased by 2.35 times compared with the FTO/SAM sample, indicating a dense and uniform deposition of SAM on the NiO_x substrate. The integrated intensity of P 2p increased 3.0 times on modulated NiO_x substrates compared with that deposited on FTO directly. In addition, the Sn 4s peak had almost disappeared, consistent with full coverage of modulated NiO_x on the FTO substrate.

The energy levels for a very thin film can vary with the thicknesses and also be affected by the underlying substrate (*26*). Ultraviolet photoelectron spectroscopy was used to measure the highest occupied molecular orbital (HOMO) of Me-4PACz deposited on different surfaces, which were –5.35, –5.62, and –5.68 eV for the FTO, control NiO_x, and modulated NiO_x surfaces, respectively (fig. S11). The value of HOMO levels is more consistent with the intrinsic properties of Me-4PCAz (*27*) when depositing on NiO_x surface, which could be the result of better SAM coverage on NiO_x. We also measured the corresponding energy level of nearly pure $FAPbI_3$ we used. The calculated valence band of perovskite at –5.67 eV (fig. S12), was near the HOMO level of the modulated NiO_x/SAM interface (–5.68 eV). These band alignment values could lead to small energy loss at the interface for the solar cell devices (fig. S13 and table S1).

We also measured contact angles to study the wetting properties of the different surfaces (Fig. 3, A to C). The perovskite precursor on Me-4PACz–only substrates had a large contact angle of 39.8°, which is consistent with previous reports that perovskite deposition on the Me-4PACz surface is relatively challenging (*20*, *28*). The contact angle decreased to 27.4° on the control NiO_x/Me-4PACz surface and further decreased to 20.6° on the modulated NiO_x/Me-4PACz surface, indicating that the NiO_x buffer layer enabled better wetting for perovskite growth. Improved hydrophilicity could be caused by the formation of homogeneous SAM (*9*) or NiO_x with more hydroxyl groups (fig. S6). The top perovskite layers had similar morphologies (fig. S14). We also examined the morphologies of the buried surface of perovskite layer in contact with the charge transport layer by peeling off the perovskite layer from the substrate (*9*). Obvious morphology

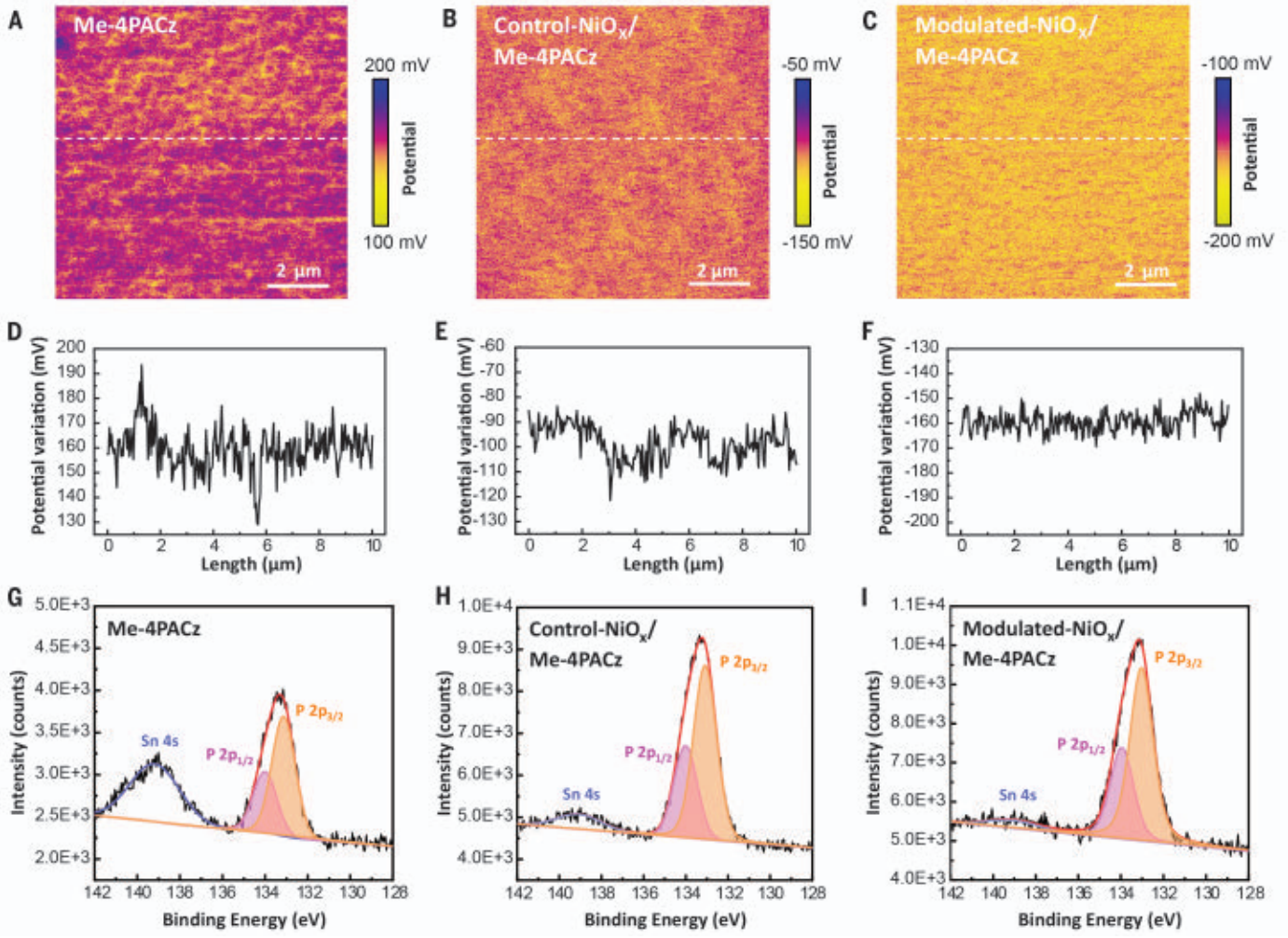

Fig. 2. Characterization of the SAM and NiO_x/SAM layers. (**A** to **C**) KPFM images of surface potential of Me-4PACz, control-NiO_x/Me-4PACz, and modulated-NiO_x/Me-4PACz, respectively. (**D** to **F**) Corresponding line profiles of Me-4PACz, control-NiO_x/Me-4PACz, and modulated-NiO_x/Me-4PACz, respectively. (**G** to **I**) XPS spectra of P 2p core levels for Me-4PACz, control-NiO_x/Me-4PACz, and modulated-NiO_x/Me-4PACz films, respectively.

defects such as pinholes were observed for the perovskite film deposited on the Me-4PACz–only surface, which could be caused by the dewetting of the Me-4PACz surface (Fig. 3D). After inserting the NiO_x layer between SAM and FTO, the bottom surface of perovskite became denser and the crystal was more homogeneous (Fig. 3, E and F).

We studied the charge transfer and the recombination properties at the perovskite buried interface using photoluminescence (PL) and time-resolved photoluminescence (TRPL) measurements with the stack of FTO/HTL/perovskite; for comparison, the results of perovskite directly deposited on FTO were also included (Fig. 3, G and H). The PL intensity of perovskite deposited on SAM surface was greater than that on the FTO surface (Fig. 3G), indicating that the SAM could passivate the buried surface of the perovskite layer (*8*). The PL intensity gradually increased with the coverage of the SAM, inferring that the more compact SAM surface provides more passivation sites for the perovskite layer. In addition to the PL enhancement, a blue shift from 815 to 809 nm was observed, further confirming suppression of the interface recombination.

The perovskite TRPL results could be fit by two exponent decays, except for the film on FTO directly (Fig. 3H). The fast decay was attributed to the charge extraction (*29*). The lifetimes were 54, 46, and 42 ns for Me-4PACz, control NiO_x/Me-4PACz, and modulated NiO_x/Me-4PACz, respectively, indicating that the hole extraction became more efficient after inserting and modulating the NiO_x. This improvement could have resulted from the better coverage of the SAM layer (Fig. 2) and the enhanced electronic properties of the NiO_x (fig. S9). A longer decay time was observed for all perovskites on SAM layers; the perovskite on SAM only had a lifetime of 0.7 μs, but the lifetime was 2.3 μs for the modulated NiO_x surface (Fig. 3H), indicating that the fully covered Me-4PACz efficiently passivated the buried interface of the perovskite.

Photovoltaic properties

We fabricated the devices with the architecture of glass/FTO/NiO_x/Me-4PACz/$FAPbI_3$/PCBM/SnO_2/Cu, where PCBM is [6,6]-phenyl-C_{61}-butyric acid methyl ester. The fabrication details can be found in the supplementary materials. $FAPbI_3$ was used as the perovskite absorber with a bandgap around 1.52 eV, and the thickness of perovskite film was ~700 nm with large grains spanning the film. The grain size was ~1 μm, as determined from the cross-sectional and top-view SEM images (figs. S14 and S15). The NiO_x layer improved the device performance (Fig. 4A). For the device based on Me-4PACz without NiO_x, the PCE for an illuminated area of 0.1 cm^2 was 22.2% with an open-circuit voltage (V_{OC}) of 1.11 V, short circuit current (J_{SC}) of 26 mA/cm^2, and fill factor (FF) of 77.1%. For devices with the NiO_x layer, the V_{OC} and FF increased

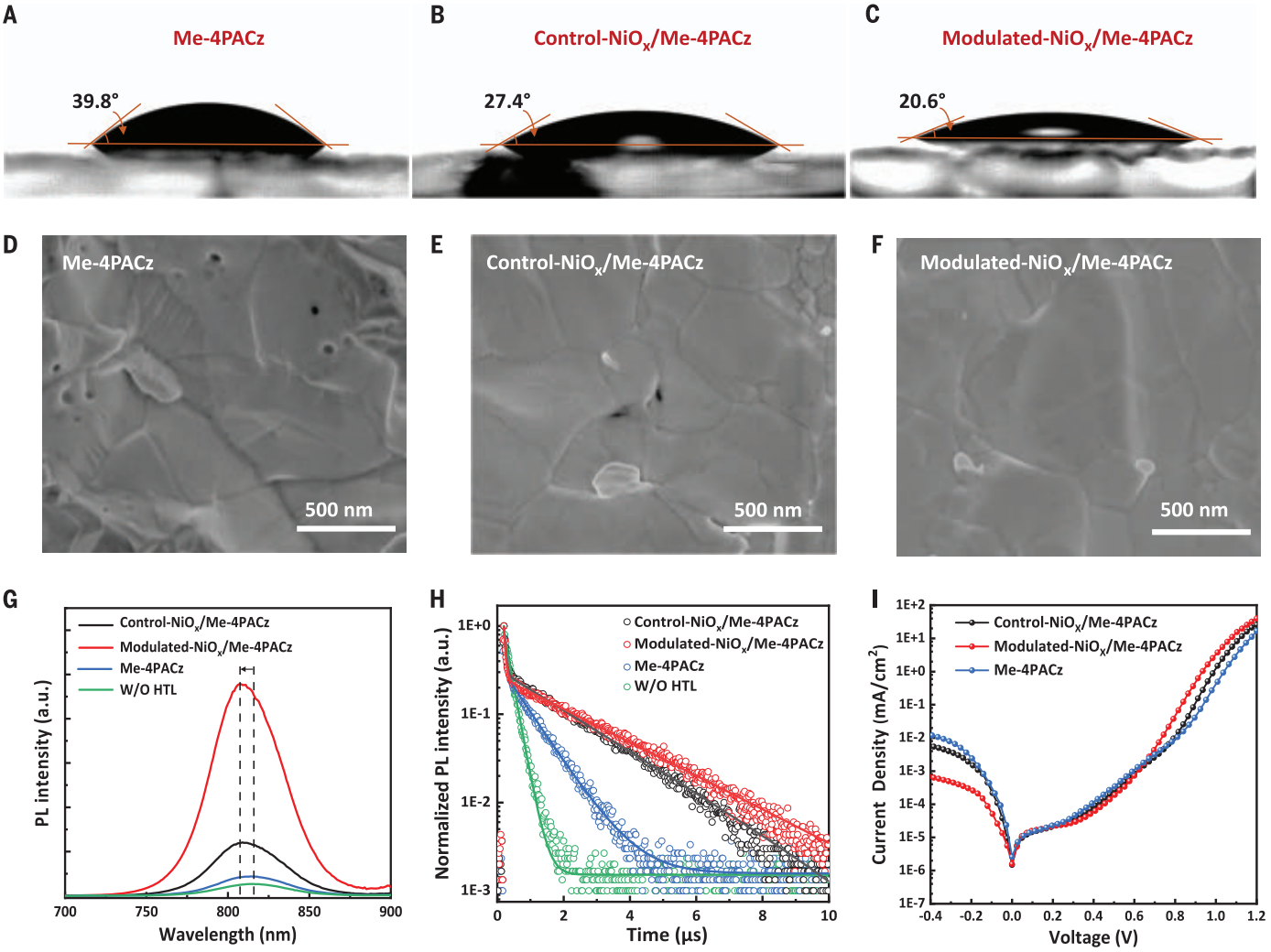

Fig. 3. Surface and electronic properties of SAM and NiO_x/SAM layers. (**A** to **C**) Contact angles of the perovskite precursor solution on different HTL layers. (**D** to **F**) Top-view SEM images of the bottom surface of perovskite deposited on different HTLs. (**G** and **H**) PL and TRPL measurements of perovskite films on different HTL layers. (**I**) Dark *J-V* measurements of different HTL layer–based inverted devices.

to 1.14 V and 81.1%, respectively, and a PCE of 24.1% was achieved. For PSCs based on H_2O_2-modulated NiO_x, a PCE up to 25.5% was achieved with a V_{OC} of 1.16 V, a J_{SC} of 26.15 mA/cm^2, and an FF of 84.1% (Fig. 4A). We also found that the modulated NiO_x/SAM devices showed neglected hysteresis compared with the NiO_x without modification (Fig. 4B and fig. S16). The detailed device parameters are listed in tables S2 and S3. To show that the enhancement after NiO_x insertion is universal, we replaced the substrates and self-assembled molecule by using ITO and MeO-2PACz, respectively, and a similar trend was observed even though the device performance was not optimized (figs. S17 and S18 and tables S4 and S5).

The typical external quantum efficiency result of the device is shown in fig. S19, which is almost consistent with the J_{SC} from current density-voltage (*J-V*) sweeps. One of our best-performing PSCs was sent to an accredited laboratory (Newport Corporation) for certification. The device with an illuminated mask area of 0.074 cm^2 delivered a certified quasi–steady-state efficiency of 25.2% with a V_{OC} of 1.18 V, J_{SC} of 26.2 mA/cm^2, and FF of 81.2% (fig. S20). Compared with the in-house measurement results, we found that the certificated results showed a 2% reduction in FF, which could be caused by the contact degradation during the transportation. Moreover, we collected the PV parameters of 50 devices for each condition (control and H_2O_2-modulated) in fig. S21. The high reproducibility was evidenced by the narrow PCE distribution, and the average PCE with modulation increased from 23.5 to 25.0%, which mainly reflected increases in V_{OC} and FF.

The reverse leakage current density was reduced by more than one order after the modulation of NiO_x via H_2O_2, further indicating that recombination at the buried surface was suppressed (Fig. 3I). The current density of the NiO_x-modulated sample under forward bias was higher than that of the SAM-only and control NiO_x samples and reflects better charge-transport properties.

We measured the transit photovoltage to compare charge recombination (fig. S22). The decay time increased from 1.44 μs for the SAM-only device to 2.02 μs for modulated NiO_x/SAM–based devices, indicating that the recombination had been suppressed, which was consistent with the TRPL results (Fig. 3H). We also measured the V_{OC}-light intensity dependence (fig. S23) and found that the ideality factor for the device without NiO_x was 1.71, an indicator of substantial recombination in the SAM-only device. With the NiO_x layer, the ideal factor decreased to 1.50 and decreased to 1.22 for modulated NiO_x-based devices, which is near the value of 1.14 for the champion normal structure (n-i-p) devices (*30*).

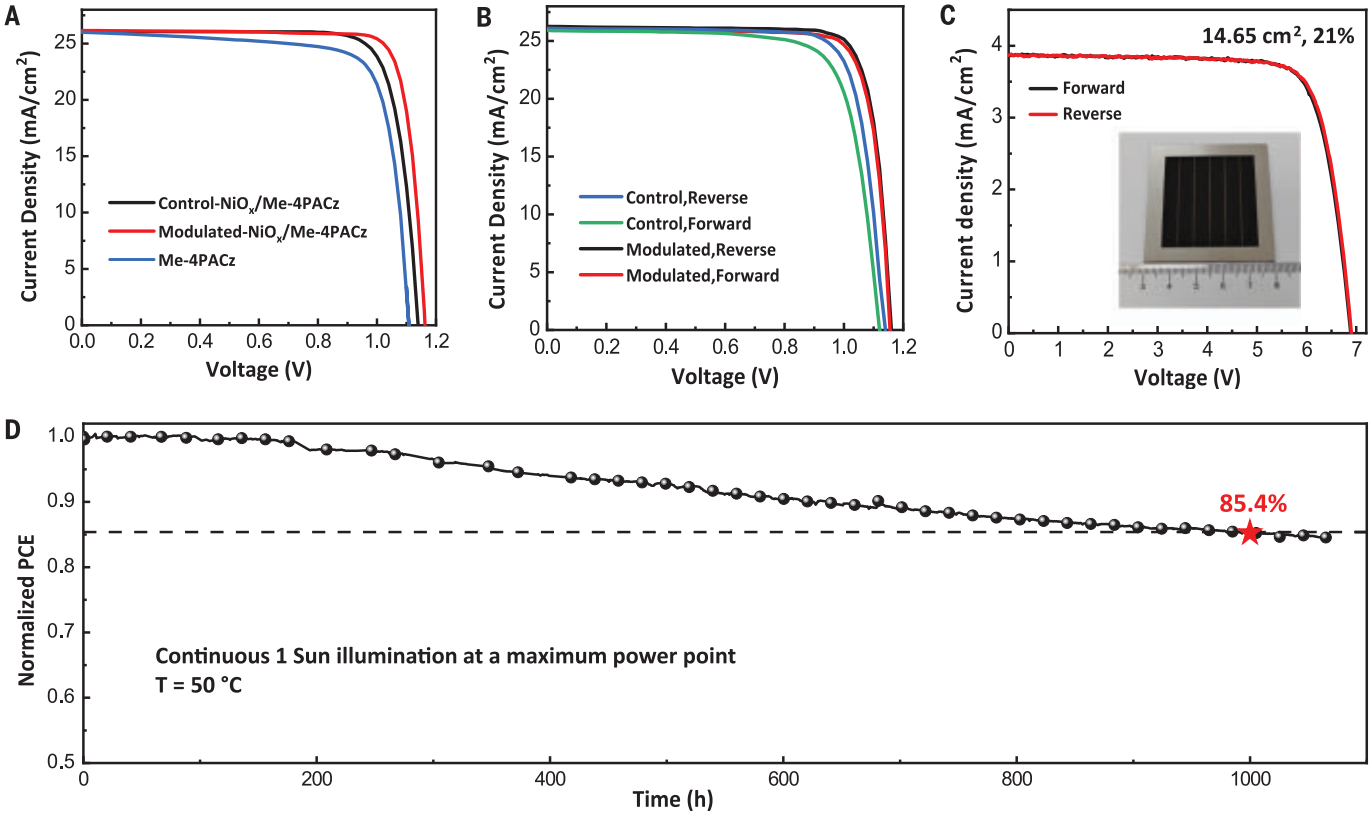

Fig. 4. Photovoltaic performance and stability of devices. (**A**) *J-V* curves of the Me-4PACz–, control-NiO_x/Me-4PACz–, and modulated-NiO_x/Me-4PACz–based devices (device area is 0.108 cm^2 and the mask size is 0.0737 cm^2) measured under AM 1.5G (100 mW/cm^2) illumination. (**B**) *J-V* curves of the devices under reverse and forward scan for the control-NiO_x and modulated NiO_x devices, respectively. (**C**) *J-V* curves of the modulated-NiO_x/Me-4PACz–based devices (14.65 cm^2) measured under AM 1.5G (100 mW/cm^2) illumination. (**D**) Steady power output tracking for the modulated devices (0.1 cm^2). The device was applied at maximum power point with continuous bias voltage of 1.02 V under 1-sun illumination at ~50°C, for enhancing the stability. A 5-nm thin film of ITO was used as a buffer layer between SnO_2 and Cu.

We also studied the electroluminescence performance of the devices working as light-emitting diodes. The modulated NiO_x device had a 2.53% external quantum efficiency versus 0.32% for the Me-4PACz device (fig. S24). This ~8 factor electroluminescence efficiency enhancement was consistent with a 50 meV V_{OC} increase (Fig. 4A). We conclude that increase in V_{OC} was mainly caused by suppression of the defect-related recombination. For the FF and hysteresis improvement, the better physical contact from improved wetting (Fig. 2, A to C) and improved charge transport from better band alignment (fig. S13) or enhanced NiO_x conductivity (fig. S9) could also play a role.

Large-area devices and device stability

We fabricated the minimodules with six subcells with an aperture area of 14.65 cm^2. The structural schematic and photomicrograph of the subcell interconnection region are shown in fig. S25, and details of the minimodule fabrication process can be found in the experimental section. The device parameters were as follows: V_{OC} of 6.9 V connected in series, J_{SC} of 3.87 mA/cm^2, and FF of 78.7%, resulting in a PCE of 21% (Fig. 4C and table S6), which is among the highest efficiencies for the large-area PSCs. On the basis of the geometry design and the SEM images of subcell interconnection region (fig. S25), the geometric FF can be calculated as 94.5%, which still has some room for improvement. Compared with the small device, the performance loss for the minimodule is mainly from the J_{SC} and FF, and it can be further improved by depositing more uniform perovskite layer.

To determine the device stabilities, we first compared the stability of NiO_x-based devices without the SAM layer using the small-size device (0.1 cm^2). The H_2O_2-modulated strategy had slightly better stability both in stabilized power output tracking at 50°C and accelerated aging testing at 85°C (fig. S26), which could be due to the contact improvement (*16*). The device with the modulated NiO_x/Me-4PACz bilayer (small-size device) maintained ~79% of its initial PCE of 24.1% at maximum power point tracking under 1 sun illumination at 50°C (figs. S27 and S28). The device used for stability did not have an antireflection coating, leading to a 2% loss of J_{SC} compared with the champion devices.

We then fabricated a device in which we deposited a 5-nm layer of ITO between the Cu electrode and SnO_2 to avoid diffusion. This device retained 85.4% of its initial 23.6% PCE (fig. S29A) after continuous operation for 1000 hours at 50°C (Fig. 4D), tested under the continuous bias voltage of 1.02 V, which is the output voltage at the maximum power point. The enhanced stability of the device after inserting the ITO buffer layer could be caused by suppression of ion migration under external stress.

We also investigated the stability of the minimodule. After 400 hours of stabilized power output tracking, the device still showed 90% of its original PCE of 20.5% under 1 sun illumination at 50°C (figs. S30 and S31). The small-size unencapsulated device with an initial PCE of 23.5% without antireflection coating (fig. S29B) was subjected to accelerated aging stability by being heated at 85°C in nitrogen conditions. The device retained 85.1% of the initial PCE after 500 hours (fig. S32).

Discussion

Self-assembled molecules are widely used for designing efficient inverted perovskite solar cells, but inhomogeneous SAM could lead to leakage and recombination, both of which limit the device's performance and reproducibility.

We incorporated homogeneous NiO_x nanoparticles for better SAM growth based on this hole-selecting layer, and small-size PSCs with a certified efficiency of 25.2% and a 14.6-cm^2 minimodule with 21% efficiency were obtained; these configured devices exhibited good stability. Further improvement in device performance could be achieved by optimizing the buried surface and the top surface. Depositing a more uniform perovskite layer will be helpful for further enhancing module device performance. In addition to solar cells, this bilayer HTL could be used in other optoelectronic devices such as light-emitting diodes and photodetectors.

REFERENCES AND NOTES

1. Q. Jiang *et al.*, *Nature* **611**, 278–283 (2022).
2. X. Li *et al.*, *Science* **375**, 434–437 (2022).
3. Z. Li *et al.*, *Science* **376**, 416–420 (2022).
4. H. Chen *et al.*, *Nat. Photonics* **16**, 352–358 (2022).
5. X. Wu *et al.*, *Adv. Mater.* **35**, e2208431 (2023).
6. Y. Kim *et al.*, *Adv. Energy Mater.* **8**, 1801668 (2018).
7. Z. Ni *et al.*, *Science* **367**, 1352–1358 (2020).
8. A. Al-Ashouri *et al.*, *Science* **370**, 1300–1309 (2020).
9. S. Zhang *et al.*, *Science* **380**, 404–409 (2023).
10. N. Phung *et al.*, *ACS Appl. Mater. Interfaces* **14**, 2166–2176 (2022).
11. C. Li *et al.*, *Science* **379**, 690–694 (2023).
12. J. Sun *et al.*, *Sol. RRL* **5**, 2100663 (2021).
13. L. Li *et al.*, *Nat. Energy* **7**, 708–717 (2022).
14. C. C. Boyd *et al.*, *Joule* **4**, 1759–1775 (2020).
15. N. Sasirekha, B. Rajesh, Y.-W. Chen, *Thin Solid Films* **518**, 43–48 (2009).
16. M. Du *et al.*, *Joule* **6**, 1931–1943 (2022).
17. Q. Liu *et al.*, *J. Mater. Chem. C Mater. Opt. Electron. Devices* **6**, 646–653 (2018).
18. J.-L. Yang, Y.-S. Lai, J. S. Chen, *Thin Solid Films* **488**, 242–246 (2005).
19. X. Cui *et al.*, *Adv. Funct. Mater.* **32**, 2203049 (2022).
20. L. Mao *et al.*, *Adv. Mater.* **34**, e2206193 (2022).
21. M. Casas-Cabanas *et al.*, *J. Mater. Chem. A Mater. Energy Sustain.* **6**, 19256–19265 (2018).
22. Y. Ren *et al.*, *Sol. Energy Mater. Sol. Cells* **116**, 83–88 (2013).
23. A. C. Gandhi *et al.*, *J. Phys. Chem. C Nanomater. Interfaces* **117**, 18666–18674 (2013).
24. A. Wang *et al.*, *J. Energy Chem.* **48**, 426–434 (2020).
25. H. Bin *et al.*, *ACS Appl. Mater. Interfaces* **14**, 16497–16504 (2022).
26. P. Schulz *et al.*, *Energy Environ. Sci.* **7**, 1377–1381 (2014).
27. X. Zheng *et al.*, *Nat. Energy* **8**, 462–472 (2023).
28. Z. Ying *et al.*, *Joule* **6**, 2644–2661 (2022).
29. R. Lin *et al.*, *Nature* **620**, 994–1000 (2023).
30. Y. Zhao *et al.*, *Science* **377**, 531–534 (2022).

ACKNOWLEDGMENTS

We thank Q. Jiang from the Institute of Semiconductors, Chinese Academy of Sciences (CAS), for discussion and C. Yi from Tsinghua University for help with the TPV measurements. We also thank Y. Yang from the Shanghai Synchrotron Radiation Facility (SSRF) and User Experiment Assist System of SSRF for the help during our research process. **Funding:** This work was supported by the National Key Research and Development Program of China (grant 2020YFB1506400), the National Science Fund for Distinguished Young Scholars (grant 61925405), and the CAS Project for Young Scientists in Basic Research (grant YSBR-090). **Author contributions:** J.Y., Z.X., and S.Y. conceived the idea. J.Y. directed and supervised the project. S.Y. initialized inverted PSCs based on NiO_x nanoparticles and developed the device structure. Z.X. modulated NiO_x particles and applied them to the inverted PSCs. H.Z., Q.Z., F.M., Z.Q., Y.Z., X.C., and X.Z. analyzed the data. J.Y., S.Y., and. Z.X. cowrote the manuscript. All authors contributed to discussions and finalizing the manuscript. **Competing interests:** A Chinese patent application (CN 202310148064.5) was submitted by the Institute of Semiconductors, CAS, which covers the homogenized NiO_x nanoparticles for efficient inverted PSCs. **Data and materials availability:** All data needed to evaluate the conclusions in this study are present in the main text or the supplementary materials. **License information:** Copyright © 2023 the authors, some rights reserved; exclusive licensee American Association for the Advancement of Science. No claim to original US government works. https://www.science.org/about/science-licenses-journal-article-reuse

SUPPLEMENTARY MATERIALS
science.org/doi/10.1126/science.adj8858
Materials and Methods
Figs. S1 to S32
Tables S1 to S6
References (*31*–*33*)

Submitted 13 August 2023; resubmitted 14 September 2023
Accepted 13 November 2023
Published online 23 November 2023
10.1126/science.adj8858

STRUCTURAL BIOLOGY

Rab29-dependent asymmetrical activation of leucine-rich repeat kinase 2

Hanwen Zhu[1]†, Francesca Tonelli[2,3]†, Martin Turk[4], Alan Prescott[2], Dario R. Alessi[2,3], Ji Sun[1]*

Gain-of-function mutations in *LRRK2*, which encodes the leucine-rich repeat kinase 2 (LRRK2), are the most common genetic cause of late-onset Parkinson's disease. LRRK2 is recruited to membrane organelles and activated by Rab29, a Rab guanosine triphosphatase encoded in the *PARK16* locus. We present cryo–electron microscopy structures of Rab29–LRRK2 complexes in three oligomeric states, providing key snapshots during LRRK2 recruitment and activation. Rab29 induces an unexpected tetrameric assembly of LRRK2, formed by two kinase-active central protomers and two kinase-inactive peripheral protomers. The central protomers resemble the active-like state trapped by the type I kinase inhibitor DNL201, a compound that underwent a phase 1 clinical trial. Our work reveals the structural mechanism of LRRK2 spatial regulation and provides insights into LRRK2 inhibitor design for Parkinson's disease treatment.

Parkinson's disease (PD) is the second most prevalent neurodegenerative disorder, affecting 1 to 2% of the population over the age of 65 (*1*). Mutations in the *LRRK2* gene, which encodes the leucine-rich repeat kinase 2 (LRRK2) protein, are among the most frequent genetic causes of late-onset PD and account for ~5% of familial and ~1% of sporadic cases (*2*–*4*). More than 250 mutations in *LRRK2* have been identified, and ~100 were biochemically characterized (*5*–*7*). Most LRRK2-related PD mutations, such as G2019S (Gly^{2019}→Ser), have increased kinase activity. Therefore, LRRK2 inhibitors are of great interest to researchers in PD treatment (*2*).

Much effort has been directed at exploring the structure-function relationship in LRRK2 to gain a mechanistic understanding and to guide rational drug discovery (*8*). Previous work revealed high-resolution structures of inactive LRRK2 (*9*, *10*), whereas our understanding of LRRK2 activation is limited to microtubule-associated LRRK2 structures of disease mutations at mediate and low resolutions (*11*, *12*) or molecular dynamics (MD) simulations in combination with hydrogen-deuterium exchange mass spectrometry (HDX-MS) analyses (*13*–*16*). Furthermore, LRRK2 activation in both physiological and pathogenic conditions is tightly associated with membrane recruitment and Rab guanosine triphosphatases (GTPases) (*17*–*19*), the molecular basis of which remains enigmatic.

This study aimed to explore the kinase activation mechanism of LRRK2 that is induced by Rab29, a membrane-anchored Rab GTPase. Rab GTPases are master regulators of intracellular-vesicle trafficking, whose disruption is a hallmark of PD pathogenesis (*20*). Rab29, encoded in the *PARK16* locus and associated with late-onset PD, is believed to function in the same pathway as LRRK2. Although mouse genetic data suggest that alternative activation mechanisms of LRRK2 exist (*21*), physiological connections between Rab29 and LRRK2 are supported by human and *Caenorhabditis elegans* genetic data, similar mouse knockout histological phenotypes, cellular colocalization, and physical interactions (*22*–*27*). Moreover, Rab29, but not its close homologs Rab32 or Rab38, stimulates LRRK2 kinase activity by monitoring S1292 autophosphorylation (*28*), suggesting that Rab29 does more than membrane recruitment to stimulate LRRK2 activity.

Structural determination of Rab29–LRRK2 complexes

To structurally characterize the Rab29–LRRK2 interaction, we first reconstituted a stable complex in vitro. Previous studies have suggested an emerging "Rab29–LRRK2–Rabs" cascade for LRRK2 signaling (Fig. 1A) (*19*, *29*), in which GTP-bound Rab29 (Rab29•GTP) facilitates LRRK2 membrane recruitment and activation,

[1]Department of Structural Biology, St. Jude Children's Research Hospital, Memphis, TN 38105, USA. [2]MRC Protein Phosphorylation and Ubiquitylation Unit, School of Life Sciences, University of Dundee, Dundee DD1 5EH, UK. [3]Aligning Science Across Parkinson's (ASAP) Collaborative Research Network, Chevy Chase, MD, USA. [4]Cryo-EM and Tomography Center, St. Jude Children's Research Hospital, Memphis, TN 38105, USA.
***Corresponding author. Email: ji.sun@stjude.org**
†These authors contributed equally to this work.

then activated LRRK2 phosphorylates Rab GTPases, including Rab29 itself. Phosphorylated Rab29, which was reported not to activate LRRK2, could potentially serve as negative feedback (*28*). We thus introduced three point mutations (Q67L, T71A, and S72A) to Rab29 ($Rab29_{EM}$) to maximize the opportunity of capturing the active Rab29•GTP–LRRK2 complex (where Q is glutamine, L is leucine, T is threonine, A is alanine, and S is serine). T71A and S72A prevent Rab29 phosphorylation, and Q67L abolishes GTPase activity and enhances the interaction between Rab29 and LRRK2 (*26*). Although Q67L also diminishes the membrane localization of Rab29 in cells (*26*), we reasoned that the interaction between Rab29 and LRRK2 is independent of membrane environment or composition (*30*) and should not be affected in vitro by this mutation. Indeed, glutathione *S*-transferase (GST) pulldown assays validated the $Rab29_{EM}$–LRRK2 interaction and complex formation (fig. S2G).

We determined cryo–electron microscopy (cryo-EM) structures of the Rab29–LRRK2 complex, reconstituted by mixing LRRK2, $Rab29_{EM}$, GTP analog (GppNHp), adenosine triphosphate (ATP), and Mg^{2+}. The final cryo-EM reconstruction resulted in Rab29–LRRK2 structures of three distinct oligomeric assemblies (Fig. 1, B and C; fig. S1; and table S1): Rab29–LRRK2 monomer with one LRRK2 and one Rab29; Rab29–LRRK2 dimer with two LRRK2 and two Rab29; and Rab29–LRRK2 tetramer with four LRRK2 and two visible Rab29 (Fig. 1, B and C). Focused three-dimensional (3D) refinement improved the cryo-EM density surrounding the Rab29–LRRK2 interface (fig. S1A), and C2 symmetry was imposed for Rab29–LRRK2 dimer and tetramer during data analysis (fig. S1A).

Rab29-dependent recruitment of LRRK2

In the Rab29–LRRK2 monomer, LRRK2 is almost identical to the inactive LRRK2-alone structure (*10*) (fig. S2A). Rab29 binds to the N-terminal armadillo repeat (ARM) domain of LRRK2, burying a surface area of ~800 $Å^2$ (Fig. 2A), and adopts a GTP-bound Switch I closed configuration often observed in GTP-bound small GTPases (fig. S2, B to E). Docking of the GDP-bound Rab29 structure (*25*) into the cryo-EM density shows obvious steric clashes with LRRK2 (fig. S2F), explaining why the GTP-bound state promotes Rab29-dependent recruitment of LRRK2 (*24*, *25*, *27*, *28*, *30*, *31*).

The Rab29–LRRK2 interface is formed by the ARM9-10 of LRRK2 and the Switch I-Interswitch-Switch II surface and CDR1 (*32*) of Rab29 (fig. S2E). The interaction conforms with a general Rab-effector recognition mode, in which effectors associate with the GTP-bound form of Rabs through the Switch I-Interswitch-Switch II surface (*32*). Sequence alignment of Rab GTPases, including the Rab32 subfamily (Rab29, Rab32, and Rab38) and several LRRK2 substrates, revealed that key residues in the Rab29–LRRK2 interface were conserved among the Rab32 subfamily (fig. S2H). Single mutations at the center of the interface (Rab29 D43A or W62A) were sufficient to abolish the interaction, whereas Rab29 L7Q or L76M substitutions at the edge of the interface had moderate or little impact (fig. S2G). The surfaces of Rab29 and Rab10 predicted to interact with LRRK2 had almost identical interface residues, which is consistent with previous work suggesting that Rab10 interacts with LRRK2 at the Rab29 site (*33*). Rab5A, 5B, and 5C, which can be phosphorylated by LRRK2 (*34*), contain an alanine in the position corresponding to Asp^{43} in Rab29 (fig. S2H).

Consistent with the pulldown-assay results, confocal microscopy revealed that Rab29 D43A or W62A mutations diminished the membrane recruitment of LRRK2, whereas Rab29 L7Q or L76M substitutions had moderate or little disruptive effects (Fig. 2B and fig. S3A). Similarly, LRRK2 mutations (R399E and L403E) at the center of the Rab29–LRRK2 interface significantly reduced the Rab29-dependent membrane recruitment, whereas a mutation at the periphery of the interface (M402A) had a moderate impact (Fig. 2C and fig. S3B). We also assessed the effect of interface mutations on LRRK2 kinase activity in cells by monitoring the phosphorylation status of Rab10-Thr^{73}, Rab29-Thr^{71}, and LRRK2-Ser^{1292} (*28*). In agreement with the pulldown and membrane-localization results, mutations at the center of the interface on either the Rab29 (Fig. 2D and fig. S3, C and E) or LRRK2 side (Fig. 2E and fig. S3D) abolished the Rab29-stimulated kinase activity, whereas mutations at the periphery had only a minor impact. These data confirmed the observed Rab29–LRRK2 interface and suggested the importance of membrane recruitment for LRRK2 activation. All mutations introduced to the Rab29–LRRK2 interface had minor impacts on the basal activity of LRRK2 on Rab10 and Ser^{1292}, supporting the view that the observed interface is important for LRRK2 recruitment but probably not for substrate recognition.

In the Rab29–LRRK2 dimer assembly, each LRRK2 protomer binds a single Rab29 molecule at the ARM9-10 interface (Fig. 1B). In this X-shaped complex, LRRK2 protomers adopt the same inactive conformation observed in the Rab29–LRRK2 monomer and the LRRK2-alone structure (fig. S4) (*10*). The two LRRK2 protomers interact via their COR-B domains, in a way that is similar to what we described for the LRRK2 homodimer (fig. S4B) (*10*). The observation of LRRK2 dimers both in the presence and absence of Rab29 suggests that

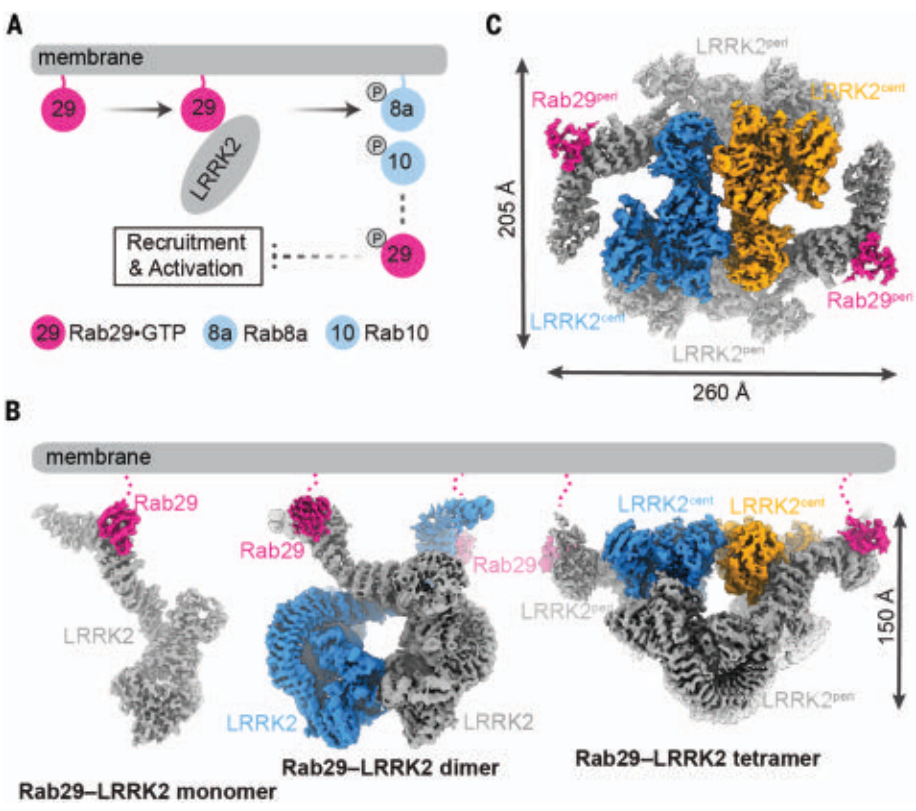

Fig. 1. Structural determination of the Rab29–LRRK2 complex. (**A**) Schematic diagram showing Rab29-mediated LRRK2 membrane recruitment and activation. (**B**) Cryo-EM structures of the Rab29–LRRK2 complex in three oligomerization states. (**C**) Top view of the cryo-EM structure of the Rab29–LRRK2 tetramer.

COR-B–mediated dimerization of LRRK2 could occur under physiological settings.

A tetrameric assembly of LRRK2

We captured the Rab29–LRRK2 complex in an unexpected tetrameric assembly and determined its structure to an overall resolution of 3.5 Å (fig. S1 and table S1). With a ~205 Å by 260 Å by 150 Å dimension (Fig. 1, B and C), the Rab29–LRRK2 tetramer is an assembly with a twofold rather than fourfold symmetry, featuring two types of LRRK2 protomers: LRRK2^{peri} (peripheral) and LRRK2^{cent} (central) (Fig. 1, B and C, and Fig. 3A). We were able to resolve and model near full-length LRRK2^{peri} and associated Rab29^{peri}. By contrast, LRRK2^{cent} protomers have flexible LRR, ankyrin repeat (ANK), and ARM domains, and neither those domains nor the associated Rab29^{cent} molecules could be resolved (Fig. 3A and fig. S5, A to C). By contrast, the catalytic halves of LRRK2^{cent}, including ROC, COR, KIN, and WD40 domains (ROC, Ras of complex proteins; COR, C-terminal of ROC; KIN, kinase), were rigid and could be refined to an overall resolution of 3.2 Å with focused refinement (fig. S1A).

The LRRK2^{peri}–LRRK2^{cent} interaction within each asymmetric unit is mediated by the COR-B domains (fig. S5, C and D), and the COR-B–COR-B interface is similar to that seen in LRRK2 homodimers or Rab29–LRRK2 dimers, with a subtle rotational motion (fig. S5D). In addition, LRRK2^{peri} directly interacts with LRRK2^{cent} from the other asymmetric unit (Fig. 3, A to C), with regions near the LRRK2^{peri} ARM–ANK boundary packing against the LRRK2^{cent} WD40 domain and the LRRK2^{peri} ARM domain associated with the LRRK2^{cent} ROC domain. The two LRRK2^{cent} protomers pack in a "head-to-tail" mode through WD40–KIN interfaces (Fig. 3, A and D). The flexible N-terminal part of LRRK2^{cent} might also interact with the Rab29^{peri} and the ARM domain of LRRK2^{peri}, but the low local resolution of the cryo-EM map prevents further interpretation (fig. S5A).

The catalytic halves of LRRK2^{cent} and LRRK2^{peri} show substantial conformational differences (Fig. 3E and movie S1). Upon aligning the COR-B domain, KIN and WD40 are displaced about 40° toward the COR-A and ROC domains in LRRK2^{cent} (fig. S5E). This conformational rearrangement closes a central cavity shaped by the ROC, COR, and KIN domains (Fig. 3E). In this conformation, COR-B, ROC-COR-A, KIN N-lobe, and KIN C-lobe-WD40 appear to move as rigid bodies (fig. S5F). Repositioning of KIN C-lobe-WD40 in LRRK2^{cent} disrupts the connection between the WD40 and ARM-ANK-LRR domains in the inactive state, which was stabilized by the scaffolding hinge helix and C-terminal helix (fig. S5, G and H) (*10*). Additionally, the KIN C-lobe would clash into the LRR domain (fig. S5I), contributing to the displacement and flexibility of the ARM-ANK-LRR domains in LRRK2^{cent} protomers (fig. S5A).

LRRK2^{cent} has an active kinase domain

The KIN domain of LRRK2^{cent} has structural features of an active kinase. The LRR domain that shields the KIN domain in the inactive conformation (*10*) is flexible in LRRK2^{cent}, leaving the KIN domain accessible to substrates from the membrane side (fig. S5, A and B). Critically, the LRRK2^{cent} KIN domain adopts a closed conformation (Fig. 4A), with the αC helix positioned toward the active site and the "DYG motif" flipped in. Lys^{1906} and Glu^{1920} form a salt bridge, an interaction blocked by Tyr^{2018} in the inactive conformation (Fig. 4, B and C). There is a well-defined cryo-EM density for ATP in the active site, and the distance between Asp^{2017} and ATP shortens to 3.8 Å (from 13.8 Å in the inactive state) (Fig. 4, A and C), permitting ATP hydrolysis in the presence of

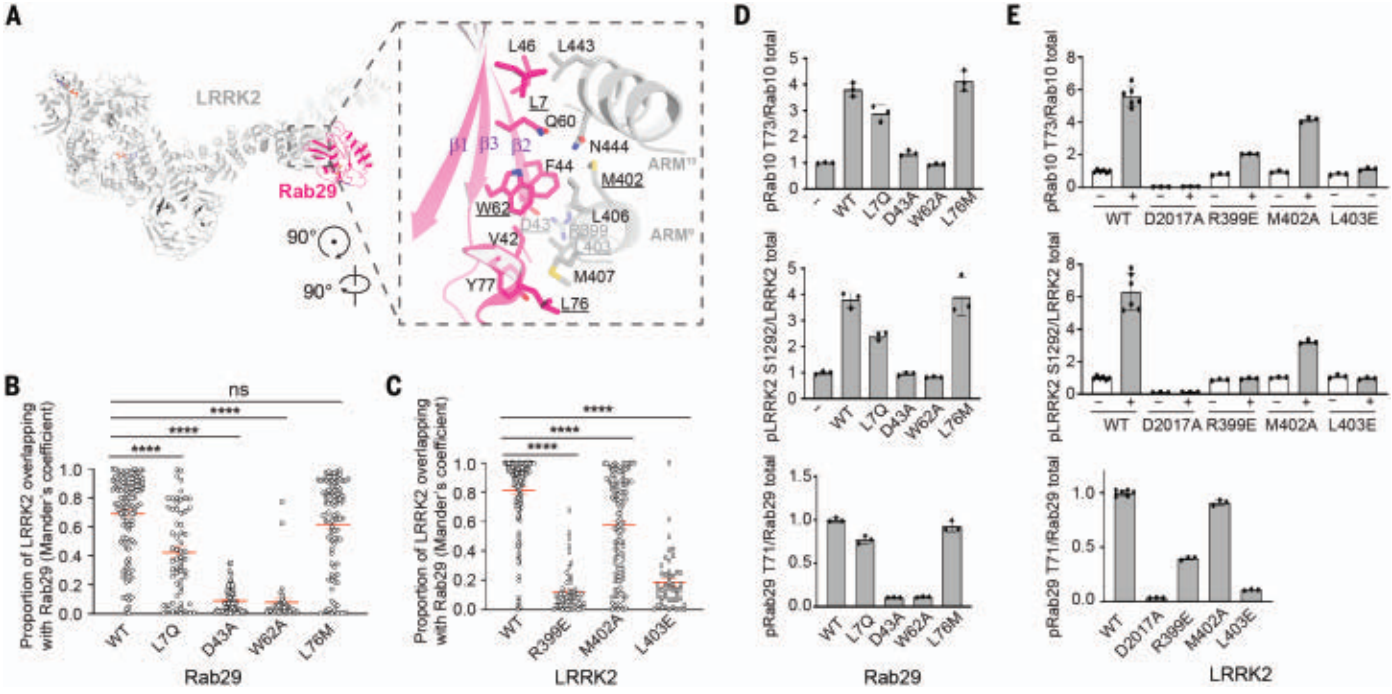

Fig. 2. Molecular basis of Rab29-dependent LRRK2 recruitment. (**A**) Rab29–LRRK2 interface in the LRRK2 monomer state. LRRK2 and Rab29 are colored gray and hot pink, respectively. Side chains of interface residues are shown as sticks. (**B** and **C**) Impact of Rab29 or LRRK2 mutations on LRRK2 localization in HEK293 cells. Quantification of a portion of LRRK2 overlapping with Rab29 according to Mander's coefficient for confocal analysis is shown in fig. S3, A and B. Each empty circle represents colocalization coefficient (Mander's coefficient) measured in one cell. Error bars represent SEM. Significance was determined by the Kruskal-Wallis one-way analysis of variance (ANOVA) test. ****P < 0.0001; ns (not significant). (**D** and **E**) Quantification of the immunoblotting data shown in fig. S3, C and D. Data are presented as ratios of pRab10-Thr^{73}/total Rab10, pLRRK2-Ser^{1292}/total LRRK2, and pRab29-Thr^{71}/total Rab29, normalized to the average of LRRK2 WT values. The data shown are the mean ± SD of three determinations. Single-letter abbreviations for the amino acid residues are as follows: A, Ala; C, Cys; D, Asp; E, Glu; F, Phe; G, Gly; H, His; I, Ile; K, Lys; L, Leu; M, Met; N, Asn; P, Pro; Q, Gln; R, Arg; S, Ser; T, Thr; V, Val; W, Trp; and Y, Tyr.

substrates. The regulatory spine (R-spine), formed by Leu^{1935}, Leu^{1924}, Tyr^{2018}, and Tyr^{1992} becomes continuous (Fig. 4D). Docking of the LRRK2^{cent} model into the 14-Å in situ cryo–electron tomography (cryo-ET) map of microtubule-bound LRRK2 (Fig. 4E), which was proposed to represent an active conformation (*11*), reveals close correspondence, supporting our conclusion that the LRRK2^{cent} KIN domain is in an active conformation.

We next examined the interdomain interactions that stabilize the active conformation of the LRRK2^{cent} KIN domain. The activation loop of the KIN domain (*35*) dips into the open pocket between COR-A and COR-B (Fig. 4F). We hypothesized that this interdomain interaction stabilizes the closed conformation of the KIN domain and would thus be crucial for LRRK2 kinase activity. Indeed, single point mutations at the KIN–COR interface (P1588A, N1710A, and W1791A) reduced the LRRK2 kinase activity induced by Rab29 (Fig. 4G and fig. S6). LRRK2 W1791A almost completely abolished LRRK2 activity in the absence of Rab29, indicating that the observed interactions (Fig. 4F) are also critical for the basal activity of LRRK2 (Fig. 4G and fig. S6C). Therefore, blocking the COR–KIN interaction could be a potential strategy to inhibit LRRK2 allosterically.

Compared with the inactive state, the KIN N-lobe rotates slightly toward the COR-B domain in LRRK2^{cent}, leading to more-extensive interactions between the αC helix of the KIN domain and the docking (Dk) helix of the COR-B domain (Fig. 4F). These observations are consistent with previous HDX-MS and MD simulation studies that indicated an altered interface between the COR-B Dk helix and the KIN αC helix and the stabilization of a nearby COR-B loop (residues 1721 to 1725) upon binding of type I inhibitors (fig. S5J) (*15*).

The ROC domain is displaced relative to the COR-B domain upon LRRK2 activation (fig. S5K). COR-B structurally bridges the catalytic ROC and KIN domains, and GTP binding in the former modulates the kinase activity of the latter (*36*–*39*). The movement of the ROC domain relative to the COR-B domain upon activation involves a "seesaw-like" motion of the ROC αC helix, with Tyr^{1699} as the pivot point (fig. S5K and movie S2). Our structural observations indicate that conformational coupling between the ROC and COR-B domains is vital for LRRK2 activity by contributing to the crosstalk between GTPase and kinase activities (*10*).

We then determined the cryo-EM structure of LRRK2^{RCKW} (RCKW: ROC-COR-KIN-WD40) in complex with DNL201/GNE-0877, a compound reported to be safe and well tolerated in a phase 1 clinical trial (*40*) (Fig. 5A and fig. S7, A to H). LRRK2^{RCKW} is used to simplify the structure determination caused by the flexibility of the N-terminal domains. DNL201 is a type I kinase inhibitor that fixes the LRRK2 kinase domain in an active-like conformation, as judged by the compound's ability to induce dephosphorylation of Ser^{935} (*40*, *41*). The well-resolved kinase domain structure revealed a binding site for DNL201 within LRRK2 at the ATP-binding pocket (Fig. 5B and fig. S7, F to H). In the LRRK2^{cent} and LRRK2^{RCKW}–DNL201 structures, KIN domains adopted a highly similar structure [root mean square deviation (RMSD), 0.7 Å] (Fig. 5C), further supporting the active conformation of LRRK2^{cent} KIN domain.

Comparing the active conformations of LRRK2^{cent} and LRRK2^{RCKW}–DNL201, we observed several common features. The αC helix, activation loop, APE-αF, and αH-αI linkers from the KIN domain are the major contributors for interactions with COR, and the interface between the KIN and COR domains are almost identical (Fig. 5D) despite a small displacement of COR domains (Fig. 5C). The seesaw motion between the COR-B and ROC domains is also observed, as seen by the Tyr^{1699} side-chain flipping (fig. S8A).

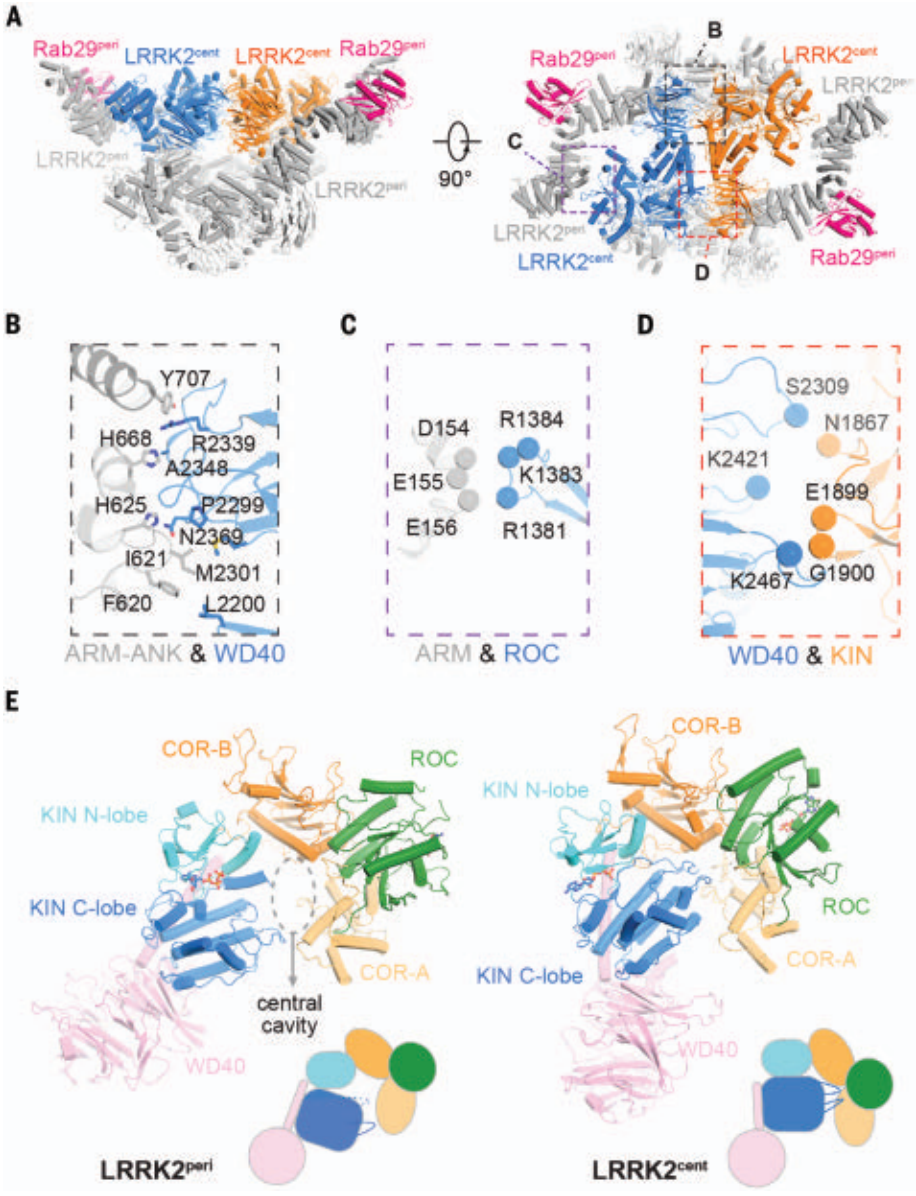

Fig. 3. Structure of the Rab29–LRRK2 tetramer. (**A**) Cryo-EM structure of the Rab29–LRRK2 tetramer with two different views. Peripheral Rab29 (Rab29^{peri}) and LRRK2 (LRRK2^{peri}) are colored in hot pink and gray, respectively; central LRRK2 (LRRK2^{cent}) copies are colored in blue and orange. (**B** and **C**) Interactions between (B) the WD40 domain of LRRK2^{cent} and ARM-ANK domains of LRRK2^{peri} and (C) the ROC domain of LRRK2^{cen} and the ARM domain of LRRK2^{peri}. (**D**) Interactions between two LRRK2^{cent} copies. (**E**) Conformational changes in the C-terminal halves of LRRK2 upon activation. A dashed circle indicates the central cavity between the KIN and COR domains. Color codes for different parts of LRRK2 are as follows: ROC, green; COR-A, light orange; COR-B, bright orange; N-lobe of KIN, cyan; C-lobe of KIN, marine; WD40, pink.

However, these activation features are different from or were not observed in the previous microtubule-based LRRK2 model (PDB 6XR4) (fig. S8B) (*11*). Additionally, there are global differences between Rab29-dependent and microtubule-based activation of LRRK2 because the Rab29–LRRK2 tetramer contains asymmetric dimers and microtubule-based LRRK2 oligomers are symmetric (fig. S8, C and D).

The conformational changes revealed by comparing active LRRK2^{cent} or active-like LRRK2–DNL201 with inactive LRRK2 align very well with previous HDX-MS data (*13*–*16*). Overall, the active conformation has a more compact arrangement; the αC helix, activation loop, APE-αF loop of the KIN domain (Fig. 4F and Fig. 5D), and C-terminal part of COR-B helix (residues 1788 to 1797) showed lower deuterium exchange (*14*, *15*), owing to the closure of the central cavity upon activation (Fig. 3E). The only exception was the C-terminal half of the αC helix of ROC domain (residues 1426 to 1449), which became more accessible and showed increased deuterium exchange because of the seesaw motion (fig. S5K).

Rab29–LRRK2 tetramer and Rab29-dependent activation

As the Rab29–LRRK2 tetramer has two protomers in active kinase conformation, we hypothesized

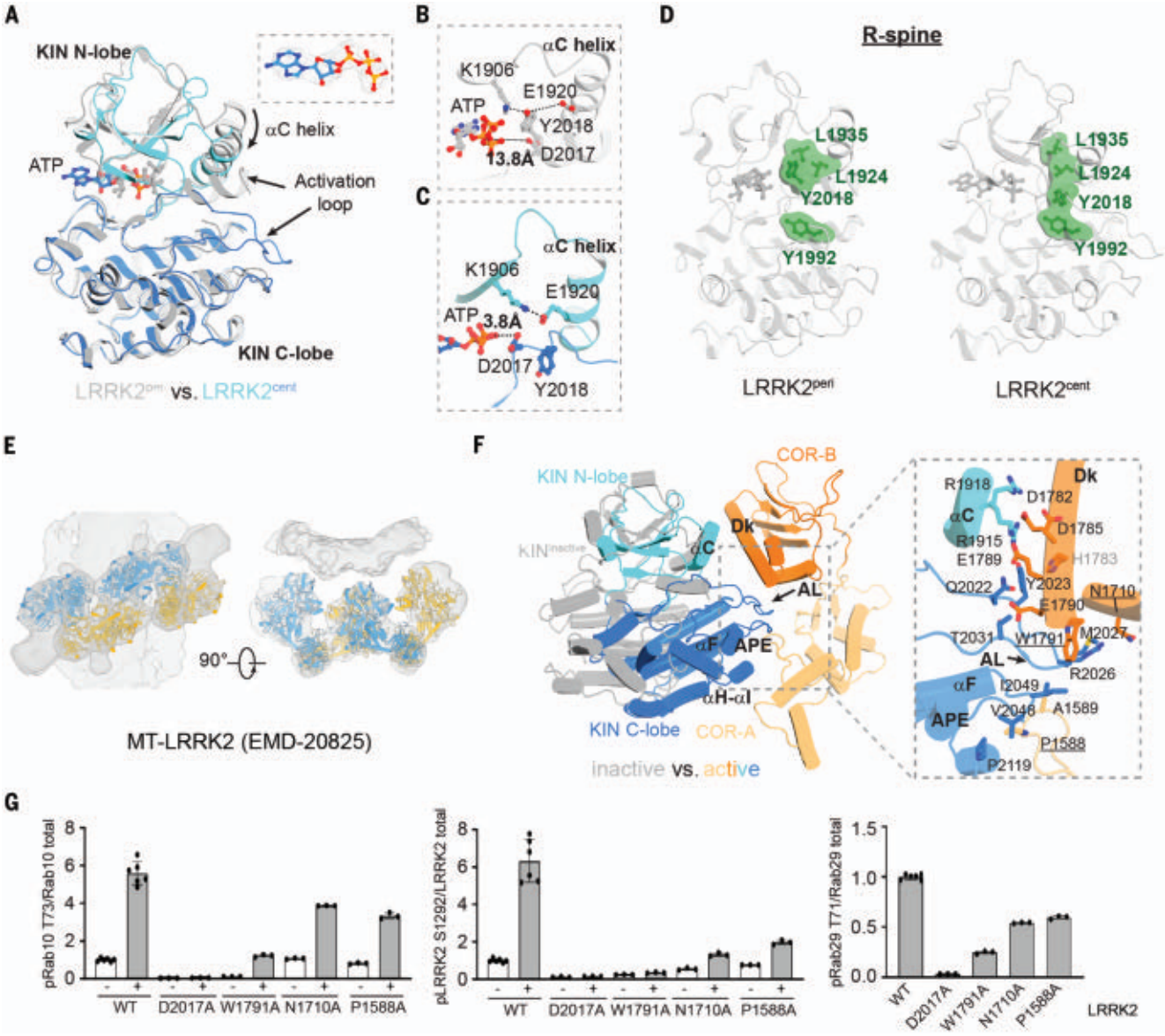

Fig. 4. An active conformation of LRRK2. (**A**) Superposition of kinase domains of LRRK2^{cent} and LRRK2^{peri}. N- and C-lobes of the LRRK2^{cent} kinase domain are colored in cyan and marine, respectively; the LRRK2^{peri} KIN domain is colored in gray. (Inset) Image shows the Cryo-EM density of the ATP molecule. (**B** and **C**) Key catalytic residues in LRRK2^{peri} (B) and LRRK2^{cent} (C) KIN domain with side chains shown as ball-and-stick models. The distances between the side chain of D2017 and the phosphate group of ATP are indicated with dashed lines. (**D**) R-spine of the LRRK2^{peri} (left) and LRRK2^{cent} (right) KIN domains. The four residues forming the R-spine (L1935, L1924, Y2018, and Y1992) are shown as green surfaces. (**E**) Docking of C-terminal catalytic halves of LRRK2^{cent} into the cryo-ET map of microtubule-bound LRRK2. (**F**) Movement of the KIN domain relative to the COR domain upon activation. (Inset) Interactions between the KIN and COR domains in the active conformation; side chains of the interface residues are shown as sticks. Dk, docking helix; APE, conserved APE motif; AL, activation loop. (**G**) Quantitative immunoblotting analysis of the cellular kinase activity of LRRK2-bearing mutations in the interface between the KIN and COR domains in fig. S6C. Data are presented as ratios of pRab10-Thr^{73}/total Rab10, pLRRK2-Ser^{1292}/total LRRK2, and pRab29-Thr^{71}/total Rab29, normalized to the average of LRRK2 WT values. The data shown are the mean ± SD of three experiments.

that the tetrameric assembly could explain the increased Rab29-induced LRRK2 Ser^{1292} autophosphorylation (*28*). To test the hypothesis, we first verified that the tetramer state was not caused by the Rab29 Q67L mutation, which disrupts Rab29 membrane localization and impacts the Rab29-dependent LRRK2 activation in cells (*23*, *27*). Thus, we characterized the Rab29 T71A/S72A–LRRK2 complex because Rab29 T71A/S72A has minimal impacts on LRRK2 cellular localization or kinase activity (fig. S9, A to D) (*28*). Our cryo-EM analysis showed that Rab29 T71A/S72A–LRRK2 forms tetramers during 2D classification performed with cross-correlation (fig. S9E), although there was a lower ratio of tetramer particles than with $Rab29_{EM}$–LRRK2, likely because of a lower percentage of GTP-bound Rab29.

We then compared Rab29–LRRK2 and Rab32–LRRK2 complexes to dissect the role of LRRK2 tetramerization in kinase activation. Rab32, a close homolog of Rab29 (~56% sequence identity and ~70% similarity) can mediate LRRK2 membrane recruitment (*31*) but does not support LRRK2 activation in human embryonic kidney 293 (HEK293) cells, as indicated by low Ser^{1292} autophosphorylation levels (*28*) and by a higher level of Ser^{935} phosphorylation (Fig. 6, A and B), which is associated with inactive LRRK2 (*41*). We determined the cryo-EM structure of Rab32–LRRK2 complexes (fig. S10, A to C). Rab32 interacts with LRRK2 through an interface that is almost identical to that used by Rab29 (fig. S10, D and E), but the Rab32–LRRK2 complex was captured in two oligomerization states: Rab32–LRRK2 monomer and Rab32–LRRK2 dimer (Fig. 6C). Furthermore, reprocessing of our previous LRRK2-alone dataset (*10*) showed no LRRK2 tetrameric assembly (Fig. 6D and fig. S10F). Therefore, we conclude that the Rab29–LRRK2 tetramer is associated with the Rab29-dependent activation of Ser^{1292} autophosphorylation.

In contrast to our results for Ser^{1292} autophosphorylation, we found that phosphorylation of Rab10 by LRRK2 is stimulated by both Rab29 and Rab32 (Fig. 6B), suggesting that membrane recruitment of LRRK2 is sufficient to activate Rab10 phosphorylation without a requirement for tetramerization. Rab10 phosphorylation and Ser^{1292} autophosphorylation are thus independent molecular events during LRRK2 signaling (*42*, *43*). Endogenous Rab38 was also reported to increase Rab10 phosphorylation but not Ser^{1292} autophosphorylation in melanocytes (*44*). Therefore, we predict that Rab38 should mediate LRRK2 membrane recruitment but not the tetramerization of LRRK2.

Discussion

In this study, we have presented Rab29–LRRK2 structures in both active and inactive states, which allowed us to analyze PD mutations in the context of kinase activation. Gain-of-function mutations at six sites—G2019S, I2020T, Y1699C, N1437H, R1441C/G/H, and S1761R (fig. S11A)—have been proposed to be high risk and PD-causing (*45*). Our previous structure of LRRK2 bearing the G2019S substitution showed little difference from the wild-type (WT) LRRK2 in the inactive state (*10*). However, this mutation could induce additional interactions with Glu^{1920} and stabilize the critical Lys^{1906}-Glu^{1920} salt bridge in the active conformation (fig. S11C). Ile^{2020} moves from a hydrophobic to a hydrophilic environment upon LRRK2 activation (fig. S11B), and the I2020T mutation would destabilize the inactive conformation and favor the active conformation. Tyr^{1699}, Asn^{1437}, and Arg^{1441} are at the interface between the αC helix of ROC and the COR-B domain, where a seesaw-like motion of the ROC-αC helix occurs upon LRRK2 activation (fig. S11D, fig. S5K, and movie S2). Asn^{1437} and Arg^{1441} are located at one side of the seesaw and anchor the C-terminal part on the αC helix of ROC to the surface of the COR-B domain in the inactive state (fig. S11D). Therefore, mutations of Asn^{1437} and Arg^{1441} should weaken the anchoring effect, shifting the balance of the seesaw toward the N-terminal of the ROC αC helix, hence promoting LRRK2 activation. Tyr^{1699} functions as the pivot point (fig. S11D and movie S2), and its substitution with a smaller residue would lower the energy barrier for the seesaw motion and for the transition from the inactive to the active state. The above structural observations lead us to conclude that increased conformational dynamics of G2019S, I2020T, Y1699C, N1437H, and R1441C/G/H mutations play an important role in PD pathogenesis.

The different modes of activation of LRRK2 with Rab29 or its close homologs, Rab32 or Rab38, are intriguing. Although Rab29, Rab32, and Rab38 could all activate Rab10 phosphorylation by LRRK2, only Rab29 promotes the formation of LRRK2 tetrameric assembly, boosts Ser^{1292} autophosphorylation, and is associated with late-onset PD. Moreover, LRRK2 Ser^{1292} autophosphorylation is elevated in urinary exosomes of *LRRK2* mutation carriers (*46*–*48*), but the association between Rab10 phosphorylation and *LRRK2* mutations varies across different studies (*46*–*50*). We thus speculate a pathogenic association between Rab29-dependent LRRK2 tetramerization and Ser^{1292} autophosphorylation

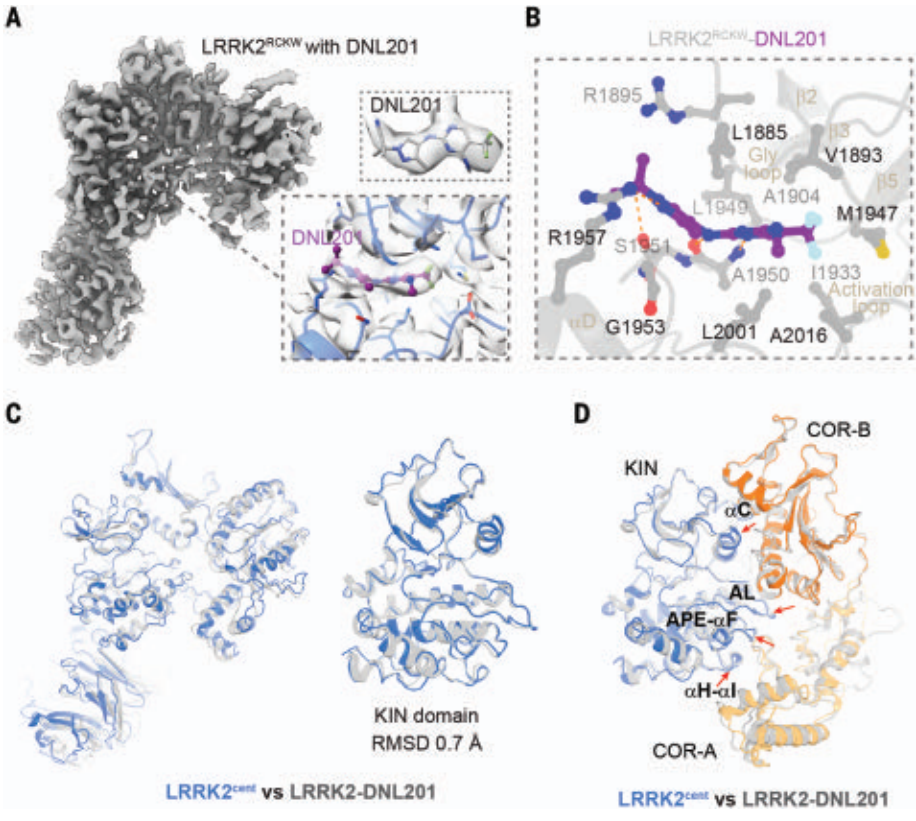

Fig. 5. Structure of $LRRK2^{RCKW}$ with DNL201. (**A**) Cryo-EM map of $LRRK2^{RCKW}$ in complex with type I inhibitor DNL201. (Insets) Cryo-EM densities of the DNL201 inhibitor (top) and the surrounding residues (bottom) are shown. (**B**) DNL201 binding site [magnified from bottom inset of (A)]. Side chains of DNL201-interacting residues are shown as sticks. (**C**) Structural comparison of DNL201-bound $LRRK2^{RCKW}$ (gray) and $LRRK2^{cent}$ (blue) structures. The kinase domain alignment is shown on the right. (**D**) Comparison of KIN-ROC interface between $LRRK2^{RCKW}$-DNL201 (gray) and $LRRK2^{cent}$ (blue and orange). Key structural elements from KIN domain involved in the interaction are labeled.

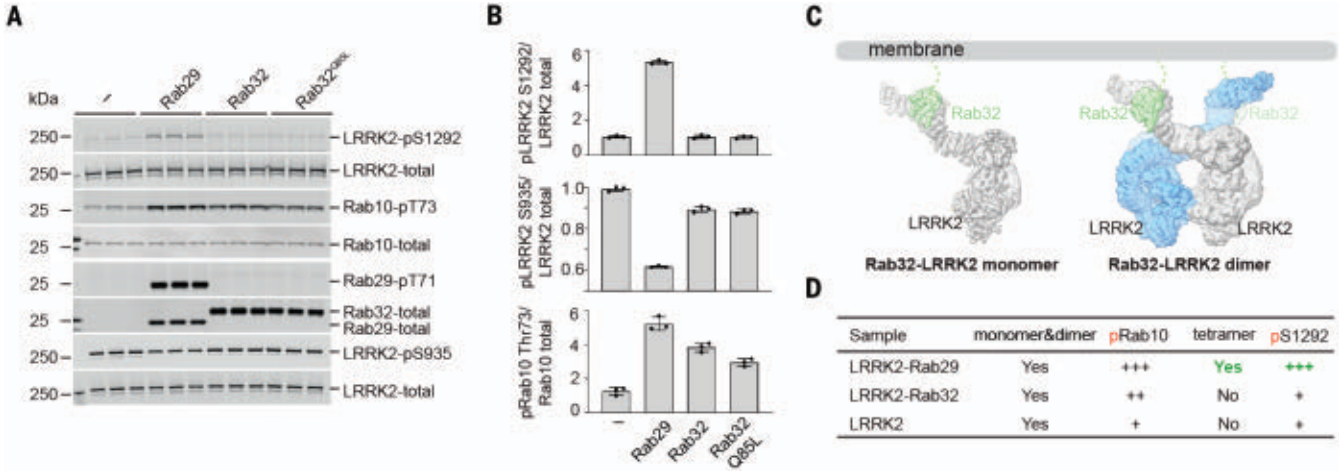

Fig. 6. Rab29-LRRK2 tetramer and kinase activation. (**A** and **B**) Quantitative immunoblotting analysis of the cellular kinase activity of LRRK2 in the presence of Rab29 or Rab32. HEK293 cells were transiently cotransfected with WT LRRK2 and hemagglutinin (HA)–tagged empty vector ("–"), HA-tagged Rab29, or HA-tagged Rab32 (WT or Q85L mutant). Data are presented as ratios of pLRRK2-Ser^{1292}/total LRRK2, pRab10-Thr^{73}/total Rab10, and pLRRK2-Ser^{935}/total LRRK2, normalized to the average of LRRK2 WT values. The data shown are the mean ± SD of three determinations. (**C**) Cryo-EM maps of the Rab32–LRRK2 complex. (**D**) Summary of LRRK2 kinase activity and LRRK2 states observed in the cryo-EM study of LRRK2 alone, in the presence of Rab32, or in the presence of Rab29.

in patients with *LRRK2* mutations. It would also be interesting to examine the Ser^{1292} autophosphorylation in PD patients with *PARK16* variations.

LRRK2 activation features a striking dimer-of-asymmetric dimer assembly containing two active core subunits encased by two inactive peripheral protomers. Intermolecular interactions between two asymmetric LRRK2 dimers stabilize the active Rab29–LRRK2 tetramer (Fig. 3, A to D). The formation of active tetramers is Rab29-dependent because such an assembly was not observed with Rab32 or without Rab29 under similar experimental conditions (Fig. 6, C and D) (*10*). Furthermore, Rab29 binding to the extended ARM-ANK-LRR portion of LRRK2^{cent} appears to unlock or facilitate LRRK2^{cent} activation (fig. S5A). However, the low resolution of LRRK2^{cent} ARM-ANK-LRR domains prevents us from dissecting these putative mechanisms in atomic details. Nevertheless, this Rab29- and oligomerization-controlled asymmetric activation of LRRK2 adds a new mode of kinase asymmetric activation, currently represented by EGFR (*51*), IRAK4 (*52*), and B-Raf (*53*, *54*).

Lastly, LRRK2 activation is clearly a complex process and could be achieved by other mechanisms, such as lipid oxidation, Rab12, and microtubule-based filamentation (*11*, *12*, *55*–*58*). This study focuses on Rab29-induced LRRK2 activation and provides a framework for interpreting disease mutations in the context of kinase activation. Our data suggest that allosteric inhibition of LRRK2 could be potentially achieved by disrupting Rab29–LRRK2 interaction, blocking LRRK2 oligomerization, or preventing the conformational transition from the inactive to the active states. Thus, our findings provide novel insights into LRRK2-based drug development and PD treatment.

REFERENCES AND NOTES

1. A. J. Lees, J. Hardy, T. Revesz, *Lancet* **373**, 2055–2066 (2009).
2. E. Tolosa, M. Vila, C. Klein, O. Rascol, *Nat. Rev. Neurol.* **16**, 97–107 (2020).
3. C. Paisán-Ruíz *et al.*, *Neuron* **44**, 595–600 (2004).
4. A. Zimprich *et al.*, *Neuron* **44**, 601–607 (2004).
5. M. B. Ramírez *et al.*, *Curr. Protein Pept. Sci.* **18**, 677–686 (2017).
6. N. Bryant *et al.*, *Hum. Mol. Genet.* **30**, 454–466 (2021).
7. A. F. Kalogeropulou *et al.*, *Biochem. J.* **479**, 1759–1783 (2022).
8. A. Usmani, F. Shavarebi, A. Hiniker, *Mol. Cell. Biol.* **41**, e00660–20 (2021).
9. C. K. Deniston *et al.*, *Nature* **588**, 344–349 (2020).
10. A. Myasnikov *et al.*, *Cell* **184**, 3519–3527.e10 (2021).
11. R. Watanabe *et al.*, *Cell* **182**, 1508–1518.e16 (2020).
12. D. M. Snead *et al.*, *Nat. Struct. Mol. Biol.* **29**, 1196–1207 (2022).
13. J. H. Weng *et al.*, *J. Mol. Biol.* **435**, 167999 (2023).
14. J. H. Weng *et al.*, *ACS Chem. Biol.* **18**, 810–821 (2023).
15. J. H. Weng *et al.*, *PLOS Biol.* **20**, e3001427 (2022).
16. S. H. Schmidt *et al.*, *Proc. Natl. Acad. Sci. U.S.A.* **118**, e2100844118 (2021).
17. S. R. Pfeffer, *FEBS Lett.* **597**, 811–818 (2023).
18. S. R. Pfeffer, *Biochem. Soc. Trans.* **46**, 1707–1712 (2018).
19. T. Kuwahara, T. Iwatsubo, *Front. Neurosci.* **14**, 227 (2020).
20. K. Ebanks, P. A. Lewis, R. Bandopadhyay, *Front. Neurosci.* **13**, 1381 (2020).
21. A. F. Kalogeropulou *et al.*, *Biochem. J.* **477**, 4397–4423 (2020).
22. T. Kuwahara *et al.*, *Sci. Rep.* **6**, 29945 (2016).
23. T. Fujimoto *et al.*, *Biochem. Biophys. Res. Commun.* **495**, 1708–1715 (2018).
24. Z. Liu *et al.*, *Hum. Mol. Genet.* **27**, 385–395 (2018).
25. E. McGrath, D. Waschbüsch, B. M. Baker, A. R. Khan, *Small GTPases* **12**, 133–146 (2021).
26. A. Beilina *et al.*, *Proc. Natl. Acad. Sci. U.S.A.* **111**, 2626–2631 (2014).
27. D. A. MacLeod *et al.*, *Neuron* **77**, 425–439 (2013).
28. E. Purlyte *et al.*, *EMBO J.* **37**, 1–18 (2018).
29. D. C. Berwick, G. R. Heaton, S. Azeggagh, K. Harvey, *Mol. Neurodegener.* **14**, 49 (2019).
30. R. C. Gomez, P. Wawro, P. Lis, D. R. Alessi, S. R. Pfeffer, *J. Cell Biol.* **218**, 4157–4170 (2019).
31. D. Waschbüsch *et al.*, *PLOS ONE* **9**, e111632 (2014).
32. O. Pylypenko, H. Hammich, I. M. Yu, A. Houdusse, *Small GTPases* **9**, 22–48 (2018).
33. E. G. Vides *et al.*, *eLife* **11**, e79771 (2022).
34. M. Steger *et al.*, *eLife* **6**, e31012 (2017).
35. S. S. Taylor *et al.*, *Front. Mol. Neurosci.* **13**, 538219 (2020).
36. A. Biosa *et al.*, *Hum. Mol. Genet.* **22**, 1140–1156 (2013).
37. J. M. Taymans *et al.*, *PLOS ONE* **6**, e23207 (2011).
38. A. B. West *et al.*, *Hum. Mol. Genet.* **16**, 223–232 (2007).
39. G. Ito *et al.*, *Biochemistry* **46**, 1380–1388 (2007).
40. D. Jennings *et al.*, *Sci. Transl. Med.* **14**, eabj2658 (2022).
41. A. Tasegian, F. Singh, I. G. Ganley, A. D. Reith, D. R. Alessi, *Biochem. J.* **478**, 3555–3573 (2021).
42. P. Rivero-Ríos, M. Romo-Lozano, B. Fernández, E. Fdez, S. Hilfiker, *Cells* **9**, 1719 (2020).
43. A. Fellgett *et al.*, *J. Parkinsons Dis.* **11**, 1805–1820 (2021).
44. A. Unapanta *et al.*, *J. Biol. Chem.* **299**, 105192 (2023).
45. K. V. Christensen *et al.*, LRRK2 exonic variants associated with Parkinson's disease augment phosphorylation levels for LRRK2-Ser1292 and Rab10-Thr73. bioRxiv 447946 [Preprint] (2018). https://doi.org/10.1101/447946.
46. Y. Fan *et al.*, *Acta Neuropathol.* **142**, 475–494 (2021).
47. Y. Fan *et al.*, *Biochem. J.* **475**, 23–44 (2018).
48. A. Garrido *et al.*, *Mov. Disord.* **37**, 1004–1015 (2022).
49. F. Atashrazm *et al.*, *Mov. Disord.* **34**, 406–415 (2019).
50. Ö. Karayel *et al.*, *Mol. Cell. Proteomics* **19**, 1546–1560 (2020).
51. X. Zhang, J. Gureasko, K. Shen, P. A. Cole, J. Kuriyan, *Cell* **125**, 1137–1149 (2006).
52. R. Ferrao *et al.*, *Mol. Cell* **55**, 891–903 (2014).
53. Y. Kondo *et al.*, *Science* **366**, 109–115 (2019).
54. E. Park *et al.*, *Nature* **575**, 545–550 (2019).
55. S. H. Schmidt *et al.*, *Proc. Natl. Acad. Sci. U.S.A.* **116**, 14979–14988 (2019).
56. V. V. Bondar *et al.*, Rab12 regulates LRRK2 activity by promoting its localization to lysosomes. bioRxiv 2023.02.21.529466 [Preprint] (2023). https://doi.org/10.1101/2023.02.21.529466.
57. H. S. Dhekne *et al.*, Genome-wide screen reveals Rab12 GTPase as a critical activator of pathogenic LRRK2 kinase. bioRxiv 2023.02.17.529028 [Preprint] (2023). https://doi.org/10.1101/2023.02.17.529028
58. R. Di Maio *et al.*, *Sci. Transl. Med.* **10**, eaar5429 (2018).
59. F. Tonelli, Structural basis of LRRK2 membrane recruitment and activation, Version v2, Zenodo (2023); https://doi.org/10.5281/zenodo.7601062

ACKNOWLEDGMENTS

We thank the support of the Cryo-Electron Microscopy Center at St. Jude Children's Research Hospital for help with cryo-EM data collection, members of the Sun lab for helpful discussion, P. Hixson for cell-culture support, M. Esmaili for initial setup of the kinase inhibition assay and P. Hixson for cross validation, N. Luo for illustrations, and I. Chen and J. Payandeh for valuable inputs for manuscript preparation. We thank the excellent technical support

of the Medical Research Council (MRC) Protein Phosphorylation and Ubiquitylation Unit (PPU) DNA cloning team (coordinated by R. Toth), sequencing service (coordinated by G. Hunter), and tissue culture team (coordinated by E. Allen). We also want to thank P. Lis and the MRC PPU at the University of Dundee for their help in preparing the confocal microscopy images. **Funding:** This work was funded by the American Lebanese Syrian Associated Charities (ALSAC), NIH (R00HL143037 and R01NS129795), the UK MRC (MC_UU_00018/1), and Aligning Science Across Parkinson's (ASAP). This research was funded in part by ASAP [ASAP-000463] through the Michael J. Fox Foundation for Parkinson's Research (MJFF) to D.R.A. **Author contributions:** H.Z. and J.S. designed the project. H.Z. performed sample preparation, biochemical analysis, and structural determination. F.T. designed, performed, and analyzed the cellular assays. F.T. and D.R.A. interpreted the activity assays. A.P. acquired and quantified the confocal microscopy images blindly. H.Z. optimized and performed the kinase inhibition assay. M.T. performed the 2D classification cross-correlation analysis. All authors were involved in data analysis. H.Z. and J.S. wrote the manuscript with input from all authors. **Competing interests:** The authors declare that they have no competing interests. **Data and materials availability:** The cryo-EM maps of Rab29-LRRK2 monomer, dimer, tetramers and LRRK2^{RCKW}-DNL201 complexes have been deposited in the Electron Microscopy Data Bank under accession codes EMD-29339, EMD-29341, EMD-29342, and EMD-40588. The corresponding coordinates have been deposited in the Protein Data Bank under accession codes 8FO2, 8FO8, 8FO9, and 8SMC, respectively. Raw micrographs of the Rab29-LRRK2 complex have been deposited in the Electron Microscopy Public Image Archive (EMPIAR) with accession code 47485217. Plasmids encoding constructs used for cryo-EM in this study are available upon request. All the primary immunoblotting and confocal microscopy data that are presented in this study have been deposited at Zenodo (*59*). Plasmids and antibodies (and associated datasheets) generated at the MRC PPU at the University of Dundee can be requested through our website: https://mrcppureagents.dundee.ac.uk/. **License information:** Copyright © 2023 the authors, some rights reserved; exclusive licensee American Association for the Advancement of Science. No claim to original US government works. https://www.science.org/about/science-licenses-journal-article-reuse. This research was funded in whole or in part by UK Medical Research Council (MC_UU_00018/1). The author will make the Author Accepted Manuscript (AAM) version available under a CC BY public copyright license.

SUPPLEMENTARY MATERIALS

science.org/doi/10.1126/science.adi9926
Materials and Methods
Figs. S1 to S11
Table S1
Movies S1 and S2
References (*60*–*72*)
MDAR Reproducibility Checklist

Submitted 30 May 2023; accepted 16 November 2023
10.1126/science.adi9926

ASTROCHEMISTRY

Polycyclic aromatic hydrocarbons in samples of Ryugu formed in the interstellar medium

Sarah S. Zeichner[1]*, José C. Aponte[2], Surjyendu Bhattacharjee[1], Guannan Dong[1], Amy E. Hofmann[1,3], Jason P. Dworkin[2], Daniel P. Glavin[2], Jamie E. Elsila[2], Heather V. Graham[2], Hiroshi Naraoka[4], Yoshinori Takano[5], Shogo Tachibana[6,7], Allison T. Karp[8,9,10], Kliti Grice[11], Alex I. Holman[11], Katherine H. Freeman[8], Hisayoshi Yurimoto[12], Tomoki Nakamura[13], Takaaki Noguchi[14], Ryuji Okazaki[4], Hikaru Yabuta[15]†, Kanako Sakamoto[7], Toru Yada[7], Masahiro Nishimura[7], Aiko Nakato[7], Akiko Miyazaki[7], Kasumi Yogata[7], Masanao Abe[7,16], Tatsuaki Okada[6,17], Tomohiro Usui[6,7], Makoto Yoshikawa[7,16] Takanao Saiki[7], Satoshi Tanaka[7,16], Fuyuto Terui[18], Satoru Nakazawa[7], Sei-ichiro Watanabe[19], Yuichi Tsuda[7], Kenji Hamase[20], Kazuhiko Fukushima[21], Dan Aoki[21], Minako Hashiguchi[19], Hajime Mita[22], Yoshito Chikaraishi[23], Naohiko Ohkouchi[5], Nanako O. Ogawa[5], Saburo Sakai[5], Eric T. Parker[2], Hannah L. McLain[2], Francois-Regis Orthous-Daunay[24], Véronique Vuitton[24], Cédric Wolters[24], Philippe Schmitt-Kopplin[25,26,27], Norbert Hertkorn[25,28], Roland Thissen[29], Alexander Ruf[30,31,32], Junko Isa[33, 34], Yasuhiro Oba[23], Toshiki Koga[5], Toshihiro Yoshimura[5], Daisuke Araoka[35], Haruna Sugahara[7], Aogu Furusho[36]‡, Yoshihiro Furukawa[13], Junken Aoki[37], Kuniyuki Kano[37], Shin-ichiro M. Nomura[38], Kazunori Sasaki[39,40], Hajime Sato[40], Takaaki Yoshikawa[41], Satoru Tanaka[42], Mayu Morita[42], Morihiko Onose[42], Fumie Kabashima[43], Kosuke Fujishima[33,44], Tomoya Yamazaki[23], Yuki Kimura[23], John M. Eiler[1]

Polycyclic aromatic hydrocarbons (PAHs) contain ≲20% of the carbon in the interstellar medium. They are potentially produced in circumstellar environments (at temperatures ≳1000 kelvin), by reactions within cold (~10 kelvin) interstellar clouds, or by processing of carbon-rich dust grains. We report isotopic properties of PAHs extracted from samples of the asteroid Ryugu and the meteorite Murchison. The doubly-^{13}C substituted compositions ($\Delta 2\times^{13}$C values) of the PAHs naphthalene, fluoranthene, and pyrene are 9 to 51‰ higher than values expected for a stochastic distribution of isotopes. The $\Delta 2\times^{13}$C values are higher than expected if the PAHs formed in a circumstellar environment, but consistent with formation in the interstellar medium. By contrast, the PAHs phenanthrene and anthracene in Ryugu samples have $\Delta 2\times^{13}$C values consistent with formation by higher-temperature reactions.

Polycyclic aromatic hydrocarbons (PAHs)—organic molecules consisting of multiple aromatic rings—are ubiquitous in the interstellar medium (ISM). Based on observations of mid-infrared emission bands in the ISM, PAHs are present in abundances ~10^{-7} times that of hydrogen (*1*). PAHs are estimated to contain ≲20% of the carbon atoms in the ISM of the Milky Way (*1*, *2*) and other galaxies (*3*). PAHs have been proposed as building blocks of carbon-rich dust grains, which are abundant in the ISM (*4*), and of higher molecular weight–insoluble organic material (IOM) that comprises most of the carbon within meteorites (*5*). However, it is unknown which chemical processes produce these forms of reduced carbon or where they occur (Fig. 1) (*6*).

Small aromatic organics, such as PAHs containing only a few rings, can form through reactions of free radicals in the gas phase, particularly the hydrogen-abstraction-carbon-addition (HACA) reaction mechanism, which is expected to occur in hot (>1000 K) circumstellar environments around carbon-rich asymptotic giant branch (AGB) stars and on Earth by combustion (Fig. 1A) (*6*). Carbon-rich dust grains and IOM could potentially be formed through similar processes. However, the reaction rates of these high-temperature mechanisms are too slow to account for the amount of PAHs present within the ISM and there is no complete model of the synthesis of PAHs within the outflows of AGB stars (*6*, *7*).

PAHs could also be formed through the breakdown of carbon-rich dust grains by shock waves, cosmic rays, or ultraviolet photolysis (*8*). However, these same processes destroy PAHs (Fig. 1B). This destruction occurs on time scales (*9*, *10*) that are shorter than those expected for production of PAHs in circumstellar envelopes of AGB stars (*11*, *12*).

A third location where PAHs could form is in cold (~10 K) molecular clouds within the ISM, through either ion-molecule reactions (*13*), or rapid barrierless reactions involving radicals (Fig. 1C) (*7*). Laboratory experiments have characterized these chemical mechanisms but it is difficult to directly observe specific PAH molecules within interstellar molecular clouds using spectroscopic methods. The only species that have been identified within molecular clouds are nitriles derived from PAHs: benzonitrile (*14*) and cyanonaphthalenes (*15*). Therefore, it is unlikely that circumstellar synthesis dominates the formation of extraterrestrial PAHs, but there is little evidence for interstellar formation either.

Later secondary processing reactions within a parent body—the asteroid or other Solar System object that meteorites originate from—could also synthesize PAHs or alter their composition. These reactions are often related to aqueous alteration, the modification of solid material by reactions with liquid water, which is known to have occurred on parent bodies. Potential secondary reactions include Fischer-Trospch-type (FTT) synthesis of alkanes from carbon monoxide (CO) (*16*) followed by aromatization; exchange with dissolved inorganic carbon (DIC) (*17*) or aqueous H_2; or the breakdown of IOM into smaller organic molecules

by catagenesis (*18*), which thermally cracks large organic molecules (on Earth this forms oil and gas deposits).

Soluble PAHs have been studied in samples of carbonaceous chondrite (CC) meteorites but as a result of the terrestrial exposure of meteorite samples, it is possible that endogenous PAHs in meteorites could be contaminated with PAHs formed on Earth. Samples of the near-Earth carbonaceous asteroid (162173) Ryugu were collected by the Hayabusa2 spacecraft under controlled conditions, and so underwent fewer opportunities for terrestrial contamination. We studied the isotopic properties of PAHs in the CC meteorite Murchison and a sample of Ryugu to investigate PAH formation processes.

Principles of isotope analysis

The rare-isotope distributions of organic molecules can be used to constrain the source, substrate, and chemical mechanisms responsible for their formation (*19*, *20*). The molecular-average $^{13}C/^{12}C$ and D/H ratios of organic molecules are conventionally reported as $\delta^{13}C_{VPDB}$ and δD_{VSMOW}, respectively, where δ notation is defined in equation S7, and VPDB and VSMOW are standard reference scales (*21*). Measured isotope ratios of extraterrestrial organics are often outside the ranges of ratios measured in terrestrial organics. Some extraterrestrial organic molecules such as amino acids (*22*) are enriched in ^{13}C and have been interpreted as products of precursor molecules that were themselves derived from a reservoir of CO in the ISM that was enriched in ^{13}C (*23*, *24*). By contrast, interstellar PAHs exhibit only small ^{13}C enrichments, consistent with formation in a range of extraterrestrial environments. Heterogeneities in the carbon isotope compositions of interstellar, circumstellar, and parent body carbon reservoirs prevent unique interpretation of such data (Fig. 1).

Multiple substitutions of heavy isotopes within molecules (hereafter referred to as clumping)

Table 1. PAH abundance and isotope ratio measurements. $\delta^{13}C_{VPDB}$, δD_{VSMOW}, $2\times^{13}C/^{12}C$ ratios, and $\Delta 2\times^{13}C$ values of PAHs extracted from Ryugu samples A0106 and C0107, the Murchison (Murch) meteorite, and terrestrial standards. $\delta^{13}C_{VPDB}$, δD_{VSMOW}, and $\Delta 2\times^{13}C$ values are reported in units of ‰. The number of replicate analyses, *n*, is included in parentheses (*21*). σ is the standard error propagated in quadrature (*21*). All uncertainties on the abundances of PAHs in Ryugu samples are 25% (*21*).

Compound	Abundances of PAHs in Ryugu samples/ppm		$\delta^{13}C_{VPDB} \pm \sigma$ (*n*)				$\delta D_{VSMOW} \pm \sigma$ (*n*)		$2\times^{13}C/^{12}C \pm \sigma$ (*n*)			$\Delta 2\times^{13}C \pm \sigma$ (*n*)	
	Ryugu A0106	Ryugu C0107	Terrestrial standard	Ryugu A0106	Ryugu C0107	Murch	Terrestrial standard	Ryugu C0107	Terrestrial standard	Ryugu C0107	Murch	Ryugu C0107	Murch
Naphthalene	0.20	0.06	−23.8 ± 0.5 (2)	−27.5 ± 24.6 (2)	−20.3 ± 4.9 (3)	-	−67.3 ± 0.4 (3)	−7.2 ± 36.0 (4)	0.0048 ± 0.0060 (7)	0.0050 ± 0.0107 (7)	-	35 ± 20 (7)	-
Phenanthrene	0.33	0.04	−24.4 ± 0.6 (2)	−14.9 ± 6.9 (2)	−12.6 ± 4.2 (3)	-	−115.0 ± 1.1 (3)	−458.9 ± 31.0 (4)	0.0095 ± 0.0046 (7)	0.0097 ± 0.0066 (7)	-	−4 ± 10 (7)	-
Anthracene	0.15	0.04	−24.1 ± 0.5 (2)	−10.5 ± 0.5 (2)	−16.7 ± 4.5 (3)	-	−98.4 ± 0.7 (6)	−581.3 ± 41.2 (4)	0.0095 ± 0.0043 (7)	0.0097 ± 0.0088 (7)	-	3 ± 10 (7)	-
Fluoranthene	1.33	0.30	−24.2 ± 0.4 (2)	−27.1 ± 9.8 (2)	−17.1 ± 2.5 (3)	−9.9 ± 1.0 (3)	−102.0 ± 1.1 (6)	−137.0 ± 18.9 (4)	0.0122 ± 0.0025 (7)	0.0125 ± 0.0050 (7)	0.0133 ± 0.008 (3)	9 ± 5 (7)	51 ± 13
Pyrene	6.19	1.13	−25.2 ± 0.5 (2)	−29.6 ± 1.3 (2)	−23.6 ± 2.1 (3)	−11.3 ± 1.1 (3)	−66.8 ± 1.0 (6)	−68.0 ± 15.3 (4)	0.0122 ± 0.0023 (7)	0.0124 ± 0.0039 (7)	0.0126 ± 0.009 (7)	11 ± 4 (7)	1 ± 13

[1]Geological and Planetary Science Division, California Institute of Technology, Pasadena, CA 91125, USA. [2]Solar System Exploration Division, NASA Goddard Space Flight Center, Greenbelt, MD 20771, USA. [3]Jet Propulsion Laboratory, California Institute of Technology, Pasadena, CA 91109, USA. [4]Department of Earth and Planetary Sciences, Kyushu University, Fukuoka 819-0395, Japan. [5]Biogeochemistry Research Center, Japanese Agency for Marine-Earth Science and Technology, Yokosuka, Kanagawa 237-0061, Japan. [6]Department of Earth and Planetary Science, University of Tokyo, Tokyo 113-0033, Japan. [7]Institute of Space and Astronautical Science, Japan Aerospace Exploration Agency, Sagamihara 252-5210, Japan. [8]Department of Geosciences, The Pennsylvania State University, University Park, PA 16802, USA. [9]Ecology and Evolutionary Biology Department, Yale University, New Haven, CT, USA. [10]Department of Environmental, Earth, and Planetary Sciences, Brown University, Providence, RI 02912, USA. [11]Western Australia Organic & Isotope Geochemistry Centre, The Institute for Geoscience Research, School of Earth and Planetary Sciences, Curtin University, Perth, Western Australia 6102, Australia. [12]Department of Earth and Planetary Sciences, Hokkaido University, Sapporo 060-0810, Japan. [13]Department of Earth Science, Tohoku University, Sendai 980-8578, Japan. [14]Division of Earth and Planetary Sciences, Kyoto University, Kyoto 606-8502, Japan. [15]Department of Earth and Planetary Systems Science, Hiroshima University, Higashi-Hiroshima 739-8526, Japan. [16]School of Physical Sciences, The Graduate University for Advanced Studies, Hayama 240-0193, Japan. [17]Department of Chemistry, University of Tokyo, Tokyo 113-0033, Japan. [18]Department of Mechanical Engineering, Kanagawa Institute of Technology, Atsugi 243-0292, Japan. [19]Graduate School of Environmental Studies, Nagoya University, Nagoya 464-8601, Japan. [20]Graduate School of Pharmaceutical Sciences, Kyushu University, Fukuoka 812-8582, Japan. [21]Graduate School of Bioagricultural Sciences, Nagoya University, Nagoya 464-8601, Japan. [22]Department of Life, Environment and Material Science, Fukuoka Institute of Technology, Fukuoka 811-0295, Japan. [23]Institute of Low Temperature Science, Hokkaido University, Sapporo 060-0189, Japan. [24]Institut de Planétologie et d'Astrophysique de Grenoble, Université Grenoble Alpes, Centre National de la Recherche Scientifique, 38000 Grenoble, France. [25]Analytical BioGeoChemistry, Helmholtz Zentrum München, 85764 Neuherberg, Germany. [26]Technische Universität München, Analytische Lebensmittel Chemie, 85354 Freising, Germany. [27]Max Planck Institute for Extraterrestrial Physics, 85748 Garching bei München, Germany. [28]Department of Thematic Studies, Environmental Sciences, Linköping University, 58183 Linköping, Sweden. [29]Institut de Chimie Physique, Université Paris-Saclay, Centre National de la Recherche Scientifique, 91405 Orsay, France. [30]Laboratoire de Physique des Interactions Ioniques et Moléculaires, Université Aix-Marseille, Centre National de la Recherche Scientifique, 13397 Marseille, France. [31]Faculty of Physics, Ludwig-Maximilians-University, 80799 Munich, Germany. [32]Excellence Cluster Origins, 85748 Garching, Germany. [33]Earth-Life Science Institute, Tokyo Institute of Technology, Tokyo 1528550, Japan. [34]Planetary Exploration Research Center, Chiba Institute of Technology, Narashino 275-0016, Japan. [35]Geological Survey of Japan, National Institute of Advanced Industrial Science and Technology, Tsukuba, Ibaraki 305-8567, Japan. [36]Graduate School of Pharmaceutical Sciences, Kyushu University, Fukuoka 819-0395, Japan. [37]Graduate School of Pharmaceutical Sciences, University of Tokyo, Tokyo 113-0033, Japan. [38]Department of Robotics, Tohoku University, Sendai 980-8578, Japan. [39]Human Metabolome Technologies Inc., Kakuganji, Tsuruoka, Yamagata, 997-0052, Japan. [40]Institute for Advanced Biosciences, Keio University, Kakuganji, Tsuruoka, Yamagata 997-0052, Japan. [41]Horiba Advanced Technologies Co. Ltd., Kisshoin, Minami-ku, Kyoto 601-8510, Japan. [42]Horiba Technology Services Co. Ltd., Kisshoin, Minami-ku, Kyoto 601-8510, Japan. [43]Laboratory Equipment Corporation Japan, Tokyo 105-0014, Japan. [44]Graduate School of Media and Governance, Keio University, Fujisawa, Kanagawa 252-0882, Japan.

***Corresponding author. Email: szeichner@caltech.edu**

†Present address: International Institute for Sustainability with Knotted Chiral Meta Matter, Hiroshima University, Hiroshima 739-8526, Japan.

‡Present address: School of Pharmaceutical Sciences, University of Shizuoka, Shizuoka 422-8526, Japan.

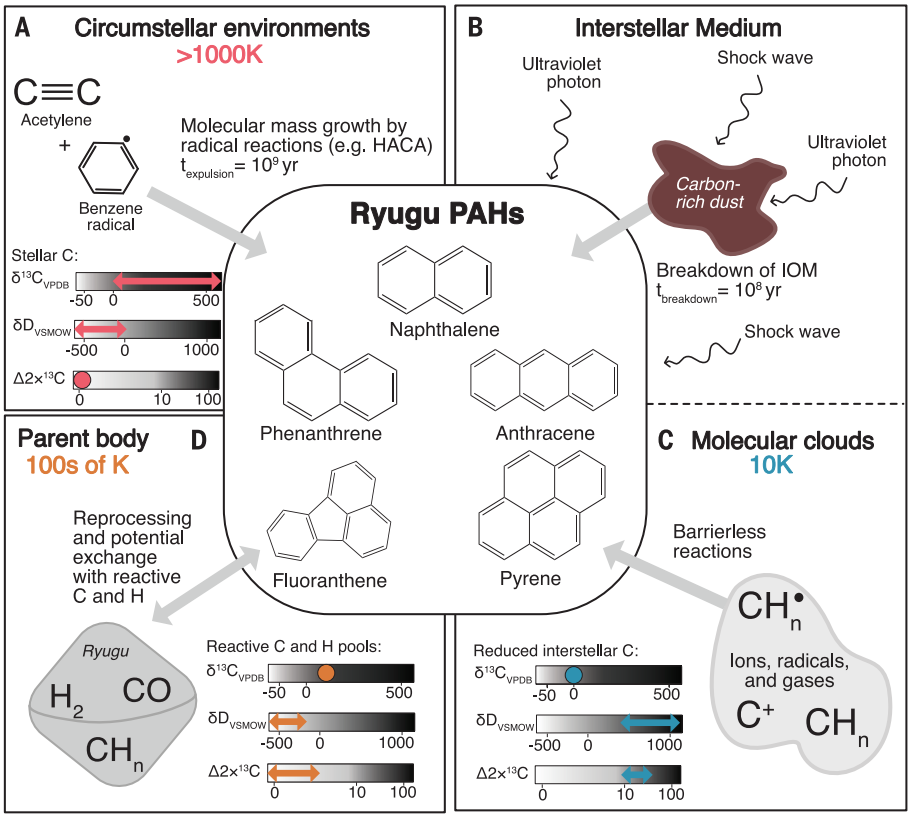

Fig. 1. Potential pathways for extraterrestrial PAH formation. The central inset shows the molecular structures of the five PAHs we investigated. The surrounding panels schematically illustrate potential formation pathways for those PAHs. In (**A**), (**C**), and (**D**), grayscale color bars show $\delta^{13}C_{VPDB}$, δD_{VSMOW}, and $\Delta 2\times^{13}C$ values measured or predicted in extraterrestrial materials. White is isotopically depleted and black is isotopically enriched. Dots and arrows indicate values and ranges, respectively, of the source carbon and hydrogen. $\Delta 2\times^{13}C$ values are estimated predictions (*21*) based on model results (Fig. 2), see text. (A) PAH formation in hot (≳1000 K, red) circumstellar environments by molecular mass growth reactions (*6*, *11*). $\delta^{13}C_{VPDB}$ values in AGB stars are expected to range from 0 to hundreds of per-mille depending on the stellar evolution (*35*, *36*). δD_{VSMOW} values are expected to be low or zero as a result of the fusion of D in stars (*35*, *36*). $t_{expulsion}$ is the time scale for PAH expulsion from stellar envelopes. (**B**) Shock waves and ultraviolet radiation form PAHs by breaking down carbon-rich dust but also destroy them. $t_{breakdown}$ is the time scale for PAH breakdown in the ISM. (C) PAH formation in cold (10 K, blue) interstellar environments through barrierless reactions (*6*, *12*). Reduced carbon in molecular clouds is depleted in ^{13}C compared with interstellar CO (*47*), whereas interstellar hydrogen is typically D-enriched (*33*). (D) PAH formation or modification on a parent body at moderate temperatures (100s of K, orange). Isotopic exchange can occur with carbon reservoirs such as CO and DIC, and hydrogen reservoirs such as H_2. Murchison carbonate has $\delta^{13}C_{VPDB}$ values of +20 to +80‰ (*48*) whereas the water in parent bodies of CC meteorites has been found to be D-depleted (*40*, *42*).

reflect temperature-dependent chemical reactions and physical processes (*19*) thus providing additional information on a given molecule's source and formation/degradation history. For any given molecular-average $\delta^{13}C_{VPDB}$ value of PAHs, a smaller proportion of each molecule is doubly-^{13}C substituted (denoted $2\times^{13}C$). We report the ratio '$2\times^{13}C/^{12}C$' of clumped ^{13}C isotopologues to the unsubstituted isotopologues as well as the differences—$\Delta 2\times^{13}C$—between the measured $2\times^{13}C/^{12}C$ ratios and the expected stochastic $2\times^{13}C/^{12}C$ ratios. Expected $2\times^{13}C/^{12}C$ ratios are calculated based on the random probability of a double-^{13}C-substitution given its molecular-average ^{13}C abundance (*21*). A formation process that leads to a higher (lower) number of heavy isotope substitutions than the stochastic expectation leads to a positive (negative) $\Delta 2\times^{13}C$ value.

Variations in $2\times^{13}C$ clumping can be temperature-dependent because heavy isotopic substitution lowers the molecular vibrational energy (fig. S4) of the C-C bond and therefore stabilizes it. Isotopic clumping is therefore more energetically favored at lower temperatures. We used acetylene as a model compound to predict $2\times^{13}C$ clumping at different temperatures, because it is thought to be a precursor to the formation of interstellar aromatic reduced carbon (*25*) including

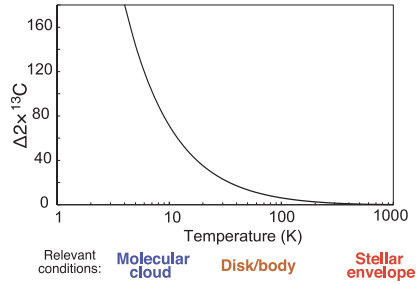

Fig. 2. Predicted $\Delta 2\times^{13}C$ values from our model. The black curve shows our theoretical calculations of the $\Delta 2\times^{13}C$ values expected for acetylene at different temperatures (*21*). Labels below the plot indicate the relevant environments at each temperature and use the same colors as Fig. 1.

PAHs (*26*, *27*) (Fig. 1A). The equilibrium exchange reaction between single and double-^{13}C substitution in acetylene is:

$$2\times^{13}C^{12}CH_2 \rightleftharpoons {}^{13}C_2H_2 + {}^{12}C_2H_2 \quad (1)$$

The products on the right-hand side of Eq. 1 are favored at all temperatures (Fig. 2) (*21*). We therefore predict that PAHs formed in the cold ISM have $\Delta 2\times^{13}C$ values substantially different from zero (positive if formed by reversible reactions; Figs. 1C and 2). By contrast, we expect PAHs formed in hot circumstellar envelopes or in the parent body to have $\Delta 2\times^{13}C$ close to zero (Figs. 1A and 2).

Isotopic measurements of PAH samples

The Hayabusa2 spacecraft collected 5.4 g of material from two locations on Ryugu (*28*). Previous analysis of Ryugu samples has demonstrated that Ryugu is compositionally similar to Ivuna-type carbonaceous (CI) meteorites (*29*). Soluble organic molecules previously have been extracted (*22*, *30*) from Ryugu samples A0106 and C0107, which are aggregates of submillimeter grains collected from the first and second touchdown sites, respectively (*22*, *28*). Endogenous, complex soluble aromatic organics have been identified among the compounds extracted from these samples using the solvent dichloromethane (DCM) (*30*). The molecules identified included several PAHs: the 2-ring naphthalene, 3-ring isomers phenanthrene and anthracene, and 4-ring isomers fluoranthene and pyrene. The total PAH abundances in the Ryugu samples (8.6 to 32.4 nmol g^{-1}; Table 1 and fig. S2) were too low for isotopic analysis using gas-source isotope ratio mass spectrometry (*22*, *30*).

We analyzed PAHs within the same DCM extracts of Ryugu as those previous studies (*22*, *30*) using gas chromatography coupled with Orbitrap mass spectrometry (GC-Orbitrap) (*31*). We measured the $\delta^{13}C_{VPDB}$ values of the five PAHs previously identified in Hayabusa2 sample A0106 and the $\delta^{13}C_{VPDB}$, δD_{VSMOW} and $\Delta 2\times^{13}C$

values of the same five PAHs from C0107 (*21*). We compared these measurements with those of fluoranthene and pyrene extracted from the CC meteorite Murchison (*21*, *31*). We also measured $\delta^{13}C_{VPDB}$ and $\Delta2\times^{13}C$ values of combusted plant biomass as a high-temperature comparison (*21*). As a control sample, we used a serpentine blank processed in parallel with the Ryugu samples and within this blank we detected no PAHs above the instrumental background (table S1). Measured isotope values are listed in Table 1 and plotted in Fig. 3.

We found elevated $\Delta2\times^{13}C$ values of 9 to 51‰ for naphthalene, fluoranthene, and pyrene from Ryugu and fluoranthene from Murchison, which significantly exceed the expected stochastic values (all *P*-values < 0.005) (*21*). The $\delta^{13}C_{VPDB}$ values are the same (within analytical uncertainties) for PAHs with even and odd numbers of rings in Ryugu and for fluoranthene and pyrene in Murchison. δD_{VSMOW} values for naphthalene, fluoranthene, and pyrene from Ryugu are 320 to 570‰ higher than Ryugu's phenanthrene and anthracene (Table 1).

Cold PAH formation processes

The $\Delta2\times^{13}C$ values we measured for naphthalene, fluoranthene, and pyrene from Ryugu and fluoranthene from Murchison are larger than previously measured $\Delta2\times^{13}C$ values of ethane formed by processes at Earth-surface conditions (~1‰) (*32*). These large positive anomalies are consistent with the hypothesis that some (or all) of these PAHs were synthesized within cold (<50 K) environments (Figs. 1C and 3, A and C) by means of a process that preferentially forms ^{13}C-^{13}C bonds. The clumped-^{13}C composition of all PAHs we measured is independent of molecular-average $\delta^{13}C_{VPDB}$ values, which span a narrow range. This is consistent with the low-temperature process that formed these PAHs having a high yield, such that the overall ^{13}C abundances of product PAHs approached those of the reactants. We expect PAHs formed within molecular clouds to have higher δD_{VSMOW} values than those of PAHs formed within other environments (Fig. 1C) (*33*) for the same chemical physics reasons that cause interstellar CO or acetylene to be enriched in ^{13}C or ^{13}C-clumping, respectively.

The highest $\Delta2\times^{13}C$ value we measure, 51 ± 13‰ for Murchison fluoranthene, is close to the acetylene equilibrium value at ~10 K, which we interpret as evidence that most of the fluoranthene in Murchison was synthesized in the ISM (*34*). We suggest that low-temperature reactions were responsible for both the initial formation of C-C bonds and the subsequent assembly of high-molecular-weight aromatic compounds from smaller molecules, because otherwise the assembly of larger structures would dilute the initial clumping. The $\Delta2\times^{13}C$ value of 4-ring fluoranthene from Murchison is higher than those of the 2- and 4-ring PAHs from Ryugu, which have positive but lower $\Delta2\times^{13}C$ values. We suggest three scenarios for Ryugu's 2- and 4-ring PAHs: (i) They could have formed at higher (but still low) temperatures than Murchison's fluoranthene, 20 to 50 K; (ii) they might be mixtures from two or more sources, with 20 to 50% formed in cold interstellar environments and the remainder formed (or reprocessed) at higher temperatures in other environments; (iii) they could have formed from 2- or 3-carbon precursors with large positive $\Delta2\times^{13}C$ values produced at low ISM temperatures, which were subsequently converted into larger aromatic molecules through reactions that diluted the initial $\Delta2\times^{13}C$ signature.

Hot PAH formation processes

Three of the extraterrestrial PAHs we examined have $\Delta2\times^{13}C$ values that are consistent with calculated stochastic values (*P*-values > 0.15) (*21*): the 3-ring PAHs phenanthrene and anthracene from Ryugu and 4-ring PAH pyrene from Murchison. We do not expect synthesis of PAHs at high temperatures to produce $\Delta2\times^{13}C$ values that can be distinguished from zero using our methods (*21*). We also measured no statistically significant (*P*-values > 0.04) deviations from the stochastic distributions of doubly-^{13}C-substituted species in the PAHs from combusted plant biomass (Fig. 3, B and C, and table S3) (*21*).

High-temperature processes that could have formed the 3-ring PAHs from Ryugu and pyrene from Murchison include: (i) condensation in the outflows of carbon-rich AGB stars through bottom-up synthesis, such as the HACA mechanism, or (ii) top-down catagenetic breakdown of larger carbonaceous dust grains. We expect that the formation of aromatic compounds

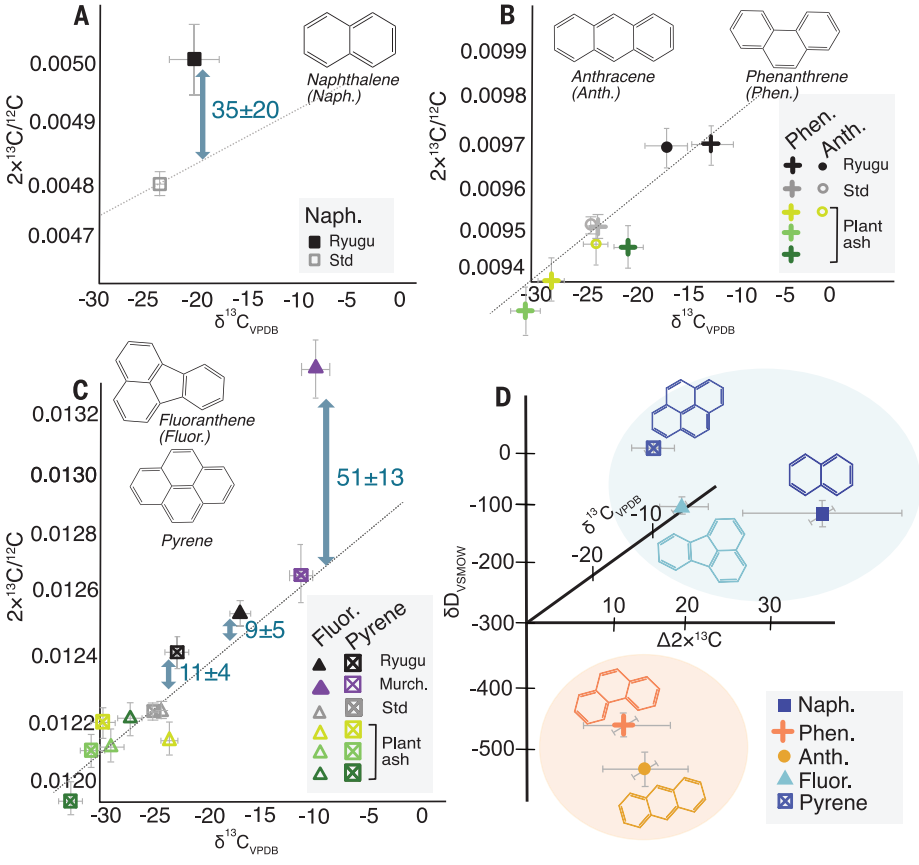

Fig. 3. ^{13}C clumping measured from PAHs in the Ryugu samples. $2\times^{13}C/^{12}C$ ratios are plotted as a function of $\delta^{13}C_{VPDB}$ for: (**A**) the 2-ring PAH naphthalene (black square); (**B**) 3-ring PAHs phenanthrene (black cross) and anthracene (black circle); and (**C**) 4-ring PAHs fluoranthene (black triangle) and pyrene (black open crossed square). Black symbols were measured from Ryugu sample C0107; terrestrial standards (Std) are shown with unfilled gray symbols. (C) includes measured values for Murchison (Murch) meteorite (purple symbols). Panels B and C include residues of combusted plants (green symbols) (*21*, *49*). Predicted stochastic distributions are plotted as dotted gray lines (*21*). Departures from stochasticity ($\Delta2\times^{13}C\pm\sigma$ values) are indicated with labeled blue arrows (*21*). All error bars are 1σ and numerical values are listed in Table 1 and table S3. (**D**) $\delta^{13}C_{VPDB}$, δD_{VSMOW}, and $\Delta2\times^{13}C$ values measured for all five PAHs (see legend) in the Ryugu samples. Blue and orange ovals indicate PAHs that we interpret as formed by interstellar and circumstellar/parent body processes, respectively.

by high-temperature processes in circumstellar environments would produce PAHs with high $\delta^{13}C_{VPDB}$ (*35*) and low δD_{VSMOW} values, due to the nuclear fusion of deuterium lowering its abundance, and the subsequent convective mixing of D-poor ashes from the core of the star to the outer layers (Fig. 1A) (*36*). This interpretation is consistent with our measurements of Ryugu phenanthrene and anthracene. A previous computational study of HACA formation of PAHs predicted an excess of the 3-ring PAHs phenanthrene and anthracene (compared with other PAHs with different numbers of rings) (*37*). Thus, PAHs formed by HACA could dominate the 3-ring species in Ryugu while making a small contribution to other PAH species.

Contributions from parent body processes

PAHs in Ryugu or Murchison samples that have $\Delta 2\times^{13}C$ values close to zero alternatively could have been formed or altered by secondary processes (Fig. 1D). Previous experiments that performed pyrolysis (reactions that simulate catagenesis), on meteoritic IOM formed the same 2-, 3-, and 4-ring PAHs that we found in A0106 and C0107, at temperatures experienced by Ryugu's parent body (<200°C) (*38*). FTT synthesis is a less likely explanation for these samples because FTT products such as alkanes are unlikely to undergo aromatization below 200°C (*39*).

We expect PAHs that formed on the parent body or experienced secondary processing to have low δD_{VSMOW} values (Fig. 1D). A previous experiment demonstrated that organic molecules formed under hydrothermal conditions from CO have δD_{VSMOW} values of −450 to −580‰ (*40*), which is consistent with the values we measured for phenanthrene and anthracene from Ryugu (Fig. 3B). Hydrogen atoms in PAHs that were formed by primary interstellar processes could exchange isotopes and equilibrate with the parent body water (*41*). Ryugu is known to have experienced aqueous alteration (*29*). Some CC meteorites are known to contain water depleted in D [including Murchison, which has δD_{VSMOW} ~−440‰ (*42*)], but the δD_{VSMOW} value of Ryugu parent body water is unknown. Carbon-rich grains in Ryugu samples have heterogeneous δD_{VSMOW} values, ranging from −1000‰ (no D detected) to +10,000‰ (*40*), indicating that parent body processes did not fully equilibrate hydrogen isotopic distributions in the Ryugu samples.

Formation of PAHs by means of synthesis in the parent body could explain the differences between the $\Delta 2\times^{13}C$ values of fluoranthene and pyrene from Murchison. Murchison is known to have experienced aqueous alteration, which is variable even among different chips of the same specimen (*43*). Our measurements show that fluoranthene—which is the metastable isomer of the two four-ring PAHs that we studied (*44*)—has $\Delta 2\times^{13}C$ of 51 ± 13‰, which is consistent with preferential ^{13}C-clumping at cold interstellar temperatures. Pyrene—the more stable isomer (*44*)—has $\Delta 2\times^{13}C$ values close to the stochastic distribution. Formation of PAHs under parent body conditions would be closer to thermodynamic equilibrium, favoring production of more stable isomers (pyrene is preferred to fluoranthene) (*45*). After mixing with preexisting PAHs formed through other pathways, the additional stable PAHs would dilute and potentially erase any preexisting interstellar isotopic fingerprints, such as ^{13}C clumping (see Supplementary Text).

Conclusions

We suggest that the diversity in $\delta^{13}C_{VPDB}$, δD_{VSMOW}, and $\Delta 2\times^{13}C$ values measured in PAHs from Ryugu and Murchison is consistent with PAHs being formed in at least two different settings (*21*, *46*). Most of the 2- and 4-ring PAHs were synthesized in cold interstellar environments whereas the other PAHs we measured (including the 3-ring PAHs) were formed by synthesis or reprocessing within high- to moderate-temperature settings, such as circumstellar environments or the parent body. The non-zero ^{13}C clumping was measured in multiple PAHs from two samples that have different histories of alteration, collection, and (potentially) formation. By extrapolation, we infer that a large fraction of extraterrestrial PAHs were formed by interstellar processes.

REFERENCES AND NOTES

1. A. G. G. M. Tielens, *Rev. Mod. Phys.* **85**, 1021–1081 (2013).
2. L. J. Allamandola, S. A. Sandford, B. Wopenka, *Science* **237**, 56–59 (1987).
3. J. D. T. Smith *et al*., *Astrophys. J.* **656**, 770–791 (2007).
4. B. T. Draine, *Astrophys. J.* **831**, 109 (2016).
5. A. G. G. M. Tielens, *Annu. Rev. Astron. Astrophys.* **46**, 289–337 (2008).
6. R. I. Kaiser, N. Hansen, *J. Phys. Chem. A* **125**, 3826–3840 (2021).
7. R. I. Kaiser, D. S. N. Parker, A. M. Mebel, *Annu. Rev. Phys. Chem.* **66**, 43–67 (2015).
8. J. E. Chiar, A. G. G. M. Tielens, A. J. Adamson, A. Ricca, *Astrophys. J.* **770**, 78 (2013).
9. E. R. Micelotta, A. P. Jones, A. G. G. M. Tielens, *Astron. Astrophys.* **510**, A36 (2010).
10. E. R. Micelotta, A. P. Jones, A. G. G. M. Tielens, *Astron. Astrophys.* **510**, A37 (2010).
11. M. Frenklach, E. D. Feigelson, *Astrophys. J.* **341**, 372–384 (1989).
12. S. Doddipatla *et al*., *Sci. Adv.* **7**, eabd4044 (2021).
13. O. Martinez Jr. *et al*., *Astrophys. J.* **686**, 1486–1492 (2008).
14. B. A. McGuire *et al*., *Science* **359**, 202–205 (2018).
15. B. A. McGuire *et al*., *Science* **371**, 1265–1269 (2021).
16. M. Zolotov, E. Shock, *J. Geophys. Res.* **104** (E6), 14033–14049 (1999).
17. H. V. Graham, J. E. Elsila, J. P. Dworkin, S. A. Sandford, J. C. Aponte, *Life* **12**, 1368 (2022).
18. K. Pehr *et al*., *Astrobiology* **21**, 1049–1075 (2021).
19. J. M. Eiler, *Annu. Rev. Earth Planet. Sci.* **41**, 411–441 (2013).
20. J. Bigeleisen, M. Wolfsberg, *Adv. Chem. Phys.* **1**, 15–76 (1957).
21. Materials and methods are available as supplementary materials.
22. H. Naraoka *et al*., *Science* **379**, eabn9033 (2023).
23. D. P. Glavin *et al*., in *Primitive Meteorites and Asteroids*, N. Abreu, Ed. (Elsevier, 2018), pp. 205–271.
24. J. E. Elsila, S. B. Charnley, A. S. Burton, D. P. Glavin, J. P. Dworkin, *Meteorit. Planet. Sci.* **47**, 1517–1536 (2012).
25. F. Lahuis, E. F. Van Dishoeck, *Astron. Astrophys.* **355**, 699–712 (2000).
26. M. J. Abplanalp, R. I. Kaiser, *Astrophys. J.* **889**, 3 (2020).
27. A. M. Mebel, A. Landera, R. I. Kaiser, *J. Phys. Chem. A* **121**, 901–926 (2017).
28. S. Tachibana *et al*., *Science* **375**, 1011–1016 (2022).
29. T. Yokoyama *et al*., *Science* **379**, eabn7850 (2023).
30. J. C. Aponte *et al*., *Earth Planets Space* **75**, 28 (2023).
31. S. S. Zeichner *et al*., *Int. J. Mass Spectrom.* **477**, 116848 (2022).
32. M. Clog *et al*., *Geochim. Cosmochim. Acta* **223**, 229–244 (2018).
33. S. A. Sandford, *Planet. Space Sci.* **50**, 1145–1154 (2002).
34. K. I. Öberg, *Chem. Rev.* **116**, 9631–9663 (2016).
35. C. Abia *et al*., *Publ. Astron. Soc. Aust.* **20**, 314–323 (2013).
36. M. Busso, R. Gallino, G. J. Wasserburg, *Annu. Rev. Astron. Astrophys.* **37**, 239–309 (1999).
37. V. V. Kislov, A. I. Sadovnikov, A. M. Mebel, *J. Phys. Chem. A* **117**, 4794–4816 (2013).
38. V. Vinogradoff *et al*., *Geochim. Cosmochim. Acta* **212**, 234–252 (2017).
39. H. Yabuta *et al*., *Science* **379**, eabn9057 (2023).
40. T. M. McCollom, B. S. Lollar, G. Lacrampe-Couloume, J. S. Seewald, *Geochim. Cosmochim. Acta* **74**, 2717–2740 (2010).
41. R. Alexander, R. I. Kagi, A. V. Larcher, *Geochim. Cosmochim. Acta* **46**, 219–222 (1982).
42. C. M. O. D. Alexander *et al*., *Science* **337**, 721–723 (2012).
43. C. M. O. D. Alexander, R. Bowden, M. L. Fogel, K. T. Howard, *Meteorit. Planet. Sci.* **50**, 810–833 (2015).
44. W.-K. Wong, E. F. Westrum Jr., *J. Chem. Thermodyn.* **3**, 105–124 (1971).
45. N. Thiagarajan *et al*., *Proc. Natl. Acad. Sci. U.S.A.* **117**, 3989–3995 (2020).
46. M. A. Sephton *et al*., *Astrobiology* **15**, 779–786 (2015).
47. M. A. Cordiner, M. Y. Palmer, S. B. Charnley, L. Paganini, G. Villanueva, *Astrophys. J. Lett.* **870**, L26 (2019).
48. M. A. Sephton, *Nat. Prod. Rep.* **19**, 292–311 (2002).
49. A. T. Karp, A. I. Holman, P. Hopper, K. Grice, K. H. Freeman, *Geochim. Cosmochim. Acta* **289**, 93–113 (2020).
50. S. Zeichner, szeichner/RyuguPAHs: Ryugu PAHs v1.0.7, v1.0.7, Zenodo (2022).

ACKNOWLEDGMENTS

We thank G. Blake, K. Oberg, L. Nittler, and L. Remusat for enlightening discussions. N. Kitchen, A. Sessions, and F. Wu provided invaluable experimental insights. T. Csernica, E. Mueller, G. Weiss, P. Martin, M. Lloyd, A. Hilkert, K. Ayzikov, and C. Neubauer contributed to the development of the data analysis software. We thank the project members of the Extraterrestrial Samples Curation Center (ESCuC) and the Astromaterials Science Research Group (ASRG) at Institute of Space and Astronautical Science (ISAS) for the sample processes. This project was supported by the Centre National d'Etudes Spatiales focus on Hayabusa2. The Jet Propulsion Laboratory is operated by the California Institute of Technology under contract with the National Aeronautics and Space Administration (80NM0018D0004). **Funding:** S.S.Z. was funded by the NSF Graduate Research Fellowship. S.S.Z., A.E.H., and J.M.E. were funded by the NASA Emerging Worlds Grant (18-EW18_2-0084). S.S.Z., S.B., and J.M.E. were funded by the Simons Foundation Collaboration on the Origins of Life. J.M.E. was funded by the US Department of Energy BES Grant (DE-SC0016561). J.C.A., J.P.D., D.P.G., E.T.P., and J.E.E. were funded by the NASA Consortium for Hayabusa2 Analysis of Organic Solubles. H.N. and Y.Ta. were funded by the Japan Society for the Promotion of Science (grants 21KK0062 to Y.Ta; 20H00202, JP20H00202, and JP20H05846 to H.Nar.). K.G. was funded by the Australian Research Council through a Discovery Outstanding Research Award (DP130100577) and ARC Laureate fellowship (FL210100103). **Author contributions:** Conceptualization: S.S.Z., J.C.A., J.M.E., H.N., Y.T., and J.P.D. Methodology: S.S.Z., A.E.H., G.D., and J.M.E. Investigation: S.S.Z., J.M.E., S.B., A.E.H., G.D., J.C.A., J.P.D., D.P.G., J.E.E., H.V.G., H.N., Y.Tac., S.Tac., A.T.K., A.I.H., K.G., K.H.F., H.Yu., T.Na., T.No., R.O., H.Ya., K.Sak., T.Yad., M.N., A.N., A.M., K.Y., M.A., T.O., T.U., M.Y., T.S., SatoshiT., F.T., S.N., S.W., Y.Ts., K.H., K.Fuk., D.Ao., M.H., H.M., Y.C., N.O., N.O.O., S.S., E.T.P., H.L.M,. F.-R.O.-D., V.V., R.T., C.W., P.S.K., A.R., T.K., J.I., N.H., Y.O., T.Yoshimura, D.Ara., H.S., A.F., K.Sas., H.Sa., Y.F., J.A., K.K., S.M.N., T.Yoshikawa, SatoruT., M.M., M.O., F.K., K.Fuj., T.Yam., and Y.K. Visualization:

S.S.Z. and S.B. Data analysis: S.S.Z., A.E.H., G.D., S.B., and J.M.E.. Modeling: S.S.Z., S.B., and J.M.E. Funding acquisition: S.S.Z., A.E.H., J.M.E., and J.P.D. Project administration: S.S.Z., J.M.E., J.C.A., J.P.D., S.Tac., H.N., and Y.T. Supervision: J.M.E. and J.P.D. Writing – original draft: S.S.Z., S.B., and J.M.E. Writing – review and editing: All authors **Competing interests:** The authors declare no competing interests. **Data and materials availability:** Summary processed isotope measurements are listed in Tables 1 and S3-S4. Raw experimental data are archived at Zenodo (*50*) in a form that complies with ISAS data policies (www.isas.jaxa.jp/en/researchers/data-policy/). Additional raw data and properties of the asteroid Ryugu are available in the Hayabusa2 Science Data Archives (DARTS, https://www.darts.isas.jaxa.jp/planet/project/hayabusa2/). Samples of the Ryugu asteroid were allocated by the JAXA Astromaterials Science Research Group; the sample catalog is available at https://darts.isas.jaxa.jp/curation/hayabusa2/ and distribution for analysis is through Announcements of Opportunity available at https://jaxa-ryugu-sample-ao.net. Samples of the Murchison meteorite were obtained from Clifford Matthew at the Field Museum in Chicago, IL (*31*). The solvent extracted organic fractions of Ryugu and Murchison were fully consumed during the analyses in this study and in previous work (*31*), respectively. The larger chip of Murchison from which the sample was taken remains at the Field Museum. **License information:** Copyright © 2023 the authors, some rights reserved; exclusive licensee American Association for the Advancement of Science. No claim to original US government works. https://www.sciencemag.org/about/science-licenses-journal-article-reuse

SUPPLEMENTARY MATERIALS

science.org/doi/10.1126/science.adg6304
Materials and Methods
Supplementary Text
Figs. S1 to S4
Tables S1 to S5
References (*51*–*86*)

Submitted 11 January 2023; accepted 13 November 2023
10.1126/science.adg6304

WEATHER FORECASTING

Learning skillful medium-range global weather forecasting

Remi Lam[1]*†, Alvaro Sanchez-Gonzalez[1]*†, Matthew Willson[1]*†, Peter Wirnsberger[1]†, Meire Fortunato[1]†, Ferran Alet[1]†, Suman Ravuri[1]†, Timo Ewalds[1], Zach Eaton-Rosen[1], Weihua Hu[1], Alexander Merose[2], Stephan Hoyer[2], George Holland[1], Oriol Vinyals[1], Jacklynn Stott[1], Alexander Pritzel[1], Shakir Mohamed[1]*, Peter Battaglia[1]*

Global medium-range weather forecasting is critical to decision-making across many social and economic domains. Traditional numerical weather prediction uses increased compute resources to improve forecast accuracy but does not directly use historical weather data to improve the underlying model. Here, we introduce GraphCast, a machine learning–based method trained directly from reanalysis data. It predicts hundreds of weather variables for the next 10 days at 0.25° resolution globally in under 1 minute. GraphCast significantly outperforms the most accurate operational deterministic systems on 90% of 1380 verification targets, and its forecasts support better severe event prediction, including tropical cyclone tracking, atmospheric rivers, and extreme temperatures. GraphCast is a key advance in accurate and efficient weather forecasting and helps realize the promise of machine learning for modeling complex dynamical systems.

It is 05:45 UTC (coordinated universal time) in mid-October 2022 in Bologna, Italy, at the recently opened high-performance computing facility of the European Centre for Medium-Range Weather Forecasts (ECMWF). For the past several hours, the Integrated Forecasting System (IFS) has been running sophisticated calculations to forecast Earth's weather over the next days and weeks, and its first predictions have just begun to be disseminated to users. This process repeats every 6 hours, every day, to supply the world with the most accurate weather forecasts available.

The IFS, and modern weather forecasting more generally, are triumphs of science and engineering. The dynamics of weather systems are among the most complex physical phenomena on Earth, and each day, countless decisions made by individuals, industries, and policy-makers depend on accurate weather forecasts, from deciding whether to wear a jacket to deciding whether to flee a dangerous storm. The dominant approach for weather forecasting today is numerical weather prediction (NWP), which involves solving the governing equations of weather using supercomputers. The success of NWP lies in the rigorous and ongoing research practices that provide increasingly detailed descriptions of weather phenomena and in how well NWP scales to greater accuracy with greater computational resources (*1*, *2*). As a result, the accuracy of weather forecasts has increased year after year, to the point where the path of a hurricane can be predicted many days ahead—a possibility that was unthinkable even a few decades ago.

But while traditional NWP scales well with compute, capitalizing on the vast amount of historical weather data to improve accuracy is not straightforward. Rather, NWP methods are improved by highly trained experts innovating better models, algorithms, and approximations, which can be a time-consuming and costly process.

Machine learning–based weather prediction (MLWP)—wherein forecast models are trained from historical data, including observations and analysis data—offers an alternative to traditional NWP. MLWP has the potential to improve forecast accuracy by capturing patterns in the data that are not easily represented in explicit equations. MLWP also offers opportunities for greater efficiency by exploiting modern deep learning hardware, rather than supercomputers, and striking more favorable speed–accuracy trade-offs. Recently, MLWP has helped improve on NWP-based forecasting in regimes where traditional NWP is relatively weak, for example, in subseasonal heat wave prediction (*3*) and precipitation nowcasting from radar images (*4*–*7*), where accurate equations and robust numerical methods are not as available.

In medium-range weather forecasting—the prediction of atmospheric variables up to 10 days ahead—NWP-based systems such as the IFS are still most accurate. The top deterministic operational system in the world is ECMWF's high-resolution forecast (HRES), a configuration of IFS that produces global 10-day forecasts at 0.1° latitude and longitude resolution, in

Table 1. Weather variables and levels modeled by GraphCast. The numbers in parentheses in the column headings are the number of entries in the column. Boldfaced variables and levels indicate those that were included in the scorecard evaluation. All atmospheric variables are represented at each of the pressure levels.

Surface variables (5)	Atmospheric variables (6)	Pressure levels (37)
2-m temperature (*2T*)	**Temperature** (*T*)	1, 2, 3, 5, 7, 10, 20, 30, **50**, 70,
10-m u wind component (*10U*)	**U component of wind** (*U*)	**100**, 125, **150**, 175, **200**, 225,
10-m v wind component (*10V*)	**V component of wind** (*V*)	**250**, **300**, 350, **400**, 450, **500**,
Mean sea level pressure (*MSL*)	**Geopotential** (*Z*)	550, **600**, 650, **700**, 750, 775,
Total precipitation (*TP*)	**Specific humidity** (*Q*)	800, 825, **850**, 875, 900, **925**,
	Vertical wind speed (*W*)	950, 975, and **1000** hPa

[1]Google DeepMind, London, UK. [2]Google Research, Mountain View, CA, USA.
***Corresponding author. Email: remilam@google.com (R.L.); alvarosg@google.com (A.S.-G.); matthjw@google.com (M.W.); shakir@google.com (S.M.); peterbattaglia@google.com (P.B.)**
†These authors contributed equally to this work.

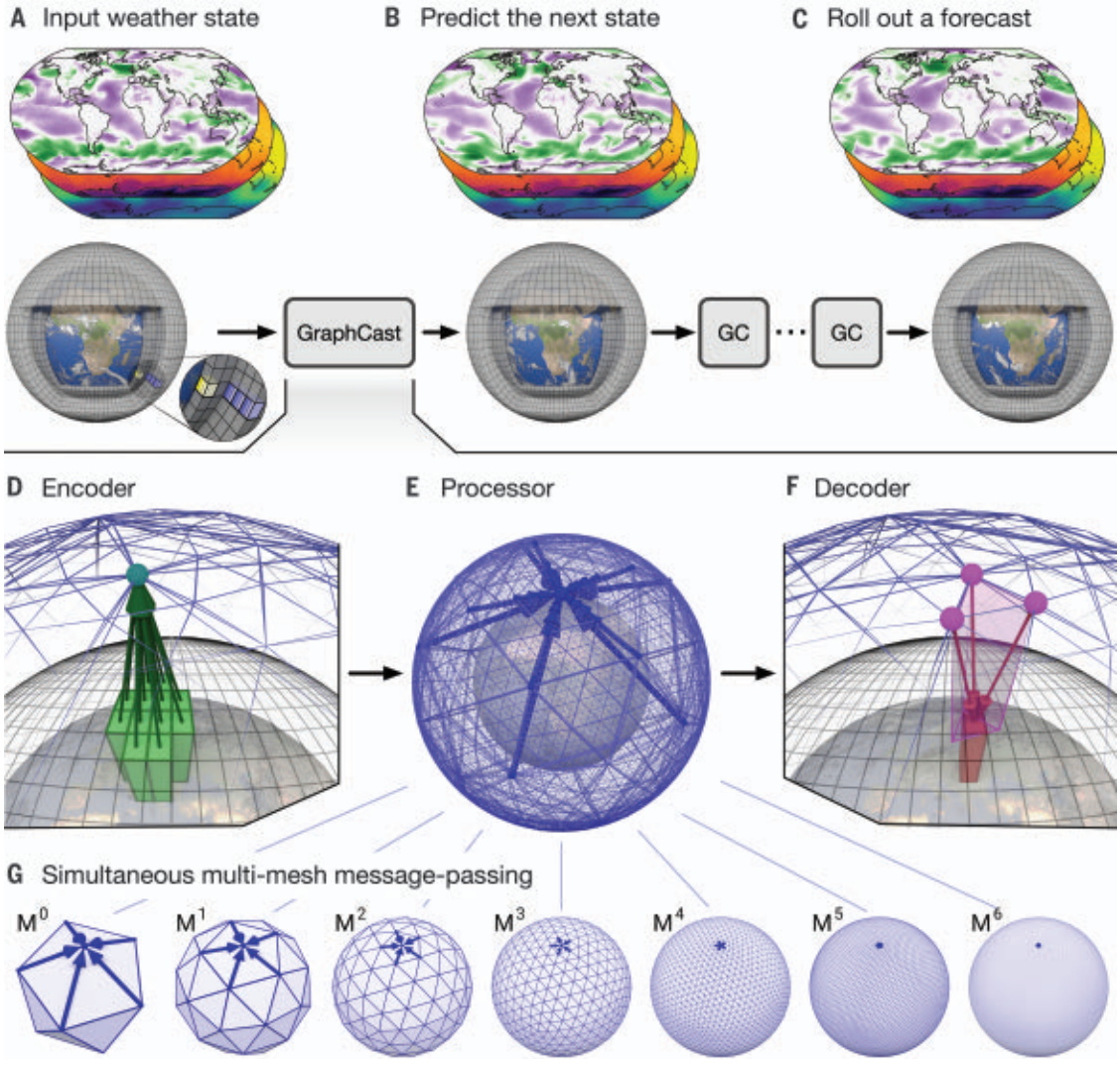

Fig. 1. Model schematic. (**A**) The input weather state(s) are defined on a 0.25° latitude-longitude grid comprising a total of 721 × 1440 = 1,038,240 points. Yellow layers in the close-up pop-out window represent the five surface variables, and blue layers represent the six atmospheric variables that are repeated at 37 pressure levels (5 + 6 × 37 = 227 variables per point in total), resulting in a state representation of 235,680,480 values. (**B**) GraphCast predicts the next state of the weather on the grid. (**C**) A forecast is made by iteratively applying GraphCast (GC) to each previous predicted state, to produce a sequence of states that represent the weather at successive lead times. (**D**) The encoder component of the GraphCast architecture maps local regions of the input (green boxes) into nodes of the multimesh graph representation (green, upward arrows that terminate in the green-blue node). (**E**) The processor component updates each multimesh node using learned message-passing (heavy blue arrows that terminate at a node). (**F**) The decoder component maps the processed multimesh features (purple nodes) back onto the grid representation (red, downward arrows that terminate at a red box). (**G**) The multimesh is derived from icosahedral meshes of increasing resolution, from the base mesh (M^0, 12 nodes) to the finest resolution (M^6, 40,962 nodes), which has uniform resolution across the globe. It contains the set of nodes from M^6 and all the edges from M^0 to M^6. The learned message-passing over the different meshes' edges happens simultaneously, so that each node is updated by all of its incoming edges. [The Earth texture in the figure is used under CC BY 4.0 from https://www.solarsystemscope.com/textures/]

around an hour (*8*). However, over the past several years, MLWP methods for medium-range forecasting trained on reanalysis data have been steadily advancing, facilitated by benchmarks such as WeatherBench (*8*). Deep learning architectures based on convolutional neural networks (*9*–*11*) and Transformers (*12*) have shown promising results at latitude and longitude resolutions coarser than 1.0°, and recent works—which use graph neural networks (GNNs), Fourier neural operators, and Transformers (*13*–*16*)—have reported performance that begins to rival IFS's at 1.0° and 0.25° for a handful of variables and lead times up to 7 days.

GraphCast

Here, we introduce an MLWP approach for global medium-range weather forecasting called GraphCast, which produces an accurate 10-day forecast in under a minute on a single Google Cloud TPU (Tensor Processing Unit) v4 device and supports applications including predicting tropical cyclone tracks, atmospheric rivers, and extreme temperatures.

GraphCast takes as input the two most recent states of Earth's weather—the current time and 6 hours earlier—and predicts the next state of the weather 6 hours ahead. A single weather state is represented by a 0.25° latitude-longitude grid (721 by 1440), which corresponds to roughly 28 km by 28 km resolution at the equator (Fig. 1A), where each grid point represents a set of surface and atmospheric variables (listed in Table 1). Like traditional NWP systems, GraphCast is autoregressive: It can be "rolled out" by feeding its own predictions back in as input, to generate an arbitrarily long trajectory of weather states (Fig. 1, B and C).

GraphCast is implemented as a neural network architecture, based on GNNs in an "encoder-processor-decoder" configuration (*13*, *17*), with a total of 36.7 million parameters (code, weights, and demos can be found at https://github.com/deepmind/graphcast). Previous GNN-based learned simulators (*18*–*20*) have been very effective at learning the complex dynamics of fluid and other systems modeled by partial differential equations, which supports their suitability for modeling weather dynamics.

The encoder (Fig. 1D) uses a single GNN layer to map variables (normalized to zero-mean unit variance) represented as node attributes on the input grid to learned node attributes on an internal "multimesh" representation. The

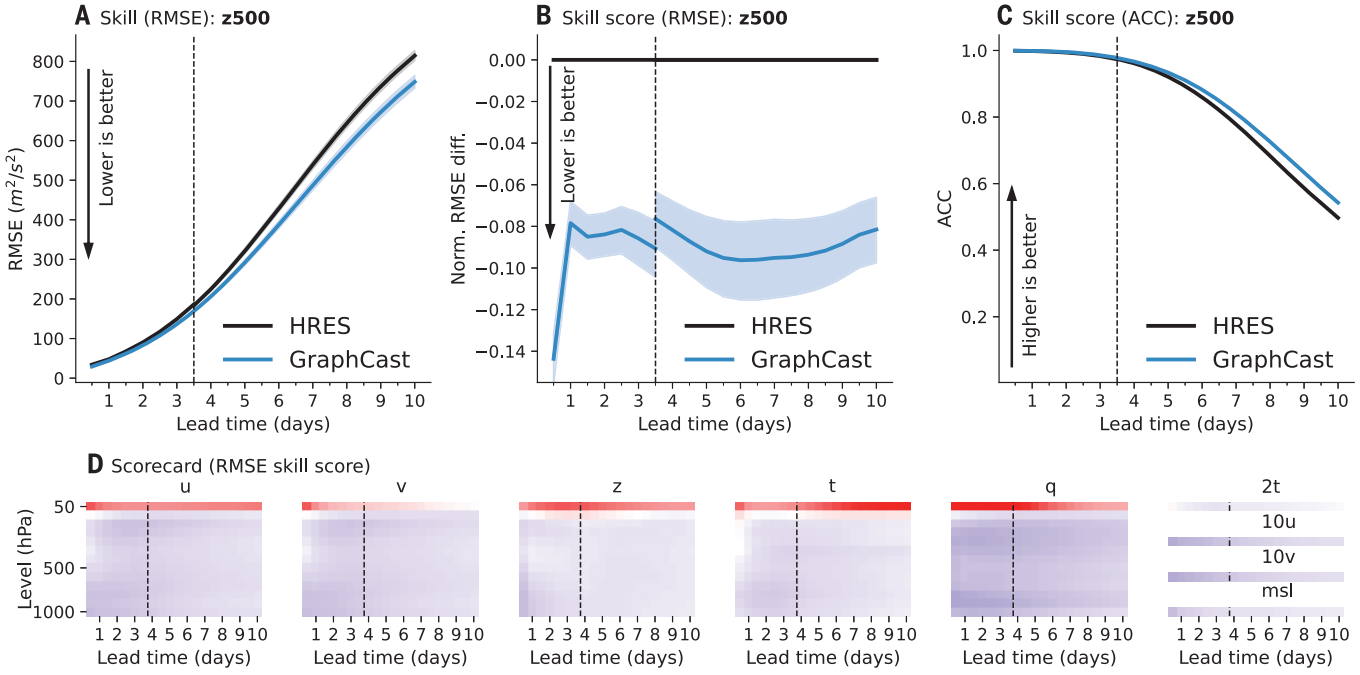

Fig. 2. Global skill and skill scores for GraphCast and HRES in 2018. (**A**) RMSE skill (*y* axis) for GraphCast (blue lines) and HRES (black lines), on *Z*500, as a function of lead time (*x* axis). Error bars represent 95% confidence intervals. The vertical dashed line represents 3.5 days, which is the last 12-hour increment of the HRES 06z/18z forecasts. The black line represents HRES, where lead times earlier and later than 3.5 days are from the 06z/18z and 00z/12z initializations, respectively. (**B**) RMSE skill score (*y* axis) for GraphCast versus HRES, on *Z*500, as a function of lead time (*x* axis). Error bars represent 95% confidence intervals for the skill score. We observe a discontinuity in GraphCast's curve because skill scores up to 3.5 days are computed between GraphCast (initialized at 06z/18z) and HRES's 06z/18z initialization, whereas skill scores after 3.5 days are computed with respect to HRES's 00z/12z initializations. (**C**) ACC skill (*y* axis) for GraphCast (blue lines) and HRES (black lines), on *Z*500, as a function of lead time (*x* axis). (**D**) Scorecard of RMSE skill scores for GraphCast, with respect to HRES. Each subplot corresponds to one variable: *U*, *V*, *Z*, *T*, *Q*, *2T*, *10U*, *10V*, and *MSL*. The rows of each heatmap correspond to the 13 pressure levels (for the atmospheric variables), from 50 hPa at the top to 1000 hPa at the bottom. The columns of each heatmap correspond to the 20 lead times at 12-hour intervals, from 12 hours on the left to 10 days on the right. Each cell's color represents the skill score, as shown in (B), where blue represents negative values (GraphCast has better skill) and red represents positive values (HRES has better skill).

multimesh (Fig. 1G) is a graph that is spatially homogeneous, with high spatial resolution over the globe. It is defined by refining a regular icosahedron (12 nodes, 20 faces, 30 edges) iteratively six times, where each refinement divides each triangle into four smaller ones (leading to four times more faces and edges), and reprojecting the nodes onto the sphere. The multimesh contains the 40,962 nodes from the highest-resolution mesh (which is roughly 1/25 the number of latitude-longitude grid points at 0.25°) and the union of all the edges created in the intermediate graphs, forming a flat hierarchy of edges with varying lengths. The processor (Fig. 1E) uses 16 unshared GNN layers to perform learned message-passing on the multimesh, enabling efficient local and long-range information propagation with few message-passing steps. The decoder (Fig. 1F) maps the final processor layer's learned features from the multimesh representation back to the latitude-longitude grid. It uses a single GNN layer and predicts the output as a residual update to the most recent input state (with output normalization to achieve unit variance on the target residual). See supplementary materials section 3 for further architectural details.

During model development, we used 39 years (1979–2017) of historical data from ECMWF's ERA5 (*21*) reanalysis archive. As a training objective, we averaged the mean squared error (MSE) between GraphCast's predicted states over N autoregressive steps and the corresponding ERA5 states, with the error weighted by vertical level (see supplementary materials eq. 19). The value of N was increased incrementally from 1 to 12 (i.e., from 6 hours to 3 days) over the course of training, and the gradient of the loss was computed by backpropagation through time (*22*). GraphCast was trained to minimize the training objective using gradient descent, which took roughly 4 weeks on 32 Cloud TPU v4 devices using batch parallelism. See supplementary materials section 4 for further training details. Consistent with real deployment scenarios, where future information is not available for model development, we evaluated GraphCast on the held-out data from the years 2018 onward (see supplementary materials section 5.1).

Verification methods

We verified GraphCast's forecast skill comprehensively by comparing its accuracy to that of HRES on a large number of variables, levels, and lead times. We quantified the respective skills of GraphCast, HRES, and ML baselines with two skill metrics: the root mean square error (RMSE) and the anomaly correlation coefficient (ACC).

Of the 227 variable and level combinations predicted by GraphCast at each grid point, we evaluated its skill versus HRES on 69 of them, corresponding to the 13 levels of WeatherBench (*8*) and variables (*23*) from the ECMWF Scorecard (*24*); see boldface variables and levels in Table 1 and supplementary materials section 1.2 for which HRES cycle was operational during the evaluation period. In addition to the aggregate performance reported in the main text, supplementary materials section 7 provides further detailed evaluations, including other variables, precipitation, regional performance, latitude and pressure level effects, spectral properties, blurring, biases, comparisons to other ML-based forecasts, and effects of model design choices.

In making these comparisons, skill was established on the basis of two key elements: (i) the selection of the ground truth for comparison and (ii) a careful accounting of the data

assimilation windows used to infer this data from observations. We used ERA5 as the ground truth for evaluating GraphCast, because it was trained to take ERA5 data as input and predict ERA5 data as outputs. However, evaluating HRES forecasts against ERA5 would result in nonzero error on the initial forecast step. Instead, we constructed an "HRES forecast at step 0" (HRES-fc0) dataset to use as ground truth for HRES. HRES-fc0 contains the inputs to HRES forecasts at future initializations (see supplementary materials section 1.2), ensuring that each data point is grounded by recent observations and that the zeroth step of HRES forecasts will have zero error.

For a fair comparison, we had to ensure that the ERA5 initial conditions for GraphCast were derived from assimilation windows that look no further into the future than those used by HRES. HRES initializations (00z/06z/12z/18z, where 00z means 00:00 UTC in Zulu convention) always assimilate observations 3 hours into the future, whereas ERA5 initializations assimilate observations 9 hours into the future at 00z/12z and 3 hours into the future at 06z/18z. This constrained the choice of initialization times for GraphCast to 06z/18z in all our results. We used the same initializations for HRES when comparing performance up to 3.75 days. Beyond that, HRES archived forecasts are only available from 00z/12z initializations. The transition from 06z/18z to 00z/12z initializations for HRES induced a small discontinuity in our plots, which is indicated by a vertically dashed line at the appropriate lead time. Supplementary materials section 5 contains further verification details, including details of the comparisons protocol between GraphCast and HRES (supplementary materials section 5.2) and the effect of initialization lookahead on both models' performance (supplementary materials section 5.2.2).

Forecast verification results

We find that GraphCast has greater weather forecasting skill than HRES when evaluated on 10-day forecasts at a horizontal resolution of 0.25° for latitude and longitude and at 13 vertical levels. Figure 2, A to C, shows how GraphCast (blue lines) outperforms HRES (black lines) on the *Z*500 (geopotential at 500 hPa) "headline" field in terms of RMSE skill, RMSE skill score [i.e., the normalized RMSE difference between model *A* and baseline *B* defined as $(RMSE_A - RMSE_B)/(RMSE_B)$], and ACC skill. Using *Z*500, which encodes the synoptic-scale pressure distribution, is common in the literature, as it has strong meteorological importance (*8*). The plots show that GraphCast has better skill scores across all lead times, with a skill score improvement of around 7 to 14%. Plots for additional headline variables are given in supplementary materials section 7.1.

Figure 2D summarizes the RMSE skill scores for all 1380 evaluated variables and pressure levels, across the 10-day forecasts, in a format analogous to the ECMWF Scorecard. The cell colors are proportional to the skill score, where blue indicates that GraphCast had better skill, and red indicates that HRES had better skill. GraphCast outperformed HRES on 90.3% of the 1380 targets and significantly ($P \leq 0.05$, nominal sample size $n \in \{729, 730\}$) outperformed HRES on 89.9% of targets. See supplementary materials section 5.4 for methodology and table S4 for *P* values, test statistics, and effective sample sizes.

The regions of the atmosphere in which HRES had better performance than GraphCast (top rows in red in the scorecards) were disproportionately localized in the stratosphere and had the lowest training loss weight (see supplementary materials section 7.2.2). When excluding the 50 hPa level, GraphCast significantly outperforms HRES on 96.9% of the remaining 1280 targets. When excluding levels 50 and 100 hPa, GraphCast significantly outperforms HRES on 99.7% of the remaining 1180 targets. When conducting per-region evaluations, we found that the previous results generally hold across the globe, as detailed in figs. S14 to S16.

We found that increasing the number of autoregressive steps in the MSE loss improves GraphCast performance at longer lead times (see supplementary materials section 7.3.2). It also encourages GraphCast to blur to a degree at longer lead times (see fig. S38), which means that its forecasts will lie somewhere between a traditional deterministic forecast and an ensemble mean. HRES's underlying physical equations, however, do not lead to blurred predictions. To assess whether GraphCast's relative advantage over HRES on RMSE skill is due to blurrier forecasts better optimizing RMSE, we artificially blurred HRES's forecasts with blurring filters. We fit filters for GraphCast and HRES by minimizing the RMSE between filtered predictions and the models' respective ground truths. We found that RMSE-optimized blurring applied to GraphCast has greater skill than analogous blurring applied to HRES on 88.0% of our 1380 verification targets, which is generally consistent with our above conclusions (see supplementary materials section 7.4).

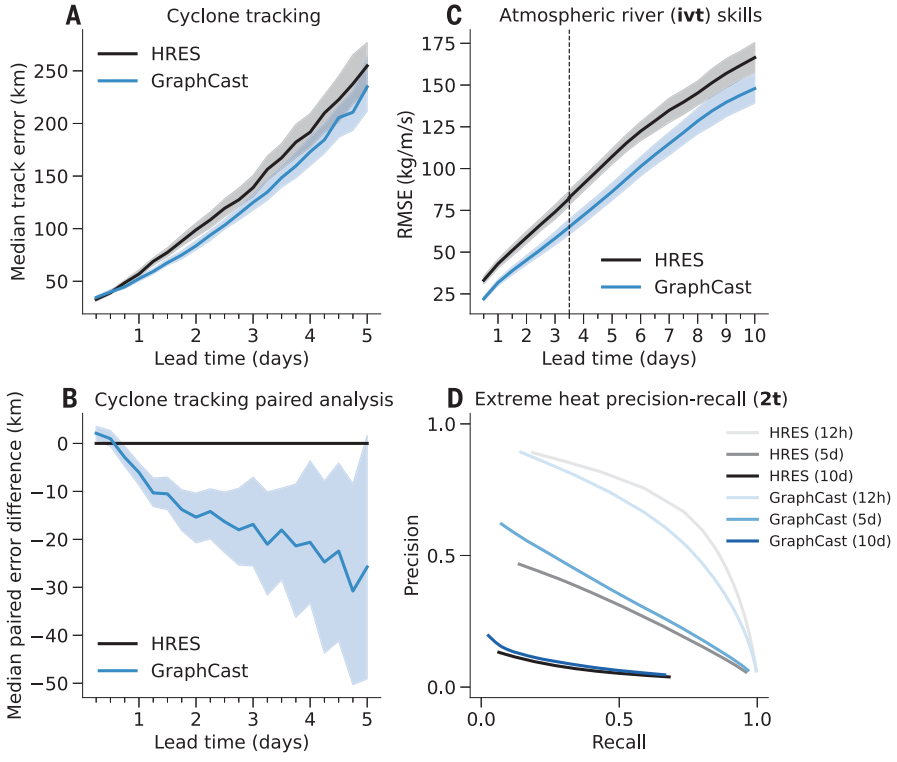

Fig. 3. Severe event prediction. (**A**) Cyclone tracking performances for GraphCast and HRES. The *x* axis represents lead times (in days), and the *y* axis represents median track error (in kilometers). Error bars represent bootstrapped 95% confidence intervals for the median. (**B**) Cyclone tracking paired error difference between GraphCast and HRES. The *x* axis represents lead times (in days), and the *y* axis represents median paired error difference (in kilometers). Error bars represent bootstrapped 95% confidence intervals for the median difference (see supplementary materials section 8.1). (**C**) Atmospheric river prediction (*IVT*) skills for GraphCast and HRES. The *x* axis represents lead times (in days), and the *y* axis represents RMSE. Error bars are 95% confidence intervals. (**D**) Extreme heat prediction precision-recall for GraphCast and HRES. The *x* axis represents recall, and the *y* axis represents precision. The curves represent different precision-recall trade-offs when sweeping over gain applied to forecast signals (see supplementary materials section 8.3).

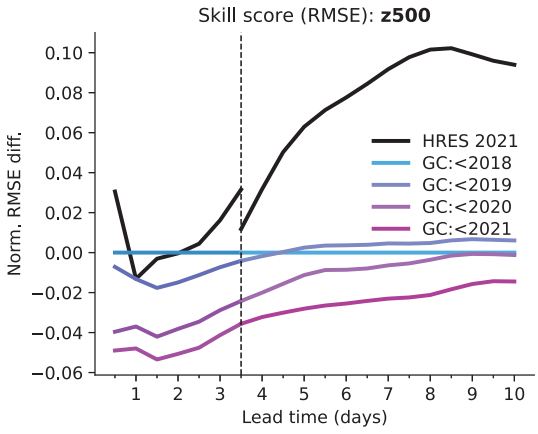

Fig. 4. Training GraphCast on more recent data. Each colored line represents GraphCast trained with data ending before a different year, from 2018 (blue) to 2021 (purple). The *y* axis represents RMSE skill scores on 2021 test data, for *Z*500, with respect to GraphCast trained up to before 2018, over lead times (*x* axis). The vertical dashed line represents 3.5 days, where the HRES 06z/18z forecasts end. The black line represents HRES, where lead times earlier and later than 3.5 days are from the 06z/18z and 00z/12z initializations, respectively.

Still, blurrier forecasts may not be desirable for some applications, which we discuss further in the Conclusions section. We also compared GraphCast's performance to the top competing ML-based weather model, Pangu-Weather (*16*), and found that GraphCast outperformed it on 99.2% of the 252 targets presented (see supplementary materials section 6 for details).

Severe event forecasting results

Beyond evaluating GraphCast's forecast skill against HRES's on a wide range of variables and lead times, we also evaluated how its forecasts support predicting severe events, including tropical cyclones tracks, atmospheric rivers, and extreme temperature. These are key downstream applications for which GraphCast is not specifically trained, but which are very important for human activity.

Tropical cyclone tracks

Improving the accuracy of tropical cyclone tracking can help avoid injury and loss of life and can reduce economic harm (*25*). A cyclone's existence and trajectory are predicted by applying a tracking algorithm to forecasts of geopotential (*Z*), horizontal wind (10*U*/10*V*, *U*/*V*), and mean sea level pressure (*MSL*). We implemented a tracking algorithm based on ECMWF's published protocols (*26*) and applied it to GraphCast's forecasts to produce cyclone track predictions (see supplementary materials section 8.1). As a baseline for comparison, we used the operational tracks obtained from HRES's 0.1° forecasts with ECMWF's own tracker, stored in the TIGGE (THORPEX Interactive Grand Global Ensemble) archive (*27*, *28*). The reason we used different trackers for GraphCast and HRES is because no single tracker should necessarily give best performance across different forecasts, therefore, we used the best tracker for each model. We measured errors for both models against the tracks from IBTrACS [International Best Track Archive for Climate Stewardship (*29*, *30*)], a separate reanalysis dataset of cyclone tracks aggregated rom various analysis and observational sources. To be consistent with established evaluation of tropical cyclone prediction (*26*), we evaluate all tracks when both GraphCast and HRES detect a cyclone, ensuring that both models are evaluated on the same events, and verify that each model's true-positive rates are similar.

Figure 3A shows that GraphCast has lower median track error than HRES over the period 2018–2021 (median was chosen to resist outliers). As per-track errors for HRES and GraphCast are correlated, we also measured the per-track paired error difference between the two models and found that GraphCast is significantly better than HRES for lead times of 18 hours to 4.75 days, as shown in Fig. 3B. The error bars show the bootstrapped 95% confidence intervals for the median (see supplementary materials section 8.1 for details).

Atmospheric rivers

Atmospheric rivers are narrow regions of the atmosphere that are responsible for most of the poleward water vapor transport across the mid-latitudes and generate 30 to 65% of annual precipitation on the US West Coast (*31*). Their strength can be characterized by the vertically integrated water vapor transport *IVT* (*32*, *33*), indicating whether an event will provide beneficial precipitation or be associated with catastrophic damage (*34*). *IVT* can be computed from the nonlinear combination of the horizontal wind speed (*U* and *V*) and specific humidity (*Q*), which GraphCast predicts. We evaluated GraphCast forecasts over coastal North America and the Eastern Pacific during cold months (October to April), when atmospheric rivers are most frequent. Despite not being specifically trained to characterize atmospheric rivers, Fig. 3C shows that GraphCast improves the prediction of *IVT* compared with HRES, from 25% at short lead time to 10% at longer horizons (see supplementary materials section 8.2 for details).

Extreme heat and cold

Extreme heat and cold are characterized by large anomalies with respect to typical climatology (*3*, *35*, *36*), which can be dangerous and disrupt human activities. We evaluated the skill of HRES and GraphCast in predicting events above the top 2% of historical values across location, time of day, and month of the year, for 2*T* at 12-hour, 5-day, and 10-day lead times, for land regions across the Northern and Southern hemispheres over their respective summer months. We plotted precision-recall curves (*37*) to reflect different possible trade-offs between reducing false positives (high precision) and reducing false negatives (high recall). For each forecast, we obtained the curve by varying a "gain" parameter that scales the 2*T* forecast's deviations with respect to the median climatology.

Figure 3D shows that GraphCast's precision-recall curves are above HRES's for 5- and 10-day lead times, suggesting that GraphCast's forecasts are generally superior to those of HRES at extreme classification over longer horizons. By contrast, HRES has better precision-recall at the 12-hour lead time, which is consistent with the *2T* skill score of GraphCast over HRES being near zero, as shown in Fig. 2D. We generally find these results to be consistent across other variables relevant to extreme heat, such as *T*850 (temperature at 850 hPa) and *Z*500 (geopotential at 500 hPa) (*36*), other extreme thresholds (5, 2, and 0.5%), and extreme cold forecasting in winter. See supplementary materials section 8.3 for details.

Effect of training data recency

GraphCast can be retrained periodically with recent data, which in principle allows it to capture weather patterns that change over time—in response to, for example, the effects of climate change—and long climate oscillations. We trained four variants of GraphCast from scratch, with data that always began in 1979 but ended in 2017, 2018, 2019, and 2020, respectively (we label the variant ending in 2017 as "GraphCast: <2018," etc.). We compared their performances to HRES on 2021 test data.

Figure 4 shows the skill scores (normalized by GraphCast:<2018) of the four variants and HRES for *Z*500. We found that while GraphCast's performance when trained up to before 2018 is still competitive with HRES in 2021, training it up to before 2021 further improves its skill scores (see supplementary materials section 7.1.3). We speculate that this recency effect allows recent weather trends to be captured to improve accuracy. This shows that GraphCast's performance can be improved by retraining on more recent data.

Conclusions

GraphCast's forecast skill and efficiency compared with HRES shows that MLWP methods are now competitive with traditional weather forecasting methods. Additionally, GraphCast's performance on severe event forecasting, which

it was not directly trained for, demonstrates its robustness and potential for downstream value. We believe this marks a turning point in weather forecasting, which helps open new avenues to strengthen the breadth of weather-dependent decision-making by individuals and industries by making cheap prediction more accurate and accessible as well as suitable for specific applications.

With 36.7 million parameters, GraphCast is a relatively small model by modern ML standards, chosen to keep the memory footprint tractable. And while HRES is released on 0.1° resolution, 137 levels, and up to 1-hour time steps, GraphCast operates on 0.25° latitude and longitude resolution, 37 vertical levels, and 6-hour time steps, because of the ERA5 training data's native 0.25° resolution and engineering challenges in fitting higher-resolution data on hardware. Generally, GraphCast should be viewed as a family of models, with the current version being the largest we can practically fit under current engineering constraints, but which have the potential to scale much further in the future with greater compute resources and higher-resolution data.

One key limitation of our approach is in how uncertainty is handled. We focused on deterministic forecasts and compared against HRES, but the other pillar of ECMWF's IFS, the ensemble forecasting system ENS, is especially important for quantifying the probability of extreme events and as the skill of the forecast decreases at longer lead times. The nonlinearity of weather dynamics means that there is increasing uncertainty at longer lead times, which is not well captured by a single deterministic forecast. ENS addresses this by generating multiple, stochastic forecasts, which approximate a predictive distribution over future weather; however, generating multiple forecasts is expensive. By contrast, GraphCast's MSE training objective encourages it to spatially blur its predictions in the presence of uncertainty, which may not be desirable for some applications where knowing tail, or joint, probabilities of events is important. Building probabilistic forecasts that model uncertainty more explicitly, along the lines of ensemble forecasts, is a crucial next step.

It is important to emphasize that data-driven MLWP relies critically on large quantities of data and their quality, which, in the case of models trained on reanalysis, depend on the fidelity of NWPs. Therefore, rich high-quality data sources such as ECMWF's MARS (Meteorological Archival and Retrieval System) archive (*38*) are invaluable. Our approach should not be regarded as a replacement for traditional weather forecasting methods, which have been developed for decades, rigorously tested in many real-world contexts, and offer many features we have not yet explored. Rather, our work should be interpreted as evidence that MLWP is able to meet the challenges of real-world forecasting problems and has the potential to complement and improve the current best methods.

Beyond weather forecasting, GraphCast can open new directions for other important geospatiotemporal forecasting problems, including climate and ecology, energy, agriculture, and human and biological activity, as well as other complex dynamical systems. We believe that learned simulators, trained on rich, real-world data, will be crucial in advancing the role of machine learning in the physical sciences.

REFERENCES AND NOTES

1. S. G. Benjamin *et al*., *Meteorol. Monogr.* **59**, 13.1–13.67 (2019).
2. P. Bauer, A. Thorpe, G. Brunet, *Nature* **525**, 47–55 (2015).
3. I. Lopez-Gomez, A. McGovern, S. Agrawal, J. Hickey, *Artif. Intell. Earth Syst.* **2**, e220035 (2022).
4. X. Shi *et al*., *Adv. Neural Inf. Process. Syst.* **30**, 5617–5627 (2017).
5. C. K. Sønderby *et al*., arXiv:2003.12140 [cs.LG] (2020).
6. S. Ravuri *et al*., *Nature* **597**, 672–677 (2021).
7. L. Espeholt *et al*., *Nat. Commun.* **13**, 5145 (2022).
8. S. Rasp *et al*., *J. Adv. Model. Earth Syst.* **12**, e2020MS002203 (2020).
9. J. A. Weyn, D. R. Durran, R. Caruana, *J. Adv. Model. Earth Syst.* **11**, 2680–2693 (2019).
10. J. A. Weyn, D. R. Durran, R. Caruana, *J. Adv. Model. Earth Syst.* **12**, e2020MS002109 (2020).
11. S. Rasp, N. Thuerey, *J. Adv. Model. Earth Syst.* **13**, e2020MS002405 (2021).
12. T. Nguyen, J. Brandstetter, A. Kapoor, J. K. Gupta, A. Grover, arXiv:2301.10343 [cs.LG] (2023).
13. R. Keisler, Forecasting global weather with graph neural networks. arXiv:2202.07575 [physics.ao-ph] (2022).
14. J. Pathak *et al*., arXiv:2202.11214 [physics.ao-ph] (2022).
15. T. Kurth *et al*., arXiv:2208.05419 [physics.ao-ph] (2022).
16. K. Bi *et al*., arXiv:2211.02556 [physics.ao-ph] (2022).
17. P. W. Battaglia *et al*., arXiv:1806.01261 [cs.LG] (2018).
18. A. Sanchez-Gonzalez *et al*., *Proc. Mach. Learn. Res.* **119**, 8459–8468 (2020).
19. T. Pfaff, M. Fortunato, A. Sanchez-Gonzalez, P. Battaglia, "Learning mesh-based simulation with graph networks," International Conference on Learning Representations (ICLR 2021), 3 to 7 May 2021.
20. F. Alet *et al*., *Proc. Mach. Learn. Res.* **97**, 212–222 (2019).
21. H. Hersbach *et al*., *Q. J. R. Meteorol. Soc.* **146**, 1999–2049 (2020).
22. P. Werbos, *Proc. IEEE* **78**, 1550–1560 (1990).
23. Because precipitation in ERA5 has known biases (*39*), no development decision for GraphCast was made to improve performance on precipitation, and GraphCast simply uses precipitation as an auxiliary input and output. Note that precipitation is sparse and non-Gaussian and would have possibly required different modeling decisions than the other variables. Additionally, precipitation is not available in the HRES analysis products in a form amenable to our evaluation protocol (see next paragraphs). Thus, any claim about precipitation prediction is left out of the scope of this work, and we show precipitation evaluation using a different protocol in supplementary materials section 7.1.4 for completeness only.
24. T. Haiden *et al*., "Evaluation of ECMWF forecasts, including the 2018 upgrade," ECMWF Technical Memorandum No. 831 (European Centre for Medium-Range Weather Forecasts, 2018); https://doi.org/10.21957/ldw15ckqi.
25. A. B. Martinez, *Econometrics* **8**, 18 (2020).
26. L. Magnusson *et al*., "Tropical cyclone activities at ECMWF," ECMWF Technical Memorandum No. 888 (European Centre for Medium-Range Weather Forecasts, 2021); https://doi.org/10.21957/zzxzzygwv.
27. P. Bougeault *et al*., *Bull. Am. Meteorol. Soc.* **91**, 1059–1072 (2010).
28. R. Swinbank *et al*., *Bull. Am. Meteorol. Soc.* **97**, 49–67 (2016).
29. K. R. Knapp, M. C. Kruk, D. H. Levinson, H. J. Diamond, C. J. Neumann, *Bull. Am. Meteorol. Soc.* **91**, 363–376 (2010).
30. K. R. Knapp, H. J. Diamond, J. P. Kossin, M. C. Kruk, C. J. Schreck III, International Best Track Archive for Climate Stewardship (IBTrACS) Project, version 4, NOAA National Centers for Environmental Information (2018); https://doi.org/10.25921/82ty-9e16.
31. W. Chapman, A. Subramanian, L. Delle Monache, S. Xie, F. Ralph, *Geophys. Res. Lett.* **46**, 10627–10635 (2019).
32. P. J. Neiman, F. M. Ralph, G. A. Wick, J. D. Lundquist, M. D. Dettinger, *J. Hydrometeorol.* **9**, 22–47 (2008).
33. B. J. Moore, P. J. Neiman, F. M. Ralph, F. E. Barthold, *Mon. Weather Rev.* **140**, 358–378 (2012).
34. T. W. Corringham, F. M. Ralph, A. Gershunov, D. R. Cayan, C. A. Talbot, *Sci. Adv.* **5**, eaax4631 (2019).
35. L. Magnusson, T. Haiden, D. Richardson, "Verification of extreme weather events: Discrete predictands," ECMWF Technical Memorandum No. 731 (European Centre for Medium-Range Weather Forecasts, 2014); https://doi.org/10.21957/1iql31n2c.
36. L. Magnusson, ECMWF confluence wiki: 202208 - Heatwave - UK (2022); https://confluence.ecmwf.int/display/FCST/202208+-+Heatwave+-+UK.
37. T. Saito, M. Rehmsmeier, *PLOS ONE* **10**, e0118432 (2015).
38. C. Maass, E. Cuartero, MARS user documentation (2022); https://confluence.ecmwf.int/display/UDOC/MARS+user+documentation.
39. D. A. Lavers, A. Simmons, F. Vamborg, M. J. Rodwell, *Q. J. R. Meteorol. Soc.* **148**, 3152–3165 (2022).
40. D. Fan *et al*., *Sci. Robot.* **4**, eaay5063 (2019).
41. T. Ewalds, Source code for GraphCast, google-deepmind/graphcast: Version 0.1, Zenodo (2023); https://doi.org/10.5281/zenodo.10058758.

ACKNOWLEDGMENTS

In alphabetical order, we thank K. Allen, C. Blundell, M. Botvinick, Z. B. Bouallegue, M. Brenner, R. Carver, M. Chantry, M. Deisenroth, P. Deuben, M. Garnelo, R. Keisler, D. Kochkov, C. Mattern, P. Mirowski, P. Norgaard, I. Price, C. Qin, S. Racanière, S. Rasp, Y. Rubanova, K. Shah, J. Smith, D. Worrall, and countless others at Alphabet and ECMWF for advice and feedback on our work. We also thank ECMWF for providing invaluable datasets to the research community. The style of the opening paragraph was inspired by (*40*). **Funding:** All research in this study was funded by Google DeepMind and Alphabet. There was no external funding. **Author contributions:** Conceptualization: R.L., A.S.-G., M.W., S.M., and P.B. Data curation: R.L., A.S.-G., M.W., A.M., and P.B. Formal analysis: R.L., A.S.-G., M.W., P.W., M.F., F.A., S.R., T.E., Z.E.-R., W.H., A.P., S.M., and P.B. Investigation: R.L., A.S. -G., M.W., P.W., M.F., F.A., S.R., T.E., Z.E.-R., W.H., A.P., S.M., and P.B. Methodology: R.L., A.S.-G., M.W., P.W., M.F., F.A., S.R., T.E., Z.E.-R., W.H., A.P., S.M., and P.B. Project administration: R.L., A.S.-G., M.W., G.H., O.V., J.S., S.M., and P.B. Software: R.L., A.S.-G., M.W., P.W., M.F., F.A., S.R., T.E., Z.E.-R., W.H., A.P., and P.B. Supervision: R.L., S.M., and P.B. Validation: R.L., A.S.-G., M.W., P.W., M.F., F.A., S.R., T.E., Z.E.-R., W.H., A.P., S.M., and P.B. Visualization: R.L., A.S.-G., M.W., F.A., and P.B. Writing – original draft: R.L., A.S.-G., M.W., P.W., M.F., F.A., S.R., T.E., Z.E.-R., S.H., A.P., S.M., and P.B. Writing – review & editing: R.L., A.S.-G., M.W., P.W., M.F., F.A., S.R., T.E., Z.E.-R., S.H., A.P., S.M., and P.B. **Competing interests:** This work was done in the course of employment at Google DeepMind, with no other competing financial interests. A.S.-G., R.L., P.B., M.W., P.W., M.F., and A.P. have filed a provisional patent application relating to machine learning for learned medium-range global weather forecasting (US Provisional App. no. US63/435,163). **Data and materials availability:** GraphCast's code and trained weights are publicly available on GitHub at https://github.com/deepmind/graphcast (*41*). This work used publicly available data from the ECMWF. We used the ECMWF archive (expired real-time) products for ERA5, HRES, and TIGGE products, whose use is governed by the Creative Commons Attribution 4.0 International (CC BY 4.0). We used IBTrACS Version 4 from https://www.ncei.noaa.gov/products/international-best-track-archive and (*29*, *30*), as required.

License information: Copyright © 2023 the authors, some rights reserved; exclusive licensee American Association for the Advancement of Science. No claim to original US government works. https://www.science.org/about/science-licenses-journal-article-reuse

SUPPLEMENTARY MATERIALS

science.org/doi/10.1126/science.adi2336
Materials and Methods
Supplementary Text
Figs. S1 to S53
Tables S1 to S4
References (*42*–*75*)

Submitted 18 April 2023; accepted 1 November 2023
Published online 14 November 2023
10.1126/science.adi2336

SUPERCONDUCTIVITY

Time-reversal symmetry breaking superconductivity between twisted cuprate superconductors

S. Y. Frank Zhao[1]†, Xiaomeng Cui[1]†, Pavel A. Volkov[1,2,3], Hyobin Yoo[4], Sangmin Lee[5], Jules A. Gardener[6], Austin J. Akey[6], Rebecca Engelke[1], Yuval Ronen[1], Ruidan Zhong[7]‡, Genda Gu[7], Stephan Plugge[8], Tarun Tummuru[8], Miyoung Kim[5], Marcel Franz[8], Jedediah H. Pixley[2], Nicola Poccia[1,9]*, Philip Kim[1]*

Twisted interfaces between stacked van der Waals (vdW) cuprate crystals present a platform for engineering superconducting order parameters by adjusting stacking angles. Using a cryogenic assembly technique, we construct twisted vdW Josephson junctions (JJs) at atomically sharp interfaces between $Bi_2Sr_2CaCu_2O_{8+x}$ crystals, with quality approaching the limit set by intrinsic JJs. Near 45° twist angle, we observe fractional Shapiro steps and Fraunhofer patterns, consistent with the existence of two degenerate Josephson ground states related by time-reversal symmetry (TRS). By programming the JJ current bias sequence, we controllably break TRS to place the JJ into either of the two ground states, realizing reversible Josephson diodes without external magnetic fields. Our results open a path to engineering topological devices at higher temperatures.

Weak van der Waals (vdW) bonding between neighboring atomic layers offers a distinct opportunity for engineering atomic interfaces with controlled twist angles (*1*). Careful adjustment of the twist angle can create the spatial periodicity of a moiré superlattice (*2*) with narrow electronic bands and topological structure (*3*). Such twisted structures of various vdW materials, including graphene (*3*) and transition metal dichalcogenides (*4*), have been shown to host a plethora of emergent electronic states, including superconductivity (*5*), magnetism (*6*), Chern insulators (*7*), generalized electronic Wigner crystals (*8*), and correlated insulating states (*9*).

Atomically layered cuprate high-temperature superconductors also offer a platform for twistronics by enabling the engineering of the coupling between nodal superconducting order parameters (SOPs) across a twisted vdW interface (*10*–*15*). In $Bi_2Sr_2CaCu_2O_{8+x}$ (BSCCO), superconducting CuO_2 bilayers are Josephson-coupled through insulating [SrO-BiO] bilayers (*16*), where the crystal can be mechanically cleaved into atomically flat crystals (*17*, *18*) exhibiting high-temperature superconductivity even in the monolayer limit (*19*).

Josephson junctions (JJs) formed at twist boundaries between cuprate crystals directly probe the pairing symmetry of Cooper pairs (*20*, *21*). For example, using *ab*-planar tilt grain boundaries, measurements of angle-dependent critical currents (*22*), nonsinusoidal Josephson current-phase relations (*23*), and spontaneous supercurrents (*21*) established the cuprates as d-wave superconductors where the SOP changes sign when Cooper pair momentum is rotated by 90°.

Similarly, interfacial Josephson coupling between twisted nodal d-wave superconductors is strongly modulated by the twist angle (*15*). Particularly, at a twist angle of $\theta = 45°$, direct Cooper pair tunneling is forbidden because of the complete mismatch between the $d_{x^2-y^2}$ symmetric SOPs across the interface (*15*). Any remaining Josephson supercurrents are mediated through second-order processes (*10*–*12*, *24*); the system is expected to support topological time-reversal symmetry (TRS)–breaking superconducting phases persisting up to the junction superconducting transition temperature T_C (*11*, *12*). Alternatively, TRS can be broken away from $\theta = 45°$ by an applied current, which is predicted to induce a topological superconducting state (*13*).

Building twisted BSCCO junctions

The preservation of surface superconductivity of BSCCO crystals after vdW stacking remains an outstanding experimental challenge (*17*, *18*). BSCCO crystals react with moisture (*19*, *25*), and their oxygen dopants become mobile above 200 K (*19*, *26*). BSCCO twist junctions previously required high-temperature oxygen annealing to restore interfacial superconductivity (*27*–*31*), often at the cost of considerable interfacial structural reconstruction (*29*, *31*–*33*), suppressed T_C (*28*–*31*), low critical current density J_C at zero twist angle (*27*–*29*, *31*), and pronounced anomalies in the resistance-temperature (*R*-*T*) curves (*28*, *29*, *31*). Most experiments observed no angular sensitivity (*27*–*29*), except two (*30*, *31*) where the Josephson coupling angular dependence deviated strongly from conventional models of d-wave superconductivity (*15*).

We overcome these challenges by developing a cryogenic, solvent-free vdW transfer technique in pure argon using a liquid nitrogen–cooled stage kept at <−90°C. We cleave an exfoliated BSCCO crystal into two copies between BiO planes, while thermally freezing out oxygen migration and other chemical processes at the surface (Fig. 1A and fig. S1). One of the crystals is quickly rotated to the targeted twist angle and reassembled with the other. A Josephson junction forms in the overlapping region upon contact (Fig. 1, B to D). Two sets of electrical contacts, both defined by stencil masks and evaporated on a −30°C cold stage (*17*), are prefabricated nearby before cleaving and placed on the top surface of the bottom crystal after reassembly. This contact geometry probes the twist junction while minimizing bulk crystal contributions (Fig. 1H, upper inset). Additional details are given in section S1 of (*34*).

Cryogenic handling in argon is critical to maintaining pristine atomic interfaces without interfacial reconstruction and oxygen dopant changes. Figure 1D shows cross-sectional high-angle annular dark field (HAADF) scanning transmission electron microscope (STEM) image of a $\theta = 46°$ junction, simultaneously viewing both BSCCO crystals on two different zone axes. Notably, crystalline order is maintained at the interfacial layer with no change to the lattice structure (*35*) in the [001] direction between atomic layers (Fig. 1E) or along CuO_2 planes (Fig. 1, F and G, and figs. S2 to S4). Detailed analysis of the interfacial BiO atomic layer places an upper bound of the twist-angle disorder below 0.2° [section S2 of (*34*)]. Similar interface quality is uniformly observed across large areas in several additional junctions (see figs. S2 to S4, for example). We compare 26 devices with θ ranging from 0° to 180°, with $T_C >$ 79 K and average T_C of 84 K (Fig. 1H, lower inset), demonstrating high oxygen dopant uniformity even at the junction. Neither T_C nor the normal-state conductivity are systematically correlated with θ (fig. S8).

At $\theta = 0°$, our devices exhibit electronic characteristics similar to the intrinsic Josephson junctions (IJJs) that naturally form between CuO_2 layers in BSCCO single crystals (*16*), demonstrating the high interfacial quality of our JJs. Figure 1I shows the current-voltage (*I*-*V*) characteristics (IVCs) measured with four terminals at temperature $T = 9$ K. In this low-temperature regime, the JJ exhibits a large hysteresis. As we increase current bias from a large negative value,

[1]Department of Physics, Harvard University, Cambridge, MA 02138, USA. [2]Center for Materials Theory, Department of Physics and Astronomy, Rutgers University, Piscataway, NJ 08854, USA. [3]Department of Physics, University of Connecticut, Storrs, CT 06269, USA. [4]Department of Physics, Institute of Emergent Materials, Sogang University, Seoul 04107, Korea. [5]Department of Materials Science and Engineering, Seoul National University, Seoul 08826, Korea. [6]Center for Nanoscale Systems, Harvard University, Cambridge, MA 02138, USA. [7]Department of Condensed Matter Physics and Materials Science, Brookhaven National Laboratory, Upton, NY 11973, USA. [8]Department of Physics and Astronomy and Stewart Blusson Quantum Matter Institute, University of British Columbia, Vancouver, BC V6T 1Z4, Canada. [9]Leibniz Institute for Solid State and Materials Research Dresden (IFW Dresden), 01069 Dresden, Germany.
***Corresponding author. Email: n.poccia@ifw-dresden.de (N.P.); pkim@physics.harvard.edu (P.K.)**
†These authors contributed equally to this work.
‡Present address: Tsung-Dao Lee Institute and School of Physics and Astronomy, Shanghai Jiao Tong University, Shanghai 200240, China.

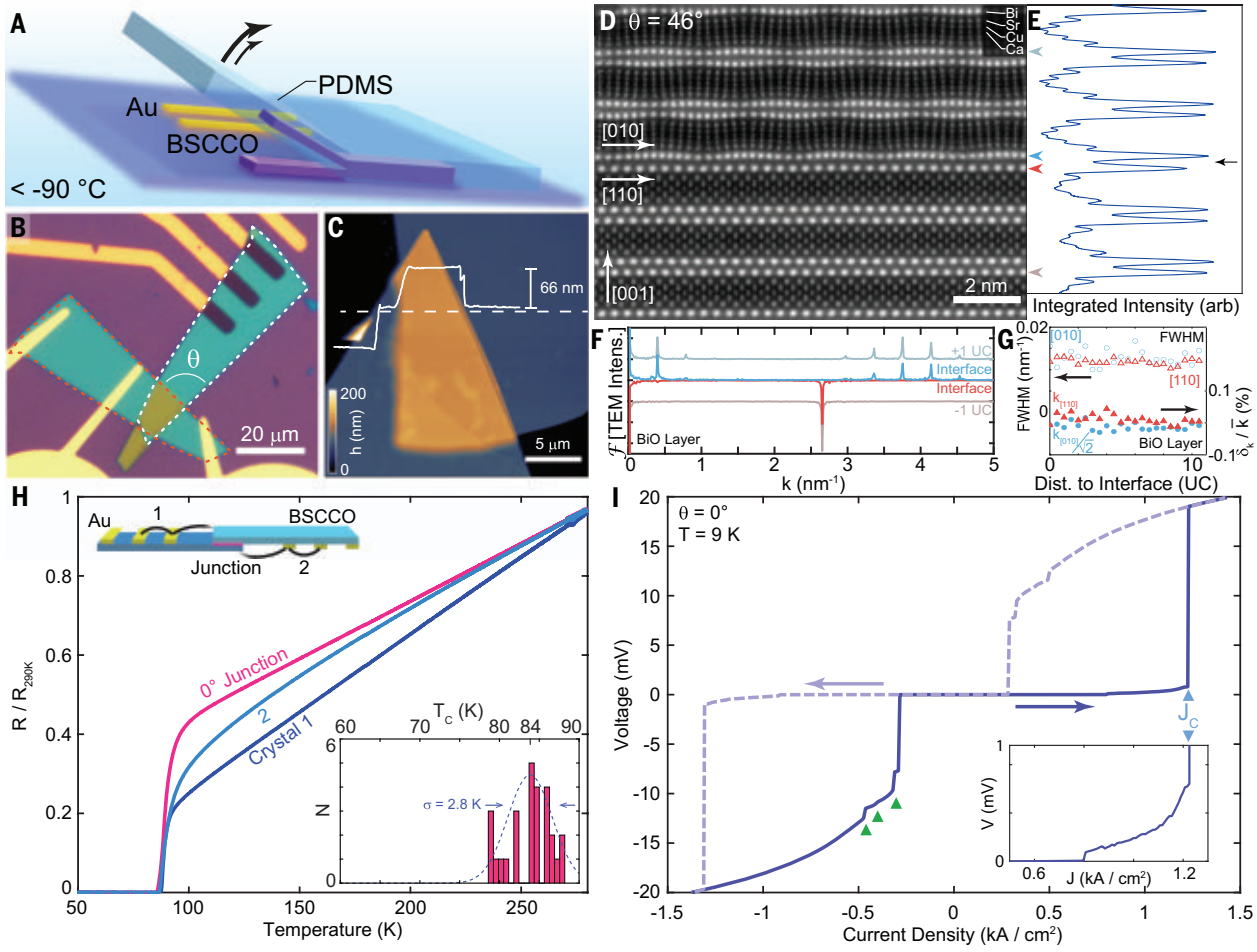

Fig. 1. Twist Josephson junctions with intrinsic junction quality. (**A**) Schematic of key fabrication step: a single BSCCO crystal is cleaved using polydimethylsiloxane (PDMS) below −90°C. (**B**) Optical micrograph of a BSCCO twist junction. Dashes outline identical copies of the same crystal. Corresponding schematic in upper inset of (H). (**C**) Atomic force microscope topography showing atomically flat interface. Line trace shows topography along dotted line. (**D**) Cross-sectional annular dark field scanning TEM image of θ = 46° junction, showing bulk-like crystalline order at the interface. Bright spots are columns of atoms identified in the upper right corner. (**E**) Integrated intensity of each layer. arb, arbitrary units. (**F**) Fourier transform of TEM line cuts at BiO layers highlighted in (E), showing atomically sharp structural transition at the interface. (**G**) BiO layer lattice periodicity variation, $\delta_k/\bar{k}$, and peak full width at half maximum (FWHM) from (F), whose fluctuations are within 0.05%, with peak FWHM at fast Fourier transform resolution (0.014 nm^{-1}). (**H**) In-plane resistance in each bulk crystal versus resistance through the artificial junction between them, showing nearly identical junction T_C. Lower inset shows T_C distribution among all 26 JJs in the angle-dependence analysis. (**I**) *I-V* curve for a θ = 0° junction in both sweep directions (arrows). Blue triangle highlights J_C comparable to IJJs. Green triangles highlight inelastic scattering features seen at the same voltages in IJJs (*16*). Inset shows low-voltage region of IVC.

the resistive quasiparticle branch of the IVC undergoes a series of jumps (green arrows) before retrapping into the superconducting state. Similar jumps were seen in IJJs [see section S5 of (*34*)] (*16*). Under positive bias current, V first becomes nonzero at I_{C1} (Fig. 1I, inset) before jumping about 20 mV to the resistive state at the critical current I_C, marked by the blue triangle. The small voltage rise at I_{C1} was previously seen in some IJJs (*16*, *36*, *37*) and was attributed to self-field effects (*16*, *38*), whereas the V jump at I_C is comparable in magnitude to the corresponding jump in IJJs (*16*, *39*, *40*). Upon reversing the bias current polarity (dashed line), the JJ's *I-V* behavior is mirrored along $I = 0$. Normalizing to junction area, we obtain a critical current density $J_C \approx 1.2$ kA/cm^2 for this junction, similar to the J_C of intrinsic junctions (*41*). Together, these observations indicate that our θ = 0° JJ reaches electronic quality comparable to IJJs of single-crystal BSCCO.

Twist angle and temperature–dependent transport

To compare transport characteristics of different twisted JJs, we normalized the bias current I with the junction normal resistance R_N [see section S4 of (*34*) for experimental definition]. Because I_C and R_N^{-1} are both proportional to the area of the junction, the product I_CR_N is independent of junction area. Figure 2A shows the normalized dynamic resistance $[dV/dI]/R_N$ as a function of T and IR_N at θ = 0°, 31°, and 44.9° (similar data for 26 JJs studied are shown in fig. S11). Several features are apparent in these datasets. First, as the current sweeps from left to right, on the retrapping side ($IR_N < 0$), constant-voltage inelastic tunneling features appear in arcs of constant V. Next, on the switching side ($IR_N > 0$), both V and dV/dI jump at critical current I_C, which depends on T. The detailed behavior of $I_C(T)R_N$ depends on θ, as we detail below. Finally, we find the hysteresis of JJs to be reduced in the high-temperature regime as $I_C(T)R_N$ decreases.

The analysis of I_CR_N for 26 devices with θ between 0° and 180° indicates that the magnitude of I_CR_N becomes smaller closer to 45° and 135°, where the JJs also appear less hysteretic. In Fig. 2B, we plot I_CR_N at two representative temperatures, 12 and 30 K, as a

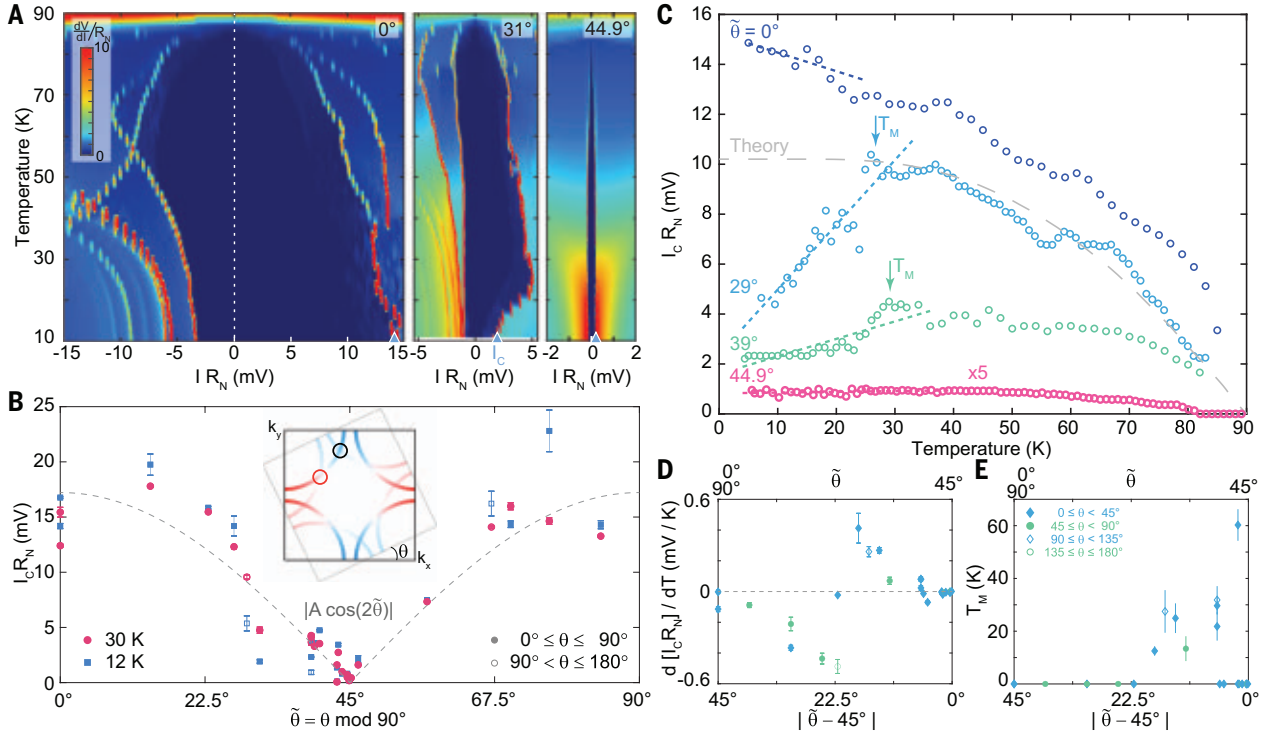

Fig. 2. d-wave SOP symmetry revealed by supercurrent tunneling. (**A**) Normalized differential resistance $[dV/dI]/R_N$ versus characteristic voltage IR_N and temperature T. Current is swept to the right. Blue arrows highlight I_CR_N. (**B**) Angular dependence of I_CR_N at 30 and 12 K. The points follow the $|\cos(2\tilde{\theta})|$ curve predicted for nearly incoherent tunneling between d-wave superconductors (*15*). (Inset) Schematic diagram of the Fermi surface of both crystals, with sign and magnitude of superconducting gap $\Delta(\vec{k})$ superposed in color. At $\theta > 10°$, Fermi surfaces intersect at two points per quadrant (circles) with different relative signs of SOPs. (**C**) Temperature dependence of the critical current for select devices. Dashed lines are linear fits to the low-temperature data. T_M is the temperature where I_C is maximal. Gray theory line shows expected $I_CR_N(T)$ behavior [see section S8 of (*34*)]. (**D**) The slope of the low-temperature linear fit, $d(I_CR_N)/dT$. (**E**) T_M as a function of angle $\tilde{\theta}$.

function of a new variable $\tilde{\theta} = \theta \bmod \pi/2$. We observe that $I_CR_N(\tilde{\theta})$ follows $|\cos(2\tilde{\theta})|$, which is expected for nearly incoherent Cooper pair tunneling between d-wave superconductors (*15*). Similar angular dependence is seen in junction critical current density and junction voltage just above the critical current $V(I_C)$ (see fig. S8). In conventional tunneling JJs, $eV(I_C) \approx 2\Delta$ (*42*). In BSCCO IJJs, $eV(I_C)$ usually reaches about half the spectroscopic gap value (*16*).

The temperature dependence of Josephson coupling in our twisted junctions provides further insight into the pairing symmetry of the Cooper pairs in BSCCO. Figure 2C shows $I_C(T)R_N$ for several representative JJs with different $\tilde{\theta}$. For $\tilde{\theta} \sim 0$, we find that $I_C(T)R_N$ monotonically decreases as T increases, approximately following the theory curve for nearly incoherent tunneling between d-wave superconductors [dashed line; see section S8 of (*34*)]. As $\tilde{\theta}$ increases, however, a surprising nonmonotonic behavior of $I_C(T)R_N$ appears. For example, for $\tilde{\theta}$ = 29° and 39° in Fig. 2C, $I_C(T)R_N$ increases alongside T, reaching a maximum value at $T = T_M$, and then decreases as T approaches T_C. More quantitative analysis can be found in Fig. 2, D and E, where we plot the low-temperature slope $d(I_CR_N)/dT$ (dashed lines in Fig. 2C and fig. S12) and observed T_M, respectively. These plots show a nonmonotonic behavior of $I_CR_N(T)$, signaled by the positive slope of $I_CR_N(T)$ at low temperatures with finite T_M, appearing within $|\tilde{\theta} - \pi/4| < \pi/8$.

The strong $\tilde{\theta}$ dependence of the nonmonotonic $I_C(T)R_N$ in Fig. 2, D and E, points to SOP d-wave symmetry as its origin. For this explanation, we consider a gap function $\Delta_{1,2}(\mathbf{k})$ superimposed on top of the Fermi surface $E_F^{1,2}(\mathbf{k})$ (*43*), where $\mathbf{k}$ is the in-plane Cooper pair wave vector in the first Brillouin zone and the index 1 or 2 denotes the top and bottom layer of BSCCO, respectively. In the twisted JJ, $E_F^1(\mathbf{k})$ and $E_F^2(\mathbf{k})$ are rotated relative to each other by angle θ (Fig. 2B, inset). At $\theta \approx 0$, $E_F^1(\mathbf{k})$ and $E_F^2(\mathbf{k})$ overlap almost completely and $\Delta_1(\mathbf{k})\Delta_2(\mathbf{k})$ is >0, yielding a uniformly positive contribution to critical current for coherent tunneling (*15*). As θ increases to ~10°, the Fermi surfaces overlap at two points per quadrant in $\mathbf{k}$-space, but with opposite phase difference between layers, yielding nodal and antinodal contribution where $\Delta_1(\mathbf{k})\Delta_2(\mathbf{k})$ alternates in sign. Because the supercurrents from these two components carry the opposite sign, their contributions to the total critical current compete. As the gap in the nodal region is much smaller than the antinodal one, nonmonotonic temperature-dependent $I_C(T)$ is expected for $\tilde{\theta} \approx \pi/8$, where the competition is strongest [see section S8 of (*34*) and (*44*) for more quantitative discussion]. We also note that near $\tilde{\theta} \approx \pi/4$, the JJ coupling is strongly suppressed but remains nonzero. For the θ = (44.9±.1)° junction, Josephson critical current can be measured up to 79 K, with I_CR_N about two orders of magnitude smaller than the 0° value.

Second-order Josephson coupling near θ = 45°

The origin of the finite supercurrent near 45° is encoded in the Josephson current-phase relation (CPR) $j(\varphi) = j_1\sin(\varphi) + j_2\sin(2\varphi)$, where j and φ are the Josephson current density and phase, respectively (*10*, *12*, *24*). At $\tilde{\theta} = 45°$, the maximally mismatched SOP phase eliminates the conventional direct Cooper pair tunneling term j_1. The supercurrent must then flow through second-order mechanisms, which are predicted to support an interfacial superconductivity with doubly degenerate Josephson energy owing to the inherent $d_{x^2-y^2}$ symmetry of the SOP within each flake (*10*–*12*). The CPR corresponding to this unusual SOP leaves an experimental signature in the in-plane magnetic interference ("Fraunhofer") pattern and microwave-induced Shapiro steps in the IVC, which are both sensitive to the presence of two

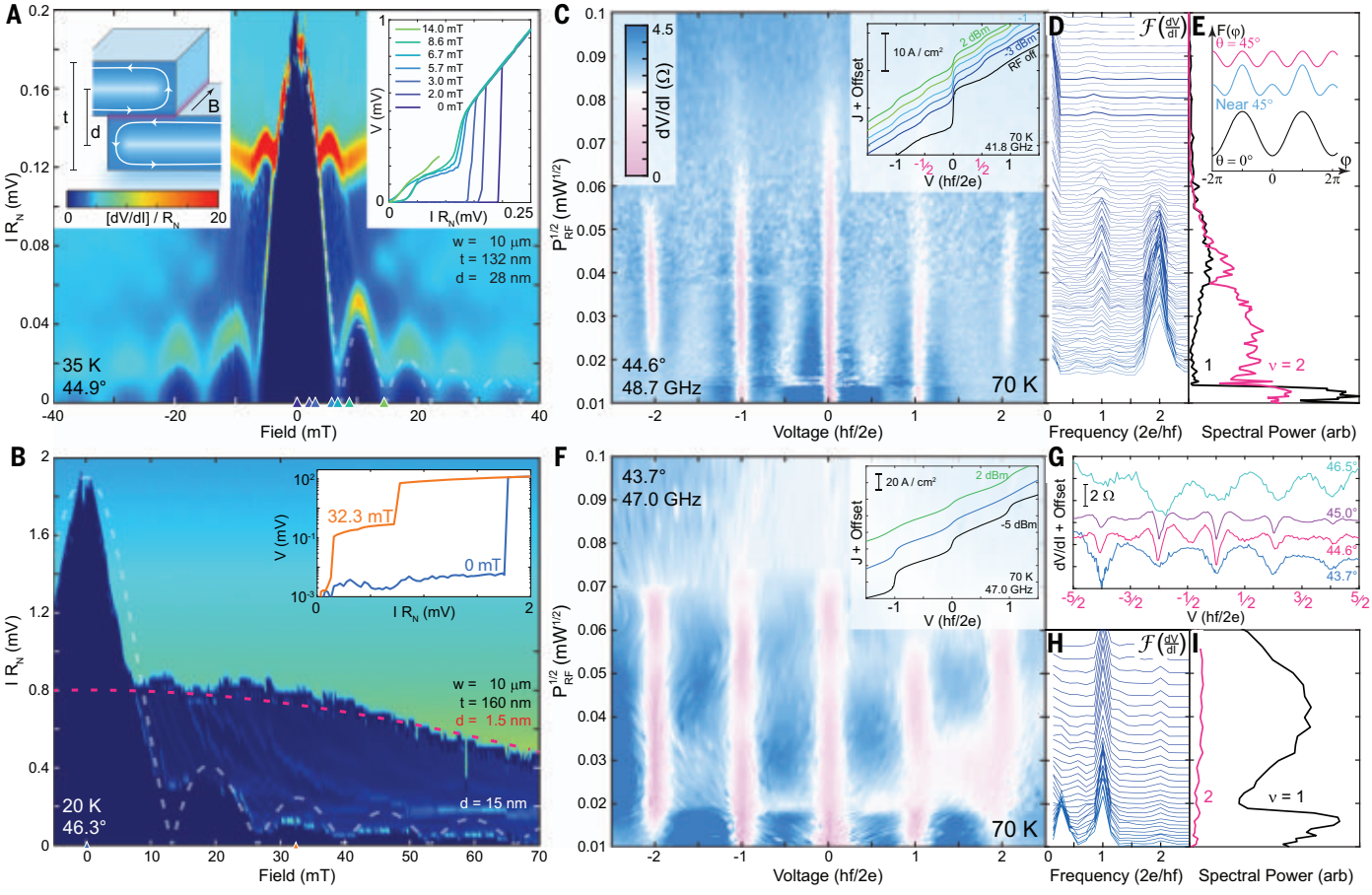

Fig. 3. Half-integer Shapiro steps and magnetic interference patterns emerge close to θ = 45°. (**A**) Response to in-plane magnetic field $B_{||}$ at θ = 44.9°. One well-developed Fraunhofer pattern corresponding to d = 28 nm (14 nm for a second-harmonic CPR) appears, as indicated by the gray dashed line. (Left inset) Junction schematic. The Meissner currents (white lines) in the flakes affect the phase difference at the twist junction, enhancing its effective thickness d for the magnetic flux (*42*) [see section S13 of (*34*)]. (Right inset) IVCs at fields highlighted with arrows in the main panel. (**B**) θ = 46.3° JJ. Two Fraunhofer patterns with different magnetic field periodicity appear (dashed lines), with an estimated d = 15 nm (gray) and d =1.5 nm (red). (Inset) *I-V* characteristics at two different $B_{||}$ values, showing two jumps in *V*. (**C**) θ = 44.6° JJ. dV/dI as a function of voltage across the junction and microwave illumination power $P_{RF}^{1/2}$ at 70 K. dV/dI dips (white, pink) correspond to Shapiro steps. (Inset) *I-V* characteristic with half-integer Shapiro steps. (**D**) Fourier transform of $dV/dI(V)$ and (**E**) the spectral power at ν_f = 1 and $2{\cdot}2e/hf$ for the θ = 44.6° JJ. (Inset) Schematic of the junction free energy F versus Josephson phase φ as twist angle changes. At 45°, the second harmonic dominates the current-phase relation. (**F**, **H**, and **I**) As in (C) to (E), but for the 43.7° device, where only integer Shapiro steps appear. (**G**) Representative dV/dI for all four devices with Shapiro step measurements at different twist angles. Half-integer Shapiro steps are only observed in junctions closest to 45°.

degenerate local minima in Josephson energy that are connected by TRS (*10*, *11*, *24*).

Figure 3, A and B, shows Fraunhofer interference patterns (FIPs) obtained at two different angles by applying parallel magnetic field $B_{||}$. Figure 3A shows θ = 44.9° JJ with $I_C(B_{||})$ oscillation with a period about 20 times shorter than that expected for intrinsic junctions. At a nearby angle θ = 46.3° (Fig. 3B), the short-period oscillations appear to coexist with a long-period oscillation characteristic of IJJs (*41*). A reduction in the FIP period implies an increase in d, the thickness of the interfacial region where magnetic field penetrates owing to field-induced currents extending into the crystal bulk (*42*). The ratio d/t, where t is the total junction thickness, depends only on the properties of the crystal and junction geometry and should not depend strongly on the twist angle [see section S13 of (*34*)]. Notably, for the devices in Fig. 3, A and B, which share similar geometry, we obtain $d/t \approx 0.1$ for both devices only if we assume that the 44.9° junction is coupled purely through the second-order process with a doubled FIP period.

The presence of higher-order harmonics in the CPR near 45° is further revealed by measuring Shapiro steps in *I-V* under microwave illumination of frequency f (Fig. 3, C and F, inset) (*11*, *24*). In conventional JJs, where the CPR is dominated by the first harmonic of φ, Shapiro steps appear as plateaus of constant voltage whenever V approaches $n{\cdot}hf/2e$, where n is an integer. We observe these conventional integer Shapiro steps in the JJs substantially away from $\tilde{\theta} = \pi/4$, as shown in the θ = 43.7° device (Fig. 3F). Consistent with the FIP discussed above, the experimentally observed Shapiro steps also show signatures of the second-harmonic CPR as $\tilde{\theta}$ approaches π/4 (Fig. 3C): specifically, when our devices are within (45±1)°, additional steps at half-integer n appear. As shown in Fig. 3C, microwave illumination causes a series of dV/dI dips corresponding to steps in *I-V* at both integer and half-integer n to emerge from the symmetric *I-V* curve of an overdamped JJ.

The Fourier components of $dV/dI(V)$ show the relative strengths of integer and half-integer Shapiro steps. For the conventional Shapiro steps appearing in the 43.7° device, the Fourier transform shows dominant spectral power for the first harmonic $\nu_1 = 2e/hf$ (Fig. 3, H and I). In contrast, for the devices exhibiting half-integer Shapiro steps (e.g., the 44.6° device at low microwave power), the Fourier transform is dominated by the second harmonic $\nu_2 = 4e/hf$.

The corresponding dV/dI shows dips of similar strength at half-integer and integer steps, indicating that second-order processes dominate over the conventional Josephson coupling close to 45°.

Similar second-harmonic Josephson effects have been observed in parallel-connected arrays of 0- and π-JJs, where multiple degenerate ground states can form (*45*–*48*). Electronically, Josephson currents across distributions of facets in such junctions create disordered magnetic interference patterns, often with prominent peaks symmetrically centered about zero magnetic field (*49*–*52*). This is at odds with our Fraunhofer-like $J_C(B_\parallel)$ measurements. Moreover, our TEM analysis [see section S2 of (*34*)] quantitatively bounds our interfacial twist angle disorder to 0.2°, which excludes the scenario of angle inhomogeneity–induced TRS breaking in this device (*53*).

Current-trainable Josephson diode effect

The sign of j_2 in CPR plays an important role in the quantum properties of twist Josephson junctions when it exceeds j_1 in magnitude. When j_2 is negative, the JJ ground state splits into a pair of degenerate states with complex phase angle $\varphi = \pm\varphi_0$ lying between 0 and π (*12*, *24*) (Fig. 3E, inset). When θ is tuned slightly away from 45°, both CPR harmonics coexist, creating asymmetric potential barrier heights around each of the degenerate energetic minima. We observe such TRS breaking through an asymmetric critical current, when the Josephson phase particle begins to roll down the resistively and capacitively shunted Josephson (RCSJ) washboard potential at different tilt angles, corresponding to different bias currents, in each direction (Fig. 4A, schematic) (*54*).

We find that twist JJs slightly away from θ = 45° exhibit nonreciprocal Josephson critical current, which can be controlled by the current sweep sequence. In this scheme, one can controllably prepare the TRS broken initial $\pm\varphi_0$ states by the "training current sequence," as shown in Fig. 4A. We use both positive and negative direction (+/−) and full and half sweep (F/H) to control the location of the phase particle during the retrapping process with high probability (*24*), where the switching critical current density $J_{C\pm}^{F/H}$ is defined from supercurrent to normal current transition. We note that $J_{C+}^{F/H} \approx -J_{C-}^{F/H}$, reflecting the symmetry between $\pm\varphi_0$ states due to TRS in the absence of magnetic field.

Controlled placement of Josephson phase particles in a specific $\pm\varphi_0$ valley (broken TRS) and the directionally asymmetric barrier associated with each valley (broken spatial inversion symmetry) are the critical ingredients for a Josephson diode (*55*–*64*), as shown in Fig. 4, B and C. Here, by biasing the "training" current into the voltage state in the forward (reverse) direction with the amplitude between $\left|J_{C\pm}^{F/H}\right|$, and then back to zero, the running JJ phase particle is retrapped into the $-\varphi_0$ (or $+\varphi_0$) valleys, respectively. A subsequent test sweep measures a critical current whenever the RCSJ washboard potential is tilted sufficiently to overcome the potential barrier, giving rise to asymmetric critical current densities $\left|J_{C+}^{F}\right|$ and $\left|J_{C-}^{H}\right|$. Note that we can flip the polarity of this Josephson

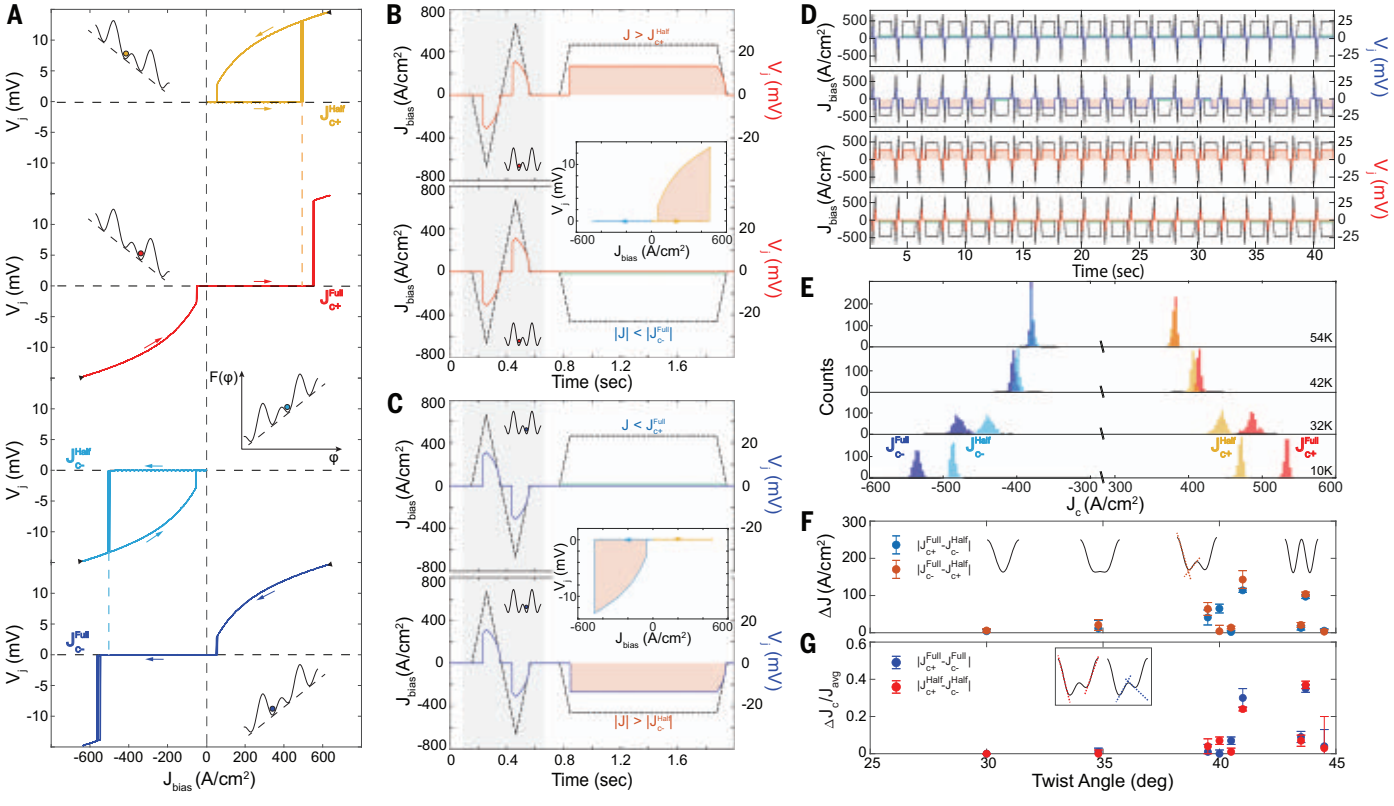

Fig. 4. Time-reversal symmetry breaking Josephson diode effects. (**A**) Junction *I*-*V* characteristics obtained from a JJ with θ = 39.5° at 12 K, revealing four distinct J_C accessible via different current sweep directions and histories. Schematics show RCSJ phase particle on the washboard potential just before reaching J_C. (**B** and **C**) Junction current bias (dashes) and voltage response (lines) across training (gray shading) and test pulses. For each subpanel, identical training pulses place the RCSJ phase particle in the same state (schematics). Insets show IVC of each test pulse. (**D**) Junction response to consecutive training and test pulses, showing controllable behavior. (**E**) Temperature-dependent switching current distributions of the four different critical currents. (**F**) Difference between mean full and half sweep $\Delta J = \left|J_{C\pm}^{F/H} - J_{C\mp}^{H/F}\right|$ versus twist angle θ, and the standard deviation measured at 30 K. Schematics show the shape of the potential with respect to twist angle, with the phase particle in the same well before switching. (**G**) Difference between positive and negative $\Delta J_c = \left|J_{C+}^{F/H} - J_{C-}^{F/H}\right|$, normalized by average $J_{avg} = \left(J_{C+}^{F/H} + J_{C-}^{F/H}\right)/2$ measured at 30 K. Schematic shows corresponding potential shape near 45°, where the phase particle is in different wells before switching.

diode by flipping polarity of the training current (Fig. 4C). In this way, we repeatedly and controllably prepare the JJ into either ground state (Fig. 4D). At higher temperatures, the phase dynamics become damped, which hinders the processes depicted in Fig. 4A by trapping φ in the local minima of the washboard potential. As a result, the $J_C^{F/H}$ asymmetry becomes less prominent upon heating and vanishes at about 50 K (Fig. 4E).

In this study, we investigated the Josephson diode effect in several JJs with different twist angles. For each JJ, the critical current difference $\Delta J = J_{C\pm}^{F/H} - J_{C\mp}^{H/F}$ reflects the asymmetry in potential barriers for each $\pm\varphi_0$ valley (Fig. 4F), whereas the difference $\Delta J_c = J_{C+}^{F/H} - J_{C-}^{F/H}$ reflects asymmetries between the two free energy minima (Fig. 4G). In both cases, the differences are strongest near 43° and weaken at both 45° and ~35°, where j_1 and j_2 terms become negligible, respectively. Away from 45°, the absence of the diode effect is caused by the restoration of time-reversal symmetry. At exactly 45°, on the other hand, the purely second-harmonic Josephson potential has an additional symmetry around $\pm\varphi_0$: $\pm\varphi_0 \pm \varphi \leftrightarrow \pm\varphi_0 \mp \varphi$, which forbids the diode effect. Therefore, the diode effect is expected to vanish at 45° and at sufficiently low twist angles, which is consistent with our results. Thus, the observed diode effect is closely related to the free energy landscape of coexisting first- and second-harmonic CPR terms. The asymmetry between the two ground state valleys as observed in Fig. 4G can arise from an additional $\cos\varphi$ term in the CPR [see section S14 of (*34*) for details]. Our demonstration of the polarity-tunable Josephson diode effect in near-45° twist BSCCO JJs thus provides strong experimental evidence for TRS broken superconductivity based on the emergent interfacial SOP.

REFERENCES AND NOTES

1. R. Ribeiro-Palau *et al*., *Science* **361**, 690–693 (2018).
2. H. Yoo *et al*., *Nat. Mater.* **18**, 448–453 (2019).
3. S. Carr, S. Fang, E. Kaxiras, *Nat. Rev. Mater.* **5**, 748–763 (2020).
4. D. M. Kennes *et al*., *Nat. Phys.* **17**, 155–163 (2021).
5. Y. Cao *et al*., *Nature* **556**, 43–50 (2018).
6. X. Lu *et al*., *Nature* **574**, 653–657 (2019).
7. Y. Saito *et al*., *Nat. Phys.* **17**, 478–481 (2021).
8. Y. Zhou *et al*., *Nature* **595**, 48–52 (2021).
9. Y. Cao *et al*., *Nature* **556**, 80–84 (2018).
10. M. Sigrist, *Prog. Theor. Phys.* **99**, 899–929 (1998).
11. Z. Yang, S. Qin, Q. Zhang, C. Fang, J. Hu, *Phys. Rev. B* **98**, 104515 (2018).
12. O. Can *et al*., *Nat. Phys.* **17**, 519–524 (2021).
13. P. Volkov, J. Wilson, K. Lucht, J. Pixley, *Phys. Rev. B* **107**, 174506 (2023).
14. P. A. Volkov, J. H. Wilson, K. P. Lucht, J. H. Pixley, *Phys. Rev. Lett.* **130**, 186001 (2023).
15. R. A. Klemm, *Philos. Mag.* **85**, 801–853 (2005).
16. K. Schlenga *et al*., *Phys. Rev. B* **57**, 14518–14536 (1998).
17. S. Y. F. Zhao *et al*., *Phys. Rev. Lett.* **122**, 247001 (2019).
18. M. Liao *et al*., *Nano Lett.* **18**, 5660–5665 (2018).
19. Y. Yu *et al*., *Nature* **575**, 156–163 (2019).
20. H. Hilgenkamp, J. Mannhart, *Rev. Mod. Phys.* **74**, 485–549 (2002).
21. C. C. Tsuei, J. R. Kirtley, *Rev. Mod. Phys.* **72**, 969–1016 (2000).
22. F. Lombardi *et al*., *Phys. Rev. Lett.* **89**, 207001 (2002).
23. E. Il'ichev *et al*., *Phys. Rev. Lett.* **81**, 894–897 (1998).
24. E. Goldobin, D. Koelle, R. Kleiner, A. Buzdin, *Phys. Rev. B* **76**, 224523 (2007).
25. L. J. Sandilands *et al*., *Phys. Rev. B* **90**, 081402 (2014).
26. M. Fratini *et al*., *Nature* **466**, 841–844 (2010).
27. Q. Li *et al*., *Phys. Rev. Lett.* **83**, 4160–4163 (1999).
28. Y. I. Latyshev, A. P. Orlov, A. M. Nikitina, P. Monceau, R. A. Klemm, *Phys. Rev. B* **70**, 094517 (2004).
29. Y. Zhu *et al*., *Phys. Rev. X* **11**, 031011 (2021).
30. Y. Takano *et al*., *Phys. Rev. B* **65**, 140513 (2002).
31. J. Lee *et al*., *Nano Lett.* **21**, 10469–10477 (2021).
32. Y. Zhu *et al*., *Phys. Rev. B* **57**, 8601–8608 (1998).
33. Y. Takano *et al*., *Physica C* **408-410**, 296–299 (2004).
34. See supplementary materials for methods and detailed analysis.
35. N. Poccia *et al*., *Phys. Rev. Mater.* **4**, 114007 (2020).
36. N. B. Othman, G.-i. Oya, M. Kitamura, A. Irie, *IEEE Trans. Appl. Supercond.* **21**, 176–179 (2011).
37. K. Hirata, S. Ooi, T. Mochiku, *Physica C* **362**, 114–120 (2001).
38. G. Hechtfischer *et al*., *Phys. Rev. B* **55**, 14638–14644 (1997).
39. A. Yurgens, *Supercond. Sci. Technol.* **13**, R85–R100 (2000).
40. K. Tanabe, Y. Hidaka, S. Karimoto, M. Suzuki, *Phys. Rev. B* **53**, 9348–9352 (1996).
41. A. Irie *et al*., *Phys. Rev. B* **62**, 6681–6686 (2000).
42. A. Barone, G. Paterno, *Physics and Applications of the Josephson Effect* (Wiley, 1982).
43. M. Hashimoto, I. M. Vishik, R.-H. He, T. P. Devereaux, Z.-X. Shen, *Nat. Phys.* **10**, 483–495 (2014).
44. T. Tummuru, S. Plugge, M. Franz, *Phys. Rev. B* **105**, 064501 (2022).
45. H. Sickinger *et al*., *Phys. Rev. Lett.* **109**, 107002 (2012).
46. A. Zyuzin, B. Spivak, *Phys. Rev. B* **61**, 5902–5904 (2000).
47. A. Buzdin, A. Koshelev, *Phys. Rev. B* **67**, 220504 (2003).
48. N. G. Pugach, E. Goldobin, R. Kleiner, D. Koelle, *Phys. Rev. B* **81**, 104513 (2010).
49. S. Scharinger *et al*., *Phys. Rev. B* **81**, 174535 (2010).
50. W. K. Neils, D. J. Van Harlingen, *Phys. Rev. Lett.* **88**, 047001 (2002).
51. J. Mannhart *et al*., *Phys. Rev. Lett.* **77**, 2782–2785 (1996).
52. H. Hilgenkamp, J. Mannhart, B. Mayer, *Phys. Rev. B* **53**, 14586–14593 (1996).
53. A. C. Yuan, Y. Vituri, E. Berg, B. Spivak, S. A. Kivelson, *Phys. Rev. B* **108**, L100505 (2023).
54. M. Tinkham, *Introduction to Superconductivity* (Dover Publications Inc., 1996).
55. K. Misaki, N. Nagaosa, *Phys. Rev. B* **103**, 245302 (2021).
56. H. Wu *et al*., *Nature* **604**, 653–656 (2022).
57. M. Davydova, S. Prembabu, L. Fu, *Sci. Adv.* **8**, eabo0309 (2022).
58. J. Díez-Mérida *et al*., *Nat. Commun.* **14**, 2396 (2023).
59. C. Baumgartner *et al*., *Nat. Nanotechnol.* **17**, 39–44 (2022).
60. J. F. Steiner, L. Melischek, M. Trahms, K. J. Franke, F. von Oppen, *Phys. Rev. Lett.* **130**, 177002 (2023).
61. Y. Zhang, Y. Gu, P. Li, J. Hu, K. Jiang, *Phys. Rev. X* **12**, 041013 (2022).
62. C. Baumgartner *et al*., *J. Phys. Condens. Matter* **34**, 154005 (2022).
63. R. S. Souto, M. Leijnse, C. Schrade, *Phys. Rev. Lett.* **129**, 267702 (2022).
64. B. Pal *et al*., *Nat. Phys.* **18**, 1228–1233 (2022).
65. X. Cui *et al*., Replication Data for: Time-Reversal Symmetry Breaking Superconductivity between Twisted Cuprate Superconductors, version 1, Harvard Dataverse (2023); https://doi.org/10.7910/DVN/BYQDSP.

ACKNOWLEDGMENTS

The authors are grateful for sample shipping coordination with J. Y. Park and for fruitful discussions with D. K. Bediako, K. S. Burch, S. Chakram, G.-H. Lee, R. Mélin, J. Wilson, B. Spivak, and S. Kivelson. **Funding:** The experiments were supported by the NSF (DMR-1809188 and DMR-1922172). P.K. acknowledges support from the US Department of Defense (DOD) Vannevar Bush Faculty Fellowship N00014-18-1-2877. Work at the University of British Columbia was supported by NSERC and CFREF. Stencil masks were fabricated at Harvard CNS, a part of the National Nanotechnology Coordinated Infrastructure (NSF 1541959). STEM imaging was performed at Harvard CNS Imaging and Analysis Facility (NSF ECCS-2025158) and at Seoul National University. N.P. acknowledges the Deutsche Forschungsgemeinschaft (DFG-452128813) for partial support of the project. P.A.V. is supported by a Rutgers Center for Materials Theory Postdoctoral Fellowship, and J.H.P. is partially supported by the Air Force Office of Scientific Research under grant FA9550-20-1-0136, NSF CAREER grant DMR-1941569, and the Alfred P. Sloan Foundation through a Sloan Research Fellowship. P.A.V. and J.H.P. acknowledge the Aspen Center for Physics, where part of this work was performed, which is supported by National Science Foundation grant PHY-1607611. This work was partially supported by a grant from the Simons Foundation (P.A.V.). The work at Brookhaven National Laboratory was supported by the US Department of Energy, Office of Basic Energy Sciences, under contract DOE-sc0012704. **Author contributions:** S.Y.F.Z., N.P., and P.K. conceived of and designed the experiment. S.Y.F.Z. and N.P. developed the air-sensitive cryogenic stacking technique. S.Y.F.Z., X.C., and N.P. performed the experiments. S.L., M.K., H.Y., A.J.A., J.A.G., and R.E. performed the focused ion beam lamella sample preparation and TEM and STEM imaging. R.Z. and G.G. provided the crystals. P.A.V. and J.H.P. performed theoretical analysis of the Fraunhofer patterns and contributed to the analysis of the critical current. M.F., S.P., and T.T. performed theoretical analysis of the critical current. S.Y.F.Z., N.P., X.C., and P.K. analyzed the data and wrote the manuscript, with contributions from P.A.V., J.H.P., M.F., and Y.R. **Competing interests:** The authors declare that they have no competing interests. **Data and materials availability:** The data from this study are available at the Harvard Dataverse (*65*).

License information: Copyright © 2023 the authors, some rights reserved; exclusive licensee American Association for the Advancement of Science. No claim to original US government works. https://www.science.org/about/science-licenses-journal-article-reuse

SUPPLEMENTARY MATERIALS

science.org/doi/10.1126/science.abl8371
Materials and Methods
Supplementary Text
Figs. S1 to S24
Table S1
References (*66*–*99*)

Submitted 8 August 2021; resubmitted 7 February 2023
Accepted 7 November 2023
Published online 7 December 2023
10.1126/science.abl8371

ScienceCareers.org
ScienceCareers

What's Your Next Career Move?

From networking to mentoring to evaluating your skills, find answers to your career questions on *Science* Careers

To view the complete collection, visit
ScienceCareers.org/booklets

ScienceCareers
FROM THE JOURNAL SCIENCE AAAS

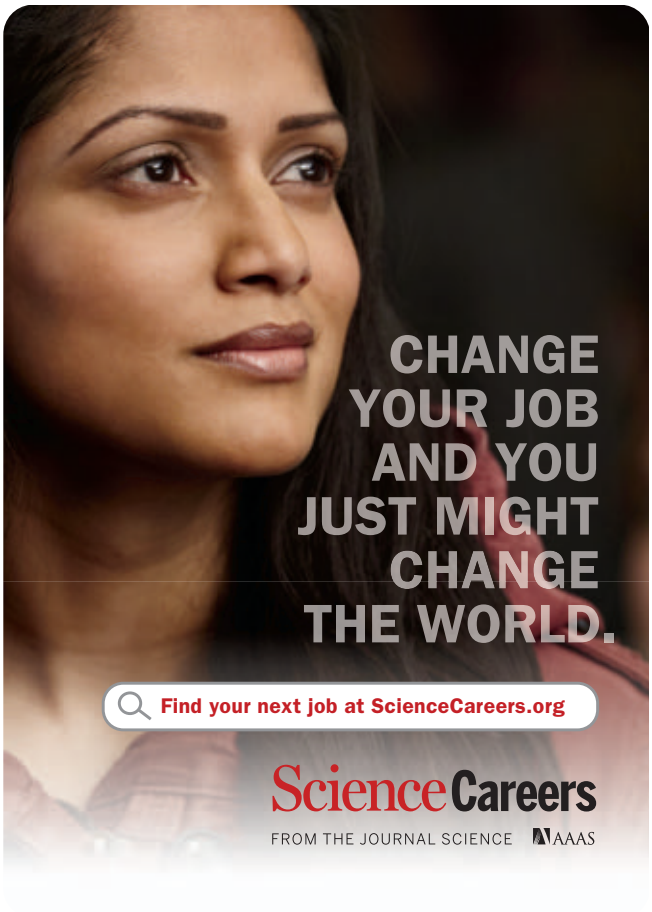

深圳理工大学

USIAT Welcome Worldwide Talent

The University of SIAT seeks highly qualified candidates for faculty positions in the Tenure-track at the Assistant and Associated Professor ranks. Position information please see below:

1. Position: Tenure-Track Assistant Professor, and Associate Professor
2. Qualification:
   (a) Applicant must have a Ph.D. and/or M.D or equivalent degree;
   (b) Applicant must birth after January 1, 1984;
   (c) The research area is mainly in natural science, engineering technology;
   (d) Before March 15, 2024, the applicant should have obtained a formal teaching or research position in an overseas university, scientific research institution, or corporate research and development institution, and have more than 36 months of continuous work experience; for those who have obtained a doctorate overseas and have particularly outstanding performance, the limitation of work experience may be appropriately relaxed
   (e) The applicant has not yet returned to work in China (to China) on a full-time basis or returned (came) to work in China after January 1, 2023. The applicant must resign from the overseas work or have no work overseas after being notified of the grant of funding and return (come) to work in China full-time for at least 3 years.

The application deadline is 15 February 2024, please apply through the link: https://newtds.cingta.com/apply/form?id=520

The University of SIAT was established in partnership between the Chinese Academy of Sciences and the Shenzhen Municipal Government. We are a newly-created university to become the world's preeminent institute for emerging science and engineering programs. The University of SIAT is equipped with state-of-the-art teaching and research facilities and is dedicated to cultivating international, visionary, and interdisciplinary talents while delivering research support to pursue innovation-driven development. We are seeking applications for faculty positions of all ranks in the following academic programs: Computer Science and Engineering, Bioinformatics, Robotics, Life Sciences, Material Science and Engineering, Biomedical Engineering, Pharmaceutical Sciences, Synthetic Biology, Neurosciences, etc. We are seeking individuals with a strong record of scholarship who possess the ability to develop and lead high-quality teaching and research programs. We offer a comprehensive benefits package and are committed to faculty success throughout the academic career trajectory, providing support for ambitious and world-class research projects and innovative, interactive teaching methods.

Who's the top employer for 2023?

Science Careers' annual survey reveals the top companies in biotech & pharma voted on by *Science* readers.

Read the article at sciencecareers.org/topemployers

Science 2023 TOP EMPLOYER

By **Rosalind A. Coleman**

Facing fraud in my lab

On the Monday when C.B. came into my office, his worried face told me the news was bad. Three weeks earlier, two of my postdocs had appeared at my door, barely holding back tears. They were certain that another postdoc colleague had fabricated his work because they had never seen him—let's call him John—use the equipment necessary for the latest data he had presented in our lab meeting. Initially, I was certain they were mistaken. I had already presented John's data at several national conferences, and we were writing a paper I thought would have a huge impact on our field. But I could not ignore their suspicions. I phoned the university integrity officer and met with my dean. I also hired C.B., a former senior scientist in my lab, to repeat the most critical experiments. Now, the fraud was confirmed.

I was devastated. What should I do? How could I face my colleagues and the people working in my lab?

It wasn't easy on any of us. The two postdocs who had identified the fraud had spent countless hours in the lab with John and felt guilty about informing on him. They worried they might be wrong, that they might be needlessly ruining the life of someone they liked and respected. They were distraught when he sent them sorrowful emails, and finally terrified when he left angry messages on their home answering machines. We had to call the campus police and change the locks on our lab doors. John eventually announced he would be leaving with his wife, who had found a job in another state.

"I felt humiliated. ... Why had I not been more vigilant?"

In the weeks that followed the discovery, university investigators rifled through lab notebooks and sorted through freezer boxes full of samples. Machines, printouts, and computers were carted away to be forensically examined. Lab members gave recorded testimony, and I met with a faculty board of enquiry. My dean, though sympathetic, probed John's possible motivation as well as why I had failed to prevent the fraud. Although everyone strained to remain polite, it was clear they faulted me, too, for accepting John's data so readily. As a senior scientist, I felt humiliated, but I also felt I deserved the humiliation. Why had I not been more vigilant?

I was forced to confront my own complicity. I understood perfectly why I had been duped. Although I was well-known in my field, had presented keynote lectures at major conferences and mentored successful junior scientists, I longed to be known for making a true breakthrough, for discovering something amazing. Thus, after seeing John's exciting initial results, I stopped reviewing his original data. I wanted to believe the findings underpinning the novel concepts were real, and I was satisfied with the beautiful graphs he produced, which I imagined would bring us recognition as conceptual innovators.

I was profoundly disappointed in myself. I had barely escaped the shame of having to retract a published article, and the investigation and the monthslong impact on my working life were wrenching. For my lab, the aftermath was so disruptive that several people sought counseling.

I retired several years after this incident. With time to consider what had occurred, I began to wonder how frequently other lab directors are forced to confront their own errors and culpability. At the time, I felt more personally guilty than I cared to admit, and I concealed the fraud from my colleagues. I now think that was the wrong approach; others could surely have learned from the mistakes I made.

John's fraud left me feeling personally violated, as if a thief had come to my home and rifled through my drawers and closets. Scientific fraud is, indeed, a kind of theft. Apart from the wasted time and ill-spent money, it is a blow to one's reputation, and it damages a lab's credibility.

The worst of it was that my deepest beliefs had been shaken. I had depended on the idea that scientific research is a sacred trust, not only to the other individuals in one's group, but also to the research enterprise as a whole. John's betrayal was a warning lesson—one I am sorry I had to learn. ■

Rosalind A. Coleman is a professor emeritus at the University of North Carolina at Chapel Hill. Send your career story to SciCareerEditor@aaas.org.

ILLUSTRATION: ROBERT NEUBECKER

QUALITY CONTENT FOR THE GLOBAL SCIENTIFIC COMMUNITY

Multiple ways to stay informed on issues related to your research

Posters

Podcasts

Sponsored Collection Booklets

Advertorials

Webinars

Science

AAAS

Scan the code and start exploring the latest advances in science and technology innovation!

Science.org/custom-publishing

Brought to you by the *Science*/AAAS Custom Publishing Office.

YOUR RESEARCH HAS ITS REWARDS.

Submit an essay by 3/15/24 to enter to win $25K.

The prestigious international *Science* & PINS Prize is awarded annually to outstanding early-career researchers in the emerging field of neuromodulation. Findings already show improved outcomes in several neurological disorders. To enter, just write a 1000-word essay about your research performed in the last three years. The Grand Prize winner will be presented a US$25,000 award, as well as have their essay published in *Science* magazine and on *Science* Online. A runner-up will have their essay published online. For additional inquiries, email SciencePINSPrize@aaas.org.

SCIENCE-PINS PRIZE FOR NEUROMODULATION

SCIENCE-PINS

SCIENCE.ORG/PINS